coatings

Special Issue Reprint

Plasma Electrolytic Oxidation (PEO) Coatings, 2nd Edition

Edited by
Marta Mohedano and Raul Arrabal

mdpi.com/journal/coatings

MDPI

Plasma Electrolytic Oxidation (PEO) Coatings, 2nd Edition

Plasma Electrolytic Oxidation (PEO) Coatings, 2nd Edition

Editors

Marta Mohedano
Raul Arrabal

MDPI

Basel • Beijing • Wuhan • Barcelona • Belgrade • Novi Sad • Cluj • Manchester

Editors

Marta Mohedano
Universidad Complutense de Madrid
Madrid
Spain

Raul Arrabal
Universidad Complutense de Madrid
Madrid
Spain

Editorial Office
MDPI AG
Grosspeteranlage 5
4052 Basel, Switzerland

This is a reprint of articles from the Special Issue published online in the open access journal *Coatings* (ISSN 2079-6412) (available at: https://www.mdpi.com/journal/coatings/special_issues/0Q40460C62).

For citation purposes, cite each article independently as indicated on the article page online and as indicated below:

Lastname, A.A.; Lastname, B.B. Article Title. *Journal Name* **Year**, *Volume Number*, Page Range.

ISBN 978-3-7258-2031-3 (Hbk)
ISBN 978-3-7258-2032-0 (PDF)
doi.org/10.3390/books978-3-7258-2032-0

Cover image courtesy of Raul Arrabal

Contents

About the Editors

Marta Mohedano

Marta Mohedano completed her PhD in Materials Science and Technology (Extraordinary Award) from Complutense University of Madrid—UCM—(Spain) in 2011 with the support of a UCM Pre-doctoral Fellowship, including a predoctoral stay at the University of Cambridge (UK) for six months. She then continued at the UCM with a postdoctoral research contract until 2013, when she was awarded the prestigious Humboldt Research Fellowship for Postdoctoral Researchers and moved to Helmholtz Zentrum Geesthacht—HZG (Germany). After 32 months at HZG, she returned to UCM in June 2016, first as a Juan de la Cierva Incorporaci´on Fellow and then in 2017 as a Principal Investigator of the national project MAT2015-73355-JIN under the umbrella of the National Programme for Research Aimed at the Challenges of Society. In 2019, she became a Ramon y Cajal Researcher, later advancing to Associate Professor in 2024. Dr Mohedano has contributed to the field of the corrosion and protection of light alloys (up to 2024) with a total of 100 publications with ¿4500 citations and an h-index = 42 (Scopus), more than 60 communications to national/international conferences, participation in 13 research projects, 14 technology transfer contracts and 1 utility model.

has been internationally recognized with prestigious awards: in 2015, the international EFC (European Federation of Corrosion)—Kurt Schwabe Prize, in 2021, the Coatings young Investigator Awards—Journal *Coatings* (MDPI) and in 2023, the International Magnesium Award for the Youth 2023—International Magnesium Society.

She has contributed to more than 800 h of lectures at UCM and HZG (including training and supervision of more than 20 bachelor's/master's/PhD students) and has participated in scientific and organization committees (Young EFC, Local organizer Eurocorr, Advanced Chemistry Symposium), dissemination activities (Escuelab, in-school workshops) and the revision of manuscripts (*Corr. Sci*, *JES*, *Surf. Coat. Tech*, etc.).

Raul Arrabal

Raul Arrabal completed his PhD in Materials Science and Technology (Extraordinary Award) from Universidad Complutense de Madrid—UCM—(Spain) in 2006 with the support of a FPU Pre-doctoral Fellowship, including a four-month stay at the University of Manchester (UoM, UK). He then received an MEC postdoctoral grant (2006-2008) to continue his research at UoM under the supervision of G.E. Thompson. In 2008, he joined UCM as a Ramon y Cajal fellow, later advancing to Associate Professor in 2013. Dr Arrabal has been actively engaged in the field of the characterization, corrosion and protection of light metals since 2003, with a particular focus on developing coatings for Mg, Al and Ti alloys using PEO. His research interests also include alloy design, additive manufacturing, composites and biocompatible materials. As of 2024, Dr Arrabal has published 156 articles (139 JCR, 74%Q1, 35%D1, 5 reviews), authored 3 patents, contributed 4 book chapters and contributed to 168 communications to national (43, CNMAT, MATCOMP, etc.) and international conferences (105, Eurocorr, Euromat, SMT, etc.). His work has significantly advanced our understanding of corrosion mechanisms in light alloys and their surface functionalization (e.g., conversion, thermal spray, anodizing, PEO, sol-gel). His scholarly impact is evidenced by an h-index of 53 and over 10254 citations. Dr Arrabal has participated in 25 R&D projects (7 as principal investigator, PI) and 25 contracts (9 as PI), collaborating with researchers across Europe, Asia, Australia and the USA. Since 2019, he has led the Preparation and Degradation of Materials Research Group at UCM, which has been recognized as Excellent by the state research agency. Additionally, Dr Arrabal has more than 15 years of teaching experience in BSc and MSc programs in Chemistry and

Materials Engineering and has served in administrative roles, including Secretary and Deputy Head of the Department of Chemical and Materials Engineering at UCM.

coatings

MDPI

Review

Plasma Electrolytic Oxidation (PEO) as a Promising Technology for the Development of High-Performance Coatings on Cast Al-Si Alloys: A Review

Patricia Fernández-López [1,2], Sofia A. Alves [1], Jose T. San-Jose [2], Eva Gutierrez-Berasategui [1] and Raquel Bayón [1,*]

[1] TEKNIKER, Basque Research and Technology Alliance (BRTA), Plasma Coating Technologies Unit, C/Iñaki Goenaga 5, 20600 Eibar, Spain; patricia.fernandez@tekniker.es (P.F.-L.); sofia.alves@tekniker.es (S.A.A.); eva.gutierrez@tekniker.es (E.G.-B.)

[2] Department of Engineering in Mining, Metallurgy and Science of Materials, Faculty of Engineering in Bilbao, Building I, University of the Basque Country (UPV/EHU), Plaza Ingeniero Torres Quevedo 1, 48013 Bilbao, Spain

* Correspondence: raquel.bayon@tekniker.es

Abstract: Cast Al-Si alloys, recognized for their excellent mechanical properties, constitute one of the most widely employed non-ferrous substrates in several sectors, and are particularly relevant in the transport industry. Nevertheless, these alloys also display inherent limitations that significantly restrict their use in several applications. Among these limitations, their low hardness, low wear resistance, or limited anti-corrosion properties, which are often not enough when the component is subjected to more severe environments, are particularly relevant. In this context, surface modification and the development of coatings are essential for the application of cast Al-Si alloys. This review focuses on the development of coatings to overcome the complexities associated with improving the performance of cast Al-Si alloys. Against this background, plasma electrolytic oxidation (PEO), an advanced electrochemical treatment that has revolutionized the surface modification of several metallic alloys in recent years, emerges as a promising approach. Despite the growing recognition of PEO technology, the achievement of high-performance coatings on cast Al-Si is still a challenge nowadays, for which reason this review aims to provide an overview of the PEO treatment applied to these alloys. In particular, the impact of the electrolyte chemical composition on the properties of the coatings obtained on different alloys exposed to harsh environments has been analyzed and discussed. By addressing the existing gaps and challenges, this paper contributes to a better understanding of the intricacies associated with the development of robust PEO coatings on cast Al-Si alloys.

Keywords: plasma electrolytic oxidation (PEO); cast Al-Si alloys; coatings; lightweighting

Citation: Fernández-López, P.; Alves, S.A.; San-Jose, J.T.; Gutierrez-Berasategui, E.; Bayón, R. Plasma Electrolytic Oxidation (PEO) as a Promising Technology for the Development of High-Performance Coatings on Cast Al-Si Alloys: A Review. *Coatings* **2024**, *14*, 217. https://doi.org/10.3390/coatings14020217

Academic Editor: Jinyang Xu

Received: 28 December 2023
Revised: 4 February 2024
Accepted: 7 February 2024
Published: 9 February 2024

1. Introduction

Aluminum (Al) is frequently alloyed with various elements to produce a diverse range of commercial alloys. Among these, cast aluminum–silicon (Al-Si) alloys stand out, constituting over 80% of the globally produced cast Al alloys [1,2]. These alloys offer interesting advantages, including excellent castability and weldability, a high strength-to-weight ratio, optimal melt fluidity, and cost-effective manufacturing [2–4]. The alloying of cast Al-Si alloys involves elements such as Si, Cu, Mg, Zn, Ni, or Fe, among others. The specific properties of these alloys are determined by their chemical composition. Si serves as the principal alloying element of cast Al-Si alloys, typically ranging between 4% and 24% [5]. These alloys are classified as hypoeutectic (Si wt.% < 11), eutectic (Si wt.%~11), and hypereutectic (Si wt.% > 11) based on their Si content [1,6]. During the manufacturing of castings, the inclusion of Si requires longer solidification times, favoring a higher fluidity and lower shrinkage, and enhancing castability and weldability [1,3,6]. Furthermore, the

addition of Si reduces the melting point of the resulting alloy, which is beneficial for the industrial casting processes [7]. Cu and Mg are other commonly added alloying elements in cast Al-Si alloys. The addition of Cu, typically ranging from 1% to 5%, improves the hardening of the alloy in both the as-cast condition and during heat treatments [5,6]. On the other hand, Mg is usually added in lower quantities (usually 0.2%–0.6%) [5] and serves as a precipitation hardener, improving both the tensile properties at high temperatures (up to 200 °C) and enhancing creep resistance [1,6]. Other alloying elements, such as Ni or Zn, are usually incorporated to enhance the tensile strength or to improve the properties after heat treatment without compromising ductility, respectively.

In cast Al-Si alloys, Fe typically emerges as the predominant undesirable impurity [1,8], with its concentration being higher in recycled alloys, where it can elevate to approximately 1% [9]. Due to the limited solubility of Si and Fe in the Al matrix, brittle intermetallic compounds, such as $Al_{15}(FeMn)_3Si_2$ or $Al_{15}(FeMnCr)_3Si_2$, can be formed (Figure 1) [4,10], often resulting in a degradation of the mechanical properties of the alloy [9]. Nevertheless, in the manufacturing of cast Al-Si alloys using specific techniques like high-pressure die-casting (HPDC), the presence of Fe could be advantageous due to its role in preventing molten alloys from adhering to the casting matrix [8] and reducing adhesion [11]. HPDC, renowned for its cost-effectiveness and capability to manufacture components with complex geometry and thin walls, stands as the predominant method for the manufacturing of cast Al-Si components [12,13]. Nonetheless, the turbulences generated by the high-speeds applied result in both superficial and internal porosities in HPDC components, which could compromise some mechanical properties [4,14].

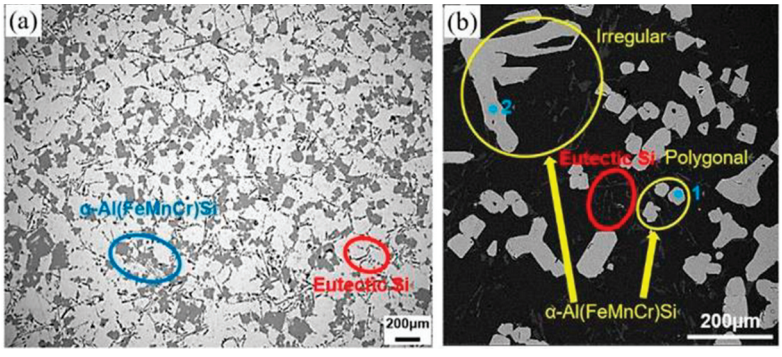

Figure 1. Optical (**a**) and SEM (**b**) micrographs of an $AlSi_7FeMn_{1.5}Cr_{0.5}$ alloy containing iron-rich intermetallic compounds [15]. Reprinted from Materials Letters; 277; Dongtao Wang, Xiaozu Zhang, Hiromi Nagaumi, Xinzhong Li, Haitao Zhang; 3D morphology and growth mechanism of cubic α-Al(FeMnCr)Si intermetallic in an Al-Si cast alloy; 128384; Copyright (2020), with permission from Elsevier.

Due to their outstanding properties, cast Al-Si alloys are extensively used in the automotive industry [4], and their application in the aerospace industry is also growing [7,16] (Figure 2). The primary advantage of the use of cast Al-Si alloys in the transport sector resides in the lightweighting achieved in comparison with other conventional materials, like steel or cast iron [17,18], offering a substantial reduction of fuel consumption, CO_2 emissions, and overall carbon footprint [19,20]. In a mid-size vehicle, one ton of Al replacing conventional materials can lead to an 18-ton reduction in GHG emissions throughout its whole life cycle [21]. Cast Al-Si alloys serve as effective substitutes for cast iron or steel in several automotive components, including those with complex geometries, like engine blocks or cylinder heads [20,22], cylinder liners [23], and pistons [1]; power train applications [18]; brake parts [24]; wheels [25]; and larger structural components [26].

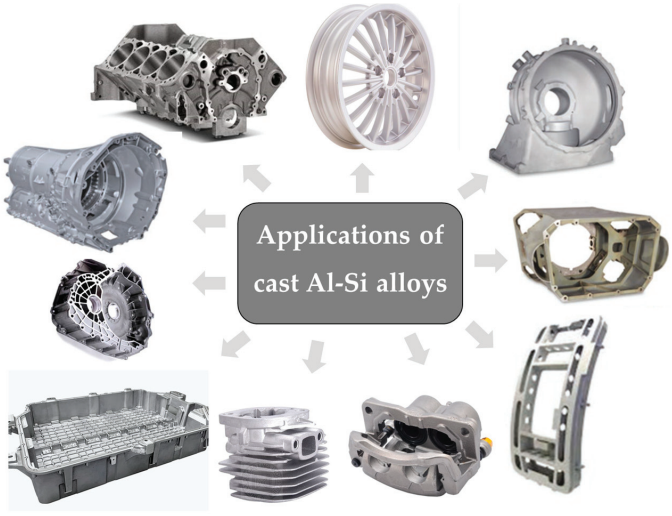

Figure 2. Schematic representation of components manufactured from cast aluminum alloys.

Despite the promising features offered by cast Al-Si alloys, their industrial implementation faces significant limitations, especially in applications that require prolonged durability under aggressive environments. Their poor tribological features, including low wear and abrasion resistances [4,16,27], low hardness, and high tendency to adhesion [28,29], constitute the primary drawbacks. Concerning corrosion resistance, although Al alloys generally provide acceptable corrosion resistance due to their natural oxide layer, this protection is often inadequate under harsh environments, particularly for cast Al-Si alloys, due to the relevant heterogeneities in their chemical composition. Furthermore, the high Si content promotes localized corrosion, rendering them unsuitable for applications with severe requirements compared to wrought Al alloys [4,16,30–32].

Surface engineering, which emerged in the 1970s, entails the modification of coating material surfaces and serves as a powerful tool, not only for the enhancement of the materials, but also to provide them with novel functionalities. Reinforcement, modification, functionalization, or embellishment are among the technological and functional demands faced by materials across several industrial sectors. Addressing these requirements, alongside considerations such as sustainability and durability, constitutes critical elements in the design and advancement of the latest generation of surface solutions to overcome the most demanding challenges imposed by strategic industrial sectors.

Anodic oxidation, commonly known as anodizing, stands as a traditional and extensively used technique for enhancing the surface properties of Al alloys, particularly for the improvement of the anti-wear and anti-corrosion capabilities. During this process, an anodic oxide film is electrochemically generated on the surface of Al under anodic polarization. This involves the anodic dissolution of the metal and the subsequent reaction between the Al cations (Al^{3+}) and the negatively charged anions from the acid solution in which the treated component has been immersed, resulting in the formation of a metal oxide film [33]. Different types of anodizing are available, such as chromic acid anodizing for high protection, sulphuric anodizing for aesthetic and protective films, and hard anodizing for thicker coatings. Despite its widespread application in recent years, the current use of anodizing is facing limitations due to stringent EU policies restricting the use of acid electrolytes. Furthermore, anodizing proves inadequate for treating the surfaces of cast Al-Si alloys, particularly those with higher Si contents. This challenge is exacerbated when dealing with recycled cast Al-Si alloys containing complex intermetallic compounds. Challenges associated with the treatment of these alloys arise from silicon phases hindering the proper development of the anodic layer [16], which results in differing conductive behavior

between the Al matrix and the dispersed Si phases, leading to variations in the growth rate of the anodic oxide coating [3]. These discrepancies in the growth rates give rise to the oxide layers of reduced thickness and hardness (up to 800 HV), increased heterogeneity [4], as well as heightened porosity and brittleness [34], rendering their application unfeasible, especially in more severe environments.

The growing demand for lightweight materials within the transport sector, especially in automotive manufacturing, has prompted the exploration and refinement of advanced technologies for the surface modification of Al alloys, particularly targeting cast Al-Si alloys. Among these techniques, plasma electrolytic oxidation (PEO) has emerged as a promising method garnering significant interest for its capability to enhance the durability and corrosion resistance of these alloys. Surface treatment of cast Al-Si alloys resultsmore complex compared to wrought Al alloys due to their complex microstructure, which presents unique challenges. The widespread usage of these alloys in the transport sector underlines the necessity for robust and effective surface engineering solutions.

This review provides a comprehensive description of the complexities associated with the PEO treatment of cast Al-Si alloys, placing its relevance in context with conventional surface modification techniques such as anodizing. A detailed examination of PEO technology delves into the coating growth mechanism and the key influencing process parameters, encompassing substrate composition, electrolyte composition, and the type of power supply used. This is succeeded by a thorough review of the pertinent literature, exploring the impact of different electrolyte formulations (silicate based, phosphate based, and aluminate based) on the development of high-performance PEO coatings for cast Al-Si substrates. Given the challenges linked with the treatment of cast Al-Si alloys, in addition to addressing considerations related to the type of electrolyte used, strategies for improving PEO coatings are addressed. This encompasses the examination of pre- and post-treatments, as well as the incorporation of nanoparticles and microparticles into the electrolyte, a promising frontier to further improve the functional attributes of PEO-treated cast Al-Si alloys. By synthesizing these insights, this review aims to offer an overview of the current state of knowledge, identify critical research gaps, and lay the basis for future advances in the search for surface modification solutions for cast Al-Si alloys in different applications within the transport sector.

2. Plasma Electrolytic Oxidation (PEO)

Plasma electrolytic oxidation (PEO), also known as microarc oxidation (MAO), represents an electrochemical plasma-assisted technology employed for the development of multifunctional ceramic coatings on diverse valve metals. PEO combines electrochemical oxidation processes with plasma discharges, thereby sintering the treated metal surface. Within the metallic substrates treated by PEO, Al [35,36], Ti [37,38], and Mg [39,40] alloys outstand, while nowadays the technology is also being extended to other metallic substrates, like Zr [41], Nb [42], Ta [43], and even steel [44–46].

The properties of the PEO coatings are strongly related to the type of alloy treated [4,47], the chemical composition of the electrolyte used [4,23,48], and the electrical parameters applied during the process [49–51]. Notable properties of PEO coatings include high wear resistance [4,23,52], strong corrosion protection [53,54], high hardness [55,56], and excellent adhesion to the metallic substrate [57]. The morphology of PEO coatings is also suitable for the adhesion of other top coats, like sol–gel layers, while it could act as a reservoir for liquid or solid lubricants, providing self-lubricating properties [58–60]. Furthermore, PEO coatings exhibit high thermal resistance [61,62], superior dielectric properties [63,64], or photo-catalytical features [38,65,66]. In the biomedical industry, PEO coatings provide desirable properties such as biocompatibility [67,68], antibacterial properties [67,69], and bioactivity [70,71].

Discharge phenomena that occurred during electrolysis were initially observed by Sluginov around the year 1880 [72]. However, the technologies related to this phenomenon and their applications gained more attention during the 20th century. Researchers such

as Snezhko et al. [73], Markov et al. [74,75], Kurze et al. [76,77], and Yerokhin et al. [78] significantly contributed to the understanding of these technologies. During this period, various terms have been employed to describe PEO technology, including micro-plasma oxidation, anode spark electrolysis, or plasma electrolytic anode treatment [79].

The PEO process constitutes an electrochemical procedure wherein the treated sample or component is immersed in an electrolytic bath [80,81], while an electric current and a potential are applied. This process requires two electrodes: the treated sample, serving as the anode and connected to the positive output of the power supply; and a cathode enveloping the treated sample [80,82], usually made of stainless steel [83–85] and connected to the negative output of the power supply [80] (Figure 3a).

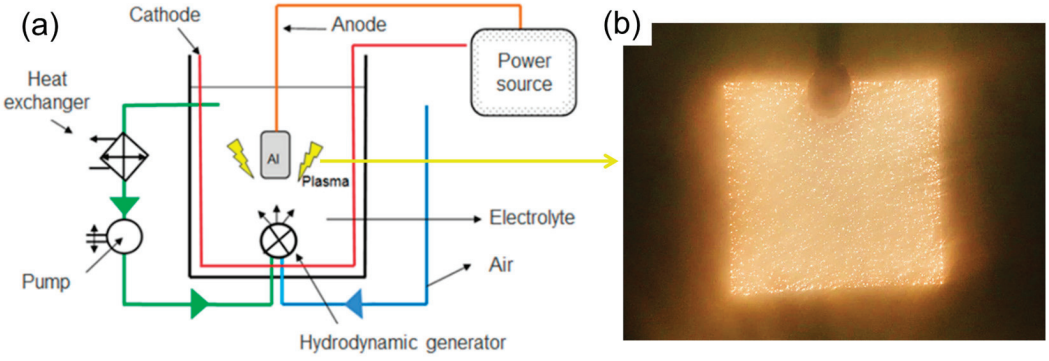

Figure 3. (**a**) Schematic representation of the PEO equipment and (**b**) plasma micro-discharges occurring during a PEO process on an Al sample carried out at Tekniker.

During a PEO process, the treated sample undergoes anodic polarization to high voltages, typically ranging from 300 V to 700 V, exceeding the dielectric breakdown voltage threshold of the pre-existing oxide layer [86–88]. During the treatment, there is also a continuous release of gas in the form of gas bubbles surrounding the anode. The establishment of a high electric field between the anode and the cathode results in the ionization of these gas bubbles, leading to the generation of plasma micro-discharges (Figure 3b) characterized by high temperatures, around 1500 °C, resulting in localized melting of the metal substrate. As a result, multiple and complex electrochemical reactions take place simultaneously, involving specific reactions with ions from the electrolyte, mainly oxygen. These plasma-chemical reactions culminate in the formation of the coating oxides, which solidify instantaneously as the overall temperature of the system remains refrigerated [89,90]. Therefore, the PEO treatment requires the development of specific electrochemical processes that include anodic oxidation of the treated metallic substrate [91–93], electrolysis of water, promoting gas evolution [57,91], and thermo-chemical reactions including the deposition of electrolyte-discharged anions [93–95].

PEO technology could be considered an evolution of anodizing for metal protection [16]. However, although both technologies work under a similar basic procedure, PEO involves higher potentials, reaching hundreds of volts [96], leading to more complex reactions and growth mechanisms [97]. Furthermore, compared with anodization, PEO technology results in thicker and denser coatings [98], which are also less detrimental to the fatigue limit of the alloy [99]. From an industrial perspective, PEO would be easier to apply than anodization, with less critical pre-treatment requirements and PEO can be carried out under atmospheric working environments, which would greatly simplify the whole manufacturing process [98,100]. Moreover, another outstanding advantage that makes PEO be viewed as a promising technology is the fact that employs water-based alkaline electrolytes without heavy metals, which are much less harmful to the environment than

the acidic solutions used in anodizing [88,101]. The main differences between anodizing, hard anodizing and PEO have been summarized in Table 1.

Table 1. Comparison of the processing conditions and properties obtained in anodizing, hard anodizing, and PEO treatments.

Parameter	Anodizing	Hard Anodizing	PEO
Pre-treatment	Critical		Not necessary
Electrolyte	Acidic (sulphuric, chromic, oxalic, etc.)		Alkaline without heavy metals
Potential applied	10–50 V	20–120 V	Higher than breakdown voltage
Current density	Low: <10 $A \cdot dm^{-2}$		Medium-high: 5–25 $A \cdot dm^{-2}$
Metallic substrate	Critical	Medium	High versatility
Adhesion to the substrate	Good	Moderate	High
Time	Moderate: 10–60 min	High: 30–120 min	Low < 10 min *
Coating growth rate	Low: <1 $\mu \cdot min^{-1}$	Medium: 1–3 $\mu \cdot min^{-1}$	High: 1–5 $\mu \cdot min^{-1}$
Microstructure	Amorphous		Amorphous and crystalline
Energy consumes	Low	Medium	Medium-high
Eco-friendly	No	No	Yes

* For the development of coatings with thicknesses typically applied by anodising. Thicker PEO coatings will require longer treatment times.

The assessment of PEO technology in relation to other conventional surface modification methods is context dependent, with each technique offering distinct advantages and drawbacks based on factors like material properties, specific requirements, and intended use cases. Regarding the surface modification of Al alloys, it is generally accepted that PEO technology results in coatings of considerable thickness, superior substrate adhesion, and exceptional wear and corrosion resistance, all while maintaining an environmentally sustainable profile. The PEO process also offers versatility across alloys and geometries, but requires precise control of parameters and can consume more energy than other conventional techniques. Moreover, the relatively high surface roughness and scalability issues are relevant constraints that are currently limiting the industrialization of this technology.

2.1. PEO Coating Growth Mechanism

The PEO coating growth is governed by two main mechanisms: the micro-discharge mechanism and the coating growth mechanism [102]. The micro-discharge mechanism, although not fully understood, is explained by three main theories [103]. The first, referred to as local avalanche breakdown [104,105], proposes that each micro-discharge results from localized electron avalanches in the bulk of the anodic film, leading to the breakdown of the solid insulating coating. Albella et al. proposed an extension of this theory, suggesting that the electrolyte species incorporated into the coating initiate electron avalanches, leading to plasma micro-discharges [106,107]. However, the expected linear relationship between applied voltage and coating thickness does not match practical observations [108]. The second theory, usually referred to as glow discharge electrolysis, suggests that the initial breakdown of the barrier layer is induced by free electrons from the electrolyte that are injected into the gas bubbles at the oxide/electrolyte interface. This theory was defended by Wang et al. [109], who found that anions from the electrolyte, other than OH^-, minimally influenced the composition of the active plasma species. According to this theory, the glow discharges would promote the melting and sintering of the underlaying ceramic coating. The third model, known as the discharge-in-pore theory, assumes that micro-discharge initiation occurs at the bottom of the micropores of the coating by gas discharge [110].

Among these, the local avalanche breakdown is the most widely accepted theory [111], suggesting that electron avalanches promoting the micro-discharges would also form

discharge channels in the oxide layer [112]. To explain the growth of a PEO coating on pure Al, Monfort et al. [113] used a silicate- and phosphate-based electrolyte and studied the distribution of the electrolyte species throughout the coating, finding that coating growth occurred at dielectric breakdown sites, creating short-circuit pathways. These pathways, enriched with phosphorus at the metal/coating interface, facilitated the penetration of species from the electrolyte into the interior of the coatings.

The development of a PEO process and the associated coating growth mechanism is typically divided into four stages [114–116] (Figure 4). During the first stage, the voltage experiences a rapid and linear increase, similar to conventional anodic oxidation, and the substrate is covered only by a thin layer of Al_2O_3. After reaching the breakdown voltage, plasma micro-discharges gradually appear on the surface of the treated sample [25,117] (Figure 4). In the second stage, the voltage increases more slowly, promoting the growth of the PEO coating through the formation of the oxide phases. During the third stage, the potential remains at a near-stable value, indicating the transformation of the previously formed oxides into crystalline phases [118]. At this stage, the growth thickness of the coating is also almost unaffected by the total current density.

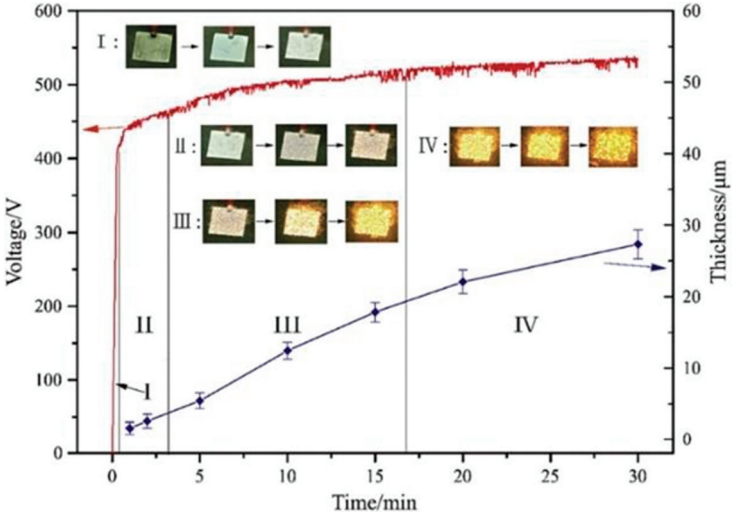

Figure 4. Typical evolution of the potential over time during a PEO process, with the corresponding plasma micro-discharges on the surface of the treated Al alloy [114]. Reprinted from Journal of Alloys and Compounds; 753; Rui-qiang Wang, Ye-kang Wu, Guo-rui Wu, Dong Chen, Dong-lei He, Dalong Li, Changhong Guo, Yefei Zhou, Dejiu Shen, Philip Nash; An investigation about the evolution of microstructure and composition difference between two interfaces of plasma electrolytic oxidation coatings on Al; 272–281; Copyright (2018), with permission from Elsevier.

In certain PEO processes, the potential evolution may not follow the typical pattern shown in Figure 4, leading to a phenomenon known as "soft sparking". This particular regime occurs in those PEO processes where the applied cathodic current density is higher than the anodic current density, $R = J_{cathodic}/J_{anodic} > 1$, resulting in a drop in the positive potential [119], and typically leads to a refinement of the plasma micro-discharges, in terms of light and sound emissions [88,120].

Although the mechanism behind soft sparking, is not yet fully understood, it is correlated with an increased resistance to energy transfer due to the thicker and denser coating formed [121]. The earlier appearance of the soft sparking regime has also been associated with the use of aged electrolytes, due to the decrease in ionic species that reduce the electrical conductivity of the electrolyte while modifying the plasma discharges [122]. This regime would not only avoid the occurrence of aggressive plasma discharges, but

the more refined discharges associated with it would promote the development of PEO coatings with enhanced properties [57]. For example, it has been found that soft sparking promotes denser inner layers in PEO coatings developed on Al substrates, together with a higher formation of α-Al_2O_3 [119]. Furthermore, the transition to the soft sparking regime will also favor an improved energy efficiency of the process, due to the reduction of the total power consumption as a consequence of the lower potential during the process [87].

The morphological structure of PEO coatings typically shows three distinct layers. The outer layer, usually comprising between 5 and 30% of the coating thickness, usually shows defects (i.e., cracks and/or pores) and is mainly composed of γ-Al_2O_3 with relatively low hardness values, around 500 HV and 1000 HV [31,115]. The intermediate layer, which accounts for between 70 and 95% of the total coating thickness, is denser and consists of both γ-Al_2O_3 and α-Al_2O_3, with higher hardnesses ranging from 900 HV to 2000 HV [31,115,123]. Adjacent to the substrate, an amorphous Al oxide inner layer promotes strong adhesion to the coating [102,124]. Nevertheless, recent advances have reported bi-layered PEO coatings, where the outermost layer promotes higher density. This particular structure has been observed in PEO coatings developed on cast Al-Si alloys using aluminate-based electrolytes that promote a higher rate of Al_2O_3 into the coating [4,14,23]. This particular morphology would be explained by the fact that the oxidation and incorporation of the Si from the substrate promotes the formation of Si- or aluminosilicate oxides, with a lower density than the Al oxides, while the $NaAlO_2$ from the electrolyte promotes a higher proportion of Al_2O_3 in the outermost layer [54,125].

2.2. PEO Process Parameters

The key factors influencing the properties of PEO coatings on cast Al-Si alloys include substrate composition, electrolyte composition, and electrical process parameters such as the type of power supply or the voltage and current density applied. These factors affect the thickness, composition, and morphology of the coating and ultimately the performance of the coating in various environments. For example, variations in substrate composition can alter the adhesion and mechanical properties of PEO coatings, while the chemical composition of the electrolyte can directly influence the formation of specific oxide phases, thereby affecting the corrosion resistance and tribological properties of the developed coatings.

2.2.1. Substrate Composition

During the PEO process, part of the metallic substrate is dissolved. This actively contributes to the formation of the ceramic coating. Consequently, the chemical composition of the treated alloy plays a key role in determining the composition, microstructure, and characteristics of the resulting coating [52,126,127]. Previous investigations have shown that the presence of alloying elements, such as Cu, Mg or Zn in Al alloys, inhibits the transition of γ-Al_2O_3 to α-Al_2O_3 [102,128]. This suppression of the phase transformation is attributed to the lower bond energy between the oxygen and these alloying elements, compared to the robust interaction between Al and O_2. Under the influence of the electric field, Cu^{2+}, Mg^{2+}, and Zn^{2+} ions would migrate to the outer part of the coating faster than the Al^{2+} ions. The presence of these weaker bonds in the lattice would disrupt the grain growth, as the transformation from γ-Al_2O_3 to α-Al_2O_3 involves a shift from cubic to hexagonal packing, typically accompanied by grain growth and an increase in the transition temperature [127]. In the particular case of cast Al-Si alloys, the Si will also significantly inhibit the effective growth of the PEO coating [127,129].

2.2.2. Electrical Parameters

A PEO process can be carried out under direct current (DC), alternating current (AC), and unipolar pulsed (UP) or bipolar pulsed (BP) current, with the type of power supply being a determining factor in the characteristics of the PEO coating. DC, which provides the lowest energy efficiency, represents the simplest mode and its application is best suited

for treating components with a simple geometry that requires low thicknesses [130]. The AC mode improves the process control but has limitations in terms of power and current frequency. This mode provides coatings with better properties than those obtained with DC sources and also allows better control of the discharge parameters and processes. However, the control provided is sometimes insufficient for the design of PEO coatings with certain requirements [131]. According to the literature [132], the processes performed using pulsed sources show the most successful results in terms of energy efficiency.

In addition to the type of power supply, precise control of various electrical parameters is essential, including anodic and cathodic potentials, applied current density, frequency, duty cycle, process time, and temperature. Among these, the most relevant parameters to control are the current density, frequency, and anodic potential. The anodic potential is particularly relevant because it provides the energy required to form the coatings and significantly influences the microstructure and properties of the PEO coatings [102]. Once the applied anodic potential exceeds the value of the critical breakdown voltage of the barrier layer of the metal substrate, plasma micro-discharges occur on the treated sample [57]. Increasing the anodic potential leads to an increase in the number, brightness, and size of the plasma micro-discharges, as long as a limiting voltage value is not exceeded, and beyond which the above-mentioned behavior of the plasma discharges is reversed. The same pattern is observed for micropores, where higher anodic potentials lead to an increase in both size and number [133].

The applied current density, which directly determines the growth rate of the PEO coating, is primarily determined by the nature of the alloy being treated. Typically, applying too low current densities would lead to a relatively slow coating growth rate, which would impair the energy efficiency of the process. On the other hand, the use of excessive current densities will promote a PEO coating with lower mechanical properties and higher roughness, a higher releasement of gaseous products, and the treated sample may even be burnt [100,134]. Al alloys containing low amounts of alloying elements will typically require current densities between 5 $A \cdot dm^{-2}$ and 15 $A \cdot dm^{-2}$. However, Al alloys with higher amounts of alloying elements, and especially cast Al-Si alloys, will require current densities of around 25 $A \cdot dm^{-2}$ [4,14,23]. In terms of frequency, higher frequencies usually result in coatings with lower roughness and provide shorter plasma discharge lifetimes, reducing the occurrence of large destructive discharges [134]. The roughness of the coating is also proportional to the process time applied: longer processes will increase the arc force occurring at the surface and promote higher discharges, resulting in more uneven surfaces [134].

2.2.3. Electrolyte

The electrolyte is probably the most important parameter in a PEO process, as it determines not only the course of the process, but also the microstructure, composition, and properties of the developed coatings [135,136]. Typically, PEO electrolytes are water-based alkaline solutions, enriched with various inorganic salts, nanoparticles, or additives [100]. This makes PEO electrolytes environmentally friendly, which is a major advantage over anodizing, which employs acidic electrolytes.

The chemical composition of the electrolyte is critical because its constituents are incorporated into the PEO coating through the plasma-chemical reactions that take place during the process [37,101]. PEO electrolytes also provide oxygen, which reacts with the molten cations of the metal substrate, resulting in the formation of ceramic oxides, such as Al_2O_3 or TiO_2 for Al and Ti alloys, respectively [38]. The movement of OH^- through the electrolyte, under the influence of the electric field, favors the oxygen transport mechanism to the metallic substrate [57]. In addition, the electrolytes contain other compounds that confer anionic or cationic components to the PEO coating [38].

PEO electrolytes are typically categorized based on the predominant inorganic compound in their formulation, with common classifications including silicate-, aluminate- and phosphate-based electrolytes. Among these, silicate-based electrolytes, with Na_2SiO_3

being the most common reagent, are the most widely used electrolytes in PEO technology [64,137,138]. In general, silicate-based electrolytes have been found to be more stable than phosphate-based electrolytes [101]. However, for certain alloys and applications, such as cast Al-Si alloys with high tribological requirements, these electrolytes may not be the most appropriate. This is attributed to their tendency to promote an excessive presence of Si oxides, mullite, and aluminosilicates within the coating, which are also derived from the Si in the metal substrate. Consequently, these coatings exhibit inferior tribological properties compared to Al oxides [139]. In the case of phosphate-based electrolytes, some studies have reported their ability to enhance the density and tribological performance of the coating [140]. Furthermore, it is common for phosphorus salts to be incorporated into silicate- or aluminate-based electrolytes at lower concentrations than the latter [141,142]. Although research on aluminate-based electrolytes is comparatively recent, observations suggest that they favor the development of coatings with high tribological and anti-corrosion performance. This is particularly notable in the treatment of complex cast Al-Si alloys, where the main interest resides in increasing the Al oxides in the coating to counteract the formation of Si oxides originating from the substrate [54,128,136].

The chemical stability of the electrolyte also plays a key role, as inadequate dispersion of the reagents can lead to the formation of precipitates. This would not only hinder the reaction and incorporation of the components into the coating, but could also cause blockages in the electrochemical cell pipes. Continuous use induces aging of the electrolyte, gradually depleting its ionic species and decreasing its electrical conductivity, thereby affecting the potential breakdown value and the plasma discharge formation during the process [122]. Nevertheless, it has also been observed that electrolyte aging would favor the occurrence of soft sparking by increasing the α-Al_2O_3 content in the coating [122]. Therefore, the evaluation of the electrolyte quality must be analyzed on a case-by-case basis. The pH values of the PEO electrolytes typically range between 10 and 13, and this is usually regulated by the addition of KOH or NaOH [57,88]. However, it is critical to control the concentration of these reagents, as their higher concentration has previously been found to result in a lower coating growth rate due to an increased anodic dissolution [130,143]. The electrical conductivity of the electrolyte, which typically varies between 5 and 100 $mS{\cdot}cm^{-1}$, is also a crucial parameter, directly influencing the breakdown value during the PEO process (higher electrical conductivity corresponds to a lower breakdown potential) [57,144]. Unlike anodizing, the temperature control during PEO processes, especially in Al alloys, is less sensitive [145]. However, for titanium alloys, the temperature of the electrolyte during the process plays a more significant role. For example, an aluminate-based electrolyte used in the PEO coating of Ti showed an increased amount of α-Al_2O_3 at lower electrolyte temperatures [146].

Structural defects such as porosity and microcracking are common despite the improved wear and corrosion resistance of PEO coatings. These defects usually result from gas release or rapid cooling during the formation of the micro-electrical discharges. Consequently, the high porosity and the presence of defects will induce the development of more brittle layers, limiting their long-term barrier efficacy. In particular, the incorporation of specific chemical elements, such as certain salts or nanoparticles, into PEO coatings is of great interest to reduce the intrinsic porosity of these layers, thereby providing coatings with a broader range of properties [147,148]. Each additive, depending on the concentration used and how it is combined with the other additives, will provide unique properties to the developed PEO coating, such as higher growth rate, higher thickness and hardness, lower roughness, or enhanced tribological and anti-corrosion performance [86,149–151].

One of the major challenges in PEO technology involves the mitigation of the intrinsic porosity of PEO coatings, which typically compromises an optimal tribological and corrosion performance. Porosity can be reduced through the use of several approaches, including the adjustment of electrical parameters, the development of duplex coatings, and the modification of the electrolyte composition. Among these methods, the formulation of the electrolyte emerges as the most effective method of porosity reduction, with emphasis

on the incorporation of micro- or nanoparticles. Generally, particles are directly introduced into the electrolyte in the form of powders or sols comprising different compounds [62]. The incorporation of the particles or nanoparticles can be accomplished through either an inert or reactive mechanism [152]. The type of incorporation will depend on the substrate, electrical process parameters, electrolyte composition, and inherent properties of the particles. In the case of an inert incorporation, no reaction nor formation of a new phase occurs. Additionally, the size and shape of the particles undergo minimal alteration after their incorporation. Conversely, in reactive incorporation, the particles react with compounds from both the electrolyte and the metal substrate. This process is more complex and influenced by several parameters [153]. The reactive incorporation is more feasible in particles with smaller sizes and relatively low melting points [153,154].

Achieving a proper and adequate dispersion of the particles in the electrolyte is critical for the optimal incorporation of the particles into the coating. When dispersion is unstable, particles tend to agglomerate, forming clusters of larger size, even micrometric. In addition, introducing pigments and/or dyes to the electrolyte can confer aesthetic functionality, leading to the generation of PEO coatings with different colors. In general, black is the most demanded color due to its aesthetical functionality and its ability to provide coatings with high emittance and absorbance, properties required in aerospace internal components subjected to significant thermal gradients in space [35,155]. However, producing black PEO coatings remains challenging, particularly on more challenging alloys like cast Al-Si alloys. Three reagents, namely potassium fluorotitanate (K_2TiF_6), sodium tungstate (Na_2WO_4), and ammonium metavanadate (NH_4VO_3), have been extensively studied for obtaining black PEO coatings. It should be noted that, unlike anodizing which uses coloring agents, the black coloring in PEO coatings can also be obtained by the reaction and dissociation of these reagents during the process, resulting in oxides with a dark grey or black color. Among the aforementioned reagents, K_2TiF_6 stands out for the dark color that it provides to the coating, increased thickness [86], enhanced wear and corrosion resistance [82,156–159], as well as heightened absorbance and emissivity values [35]. Na_2WO_4 is widely used in formulating silicate- [86,97,160–162], aluminate- [155], and phosphate-based [163,164] electrolytes, resulting in black coatings on Al [162,164] and titanium [163] substrates. Tungsten-containing electrolytes, when applied to Al substrates, typically form an $Al_2(WO_4)_3/Al_2O_3/Al$ composite [165]. The surface energy of the $Al_2(WO_4)$/electrolyte interface is higher than that of the Al_2O_3/electrolyte interface, so the tungsten-containing oxides are located in the outer part of the coating, providing a darker color. Furthermore, the addition of Na_2WO_4 improved the corrosion resistance [35,155], and catalytic properties [66,165] of the coatings.

NH_4VO_3 has also been employed for the development of black coatings [164,166], but its toxicity significantly limits its use. Besides black, PEO coatings with other colors have also been obtained, through the additivation of the electrolytes with dyes or pigments [167] (Figure 5).

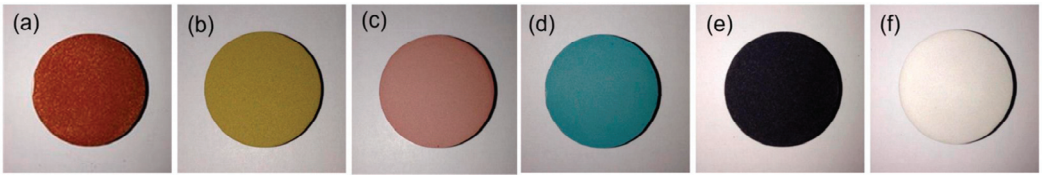

Figure 5. (**a**) Red, (**b**) yellow, (**c**) orange, (**d**) blue, (**e**) black, and (**f**) white PEO coatings obtained by adding dye emulsions to an electrolyte in an Al substrate [168]. Reprinted from Surface and Coatings Technology; 287; Shang-Chun Yeh, Dah-Shyang Tsai, Jian-Mao Wang, Chen-Chia Chou; Coloration of the aluminum alloy surface with dye emulsions while growing a plasma electrolytic oxide layer; 61–66; Copyright (2016), with permission from Elsevier.

3. Surface Modification of Cast Al-Si Alloys through PEO Technology: A Current Challenge

The development of protective coatings on cast Al-Si alloys by conventional anodizing is challenging, mainly due to the hydration of the silicon phases [34,169]. Although PEO technology has been widely used for the development of coatings on several Al alloys (2024, 6061, 7075, etc.), and has obtained high-performance coatings, the development of competitive PEO coatings on cast Al-Si alloys remains a challenge nowadays. However, despite the higher complexity of this type of alloy, there has been an increase in the number of publications in recent years, highlighting the interest and the need for the surface improvement of these alloys using PEO technology.

The chemical composition of the electrolyte used in the PEO process is a critical determinant of the microstructure, composition, and performance of the coatings. Different electrolyte formulations, such as silicate-, phosphate-, and aluminate-based solutions, offer different advantages and challenges. Selecting the electrolyte composition is therefore critical to tailoring the properties of PEO coatings to meet the specific performance requirements of cast Al-Si alloys. The published findings related to the growth of PEO coatings on different cast Al-Si alloys have been analyzed and classified according to the type of electrolyte used: silicate-, phosphate- or aluminate-based. The factors hindering the surface treatment of cast Al-Si alloys using PEO technology have been analyzed, as well as the different strategies described in the literature for the improvement of the coatings obtained.

3.1. PEO Coatings Developed on Cast Al-Si Alloys Using Silicate-Based Electrolytes

Silicate-based electrolytes are the most widely used within PEO technology. In one of the first studies carried out concerning the development of PEO on cast Al-Si alloys, Krishtal et al. [170] studied the influence of Si content on the properties of the developed PEO coating. For this aim, they treated hypoeutectic, eutectic, and hypereutectic alloys. The authors showed that the composition and microstructure of the cast Al-Si alloy directly influenced the growth of the PEO coating, determining the morphology of the PEO coating. Furthermore, the authors observed that the Si particles present in the Al matrix inhibited the reaction between Al and O_2, hindering the growth of the PEO coating due to the lower electrical conductivity of the Si phases with respect to the Al matrix. As a consequence, the layers obtained not only showed lower thickness, but also poorer hardness and adhesion, together with higher porosity [170].

In another early research project on this topic, Wang & Nie [171] studied the influence of Si content on the growth mechanism, composition, and morphology of the coating. For that purpose, they worked with a hypoeutectic (A319) and a hypereutectic (A390) alloy, using an electrolyte composed of 4 $g \cdot L^{-1}$ Na_2SiO_3 [171]. The authors observed that the Si content significantly influenced the lifetime and morphology of the coating during stages I, II, and III of the PEO process. Although the breakdown voltage value was similar for the hypo- and hypereutectic alloys—390 V and 400 V, respectively—the hypoeutectic alloy reached that value in 1 min, while the hypereutectic alloy required 5 min to reach 400 V. This slower rise in potential at the beginning of the process would indicate a lower coating growth rate on the alloy with the higher Si content. This reduced coating growth would be a consequence of the lower Al area to be passivated in the hypereutectic alloy during this initial stage [171]. A similar pattern was observed in the rate of increase in the potential during stages II and III. In the second stage, the alloy A319 required 1 min to raise the positive voltage by 50 V, while the alloy A390 required 5 min to increase the voltage value up to 65 V. In the third stage, the rate of potential rise was 2.79 $V \cdot min^{-1}$ and 1.65 $V \cdot min^{-1}$ for alloys 319 and 390, respectively. The coatings obtained during stage IV showed a similar composition, mainly γ-Al_2O_3, and similar roughness for both alloys. In addition, the authors also determined that the alloy composition did not lead to significant variations in the coating for thicknesses above 50 microns [171].

Wang & Nie [171] also studied the variation in coating morphology throughout stages II, III, and IV for A319 and A390. In the second stage, it was observed, by means of

SEM and EDS analysis, that the plasma micro-discharges started at the interface between the Al matrix and the Si grains due to a concentration effect of the electric field in that interface. That discharge would melt the Si phase, mixing it with the Al oxide, leading to the formation of aluminosilicates (Al-O-Si), which have a lower melting point than the Al oxides, and whose morphology presented cavities and bubbles. Since the A390 alloy contained higher Si content and, therefore, higher discharge points at the Al-Si interface, it required a higher potential for the occurrence of the discharges. During stage III, due to the higher presence of Al-O-Si compounds in the coating, with a lower melting point and higher porosity, more discharge points appeared in those areas, leading to a clustering of the aluminosilicate phases. In stage IV, due to the increased thickness of the coating, the chemical reactions involved more elements from the electrolyte than from the substrate. In addition, at this stage, the morphology and composition of the coatings developed on the A319 and A390 alloys became more uniform [171].

Xue et al. [169] investigated the development of PEO coatings with high anti-corrosion performance on cast Al-Si alloys with a 7% Si content. They developed coatings with different thicknesses, comparing the morphology and chemical composition of each one, using an electrolyte composed of Na_2SiO_3 and KOH. In this study, the results concerning the coating growth and the evolution of the potential agreed with those obtained by Wang & Nie [171]. The coating growth rate increased during the second stage of the process, decreasing during the third stage. The coatings obtained in that study exhibited three distinct regions: the inner layer, which showed high adhesion to the metal substrate, an intermediate layer, with high density, and a porous outer layer (Figure 6). From the EDS analysis, it was found that the intermediate dense layer was mainly composed of Al oxides, while a significantly higher amount of Si was detected in the porous outermost layer. The porous outer layer, besides Si, also showed higher Na and K content (Figure 6).

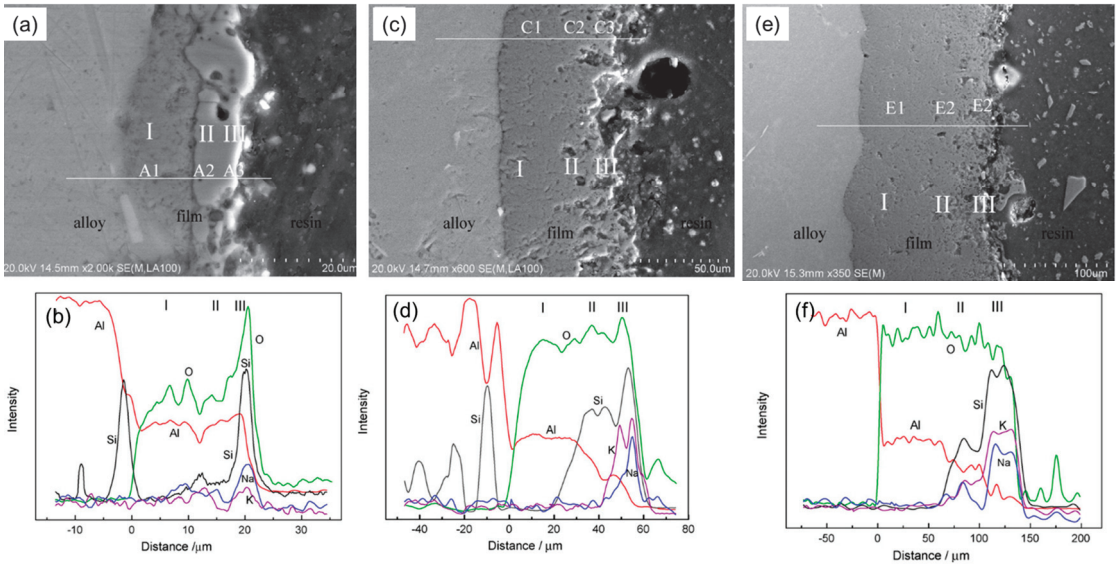

Figure 6. Cross-sections and their corresponding EDS analysis of PEO coatings developed using a silicate-based electrolyte, with thicknesses of 20 μm (**a**,**b**); 60 μm (**c**,**d**); and 140 μm (**e**,**f**) [169]. Reprinted from Applied Surface Science; 253; Wenbin Xue, Xiuling Shi, Ming Hua, Yongliang Li; Preparation of anti-corrosion films by microarc oxidation on an Al–Si alloy; 6118–6124; Copyright (2007) with permission from Elsevier.

According to the authors [169], the Si, Na, and K present in the porous outer layer would have come from the electrolyte (more specifically, Na and K were not present in the alloy, only in the electrolyte), and did not diffuse into the intermediate dense layer. Xue et al. [169] suggested that this result was mainly due to the use of an AC power supply, which favors the obtention of denser coatings on cast Al-Si alloys. The higher density of the coatings would prevent the diffusion of the ions from the electrolyte towards the innermost layers, remaining in the external zone, where the higher porosity of this region would favor their permanence. Concerning the oxide phases detected in the coatings, γ-Al_2O_3 phases were detected in all coatings, while α-Al_2O_3 was only found in the thickest coatings (60 μm and 140 μm). Mullite phases were also detected in all the coatings, although their content increased with increasing the coating thickness. It also investigated the influence of PEO treatment on the corrosion behavior of the cast Al-Si alloy [169]. For this purpose, they compared the corrosion resistance of the cast Al-Si reference alloy against three samples treated by PEO, with thicknesses of 20 μm, 60 μm, and 140 μm. Electrochemical corrosion tests showed that both general and pitting corrosion resistance improved considerably with the application of the PEO coating. Moreover, the improvement is even more pronounced with increasing coating thickness, with the best results being obtained for the coating of 140 μm.

The influence of Si phases on the growth, composition, and morphology of PEO coatings on cast Al-Si was also studied by He et al. [34]. In this study, cast Al-7Si alloys were treated using an electrolyte composed of Na_2SiO_3, KOH, and Na_3AlF_6, using a pulsed bipolar power supply at a frequency of 700 Hz. Based on SEM and EDS analysis, it was observed that the coating grown on the Al primary phases was mostly composed of Al_2O_3, while Si and O_2 content increased in the eutectic α phase areas, due to the relative oxidation of Si. The eutectic β phase regions showed a higher Si and O_2 content, but there was no evidence of plasma discharge in these regions. This would indicate that Si oxides could have been formed by melting and oxidation due to the high temperature of the plasma discharges in the Al substrate regions, mixing with the Al_2O_3 phases during the coating growth process. He et al. also observed that the Si content decreased from the outer to the inner region of the coating, suggesting that the higher Si content in the outer region would come from the silicate-based electrolyte. In a further step, Xu et al. [129] treated hypereutectic cast Al-Si alloys with a Si content between 27 and 32%, using an electrolyte composed of Na_2SiO_3 and NaOH, and an AC power supply. It was observed that longer PEO processes, up to 300 min, resulted in more uniform coatings, both in terms of element distribution and coating morphology.

Sabitini et al. [29] carried out research in which the main objective was the comparison of the growth, properties, and wear resistance of the PEO layers grown, under the same process conditions, on a cast A359 and a wrought 7075 alloys. The authors used a 50 Hz AC power supply and a commercial silicate-based electrolyte. Due to the higher presence of microstructural defects in the cast alloy caused by the presence of Si phases in the substrate (Figure 7), the coatings grown on this material showed lower hardness and lower elastic modulus, as well as higher roughness (Figure 8). Both PEO coatings on cast and wrought alloys showed an improvement in wear resistance compared to the base materials. At high loads, the coating developed on the 7075 wrought alloy showed a stronger tribological performance than the coating grown on the cast Al-Si alloy, due to the higher hardness and homogeneity of the former. Feng Su et al. [172] also studied the development of a PEO coating with high tribological performance on an A356 casting alloy. In this case, they employed a pulsed power supply under a frequency of 2000 Hz, and two different electrolytes, containing only $K_4P_2O_7$, and $K_4P_2O_7$ combined with Na_2SiO_3. In the tests, carried out under minimum lubrication, a tribological improvement (lower COF, wear, and plastic deformation) was found in the PEO coatings compared to a PTWA coating.

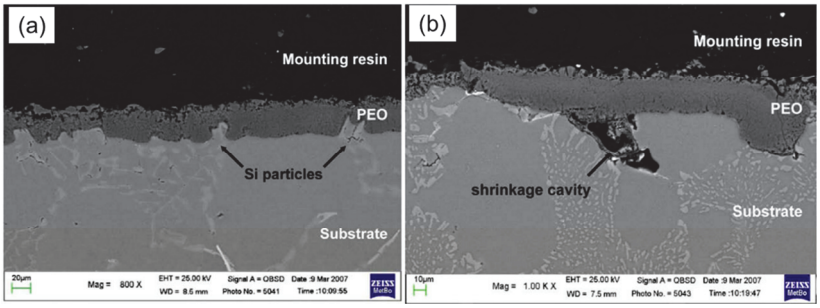

Figure 7. Cross-sectional SEM micrographs of the PEO coating developed on an A359 cast Al-Si alloy showing particular morphologies, such as eutectic Si particles (**a**) and shrinkage cavities (**b**) [29]. Reprinted from Materials & Design; 31; G. Sabatini, L. Ceschini, C. Martini, J.A. Williams, I.M. Hutchings; Improving sliding and abrasive wear behaviour of cast A356 and wrought AA7075 aluminium alloys by plasma electrolytic oxidation; 816–828; Copyright (2010), with permission from Elsevier.

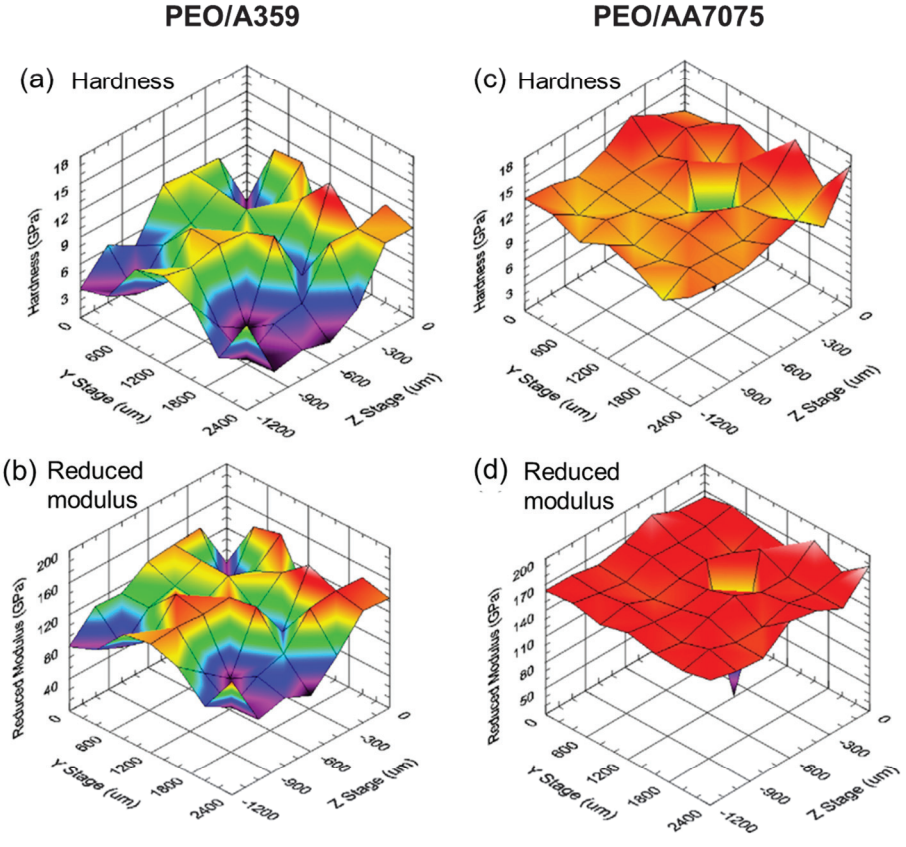

Figure 8. 2D profiles of hardness and reduced modulus of the PEO coatings grown on an A359 (**a**,**b**) and AA7075 (**c**,**d**) alloys [29]. Reprinted from Materials & Design; 31; G. Sabatini, L. Ceschini, C. Martini, J.A. Williams, I.M. Hutchings; Improving sliding and abrasive wear behaviour of cast A356 and wrought AA7075 aluminium alloys by plasma electrolytic oxidation; 816–828; Copyright (2010), with permission from Elsevier.

Gulec et al. [3] carried out a systematic study to analyze the influence of the Si content on PEO coatings grown on binary cast Al-Si alloys with Si contents between 1% and 32%, by performing PEO processes of 120 min with a silicate-based electrolyte. The researchers observed that, as the Si content increased, the thickness of the developed PEO coating decreased. In addition, α-Al_2O_3 phases were only observed for the alloys containing 1 and 2 at. % Si. Furthermore, it was observed that as the Si content of the alloy increased, the coatings had a smoother appearance and lower roughness, which would be explained by the fact that the melting temperature of SiO_2 (1726 °C) is lower than the melting temperatures of mullite (1828 °C) and Al_2O_3 (2054 °C). The alloys with higher Si content will contain a higher relative amount of Si in the coating, decreasing the melting temperature of the mixed oxides that form the coating, and thus leading to an increase in the fluidity of the materials transported through the plasma channels, covering all the surfaces of the coating as they are sprayed outwards. In addition, the plasma microarcs occurring during the treatment of alloys with higher Si content are weaker, also favoring the formation of coatings with lower porosity and roughness.

Rogov et al. [28] studied the influence of the microstructure of Al-Si substrates on the PEO coating development, by comparing a cast Al-12Si alloy against an Al alloy with a 12% Si content fabricated by additive manufacturing. In this study, an electrolyte composed of 10 $g \cdot L^{-1}$ Na_2SiO_3 and 2 $g \cdot L^{-1}$ KOH and a pulsed bipolar power source were employed. Since the cathodic polarization could suppress the passivation of the Si grains, the authors designed a specific wave regime, where only anodic polarization was applied in the first 3 min of the process. After that time, and once the plasma was stably initiated, authors alternated bipolar and unipolar polarization cycles with cathode-only pulses. Their findings suggested that the microstructure of the alloy, i.e., the size and distribution of the Si grains in the metal substrate, had only influenced the most unstable stages of the PEO process: the initial stage and the stage of transition to the soft sparking regime. Once the corresponding micro-discharge regime has been initiated, the process proceeds normally for both alloys.

In a recent paper [25], PEO processes under pulsed bipolar current (PBC) and pulsed bipolar voltage (PBV) modes were performed on pure Al and binary Al-Si alloys with different Si contents (5 wt.% Si, 9 wt.% Si, 12 wt.% Si, and 15 wt.% Si). While under the PBC regime, the Si phases were rapidly oxidized, obtaining similar final thicknesses regardless of the Si concentration of the alloy, under the PBV regime, the Si phases were oxidized more slowly, which was reflected in a lower final thickness on the substrate with higher Si content. The growth of PEO coatings on Al-Si binary alloys was also investigated by Moshrefifar et al. [173], who in their study worked with Al-xSi alloys (x = 1 wt.%, 3 wt.%, 5 wt.%, 7 wt.%, 9 wt.%, 11 wt.%, and 13 wt.%) (Figure 9), obtaining the PEO coatings by using a $Na_2SiO_3 \cdot 5H_2O$-containing electrolyte, with and without being modified with $Na_2WO_4 \cdot 2H_2O$. As expected, it was observed that a higher Si content in the substrate led to a reduction in the size of the α-Al dendrites and an increase in the eutectic phase (Figure 9). It was reported that a higher porosity percentage and a lower average thickness were attributed to an increased Si content on the substrate. Nevertheless, the higher thicknesses obtained in the samples with lower Si contents presented greater outer layers, which normally exhibit poorer tribological properties than the dense inner layers typically observed in PEO coatings. Thus, the PEO coatings grown in the samples with lower wt.% Si presented higher wear rates, volume losses, and wear track widths (Figure 10). In a further attempt to improve the durability of a PEO coating developed on a cast Al-Si alloy, Student et al. found that the uneven growth of the PEO layers was due to the silicon crystals hindering the proper development of the coatings (Figure 11). The addition of H_2O_2 to the electrolyte significantly enhanced wear resistance by promoting the formation of high-temperature phases like α-Al_2O_3 and $3Al_2O_3 \cdot 2SiO_2$, resulting in increased durability.

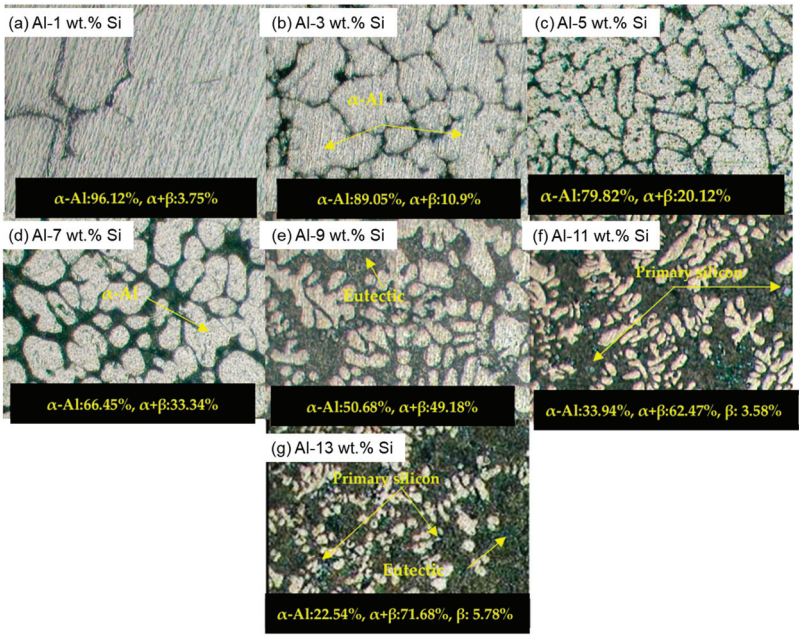

Figure 9. Optical images and each corresponding phase's percentage of the different Al-Si alloys PEO treated in reference: [173]. Reprinted from https://www.mdpi.com/2079-6412/12/10/1438, accessed on 27 December 2023: open access article distributed under the terms and conditions of the Creative Commons Attribution (CC BY) license (https://creativecommons.org/licenses/by/4.0/, accessed on 27 December 2023).

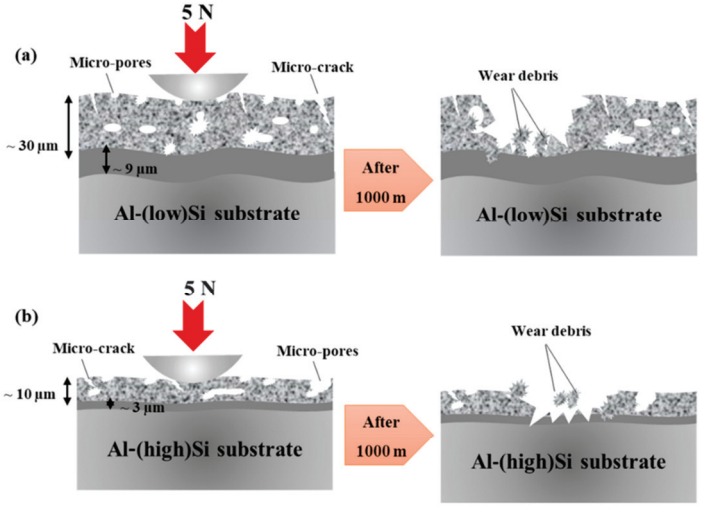

Figure 10. Schematic representation of the wear mechanism of PEO coatings developed on two different Al-Si alloys with low Si content (**a**) and high Si content (**b**) [173]. Reprinted from https://www.mdpi.com/2079-6412/12/10/1438, accessed on 27 December 2023: open access article distributed under the terms and conditions of the Creative Commons Attribution (CC BY) license (https://creativecommons.org/licenses/by/4.0/, accessed on 27 December 2023).

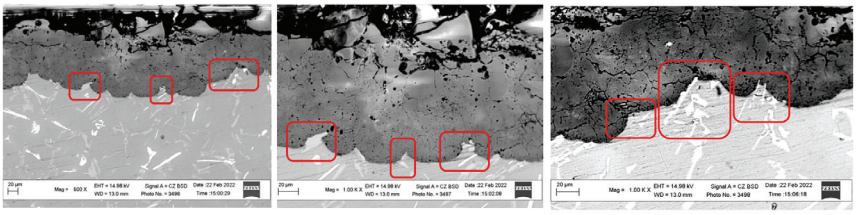

Figure 11. SEM micrographs revealing the cross-section of a PEO coating grown on a cast AlSi10 (AK9) alloy. The marked areas reveal the deceleration in the coating growth in the areas containing Si-rich crystals. Figure adapted from [174]. Reprinted from https://www.mdpi.com/2079-6412/13/3/637, accessed on 27 December 2023, open access article distributed under the terms and conditions of the Creative Commons Attribution (CC BY) license (https://creativecommons.org/licenses/by/4.0/, accessed on 27 December 2023).

The manufacturing method is also a determinant of the behavior of PEO coatings grown on Al-Si alloys. Mora-Sanchez et al. compared the growth and properties of PEO coatings grown on a conventional A361 cast alloy and on an AM) Al10SiMg alloy, using a silicate-based electrolyte [175]. Compared with the PEO grown on the AM/Al-Si substrate, the PEO coating developed on the cast Al-Si alloy showed finer and lower porosity percent. Nevertheless, the interface between the substrate and the coating was flatter for the AM substrate, since it presented a finer distribution of silicon in comparison with the cast alloy. As referenced in their works, Pezzato et al. [176,177] have demonstrated substantial enhancements in the corrosion resistance of PEO coatings applied on AM AlSi10Mg alloys, obtained by selective laser melting (SLM), in comparison to PEO coatings grown on conventionally cast AlSi10Mg substrate. In both cases, the PEO processes were carried out using a silicate-based electrolyte composed of 25 g/L of Na_2SiO_3 and 2.5 g/L of NaOH. The improved anti-corrosion performance was attributed to the more uniformly distributed Si phases present on the AM Al-Si substrates. Additionally, the absence of Fe and Mn intermetallic compounds contributed to the formation of denser and more uniformly structured PEO coatings.

3.2. PEO Coatings Developed on Cast Al-Si Alloys Using Phosphate-Based Electrolytes

The effect of the addition of NH_4VO_3 to a phosphate-based electrolyte in a PEO process on a cast Al-12Si alloy was studied by Hwang et al. [166]. It was observed that the addition of NH_4VO_3 influenced the size and duration of the plasma micro-discharges, resulting in a decrease in the breakdown voltage. Furthermore, the NH_4VO_3-containing electrolyte not only promoted a more uniform PEO coating, preventing the heterogeneous growth observed in previous studies, but also led to black PEO coatings. NH_4VO_3 was newly employed for the development of black PEO coatings on a hypoeutectic Al-Si alloy, in combination with Na_2WO_4, which is a reagent that is also a coating darkener [164]. In this study, the authors found the optimal ratio between the concentrations of Na_2WO_4 and NH_4VO_3 added to a phosphate-based electrolyte to obtain smoother and darker-colored coatings. The formation of vanadium and tungsten oxides in the coating was found to be responsible for the black color. In addition, it was found that the NH_4VO_3 reagent played the most significant role in the formation of the dark-colored coating.

In 2018, Yu et al. treated a eutectic cast Al-Si alloy using a phosphate-based electrolyte [27]. The PEO processes were performed at a low current density, between 4 and 6 $A{\cdot}dm^{-2}$, and resulted in low-thickness PEO coatings (8–10 μm), in which no α-Al_2O_3 phase was detected. In this study, the authors proposed a new and interesting model to explain the growth mechanism of the PEO coating on a cast Al-Si alloy, which contradicts the theory proposed by Wang & Nie [171]. According to Wang & Nie, after the initial passivation stage, discharges occurred at the edge between Al and Si, due to the border effect promoted by the occurrence of a critical potential value due to the electrical concentration at

that interface. Furthermore, Wang & Nie suggested that during passivation, the film grows inward, whereas when Al or Si oxides are formed, there would be some expansion in the volume of the formed layer. According to Yu et al. [27], the thickness of the layer created during the initial passivation stage (in the order of nanometers) is significantly lower than the roughness of the substrate (in the order of microns). Thus, these authors believed that the boundary effect prevented the initiation of discharges and proposed a new growth mechanism consisting of three steps: passivation, stable oxidation, and final oxidation stages. According to this novel model, during the passivation stage, which occurs before the potential reaches the dielectric breakdown value, anodic layers grow on both the Al matrix and the Si crystals (Figure 12 I). Since it is a very quick stage, the authors suggested that the thickness of the anodic layers grown on the Al and Si phases should have a similar thickness. In the stage of stable oxidation, once the breakdown potential has been exceeded, the anodic layers break down and the plasma microdischarges appear. The first areas of the anodic layers to be broken and where the plasma discharges will appear are those of Al_2O_3 formed on the Al matrix, since this oxide has a lower dielectric strength than SiO_2 (Figure 12 II) [27]. Due to the high temperature caused by the discharges, the area where the point discharge occurs is melted, further oxidizing the underlying Al matrix. At the end of the discharge, the molten oxide solidifies, due to the lower temperature of the electrolyte, rebuilding the film at that point. This process is repeated in the areas above the Al matrix, thereby creating the coating. Furthermore, as the coating grows, the discharge potential increases, corresponding to the increase in potential shown in stages II and III of Figure 4. Once the discharge voltage exceeds the value of the SiO_2 films grown on the Si phases of the alloy, discharge points start to occur in these areas as well. These new discharges start at the edges of the larger Si particles since a larger area is in contact with the Al matrix, which has far higher conductivity than Si. Through oxidation and diffusion, Al-Si-O oxides form and, as these films grow, the discharges move towards the center of the Si phases. For the smaller Si particles, the Al-Si-O layers tend to form directly, as discharges occur over their entire surface (Figure 12 III). This process is repeated, increasing the thickness of the coating and reaching the final oxidation stage. However, the discharges mostly occur in the Al_2O_3-rich areas, as the discharge voltage in these areas is lower than in the SiO_2 areas (Figure 12 IV), which cause the thickness of the coating on the Si particles to be slightly lower than that grown on the Al matrix. At this stage, in the areas where there are small, oxidized Si particles, the Al matrix underneath is oxidized, as well as small Si particles that are immersed in the oxidizing Al matrix. These processes promote the reactions between Al_2O_3 and SiO_2, including the formation of aluminosilicates [27].

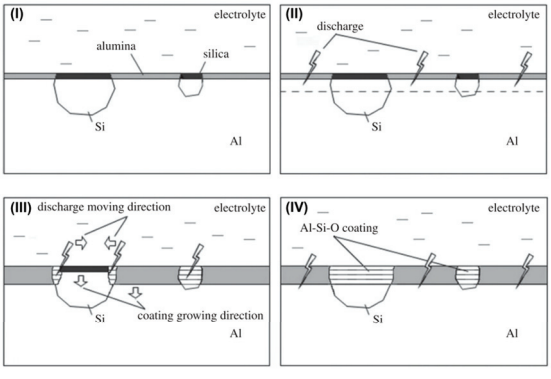

Figure 12. Schematic representation of the coating growth mechanism, with the stages I, II, III and IV described above, proposed by Yu et al. [27]. Reprinted from https://royalsocietypublishing.org/doi/10.1098/rsos.172428, accessed on 27 December 2023: open access article published by the Royal Society under the terms on the Creative Commons Attribution License http://creativecommons.org/licenses/by/4.0/4.0/ (accessed on 27 December 2023), which permits unrestricted use.

The influence of the secondary phases Al2Cu, β-Al5FeSi and eutectic Si present in an AlSi9Cu3 alloy, on the formation and growth of the PEO coating, was investigated by Wu et al. [47]. In their study, they carried out several PEO processes with durations ranging from 15 to 480 s, using an electrolyte composed of Na_3PO_4 and KOH and a unipolar-pulsed DC power supply. In this research, it was observed that the electrical field-assisted dissolution occurring at the beginning of the PEO process begins at the interface between the Al_2Cu intermetallics and the α-Al matrix. The reason for this was that these intermetallic phases presented a native oxide layer of lower coverage than the one formed spontaneously on the α-Al matrix, so the Al_2Cu particles were more exposed to the electrolyte, thus forming at these interfaces low soluble Al/Cu-based oxides and phosphates. Regarding the β-Al_5FeSi intermetallic, Fe tends to create defects and paths through which the electrolyte can penetrate, while due to its higher resistivity, Si tends to change the current flow, both resulting in a lower oxidation rate compared to the Al_2Cu intermetallic. As the coating thickness increased, the films grown on the Al_2Cu and β-Al_5FeSi intermetallics tended to overlap, presenting a more porous and less dense morphology than that formed on the Al matrix, while on the eutectic Si particles, the thinner films with cracks were formed. The sequence in which the coating was formed on this alloy was the α-Al matrix, Al_2Cu, β-Al_5FeSi, and eutectic Si.

3.3. PEO Coatings Developed on Cast Al-Si Alloys Using Aluminate-Based Electrolytes

After an in-depth study of the coating growth mechanism with silicate-based electrolytes, the conventional electrolytes most widely applied in this technology, and studies carried out with phosphate-based electrolytes, the use of aluminate-based electrolytes for the PEO treatment of cast Al-Si alloys was also investigated. Among other reasons, it had previously been observed that aluminate-based electrolytes used in Al alloys provided coatings with higher resistance than those obtained using silicate-based electrolytes [136]. In this context, Xie et al. studied for the first time the use of aluminate-based electrolytes in the PEO treatment of a cast A356 Al-Si alloy [54]. In their research, authors used pulsed bipolar polarization regimes with constant current, and analyzed the effect of $NaAlO_2$ concentration in the electrolyte, using solutions containing 2 $g{\cdot}L^{-1}$, 16 $g{\cdot}L^{-1}$, and 24 $g{\cdot}L^{-1}$ $NaAlO_2$ and 1 $g{\cdot}L^{-1}$ KOH, and compared these electrolytes against one composed of 8 $g{\cdot}L^{-1}$ Na_2SiO_3 + 1 $g{\cdot}L^{-1}$ KOH. The electrolyte composed of 24 $g{\cdot}L^{-1}$ $NaAlO_2$ provided coatings with a monolayer structure and the presence of α-Al_2O_3 phases, giving the best wear and corrosion behavior and improving the results obtained with the conventional silicate-based electrolyte.

Since the best results in the previous study were obtained with the more concentrated electrolyte, Cheng et al. investigated the use of an electrolyte consisting of 32 $g{\cdot}L^{-1}$ $NaAlO_2$ in the PEO treatment of alloy A356 [125]. However, the use of highly concentrated aluminate-based electrolytes can lead to instability and precipitation of the solution, which would be detrimental during PEO treatment. NaOH is a reactant that can improve the stability of the electrolyte, making it more durable, although if the amount of NaOH added is excessive, the electrolyte would become corrosive and detrimental to the PEO process. In this regard, the addition of 1 $g{\cdot}L^{-1}$, 5 $g{\cdot}L^{-1}$, and 10 $g{\cdot}L^{-1}$ NaOH to the electrolyte with 32 $g{\cdot}L^{-1}$ $NaAlO_2$ and its effects on the properties of the developed coatings were studied. Cheng et al. [125] observed that increasing the NaOH concentration from 1 to 5 $g{\cdot}L^{-1}$ increased the storage time of the electrolyte under good conditions from 1 day to at least 35 days, and this improvement was even greater when the NaOH concentration was 10 $g{\cdot}L^{-1}$. However, for the PEO process, the use of an electrolyte with such a high $NaAlO_2$ concentration requires the application of a PEO pre-treatment using an electrolyte with a lower $NaAlO_2$ concentration for the formation of the passive layer necessary for the initiation of the plasma discharges, which cannot form by itself when the electrolyte is too concentrated due to excessive dissolution of the metal substrate. Thus, although increasing the NaOH concentration improved the stability of the electrolyte, it also required a significantly longer pre-treatment, which would not be practical on an industrial scale due

to the increased time and energy costs. Therefore, the authors concluded that the electrolyte offering the best compromise between all requirements, both in terms of stability and coating performance, was the electrolyte composed of 32 $g \cdot L^{-1}$ $NaAlO_2$ and 5 $g \cdot L^{-1}$ NaOH.

Fernández-López et al. [4] developed and characterized the PEO coatings grown on a secondary cast Al-Si alloy (EN AC 46-500) using two novel aluminate-based electrolytes whose main component was $NaAlO_2$, while the effect of the addition of K_2TiF_6 was also evaluated. Compared to the uncoated cast Al-Si reference, the novel coatings showed a remarkable increase in hardness (with values around 1600 $HV_{0.025}$), as well as a high coating growth rate, corresponding to 1 $\mu m \cdot min^{-1}$ and 1.41 $\mu m \cdot min^{-1}$ for coatings obtained using the electrolytes without and with K_2TiF_6, respectively. The tribological analysis of the PEO coatings showed a very stable evolution of friction during the wear tests and a notable reduction of the wear rates compared to the base material (Figure 13). Moreover, the novel PEO coatings also provided an enhancement in corrosion protection compared to the uncoated reference. The most promising results, both in terms of tribology and corrosion protection, were obtained with the PEO coatings developed using the aluminate-based electrolyte containing K_2TiF_6 [4].

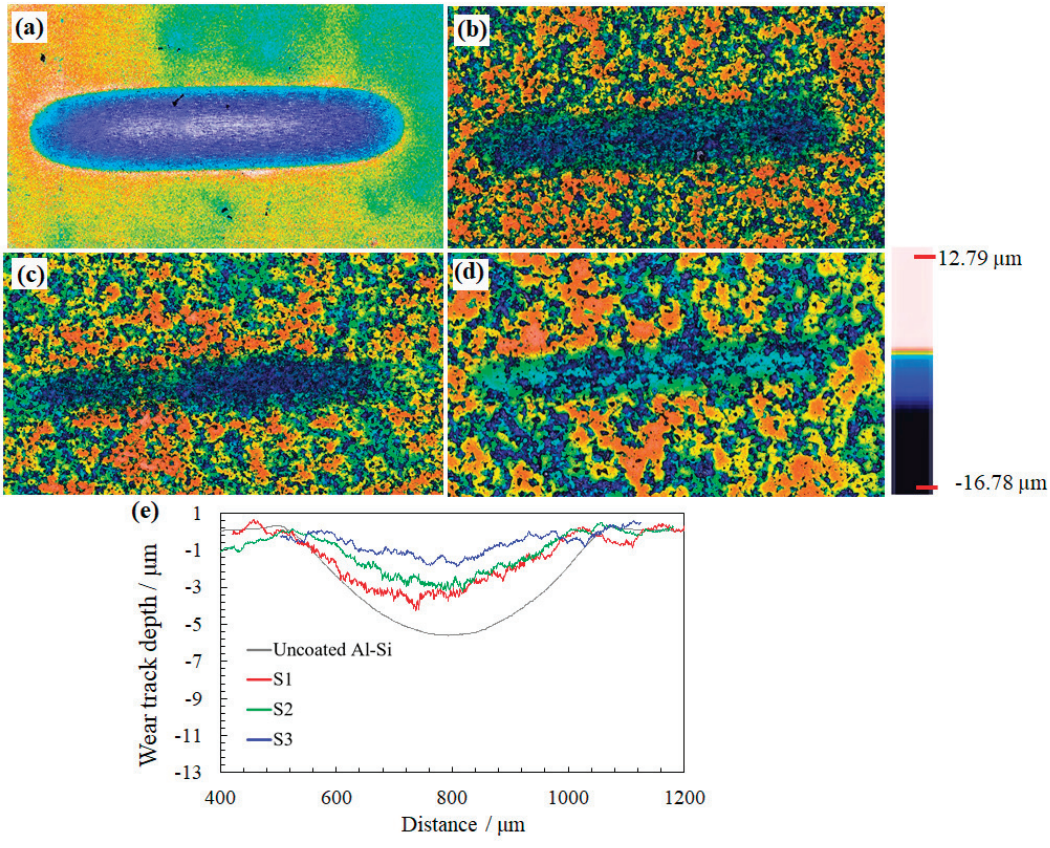

Figure 13. 3D displays of the wear tracks after the tribological tests: uncoated cast Al-Si alloy (**a**), PEO coatings developed using the aluminate-based electrolyte without thermal treatment (**b**) and with thermal treatment (**c**), the aluminate-based electrolyte additivated with K_2TiF_6 (**d**), and corresponding wear depth profiles along the whole width scar (**e**) [4]. Reprinted from Ceramics International; 47; P. Fernández-López, S.A. Alves, A. López-Ortega, J.T. San José-Lombera, R. Bayón; High performance tribological coatings on a secondary cast Al–Si alloy generated by Plasma Electrolytic Oxidation; 31238–31250; Copyright (2021), with permission from Elsevier.

The tribological behavior of PEO-coated high-Si cast Al-Si cylinder liners was recently investigated by Alves et al. [23]. The novel PEO coating was successfully grown on the hypereutectic cylinder liners obtained using the aluminate-based electrolyte formulated in [4]. It was thoroughly evaluated and compared with a PEO coating grown using a commercial silicate-based electrolyte, also additivated with BN nanoparticles. The findings revealed that the properties of the PEO coatings were drastically determined by the composition of the electrolyte used during the PEO processes. Thus, the PEO coatings developed using the aluminate-based electrolyte provided a significant improvement in the tribological performance for the studied application (i.e., lower wear damage and lower friction values), which was even comparable to the results provided by the cylinder liners made of cast iron, the conventional material.

Fernández-López et al. [14] successfully developed novel PEO coatings on a recycled cast Al-Si alloy with improved corrosion and tribocorrosion protection. For this purpose, a new aluminate-based electrolyte was developed, which also Na_2WO_4 and K_2TiF_6. All the elements present in the electrolyte were satisfactorily incorporated into the layer, resulting in a coating composed of several oxides, although its main crystalline component was α-Al_2O_3 (Figure 14). Another noteworthy finding was obtained with regard to the chemical composition of the two sub-layers that made up the coating, where the analysis revealed a higher Si content in the inner regions, which would come from the metallic substrate, while the higher Al content in the outer region of the coating would mainly come from the aluminate-based electrolyte. It was also observed that the innermost sublayer had a lower density than the outermost one, which would have been caused by the formation of a higher proportion of Si oxides, which are more porous than Al oxides, in the areas adjacent to the substrate [14].

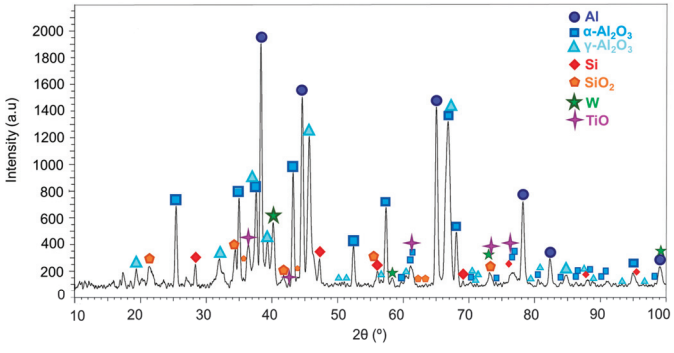

Figure 14. XRD pattern obtained for the PEO coating grown on a secondary cast Al-Si alloy [14]. Reprinted from Corrosion Science; 207; Patricia Fernández-López, Sofia A. Alves, Itziar Azpitarte, José T. San-José, Raquel Bayón; Corrosion and tribocorrosion protection of novel PEO coatings on a secondary cast Al-Si alloy: Influence of polishing and sol–gel sealing; 110548; Copyright (2022), with permission from Elsevier.

3.4. Development of High-Performance PEO Coatings on Cast Al-Si Alloys: Other Strategies

Various strategies have been pursued to develop coatings with optimal properties in combination with PEO technology, due to the difficulty of treating cast Al-Si alloys. Among the strategies pursued, pre-treatments, such as thermal, chemical, or electrochemical treatments, post-treatments, such as sealing or adding solid lubricants to the coating, as well as the incorporation of nanoparticles into the electrolyte have been, studied.

3.4.1. Pre- and Post-Treatments

Not only can the properties of a PEO coating be modified by its post-treatment, but the application of different treatments to the metallic substrate, prior to the deposition of the coating, will also have a significant influence on the growth and characteristics of the

coating. Heat treatments are one of the most widely performed pre-treatments, leading, among other effects, to the modification and/or homogenization of the microstructure, which will influence the growth rate of the PEO coating, since the different phases of the substrate possess different conducting behaviors. In this context, Krishtal et al. studied the influence of different heat treatments (i.e., T2 and T6), performed on cast Al-Si alloys, on the properties of the obtained PEO coatings. In general terms, it was determined that the coalescence and spheroidization of the silicon phases obtained by the heat treatment decreased the overall electrical resistance of the material, increased the current-carrying areas of the material, and promoted better adhesion between the coating and the matrix than between the coating and the silicon phases. The resulting changes accomplished with the heat treatments promoted the growth of coatings with increased thickness, higher adhesion to the substrate, greater hardness, and enhanced homogeneity and wear resistance [170].

The high silicon content of cast Al-Si alloys constitutes the major impediment to the establishment of a stable discharge regime at the beginning of the PEO process, which consequently promotes coatings with poorer mechanical properties. The application of a chemical etching is an effective strategy to selectively remove the surface of cast alloys with higher silicon content to promote a surface more electrically transparent. Li et al. [178] chemically etched a binary Al-Si12 alloy by immersing the samples in an acidic solution of HNO_3 and HF for 30 s. This pre-treatment favors the establishment of the micro-plasma regime during the process, not only improving the growth rate, but also decreasing energy consumption [178]. Indeed, it was also observed that the acid pre-treatment positively enhanced the evolution of the positive potential at the beginning of the process, increasing the coating growth rate from 0.50 $\mu m \cdot min^{-1}$ to 0.84 $\mu m \cdot min^{-1}$ [178]. Furthermore, surface etching promoted a decrease in amorphous SiO_2 and mullite in the coatings, as well as an improvement in the energy efficiency of the process, which decreased from 6.30 $kW \cdot h \cdot \mu m^{-1} \cdot m^{-2}$ to 4.36 $kW \cdot h \cdot \mu m^{-1} \cdot m^{-2}$. Another research also carried out an acid etching with the main aim of removing the detrimental β-Si phase contained in the skin layer of cast Al alloys with Si contents of 9 wt.%, 12 wt.%, and 15 wt.% [179]. The removal of the β-Si phase from the outermost region of the metallic substrates increased the coating growth rate and energy efficiency during early PEO stages. Extending etching time to 30 s notably improved the anticorrosion properties of the PEO coating on the Al-12Si alloy (Figure 15). Alloys with 60 s of acid etching displayed reduced Si content and larger surface pores, resembling pure Al's behavior within the initial 10 min of oxidation. However, large surface pores were filled by oxides after 30 min of PEO treatment, promoting denser layers.

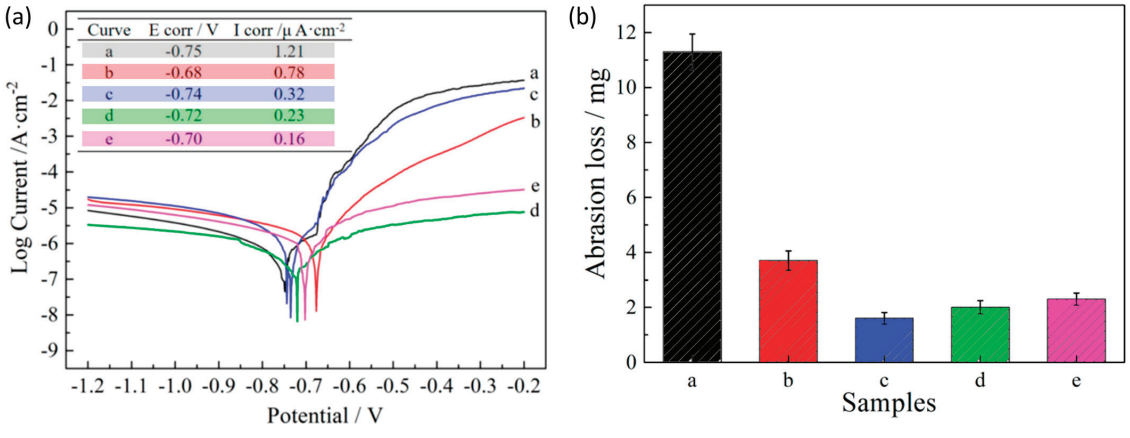

Figure 15. (**a**) Polarization curves and (**b**) weight loss evaluated for (a) the Al-12 Si matrix, (b–e) the Al-12 Si alloy subjected to etching durations of 0, 15, 30, and 60 s, respectively, followed by 30 min of PEO treatment.

The effect of refining the silicon phases on the properties of the developed PEO coating was also investigated [180]. For this purpose, a pre-treatment was carried out by adding Sr during the melting process in the fabrication of the cast Al-Si alloy. The pre-treatment effectively modified the silicon particles present in the aluminum matrix, decreasing their size and leading to a more homogeneous distribution of these phases. Consequently, the initial stage of the process was improved, leading to more uniform and thicker coatings. The final modified PEO-treated Al-Si alloys also showed a higher compactness and enhanced corrosion resistance, compared with the non-modified Al-Si substrates.

More demanding environments require the development of high-performance coatings, for which it could be necessary the application of more complex treatments. Mohedano et al. conducted a comprehensive study involving an anodizing pre-treatment and a sealing post-treatment applied to PEO coatings on an A356 alloy, using a silicate-based electrolyte and an AC power source [31]. The anodizing pre-treatment aimed to preserve the original substrate microstructure on cast A356 alloy. However, due to the presence of eutectic phases and intermetallic compounds, hindering the proper growth of the oxide layer, the resulting layers exhibited limitations. Nevertheless, the PEO coatings grown on the pre-anodized samples also exhibited the α-Al_2O_3 phase. The post-treatment involved the sealing of PEO coatings through the immersion of the coated samples on solutions containing salts of Ni (20 min of immersion), Ce (120 min of immersion), phosphonic acid (1440 min of immersion), and $KMnO_4$ (25 min of immersion). All the sealed samples exhibited not only an enhanced corrosion resistance compared with the unsealed PEO samples, but also improved hydrophobic performance. Shirani et al. developed a duplex coating by burnishing the surface of a PEO coating grown on a cast A356 alloy with graphite-MoS_2-Sb_2O_3 chameleon solid lubricant powder to reduce friction under tribological conditions [55]. The intrinsic morphology of the ceramic layer acted as an optimal supporter of the powder lubricant, while the solid powder applied reduced the surface roughness of the PEO coating. The composite coating exhibited an excellent improvement of the wear resistance, also decreasing the COF by one order of magnitude while showing high thermo-mechanical stability.

Despite the positive results obtained with a new coating developed on a recycled cast Al-Si alloy in terms of growth rate, surface appearance, and density, the typical defects of PEO layers grown on this type of substrates (i.e., high roughness and surface porosity) were still found [14]. In an attempt to improve these intrinsic limitations, the application of two post-treatments, surface polishing and the application of a sol–gel layer, was investigated. The investigated post-treatments proved to be effective in sealing pores and reducing surface roughness, resulting in a significant improvement in the corrosion and tribocorrosion performance of the coating. Nevertheless, the experimental results showed differences in corrosion and tribocorrosion resistance depending on the presence or type of post-treatment applied, and therefore the degradation mechanisms of the different types of materials under the two types of aggressive environments were considered (Figure 16). In particular, the PEO coating sealed with sol–gel proved to be more effective in terms of anti-corrosion resistance, while the polishing of the outer porous layer favored a better tribological behavior in corrosive environments [14].

3.4.2. Nanoparticles Addition

Adding nanoparticles to the electrolytes to be incorporated into the coating during the process was another strategy used to improve the properties of PEO coatings grown on cast Al-Si alloys.

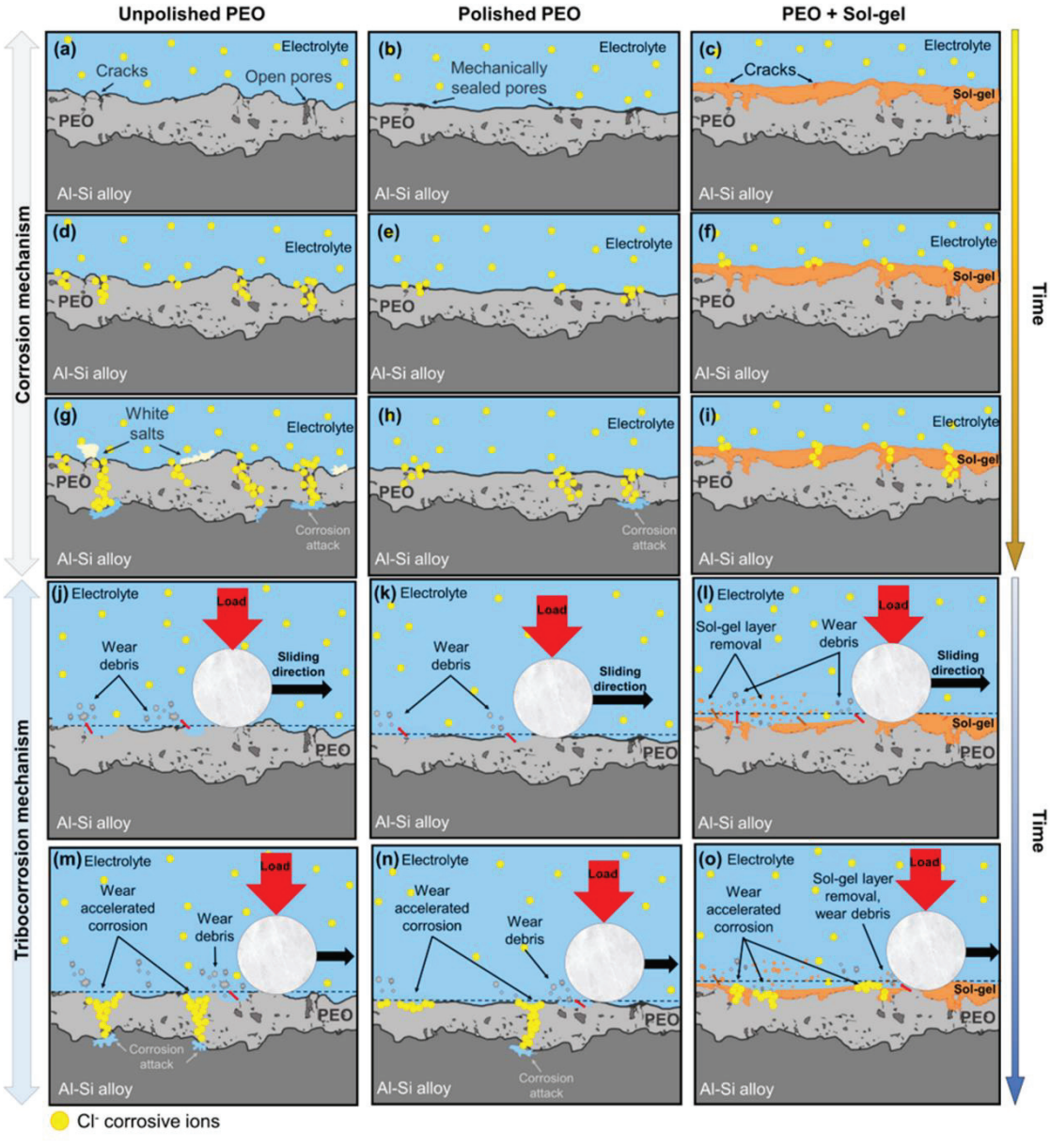

Figure 16. Corrosion (**a–i**) and tribocorrosion (**j–o**) mechanisms corresponding to the PEO coatings with different post-treatments [14]. Reprinted from Corrosion Science; 207; Patricia Fernández-López, Sofia A. Alves, Itziar Azpitarte, José T. San-José, Raquel Bayón; Corrosion and tribocorrosion protection of novel PEO coatings on a secondary cast Al-Si alloy: Influence of polishing and sol–gel sealing; 110548; Copyright (2022), with permission from Elsevier.

The incorporation of ZrO_2 into porous ceramic coatings on Al alloys improves tribological behavior by increasing the hardness of the coating and its corrosion resistance. Hu et al. added NH_4VO_3 and 200 nm ZrO_2 nanoparticles to a Na_2SiO_3 and NaOH electrolyte and studied the individual effect of each reagent on the properties of a coating grown on an Al-10Si alloy, obtained by pulsed bipolar polarization [181]. It was observed that the silicate-based electrolyte containing NH_4VO_3 resulted in an aesthetic and dark coating, but the coating exhibited poor tribological behavior. However, the addition of ZrO_2 nanoparticles to the electrolyte maintained the smooth and dark coating surface, but also reduced its surface roughness and improved its hardness, which enhanced its tribological behavior. In another study, ZrO_2 was newly incorporated into a silicate-based electrolyte with the aim of improving the properties of a PEO coating obtained on an Al-12Si cast piston [62]. In this case, it was observed that the ZrO_2 sol promoted further growth of the coating by weakening the inhibitory behavior of the Si phases while obtaining a coating with improved compactness. In addition, good thermal shock resistance results were also obtained, as the coating withstood 1000 thermal shock cycles without showing any surface cracks.

Besides ZrO_2 nanoparticles, the effect on the PEO treatment of an A356 alloy after the addition of titanium carbide (TiC) nanoparticles in two different electrolytes, containing $N_4P_2O_7$- and Na_2SiO_3, was also studied [182]. These nanoparticles, with a size below 200 nm, were incorporated by an inert mechanism, without any chemical reaction during the process. Polunin et al. achieved excellent results with the addition of TiC nanoparticles: not only the hardness and elastic modulus of the coatings were increased, but also the wear and corrosion resistance were improved by a factor of 3 and 10, respectively [182]. The effect of SiO_2 nanoparticles, with average sizes of 48 nm and 100 nm, on the PEO treatment of an A361 Al-Si alloy was further investigated [183]. The SiO_2 nanoparticles of smaller size, 48 nm, were more effectively incorporated into the PEO coatings, which also showed a finer microstructure. Compared to the coatings developed with the electrolyte without nanoparticles, the additivated electrolytes led to an improved oxidability during the processes, which promoted the development of coatings with increased thickness, which also showed a significant improvement in wear and thermal resistance.

4. Conclusions

Cast Al-Si alloys are a versatile material of great interest for many applications, highlighting their use in the automotive industry. However, their applications require the fulfillment of demanding requirements, which often require the surface enhancement of these Al alloys. In this context, a thorough understanding of the capabilities, limitations, and comparative advantages of PEO over conventional treatments such as anodizing is required.

The present work constitutes a comprehensive review concerning the development of ceramic coatings on cast Al-Si alloys using plasma electrolytic oxidation (PEO) technology. While anodizing has long been an established practice for the modification of Al alloys, PEO has emerged as a promising technology due to its distinctive characteristics, including the ability to produce thicker, more adherent coatings with increased wear and corrosion resistance, thereby positioning it as an attractive alternative. Furthermore, PEO is a more versatile technology, with a lower dependence on the substrate composition and morphology. These characteristics are particularly relevant for the surface treatment of cast Al-Si alloys, whose inherent complex microstructure has significantly hindered their anodizing and, consequently, requires novel solutions to meet the challenges arising from their singular morphology. The understanding behind the details of PEO technology, covering the coating growth mechanisms and the critical process parameters, highlights the significance of substrate composition, electrolyte formulation, and power supply selection for achieving optimal results. The systematic screening of the electrolyte types (including silicate-, phosphate-, and aluminate-based formulations), has led to a better understanding of the suitability of the development of PEO coatings for cast Al-Si alloys, with each type of formulation offering different advantages and challenges.

Innovative strategies for further enhancing PEO coatings on cast Al-Si alloys have been also discussed in this review. The analysis of the results obtained after the application of different pre- and post-treatments and the dispersion of nanoparticles into the electrolytes highlighted their potential for the optimization of the PEO coatings performance, while also addressing some of the inherent challenges associated with these coatings.

To conclude, PEO technology is proving to be a promising path for the improvement of the performance of cast Al-Si alloys, which are widely employed in the automotive sector, and a growing number of scientific publications based on this subject have been published in recent years. The identification of the fundamental understanding of PEO technology, the discussion about the influence of the chemical composition of the electrolyte, and the analysis of some innovative strategies for the surface treatment of these materials carried out in this work could provide a basis for the ongoing research efforts.

5. Future Perspective and Remarks

This comprehensive review underscores the need for continued research and innovation in the field of surface modification of cast Al-Si alloys. While the introduction of PEO technology has shown great potential, there are still interesting avenues for further exploration. Further research should prioritize the optimization of PEO coatings to address the specific challenges associated with cast Al-Si alloys. This requires a deeper understanding of the interaction between the composition of the electrolyte, process parameters, and substrate morphology in order to develop coatings with improved performance.

To summarize, while PEO technology offers significant opportunities for enhancing cast Al-Si alloys, continued interdisciplinary collaboration and exploration are essential to achieve optimal coatings that meet the needs of diverse applications in the automotive sector and beyond.

Funding: The authors would like to acknowledge the Department of Education, Linguistic Policy and Culture of the Basque Government for its support through the grant "Programa Predoctoral de Formación de Personal Investigador No Doctor (2022–2023)" awarded to the first author.

Institutional Review Board Statement: Not applicable.

Informed Consent Statement: Not applicable.

Data Availability Statement: Data are contained within the article.

Conflicts of Interest: The authors declare no conflicts of interest.

References

1. Robles Hernandez, F.C.; Herrera Ramírez, J.M.; Mackay, R. *Al-Si Alloys: Automotive, Aeronautical, and Aerospace Applications*; Springer: Berlin/Heidelberg, Germany, 2017; ISBN 9783319583792.
2. Ervina Efzan, M.N.; Kong, H.J.; Kok, C.K. Review: Effect of Alloying Element on Al-Si Alloys. *Adv. Mater. Res.* **2014**, *845*, 355–359. [CrossRef]
3. Gulec, A.E.; Gencer, Y.; Tarakci, M. The Characterization of Oxide Based Ceramic Coating Synthesized on Al-Si Binary Alloys by Microarc Oxidation. *Surf. Coat. Technol.* **2015**, *269*, 100–107. [CrossRef]
4. Fernández-López, P.; Alves, S.A.; López-Ortega, A.; San José-Lombera, J.T.; Bayón, R. High Performance Tribological Coatings on a Secondary Cast Al–Si Alloy Generated by Plasma Electrolytic Oxidation. *Ceram. Int.* **2021**, *47*, 31238–31250. [CrossRef]
5. Glazoff, M.V.; Khvan, A.V.; Zolotorevsky, V.S.; Belov, N.A.; Dinsdale, A.T. *Industrial and Perspective Casting Alloys*; Elsevier: Amsterdam, The Netherlands, 2019; ISBN 9780128118054.
6. Zamani, M. Al-Si Cast Alloys—Microstructure and Mechanical Properties at Ambient and Elevated Temperature Al-Si Cast Alloys—Microstructure and Mechanical Properties at Ambient and Elevated Temperature. Ph.D. Thesis, Jönköping University, Jonkoping, Sweden, 2015.
7. Kumar, L.; Jang, J.C.; Yu, H.; Shin, K.S. Effect of Secondary Phase on Mechanical and Thermal Conductivity of Al-Si-XFe-Mg-YCu-Mn Die Casting Alloys. *Mater. Lett.* **2022**, *314*, 131889. [CrossRef]
8. Shabestari, S.G. The Effect of Iron and Manganese on the Formation of Intermetallic Compounds in Aluminum-Silicon Alloys. *Mater. Sci. Eng. A* **2004**, *383*, 289–298. [CrossRef]
9. Otani, L.B.; Soyama, J.; Zepon, G.; Costa e Silva, A.; Kiminami, C.S.; Botta, W.J.; Bolfarini, C. Predicting the Formation of Intermetallic Phases in the Al-Si-Fe System with Mn Additions. *J. Phase Equilibria Diffus.* **2017**, *38*, 298–304. [CrossRef]

10. Cao, X.; Saunders, N.; Campbell, J. Effect of Iron and Manganese Contents on Convection-Free Precipitation and Sedimentation of Primary α-Al(FeMn)Si Phase in Liquid Al-11.5Si-0.4Mg Alloy. *J. Mater. Sci.* **2004**, *39*, 2303–2314. [CrossRef]
11. Rams, J.; Torres, B. Casting Aluminum Alloys. *Encycl. Mater. Met. Alloy.* **2021**, *1*, 123–131. [CrossRef]
12. Berlanga-Labari, C.; Biezma-Moraleda, M.V.; Rivero, P.J. Corrosion of Cast Aluminum Alloys: A Review. *Metals* **2020**, *10*, 1384. [CrossRef]
13. Yu, W.; Zhao, H.; Wang, L.; Guo, Z.; Xiong, S. The Influence of T6 Treatment on Fracture Behavior of Hypereutectic Al-Si HPDC Casting Alloy. *J. Alloys Compd.* **2018**, *731*, 444–451. [CrossRef]
14. Fernández-López, P.; Alves, S.A.; Azpitarte, I.; San-José, J.T.; Bayón, R. Corrosion and Tribocorrosion Protection of Novel PEO Coatings on a Secondary Cast Al-Si Alloy: Influence of Polishing and Sol-Gel Sealing. *Corros. Sci.* **2022**, *207*, 110548. [CrossRef]
15. Wang, D.; Zhang, X.; Nagaumi, H.; Li, X.; Zhang, H. 3D Morphology and Growth Mechanism of Cubic α-Al(FeMnCr)Si Intermetallic in an Al-Si Cast Alloy. *Mater. Lett.* **2020**, *277*, 128384. [CrossRef]
16. Xue, W.; Wang, C.; Li, Y.; Chen, R.; Zhang, T. Analyses of Microarc Oxidation Coatings Formed on Si-Containing Cast Aluminum Alloy in Silicate Solution. *ISIJ Int.* **2002**, *42*, 1273–1277. [CrossRef]
17. Peppas, A.; Kollias, K.; Dragatogiannis, D.A.; Charitidis, C.A. Sustainability Analysis of Aluminium Hot Forming and Quenching Technology for Lightweight Vehicles Manufacturing. *Int. J. Thermofluids* **2021**, *10*, 100082. [CrossRef]
18. Li, X.; Nie, X.; Wang, L.; Northwood, D.O. Corrosion Protection Properties of Anodic Oxide Coatings on an Al-Si Alloy. *Surf. Coat. Technol.* **2005**, *200*, 1994–2000. [CrossRef]
19. Gonçalves, M.; Monteiro, H.; Iten, M. Life Cycle Assessment Studies on Lightweight Materials for Automotive Applications—An Overview. *Energy Rep.* **2022**, *8*, 338–345. [CrossRef]
20. Luo, A.A.; Sachdev, A.K.; Apelian, D. Alloy Development and Process Innovations for Light Metals Casting. *J. Mater. Process. Technol.* **2022**, *306*, 117606. [CrossRef]
21. Zhang, W.; Xu, J. Advanced Lightweight Materials for Automobiles: A Review. *Mater. Des.* **2022**, *221*, 110994. [CrossRef]
22. Javidani, M.; Larouche, D. Application of Cast Al-Si Alloys in Internal Combustion Engine Components. *Int. Mater. Rev.* **2014**, *59*, 132–158. [CrossRef]
23. Alves, S.A.; Fernández-Lopéz, P.; Lopéz-Ortega, A.; Fernández, X.; Quintana, I.; San-José, J.T.; Bayón, R. Enhanced Tribological Performance of Cylinder Liners Made of Cast Aluminum Alloy with High Silicon Content through Plasma Electrolytic Oxidation. *Surf. Coat. Technol.* **2022**, *433*, 128146. [CrossRef]
24. Abdulwahab, A.; Shrestha, S.; Brooks, P.; Barton, D. *Thermal Performance of Peo Coated Lightweight Brake Rotors Compared With Grey Cast Iron*; International Federation of Automotive Engineering Societies (FISITA): Maastricht, The Netherlands, 2014; pp. 13–15.
25. Li, K.; Zhang, G.; Yi, A.; Zhu, W.; Liao, Z.; Chen, K.; Li, W.; Luo, Z. Effects of Matrix Silicon Content on the Plasma Electrolytic Oxidation of Al-Si Alloys Using Different Power Modes. *Crystals* **2022**, *12*, 123. [CrossRef]
26. Shakil, S.I.; Hadadzadeh, A.; Shalchi Amirkhiz, B.; Pirgazi, H.; Mohammadi, M.; Haghshenas, M. Additive Manufactured versus Cast AlSi10Mg Alloy: Microstructure and Micromechanics. *Results Mater.* **2021**, *10*, 100178. [CrossRef]
27. Yu, H.; Dong, Q.; Chen, Y.; Chen, C. Influence of Silicon on Growth Mechanism of Micro-Arc Oxidation Coating on Cast Al–Si Alloy. *R. Soc. Open Sci.* **2018**, *5*, 172428. [CrossRef] [PubMed]
28. Rogov, A.B.; Lyu, H.; Matthews, A.; Yerokhin, A. AC Plasma Electrolytic Oxidation of Additively Manufactured and Cast AlSi12 Alloys. *Surf. Coat. Technol.* **2020**, *399*, 126116. [CrossRef]
29. Sabatini, G.; Ceschini, L.; Martini, C.; Williams, J.A.; Hutchings, I.M. Improving Sliding and Abrasive Wear Behaviour of Cast A356 and Wrought AA7075 Aluminium Alloys by Plasma Electrolytic Oxidation. *Mater. Des.* **2010**, *31*, 816–828. [CrossRef]
30. Yoshida, H.; Uchida, H. Heat Treatment of Aluminum Alloys. *Keikinzoku/J. Jpn. Inst. Light Met.* **1995**, *45*, 41–55. [CrossRef]
31. Mohedano, M.; Matykina, E.; Arrabal, R.; Mingo, B.; Pardo, A. PEO of Pre-Anodized Al-Si Alloys: Corrosion Properties and Influence of Sealings. *Appl. Surf. Sci.* **2015**, *346*, 57–67. [CrossRef]
32. Liang, Z.X.; Ye, B.; Zhang, L.; Wang, Q.G.; Yang, W.Y.; Wang, Q.D. A New High-Strength and Corrosion-Resistant Al-Si Based Casting Alloy. *Mater. Lett.* **2013**, *97*, 104–107. [CrossRef]
33. Yerokhin, A.; Khan, R.H.U. Anodising of Light Alloys. *Surf. Eng. Light Alloy. Alum. Magnes. Titan. Alloy.* **2010**, 83–109. [CrossRef]
34. He, J.; Cai, Q.Z.; Luo, H.H.; Yu, L.; Wei, B.K. Influence of Silicon on Growth Process of Plasma Electrolytic Oxidation Coating on Al-Si Alloy. *J. Alloys Compd.* **2009**, *471*, 395–399. [CrossRef]
35. Nagumothu, R.B.; Thangavelu, A.; Nair, A.M.; Sukumaran, A.; Anjilivelil, T. Development of Black Corrosion-Resistant Ceramic Oxide Coatings on AA7075 by Plasma Electrolytic Oxidation. *Trans. Indian Inst. Met.* **2019**, *72*, 47–53. [CrossRef]
36. Akbar, A.; Adnan Qaiser, M.; Hussain, A.; Ali Mustafa, R.; Xiong, D.; Adnan Akbar, E. Surface Modification of Aluminum Alloy 6060 through Plasma Electrolytic Oxidation. *Int. J. Eng. Work. Kambohwell Publ. Enterp.* **2017**, *4*, 114–123.
37. Jiang, B.L.; Wang, Y.M. Plasma Electrolytic Oxidation Treatment of Aluminium and Titanium Alloys. *Surf. Eng. Light Alloy. Alum. Magnes. Titan. Alloy.* **2010**, 110–154. [CrossRef]
38. Aliofkhazraei, M.; Macdonald, D.D.; Matykina, E.; Parfenov, E.V.; Egorkin, V.S.; Curran, J.A.; Troughton, S.C.; Sinebryukhov, S.L.; Gnedenkov, S.V.; Lampke, T.; et al. Review of Plasma Electrolytic Oxidation of Titanium Substrates: Mechanism, Properties, Applications and Limitations. *Appl. Surf. Sci. Adv.* **2021**, *5*, 100121. [CrossRef]
39. Fattah-alhosseini, A.; Chaharmahali, R.; Babaei, K. Effect of Particles Addition to Solution of Plasma Electrolytic Oxidation (PEO) on the Properties of PEO Coatings Formed on Magnesium and Its Alloys: A Review. *J. Magnes. Alloy.* **2020**, *8*, 799–818. [CrossRef]

40. Guo, Y.; Rogov, A.; Hird, A.; Mingo, B.; Matthews, A.; Yerokhin, A. Plasma Electrolytic Oxidation of Magnesium by Sawtooth Pulse Current. *Surf. Coat. Technol.* **2022**, *429*, 127938. [CrossRef]
41. Apelfeld, A.V.; Betsofen, S.Y.; Borisov, A.M.; Vladimirov, B.V.; Savushkina, S.V.; Knyazev, E.V. Stabilization of the High-Temperature Phases in Ceramic Coatings on Zirconium Alloy Produced by Plasma Electrolytic Oxidation. *J. Phys. Conf. Ser.* **2016**, *748*, 2–7. [CrossRef]
42. Babaei, K.; Fattah-alhosseini, A.; Chaharmahali, R. A Review on Plasma Electrolytic Oxidation (PEO) of Niobium: Mechanism, Properties and Applications. *Surf. Interfaces* **2020**, *21*, 100719. [CrossRef]
43. Antonio, R.F.; Rangel, E.C.; Mas, B.A.; Duek, E.A.R.; Cruz, N.C. Growth of Hydroxyapatite Coatings on Tantalum by Plasma Electrolytic Oxidation in a Single Step. *Surf. Coat. Technol.* **2019**, *357*, 698–705. [CrossRef]
44. Wang, Y.; Jiang, Z.; Yao, Z. Effects of Na_2WO_4 and Na_2SiO_3 Additives in Electrolytes on Microstructure and Properties of PEO Coatings on Q235 Carbon Steel. *J. Alloys Compd.* **2009**, *481*, 725–729. [CrossRef]
45. Wang, Y.; Jiang, Z.; Yao, Z. Preparation and Properties of Ceramic Coating on Q235 Carbon Steel by Plasma Electrolytic Oxidation. *Curr. Appl. Phys.* **2009**, *9*, 1067–1071. [CrossRef]
46. Malinovschi, V.; Marin, A.; Mihalache, M.; Iosub, I. Preparation and Characterization of Coatings on Carbon Steel Obtained by PEO in Silicate/Carbonate Electrolyte. *Surf. Coat. Technol.* **2016**, *296*, 96–103. [CrossRef]
47. Wu, T.; Blawert, C.; Zheludkevich, M.L. Influence of Secondary Phases of $AlSi_9Cu_3$ Alloy on the Plasma Electrolytic Oxidation Coating Formation Process. *J. Mater. Sci. Technol.* **2020**, *50*, 75–85. [CrossRef]
48. Pezzato, L.; Brunelli, K.; Dabalà, M. Corrosion Properties of Plasma Electrolytic Oxidation Coated AA7075 Treated Using an Electrolyte Containing Lanthanum-Salts. *Surf. Interface Anal.* **2016**, *48*, 729–738. [CrossRef]
49. Martin, J.; Melhem, A.; Shchedrina, I.; Duchanoy, T.; Nominé, A.; Henrion, G.; Czerwiec, T.; Belmonte, T. Effects of Electrical Parameters on Plasma Electrolytic Oxidation of Aluminium. *Surf. Coat. Technol.* **2013**, *221*, 70–76. [CrossRef]
50. An, L.Y.; Ying, M.A.; Yan, X.X.; Sheng WA, N.G.; Wang, Z.Y. Effects of Electrical Parameters and Their Interactions on Plasma Electrolytic Oxidation Coatings on Aluminum Substrates. *Trans. Nonferrous Met. Soc. China (Engl. Ed.)* **2020**, *30*, 883–895. [CrossRef]
51. Dehnavi, V.; Liu, X.Y.; Luan, B.L.; Shoesmith, D.W.; Rohani, S. Phase Transformation in Plasma Electrolytic Oxidation Coatings on 6061 Aluminum Alloy. *Surf. Coat. Technol.* **2014**, *251*, 106–114. [CrossRef]
52. Sieber, M.; Simchen, F.; Morgenstern, R.; Scharf, I.; Lampke, T. Plasma Electrolytic Oxidation of High-Strength Aluminium Alloys—Substrate Effect on Wear and Corrosion Performance. *Metals* **2018**, *8*, 356. [CrossRef]
53. del Olmo, R.; Mohedano, M.; Visser, P.; Matykina, E.; Arrabal, R. Flash-PEO Coatings Loaded with Corrosion Inhibitors on AA2024. *Surf. Coat. Technol.* **2020**, *402*, 126317. [CrossRef]
54. Xie, H.J.; Cheng, Y.L.; Li, S.X.; Cao, J.H.; Li, C.A.O. Wear and Corrosion Resistant Coatings on Surface of Cast A356 Aluminum Alloy by Plasma Electrolytic Oxidation in Moderately Concentrated Aluminate Electrolytes. *Trans. Nonferrous Met. Soc. China (Engl. Ed.)* **2017**, *27*, 336–351. [CrossRef]
55. Shirani, A.; Joy, T.; Rogov, A.; Lin, M.; Yerokhin, A.; Mogonye, J.E.; Korenyi-Both, A.; Aouadi, S.M.; Voevodin, A.A.; Berman, D. PEO-Chameleon as a Potential Protective Coating on Cast Aluminum Alloys for High-Temperature Applications. *Surf. Coatings Technol.* **2020**, *397*, 126016. [CrossRef]
56. Wang, R. High Current Plasma Electrolytic Oxidation Coating Processes for Wear and Corrosion Prevention of Al 2024. *Electron. Theses Diss.* **2018**, *116*, 7405.
57. Clyne, T.W.; Troughton, S.C. A Review of Recent Work on Discharge Characteristics during Plasma Electrolytic Oxidation of Various Metals. *Int. Mater. Rev.* **2019**, *64*, 127–162. [CrossRef]
58. Pezzato, L.; Rigon, M.; Martucci, A.; Brunelli, K.; Dabalà, M. Plasma Electrolytic Oxidation (PEO) as Pre-Treatment for Sol-Gel Coating on Aluminum and Magnesium Alloys. *Surf. Coat. Technol.* **2019**, *366*, 114–123. [CrossRef]
59. Li, T.; Li, L.; Qi, J.; Chen, F. Corrosion Protection of Ti6Al4V by a Composite Coating with a Plasma Electrolytic Oxidation Layer and Sol-Gel Layer Filled with Graphene Oxide. *Prog. Org. Coat.* **2020**, *144*. [CrossRef]
60. Phuong, N.V.; Fazal, B.R.; Moon, S. Cerium- and Phosphate-Based Sealing Treatments of PEO Coated AZ31 Mg Alloy. *Surf. Coat. Technol.* **2017**, *309*, 86–95. [CrossRef]
61. Curran, J.A.; Kalkanci, H.; Magurova, Y.; Clyne, T.W. Mullite-Rich Plasma Electrolytic Oxide Coatings for Thermal Barrier Applications. *Surf. Coat. Technol.* **2007**, *201*, 8683–8687. [CrossRef]
62. Wang, P.; Li, J.; Guo, Y.; Wang, J.; Yang, Z.; Liang, M. Effect of Zirconia Sol on the Microstructures and Thermal-Protective Properties of PEO Coating on a Cast Al-12Si Piston Alloy. *J. Alloys Compd.* **2016**, *657*, 703–710. [CrossRef]
63. Dou, B.; Wang, Y.; Zhang, T.; Liu, B.; Shao, Y.; Meng, G.; Wang, F. Growth Behaviors of Layered Double Hydroxide on Microarc Oxidation Film and Anti-Corrosion Performances of the Composite Film. *J. Electrochem. Soc.* **2016**, *163*, C917–C927. [CrossRef]
64. Lee, J.H.; Jung, K.H.; Kim, S.J. Characterization of Ceramic Oxide Coatings Prepared by Plasma Electrolytic Oxidation Using Pulsed Direct Current with Different Duty Ratio and Frequency. *Appl. Surf. Sci.* **2020**, *516*, 146049. [CrossRef]
65. Stojadinović, S.; Radić, N.; Grbić, B.; Maletić, S.; Stefanov, P.; Pačevski, A.; Vasilić, R. Structural, Photoluminescent and Photocatalytic Properties of TiO2: Eu 3+ Coatings Formed by Plasma Electrolytic Oxidation. *Appl. Surf. Sci.* **2016**, *370*, 218–228. [CrossRef]
66. Tadić, N.; Stojadinović, S.; Radić, N.; Grbić, B.; Vasilić, R. Characterization and Photocatalytic Properties of Tungsten Doped TiO_2 Coatings on Aluminum Obtained by Plasma Electrolytic Oxidation. *Surf. Coat. Technol.* **2016**, *305*, 192–199. [CrossRef]

67. Chen, Z.; Yan, X.; Chang, Y.; Xie, S.; Ma, W.; Zhao, G.; Liao, H.; Fang, H.; Liu, M.; Cai, D. Effect of Polarization Voltage on the Surface Componentization and Biocompatibility of Micro-Arc Oxidation Modified Selective Laser Melted Ti6Al4V. *Mater. Res. Express* **2019**, *6*, 086425. [CrossRef]
68. Yeung, W.K.; Sukhorukova, I.V.; Shtansky, D.V.; Levashov, E.A.; Zhitnyak, I.Y.; Gloushankova, N.A.; Kiryukhantsev-Korneev, P.V.; Petrzhik, M.I.; Matthews, A.; Yerokhin, A. Characteristics and in Vitro Response of Thin Hydroxyapatite-Titania Films Produced by Plasma Electrolytic Oxidation of Ti Alloys in Electrolytes with Particle Additions. *RSC Adv.* **2016**, *6*, 12688–12698. [CrossRef] [PubMed]
69. Fattah-alhosseini, A.; Molaei, M.; Nouri, M.; Babaei, K. Antibacterial Activity of Bioceramic Coatings on Mg and Its Alloys Created by Plasma Electrolytic Oxidation (PEO): A Review. *J. Magnes. Alloy.* **2022**, *10*, 81–96. [CrossRef]
70. Gnedenkov, S.V.; Sinebryukhov, S.L.; Zavidnaya, A.G.; Egorkin, V.S.; Puz', A.V.; Mashtalyar, D.V.; Sergienko, V.I.; Yerokhin, A.L.; Matthews, A. Composite Hydroxyapatite-PTFE Coatings on Mg-Mn-Ce Alloy for Resorbable Implant Applications via a Plasma Electrolytic Oxidation-Based Route. *J. Taiwan Inst. Chem. Eng.* **2014**, *45*, 3104–3109. [CrossRef]
71. Cordeiro, J.M.; Nagay, B.E.; Ribeiro, A.L.R.; da Cruz, N.C.; Rangel, E.C.; Fais, L.M.G.; Vaz, L.G.; Barão, V.A.R. Functionalization of an Experimental Ti-Nb-Zr-Ta Alloy with a Biomimetic Coating Produced by Plasma Electrolytic Oxidation. *J. Alloys Compd.* **2019**, *770*, 1038–1048. [CrossRef]
72. Sluginov, N.P. On Luminous Phenomen, Observed in Liquids during Electrolysis. *Russ. Phys. Chem. Soc* **1880**, *12*, 193–203.
73. Snezhko, L.A.; Beskrovnyi, I.M.; Nevkrytyi, V.I.; Chernenko, V.I. Impulsnyi Rezhim Dlia Poluchenіia Silikatnykh Pokrytii v Iskrovom Razriade. *Zashch. Met.* **1980**, *16*, 365.
74. Markov, G.A.; Mironova, M.K.; Potapova, O.G.; Tatarchuk, O.A. Structure of Anodic Films Obtained by Micro Arc Oxidation of Aluminum. *Izv. Akad. Nauk SSSR Neorg. Mater.* **1983**, *19*, 1110–1113.
75. Malyshev, V.N.; Bulychev, S.I.; Markov, G.A. Physical and Mechanical Characteristics and Wear Resistance of Coatings Formed by Microarc Oxidation Method, Physika i Khimija Obrab. *Fiz. Khim. Obrab. Mater.* **1985**, *1*, 82–87.
76. Dittrich, K.-H.; Krysmann, W.; Kurze, P.; Scheneider, H.G. Structure and Properties of ANOF Layers. *Cryst. Res. Technol.* **1984**, *19*, 93–99. [CrossRef]
77. Krysmann, W.; Kurze, P.; Dittrich, K.-H.; Schneider, H.G. Process Characteristics and Parameters of Anodic Oxidation by Spark Discharge (ANOF). *Cryst. Res. Technol.* **1984**, *19*, 973–979. [CrossRef]
78. Yerokhin, A.L.; Voevodin, A.A.; Lyubimov, V.V.; Zabinski, J.; Donley, M. Plasma Electrolytic Fabrication of Oxide Ceramic Surface Layers for Tribotechnical Purposes on Aluminium Alloys. *Surf. Coatings Technol.* **1998**, *110*, 140–146. [CrossRef]
79. Yerokhin, A.L.; Nie, X.; Leyland, A.; Matthews, A.; Dowey, S.J. Plasma Electrolysis for Surface Engineering. *Surf. Coatings Technol.* **1999**, *122*, 73–93. [CrossRef]
80. Dehnavi, V.; Luan, B.L.; Shoesmith, D.W.; Liu, X.Y.; Rohani, S. Effect of Duty Cycle and Applied Current Frequency on Plasma Electrolytic Oxidation (PEO) Coating Growth Behavior. *Surf. Coatings Technol.* **2013**, *226*, 100–107. [CrossRef]
81. Chaharmahali, R.; Fattah-alhosseini, A.; Babaei, K. Surface Characterization and Corrosion Behavior of Calcium Phosphate (Ca-P) Base Composite Layer on Mg and Its Alloys Using Plasma Electrolytic Oxidation (PEO): A Review. *J. Magnes. Alloy.* **2021**, *9*, 21–40. [CrossRef]
82. Tang, M.; Li, W.; Liu, H.; Zhu, L. Influence of K 2TiF 6 in Electrolyte on Characteristics of the Microarc Oxidation Coating on Aluminum Alloy. *Curr. Appl. Phys.* **2012**, *12*, 1259–1265. [CrossRef]
83. Simchen, F.; Sieber, M.; Lampke, T. Electrolyte Influence on Ignition of Plasma Electrolytic Oxidation Processes on Light Metals. *Surf. Coatings Technol.* **2017**, *315*, 205–213. [CrossRef]
84. Zhang, P.; Nie, X.; Hu, H.; Liu, Y. TEM Analysis and Tribological Properties of Plasma Electrolytic Oxidation (PEO) Coatings on a Magnesium Engine AJ62 Alloy. *Surf. Coatings Technol.* **2010**, *205*, 1508–1514. [CrossRef]
85. Pan, J.; Wen, Y.; Wang, L.; Wu, Z.; Dong, H.; Ye, Z. Doping and Defects: The Coloring Mechanism of Black Plasma Electrolytic Oxidation (PEO) Films on Aluminum Alloys. *Surf. Coatings Technol.* **2022**, *431*, 128035. [CrossRef]
86. Arunnellaiappan, T.; Rama Krishna, L.; Anoop, S.; Uma Rani, R.; Rameshbabu, N. Fabrication of Multifunctional Black PEO Coatings on AA7075 for Spacecraft Applications. *Surf. Coatings Technol.* **2016**, *307*, 735–746. [CrossRef]
87. Rogov, A.B.; Huang, Y.; Shore, D.; Matthews, A.; Yerokhin, A. Toward Rational Design of Ceramic Coatings Generated on Valve Metals by Plasma Electrolytic Oxidation: The Role of Cathodic Polarisation. *Ceram. Int.* **2021**, *47*, 34137–34158. [CrossRef]
88. Tsai, D.S.; Chou, C.C. Review of the Soft Sparking Issues in Plasma Electrolytic Oxidation. *Metals* **2018**, *8*, 105. [CrossRef]
89. Gao, Y.; Yerokhin, A.; Matthews, A. Effect of Current Mode on PEO Treatment of Magnesium in Ca- and P-Containing Electrolyte and Resulting Coatings. *Appl. Surf. Sci.* **2014**, *316*, 558–567. [CrossRef]
90. Kaseem, M.; Yang, H.W.; Ko, Y.G. Toward a Nearly Defect-Free Coating via High-Energy Plasma Sparks. *Sci. Rep.* **2017**, *7*, 2378. [CrossRef]
91. Rogov, A.B.; Matthews, A.; Yerokhin, A. Role of Cathodic Current in Plasma Electrolytic Oxidation of Al: A Quantitative Approach to in-Situ Evaluation of Cathodically Induced Effects. *Electrochim. Acta* **2019**, *317*, 221–231. [CrossRef]
92. Mohedano, M.; Arrabal, R.; Mingo, B.; Pardo, A.; Matykina, E. Role of Particle Type and Concentration on Characteristics of PEO Coatings on AM50 Magnesium Alloy. *Surf. Coatings Technol.* **2018**, *334*, 328–335. [CrossRef]
93. Aliasghari, S.; Rogov, A.; Skeldon, P.; Zhou, X.; Yerokhin, A.; Aliabadi, A.; Ghorbani, M. Plasma Electrolytic Oxidation and Corrosion Protection of Friction Stir Welded AZ31B Magnesium Alloy-Titanium Joints. *Surf. Coatings Technol.* **2020**, *393*, 125838. [CrossRef]

94. Urban, M. Plasma Electrolytic Oxidation of Magnesium Alloys for Automotive Applications. Ph.D. Thesis, The University of Manchester, Manchester, UK, 2014; p. 116.
95. Hussein, R.O.; Nie, X.; Northwood, D.O. An Investigation of Ceramic Coating Growth Mechanisms in Plasma Electrolytic Oxidation (PEO) Processing. *Electrochim. Acta* **2013**, *112*, 111–119. [CrossRef]
96. Li, Q.; Liang, J.; Wang, Q. Plasma Electrolytic Oxidation Coatings on Lightweight Metals. *Mod. Surf. Eng. Treat.* **2013**. [CrossRef]
97. Zhu, Z.; Tu, W.; Cheng, Y.; Cheng, Y. The Formation of Metallic W and Amorphous Phase in the Plasma Electrolytic Oxidation Coatings on an Al Alloy from Tungstate-Containing Electrolyte. *Surf. Coatings Technol.* **2019**, *361*, 176–187. [CrossRef]
98. Hakimizad, A.; Raeissi, K.; Golozar, M.A.; Lu, X.; Blawert, C.; Zheludkevich, M.L. The Effect of Pulse Waveforms on Surface Morphology, Composition and Corrosion Behavior of Al_2O_3 and Al_2O_3/TiO_2 Nano-Composite PEO Coatings on 7075 Aluminum Alloy. *Surf. Coatings Technol.* **2017**, *324*, 208–221. [CrossRef]
99. Lonyuk, B.; Apachitei, I.; Duszczyk, J. The Effect of Oxide Coatings on Fatigue Properties of 7475-T6 Aluminium Alloy. *Surf. Coatings Technol.* **2007**, *201*, 8688–8694. [CrossRef]
100. Kaseem, M.; Fatimah, S.; Nashrah, N.; Ko, Y.G. Recent Progress in Surface Modification of Metals Coated by Plasma Electrolytic Oxidation: Principle, Structure, and Performance. *Prog. Mater. Sci.* **2021**, *117*, 100735. [CrossRef]
101. Toulabifard, A.; Rahmati, M.; Raeissi, K.; Hakimizad, A.; Santamaria, M. The Effect of Electrolytic Solution Composition on the Structure, Corrosion, and Wear Resistance of Peo Coatings on Az31 Magnesium Alloy. *Coatings* **2020**, *10*, 937. [CrossRef]
102. Zhu, L.; Guo, Z.; Zhang, Y.; Li, Z.; Sui, M. A Mechanism for the Growth of a Plasma Electrolytic Oxide Coating on Al. *Electrochim. Acta* **2016**, *208*, 296–303. [CrossRef]
103. Blawert, C.; Sah, S.P.; Liang, J.; Huang, Y.; Höche, D. Role of Sintering and Clay Particle Additions on Coating Formation during PEO Processing of AM50 Magnesium Alloy. *Surf. Coatings Technol.* **2012**, *213*, 48–58. [CrossRef]
104. Vijh, K. Sparking Voltages and Side Reactions during Anodization of Valve Metals in Terms of Electron Tunneling. *Corros. Sci.* **1971**, *1*, 411–417. [CrossRef]
105. Ikonopisov, S. Theory of Electrical Breakdown during Formation of Barrier Anodic Films. *Electrochim. Acta* **1977**, *22*, 1077–1082. [CrossRef]
106. Albella, J.M.; Montero, I.; Martínez-Duart, J.M. Electron Injection and Avalanche during the Anodic Oxidation of Tantalum. *J. Electrochem. Soc.* **1984**, *131*, 1101–1104. [CrossRef]
107. Albella, J.M.; Montero, I.; Martinez-Duart, J.M. A Theory of Avalanche Breakdown during Anodic Oxidation. *Electrochim. Acta* **1987**, *32*, 255–258. [CrossRef]
108. Ingenieurwissenschaften, D. Der Simulation of Plasma Electrolytic Oxidation (PEO) of AM50 Mg Alloys and Its Experimental Validation. *Dissertation* **2018**, 154.
109. Wang, L.; Chen, L.; Yan, Z.; Fu, W. Optical Emission Spectroscopy Studies of Discharge Mechanism and Plasma Characteristics during Plasma Electrolytic Oxidation of Magnesium in Different Electrolytes. *Surf. Coatings Technol.* **2010**, *205*, 1651–1658. [CrossRef]
110. Xue, W.; Deng, Z.; Chen, R.; Zhang, T. Growth Regularity of Ceramic Coatings Formed by Microarc Oxidation on Al-Cu-Mg Alloy. *Thin Solid Films* **2000**, *372*, 114–117. [CrossRef]
111. Molak, R.M.; Topolski, K.; Spychalski, M.; Dulińska-Molak, I.; Morończyk, B.; Pakieła, Z.; Nieużyła, L.; Mazurkiewicz, M.; Wojucki, M.; Gebeshuber, A.; et al. Functional Properties of the Novel Hybrid Coatings Combined of the Oxide and DLC Layer as a Protective Coating for AZ91E Magnesium Alloy. *Surf. Coatings Technol.* **2019**, *380*, 125040. [CrossRef]
112. Yaakop, N. *Plasma Electrolytic Oxidation of Aluminium for Power Electronics Applications*; The University of Manchester: Manchester, UK, 2018.
113. Monfort, F.; Matykina, E.; Berkani, A.; Skeldon, P.; Thompson, G.E.; Habazaki, H.; Shimizu, K. Species Separation during Coating Growth on Aluminium by Spark Anodizing. *Surf. Coatings Technol.* **2007**, *201*, 8671–8676. [CrossRef]
114. Wang, R.; Wu, Y.; Wu, G.; Chen, D.; He, D.; Li, D.; Guo, C.; Zhou, Y.; Shen, D.; Nash, P. An Investigation about the Evolution of Microstructure and Composition Difference between Two Interfaces of Plasma Electrolytic Oxidation Coatings on Al. *J. Alloys Compd.* **2018**, *753*, 272–281. [CrossRef]
115. Wang, D.D.; Liu, X.T.; Wu, Y.K.; Han, H.P.; Yang, Z.; Su, Y.; Zhang, X.Z.; Wu, G.R.; Shen, D.J. Evolution Process of the Plasma Electrolytic Oxidation (PEO) Coating Formed on Aluminum in an Alkaline Sodium Hexametaphosphate ($(NaPO_3)_6$) Electrolyte. *J. Alloys Compd.* **2019**, *798*, 129–143. [CrossRef]
116. Huang, X. Plasma Electrolytic Oxidation Coatings on Aluminum Alloys: Microstructures, Properties, and Applications. *Mod. Concepts Mater. Sci.* **2019**, *2*, 000526. [CrossRef]
117. Zhu, L.; Ke, X.; Li, J.; Zhang, Y.; Zhang, Z.; Sui, M. Growth Mechanisms for Initial Stages of Plasma Electrolytic Oxidation Coating on Al. *Surf. Interfaces* **2021**, *25*, 101186. [CrossRef]
118. Barati, N.; Jiang, J.; Meletis, E.I. Microstructural Evolution of Ceramic Nanocomposites Coated on 7075 Al Alloy by Plasma Electrolytic Oxidation. *Surf. Coatings Technol.* **2022**, *437*, 128345. [CrossRef]
119. Rogov, A.B.; Nemcova, A.; Hashimoto, T.; Matthews, A.; Yerokhin, A. Analysis of Electrical Response, Gas Evolution and Coating Morphology during Transition to Soft Sparking PEO of Al. *Surf. Coatings Technol.* **2022**, 128142. [CrossRef]
120. Rogov, A.B.; Yerokhin, A.; Matthews, A. The Role of Cathodic Current in Plasma Electrolytic Oxidation of Aluminum: Phenomenological Concepts of the "Soft Sparking" Mode. *Langmuir* **2017**, *33*, 11059–11069. [CrossRef] [PubMed]

121. Mohedano, M.; Matykina, E.; Arrabal, R.; Mingo, B.; Zheludkevich, M.L. PEO of Rheocast A356 Al Alloy: Energy Efficiency and Corrosion Properties. *Surf. Interface Anal.* **2016**, *48*, 953–959. [CrossRef]
122. Martin, J.; Leone, P.; Nominé, A.; Veys-Renaux, D.; Henrion, G.; Belmonte, T. Influence of Electrolyte Ageing on the Plasma Electrolytic Oxidation of Aluminium. *Surf. Coatings Technol.* **2015**, *269*, 36–46. [CrossRef]
123. Guan, Y.J.; Xia, Y.; Li, G. Growth Mechanism and Corrosion Behavior of Ceramic Coatings on Aluminum Produced by Autocontrol AC Pulse PEO. *Surf. Coatings Technol.* **2008**, *202*, 4602–4612. [CrossRef]
124. Nie, X.; Meletis, E.I.; Jiang, J.C.; Leyland, A.; Yerokhin, A.L.; Matthews, A. Abrasive Wear/Corrosion Properties and TEM Analysis of Al_2O_3 Coatings Fabricated Using Plasma Electrolysis. *Surf. Coatings Technol.* **2002**, *149*, 245–251. [CrossRef]
125. Cheng, Y.L.; Xie, H.J.; Cao, J.H.; Cheng, Y.L. Effect of NaOH on Plasma Electrolytic Oxidation of A356 Aluminium Alloy in Moderately Concentrated Aluminate Electrolyte. *Trans. Nonferrous Met. Soc. China (English Ed.)* **2021**, *31*, 3677–3690. [CrossRef]
126. Wang, L.; Wang, G.; Dong, H.; Ye, M.; Li, X.; Liu, L.; Pan, J.; Ye, Z. Plasma Electrolytic Oxidation Coatings on Additively Manufactured Aluminum–Silicon Alloys with Superior Tribological Performance. *Surf. Coatings Technol.* **2022**, *435*, 128246. [CrossRef]
127. Oh, Y.J.; Mun, J.I.; Kim, J.H. Effects of Alloying Elements on Microstructure and Protective Properties of Al_2O_3 Coatings Formed on Aluminum Alloy Substrates by Plasma Electrolysis. *Surf. Coatings Technol.* **2009**, *204*, 141–148. [CrossRef]
128. Cheng, Y.L.; Mao, M.K.; Cao, J.H.; Peng, Z.M. Plasma Electrolytic Oxidation of an Al-Cu-Li Alloy in Alkaline Aluminate Electrolytes: A Competition between Growth and Dissolution for the Initial Ultra-Thin Films. *Electrochim. Acta* **2014**, *138*, 417–429. [CrossRef]
129. Xu, F.; Xia, Y.; Li, G. The Mechanism of PEO Process on Al-Si Alloys with the Bulk Primary Silicon. *Appl. Surf. Sci.* **2009**, *255*, 9531–9538. [CrossRef]
130. Khan, R.H.U.; Yerokhin, A.; Li, X.; Dong, H.; Matthews, A. Surface Characterisation of DC Plasma Electrolytic Oxidation Treated 6082 Aluminium Alloy: Effect of Current Density and Electrolyte Concentration. *Surf. Coatings Technol.* **2010**, *205*, 1679–1688. [CrossRef]
131. Rogov, A.B.; Yerokhin, A.; Matthews, A. The Role of Cathodic Current in Plasma Electrolytic Oxidation of Aluminium: Current Density "scanning Waves" on Complex-Shape Substrates. *J. Phys. D Appl. Phys.* **2018**, *51*, 405303. [CrossRef]
132. Matykina, E.; Arrabal, R.; Mohedano, M.; Mingo, B.; Gonzalez, J.; Pardo, A.; Merino, M.C. Recent Advances in Energy Efficient PEO Processing of Aluminium Alloys. *Trans. Nonferrous Met. Soc. China (English Ed.)* **2017**, *27*, 1439–1454. [CrossRef]
133. Liu, S.; Zeng, J. Effects of Negative Voltage on Microstructure and Corrosion Resistance of Red Mud Plasma Electrolytic Oxidation Coatings. *Surf. Coatings Technol.* **2018**, *352*, 15–25. [CrossRef]
134. Molaei, M.; Fattah-alhosseini, A.; Nouri, M.; Nourian, A. Systematic Optimization of Corrosion, Bioactivity, and Biocompatibility Behaviors of Calcium-Phosphate Plasma Electrolytic Oxidation (PEO) Coatings on Titanium Substrates. *Ceram. Int.* **2022**, *48*, 6322–6337. [CrossRef]
135. Wang, S.; Liu, X.; Yin, X.; Du, N. Influence of Electrolyte Components on the Microstructure and Growth Mechanism of Plasma Electrolytic Oxidation Coatings on 1060 Aluminum Alloy. *Surf. Coatings Technol.* **2020**, *381*, 125214. [CrossRef]
136. Cheng, Y.; Cao, J.; Mao, M.; Peng, Z.; Skeldon, P.; Thompson, G.E. High Growth Rate, Wear Resistant Coatings on an Al–Cu–Li Alloy by Plasma Electrolytic Oxidation in Concentrated Aluminate Electrolytes. *Surf. Coatings Technol.* **2015**, *269*, 74–82. [CrossRef]
137. Sharma, A.; Jang, Y.J.; Jung, J.P. Effect of KOH to Na2SiO3 Ratio on Microstructure and Hardness of Plasma Electrolytic Oxidation Coatings on AA 6061 Alloy. *J. Mater. Eng. Perform.* **2017**, *26*, 5032–5042. [CrossRef]
138. Yang, Z.; Zhang, X.Z.; Wu, Y.K.; Wu, G.R.; Wang, D.D.; Liu, X.T.; Han, H.P.; Su, Y.; Shen, D.J. The Correlation between the $Na_2SiO_3{\cdot}_9H_2O$ Concentrations and the Characteristics of Plasma Electrolytic Oxidation Ceramic Coatings. *Ceram. Int.* **2019**, *45*, 19388–19394. [CrossRef]
139. Sundararajan, G.; Rama Krishna, L. Mechanisms Underlying the Formation of Thick Alumina Coatings through the MAO Coating Technology. *Surf. Coatings Technol.* **2003**, *167*, 269–277. [CrossRef]
140. Lv, G.; Gu, W.; Chen, H.; Feng, W.; Khosa, M.L.; Li, L.; Niu, E.; Zhang, G.; Yang, S.-Z. Characteristic of Ceramic Coatings on Aluminum by Plasma Electrolytic Oxidation in Silicate and Phosphate Electrolyte. *Appl. Surf. Sci.* **2006**, *253*, 2947–2952. [CrossRef]
141. Erfanifar, E.; Aliofkhazraei, M.; Fakhr Nabavi, H.; Sharifi, H.; Rouhaghdam, A.S. Growth Kinetics and Morphology of Plasma Electrolytic Oxidation Coating on Aluminum. *Mater. Chem. Phys.* **2017**, *185*, 162–175. [CrossRef]
142. Sabouri, M.; Mousavi Khoei, S.M. Plasma Electrolytic Oxidation in the Presence of Multiwall Carbon Nanotubes on Aluminum Substrate: Morphological and Corrosion Studies. *Surf. Coatings Technol.* **2018**, *334*, 543–555. [CrossRef]
143. Salehi Doolabi, D.; Ehteshamzadeh, M.; Mirhosseini, S.M.M. Effect of NaOH on the Structure and Corrosion Performance of Alumina and Silica PEO Coatings on Aluminum. *J. Mater. Eng. Perform.* **2012**, *21*, 2195–2202. [CrossRef]
144. del Olmo, R.; Mohedano, M.; Mingo, B.; Arrabal, R.; Matykina, E. LDH Post-Treatment of Flash PEO Coatings. *Coatings* **2019**, *9*, 6–20. [CrossRef]
145. Walsh, F.C.; Low, C.T.J.; Wood, R.J.K.; Stevens, K.T.; Archer, J.; Poeton, A.R.; Ryder, A. Plasma Electrolytic Oxidation (PEO) for Production of Anodised Coatings on Lightweight Metal (Al, Mg, Ti) Alloys. *Trans. Inst. Met. Finish.* **2009**, *87*, 122–135. [CrossRef]
146. Habazaki, H.; Tsunekawa, S.; Tsuji, E.; Nakayama, T. Formation and Characterization of Wear-Resistant PEO Coatings Formed on β-Titanium Alloy at Different Electrolyte Temperatures. *Appl. Surf. Sci.* **2012**, *259*, 711–718. [CrossRef]
147. Al Afghani, F.; Anawati, A. Plasma Electrolytic Oxidation of Zircaloy-4 in a Mixed Alkaline Electrolyte. *Surf. Coatings Technol.* **2021**, *426*, 127786. [CrossRef]

148. Wu, T.; Blawert, C.; Serdechnova, M.; Karlova, P.; Dovzhenko, G.; Florian Wieland, D.C.; Stojadinovic, S.; Vasilic, R.; Mojsilovic, K.; Zheludkevich, M.L. Formation of Plasma Electrolytic Oxidation Coatings on Pure Niobium in Different Electrolytes. *Appl. Surf. Sci.* **2022**, *573*, 151629. [CrossRef]
149. Hussein, R.O.; Nie, X.; Northwood, D.O. Influence of Process Parameters on Electrolytic Plasma Discharging Behaviour and Aluminum Oxide Coating Microstructure. *Surf. Coatings Technol.* **2010**, *205*, 1659–1667. [CrossRef]
150. Li, J.; Cai, H.; Jiang, B. Growth Mechanism of Black Ceramic Layers Formed by Microarc Oxidation. *Surf. Coatings Technol.* **2007**, *201*, 8702–8708. [CrossRef]
151. Kalkanci, H.; Kurnaz, S.C. The Effect of Process Parameters on Mullite-Based Plasma Electrolytic Oxide Coatings. *Surf. Coatings Technol.* **2008**, *203*, 15–22. [CrossRef]
152. Lu, X.; Mohedano, M.; Blawert, C.; Matykina, E.; Arrabal, R.; Kainer, K.U.; Zheludkevich, M.L. Plasma Electrolytic Oxidation Coatings with Particle Additions—A Review. *Surf. Coatings Technol.* **2016**, *307*, 1165–1182. [CrossRef]
153. Lu, X.; Blawert, C.; Zheludkevich, M.L.; Kainer, K.U. Insights into Plasma Electrolytic Oxidation Treatment with Particle Addition. *Corros. Sci.* **2015**, *101*, 201–207. [CrossRef]
154. Lu, X.; Blawert, C.; Huang, Y.; Ovri, H.; Zheludkevich, M.L.; Kainer, K.U. Plasma Electrolytic Oxidation Coatings on Mg Alloy with Addition of SiO_2 Particles. *Electrochim. Acta* **2016**, *187*, 20–33. [CrossRef]
155. Tu, W.; Zhu, Z.; Zhuang, X.; Cheng, Y.; Skeldon, P. Effect of Frequency on Black Coating Formation on AZ31 Magnesium Alloy by Plasma Electrolytic Oxidation in Aluminate-Tungstate Electrolyte. *Surf. Coat. Technol.* **2019**, *372*, 34–44. [CrossRef]
156. Tang, M.; Feng, Z.; Li, G.; Zhang, Z.; Zhang, R. High-Corrosion Resistance of the Microarc Oxidation Coatings on Magnesium Alloy Obtained in Potassium Fluotitanate Electrolytes. *Surf. Coatings Technol.* **2015**, *264*, 105–113. [CrossRef]
157. Sreekanth, D.; Rameshbabu, N.; Venkateswarlu, K. Effect of Various Additives on Morphology and Corrosion Behavior of Ceramic Coatings Developed on AZ31 Magnesium Alloy by Plasma Electrolytic Oxidation. *Ceram. Int.* **2012**, *38*, 4607–4615. [CrossRef]
158. Song, L.; Kou, Y.; Song, Y.; Shan, D.; Zhu, G.; Han, E.H. Fabrication and Characterization of Micro-Arc Oxidation (MAO) Coatings on Mg-Li Alloy in Alkaline Polyphosphate Electrolytes without and with the Addition of K2TiF6. *Mater. Corros.* **2011**, *62*, 1124–1132. [CrossRef]
159. Sreekanth, D.; Rameshbabu, N.; Venkateswarlu, K.; Subrahmanyam, C.; Rama Krishna, L.; Prasad Rao, K. Effect of K_2TiF_6 and $Na_2B_4O_7$ as Electrolyte Additives on Pore Morphology and Corrosion Properties of Plasma Electrolytic Oxidation Coatings on ZM21 Magnesium Alloy. *Surf. Coatings Technol.* **2013**, *222*, 31–37. [CrossRef]
160. Hakimizad, A.; Raeissi, K.; Golozar, M.A.; Lu, X.; Blawert, C.; Zheludkevich, M.L. Influence of Cathodic Duty Cycle on the Properties of Tungsten Containing Al_2O_3/TiO_2 PEO Nano-Composite Coatings. *Surf. Coatings Technol.* **2018**, *340*, 210–221. [CrossRef]
161. Wang, L.; Zhou, J.; Liang, J.; Chen, J. Thermal Control Coatings on Magnesium Alloys Prepared by Plasma Electrolytic Oxidation. *Appl. Surf. Sci.* **2013**, *280*, 151–155. [CrossRef]
162. Hakimizad, A.; Raeissi, K.; Santamaria, M.; Asghari, M. Effects of Pulse Current Mode on Plasma Electrolytic Oxidation of 7075 Al in Na_2WO_4 Containing Solution: From Unipolar to Soft-Sparking Regime. *Electrochim. Acta* **2018**, *284*, 618–629. [CrossRef]
163. Yao, Z.; Hu, B.; Shen, Q.; Niu, A.; Jiang, Z.; Su, P.; Ju, P. Preparation of Black High Absorbance and High Emissivity Thermal Control Coating on Ti Alloy by Plasma Electrolytic Oxidation. *Surf. Coatings Technol.* **2014**, *253*, 166–170. [CrossRef]
164. Li, K.; Li, W.; Zhang, G.; Guo, P. Preparation of Black PEO Layers on Al-Si Alloy and the Colorizing Analysis. *Vacuum* **2015**, *111*, 131–136. [CrossRef]
165. Lukiyanchuk, I.V.; Rudnev, V.S.; Tyrina, L.M. Plasma Electrolytic Oxide Layers as Promising Systems for Catalysis. *Surf. Coatings Technol.* **2016**, *307*, 1183–1193. [CrossRef]
166. Hwang, I.J.; Hwang, D.Y.; Kim, Y.M.; Yoo, B.; Shin, D.H. Formation of Uniform Passive Oxide Layers on High Si Content Al Alloy by Plasma Electrolytic Oxidation. *J. Alloys Compd.* **2010**, *504*, S527–S530. [CrossRef]
167. Wang, J.M.; Tsai, D.S.; Tsai, J.T.J.; Chou, C.C. Coloring the Aluminum Alloy Surface in Plasma Electrolytic Oxidation with the Green Pigment Colloid. *Surf. Coatings Technol.* **2017**, *321*, 164–170. [CrossRef]
168. Yeh, S.C.; Tsai, D.S.; Wang, J.M.; Chou, C.C. Coloration of the Aluminum Alloy Surface with Dye Emulsions While Growing a Plasma Electrolytic Oxide Layer. *Surf. Coatings Technol.* **2016**, *287*, 61–66. [CrossRef]
169. Xue, W.; Shi, X.; Hua, M.; Li, Y. Preparation of Anti-Corrosion Films by Microarc Oxidation on an Al-Si Alloy. *Appl. Surf. Sci.* **2007**, *253*, 6118–6124. [CrossRef]
170. Krishtal, M.M. Effect of Structure of Aluminum-Silicon Alloys on the Process of Formation and Characteristics of Oxide Layer in Microarc Oxidizing. *Met. Sci. Heat Treat.* **2004**, *46*, 377–384. [CrossRef]
171. Wang, L.; Nie, X. Silicon Effects on Formation of EPO Oxide Coatings on Aluminum Alloys. *Thin Solid Films* **2006**, *494*, 211–218. [CrossRef]
172. Feng Su, J.; Nie, X.; Hu, H.; Tjong, J. Friction and Counterface Wear Influenced by Surface Profiles of Plasma Electrolytic Oxidation Coatings on an Aluminum A356 Alloy. *J. Vac. Sci. Technol. A Vacuum Surf. Film.* **2012**, *30*, 061402. [CrossRef]
173. Moshrefifar, M.; Ebrahimifar, H.; Hakimizad, A. Systematic Investigation of Silicon Content Effects on the PEO Coatings' Properties on Al–Si Binary Alloys in Silicate-Based and Tungstate-Containing Electrolytes. *Coatings* **2022**, *12*, 1438. [CrossRef]
174. Student, M.; Pohrelyuk, I.; Padgurskas, J.; Posuvailo, V.; Hvozdets'kyi, V.; Zadorozhna, K.; Chumalo, H.; Veselivska, H.; Kovalchuk, I.; Kychma, A. Influence of Plasma Electrolytic Oxidation of Cast Al-Si Alloys on Their Phase Composition and Abrasive Wear Resistance. *Coatings* **2023**, *13*, 637. [CrossRef]

175. Mora-Sanchez, H.; del Olmo, R.; Rams, J.; Torres, B.; Mohedano, M.; Matykina, E.; Arrabal, R. Hard Anodizing and Plasma Electrolytic Oxidation of an Additively Manufactured Al-Si Alloy. *Surf. Coatings Technol.* **2021**, *420*, 127339. [CrossRef]
176. Pezzato, L.; Dabalà, M.; Brunelli, K. Microstructure and Corrosion Properties of PEO Coatings Produced on Am-Aluminum Alloys. *Key Eng. Mater.* **2019**, *813*, 298–303. [CrossRef]
177. Pezzato, L.; Dabalà, M.; Gross, S.; Brunelli, K. Effect of Microstructure and Porosity of AlSi10Mg Alloy Produced by Selective Laser Melting on the Corrosion Properties of Plasma Electrolytic Oxidation Coatings. *Surf. Coatings Technol.* **2020**, *404*, 126477. [CrossRef]
178. Li, K.; Li, W.; Zhang, G.; Wang, M.; Tang, P. Influence of Surface Etching Pretreatment on PEO Process of Eutectic Al-Si Alloy. *Chin. J. Chem. Eng.* **2015**, *23*, 1572–1578. [CrossRef]
179. Li, K.; Li, W.; Yi, A.; Zhu, W.; Liao, Z.; Chen, K.; Li, W. Tuning the Surface Characteristic of Al-Si Alloys and Its Impacts on the Formation of Micro Arc Oxidation Layers. *Coatings* **2021**, *11*, 453. [CrossRef]
180. Li, K.; Li, W.; Zhang, G.; Zhu, W.; Zheng, F.; Zhang, D.; Wang, M. Effects of Si Phase Refinement on the Plasma Electrolytic Oxidation of Eutectic Al-Si Alloy. *J. Alloys Compd.* **2019**, *790*, 650–656. [CrossRef]
181. Hu, C.J.; Hsieh, M.H. Preparation of Ceramic Coatings on an Al-Si Alloy by the Incorporation of ZrO_2 Particles in Microarc Oxidation. *Surf. Coatings Technol.* **2014**, *258*, 275–283. [CrossRef]
182. Polunin, A.V.; Cheretaeva, A.O.; Borgardt, E.D.; Rastegaev, I.A.; Krishtal, M.M.; Katsman, A.V.; Yasnikov, I.S. Improvement of Oxide Layers Formed by Plasma Electrolytic Oxidation on Cast Al–Si Alloy by Incorporating TiC Nanoparticles. *Surf. Coatings Technol.* **2021**, *423*, 127603. [CrossRef]
183. Krishtal, M.M.; Katsman, A.V.; Polunin, A.V. Effects of Silica Nanoparticles Addition on Formation of Oxide Layers on Al[Sbnd]Si Alloy by Plasma Electrolytic Oxidation: The Origin of Stishovite under Ambient Conditions. *Surf. Coatings Technol.* **2022**, *441*, 128556. [CrossRef]

coatings

MDPI

Article

Joining and Coating of Plasma Electrolytic Oxidated Aluminum Using a Silica Preceramic Polymer

Monica Ferraris [1,2], Alessandro Benelli [1,2,*], Valentina Casalegno [1,2], Pavel Shashkov [3] and Vincenzo Maria Sglavo [4]

[1] Department of Applied Science and Technology, Politecnico di Torino, 10129 Turin, Italy; monica.ferraris@polito.it (M.F.); valentina.casalegno@polito.it (V.C.)
[2] Inter-Departmental Multi-Disciplinary Research Centre J-TECH@PoliTO, 10129 Turin, Italy
[3] Cambridge Nanolitic Ltd., Haverhill CB9 8QP, UK; p.shashkov@nanolitic.com
[4] Department of Industrial Engineering and Technology, Università di Trento, 38122 Trento, Italy; vincenzo.sglavo@unitn.it
* Correspondence: alessandro.benelli@polito.it; Tel.: +39-38-8656-0891

Abstract: This study evaluates the effectiveness of a silica preceramic polymer for joining and coating Plasma Electrolytic Oxidated (PEO) aluminum components at temperatures below 200 °C. PEO aluminum slabs were coated and joined with a silica precursor polymer (Durazane1800, Merck, Darmstadt, Germany), both with and without the addition of 48 wt% silica nanoparticles, and cured at 180 °C for 4 h in air. Thermogravimetric analysis assessed the curing process and thermal stability, while X-ray diffraction confirmed the polymer's conversion to amorphous silica after heating at 1200 °C. Resistance to humid environments was tested by soaking coated samples in tap water for a week, with no mass variation observed. Mechanical testing through tensile mode and tensile lap tests showed that adding 48 wt% silica nanoparticles significantly improved joint cohesion and nearly quadrupled mechanical strength. Fracture surfaces were examined using Field Emission Scanning Electron Microscopy, and composition analysis was performed with Energy Dispersion X-ray Spectroscopy. Crack detection was conducted using Computer Tomography with an in situ bending test setup to obtain the mechanical resistance of the PEO coating. The results indicate that the silica preceramic polymer is suitable for joining and coating PEO aluminum components, with silica nanoparticles enhancing mechanical strength and providing excellent thermal stability and resistance to humidity.

Keywords: PEO; joining; coating; preceramic polymers; silica

Citation: Ferraris, M.; Benelli, A.; Casalegno, V.; Shashkov, P.; Sglavo, V.M. Joining and Coating of Plasma Electrolytic Oxidated Aluminum Using a Silica Preceramic Polymer. *Coatings* **2024**, *14*, 757. https://doi.org/10.3390/coatings14060757

Academic Editor: Cheng Zhang

Received: 30 April 2024
Revised: 7 June 2024
Accepted: 12 June 2024
Published: 14 June 2024

1. Introduction

Plasma Electrolytic Oxidation (PEO) of aluminum components has garnered significant interest for a variety of applications, ranging from substituting steel to enhancing electronic devices. Numerous studies in the literature have focused on optimizing the Plasma Electrolytic Oxidation process on aluminum substrates, primarily due to the advantageous combination of aluminum's low density and the high hardness of the alumina coating [1,2]. This combination is particularly beneficial for components that require rapid movement and are subject to wear.

Reducing the mass of moving parts results in increased movement speed, lower energy consumption, and diminished friction losses. Applications of PEO aluminum components include wear-resistant coatings for textiles, packaging, automotive parts, and molds, as well as abrasion-resistant coatings for turbocharger wheels. They are also used for corrosion-resistant coatings in transportation sectors such as automotive, marine, and aerospace industries; engine components; plasma erosion-resistant coatings for microplasma generator components; and decorative coatings.

In certain applications, the aforementioned PEO aluminum components require appropriate joining and coating processes that must be performed at temperatures below 200 °C. This precaution is necessary to prevent distortion or delamination of the surface layer, which can occur due to the mismatch in the thermal expansion coefficients between the metal substrate and the oxide layer.

Silica is well known for its high-temperature resistance, mechanical strength, and resistance to corrosion and wear, making it an excellent choice as a coating and joining material. Silica, particularly in its glass form, is frequently used for sealing and joining components. The typical procedure involves heating the glass above its softening temperature to reduce its viscosity sufficiently, enabling its use as a high-temperature adhesive. However, the temperatures required to soften silica are unsuitable for most metals, especially aluminum-based alloys.

Several alternatives exist for obtaining silica coatings at lower temperatures, such as chemical and vapor deposition or sol-gel techniques [3–8]. While both chemical and vapor deposition techniques necessitate expensive facilities, the sol-gel method offers a cost-effective alternative. However, the processing time required to achieve high-quality coatings through sol-gel can be extensive.

For low-temperature joining materials and technologies applicable to aluminum-based components, organic adhesives emerge as promising candidates [9–11]. Despite their advantages, these adhesives exhibit limited temperature resistance and thermal expansion properties that are often unsuitable for applications requiring thermal stability. Additionally, adhesives are sensitive to humidity [12,13], which can adversely affect the overall durability and lifespan of the components.

Silica preceramic polymers present an intriguing alternative as coating and joining materials for PEO (Plasma Electrolytic Oxidation) aluminum components. Their processing time is significantly shorter than that required for the sol-gel process, and the technology is less expensive than chemical and vapor deposition methods. Most importantly, these polymers can be converted to silica at temperatures below 900 °C.

Preceramic polymers offer considerable flexibility: despite having a basic structure composed of light elements such as C, H, O, N, and B, their structure can be modified to achieve desired properties, such as enhanced mechanical and thermal characteristics, or the introduction of new ones. Additionally, temperatures and process times (cross-linking and pyrolysis) can be easily optimized. They can be produced with significant energy and cost savings and superior properties compared to conventional ceramics [14,15].

Nonetheless, challenges must be addressed during polymer-to-ceramic conversion, including shrinkage, residual porosity, and related defects, which can significantly reduce the mechanical strength and elastic modulus of the resulting materials. One potential solution is the incorporation of active or passive fillers and the careful optimization of heat treatment protocols to minimize shrinkage [16–19].

"While the literature on silica preceramic polymers is abundant dating back to the beginning of the last century [15,20,21] the use of these materials as joining and coating materials for Plasma Electrolytic Oxidated (PEO) aluminum components has been not investigated yet, while multiple research works on other methodologies to join PEO materials have been already published [22–25]".

The aim of the present work is to study the suitability of a silica preceramic polymer for joining and coating PEO aluminum components at temperatures below 200 °C, focusing on the mechanical strength and environment resistance with or without the addition of silica nanoparticles.

2. Materials and Methods

Plasma Electrolytic Oxidated (PEO) aluminum (Al in the text) slabs have been provided by Cambridge Nanolitic, Cambridge, UK, consisting of Al (20–70 μm coated) measured using eddy currents, as reported in [26], and thick alpha and gamma nano alumina (crystallite size 30–80 nm) obtained via proprietary soft sparking PEO technology. The

average grain size was derived using X-ray diffraction measurements, as reported in [26,27]. The treatment was conducted in a phosphate–silicate electrolyte maintained at room temperature of 25 °C with the use of bipolar electrical pulses with 700 V amplitude and repetition frequency of 2 KHz.

The selected polymer was a silica precursor polymer (Durazane1800, Merck, polymer in the text [28]), cured at 180 °C for 4 h, in air, according to the available data sheet. It is a liquid, low-viscous, solvent-free polysilazane resin, which looks like a colorless liquid. Its density is 0.950–1.050 g/cm^3 at 25 °C and its viscosity 10–40 cP at 20 °C [1]. It is characterized by good adhesion, hardness, hydrophobicity, and barrier properties and it is applicable to metal, glass, and ceramic substrates. For these reasons, Durazane 1800 is suitable for industrial applications as a high-temperature coating in order to protect metals from corrosion [29–31]. The polymer consists of a silicon and nitrogen backbone functionalized with different side groups, usually hydrogen, methyl (CH3), and vinyl (CH=CH2) groups, which contribute to crosslinking via vinyl polymerization [32,33]. Typically, curing is performed using radical initiators, to allow a reduction in curing temperature or time, but catalysts can be avoided, as it in this study, when curing is performed at 180 °C, 4 h, in air, according to the polymer's data sheet.

In order to verify the thermal stability of the cured polymer, thermogravimetric analyses (TGA) were performed using NETZSCH STA 2500 Regulus apparatus (Selb, Germany) equipped with a tailor-made, ultra-micro balance with a resolution of 0.03 μg. The analysis was performed on the cured polymer in air flow (40 mL/min) with 10 °C/min heating rate, up to 1200 °C, followed by free cooling.

X-ray diffraction (XRD) analysis was performed on the polymer treated at 1200 °C, using an X'Pert Pro MRD diffractometer, with Cu Kα radiation (PANalytical X'Pert Pro, Philips, Almelo, The Netherlands), and with the aid of X-Pert HighScore software v.5.1 (JCPDS database provided by PDF-4 ICDD, International Centre for Diffraction Data, Newton Square, PA, USA).

PEO aluminum samples of 15 mm × 15 mm were cut (Brillant 220 cutting machine, QATM, Mammelzen, Germany) from a larger slab and cleaned in an ultrasonic bath (Proclean 4.5S, Ulsonix, Berlin, Germany) in ethanol (20 min, 40 °C), before being coated by the polymer through a manual process. The polymer was also sandwiched between two samples (PEO side) to obtain a joint of about 20 μm, with a pressure of about 5 kPa applied to keep the sample in position during the process; all coated and joined samples were then cured at 180 °C for 4 h in a furnace operating in air (Binder ED 23, Tuttlingen, Germany), according to the polymer datasheet.

The resistance of the coated samples in the humid environment was preliminary assessed by soaking them for 1 week in tap water at room temperature and measuring their weight variation using an analytical balance (AR2140, OHAUS Europe GmbH, Nänikon, Switzerland) with a resolution of 0.1 mg.

Joined samples were glued to steel cylinders using a two-component epoxy adhesive (DP490) and tested in tensile mode at room temperature according to a modified ASTM C633-01 [34] (on four samples) using a MTS Criterion model 43 machine (MTS Systems Corporation, Eden Prairie, MN, USA) equipped with a 5 kN load cell. The configuration used for the tensile test is reported in [35,36]. The cross-head speed was set to 0.5 mm/min to cause fracturing under quasi-static conditions. The strength (ultimate tensile stress, UTS) was calculated as

$$\sigma = F/A \quad (1)$$

where F is the peak load and A is the joined area.

The cross sections of the joined samples and fracture surfaces after mechanical tests were observed using FESEM and their composition was analyzed using EDS (JEOL JCM-6000 PLUS, Tokyo, Japan, equipped with an Energy Dispersive X-ray Spectroscopy (EDS) analyzer and FESEM-ZEISS Supra 40, Oberkochen, Germany, with EDS-SW9100 EDAX detector, Pleasanton, CA, USA).

Silica nanoparticles of up to 48 wt% (80 nm average diameter, Alfa Aesar, Haverhill, MA, USA) were added to the polymer via manually stirring at room temperature, using a metal rod in a graduated Eppendorf tube. The resulting material was highly viscous and was cured at 180 °C for 4 h in air to obtain coatings and joints as described before. Its thermal stability was tested via TGA up to 1200 °C.

Also, single-lap mechanical tests on joined samples were performed according to ASTM D1002-10 [37], in triplicate.

Computer Tomography inspection with in situ bending test (IKTS-Fraunhofer Institute, Dresden, Germany) was performed to measure the maximum resistance of the coating under bending stress. Four different tomography reconstructions were performed, the first one with no bending load and the other three with 95 N, 115 N, and 165 N bending loads applied, respectively. The tomography parameters used were 150 kV and 50 μA, with 1600 projections for each loading conditions. The reconstructed 3D volumes of the investigated specimen were obtained by using the filtered back projection algorithm through VG MAX 3.5 software (Volume Graphics GMbH, Heidelberg, Germany).

In order to calculate the stress on the coating during the bending test carried out within the CT, similar tests were carried out using a Zwick Roell Z050 machine equipped with 5 kN load cell. Specimen of 5.2 mm × 1.5 mm cross section were subjected to 4-point bending test with a load span equal to 27.5 mm and a support span equal to 67.5 mm, i.e., at the same conditions used during the in situ flexural test within the CT. The stress at which the cracks appeared in the tomography can be calculated as

$$\sigma(f_{max}) = (M(t/2))/I \quad (2)$$

where:

- $\sigma(f_{max})$ is the maximum flexural stress in the bar, occurring in the outer surface of the bar;
- M is the bending moment developed between the loading pins;
- t is the thickness of the bar;
- I is the moment of inertia of the bar.

In order to detect the presence of cracks at different flexural loading conditions, FESEM inspection were carried out on each sample (Tescan MIRA3, Brno, Czech Republic).

3. Results and Discussion

Figure 1 shows an optical and three FESEM micrographs at higher magnifications of the aluminum slabs where the nanocrystalline structure of the PEO coating is clearly visible.

Before performing the TGA analysis up to 1200 °C, the effectiveness of the curing process was verified: about 15 mg of cured polymer was put inside the crucible at an initial temperature of 20 °C, which was kept constant for 5 min; then, a heating rate of 10 °C/min was used to reach the curing temperature of 180 °C, which was kept for 1 h. A weight loss of 0.8% was observed when the temperature reached 180 °C, possibly due to the degradation of non-crosslinked volatile oligomers. After that, there was a further weight loss of 0.1%, followed by a weight increase of 0.3%. These two latter minor weight changes are likely due to buoyancy effects caused by the low weight of the sample (a few milligrams), making any conclusions about mass loss or gain speculative. Since the total weight variation was less than 1%, the curing process was considered successful.

In order to test the thermal stability of the cured polymer, TGA-DTA analysis was carried out and the results are shown in Figure 2. The overall weight loss are about 11% and it was recorded between 450 °C and 600 °C, corresponding to the ceramic conversion process. At about 800 °C, the conversion was completed, and the weight remained stable up to 1200 °C.

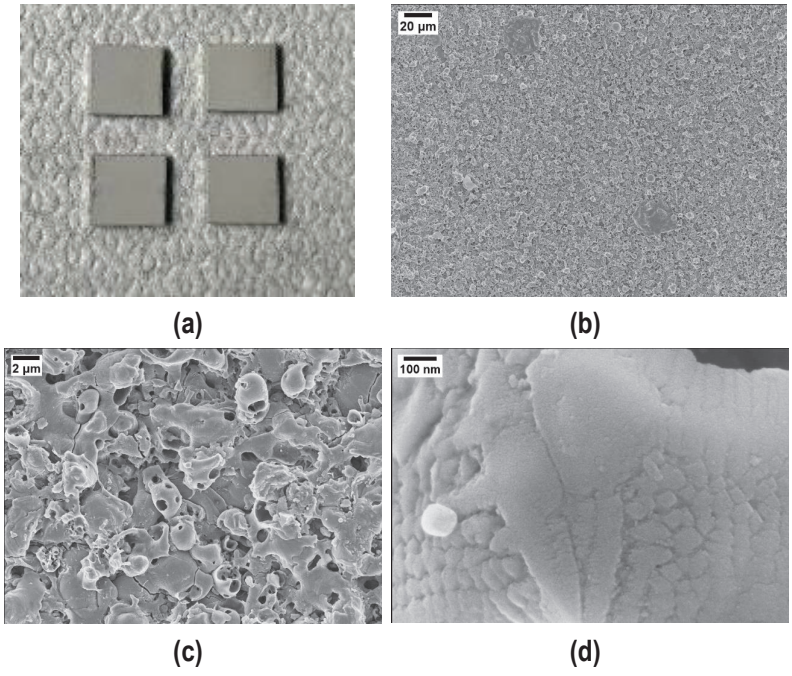

Figure 1. Visual appearance (**a**) and higher magnifications (**b**,**c**) of the Plasma Electrolytic Oxidated (PEO) alumina-coated aluminum slabs. (**d**) Evidence of the PEO alumina nanocrystalline structure.

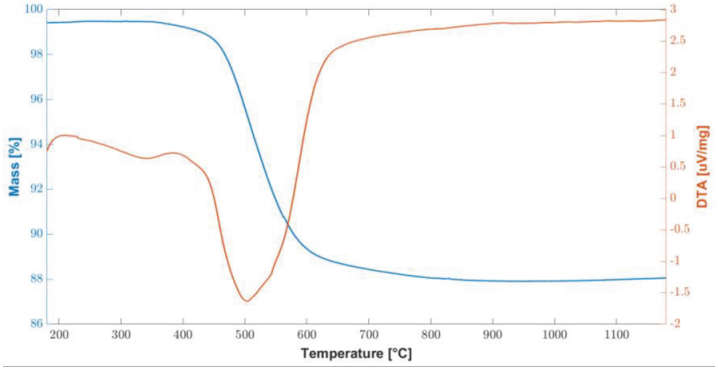

Figure 2. Combined graph of TGA/DTA curves of the cured polymer up to 1200 °C.

These results are consistent with the information found in the literature [27], in two fundamental steps were identified: the first in the temperature range 200–400 °C and the second at 500–750 °C. In particular, at temperatures above 200 °C, there is a further radical polymerization of residual vinyl groups. Up to 400 °C, further dehydrogenation and transamination reactions occur, although the total mass loss is negligible, as can be seen from the flat TGA curve in Figure 2.

Conversely, between 500 °C and 750 °C, a significant mass loss is associated with the organic–inorganic transformation of the polymer into amorphous silica. This process is also called ceramization and involves the decomposition and transformation of organic groups. During this thermal treatment, known as thermolysis, the organic components undergo significant chemical changes, breaking down and evolving into gaseous byproducts. As

the temperature rises within this specified range, the preceramic materials undergo a series of complex chemical reactions. These reactions promote the formation of strong covalent bonds between the remaining elements, leading to the development of an amorphous ceramic structure. This transformation results in the creation of amorphous covalent ceramics (ACC) [38–41]. While a mass loss of 11.4% was measured between 400 °C and 800 °C, no further mass loss was measured up to the end of the test, at 1200 °C.

XRD analysis performed on the cured polymer treated at 1200 °C (Figure 3) confirms the amorphous structure of the obtained material: once heated at 1200 °C, the polymer appears colorless. Results in the literature, such as the study by [42], confirm that pyrolysis at this temperature leads to the formation of an amorphous phase.

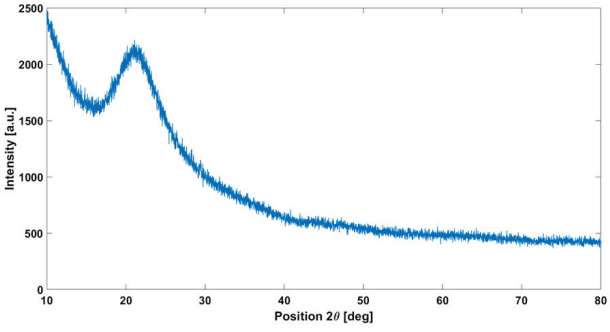

Figure 3. XRD analysis on the cured polymer heated at 1200 °C showing the typical amorphous silica halo.

Coated samples were obtained by manually depositing the polymer on the PEO side of the samples, followed by the curing process at 180 °C for 4 h. Figure 4a shows the top surface of the coating after curing; it is compact and shiny, except from some macro-cracks on the right side, probably due to an excessive thickness; the good quality of the coating is also confirmed via FESEM micrographs taken of the top surface (Figure 4b) and the cross sections (Figure 4c,d). Evidence of a sound interface between PEO Al_2O_3 and cured polymer is visible in Figure 4d.

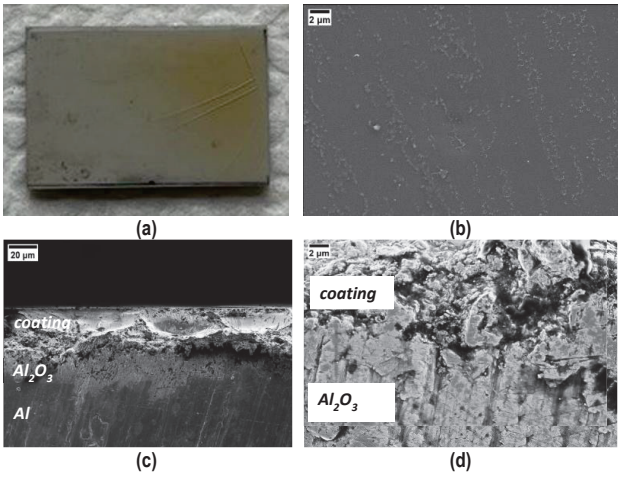

Figure 4. Visual (**a**) and FESEM (**b**) top view and cross sections (**c**,**d**) of the coating after curing. Cracks in (**a**) the thicker side of the coating. (**d**) Evidence of a sound interface between PEO Al_2O_3 and the cured polymer coating.

Joined samples were obtained by sandwiching the polymer between two samples (PEO alumina side), as in Figure 5, which shows a schematic representation (a) and a SEM polished cross section of a joined sample (b): residual porosity and cracks due to the polymer evolution (weight loss and shrinkage) upon curing are visible.

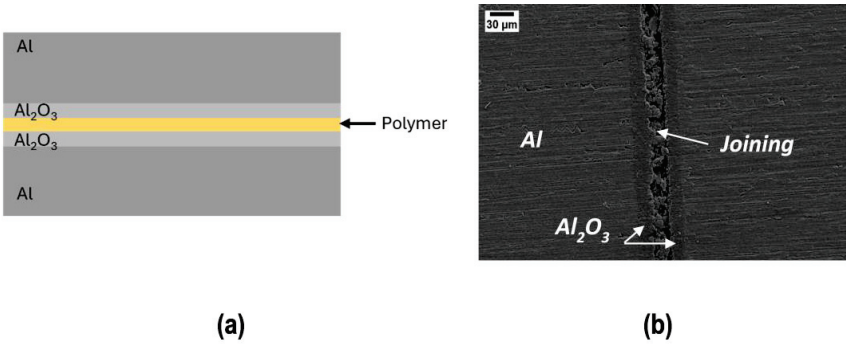

Figure 5. Schematic representation (**a**) and SEM polished cross section of the joined sample (**b**).

It is important to point out that in the case of the coating, the entire surface is available for the elimination of volatile species during curing and the coating is compact and pore free; conversely, in the joint, volatile species have only the perimeter to escape during curing. Therefore, joints are more porous than coatings, although they were produced under the same curing conditions.

Joined samples were tested in tensile mode according to a modified ASTM C633-01. Figure 6 shows the tensile test set up (a) and the typical cohesive fracture surface of joined samples after the tensile test (b). The joining material is present on both surfaces, typical of a cohesive fracture, indicating a strong interface between the PEO alumina and the coating. Figure 6c shows the stress–displacement diagrams recorded on the four joined samples subjected to the tensile test. The fracture was typically brittle, as expected for silica-based material, with an average tensile strength of 1.8 ± 0.3 MPa.

FESEM micrographs of the fracture surfaces after the tensile test are shown in Figure 7: it is possible to distinguish the joining material from the PEO alumina, with the former cracked and the latter smooth (Figure 7a). At higher magnification (Figure 7b), one can observe that the joining material has some porosity and the PEO alumina shows the nanocrystalline structure, already observed in Figure 1.

A punctual EDS analysis was performed in order to measure the elemental composition in different zones of the fracture surface. EDS of the joining material detected the polymer's main elements, i.e., Si, C, and O, with residual C associated with the non-complete transformation to silica at 180 °C (Figure 3); conversely, the main elements detected in the PEO alumina regions were, as expected: Al and O. While the PEO alumina is clearly visible in some areas of the fracture surfaces, no bare aluminum is visible, confirming the interfacial strength of Al/PEO alumina, which is more intense than the cured polymer/PEO alumina one.

In order to decrease porosity and increase the mechanical strength of the joints, an increasing amount of silica nanoparticles were added to the polymer up to 48 wt%, which was found to be the maximum amount that could be added under these experimental conditions.

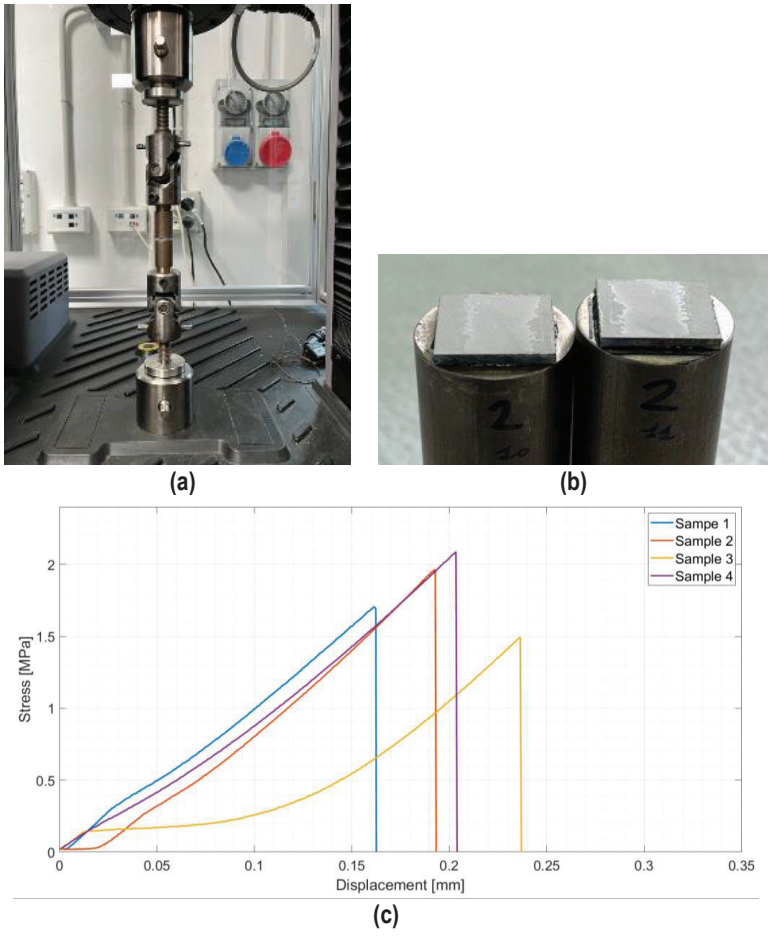

Figure 6. Tensile test on joined samples: tensile test set up (**a**), typical fracture surface of a joined sample after tensile test (**b**), and average tensile strength = 1.8 ± 0.3 MPa (**c**).

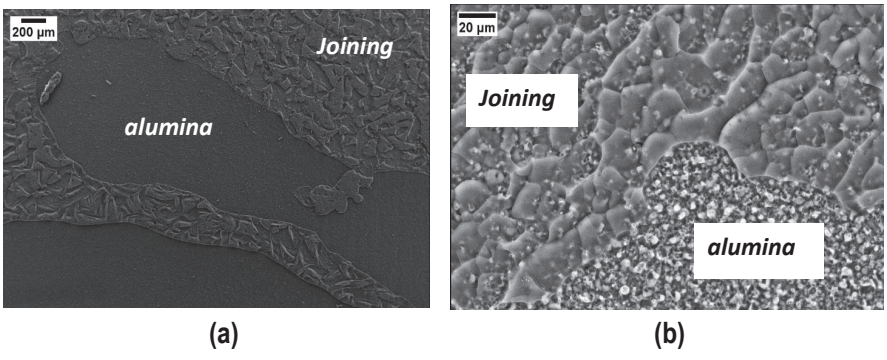

Figure 7. SEM results on the joined samples' typical fracture surface after the tensile test (**a**) and at higher magnification (**b**).

As shown in Figure 8 the total weight loss is about 10%, slightly lower than what was found without silica nanoparticles. The TGA curve is very similar to what was found for the polymer without silica nanoparticles in Figure 3; however, for temperatures below 400 °C, there is a higher mass loss (2.2%) associated with the elimination of the most volatile species, probably due to the presence of 48 wt% silica nanoparticles, which facilitate the reaction and the gaseous products elimination path. A significant mass loss of 6% occurs between 500 °C and 700 °C, corresponding to the conversion to amorphous silica.

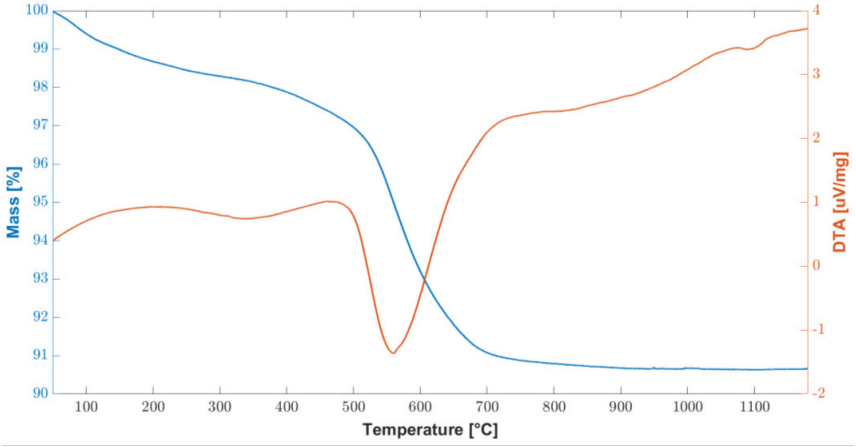

Figure 8. Combined graph of TGA/DTA curves of the cured polymer loaded with 48 wt% silica nanoparticles up to 1200 °C.

Given the low melting temperature of the Al slabs used for this work, a complete transformation to silica was not possible: however, the presence of 48 wt% of silica nanoparticles improved the mechanical strength of the joints, as discussed below.

According to the literature, an improvement in terms of reduced porosity and increased mechanical strength is expected when adding fillers to compensate for the shrinkage during the curing of a preceramic polymer. The same curing procedure at 180 °C for 4 h in air was used for the preparation of coatings and joints with 48 wt% silica. Since the addition of silica nanoparticles increased the polymer's viscosity, it was much more difficult to spread the material using the spatula to obtain a thin, uniform layer for the manual deposition. The thicker coatings became significantly more cracked than those produced without silica nanoparticles and they could be peeled off from the substrates very easily: a better deposition process is going to be developed to obtain thinner coatings with silica nanoparticles.

Figure 9 shows a FESEM top view of the coating with 48 wt% of silica nanoparticles: some "clouds" corresponding to non-homogeneously dispersed silica nanoparticles agglomerates can be seen; a better homogenization process should be tested to improve the coating compositional uniformity when silica nanoparticles are added to the polymer. Some studies are already present in the literature about increasing the uniformity of mixing nanoparticles in the polymer [20,43,44]. The EDS analysis of the coating only reported silicon, carbon, and oxygen as detected elements.

Conversely, the joints appear sound and resistant to cutting and polishing: Figure 10 shows a representative FESEM cross section of a joint, which is less porous than those obtained using the pure polymer (Figure 5). Some residual porosity is still present, but the higher magnification in Figure 10b shows a fairly good interface between PEO alumina and the joining material.

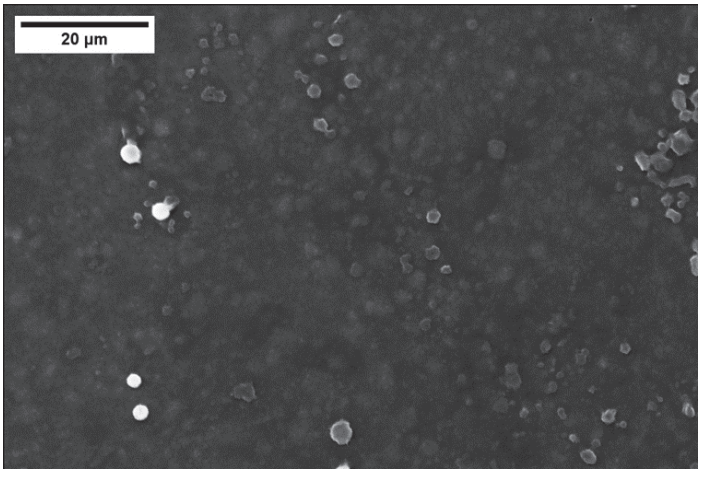

Figure 9. FESEM top view of the cured polymer coating with 48 wt% silica nanoparticles: "clouds" due to non-optimal silica dispersion.

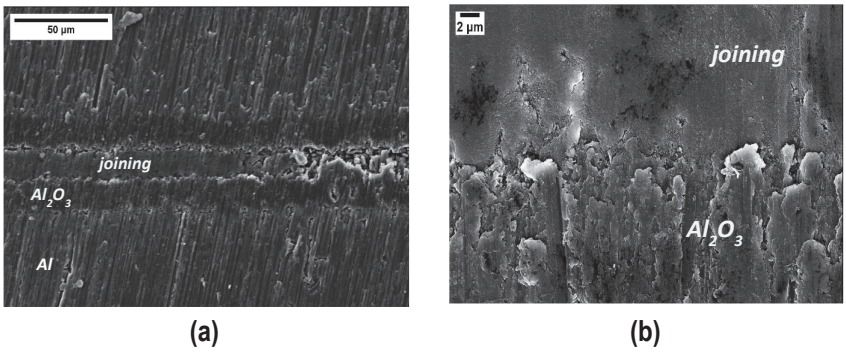

Figure 10. SEM cross section of samples joined using the cured polymer loaded with 48 wt% silica nanoparticles (**a**) and higher magnification of the interface PEO alumina and joining material (**b**).

Tensile tests on four of these joined samples gave an average tensile strength of 7.0 ± 0.6 MPa (Figure 11), which is almost four times the values obtained on joints produced by using the polymer only.

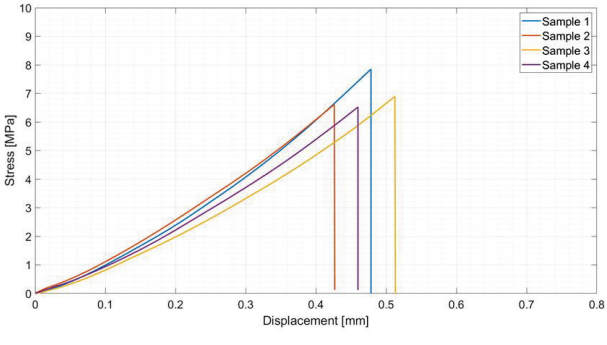

Figure 11. Tensile test results on samples joined using polymer loaded with 48 wt% silica nanoparticles: average tensile strength = 7.0 ± 0.6 MPa.

The fracture surfaces after tensile tests clearly show a cohesive fracture mode in all samples (Figure 12a): loading the polymer with silica nanoparticles decreases the joints porosity and increases their mechanical strength, this suggesting that the interface joining material/PEO alumina is stronger than before, as is the cohesion of the joining material. Figure 12 shows FESEM images of the fracture surfaces after tensile tests and the compact structure of the joining material is well visible (Figure 12b), particularly at higher magnification (Figure 12c,d). By comparing these results with those in Figure 7b, it is clear, from a morphological point of view, that the addition of silica nanoparticles improved both the cohesion and mechanical strength of the joints.

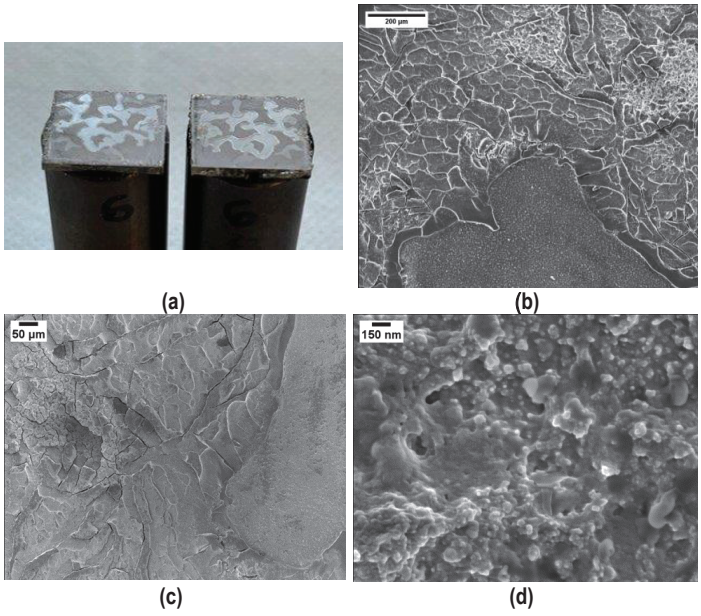

Figure 12. Typical cohesive fracture surface after tensile test on samples joined using polymer loaded with 48 wt% silica nanoparticles: visual appearance (**a**) and FESEM (**b**–**d**) of the joining material.

Given these promising results, these joints were further characterized using a tensile single lap test, according to ASTM D1002-10 [37], as shown in Figure 13: a typical cohesive fracture surface (b) was found on all samples, as reported for the tensile tests. The average lap strength was 1.2 ± 0.3 MPa and the curves show the expected brittle behavior (Figure 13c). The lower value measured for lap shear strength in tensile mode was due to the presence of bending modes, which are absent when the measure is conducted as in Figure 6.

In order to understand the mechanical resistance of the coatings better, Computed Tomography with in situ bending tests was performed on the aluminum slabs coated with the polymer and cured, as described above and by using the fixture shown in Figure 14a, where the position of the supporting pins (A), loading pins (B), and CFRP rod (C), which transfers the load, are highlighted.

The transversal sections of the reconstructed 3D volumes via CT-scan are reported in Figure 14b and the sample after test is visible in Figure 14c: the first crack appearance on the coating was observed at a bending load of 115 N. The measured bending stress on the coating was 570 MPa.

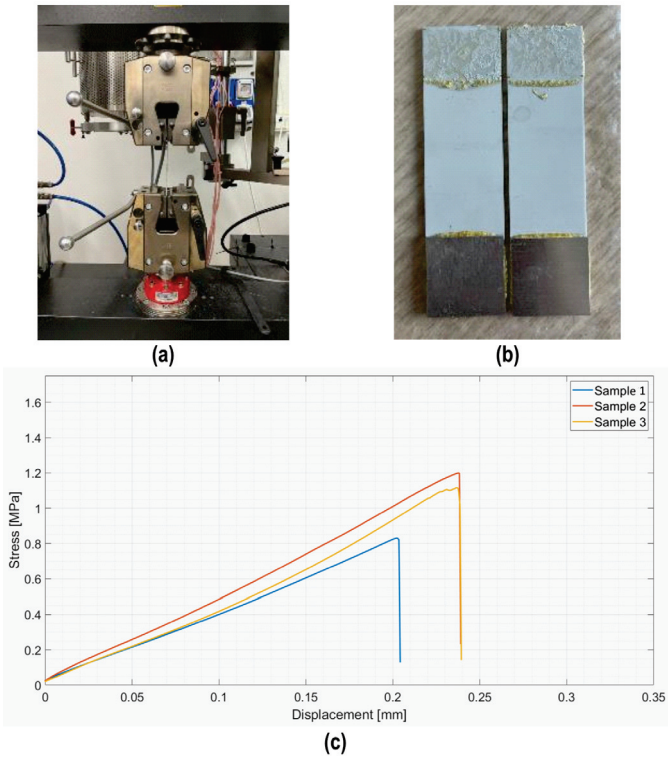

Figure 13. Single lap test in tensile mode (**a**) on samples joined using polymer loaded with 48 wt% silica nanoparticles (AISI D1002-10); typical cohesive fracture surface (**b**); and average lap strength = 1.15 ± 0.3 MPa (**c**).

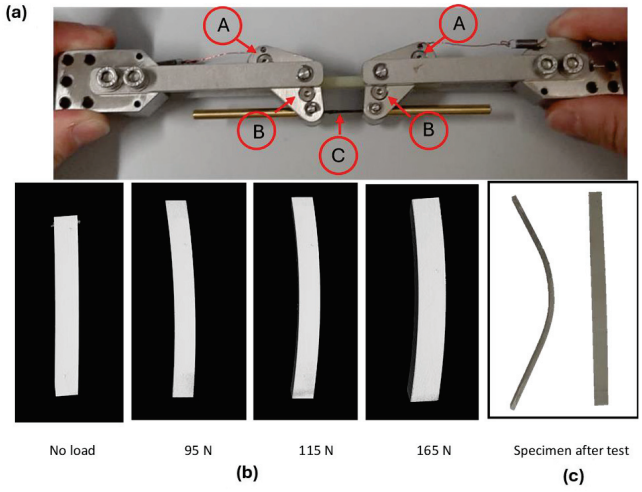

Figure 14. CT-scan in situ bending tests at different loading conditions on PEO alumina aluminum slabs, coated with the polymer and cured. Set up for the in situ bending test (**a**). Transversal section of the reconstructed 3D model via CT-scan (**b**). Specimen after test (**c**).

Figure 15 shows the cracks visible in the tomography reconstruction (b) and the FESEM inspection of the same surface (c).

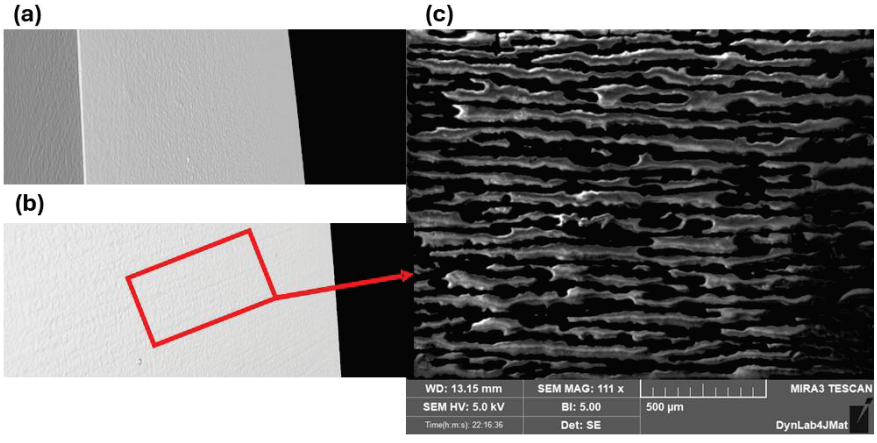

Figure 15. Surface tomography inspection of the non-loaded PEO aluminum slabs coated and cured, without cracks (**a**). First appearance of cracks on the coating during in situ bending test during tomography (**b**). Higher magnification of the cracks via FESEM (**c**).

Finally, the produced coatings were always characterized by outstanding resistance in the humid environment, with the recorded weight loss after one week soaking in tap water at room temperature always equal to zero.

4. Conclusions

The suitability of a silica preceramic polymer for joining and coating Plasma Electrolytic Oxidated (PEO) aluminum components at temperatures below 200 °C was demonstrated in this study.

The incorporation of a passive filler, specifically nanometric amorphous silica, enabled effective control over the critical aspects of the crosslinking process, resulting in significant enhancements in both joint morphology and mechanical strength. This advancement transitioned the joint from one characterized by numerous voids and cracks to a much denser and more compact structure, capable of achieving an average tensile strength of approximately 7 MPa, which is four times greater than that achieved using the pure polymer.

The bending stress at which the first crack appeared on the coating was notably 570 MPa, extending the potential applications of this coating to environments that require substantial mechanical resistance.

The water resistance, preliminarily assessed by soaking the coated samples in tap water for one week, yielded excellent results.

Further improvements in the mixing process for silica nanoparticles, as well as the coating deposition, joining procedure, and thickness, are likely to enhance the mechanical strength of the samples.

Finally, for applications requiring higher temperatures, this polymer presents itself as an intriguing joining and coating material capable of producing pure amorphous silica at approximately 800 °C.

This study explored the use of a silica preceramic polymer for joining and coating Plasma Electrolytic Oxidated aluminum components and the resistance to humid environments has been studied. The results suggest that this material, used as a joining or coating material, has potential for broader applications, including components working in harsh conditions. As a consequence, further investigations will address the behavior of this material in several liquid media showing ranges of pH values. Moreover, in the future, the influence of different wt% of silica nanoparticles will be further investigated.

Author Contributions: Conceptualization, M.F., V.M.S. and P.S.; methodology, M.F., V.C. and V.M.S.; validation, V.C. and A.B.; formal analysis, A.B.; investigation, V.C. and A.B.; resources, V.C. and A.B.; writing—original draft preparation, M.F. and A.B.; writing—review and editing, M.F., V.M.S., P.S. and V.C.; visualization, A.B.; supervision, M.F., V.M.S. and V.C.; project administration, M.F. and V.M.S.; funding acquisition, M.F. All authors have read and agreed to the published version of the manuscript.

Funding: This research received no external funding.

Institutional Review Board Statement: Not applicable.

Informed Consent Statement: Not applicable.

Data Availability Statement: Data is contained within the article.

Acknowledgments: The authors would like to thank Peter Krueger, IKTS-Fraunhofer Institute, Dresden, Germany, for providing the bending fixture for the CT-scan in situ mechanical tests and G. Soraru' and M. Biesuz at Trento University, Italy for useful discussions about the use of this polymer. A special thanks to Virginia Pastorelli, who prepared and characterized some of the samples during her master thesis at Politecnico di Torino (2023).

Conflicts of Interest: Pavel Shashkov is employed by Cambridge Nanolitic Ltd. The funders had no role in the design of the study; in the collection, analyses, or interpretation of data; in the writing of the manuscript; or in the decision to publish the results.

References

1. Rahimi, S.; Khiabani, A.B.; Yarmand, B.; Kolahi, A. Comparison of Corrosion and Antibacterial Properties of Al Alloy Treated by Plasma Electrolytic Oxidation and Anodizing Methods. 2018. Available online: www.sciencedirect.comwww.materialstoday.com/proceedings2214-7853 (accessed on 11 June 2024).
2. Ropyak, L.; Shihab, T.; Velychkovych, A.; Bilinskyi, V.; Malinin, V.; Romaniv, M. Optimization of Plasma Electrolytic Oxidation Technological Parameters of Deformed Aluminum Alloy D16T in Flowing Electrolyte. *Ceramics* **2023**, *6*, 146–167. [CrossRef]
3. Budunoglu, H.; Yildirim, A.; Bayindir, M. Flexible and mechanically stable antireflective coatings from nanoporous organically modified silica colloids. *J. Mater. Chem.* **2012**, *22*, 9671–9677. [CrossRef]
4. Chi, F.; Yan, L.; Yan, H.; Jiang, B.; Lv, H.; Yuan, X. Ultralow-refractive-index optical thin films through nanoscale etching of ordered mesoporous silica films. *Opt. Lett.* **2012**, *37*, 1406–1408. [CrossRef]
5. Castro, Y.; Ferrari, B.; Moreno, R.; Dur'an, A.; Dur'an, D. Silica Sol-Gel Coatings on Metals Produced by EPD. *J. Sol-Gel Sci. Technol.* **2003**, *26*, 735–739. [CrossRef]
6. Raut, H.K.; Ganesh, V.A.; Nair, A.S.; Ramakrishna, S. Anti-reflective coatings: A critical, in-depth review. *Energy Environ. Sci.* **2011**, *4*, 3779–3804. [CrossRef]
7. Kócs, L.; Késmárki, A.; Klébert, S.; Madarász, J.; Hórvölgyi, Z. Plasma-assisted template removal and consolidation of silica coatings on polycarbonate. *Thin Solid Film.* **2021**, *738*, 138976. [CrossRef]
8. Kócs, L.; Albert, E.; Tegze, B.; Kabai-Faix, M.; Major, C.; Szalai, A.; Basa, P.; Hórvölgyi, Z. Silica Sol-gel coatings with improved light transmittance and stability. *Period. Polytech. Chem. Eng.* **2018**, *62*, 21–31. [CrossRef]
9. Barnes, T.A.; Pashby, I.R. Joining techniques for aluminium spaceframes used in automobiles Part II Ð adhesive bonding and mechanical fasteners. *J. Mater. Process. Technol.* **2000**, *99*, 72–79. [CrossRef]
10. Lunder, O.; Olsen, B.; Nisancioglu, K. Pre-treatment of AA6060 aluminium alloy for adhesive bonding. *Int. J. Adhes. Adhes.* **2002**, *22*, 143–150. [CrossRef]
11. Cavezza, F.; Boehm, M.; Terryn, H.; Hauffman, T. A review on adhesively bonded aluminium joints in the automotive industry. *Metals* **2020**, *10*, 730. [CrossRef]
12. Petrie, E.M. How moisture affects adhesives, sealants, and coatings. *Met. Finish.* **2011**, *109*, 36–37+48. [CrossRef]
13. Del Real, J.C.; De Santayana, M.C.; Abenojar, J.; Martinez, M.A. Adhesive bonding of aluminium with structural acrylic adhesives: Durability in wet environments. *J. Adhes. Sci. Technol.* **2006**, *20*, 1801–1818. [CrossRef]
14. Fu, S.; Zhu, M.; Zhu, Y. Organosilicon polymer-derived ceramics: An overview. *J. Adv. Ceram.* **2019**, *8*, 457–478. [CrossRef]
15. Ren, Z.; Bin Mujib, S.; Singh, G. High-temperature properties and applications of Si-based polymer-derived ceramics: A review. *Materials* **2021**, *14*, 614. [CrossRef] [PubMed]
16. Chaudhary, R.P.; Parameswaran, C.; Idrees, M.; Rasaki, A.S.; Liu, C.; Chen, Z.; Colombo, P. Additive manufacturing of polymer-derived ceramics: Materials, technologies, properties and potential applications. *Prog. Mater. Sci.* **2022**, *128*, 100969. [CrossRef]
17. Colombo, P.; Mera, G.; Riedel, R.; Sorarù, G.D. Polymer-derived ceramics: 40 Years of research and innovation in advanced ceramics. *J. Am. Ceram. Soc.* **2010**, *93*, 1805–1837. [CrossRef]
18. Barroso, G.; Li, Q.; Bordia, R.K.; Motz, G. Polymeric and ceramic silicon-based coatings-a review. *J. Mater. Chem. A* **2019**, *7*, 1936–1963. [CrossRef]
19. Greil, P. Polymer derived engineering ceramics. *Adv. Eng. Mater.* **2000**, *2*, 339–348. [CrossRef]

20. Bernardo, E.; Fiocco, L.; Parcianello, G.; Storti, E.; Colombo, P. Advanced ceramics from preceramic polymers modified at the nano-scale: A review. *Materials* **2014**, *7*, 1927–1956. [CrossRef]
21. Colombo, P.; Riedel, R.; Soraru, G.D.; Kleebe, H.-J. *Polymer Derived Ceramics: From Nano-Structure to Applications*; Destech Pubns Inc.: Lancaster, PA, USA, 2010.
22. Bala Srinivasan, P.; Zettler, R.; Blawert, C.; Dietzel, W. A study on the effect of plasma electrolytic oxidation on the stress corrosion cracking behaviour of a wrought AZ61 magnesium alloy and its friction stir weldment. *Mater. Charact.* **2009**, *60*, 389–396. [CrossRef]
23. Shore, D.; Avelar-Batista Wilson, J.C.; Matthews, A.; Yerokhin, A. Adhesive bond strength of PEO coated AA6060-T6. *Surf. Coat Technol.* **2021**, *428*, 127898. [CrossRef]
24. Aliasghari, S.; Skeldon, P.; Zhou, X.; Ghorbani, M. Influence of PEO and mechanical keying on the strength of AA 5052 alloy/polypropylene friction stir spot welded joints. *Int. J. Adhes. Adhes.* **2019**, *92*, 65–72. [CrossRef]
25. Aliasghari, S.; Ghorbani, M.; Skeldon, P.; Karami, H.; Movahedi, M. Effect of plasma electrolytic oxidation on joining of AA 5052 aluminium alloy to polypropylene using friction stir spot welding. *Surf. Coat Technol.* **2017**, *313*, 274–281. [CrossRef]
26. Shashkov, P.; Khomutov, G.; Yerokhin, A.; Usov, S. Non-Metallic Coating and Method of Its Production. U.S. Patent 9,677,187,B2, 13 June 2017.
27. Bousser, E.; Rogov, A.; Shashkov, P.; Gholinia, A.; Laugel, N.; Slater, T.J.A.; Withers, P.J.; Matthews, A.; Yerokhin, A. Phase transitions in alumina films during post-sparking anodising of Al alloys. *Acta Mater.* **2023**, *244*, 118587. [CrossRef]
28. Kgaa, M. Technical Datasheet 214049 Durazane® 1800. Available online: https://www.merckgroup.com/Products/PM/global/TDS_214049_Durazane_1800_Merck.pdf (accessed on 26 April 2024).
29. Horcher, A.; Tangermann-Gerk, K.; Krenkel, W.; Schafföner, S.; Motz, G. Advanced ceramic coatings on aluminum by laser treatment of filled organosilazane-based composites. *Ceram. Int.* **2022**, *48*, 23284–23292. [CrossRef]
30. Liu, J.; Qiao, Y.L.; Zhang, P.; Xue, Y.C.; Cai, Z. Synthesis of SiC ceramics from polysilazane by laser pyrolysis. *Surf. Coat Technol.* **2017**, *321*, 491–495. [CrossRef]
31. Gardelle, B.; Duquesne, S.; Vu, C.; Bourbigot, S. Thermal degradation and fire performance of polysilazane-based coatings. *Thermochim. Acta* **2011**, *519*, 28–37. [CrossRef]
32. Barroso, G.; Döring, M.; Horcher, A.; Kienzle, A.; Motz, G. Polysilazane-Based Coatings with Anti-Adherent Properties for Easy Release of Plastics and Composites from Metal Molds. *Adv. Mater. Interfaces* **2020**, *7*, 1901952. [CrossRef]
33. Qazzazie-Hauser, A.; Honnef, K.; Hanemann, T. Crosslinking behavior of UV-cured polyorganosilazane as polymer-derived ceramic precursor in ambient and nitrogen atmosphere. *Polymers* **2021**, *13*, 2424. [CrossRef] [PubMed]
34. *ASTM C633-01*; Standard Test Method for Adhesion or Cohesion Strength of Thermal Spray Coatings. ASTM International: West Conshohocken, PA, USA, 2010.
35. Baino, F.; Vitale-Brovarone, C. Wollastonite-containing bioceramic coatings on alumina substrates: Design considerations and mechanical modelling. *Ceram. Int.* **2015**, *41*, 11464–11470. [CrossRef]
36. D'Isanto, F.; Salvo, M.; Molin, S.; Koszelow, D.; Javed, H.; Akram, S.; Chrysanthou, A.; Smeacetto, F. Glass-ceramic joining of Fe22Cr porous alloy to Crofer22APU: Interfacial issues and mechanical properties. *Ceram. Int.* **2022**, *48*, 28519–28527. [CrossRef]
37. *ASTM D1002-10*; Standard Test Method for Apparent Shear Strength of Single-Lap-Joint Adhesively Bonded Metal Specimens by Tension Loading (Metal-to-Metal). ASTM International: West Conshohocken, PA, USA, 2019. [CrossRef]
38. Santhosh, B.; Biesuz, M.; Sorarù, G.D. Thermal properties of dense polymer-derived SiCN(O) glasses. *Mater. Lett.* **2021**, *288*, 129336. [CrossRef]
39. Sorarù, G.D.; Tavonatti, C.; Kundanati, L.; Pugno, N.; Biesuz, M. Effect of the pyrolysis atmosphere on the mechanical properties of polymer-derived SiOC and SiCN. *J. Am. Ceram. Soc.* **2020**, *103*, 6519–6530. [CrossRef]
40. Santhosh, B.; Vakifahmetoglu, C.; Ionescu, E.; Reitz, A.; Albert, B.; Sorarù, G.D. Processing and thermal characterization of polymer derived SiCN(O) and SiOC reticulated foams. *Ceram. Int.* **2020**, *46*, 5594–5601. [CrossRef]
41. Ionescu, E.; Kleebe, H.J.; Riedel, R. Silicon-containing polymer-derived ceramic nanocomposites (PDC-NCs): Preparative approaches and properties. *Chem. Soc. Rev.* **2012**, *41*, 5032–5052. [CrossRef]
42. Lenz Leite, M.; Viard, A.; Galusek, D.; Motz, G. In Situ Generated β-Yb2Si2O7 Containing Coatings for Steel Protection in Extreme Combustion Environments. *Adv. Mater. Interfaces* **2021**, *8*, 2100384. [CrossRef]
43. Nguyen, V.S.; Rouxel, D.; Vincent, B. Dispersion of nanoparticles: From organic solvents to polymer solutions. *Ultrason. Sonochem.* **2014**, *21*, 149–153. [CrossRef]
44. Krishnamoorti, R. Strategies for Dispersing Nanoparticles in Polymers. *MRS Bull.* **2007**, *32*, 341–347. [CrossRef]

coatings

MDPI

Article

Comparison of Tribological Characteristics of AA2024 Coated by Plasma Electrolytic Oxidation (PEO) Sealed by Different sol–gel Layers

Hafiza Ayesha Khalid [1,2], Sajjad Akbarzadeh [1,2], Yoann Paint [3], Véronique Vitry [2] and Marie-Georges Olivier [1,3,*]

[1] Materials Science Department, Faculty of Engineering, University of Mons, 20, Place du Parc, 7000 Mons, Belgium; hafizaayesha.khalid@umons.ac.be (H.A.K.)
[2] Metallurgy Department, Faculty of Engineering, University of Mons, 20, Place du Parc, 7000 Mons, Belgium; veronique.vitry@umons.ac.be
[3] Materia Nova Research Centre, 1, Avenue N. Copernic, Parc Initialis, 7000 Mons, Belgium
* Correspondence: marjorie.olivier@umons.ac.be

Abstract: The application of sol–gel on plasma electrolytic oxidation (PEO) coatings can increase wear resistance by sealing the surface defects such as pores and cracks in the outer layer of the PEO layer and strengthen the coating. Four different sol–gel formulations based on precursors—(3-glycidyloxypropyl)trimethoxysilane (GPTMS), methyltriethoxysilane (MTES), methacryloxypropyltrimethoxysilane (MAPTMS), (3-aminopropyl)triethoxysilane (APTES), and zirconium(IV) propoxide (ZTP) along with tetraethoxysilane (TEOS)—were used to seal PEO pores, and the samples were tested tribologically. A sliding reciprocating tribometer was used to carry out a wear test with an alumina ball as the counter body in two different conditions: (a) 2.5 N load for 20 min, and (b) 3 N load for 40 min. The coefficient of friction and wear rate as volume loss per unit sliding length were obtained for all sol–gel-sealed specimens and unsealed PEO-coated and bare AA2024 substrate. 3D mechanical profilometer surface scans were used to compare the depth of wear traces. The elemental color mapping using SEM and EDS revealed that silicon remains present in the wear tracks of PEO coatings sealed with sol–gel layers containing GPTMS (PSG) and ZTP (PSG-ZT). GPTMS (PSG) was able to fill the pores of the PEO layer efficiently due to its cross-linked network. Moreover, sol–gel containing ZTP (PSG-ZT) was deposited as a thick layer on top of the PEO layer which provided good lubrication and resistance to wear. However, other sol–gel formulations (PSG-MT and PSG-AP) were worn out during tests at a higher load (3 N). The most stable friction coefficient (COF) and specific wear rates were observed with sol–gels with GPTMS and ZTP.

Keywords: plasma electrolytic oxidation; sol–gel sealing; AA2024; wear; SEM; profilometer

Citation: Khalid, H.A.; Akbarzadeh, S.; Paint, Y.; Vitry, V.; Olivier, M.-G. Comparison of Tribological Characteristics of AA2024 Coated by Plasma Electrolytic Oxidation (PEO) Sealed by Different sol–gel Layers. *Coatings* **2023**, *13*, 871. https://doi.org/10.3390/coatings13050871

Academic Editor: Marta Mohedano

Received: 5 April 2023
Revised: 28 April 2023
Accepted: 30 April 2023
Published: 5 May 2023

1. Introduction

Surface degradation by wear has recently been catching attention due to the frequent need of replacing parts in the engineering industry. This phenomenon is disastrous, leading to performance and energy losses that occur by a worn surface of the counter component when two bodies are in relative motion. The choice of material should fulfill certain criteria which are defined based on the mechanical properties, durability, mass properties, cost of production, and ease of fabrication [1]. With rising environmental concerns, lighter-weight materials with reliable strength are in focus, to be used for components and assemblies under a motion to save fuel costs. To fulfill this objective, aluminum alloys, owing to their low density and high specific resistance, have played a vital role in replacing conventional construction materials (steel) [2,3]. Nevertheless, bulk material with a hard surface that can withstand mechanical and tribological loads as well as exhibit high resistance to corrosion cannot be accomplished from aluminum alloys in their natural form. Aluminum alloys form

a soft, thin oxide layer that is easily removed when subjected to corrosive and tribological loads. Plasma electrolytic oxidation (PEO) is an electrochemical process that produces a crystalline oxide layer at a metallic substrate by generating a plasma discharge at the metal–electrolyte interface. Several-microns-thick PEO coatings reach a high hardness and present excellent adhesion to the substrate. Mora-Sanchez et al. found a significant increase in the hardness of PEO-treated cast A361 alloy—up to ~15 GPa—compared to hard anodized coatings on the same alloy which yielded a hardness of only up to ~4 GPa [4]. The PEO process is the method of choice that utilizes environmentally friendly materials such as diluted alkaline electrolytes [5–7]. Such coatings provide good resistance to fretting, abrasion, and erosion by improving the wear resistance of aluminum alloys [8–10].

There are, however, some limitations with PEO coatings, as the structure contains micropores throughout the PEO layers which results from the micro-arc generated by plasma on the metal–electrolyte interface. Moreover, the coating growth occurs with the simultaneous melting and solidification, leading to thermal stresses which generate micro-cracks radially propagated from the pores [11]. The source of power mode employed in the PEO process has an impact on the hardness, growth rate, phase composition, structure, morphology, and degree of porosity of the coatings. The PEO treatment operating in DC mode results in coatings with a lower oxide development rate and higher porosity due to its restricted control and difficulty in changing discharge characteristics. Nevertheless, the pulsed DC mode provides the opportunity to regulate the discharge duration and can potentially use less energy [12]. By using the AC mode, electrode polarization is avoided, and arc interruption may be used to conveniently manage the process. In comparison to coatings created using DC, AC, and unipolar pulsed modes, the bipolar pulsed mode greatly enhances coating characteristics, drawing the attention of numerous researchers. Since it lessens the frequency of strong plasma discharges and high-temperature spikes during the PEO process, dense coatings with superior corrosion resistance and larger coating thickness may be created in the bipolar pulsed current mode [13,14]. Under AC or bipolar-pulsed regimes, frequently using frequencies up to several thousand Hz and variable duty cycles, a three-layered PEO coating consisting of an outer porous layer rich in electrolyte-derived compounds, an intermediate relatively compact micro-cracked layer rich in α-alumina, and a submicron dense barrier layer can be obtained [15]. According to theory, increasing the quantity of α-Al_2O_3 improves the wear performance of PEO coatings [16]. Khan et al. [17] discovered that a reduced duty cycle resulted in a comparable decline in the ratio of α-Al_2O_3 to γ-Al_2O_3 in PEO coatings on 6082 aluminum alloy generated by the pulsed unipolar current. The concentration of α-Al_2O_3 in the coatings was observed to rise with the application of larger current densities and the lengthening of the deposition period, which produced thicker coatings [18,19]. V. Dehnavi et al. [20] found that increasing the pulse on time by employing a lower frequency and higher duty cycle generates micro discharges with a lower spatial density but higher intensity which results in higher concentrations of Si-rich species on the surface of the PEO coatings. V. Hutsaylyuk et al. [21] reduced the unfavorable impact of hydrogen on the plasma-electrolytic oxidation of aluminum alloys and accordingly increased the efficiency of the synthesis of PEO layers with high abrasive-wear resistance. In general, high frequencies and negative pulses help to limit the duration of individual micro discharges, preventing their reappearance at the same location and transition into destructive arc discharges [22].

Among the several post-treatments to seal PEO pores, sol–gel has been described as an efficient sealing treatment for pores to avoid the penetration of aggressive media inside the pores [23,24]. It acts as a cementing agent in the PEO layer and can provide good resistance to corrosion and wear [25]. Since the benefit of using this process allows the composition of the sol–gel to be adjusted, the surfaces can therefore be tailored to the application [26,27]. Sopchenski-Santos et al. [28] developed PEO coatings on AA2024 and sealed them with sol–gel based on silicon precursors. They observed improvement in the wear resistance of the sol–gel-sealed PEO specimens over unsealed PEO-coated and bare substrate. In the

previous studies carried out by our research group, a significant improvement in resistance to corrosion has been noticed under familiar cases [29].

Sol–gel properties are influenced by several variables, including solvent type, aging, solution pH, and the type of sol–gel precursor, particularly [30,31]. In our previous investigation, four types of sol–gel solutions using Si and Si/Zr-based precursors with different organic functional groups (epoxy, amine, and methyl) have been prepared. The hydrophobicity, compactness, and impregnation characteristics of the sol–gel layers could dramatically affect the corrosion resistance properties. It was explained that the addition of MTES reduced the cross-linking density and compactness of a sol–gel layer consisting of TEOS and GPTMS precursors due to the presence of one un-hydrolysable methyl group. GPTMS could provide pore-filling properties, leading to the identical sealing ability of two types of sol–gel coatings. It was described that the sol–gel composed of APTES and TEOS precursors had the worst corrosion protection performance due to the insufficient sealing ability and relatively hydrophilic properties. The best anti-corrosion properties were observed in a PEO/sol–gel coating system in which TEOS, ZTP, and MAPTMS were employed as sol–gel precursors. Relatively high hydrophobicity, the capability to form a uniform layer over PEO as well as the ability to penetrate intrinsic pores, and the evolution of the cage-like siloxane network along with the ladder-like structure were the crucial factors leading to the best sealing abilities [32]. This research aims to investigate the tribological behavior of PEO-coated AA2024 alloy by sealing the PEO pores with various sol–gel formulations. To the best of the author's knowledge, no investigation has been made on the tribological behavior of sol–gel-sealed PEO coatings on AA2024 alloy with different Si- and Si/Zr-based sol–gel formulations. In the continuation of our previous work [32], a tribological evaluation is carried out with the same sol–gel formulations used to seal the PEO layer, and PEO conditions were also kept identical.

2. Experimental Procedure

AA2024 alloy (Ti $\leq$ 0.15%, Ni 0.15%, Zn 0.25%, Si 0.5%, Fe 0.5%, Mn 0.3%–0.9%, Mg 1.2%–1.8%, Cu 3.8%–4.9%, and Al balance) specimen with dimensions 35 mm $\times$ 25 mm $\times$ 1.5 mm were used in this study to produce PEO layer with parameters previously defined by our research group [17,21]. A PowerPulse (Micronics Systems, Vilette d'Anthon, France) was used to coat specimens for 30 min using the following conditions: bipolar regime, 5A anodic current, 30% duty cycle, 100 Hz frequency, in an alkaline electrolytic bath consisting of 1.65 g/L Na_2SiO_3 and 1 g/L KOH (Alfa Aesar Co., Tewksbury, MA, USA). Four (4) different sol–gel formulations previously prepared by our research group were used to seal the PEO pores, the details of which can be found in an article by Akbarzadeh et al. [32]. The details of sol–gel formulations are given in Table S1. To briefly bring up the various sol–gel formulations, SG included TEOS (20% v/v) and GPTMS (10% v/v) in an electrolyte composed of distilled water (60% v/v) and ethanol (10% v/v). After bringing the pH down to 3, the solution was stirred for 24 h. The same condition was utilized to prepare PSG-MT but with one change, in which the concentration of TEOS decreased to 10% v/v and MTES with the concentration of 10% v/v was added instead to attain 30% v/v overall precursor concentration. These two solutions were applied to the PEO-coated samples, followed by curing at 150 °C for one hour to attain PSG and PSG-MT samples. To achieve the overall percentage of 30% v/v silane precursors in a solution including ethanol (56% v/v) and distilled water (14% v/v) in another sol–gel solution (SG-AP), a comparable volumetric intake of APTES (15% v/v) and TEOS (15% v/v) was used. Following this, acetic acid was gradually added to the solution to maintain the pH at 4.5. The mixture was stirred for a day at room temperature. The PEO sample coated with SG-AP was placed at ambient temperature for one day followed by placing at 150 °C for one hour to obtain PSG-AP. For the SG-ZT, two types of solution were mixed. The initial solution (Sol 1) was made up of TEOS (0.18 mol) and MAPTMS (1 mol) precursors, and the hydrolysis and condensation processes were started by adding distilled water (2.075 mol) and hydrochloric acid dropwise (0.001 mol). It was then added dropwise to Sol 2 (ZTP (0.12 mol), MAA (0.12 mol), and

isopropyl alcohol (0.4 mol)) after 150 min of stirring, then the mixture was stirred for a full day. The coated panels were dried with SG-ZT solution for one hour at 100 °C to attain the PSG-ZT sample. The sol–gel formulations were coated onto the PEO specimens through KSV Nima dip-coater instrument at a 100 mm/min withdrawal rate. To avoid confusion in the paper, the nomenclature given in Table 1 will be used throughout the paper.

Table 1. The nomenclature of the samples followed throughout the paper.

Untreated AA2024	PEO Treated	PEO + SG (TEOS + GPTMS)	PEO + SG-MT (TEOS + GPTMS + MTES)	PEO + SG-AP (TEOS + APTES)	PEO + SG-ZT (ZTP + MAPTMS + TEOS)
Substrate	PEO	PSG	PSG-MT	PSG-AP	PSG-ZT

Dry sliding tests were performed on uncoated and coated specimens at room temperature using a Bruker reciprocating sliding tribometer and a 6 mm counter body of alumina. Keeping the stroke length of 5 mm and frequency of 5 cycles/s constant, 2 sets of conditions were imposed on all specimens under ambient conditions:

(a) 2.5 N load, 1200 s (20 min) sliding duration, 60 m distance;
(b) 3 N load, 2400 s sliding duration, 120 m distance.

Two tests were carried out in each set of conditions to ensure the reproducibility of results. Tangential frictional forces were recorded to calculate the friction coefficient (COF) continuously as a function of the sliding duration by means of a load cell. The average friction coefficient was calculated from the steady state area of the graph and later averaged again over two experiments.

Both a HIROX (Tokyo, Japan) KH-870 digital optical confocal microscope and a Hitachi (Tokyo, Japan) SU8020 Scanning Electron Microscope (SEM) were used for the surface analyses of wear traces after each test. Surface roughness was measured according to ISO 4287 standard procedure. Resistance to wear and debris under a tribo-contact was assessed using confocal microscopy for wear scar depths and width of wear traces. Wear volume loss was quantified through 2D area multiplied by stroke length by averaging three profiles on each wear trace. The specific wear rate, K ($mm^3/N{\cdot}m$), is computed through the following equation (Equation (1)):

$$K = \frac{V}{F \times d} \quad (1)$$

where V is worn volume loss (mm^3), F is the normal load (N), and d is the reciprocating sliding distance (m). Consequently, the average specific wear rate was determined from two repetitions of tests. sol–gel traces were analyzed under SEM using Hitachi SU8020 equipment along with energy-dispersive X-ray spectroscopy (EDS). Color mapping of elemental composition was obtained through EDS equipped with Thermo Fisher Scientific (Waltham, MA, USA) Noran System 7 detector; 3D wear scars' profiles were drawn by P16+ profilometer from KLA Tencor (Milpitas, CA, USA).

3. Results and Discussion

3.1. SEM Analysis

The surface topography of the PEO-coated samples has been visualized via SEM images as depicted in Figure 1. The characteristic porous features of the PEO layer are caused by the repetitive melting and solidifying of the oxide layer during the process in the silicate-containing solution. Unnumbered pores with a diameter ranging from 1 to 10 μm are randomly placed throughout the surface as a result of the dielectric breakdown, plasma reactions, and the generation of such sparks. It can be noted that the trace of PEO pores and cracks has been diminished after the application of sol–gel coatings. Particularly, in the case of PSG-ZT, the formation of a layer resulted in the coverage of the porous layer in a way that flaws could barely be detectable anymore.

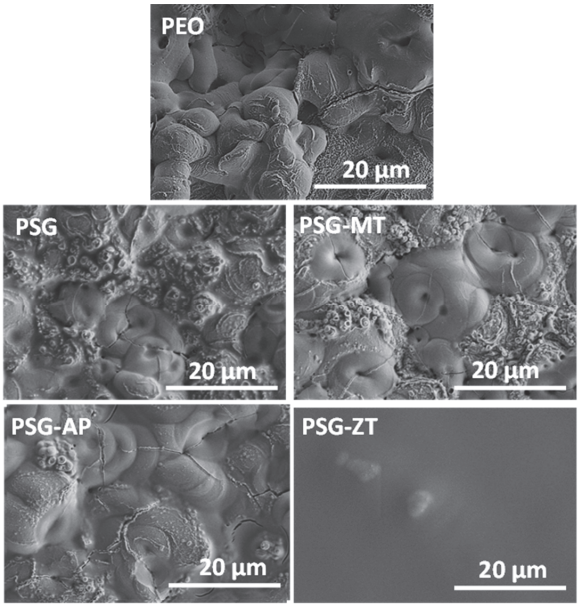

Figure 1. SEM analysis on surface morphology at 2.00 k magnification of coated samples.

The cross-section images along with the EDS mapping of the PEO/sol–gel coating systems are shown in Figure 2. The PEO oxide layer, having a thickness of 19.5 ± 5 µm, was produced by the combination of the substrate elements and the silicate solution, which is why EDS mapping images reported Al, O, and Si elements. Nevertheless, sol–gel sealing can be validated by the presence of the Si element inside the pores in the PEO/sol–gel samples compared to the distinct PEO sample. It was well-documented that the GPTMS precursor could provide the pore-filling ability to a sol–gel layer [32]. Accordingly, the almost similar sealing ability of the PSG and PSG-MT can be noticed by the EDS mapping. The PSG-AP sample contained some pores, demonstrating that the SG-AP was unable to effectively penetrate and seal the PEO pores. It appeared that the SG-AP was not likely to permeate through the pores and precipitate over the PEO surface. On the contrary, in the case of PSG-ZT, not only could a desirable pore filling be observed but also a homogenous layer over the PEO coating. In accordance with the top-view observation, the homogenous layer (with a thickness of 6.7 ± 2 µm) on top of PEO is recognized in the PSG-ZT.

The roughness measurement was performed and reported in Table 2. R_a and R_z corresponded to the arithmetical mean deviation and maximum height of the profile, respectively. The roughness of the PEO was reduced after the application of any sol–gel sealing, relating to the filling of the hollows with the sol–gel coating. Specifically, the roughness of the PSG-ZT was the minimum because of the ability of the SG-ZT sol–gel to not only seal the pores but also create a homogenous layer over the PEO layer. The roughness values of PSG and PSG-MT are somehow similar, illustrating identical sealing properties. For the PSG-AP, the R_a is a little bit lower than PSG and PSG–MT, reflecting the dominant deposition of the SG-AP rather than the sealing ability as was also depicted in the SEM cross-section images.

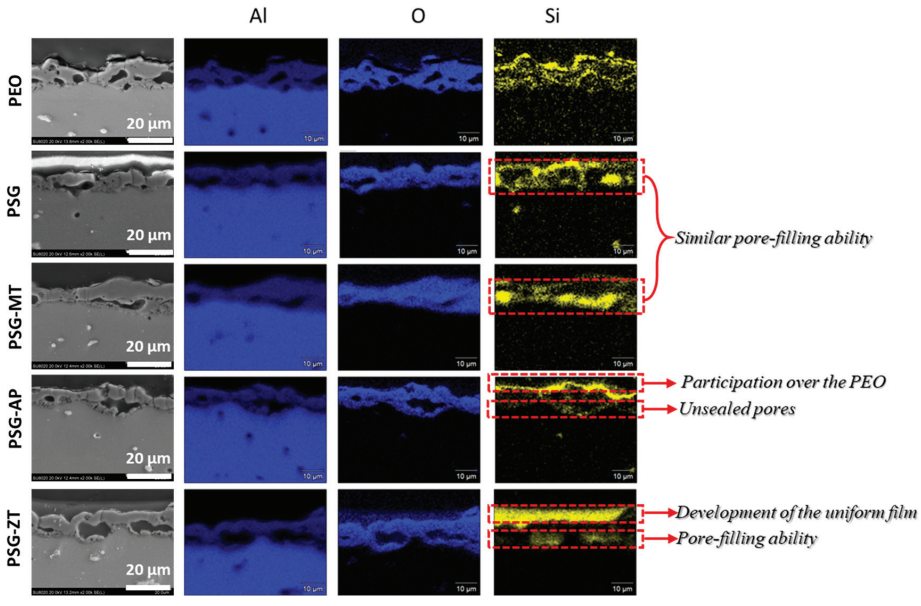

Figure 2. SEM cross-sectional analysis of coatings at 2.00 k magnification and color map.

Table 2. Roughness measurement results of different PEO/sol–gel coating systems.

Average COF	PEO	PSG	PSG-MT	PSG-AP	PSG-ZT
R_a	1.7	1.3	1.3	1.2	0.2
R_z	11.3	8.9	9.2	6.4	0.9

3.2. Tribological Evaluation

The variation of the friction coefficient (COF) with different surface treatments applied on the AA2024 alloy is illustrated in Figure 3. The COF for the substrate is selectively plotted in both conditions—(a) 2.5 N, 20 min, and (b) 3 N, 40 min—till the first highest peak and was snubbed further due to the high noise-to-signal ratio making the rest of the data unclear. The PEO-coated sample has shown a gradual increase in the coefficient of friction for Case (a), because when the loose porous structure of the PEO coating is being pressed when in contact during the wear test, it gradually exposed patches of the substrate from underneath with an average COF of 0.53. However, for Case (b), the PEO coating could not achieve a steady state as it failed to bear the load and produced more debris than the bare substrate against the alumina counter body, which led to a higher COF.

For the different sol–gels tested, PSG depicted a gradual increase in COF due to the running-in period and then stabilized for the rest of the tests with an average COF of 0.41 and 0.49 for Case (a) and Case (b), respectively. The initial gradual increase in COF is the result of a thin PSG coating, as it has a small running-in phase and helped to achieve a fast, steady state. A lubricating layer between two moving bodies known as the tribo-layer consisting of broken polymeric chains is formed. These polymeric chains being removed from the uppermost layer of the sol–gel are sheared and aligned in the direction of sliding in the contacting area between the substrate and the counter body. Hence, the third body tribo-layer formation proves that PSG has provided a good-enough sealing of the surficial defects with precursors (TEOS + GPTMS)—by making the network extendable through all hydrolyzable groups [29,33]—and when the network clusters of TEOS and GPTMS are aligned between contacting bodies after the running-in period, they facilitate the easy sliding by reducing shear stresses. Moreover, the PSG network holds well against the two

different loads (2.5 N and 3 N) by achieving a steady state rather quickly (after ~100 s) with an average COF of 0.41 and 0.49 for Cases (a) and (b), respectively. PSG-MT provided a trend similar to PSG in the COF curve at the milder conditions with an average of 0.40 for Case (a). However, a clear difference is noted in Case (b) where the sol–gel was not able to remain in the PEO pores at a higher load for a longer duration due to its less dense structure owing to the presence of the MTES precursor [34], which influences the compactness of the coating. The steady state only lasted for half of the test duration with an average COF of 0.50. Resultingly, when the sol–gel sealing was damaged, it exposed the PEO from underneath, which caused higher debris in the tribo-contact, hence the higher noise and poor lubrication. PSG-AP, owing to its -NH_2 precursor which was not able to fill the surface defects of the PEO coating, results in the inefficient sealing capability of the PEO layer [31,35]. Therefore, under load, it absorbs humidity from the surroundings and is pulled out from the superficial defects and exposed the PEO coating, showing a COF similar to the unsealed PEO coating with more debris and higher noise in the data. In the PSG-AP curves for both Cases (a) and (b), it can be noted that it is relatively difficult to obtain a steady-state range. However, the COF was averaged in the initial period having values of 0.55 in both cases with difficulty stating if the obtained COF value is due to the PSG-AP or PEO exposure. Out of all sol–gels, PSG-ZT had shown stable behavior with the longest steady-state range and the lowest average COF of 0.34 and 0.43 for both Cases (a and b), respectively. Instead of a gradual increase during the running period, a sudden increase was noticed but it still remained the lowest COF among all the sol–gels. The initial different behavior is attributed to the presence of a sol–gel layer with promising compactness properties as a top layer on the PEO layer [36]. Overall, sol–gel-sealed PEO coatings have shown promising results by effectively filling the surface defects as shown in Figure 2. The average COFs for all coatings in the steady-state range are presented in Table 3, and are in agreement with the research findings of Sopchenski-Santos et al. [28], where the bare AA2024, PEO coating, and sol–gel-sealed PEO coating were tested tribologically in a pin-on-disk tribometer at 1 N load against alumina ball.

A wear trace analysis of profile depths for the uncoated and coated samples are presented in Figures 4 and 5. The wear scar depth of PEO (Figure 4c) is much smaller than that of the bare substrate (Figure 4a) as the structure is able to withhold the load in contact for milder conditions in Case (a); nonetheless, it can be noted in Figure 4b,d that the PEO structure, owing to its relatively poor mechanical properties—since it has open, unfilled pores (Figure 2)—has, however, exposed the substrate.

The average specific wear rate is plotted, showing a significant decrease in wear rates for PEO-treated surfaces as compared to the bare substrate. This effect is more dominant in Case (a) with mild conditions, but, in Case (b), PEO, being a loose structure, is completely removed and the wear rate is close to that of the substrate. Similar outcomes were noticed by Sieber et al. [37] where PEO-coated commercial aluminum alloys showed a decrease in wear mass loss in comparison to the bare substrate.

For sol–gel-sealed specimens, a significant decrease is noted in the wear scars' depths as compared to the unsealed PEO coatings, particularly in PSG and PSG−ZT in Case (b) from 0.704 mm^3/Nm to 0.05 and 0.06 mm^3/Nm, respectively, as revealed in Figure 5 and Table 4. The sharp asperities of the PSG−coated structure have been flattened in the wear trace and look less like debris production but more like asperities pushed back into the structure as presented in Figure 5a for Case (a), and this phenomenon is more evident in Case (b) as displayed in Figure 5b. The good sealing characteristics of PSG due to four hydrolysable groups in TEOS and epoxy groups in GPTMS have helped to reduce the wear rate by a greater degree. As shown in Table 4, PSG has the lowest wear rates in both Cases (a) and (b). One thing to be noted here is that, in extreme conditions, the wear rate is further reduced by the densification of a hybrid inorganic/organic network where a higher load for a longer time has caused compactness in the surface without producing debris. This compression in the structure has caused mechanical strength in the coating, and hence it has maintained the coating integrity even better on higher loads. Contrarily, even with

a good sealing capability (with the MTES precursor), the structure of PSG−MT is not as compact as that of PSG. It is noted that the extent of damage after the wear test is higher in PSG−MT; this difference can be realized clearly in Figure 5d more than in Figure 5c for Case (b) and (a), respectively. At a low load (2.5 N) for a smaller period (1200 s), a minor pullout of sol–gel is observed from the PEO defects, hence the wear by the adhesive particles and sol–gel pullout. At the higher load (3 N for a longer period (2400 s)), the surface topography demonstrated (Figure 5d) a complete coating removal as the comparatively less compact structure does not withhold this load, and the coating is completely removed by the counter body penetration in the substrate. The adhesive wear mechanism can be explained by the high hardness of the alumina ball compared to the relatively soft coating which results in material transfer to the ball as a result, and, when exposed to air, the transferred material with free bonds oxidizes into hard particles and acts as the third body in the tribo-contact which causes more debris. In this case, wear resulted not only from third body rolling but also from PEO debris, and, ultimately, substrate exposure.

Figure 5e,f represent the surface profiles of PSG−AP for Case (a) and Case (b), respectively, and portray the worst wear resistance by producing the largest volume of material removal among all sol–gel−treated surfaces. For milder conditions, it illustrates the selective removal of material, leaving deep grooves inside the sol–gel network, with the possibility to have exposed PEO from underneath. However, for Case (b), the complete removal of the coating is rendering it inefficient in providing the necessary resistance to wear. Lastly, PSG−ZT has followed a behavior similar to that of PSG, presenting the lowest specific wear rate in extreme conditions (Case (b)). In Figure 5g, a small volume of material was removed during the running-in period as this is the thickest sol–gel layer evidenced by the cross-section analysis in Figure 2. For having a smooth run with lubricating contact, firstly, PSG−ZT flattens the asperities when under contact, and then the dense compact structure with the presence of ZTP holds against the load, leaving the coating resistant to high wear. Identical to PSG in Case (b), PSG−ZT has shown a decrease in wear rate by half as depicted in Figure 5h. This can be the result of the cement−like presence of cage−like and ladder-like siloxane structures inside the PEO pores as well as the evolution of a homogenous sol–gel layer over the PEO coating. Instead of shearing the weaker bonds among the layers of sol–gel, it compresses and maintains their structure against the load and generates lesser debris. The average specific wear rate of untreated and treated surfaces is condensed in Figure 6 and Table 4 with PSG and PSG−ZT ensuring good sealing and enhanced resistance on higher load, whereas PSG−MT and PSG−AP are associated with poor wear characteristics, respectively. In any case, the wear rate for sol–gel sealed coatings is much lower than that for the untreated substrate and PEO coatings.

Table 3. Average COF values in the steady-state range for Case (a) (2.5 N and 20 min) and Case (b) (3 N and 40 min).

Average COF	Substrate	PEO	PSG	PSG-MT	PSG-AP	PSG-ZT
Case (a) 2.5 N, 20 min	NA	0.53	0.41	0.40	0.55	0.34
Case (b) 3 N, 40 min	NA	NA	0.49	0.50	0.55	0.43

Table 4. Average specific wear rate for different surface treatments at (a) 2.5 N load for 20 min, and (b) 3 N load for 40 min.

Average Specific Wear Rate $mm^3/(Nm)$	Substrate	PEO	PSG	PSG-MT	PSG-AP	PSG-ZT
Case (a)	1.08728	0.16073	0.07049	0.09131	0.16482	0.11602
Case (b)	0.85314	0.74016	0.05883	0.40587	0.45725	0.06379

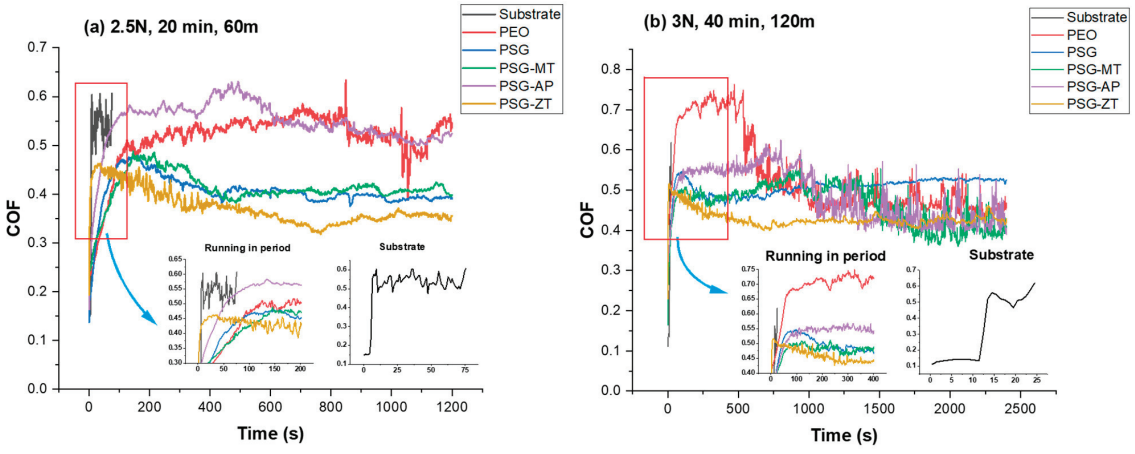

Figure 3. COF of tested sol–gels at (**a**) 2.5 N load and 20 min sliding, and (**b**) 3 N load for 40 min sliding time.

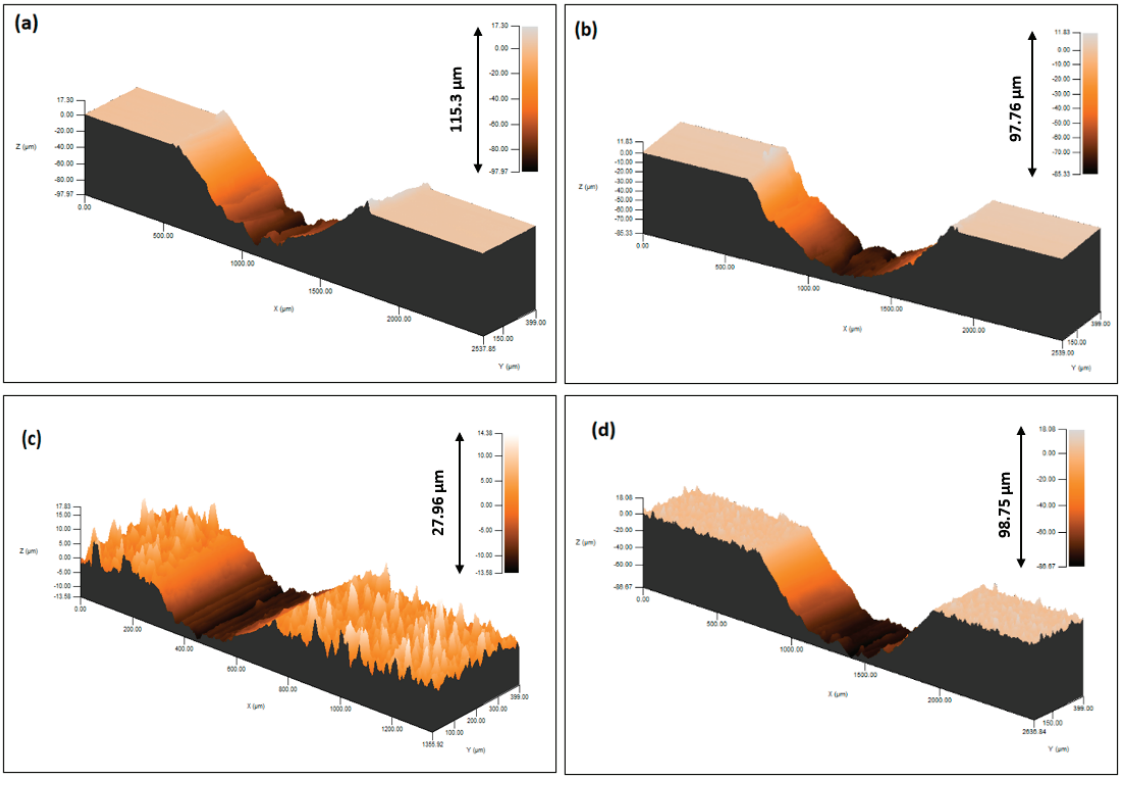

Figure 4. Mechanical profilometer 3D surface scan: (**a**,**b**) for bare AA2024 substrate, and (**c**,**d**) for PEO–coated specimens at 2.5 N load for 20 min and 3 N load for 40 min, respectively.

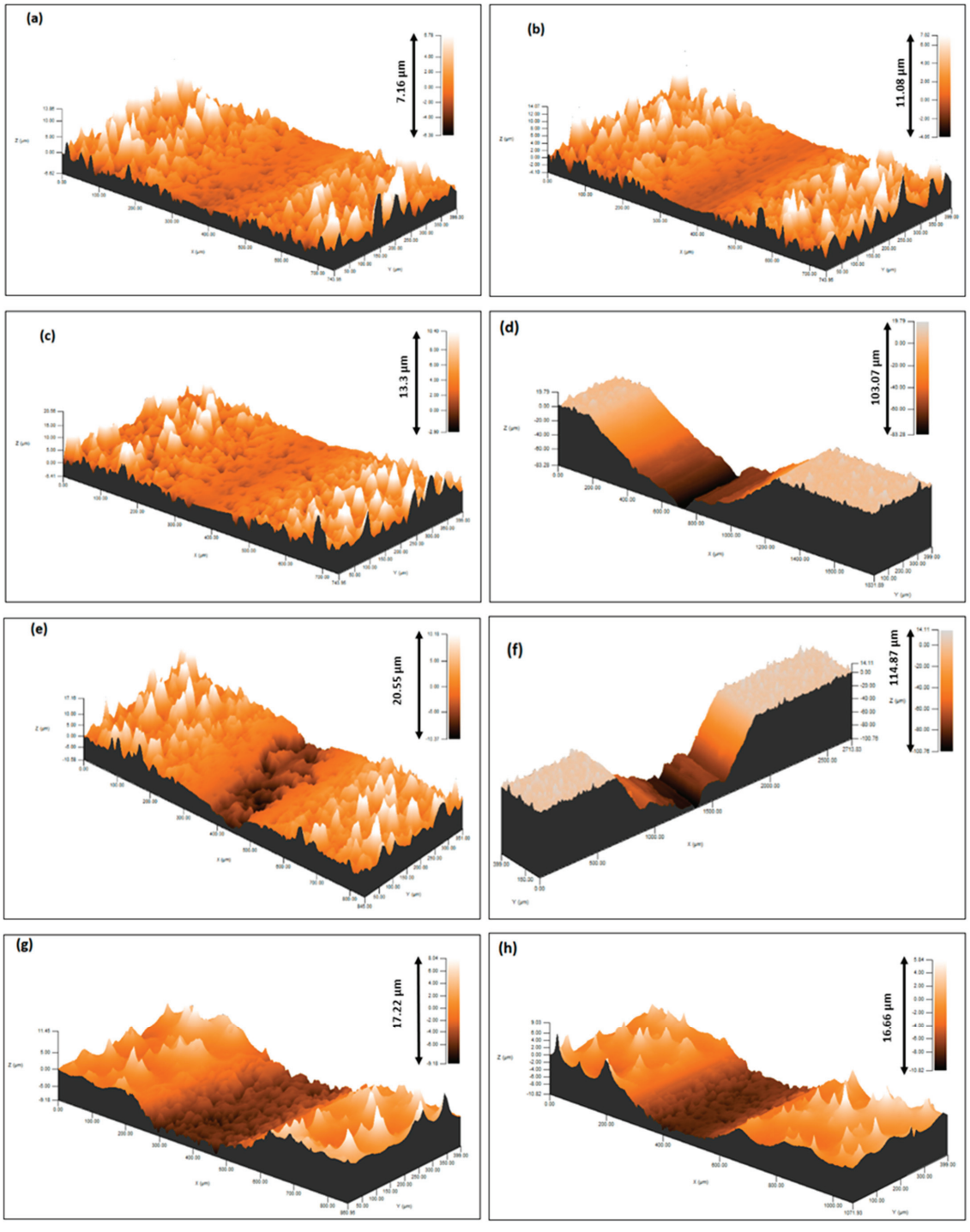

Figure 5. Mechanical profilometer 3D scan: (**a**,**b**) for PSG, (**c**,**d**) for PSG−MT, (**e**,**f**) for PSG−AP, and (**g**,**h**) for PSG−ZT, tested at 2.5 N load for 20 min and 3 N load for 40 min, respectively.

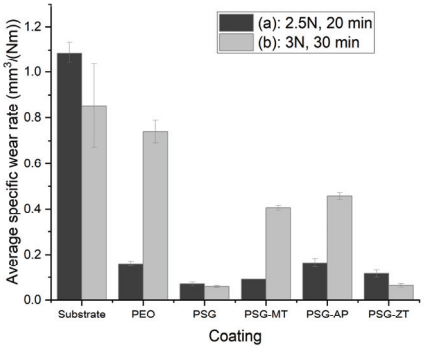

Figure 6. Graphical representation of average specific wear rate at (**a**) 2.5 N load for 20 min, and (**b**) 3 N load for 40 min for different surface treatments.

The typical distribution of elements on the wear traces of coated specimens is presented in Figure 7. It can be noted that all considered elements are distributed uniformly outside the wear trace for all sol–gel-sealed PEO coatings, ensuring uniform coating application [38]. Al is present in the wear tracks of all coatings. O exposure from the PEO coating underneath the sol–gel layer is proportional to the wear rate obtained in Figure 6. PSG and PSG-ZT exhibited a narrower removal of the sol–gel layer supporting their wear rates. With more presence of Si in the PSG wear track, it looks like PSG has a wider but shallower wear track than PSG-ZT. However, PSG-ZT has a narrower and relatively deeper wear trace. All in all, for wear scars obtained from the test at milder conditions (Case (a)), Si is still present in the wear traces of sol–gel layers of all coated samples. This means the wear test did not remove the sol–gel layers, proving the good adhesion of the coating [28].

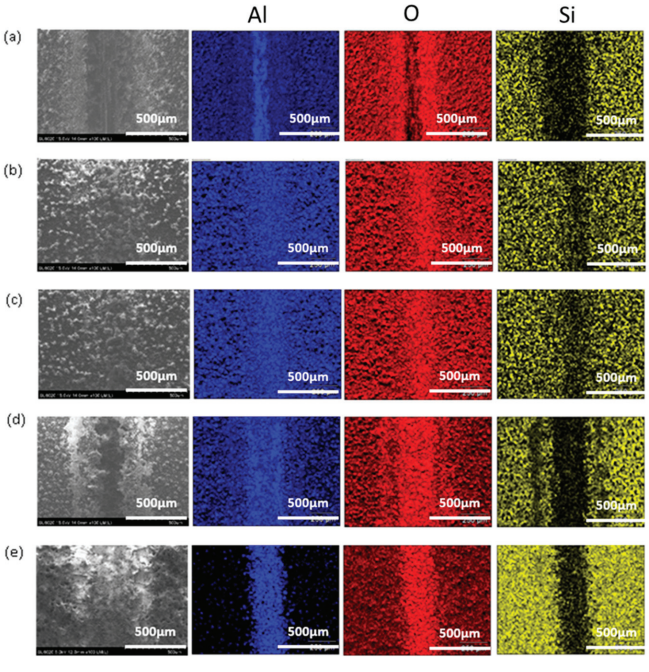

Figure 7. EDS map obtained at 100× through SEM image of coatings after wear test at 2.5 N load for 20 min: (**a**) PEO coating, (**b**) PSG, (**c**) PSG-MT, (**d**) PSG-AP, and (**e**) PSG-ZT.

In extreme conditions (3 N load for 40 min), it is clear that the wear tracks are wider in comparison to Figure 7. Specimens with unsealed PEO (Figure 8a), PSG-MT (Figure 8c), and PSG-AP (Figure 8d) show a complete absence of Si in the wear track in the color maps, indicating the pullout of sol–gel constituents from PEO pores as well as exposed substrate by the removal of the PEO layer. In addition to Si from the electrolyte, PEO coatings synthesized in an alkaline environment are primarily composed of α-Al_2O_3 and γ-Al_2O_3 [39,40]. Therefore, the depletion of O and Si elements and the high content of Al in the EDS color maps from the wear trace are proof of the Al substrate exposure and the removal of PEO layers as well. On the contrary, in PSG (Figure 8b) and PSG-ZT (Figure 8e), no parallel lines are observed, meaning that wear did not occur by abrasion. Similar results were obtained by Javadi et al. on the AA2024 alloy [25]. These two sol–gels have proven to be a good cementing agent in the sealing of PEO pores, as only a minute pullout of Si-containing species is noticed, and thus has good adhesive properties. By creating a dense structure with the PEO structure, it has improved the mechanical properties as confirmed by Pezzato et al. [41].

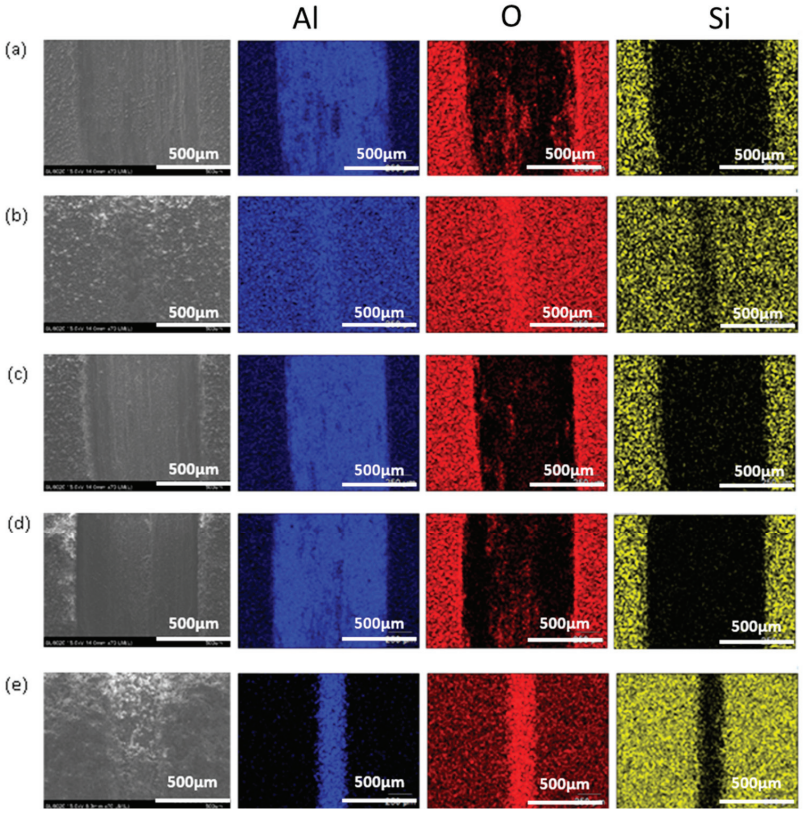

Figure 8. EDS map obtained at 70× through SEM image of coatings after wear test at 3 N load for 40 min: (**a**) unsealed PEO, (**b**) PSG, (**c**) PSG−MT, (**d**) PSG−AP, and (**e**) PSG−ZT.

Figure 9a indicates the transfer of the PEO coating from the wear track to the alumina counter body for unsealed PEO coatings, and this effect is more dominant with a higher coating transfer in Case (b). The transferred coating onto the ball could form hard abrasive particles by agglomeration, hence accelerating the wear phenomena. A similar trend is observed in PSG−MT and PSG−AP as the precursors MTES and APTES have a comparatively poor sealing performance due to a less dense network facilitating pullout during

the wear test, once the coated material transfer to the ball began after the sol–gel being pulled out of the PEO. Along with a high hardness, alumina is known for its brittle nature which limits its mechanical properties [42], resulting in the production of third body rolling brittle particles in the tribo-contact and, hence, more debris production. The PSG−MT and PSG−AP wear tracks are wider, with the complete removal of PEO coating at a higher load as well. However, PSG and PSG−ZT show no material transfer on the ball even at higher loads because of decreased shear stresses and the efficient sealing of PEO pores owing to their high branching [33] and organic groups present in the sol–gel structure [36].

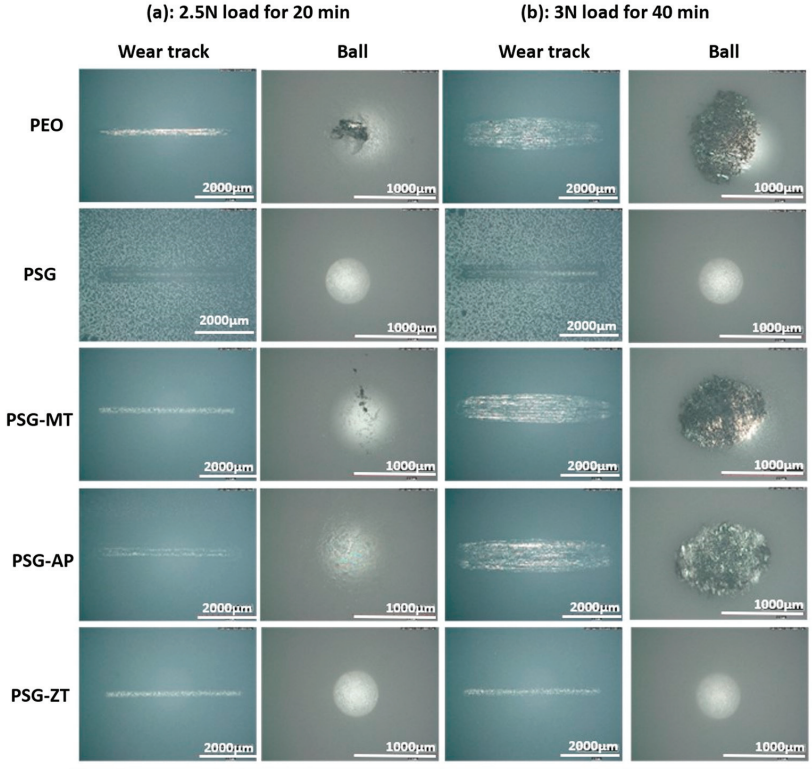

Figure 9. Optical microscopy images of wear tracks and counter body at (**a**) 2.5 N load for 20 min and (**b**) 3 N load for 40 min.

4. Conclusions

In the present work, a tribological evaluation of the previously developed sol–gel formulations have been carried out. With the aim of investigating the tribo−layer and self-healing capability of the sol–gel sealing of the PEO layer on the AA2024 alloy, i.e., coefficient of friction, the wear loss volume, elemental traces of sol–gel in the wear tracks, transfer of wear debris onto the counter body, wear track depths, and asperity profiles have been studied. The following conclusions can be drawn from the experimental results:

- The average COF values in the steady-state range for Case (a) (2.5 N and 20 min) and Case (b) (3 N and 40 min) are, respectively, followed as 0.53 and NA for PEO, 0.41 and 0.49 for PSG, 0.40 and 0.50 for PSG−MT, 0.55 and 0.55 for PSG−AP, and 0.34 and 0.43 for PSG−ZT.
- The average specific wear rate in 3 N load for the 40 min condition was 0.74016, 0.05883, 0.40587, 0.45725, and 0.06379 $mm^3/(Nm)$, for PEO, PSG, PSG−MT, PSG−AP, and PSG−ZT, respectively.

- The presence of GPTMS along with TEOS in PSG has created a dense sol–gel network in the PEO structure that has a good penetrative ability to seal the PEO layer resulting in a low COF and wear loss volume. Similarly, PSG−ZT, due to a higher sol–gel content, exhibited the same behavior. In fact, the more the hydrolyzed groups inside of a sol–gel network, the more opportunity for either the network formation or chemical adsorption of a sol–gel cluster to the PEO layer. The addition of MTES to the sol–gel formulation brought about a lower number of hydrolyzed groups possessing an un-hydrolyzed methyl functional group. Not only was the compactness of the PSG coating higher than that of PSG−MT but also its wettability, leading to the creation of more chemical bonds to the oxide groups over the PEO sample. For the PSG−ZT formulation, a high content of sol–gel precursors were utilized, which, interestingly, resulted in the formation of a dense layer over the PEO along with pore-filling ability. Hence, one could expect that, even though a high content of organic compounds was employed to obtain PSG−ZT, the wettability could be comparable with PSG.
- On the higher loads for PSG and PSG−ZT, they showed lesser wear due to the structure of the sol–gel layer being pushed together and aligning in the direction of sliding, giving lubricating characteristics to the surface.
- Moreover, the relatively low amount of wear debris in PSG and PSG−ZT with no material transfer to the counter body is indicative of the improved compactness of the coating and adhesion of the coating. Supporting EDS color maps through the SEM analysis shows the presence of sol–gel constituents in the wear tracks after the test.
- PSG−MT and PSG−AP are rendered inefficient to enhance the mechanical properties of the coatings, especially in severe conditions (Case (b)). In the case of PSG−AP, the insufficient sealing ability and the configuration of the hydrophilic amine group over the PEO sample could be the reason for such behavior. In any case, sol–gel-treated PEO layers have shown tremendous improvement in tribological properties compared to untreated samples.

Supplementary Materials: The following supporting information can be downloaded at: https://www.mdpi.com/article/10.3390/coatings13050871/s1, Table S1: Composition of the sol–gel used to seal PEO pores through dip coating.

Author Contributions: H.A.K.: investigation, methodology, validation, and writing—original draft. S.A.: investigation, methodology, validation. Y.P.: investigation, validation. V.V.: writing—review & editing, funding acquisition, and supervision. M.-G.O.: conceptualization, methodology, validation, writing—review & editing, supervision, and funding acquisition. All authors have read and agreed to the published version of the manuscript.

Funding: This work is funded by the 2018 SEALCERA project (Fédération Wallonie Bruxelles) as part of the ARC (Action de Recherche Collective). Ayesha Khalid wishes to thank the FRIA (Fonds pour la Formation à la Recherche dans l'Industrie et l'Agriculture) for funding.

Institutional Review Board Statement: Not applicable.

Informed Consent Statement: Not applicable.

Data Availability Statement: The data presented in this study are available upon request from the corresponding author.

Acknowledgments: The University of Mons provided financial support for the 2018 SEALCERA project (Fédération Wallonie Bruxelles) as part of the ARC (Action de Recherche collective), which the authors sincerely acknowledge. Ayesha Khalid wishes to thank the FRIA (Fonds pour la Formation à la Recherche dans l'Industrie et l'Agriculture) for funding. Last but not least, special thanks to Xavier Buttol and Dominique Hautcoeur for performing the roughness measurement at the Belgian Ceramic Research Center (CBRC).

Conflicts of Interest: The authors declare no conflict of interest.

References

1. Tlili, B.; Barkaoui, A.; Walock, M. Tribology and Wear Resistance of the Stainless Steel. The sol–gel Coating Impact on the Friction and Damage. *Tribol. Int.* **2016**, *102*, 348–354. [CrossRef]
2. Çam, S.; Demir, V.; Özyürek, D. Wear Behaviour of A356/TiAl3 in Situ Composites Produced by Mechanical Alloying. *Metals* **2016**, *6*, 34. [CrossRef]
3. King, R.G. *Mechanical and Textured Finishes in Surface Treatment and Finishing of Aluminium*; Chapter 1; Pergamon Press: Oxford, UK, 1988; pp. 1–12.
4. Mora-Sanchez, H.; del Olmo, R.; Rams, J.; Torres, B.; Mohedano, M.; Matykina, E.; Arrabal, R. Hard Anodizing and Plasma Electrolytic Oxidation of an Additively Manufactured Al-Si Alloy. *Surf. Coat. Technol.* **2021**, *420*, 127339. [CrossRef]
5. Yerokhin, A.L.; Nie, X.; Leyland, A.; Matthews, A.; Dowey, S.J. Plasma Electrolysis for Surface Engineering. *Surf. Coat. Technol.* **1999**, *122*, 73–93. [CrossRef]
6. Rakoch, A.G.; Bardin, I.V.; Kovalev, V.L.; Avanesyan, T.G. Microarc Oxidation of Light Constructional Alloys: Part 1. Main Notions on the Microarc Oxidation of Light Constructional Alloys. *Russ. J. Non-Ferr. Met.* **2013**, *54*, 341–344. [CrossRef]
7. Wielage, B.; Alisch, G.; Lampke, T.; Nickel, D. Anodizing—A Key for Surface Treatment of Aluminium. *Key Eng. Mater.* **2008**, *384*, 263–281. [CrossRef]
8. Mohedano, M.; Lu, X.; Matykina, E.; Blawert, C.; Arrabal, R.; Zheludkevich, M.L. Plasma Electrolytic Oxidation (PEO) of Metals and Alloys. In *Encyclopedia of Interfacial Chemistry-Surface Science and Electrochemistry*; Elsevier: Amsterdam, The Netherlands, 2018; Volume 6, pp. 423–438.
9. Zhu, M.H.; Cai, Z.B.; Lin, X.Z.; Ren, P.D.; Tan, J.; Zhou, Z.R. Fretting Wear Behaviour of Ceramic Coating Prepared by Micro-Arc Oxidation on Al–Si Alloy. *Wear* **2007**, *263*, 472–480. [CrossRef]
10. Treviño, M.; Mercado-Solis, R.D.; Colás, R.; Pérez, A.; Talamantes, J.; Velasco, A. Erosive Wear of Plasma Electrolytic Oxidation Layers on Aluminium Alloy 6061. *Wear* **2013**, *301*, 434–441. [CrossRef]
11. Curran, J.A.; Clyne, T.W. Thermo-Physical Properties of Plasma Electrolytic Oxide Coatings on Aluminium. *Surf. Coat. Technol.* **2005**, *199*, 168–176. [CrossRef]
12. Jiang, B.L.; Wang, Y.M. Plasma Electrolytic Oxidation Treatment of Aluminium and Titanium Alloys. In *Surface Engineering of Light Alloys*; Woodhead Publishing: Sawston, UK, 2010; pp. 110–154.
13. Hussein, R.O.; Zhang, P.; Nie, X.; Xia, Y.; Northwood, D.O. The Effect of Current Mode and Discharge Type on the Corrosion Resistance of Plasma Electrolytic Oxidation (PEO) Coated Magnesium Alloy AJ62. *Surf. Coat. Technol.* **2011**, *206*, 1990–1997. [CrossRef]
14. Molaeipour, P.; Allahkaram, S.R.; Akbarzadeh, S. Corrosion Inhibition of Ti6Al4V Alloy by a Protective Plasma Electrolytic Oxidation Coating Modified with Boron Carbide Nanoparticles. *Surf. Coat. Technol.* **2022**, *430*, 127987. [CrossRef]
15. Matykina, E.; Arrabal, R.; Skeldon, P.; Thompson, G.E.; Belenguer, P. AC PEO of Aluminium with Porous Alumina Precursor Films. *Surf. Coat. Technol.* **2010**, *205*, 1668–1678. [CrossRef]
16. Xue, W.; Deng, Z.; Chen, R.; Zhang, T. Growth Regularity of Ceramic Coatings Formed by Microarc Oxidation on Al–Cu–Mg Alloy. *Thin Solid Films* **2000**, *372*, 114–117. [CrossRef]
17. Khan, R.H.U.; Yerokhin, A.L.; Pilkington, T.; Leyland, A.; Matthews, A. Residual Stresses in Plasma Electrolytic Oxidation Coatings on Al Alloy Produced by Pulsed Unipolar Current. *Surf. Coat. Technol.* **2005**, *200*, 1580–1586. [CrossRef]
18. Guangliang, Y.; Xianyi, L.; Yizhen, B.; Haifeng, C.; Zengsun, J. The Effects of Current Density on the Phase Composition and Microstructure Properties of Micro-Arc Oxidation Coating. *J. Alloys Compd.* **2002**, *345*, 196–200. [CrossRef]
19. Yerokhin, A.L.; Snizhko, L.O.; Gurevina, N.L.; Leyland, A.; Pilkington, A.; Matthews, A. Discharge Characterization in Plasma Electrolytic Oxidation of Aluminium. *J. Phys. D Appl. Phys.* **2003**, *36*, 2110. [CrossRef]
20. Dehnavi, V.; Liu, X.Y.; Luan, B.L.; Shoesmith, D.W.; Rohani, S. Phase Transformation in Plasma Electrolytic Oxidation Coatings on 6061 Aluminum Alloy. *Surf. Coat. Technol.* **2014**, *251*, 106–114. [CrossRef]
21. Hutsaylyuk, V.; Student, M.; Posuvailo, V.; Student, O.; Hvozdets'kyi, V.; Maruschak, P.; Zakiev, V. The Role of Hydrogen in the Formation of Oxide-Ceramic Layers on Aluminum Alloys during Their Plasma-Electrolytic Oxidation. *J. Mater. Res. Technol.* **2021**, *14*, 1682–1696. [CrossRef]
22. Troughton, S.C.; Nominé, A.; Dean, J.; Clyne, T.W. Effect of Individual Discharge Cascades on the Microstructure of Plasma Electrolytic Oxidation Coatings. *Appl. Surf. Sci.* **2016**, *389*, 260–269. [CrossRef]
23. Li, T.; Li, L.; Qi, J.; Chen, F. Corrosion Protection of Ti6Al4V by a Composite Coating with a Plasma Electrolytic Oxidation Layer and sol–gel Layer Filled with Graphene Oxide. *Prog. Org. Coat.* **2020**, *144*, 105632. [CrossRef]
24. Toorani, M.; Aliofkhazraei, M. Review of Electrochemical Properties of Hybrid Coating Systems on Mg with Plasma Electrolytic Oxidation Process as Pretreatment. *Surf. Interfaces* **2019**, *14*, 262–295. [CrossRef]
25. Javidi, M.; Fadaee, H. Plasma Electrolytic Oxidation of 2024-T3 Aluminum Alloy and Investigation on Microstructure and Wear Behavior. *Appl. Surf. Sci.* **2013**, *286*, 212–219. [CrossRef]
26. Vasconcelos, D.C.L.; Carvalho, J.A.N.; Mantel, M.; Vasconcelos, W.L. Corrosion Resistance of Stainless Steel Coated with sol–gel Silica. *J. Non. Cryst. Solids* **2000**, *273*, 135–139. [CrossRef]
27. Innocenzi, P.; Esposto, M.; Maddalena, A. Mechanical Properties of 3-Glycidoxypropyltrimethoxysilane Based Hybrid Organic-Inorganic Materials. *J. sol–gel Sci. Technol.* **2001**, *20*, 293–301. [CrossRef]

28. Sopchenski, L.; Robert, J.; Touzin, M.; Tricoteaux, A.; Olivier, M.G. Improvement of Wear and Corrosion Protection of PEO on AA2024 via sol–gel Sealing. *Surf. Coat. Technol.* **2021**, *417*, 127195. [CrossRef]
29. Akbarzadeh, S.; Sopchenski Santos, L.; Vitry, V.; Paint, Y.; Olivier, M.G. Improvement of the Corrosion Performance of AA2024 Alloy by a Duplex PEO/Clay Modified sol–gel Nanocomposite Coating. *Surf. Coat. Technol.* **2022**, *434*, 128168. [CrossRef]
30. Balgude, D.; Sabnis, A. sol–gel Derived Hybrid Coatings as an Environment Friendly Surface Treatment for Corrosion Protection of Metals and Their Alloys. *J. sol–gel Sci. Technol.* **2012**, *64*, 124–134. [CrossRef]
31. van Ooij, W.J.; Zhu, D.; Stacy, M.; Seth, A.; Mugada, T.; Gandhi, J.; Puomi, P. Corrosion Protection Properties of Organofunctional Silanes—An Overview. *Tsinghua Sci. Technol.* **2005**, *10*, 639–664. [CrossRef]
32. Akbarzadeh, S.; Paint, Y.; Olivier, M.-G. A Comparative Study of Different sol–gel Coatings for Sealing the Plasma Electrolytic Oxidation (PEO) Layer on AA2024 Alloy. *Electrochim. Acta* **2023**, *443*, 141930. [CrossRef]
33. Deflorian, F.; Rossi, S.; Fedrizzi, L. Silane Pre-Treatments on Copper and Aluminium. *Electrochim. Acta* **2006**, *51*, 6097–6103. [CrossRef]
34. Innocenzi, P.; Abdirashid, M.O.; Guglielmi, M. Structure and Properties of sol–gel Coatings from Methyltriethoxysilane and Tetraethoxysilane. *J. sol–gel Sci. Technol.* **1994**, *3*, 47–55. [CrossRef]
35. Du, Y.J.; Damron, M.; Tang, G.; Zheng, H.; Chu, C.J.; Osborne, J.H. Inorganic/Organic Hybrid Coatings for Aircraft Aluminum Alloy Substrates. *Prog. Org. Coatings* **2001**, *41*, 226–232.
36. Rodič, P.; Mertelj, A.; Borovšak, M.; Benčan, A.; Mihailović, D.; Malič, B.; Milošev, I. Composition, Structure and Morphology of Hybrid Acrylate-Based sol–gel Coatings Containing Si and Zr Composed for Protective Applications. *Surf. Coat. Technol.* **2016**, *286*, 388–396. [CrossRef]
37. Sieber, M.; Simchen, F.; Morgenstern, R.; Scharf, I.; Lampke, T. Plasma Electrolytic Oxidation of High-Strength Aluminium Alloys—Substrate Effect on Wear and Corrosion Performance. *Metals* **2018**, *8*, 356. [CrossRef]
38. Nasirivatan, H.; Kahrizsangi, R.E.; Asgarani, M.K. Tribological Performance of PEO-WC Nanocomposite Coating on Mg Alloys Deposited by Plasma Electrolytic Oxidation. *Tribol. Int.* **2016**, *98*, 253–260. [CrossRef]
39. Serdechnova, M.; Mohedano, M.; Kuznetsov, B.; Mendis, C.L.; Starykevich, M.; Karpushenkov, S.; Tedim, J.; Ferreira, M.G.S.; Blawert, C.; Zheludkevich, M.L. PEO Coatings with Active Protection Based on In-Situ Formed LDH-Nanocontainers. *J. Electrochem. Soc.* **2017**, *164*, C36–C45. [CrossRef]
40. Xue, W.; Jiancheng, D.U.; Xiaoling, W.U.; Lai, Y. Tribological Behavior of Microarc Oxidation Coatings on Aluminum Alloy. *ISIJ Int.* **2006**, *46*, 287–291. [CrossRef]
41. Pezzato, L.; Rigon, M.; Martucci, A.; Brunelli, K.; Dabalà, M. Plasma Electrolytic Oxidation (PEO) as Pre-Treatment for sol–gel Coating on Aluminum and Magnesium Alloys. *Surf. Coat. Technol.* **2019**, *366*, 114–123. [CrossRef]
42. Mukhopadhyay, A.K.; Chakraborty, D.; Swain, M.V.; Mai, Y.W. Scratch Deformation Behaviour of Alumina under a Sharp Indenter. *J. Eur. Ceram. Soc.* **1997**, *17*, 91–100. [CrossRef]

coatings

MDPI

Article

Dissolution Behavior of Different Alumina Phases within Plasma Electrolytic Oxidation Coatings

Frank Simchen *, Roy Morgenstern, Steffen Clauß, Thomas Mehner and Thomas Lampke

Materials and Surface Engineering Group, Chemnitz University of Technology, 09111 Chemnitz, Germany
* Correspondence: frank.simchen@mb.tu-chemnitz.de

Abstract: The influence of chemical redissolution in the PEO layer-growth equilibrium on aluminum is evaluated differently in literature. In order to estimate whether and to what extent various alumina modifications could be affected by redissolution processes during PEO, immersion experiments were carried out on PEO coatings in model electrolytes of different alkalinity and silicate concentration. Their composition was determined spectroscopically before and after the experiments. The layers were characterized by XRD before and after the tests and examined at affected and unaffected zones using SEM, EDX, and EBSD. The results show that chemical oxide dissolution can only be observed at the layer/substrate interface and that primarily amorphous alumina is affected. This process is intensified by higher alkalinity and inhibited by silicate additives. The crystalline Al_2O_3 modifications show no significant attack by the electrolytes used. Transferring these observations to plasma electrolytic oxidation, they allow the conclusion that the electrochemically active zone in the pore ground of discharge channels interacts with the electrolytic and electrical process parameters throughout the entire PEO procedure. Influences of bath alkalinity and silicate content on layer growth rates are to be understood as impact on the passivation processes at the layer/substrate interface rather than chemical redissolution.

Keywords: plasma electrolytic oxidation (PEO); formation mechanisms alumina; dissolution

Citation: Simchen, F.; Morgenstern, R.; Clauß, S.; Mehner, T.; Lampke, T. Dissolution Behavior of Different Alumina Phases within Plasma Electrolytic Oxidation Coatings. *Coatings* **2021**, *12*, 1205. https://doi.org/10.3390/coatings12081205

Academic Editor: Michał Kulka

Received: 12 July 2022
Accepted: 28 July 2022
Published: 17 August 2022

1. Introduction

The plasma electrolytic oxidation (PEO) is an established process for generating oxidic conversion layers on metals, such as Al, Mg, Ti, and metal compounds of those. In contrast to conventional anodic oxidation, microarc discharges are created after initial substrate passivation by applying a sufficiently high anodic voltage and used for layer formation. In the center of the microarc discharge, there is a plasma temperature of about 7000 K [1]. With increasing distance to the center, the temperature falls below the boiling point of the oxide. In this zone, the melted substrate material reacts with the anodically formed oxygen to form molten oxide [2]. This is followed by the outer concentric zone in which the melting temperature of the oxide is no longer exceeded. In this area, thermally induced phase changes of the oxides take place. According to Rogov et al., the conversion proceeds in the direction of the Al_2O_3 modification with the lowest Gibbs free energy [3]:

$$\text{amorphous } Al_2O_3 \rightarrow \gamma\ Al_2O_3 \rightarrow \alpha\ Al_2O_3 \quad (1)$$

More precisely, the Gibbs free energy of amorphous, γ-, and α-alumina formation were quantified as -1625 kJ/mol, -1654 kJ/mol, and -1676 kJ/mol, respectively, by Naumann and Petzold [4]. Furthermore, the repeated remelting and heat treatment leads to a compaction of the inner oxide area, especially on Al materials. The result is a three-layered structure consisting of a barrier layer of a few 100 nm thickness at the substrate/layer interface, an inner, compact layer, and an outer, porous layer. The barrier layer is repeatedly formed by electrochemical oxidation at the base of a former microarc discharge and mainly consists of amorphous aluminum oxide [5,6]. The phases α- and γ-Al_2O_3 dominate within

the compact layer [6,7]. In the outer, porous layer, mixed oxides are increasingly found because of the incorporation of electrolyte constituents. They are characterized by a higher amorphous portion due to the lower thermal influence. In terms of maximum protection of the Al substrate against corrosion and/or abrasive wear, a high proportion of the compact layer of the total layer thickness is aimed for. Such PEO coatings are characterized by a low porosity and a high proportion of particularly hard and chemically resistant crystalline alumina phases. The chemical composition of the substrate alloy, the electrical regime, and the electrolyte composition were identified as the main influencing factors on the layer microstructure [7,8]. There is scientific consensus that the electrolyte composition influences the passivation behavior of the electrochemical system. With the help of potentiodynamic polarization tests, a distinction can be made between metal dissolution, metal passivation, or complex behavior, depending on the system [9,10]. Furthermore, electrolyte systems can be classified according to whether conversion of the substrate into an oxide, the incorporation of electrolyte anions into a mixed oxide, or even the deposition of a foreign oxide is sought. In the case of Al alloys, a pure conversion into the particularly wear- and corrosion-resistant, crystalline alumina phases [11] is desirable. On the other hand, the inclusion of electrolyte anions such as aluminate in the layer-formation process enables the production of $MgAl_2O_4$ spinel on Mg [12] and the deposition of Al_2O_3 layers on unalloyed steel [13]. The scientific literature shows that the rate of oxide formation increases with increasing current density and that a higher thickness [14] and oxide mass can be achieved due to increasing electrical charge [15]. Besides the oxide formation, several electrochemical side reactions may occur during the PEO process. At the beginning of the process, electrochemical metal dissolution and gas evolution are competing with the anodic passive-layer formation [8]. Anodic oxygen evolution can also be observed as a competition reaction of the oxide formation during the passive layer growth.

It has been observed that the rate of oxide formation decreases with increasing electrolyte temperature [14,16,17], alkali concentration [14,18,19], and process time [5,14,20]. On the basis of this knowledge, the theory was developed that during PEO in strongly alkaline solutions, the chemical redissolution of the oxide occurs as a competitive reaction of the anodic oxide formation. Koroleveva et al. assigned this processes to reactions according to Equation (2) [21]:

$$Al_2O_3 + 2(x-3)OH^- + 3H_2O \rightarrow 2[Al(OH)_x]^{n-}_{gel} \quad (2)$$

This would be similar to the competition of oxide formation and oxide redissolution during conventional anodizing in acidic solutions. According to Nagayama and O'Sullivan [22,23], such reactions can be promoted by strong localization of electric field lines and are designated as field-assisted chemical redissolution. To describe the chemical redissolution of PEO coatings, Snizhko and Al Bosta also refer to the reaction according to Equation (2) for the chemical dissolution of the natural passive layer [18,20]. Within the above-mentioned publications, the Al content of the electrolyte after PEO is often estimated in order to get an experimental access to conceivable redissolution reactions during the process. However, several additional reaction routes may lead to the elevated Al content after PEO. Al^{3+} ions can directly be emitted via field assisted anodic metal dissolution and emission of aluminum ions through the plasma channel [15,18]:

$$Al \rightarrow Al^{3+}_{ejected} + 3e^- \quad (3)$$

or by electrochemical etching of the metallic substrate in partial pulse periods without external polarization applied [20]:

$$2Al + 2OH^- + 6H_2O \rightarrow 2Al(OH)_4{}^- + 3H_2 \quad (4)$$

Therefore, it is not clear to what extent chemical redissolution of the plasma electrolytically formed oxide occurs during the PEO process and to what extent this affects the layer microstructure.

On the other hand, possible influences of the electrolyte temperature and the alkali concentration on the electrochemical passivation of the Al substrate were not considered in most of the studies on the chemical redissolution. The authors Moon and Pyun [24] and Snizhko et al. [25] showed that the steady state of the passive-layer growth is delayed due to increasing hydroxide concentration. This might promote side-reactions such as metal dissolution and oxygen evolution during the repassivation of the Al substrate at the base of a microarc discharge. Therefore, a decrease of the oxide growth rate and an increase of the Al ion concentration in the electrolyte might also be explained by the impairment of the substrate passivation and not necessarily point at the chemical redissolution reaction. Furthermore, it is questionable as to whether the chemical redissolution reaction described by Equation (2), which originally refers to the chemical redissolution of amorphous alumina passive layers, can also be generalized for PEO layers consisting of a high proportion of crystalline alumina phases. Additionally, the redissolution behavior of mixed oxides, which arises through the incorporation of electrolyte anions, has not yet been taken into account. This is also indicated by the fact that there is a clear discrepancy in the scientific literature with regard to the significance of chemical redissolution in PEO processes. Several research groups observed an almost linear increase of the oxide thickness over a process time of up to 45 min [26–28]. The authors Xue et al. found that the ratio of the outward growth and the total oxide thickness started to decrease after about 2 h and that the total oxide growth rate did not decrease until a process duration of about 5 h [29]. In [27,28], compact and wear-resistant PEO layers are reported, which mainly consist of the crystalline phases γ- and α-Al_2O_3. In contrast, the authors Al Bosta et al. observed a significant decrease of the layer growth rate after only about 20 min [20]. After exceeding a process time of 50 min, the layer thickness even decreased. At this point, the PEO layers consisted of around 55% γ-Al_2O_3, 18% Al_2SiO_5, 24% SiO_2, and only 8% α-Al_2O_3 [20]. From the results of [20,26–29] the conclusions might be drawn that the chemical redissolution of the oxide does not play a decisive role for PEO layers with a high proportion of crystalline alumina phases and technically relevant process times of less than one hour and that especially the presumably amorphous, Si-containing phases are characterized by a lower chemical resistance and a higher redissolution rate in alkaline solutions. This argumentation assumes that the rate of layer formation is constant over the entire process time, similar to conventional anodic oxidation, and that only the chemical redissolution rate determines the net growth rate and the maximum achievable oxide thickness. However, it is known that distribution and intensity of the microarc discharges change over the process duration due to the evolution of the oxide microstructure towards the formation of a more compact PEO layer [8,30]. The number of microarc discharges declines as the discharges focus on a decreasing number of defects in the oxide layer. The PEO process might even come to a complete standstill. In this case, redissolution would not be necessary to explain the declining rate of layer growth.

Within this work, it is intended to investigate the chemical redissolution of different oxide phases and the effect on the PEO coating's microstructure and properties for the first time. The dissolution behavior of individual phases is assessed by comparing the phase composition and layer microstructure using diffraction methods and scanning electron microscopy before and after the exposition of the PEO coatings to an alkaline solution.

2. Materials and Methods

The PEO coatings were applied on the commercially available high-strength aluminum alloy EN AW-6082 T6, the chemical composition of which is listed in Table 1. The sheets had geometrical dimension of 100 × 25 × 3 mm. The plasma electrolytic oxidation was carried out within a laboratory plant consisting of a rectifier *pe86CW-550-53-120/S* (plating electronics, Sexau, Germany) and a capsuled treatment station (Scheigenpflug, Leipzig, Germany) with a basin for 12 L electrolyte, directly cooled by a heat exchanger. Two

stainless steel sheets were used as counter electrodes. The electrolyte composition was 5 g/L KOH, 5 g/L $Na_2SiO_3 \cdot 5H_2O$, and 1 g/L Na_2HPO_4. All substances were of analytical grade (Sigma-Aldrich, St. Louis, MI, USA). The electrical regime was defined by a symmetric, bipolar, rectangular, current controlled pulse of $i_1 = -i_2 = 30$ A/dm^2 and $t_1 = t_2 = 10$ ms. The maximum anodic voltage was limited to 500 V, and the treatment time was 60 min.

Table 1. Mass fractions of the alloying elements of EN AW-6082 T6 (Al balance).

Si	Mg	Mn	Fe	Cr	Zn	Cu	Ti
0.7–1.3	0.6–1.2	0.4–1.0	≤0.5	≤0.25	≤0.2	≤0.1	≤0.1

In order to provide the data resulting from the following investigations with a suitable statistical support, five aluminum sheets were treated under the same PEO conditions. Afterwards, three samples were cut from every sheet according to the schematic representation depicted in Figure 1a.

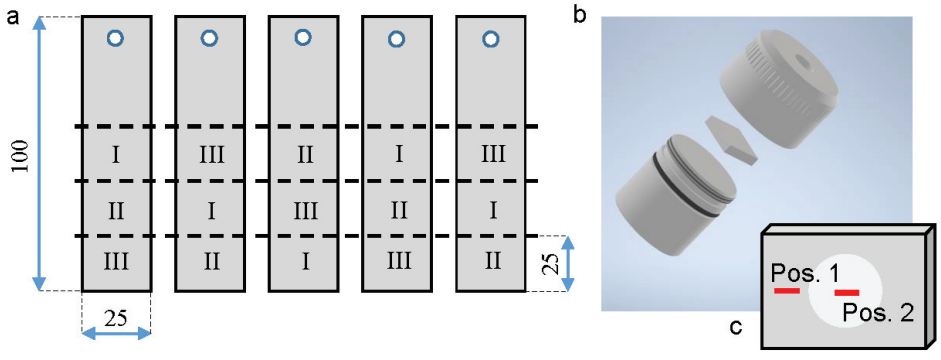

Figure 1. Schematic representation of the PEO-coated aluminum sheets, extraction positions of the individual samples and indication of the electrolytes (Table 2) used for exposition experiments (**a**) within a sample holder (**b**) as well as the position of the further SEM and EBSD investigations (**c**).

The 15 samples prepared in this way were mounted in sample holders as exemplary shown in Figure 1b and used for exposition experiments within three different electrolytes, indicated by the Roman numerals. The compositions of these are listed in Table 2.

Table 2. Composition of the electrolytes used for the exposition experiments.

Electrolyte	Composition
I	0.1 mol/L KOH, pH = 13
II	5 g/L KOH, 5 $Na_2SiO_3 \cdot 5H_2O$, 1 g/L Na_2HPO_4, pH ≈ 13
III	1.0 mol/L KOH, pH = 14

For the exposition experiments, the mounted samples were placed into glasses with 140 mL of the respective pre-heated electrolyte. Afterwards, the glasses were closed with a watch glass, positioned in a thermostat filled with water of 95 °C, and were exposed to the electrolyte for 60 min. In order to determine the exact chemical aluminum concentrations of the testing solutions before and after the experiments, test volumes of 50 mL were extracted and investigated by inductively coupled plasma optical emission spectroscopy (ICP-OES) using a *Optima 8300* (PerkinElmer, Waltham, MA, USA). In the course of these measurements, three undiluted partial volumes were shot into the flame in order to analyze the spectral information of the resulting light emission for 5 to 20 s. The characteristic Aluminium wave lengths of 394.40 nm and 396.15 nm were used to determine the Al

content by use of a N9300184-standard of $Al(NO_3)_3$ in 2% HNO_3 with 1000 µg/mL Al (PerkinElmer, Waltham, MA, USA). The phase composition of every single coated sample was examined by X-ray diffraction (XRD) before and after the exposition experiment. The setup consists of a *D8 Discover* with an 1D *LYNXEYE XE-T* detector with 192 channels (Bruker, Germany) using Co-K_α radiation. A point focus with a collimator diameter of 2 mm was chosen to gain integral information without interfering signals from the samples edges. A step size of 0.02° and a step time of 3.9 s/step, which results in an effective measurement step time of 748.8 s/step due to the use of the 1D detector.

The morphology of the coating, as well as the spatial distributions of the single alumina phases within the exposed and non-exposed coating regions (Positions 1 and 2 in Figure 1c), were investigated by using a scanning electron microscopy (SEM) and electron backscattering diffraction (EBSD). The chemical composition of the observed microstructure was determined by energy-dispersive X-ray spectroscopy (EDX) spot measurements and maps. For this purpose, one of the samples exposed to each of the electrolytes I, II, and III were prepared as listed in Table 3.

Table 3. Preparation route for EBSD measurements on ceramic PEO coatings.

No.	Working Step	Material	Duration	Device
1	cutting	diamond cutting disk	2 min	Struers MiniTom
2	grinding	600 cm^{-2} SiC	2 min	Buehler Phoenix Beta
3	grinding	800 cm^{-2} SiC	5 min	— ″ —
4	grinding	1200 cm^{-2} SiC	5 min	— ″ —
5	grinding	2500 cm^{-2} SiC	5 min	— ″ —
6	grinding	4000 cm^{-2} SiC	10 min	— ″ —
7	polishing	9 µm diamond suspension on silk	5 min	Struers DapV
8	polishing	3 µm diamond suspension on silk	5 min	— ″ —
9	polishing	1 µm diamond suspension on neoprene	5 min	— ″ —
10	vibration polishing	0.05 µm diamond suspension on neoprene	90 min	
11–15	purifying	acetone × 5	3 min	ultrasonic bath
16–20	purifying	isopropyl × 5	3 min	— ″ —
21	drying	vacuum, ϑ = 60 °C	24 h	vacuum oven
22	sputtering	Au, I = 24 mA, $p = 10^{-2}$ mbar	6 s	Emitech K550

The samples exposed to electrolyte I or II were prepared without embedding, while the sample immersed in electrolyte III, which showed layer delamination, was vacuum infiltrated with an epoxy resin (Epothin, Buehler, IL, USA). Slices of 2 mm thickness were detached by using a diamond cutting disk and mounted in a thermoplastic sample holder (Crystalbond, Buehler, IL, USA). Afterwards, the surfaces were grinded in five steps with increasing abrasive particle number. The following polishing steps were carried out on silk tie (MD-Dur, Struers, Willich, Germany), stretched on a steel disk. The resulting counterbody is relatively hard, and its use prevents roundings of the ceramic edge at the substrate/coating interface (which could be observed, for example, when using flow tie). In order to allow for Si-specific element maps during the subsequent investigations, diamond (instead of SiO_2) suspensions with decreasing particle size were used as abrasive media. The polishing and vibration polishing steps with 1 and 0.05 µm diamond particle size were carried out on neoprene tie (MD-Chem, Struers, Willich, Germany), the narrow mesh size of which allows to bind such small particles. After the sample surface was prepared for EBSD measurements in this way, it was dismounted from the sample holder and purified for investigations under vacuum conditions. Therefore, it was immersed in acetone and treated by ultrasound to dissolve the thermoplastic residuals. The procedure was repeated five times, each time using fresh acetone to gradually decrease the contamination of the sample surface. Since acetone itself showed a certain tendency to adsorb at the surfaces of the sample, they were afterwards purified in isopropyl following the same procedure. Since the typical micro- and nano sized defect structure of PEO coatings results in an intrinsic

capillary hygroscopy, the samples were dried for 24 h under vacuum at 60 °C. Afterwards, an electrical conductive layer was sputtered onto the sample surface. The Kikuchi lines showed an unsatisfying band contrast by use of carbon layers, which can be attributed to their excessive thickness and uneven thickness distribution. Therefore, thin layers of gold, invisible to the naked eye, were applied.

The micro-structure analysis was carried out by using a field-emission SEM (NEON 40EsB, Zeiss, Jena, Germany) equipped with an EDX (GENESIS, EDAX, Mahwah, NJ, USA) and EBSD system (OIM 5.31, EDAX TSL, Mahwah, NJ, USA). The SEM micrographs were taken in backscatter (BS) and secondary (SE) electron mode using an acceleration voltage of 15 kV and a working distance of 10 mm. For the EBSD measurements, the acceleration voltage was 15 kV. The samples were tilted by 70°, and the aperture was opened to 120 µm in high current mode. The sampling step size was set to 150 nm, while the sampling time was limited to some seconds in order to prevent a deterioration of the EBSD data as a result of local charging (leading to electron-beam drift) and contamination. During this measurement, the parameters of which were optimized for electron backscattering diffraction, EDX data were recorded as well. They allow for a qualitative representation of the spatial distribution of the chemical elements detected. However, the short spot measurement prohibits a quantitative interpretation.

Figure 2 summarizes the procedure used for processing and indexing the data obtained by the EBSD measurement. The raw signal intensity map with diffraction bands visible for the naked eye, Figure 2a, was transferred by using Hough transform into an dual space shown in Figure 2b. Here, seven local maxima, indicated by colored markers, were used to identify the main characteristic diffraction lines of the spot under investigation, depicted in Figure 2c. Afterwards, the OIM software was used to assign those incomplete Kikuchi patterns to one of the two crystalline aluminum oxide modifications γ- and α-Al_2O_3 previously identified by XRD. The corresponding complete Kikuchi patterns are presented in Figure 2d. This combined use of diffraction-based material-analytic methods allows for an EBSD phase map, despite the confidence index (CI) being relatively low (between 0.1 and 0.5) in this study. The CI value quantifies, via a complex algorithm, how well the detected diffraction pattern matches the indexed diffraction pattern [31,32]. As a side effect of this procedure, some grains of the aluminum-substrate alloy were indexed as alumina phases as well, which has to be considered negligible artifacts of this methodology.

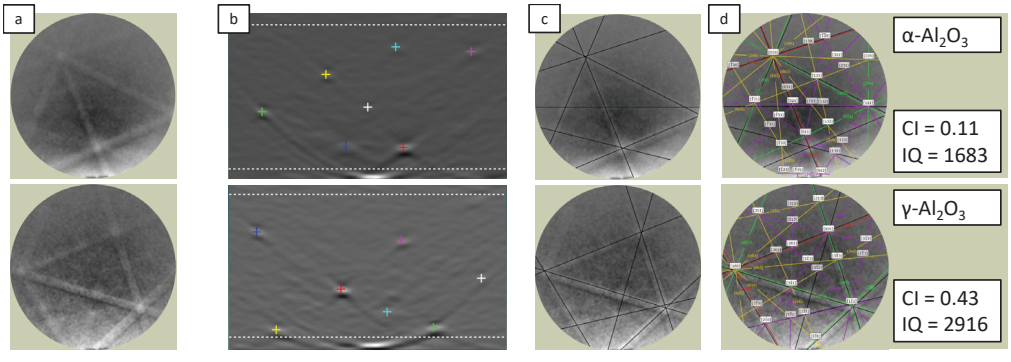

Figure 2. Graphical representation of the procedure used for indexing EBSD data, showing the raw signal intensity map with diffraction bands (**a**), the dual space resulting from the Hough transform with colored markers (**b**), indicating the characteristic diffraction lines of the spot under investigation (**c**), which were used to assign the data to the characteristic Kikuchi pattern of γ- (top) or α-Al_2O_3 (button) (**d**).

During the EBSD measurement, regions were identified in which only a few to no diffraction bands were present, which showed only a low band contrast. This leads to a reduction of the peak number and strength in the Hough space and is quantified by the so-called image quality (IQ) [31]. In addition to numerous influencing factors on the part of

preparation (topography, artefacts, edges) and the experimental setup (acceleration voltage, inclination angle, spot measurement time), the IQ is influenced by various structural features (residual stresses, distortions, dopants) along the area under investigation.

Furthermore, a low IQ can indicate amorphous areas or zones with a low crystalline order. Therefore, areas that did not allow for clear assignment to the crystalline aluminum-oxide modifications determined by XRD have been categorized into three subclasses in this work.

i IQ = 0–500: no band contrast, no pattern detectable, areas with practical no signal response, cavities, edges, amorphous zones
ii IQ $\geq$ 500–750: very low band contrast, weakly delectable diffraction patterns, no indexing possible
iii IQ $\geq$ 750–1000: low band contrast, detectable diffraction patterns, no phase assignable

3. Results

3.1. ICP-OES

The results of the ICP-OES measurements are summarized in Figure 3. The bar graphs show the determined aluminum concentrations before and after the exposition experiments for the electrolytes I–III. Furthermore, a representative stereographic close up image of a delaminated coating region observed on a sample treated in electrolyte III is depicted. Here a cavity occurred between coating and sample during the experiments, which is shown exemplary in side view in Figure 11.

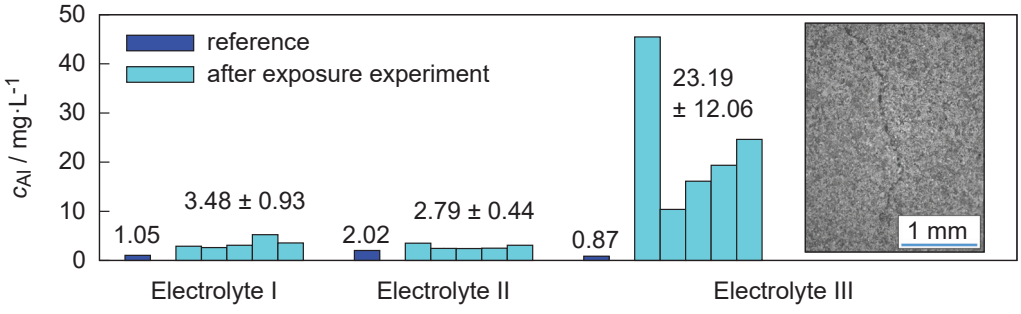

Figure 3. Aluminum concentrations of the electrolytes I-III used for the exposition experiments: reference concentration after preparing the solutions (blue), concentrations after immersing the 5 mounted samples for 60 min at 95 °C (cyan).

The reference measurements of the electrolytes before the exposition experiments showed aluminum concentrations of 0.9 to 2 mg/L, which are presumably originated from minor contaminations of the used deionized water, chemicals and laboratory equipment. The lowest aluminum concentration and deviations between the repetition measurements after the exposition were determined for the experiments in electrolyte II. Minus the reference measurement, the average concentration was 1.8 mg/L. After the subtraction of the reference concentration, the investigations in electrolyte I showed an average aluminum content of 2.5 mg/L with an elevated standard deviation. As result of the experiments in electrolyte III, a significantly higher average aluminum concentration of 22.3 mg/L was observed after subtraction the reference value. The individual test replicates show strong differences, resulting in a high standard deviation of 12 mg/L. Furthermore, the coatings showed macroscopic delaminations and cracks of various extent in the same areas.

3.2. X-ray Diffraction

The results of the XRD measurements are summarized in the Figures 4, 7 and 10. The upper subplot with the *Y*-axis labelled with "counts" shows the five diffractograms measured on the samples before (blue) and after (red) the exposition experiments. The

curves of the individual measurements are almost congruent, which indicates that the samples are practically identical with regards to XRD. While in the 2θ-range from 20° to approximately 37° a broadly drawn intensity range that indicates amorphous layer regions can be recognized, there are numerous crystalline peaks in the rest of the diffractogram. The peaks marked by blue dashed lines and indicated by blue upside down triangles at the top of the figures are originate from the aluminum substrate material. The lower subplot with the *Y*-axis labeled with "Δ counts" shows the average value of the difference between the XRD measurements of the five samples before and after the exposition experiments (purple). The positions of the peaks related to the α-Al_2O_3 phase (corundum) are indicated by green dashed lines and upside down triangles in the middle of the figure. The peaks corresponding to the γ-Al_2O_3 phase are marked by red dashed lines starting from red triangles from the bottom of the figure. The data concerning the characteristic peak positions of the detected crystalline phases were taken from corresponding powder diffraction files (PDF) [33]. While in Figure 7 (electrolyte II) the purple difference graph shows nearly no shift within the predominantly amorphous 2θ-range (20°–37°), a significant deflection can be observed in Figure 4 (electrolyte I) which is even stronger pronounced in Figure 10 (electrolyte III). Within the angular range of the substrate-related aluminum peaks, the intensity difference curves show characteristic features, which are listed in Table 4.

Table 4. Characteristic features of the substrate-related Al peaks within the XRD intensity difference curves in Figures 4, 7 and 10.

Electrolyte	2θ/°	Description
I	44	fluctuation as a result of peak shift to lower 2θ
	52	fluctuation as a result of peak shift to lower 2θ
	77	downshift
	94	amplification
	99	slight fluctuation as a result of peak shift to lower 2θ
II	44	amplification
	52	fluctuation as a result of peak shift to higher 2θ
	77	downshift
	94	no shift
	99	slight amplification
III	44	fluctuation as a result of peak shift to lower 2θ
	52	downshift
	77	fluctuation as a result of peak shift to lower 2θ
	94	downshift
	99	fluctuation as a result of peak shift to lower 2θ

The peaks related to the crystalline alumina modifications show an elevated intensity after the exposition experiments for all three electrolytes. This effect is stronger pronounced for the α-Al_2O_3 than for the γ-Al_2O_3 phase and increases for the electrolytes in the following order: II, I, III.

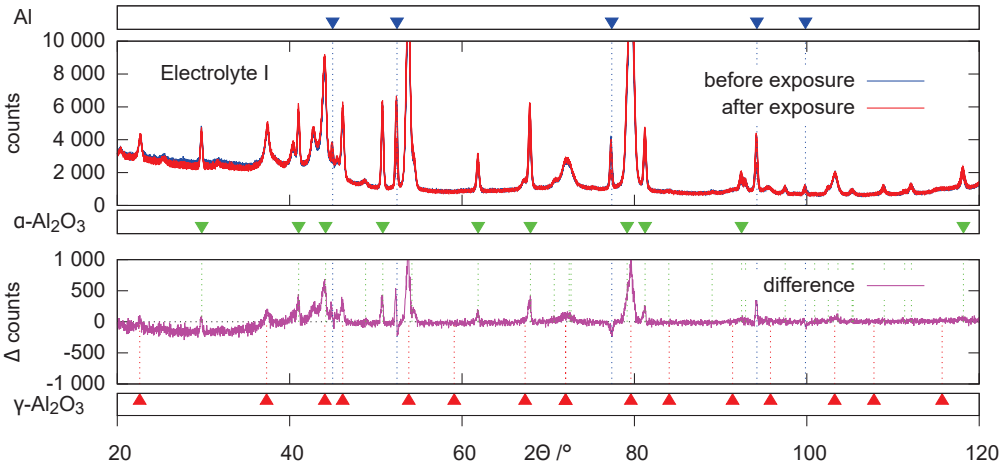

Figure 4. XRD diffractograms of the five PEO-coated samples exposed to electrolyte I before (blue) and after (red) the exposition experiments as well as the average difference graph (purple).

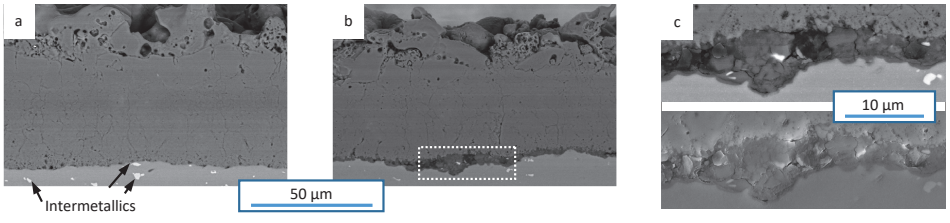

Figure 5. Backscatter SEM images of a sample which was exposed to electrolyte I at cross-sections of the unaffected (**a**) and affected region (**b**), as well as close-ups of the substrate/coating interface in backscatter (top) and secondary (bottom) electron mode (**c**).

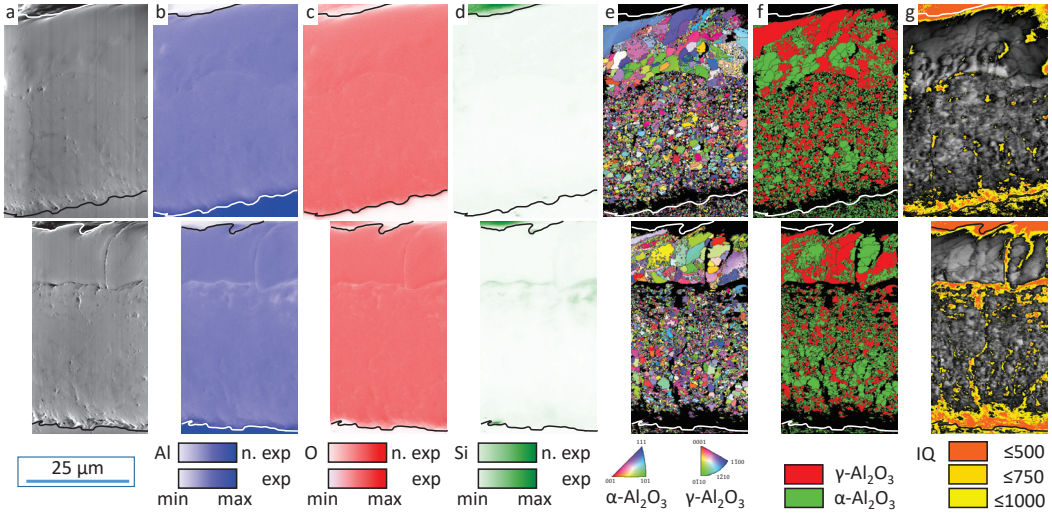

Figure 6. SEM (**a**) image as well as EDX (**b**–**d**) and EBSD (**e**–**g**) maps for the cross-section of a sample exposed to electrolyte I at unaffected (top) and affected (bottom) surface regions (Pos. 1 and 2 in Figure 1c).

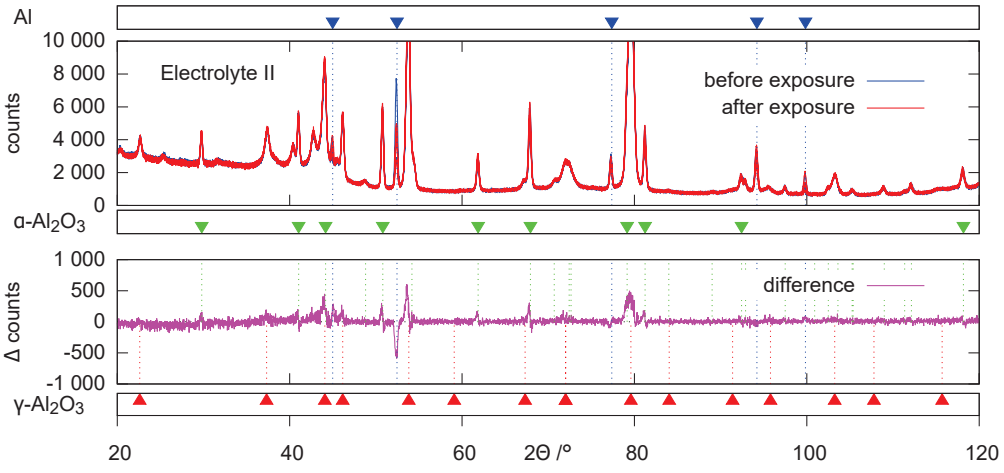

Figure 7. XRD diffractograms of the five PEO-coated samples exposed to electrolyte II before (blue) and after (red) the exposition experiments as well as the average difference graph (purple).

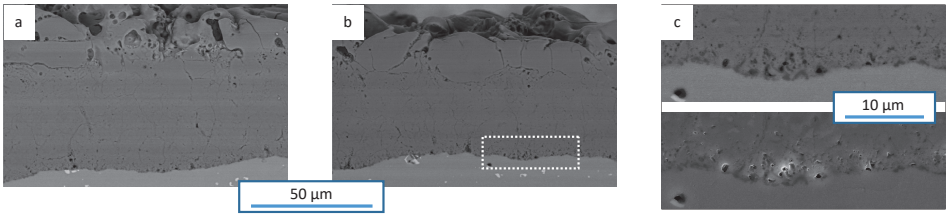

Figure 8. Backscatter SEM images of a sample which was exposed to electrolyte II at cross-sections of the unaffected (**a**) and affected region (**b**), as well as close-ups of the substrate/coating interface in backscatter (top) and seconduray (bottom) electron mode (**c**).

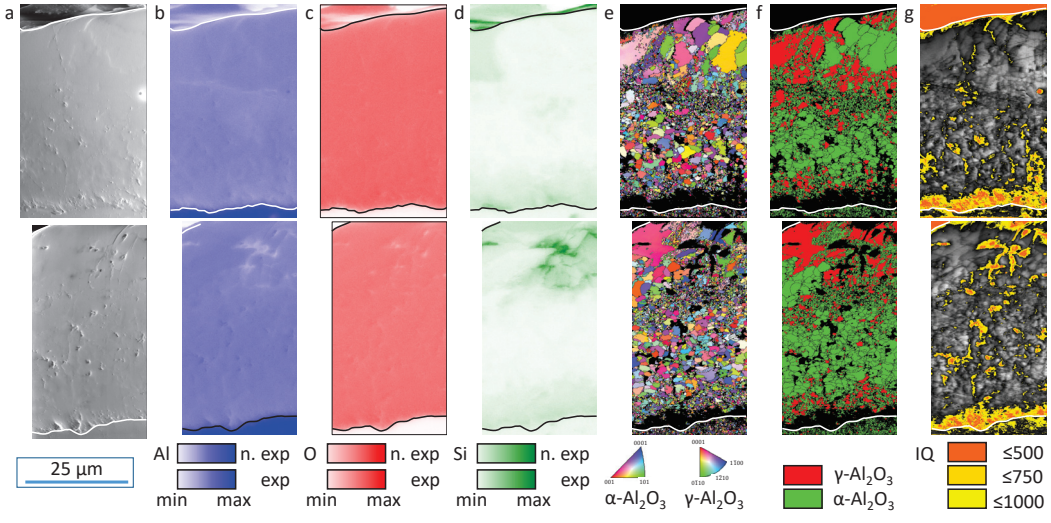

Figure 9. SEM (**a**) image as well as EDX (**b**–**d**) and EBSD (**e**–**g**) maps for the cross-section of a sample exposed to electrolyte II at unaffected (top) and affected (bottom) surface regions (Pos. 1 and 2 in Figure 1c).

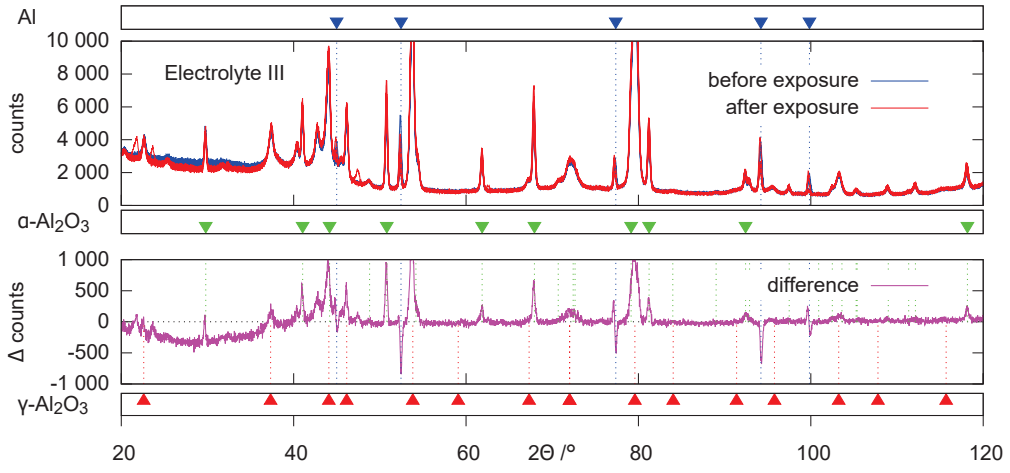

Figure 10. XRD diffractograms of the five PEO-coated samples exposed to electrolyte III before (blue) and after (red) the exposition experiments as well as the average difference graph (purple).

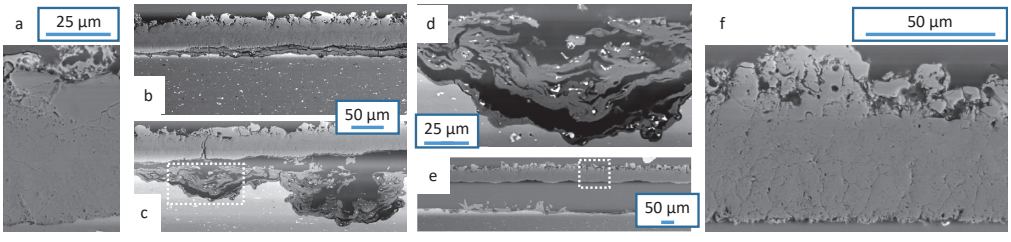

Figure 11. Backscatter SEM images of a sample which was exposed to electrolyte III at cross-sections of the unaffected (**a**) and affected region (**f**), as well at the transition zone between these areas (**b**–**e**).

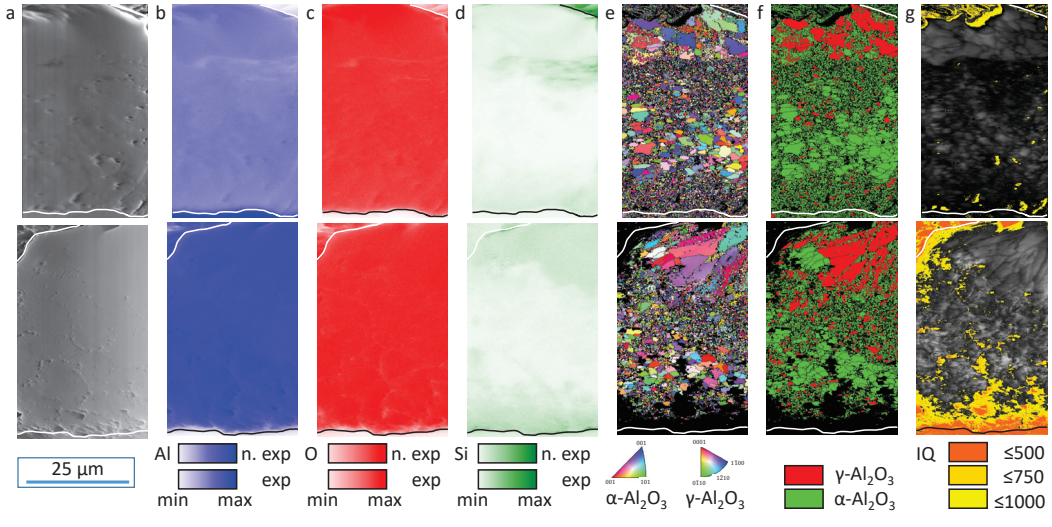

Figure 12. SEM (**a**) image as well as EDX (**b**–**d**) and EBSD (**e**–**g**) maps for the cross-section of a sample exposed to electrolyte III at unaffected (top) and affected (bottom) surface regions (Pos. 1 and 2 in Figure 1c).

3.3. SEM, EDX, and EBSD

The SEM images that show the PEO coatings and their substrate/layer interface at Pos. 1 and 2 indicated in Figure 1c are summarized in Figures 5, 8 and 11. The images of the unaffected sample regions show equivalent microstructures. The coatings exhibit the literature-known structural characteristics of inner compact areas (working layer) and outer porous zones (technological layer) as well as a good substrate bonding with slightly elevated porosity. The entire coating structure is permeated by a fine intrinsic cavity network of cracks and discharge channels. The substrate material shows small uniformly distributed bright areas in the BS mode, which correspond to intermetallic phases of the EN AW-6082 T6 alloy used. For the sample exposed to electrolyte II (Figure 8), no alteration can be recognized qualitatively between the affected and unaffected areas. Neither the bulk coating nor the near-substrate interface zone of the exposed region show visible results of interaction with the testing solution. Similarly, the PEO coating exposed to electrolyte I (Figure 5b), shows no obvious impact on the bulk layer. However, there is a significant reaction zone at the substrate/coating interface. From the BS close-up shown in Figure 5c, it can be seen that the reaction products partially enclose intermetallic phases of the substrate material. The corresponding SE image shows a preparation-related topographical contrast. These effects are much more pronounced in the sample, which was exposed to electrolyte III. The coating shows delamination already at the transition zone between unexposed and exposed layer regions, as depicted in Figure 11b,c. While the coating itself seems unaffected, the reaction products enclose intermetallics of the sample material, which indicates substrate attack by the electrolyte. While this effect is largely uniform along the substrate/layer interface in Figure 11b, two significantly localized etch depressions are visible in Figure 11c. Above the left recess, a large crack within the layer is in plane with the materialographic cross-section. The underlying areas are shown as a close-up in Figure 11d. Figure 11e shows the overview image of the center of the sample area exposed to electrolyte. Some reaction products and etch depression are visible close to the substrate. The cavity between base alloy and PEO layer is filled with embedding resin. The coating is detached completely. A close-up of the area marked by dashed lines, which shows PEO coating exposed to the electrolyte, is depicted in Figure 11f. The bulk PEO layer seems unaffected, however, despite the preparation and SEM parameters are equal to the ones of the micrograph in Figure 11a, the intrinsic cavity network is recognizable more clearly. Furthermore, the underside of the layer shows a rougher profile than in the bonded interface zones in Figure 11a (or at the equivalent layers in the Figures 5 and 8a).

The results of the EDX and EBSD measurements are summarized within Figures 6, 9 and 12 for the electrolytes I–III. While the upper lines show unaffected regions of the PEO coatings, in the lower lines, the zones affected by the electrolyte are depicted. Subfigure a shows the corresponding SEM images which were used to indicate the substrate/coating interface as well as the top edge of the tilted PEO layer by a spline. The subfigures b–d show EDX maps for the elements aluminum, oxygen, and silicon. The EBSD data are depicted in the subfigures e–g. These include: a representation of the inverse pole figures (IPF) indicating the spatial distribution of the detected grains as well as their crystallographic orientation (subfigure e); a phase map as a result of the indexing routine summarized in Figure 2, which shows the proportions of α- and γ-Al_2O_3 within the PEO layers (subfigure f); and an image quality plot (subfigure g) that shows areas of high IQ by bright gray and regions of low IQ values indicated by colors according to the categories i–iii described above. Exposure and measuring time per spot were optimized for EBSD at every investigation area to achieve a good signal/noise ratio and low electron beam drift in order to obtain a suitable band contrast within the diffraction patterns. As a result of that, the absolute count number and the range of color intensity varies between the different maps of an element. Therefore, the EDX maps only allow for a qualitative indication of the element distribution within one investigation area.

Except for the different preparation routine for the sample delaminated after interaction with electrolyte III, the images depicted in the top rows of Figures 6, 9 and 12 show

PEO layers with identical experimental histories. The elements aluminum and oxygen are distributed homogeneously within the coating and just show lowered intensities in regions of cavities and structural defects. The Si maps show an enrichment of silicon in this zones. Furthermore, an elevated Si content can be recognized close to the substrate as well as in the outer coating regions. The distribution of crystallinity, indicated by the IPF map, shows a stacked structure of characteristic zones. Near to the substrate/layer interface is a region whose oxide material cannot be assigned to any crystallographic orientation. Above this is an area with grain sizes in the submicrometer range, which merges into a zone about 15 µm in thickness with grain sizes of several micrometers. Above, the grain size decreases again with increasing substrate distance. After the transition to the outer mesoporous layer area, larger grains with chord lengths over 10 µm are also present. The phase map generated using the methodology summarized in Figure 2 shows that the identified alumina modifications are not homogeneously distributed but also exhibit a stratified structure. While the zone of larger grains above the non-crystalline substrate/coating interface predominantly consist of α-Al_2O_3, the outer mesoporous coating regions show an elevated γ-Al_2O_3 content. Interestingly, based on the direct comparison with the Si map, it can be observed that the detected Si fractions are predominantly present in areas with high γ-Al_2O_3 content, while the α-Al_2O_3 rich zones are almost free of silicon. The image quality plots show low IQ values at and above the outer coating edge because of topographic scattering. Similar effects lead to lowered IQ in regions of cracks, discharge channels and other cavities. The crystalline regions close to the substrate also show areas of low image quality, the extension of which cannot be explained based on structural effects alone. Since the element maps show the presence of aluminum, oxygen, and low amounts of silicon, a region of amorphous Al_2O_3 with dopants of Si can be assumed. The direct comparison of the element maps before and after the exposition experiments indicates local changes of the chemical composition at the substrate/coating interface: for electrolyte I and III a depletion of aluminum and oxygen, for electrolyte III an enrichment of silicon. However, due to the already mentioned limitations of EDX measurements, these indications cannot be considered valid. In contrast to that, the EBSD measurements show a significant increase of the non-crystalline zone at the substrate/coating interface for electrolyte I, which is even more pronounced for electrolyte III. The dimensions of this amorphous oxide region remain unchanged after exposure of the sample to electrolyte II.

4. Discussion

The ICP measurements, represented in Figure 3, as well as the micrographs summarized in Figures 5, 8 and 11 show that the exposition to electrolyte II barely affected the PEO coating, while electrolyte I and III lead to Al release by dissolution of the substrate/coating interface and the substrate itself. The dissolution of the substrate/coating interface can be attributed to reactions according to Equation (2). The observed substrate attack can be interpreted as reactions according to Equation (4). Since these processes require hydroxide ions, the effects were more pronounced in electrolyte III with a pH of 14 than in electrolyte I with a pH of 13. The silicate content of electrolyte II (pH $\approx$ 13, $c_{Na_2SiO_3}$ = 5 g/L) suppressed the above-mentioned reactions by passivation. Furthermore, the spatially highly localized occurrence of the dissolution processes allows for the following conclusions. On the one hand, it is proven that the present intrinsic cavity network of the fully formed PEO coating still allows the electrolyte access to the layer/substrate interface. This supports the assumption that there is an electrochemically active zone in this area over the entire process time, the characteristics of which influence the PEO to a decisive extent [34–36]. On the other hand, it becomes clear that an oxide modification must be present at the substrate/layer interface in and above the passive film, which is more prone to chemical dissolution than the oxide of the unaffected bulk coating.

The evaluation of the XRD (Figures 4, 7 and 10) and EBSD (Figures 6, 9 and 12) data provides a conclusive explanation for this. The occurrence of the characteristic deflections in the purple intensity difference curves of the diffractograms is to be interpreted as the

disappearance of amorphous parts after the exposition experiments. Accordingly, the corresponding non-crystalline oxide phases are affected preferentially by dissolution. The extent of this effect follows the same pattern that has already become clear from the ICP measurements and SEM images: hardly any oxide dissolution in electrolyte II, significant dissolution in electrolyte I, which is even stronger in electrolyte III. These observations can likewise be explained by increased dissolution of (amorphous) alumina at increased pH and inhibition of this reaction in the presence of passivating silicate constituents. The leaching of the amorphous coating parts leads to a slight relative increase of the generally much more stable crystalline oxide modifications. This directs to positive deflections in the 2θ range of the crystalline peaks in the intensity difference curves. Since this peak's superelevations are more pronounced for α-Al_2O_3 than for γ-Al_2O_3, at least the XRD data indicate that γ-Al_2O_3 is slightly affected by dissolution as well.

However, this observation cannot be supported based on the EBSD data. The phase and IQ maps give a good overview regarding the spatial distribution of the oxide modifications. However, their statistical reliability is too low for allowing a statement as to whether the volume ratio of the crystalline oxides has changed as a result of the exposition experiments. Nevertheless, the element, EBSD, and IQ maps in Figures 6 and 9 clearly show a zone of non (IQ < 500) and weakly (IQ 500–1000) crystalline oxide above the substrate/coating interface with an extension of some micrometers before the exposition experiments. This amorphous alumina can be attributed to be the freshest electrochemical formed oxide before the plasma-chemical phase-transformation processes according to Equation (1). The actual bonding character within the present Al_2O_3 modifications, as well as a conceivable gradation between the layer/substrate interface and the crystalline layer regions, could be elucidated in course of further investigations by X-ray photoelectron spectroscopy (XPS). While the extension of the non- and weakly crystalline zones remains unchanged after exposition to electrolyte II (Figure 6g), the area of low IQ is increased and oblong zones are added after exposition to electrolyte I (Figure 9g). For electrolyte III, this effect is more pronounced (Figure 12g). Therefore, it can be concluded that the amorphous oxide components, whose disappearance is proven by the deflection of the purple intensity difference curve in the X-ray diffractogram, were indeed localized directly above the layer/substrate interface. Additional areas of low IQ were created by leaching these amorphous or weakly crystalline oxides and etching the surrounding crystalline oxides. This is also in accordance with the corresponding SEM images.

The elevated Si content in porous coating zones and the vicinity of the layer/substrate interface can be explained by electrolyte residues in layer cavities and the contribution of the silicate components to the passivation reactions [13]. It is an interesting observation that within the crystalline oxide modifications, Si is preferentially bound in γ-Al_2O_3 but rarely in α-Al_2O_3. However, no significant influence on the chemical dissolution of these oxides could be observed within this study. The effect is very small, if any, since the crystalline modifications have proven to be chemically stable in general. The exposition experiments used in this study do not fully represent the conditions during PEO in that the high electric fields actually present were not applied. However, since the electric permittivity of crystalline alumina is about 10 times that of aqueous solutions, electric field lines would have been localized along the cavity network around the crystalline regions and in the layer/substrate interface. Therefore, effects of a field-assisted chemical dissolution according to [22,23] would have increased the selective dissolution of amorphous alumina, if at all.

The observations regarding substrate-related XRD peaks within the intensity difference curves summarized in Table 4 could not be clearly explained within this study and require further investigations. A changed state of internal stress as a result of the continuous or partial layer delamination, which would cause a peak shift, would be conceivable. However, the deviations in the peak positions are comparably small. The changed height of the substrate material as a result of the formation of etch pits could also have influenced the angular position of the peaks. No clear interpretation is possible at this point. Further investigations are neccessary in order to clarify the observation.

5. Conclusions

In the course of this study, by means of exposition experiments, it was proven that the intrinsic cavity network of fully formed PEO layers allows access of electrolyte solutions down to the substrate/layer interface. In this zone, amorphous alumina is present, which has an increased susceptibility to chemical dissolution. The reactions observed can be intensified by increased alkalinity and inhibited by passivating silicate components in the electrolyte. The crystalline oxide parts of the layer, on the other hand, are not attacked even under strong alkalinity and the absence of passivating silicate constituents. Transferring the results of these model experiments to PEO, chemical redissolving reactions that presumably reduce the layer thickness during the process can be classified as negligible. Literature-known interactions between bath alkalinity and layer growth rate are, therefore, more likely to be due to influences on the passivation processes in the pore base of discharge channels, i.e., the balance between the competing anodic reactions: formation of electrically insulating reaction layers, metal dissolution and electrolysis. The observations made in this study fully support the assumption that the electrochemical properties of the passive film present in the bottom of the pores are process-relevant during the entire PEO treatment time and interact with the other electrolytic and electrical process parameters.

Author Contributions: F.S. conceived and designed the experiments, analyzed the data and wrote the experimental and conclusive parts of the paper, R.M. reviewed the literature, wrote the introduction and discussed the results with F.S. in context of the state of the art, S.C. carried out the SEM and EBSD analysis and developed the corresponding preparation routine, T.M. and T.L. directed the research and contributed to the discussions and interpretations of the results. All authors have read and agreed to the published version of the manuscript.

Funding: This research was funded by the German Research Foundation (Deutsche Forschungsgemeinschaft/DFG) Grant No. LA-1274/46-1.

Institutional Review Board Statement: Not applicable.

Informed Consent Statement: Not applicable.

Data Availability Statement: The authors confirm that the data supporting the findings of this study are available within the article.

Acknowledgments: The Work of Martin Kunze and Marc Pügner who carried out the ICP-OES and XRD measurements is gratefully acknowledged.

Conflicts of Interest: The authors declare no conflict of interest.

References

1. Klapkiv, M.; Nykyforchyn, H.; Posuvailo, V. Spectral analysis of an electrolytic plasma in the process of synthesis of aluminum oxide. *Mater. Sci.* **1995**, *30*, 333–343. [CrossRef]
2. Klapkiv, M.D. Simulation of synthesis of oxide-ceramic coatings in discharge channels of a metal-electrolyte system. *Mater. Sci.* **1999**, *35*, 279–283. [CrossRef]
3. Rogov, A. The role of cathodic current in plasma electrolytic oxidation of aluminium: Current density 'scanning waves' on complex-shape substrates. *J. Phys. D Appl. Phys.* **2018**, *51*, 405303. [CrossRef]
4. Naumann, R.; Petzold, D. Die Bestimmung der Bildungsenthalpien von in thermischen Zersetzungsreaktionen auftretenden Verbindungen durch Einwurfkalorimetrie—Bildungsenthalpie $AlCl_3 \cdot 6H_2O$, amorph-Al_2O_3, γ-Al_2O_3, $Al_2O_3 \cdot 2H_2O \cdot 2HCl$. *J. Therm. Anal.* **1981**, *20*, 319–330. [CrossRef]
5. Matykina, E.; Arrabal, R.; Skeldon, P.; Thompson, G. Investigation of the growth processes of coatings formed by AC plasma electrolytic oxidation of aluminium. *Electrochim. Acta* **2009**, *54*, 6767–6778. [CrossRef]
6. Nie, X.; Meletis, E.; Jiang, J.; Leyland, A.; Yerokhin, A.; Matthews, A. Abrasive wear/corrosion properties and TEM analysis of Al_2O_3 coatings fabricated using plasma electrolysis. *Surf. Coat. Technol.* **2002**, *149*, 245–251. [CrossRef]
7. Sieber, M.; Simchen, F.; Morgenstern, R.; Scharf, I.; Lampke, T. Plasma electrolytic oxidation of high-strength aluminium alloys—Substrate effect on wear and corrosion performance. *Metals* **2018**, *8*, 356. [CrossRef]
8. Simchen, F.; Sieber, M.; Kopp, A.; Lampke, T. Introduction to Plasma Electrolytic Oxidation—An Overview of the Process and Applications. *Coatings* **2020**, *10*, 628. [CrossRef]
9. Kurze, P.; Krysmann, W.; Marx, G. About anodic oxidation of aluminum under spark discharge ANOF in aqueous electrolytes. *Wiss. Z. Techn. Hochsch.* **1982**, *6*, 665–671. (In German)

10. Simchen, F.; Sieber, M.; Mehner, T.; Lampke, T. Characterisation Method of the Passivation Mechanisms during the pre-discharge Stage of Plasma Electrolytic Oxidation Indicating the Mode of Action of Fluorides in PEO of Magnesium. *Coatings* **2020**, *10*, 965. [CrossRef]
11. Sieber, M.; Mehner, T.; Dietrich, D.; Alisch, G.; Nickel, D.; Meyer, D.; Scharf, I.; Lampke, T. Wear-resistant coatings on aluminium produced by plasma anodising—A correlation of wear properties, microstructure, phase composition and distribution. *Surf. Coat. Technol.* **2014**, *240*, 96–102. [CrossRef]
12. Sieber, M.; Simchen, F.; Scharf, I.; Lampke, T. Formation of a Spinel Coating on AZ31 Magnesium Alloy by Plasma Electrolytic Oxidation. *J. Mater. Eng. Perform.* **2016**, *25*, 1157–1162. [CrossRef]
13. Simchen, F.; Mosoud-Nia, N.; Mehner, T.; Lampke, T. Formation of corundum-rich alumina coatings on low-carbon steel by plasma electrolytic oxidation. *IOP Conf. Ser. Mater. Sci. Eng.* **2021**, *1147*, 012007. [CrossRef]
14. Raj, V.; Mubarak Ali, M. Formation of ceramic alumina nanocomposite coatings on aluminium for enhanced corrosion resistance. *J. Mater. Process. Technol.* **2009**, *209*, 5341–5352. [CrossRef]
15. Yerokhin, A.; Leyland, A.; Matthews, A. Kinetic aspects of aluminium titanate layer formation on titanium alloys by plasma electrolytic oxidation. *Appl. Surf. Sci.* **2002**, *200*, 172–184. [CrossRef]
16. Savguira, Y.; Ni, Q.; Sobrinho, P.H.; North, T.; Thorpe, S. Effect of Process Parameters on the Corrosion Resistance Properties of PEO Coatings Produced on AZ31B Magnesium Alloy. *ECS Trans.* **2016**, *72*, 91–103. [CrossRef]
17. Sobrinho, P.; Savguira, Y.; Ni, Q.; Thorpe, S. Statistical analysis of the voltage-time response produced during PEO coating of AZ31B magnesium alloy. *Surf. Coat. Technol.* **2017**, *315*, 530–545. [CrossRef]
18. Snizhko, L.; Yerokhin, A.; Pilkington, A.; Gurevina, N.; Misnyankin, D.; Leyland, A.; Matthews, A. Anodic processes in plasma electrolytic oxidation of aluminium in alkaline solutions. *Electrochim. Acta* **2004**, *49*, 2085–2095. [CrossRef]
19. Yerokhin, A.; Voevodin, A.; Lyubimov, V.; Zabinski, J.; Donley, M. Plasma electrolytic fabrication of oxide ceramic surface layers for tribotechnical purposes on aluminium alloys. *Surf. Coat. Technol.* **1998**, *110*, 140–146. [CrossRef]
20. Al Bosta, M.; Ma, K.J.; Chien, H.H. The effect of MAO processing time on surface properties and low temperature infrared emissivity of ceramic coating on aluminium 6061 alloy. *Infrared Phys. Technol.* **2013**, *60*, 323–334. [CrossRef]
21. Koroleva, E.; Thompson, G.; Hollrigl, G.; Bloeck, M. Surface morphological changes of aluminium alloys in alkaline solution: Effect of second phase material. *Corros. Sci.* **1999**, *41*, 1475–1495. [CrossRef]
22. Nagayama, M.; Tamura, K. On the mechanism of dissolution of porous oxide films on aluminium during anodizing. *Electrochim. Acta* **1968**, *13*, 1773–1783. [CrossRef]
23. O'Sullivan, J.P.; Wood, G.C. The Morphology and Mechanism of Formation of Porous Anodic Films on Aluminium. *Proc. R. Soc. Lond. Ser. A* **1970**, *317*, 511–543. [CrossRef]
24. Moon, S.M.; Pyun, S.I. The formation and dissolution of anodic oxide films on pure aluminium in alkaline solution. *Electrochim. Acta* **1999**, *44*, 2445–2454. [CrossRef]
25. Snizhko, L.; Yerokhin, A.; Gurevina, N.; Misnyankin, D.; Pilkington, A.; Leyland, A.; Matthews, A. A model for galvanostatic anodising of Al in alkaline solutions. *Electrochim. Acta* **2005**, *50*, 5458–5464. [CrossRef]
26. Dunleavy, C.; Curran, J.; Clyne, T. Self-similar scaling of discharge events through PEO coatings on aluminium. *Surf. Coat. Technol.* **2011**, *206*, 1051–1061. [CrossRef]
27. Rama Krishna, L.; Somaraju, K.; Sundararajan, G. The tribological performance of ultra-hard ceramic composite coatings obtained through microarc oxidation. *Surf. Coat. Technol.* **2003**, *163-164*, 484–490. [CrossRef]
28. Sundararajan, G.; Rama Krishna, L. Mechanisms underlying the formation of thick alumina coatings through the MAO coating technology. *Surf. Coat. Technol.* **2003**, *167*, 269–277. [CrossRef]
29. Xue, W.; Deng, Z.; Chen, R.; Zhang, T. Growth regularity of ceramic coatings formed by microarc oxidation on Al–Cu–Mg alloy. *Thin Solid Film.* **2000**, *372*, 114–117. [CrossRef]
30. Parfenov, E.; Yerokhin, A.; Matthews, A. Small signal frequency response studies for plasma electrolytic oxidation. *Surf. Coat. Technol.* **2009**, *203*, 2896–2904. [CrossRef]
31. Wright, S.; Nowell, M. EBSD image quality mapping. *Microsc. Microanal. Off. J. Microsc. Soc. Am. Microbeam Anal. Soc. Microsc. Can.* **2006**, *12*, 72–84. [CrossRef] [PubMed]
32. Field, D.P. Recent advances in the application of orientation imaging. *Ultramicroscopy* **1997**, *67*, 1–9. [CrossRef]
33. *Al: 00-004-0787, α-Al2O3: 00-010-0173, γ-Al2O3: 01-077-0396*; PDF-2 Release 2014. ICDD: Newtown Square, PA, USA, 2014.
34. Rogov, A.; Yerokhin, A.; Matthews, A. The Role of Cathodic Current in Plasma Electrolytic Oxidation of Aluminum: Phenomenological Concepts of the "Soft Sparking" Mode. *Langmuir ACS J. Surf. Colloids* **2017**, *33*, 11059–11069. [CrossRef] [PubMed]
35. Rogov, A.; Matthews, A.; Yerokhin, A. Role of cathodic current in plasma electrolytic oxidation of Al: A quantitative approach to in-situ evaluation of cathodically induced effects. *Electrochim. Acta* **2019**, *317*, 221–231. [CrossRef]
36. Rogov, A.; Nemcova, A.; Hashimoto, T.; Matthews, A.; Yerokhin, A. Analysis of electrical response, gas evolution and coating morphology during transition to soft sparking PEO of Al. *Surf. Coat. Technol.* **2022**, *442*, 128142. [CrossRef]

coatings

MDPI

Article

Chromium Luminescence in Plasma Electrolytic Oxidation Coatings on Aluminum Surface

Aleksejs Zolotarjovs [1,*], Rudolfs Piksens [1], Krisjanis Smits [1], Virginija Vitola [1], Gatis Tunens [1], Ernests Einbergs [1], Arturs Zarins [2] and Gunta Kizane [2]

[1] Laboratory of Optical Materials, Institute of Solid State Physics, University of Latvia, Kengaraga Street 8, LV-1063 Riga, Latvia
[2] Laboratory of Radiation Chemistry of Solids, Institute of Chemical Physics, University of Latvia, 1 Jelgavas Street, LV-1004 Riga, Latvia
* Correspondence: aleksejs.zolotarjovs@cfi.lu.lv

Abstract: With plasma electrolytic oxidation (PEO), one can easily obtain thick (tens of microns), mechanically resilient and chemically stable oxide coating on aluminum and other valve metal alloys. The study of luminescent PEO coatings is a relatively new subfield of the already well-established coating preparation methods. In recent years, many new luminescence-based approaches have been developed, one of which is the detection of ionizing radiation of carbon-doped PEO alumina coating. This study presents an improved approach by doping the alumina coating with chromium using citric acid as an additive in the electrolyte. Trivalent chromium ions replacing aluminum in the crystalline lattice of the coating exhibit characteristic sharp lines in the luminescence spectrum. The effectiveness of different DC voltages, process times and citric acid concentrations in electrolyte were examined. The use of citric acid in the electrolyte also provides the conditions required for the formation of an energy trap in the bandgap of the material, thus opening up the possibility for the coating to be used as an ionizing radiation detector by measuring its thermoluminescence. Chromium atoms are incorporated in the coating from the Al6082 aluminum alloy itself and are not added in the electrolyte, therefore making the process much more reliable, repeatable, and environmentally friendly.

Keywords: plasma electrolytic oxidation; PEO; dosimetry; TSL; alumina; luminescent coating

Citation: Zolotarjovs, A.; Piksens, R.; Smits, K.; Vitola, V.; Tunens, G.; Einbergs, E.; Zarins, A.; Kizane, G. Chromium Luminescence in Plasma Electrolytic Oxidation Coatings on Aluminum Surface. *Coatings* **2022**, *12*, 1733. https://doi.org/10.3390/coatings12111733

Academic Editor: Alenka Vesel

Received: 19 October 2022
Accepted: 8 November 2022
Published: 13 November 2022

1. Introduction

Electrochemical oxidation of materials has been extensively studied and applied for decades, with many established technologies like anodization and plasma electrolytic oxidation (PEO). PEO has been under extensive research for over 40 years [1–3] and is of particular interest for applications that require a thick [4], hard [5], thermally [6] and chemically resilient [7] coating. PEO uses large voltages and high current densities to produce plasma discharges through the oxide layer, thus enabling synthesis of the hardest and most stable phases, e.g., an alpha phase of alumina [8]. Due to its crystalline structure and chemical composition, this material is chemically inert with outstanding thermal stability and hardness. It is mainly exploited as a ceramic and is widely used for industrial purposes where a hard, mechanical shock-resistant, chemically inert, or biocompatible material is required [9–11].

In recent years, the PEO research branched out to studies on optical properties of coatings with subsequent application in combining functional properties (e.g., gas sensitivity [12] or ionizing radiation detection [13]) with established strengths of the PEO. Usually, a pure oxide coating is not luminescent by itself, so various approaches were developed to implement impurities (dopants) into the coating. Fortunately, the PEO process requires precise control of many variables (voltage, voltage profile, current density, electrolyte content, substrate itself) and therefore presents many possibilities for incorporation of dopants (e.g., rare earths [14]). While doping from the suspension electrolyte is the

easiest [15–17], the first one discovered was the addition of desired dopant in the substrate (aluminum alloy) itself [18]. Aluminum alloys are used in most practical applications, as the substrate already contains some concentrations of various alloying elements, of which Si, Mg, and Mn are the most abundant. These elements will introduce impurities in the crystalline structure of the coating and need to be studied.

Previous research [19–22] suggests that chromium creates deep charge carrier traps, making it suitable for detection of high dose ionizing radiation used in applications like the calibrators of equipment for radiation sterilization of plant seeds, border control vehicle scanners, power plant energy generators, and other high dose applications. This research will focus on forming α-Al_2O_3 and γ-Al_2O_3 crystalline phases on aluminum samples using the PEO process, specifically exploring impurities introduced by a common additive in most alloys—chromium. Chromium as a synthetic alumina activator is widely explored in material science, is isovalent to alumina, and does not create any meaningful point defects. α-Al_2O_3 and γ-Al_2O_3 are the most common crystalline phases of aluminum, however the alpha phase is found to possess higher hardness, resistance to wear, and thermal stability [23,24]. This paper will explore the possibilities of obtaining hard α-Al_2O_3 with intense chromium luminescence in PEO coatings by using the chromium impurities naturally present in the substrate material as luminescence centers. It is important to explore the coating process of the highly luminescent aluminum coating to a point where it can be easily, repeatably mass-produced for ionizing radiation detector usage. Cr-doped alumina has previously been reported [19], however the novelty of this research lies in the optimization of the method of coating as, to our knowledge, the usage of impurities naturally occurring in substrate material to create chromium-doped alumina for dosimetric applications has not yet been explored.

2. Materials and Methods

2.1. Samples

The substrate material (Al6082) is from the wrought aluminum–magnesium–silicon family. Although the purity is better than 95.2%, the alloy still contains traces of Cr, Cu, Fe, Mg, Mn, Si, Ti, Zn, and other metals with a concentration of chromium up to 0.25% and 0.7% of other metals. In addition, one sample using high purity (99.999%) Al was prepared. In this study, a 0.5 mm thick aluminum sheet was cut into samples $6.5 \times 25 \times 0.5$ mm^3 in size, each having a total surface area of approximately 3.5 cm^2 (used in calculations of current density, a bit less than geometric value due to the non-constant waterline). Before the PEO process, samples were cleaned in ultrasonic cleaner (ASonic (Singapore), PRO30, 40 kHz) in deionized water with soap, then rinsed in acetone.

2.2. PEO Setup

Custom 5 kW bipolar pulse electric generator ELGOO PEO V3 (Riga, Latvia) was used. The device is externally controlled via PC, which allows great repeatability and high customization of parameters like pulse timing, voltage, current, and their changes in time.

The electrolyte for "doped" samples consisted of three components: 800 mL deionized water, 1 g·L^{-1} KOH (Emplura >84% pellets) and citric acid (Sigma Aldrich (St. Louis, MO, USA), 99.5–100.5% based on anhydrous substance) with varying concentration (2/5/10/15/30 g·L^{-1}), as well as a sample without the addition of citric acid was prepared. The electrolyte was contained in a double-walled water-cooled reaction chamber, and thus a stable 30 ± 5 °C temperature was maintained. However, evaporation of the electrolyte was still present. To compensate, a constant influx of deionized water was supplied to the reactor keeping the water level constant.

According to the tested parameters, DC constant voltages were chosen (450/550/650/700/750 V) and kept constant throughout the whole process. The total process time (15/30/45/60 min) also varied between processes. Throughout the process, current density dropped, starting at approximately 178 mA·cm^{-2} in the first half of the process and declined in the second half for about 30%. The current density for the sample without citric acid

in the electrolyte was approximately 25 mA·cm^{-2} larger throughout the whole synthesis. However, the current profile throughout the synthesis is highly dependent on the citric acid concentration, as electric characteristics of the electrolyte are different. Pt plate was used as a counter electrode.

Three PEO process parameters—DC voltage, PEO process time, and concentration of citric acid in the electrolyte—were consecutively varied and tested on different samples. The samples produced with a citric acid concentration of 15 and 30 g·L^{-1} were heavily corroded during PEO and thus were not included in further measurements. From each series of tests, the sample with the highest luminescence intensity measurement in TSL was chosen to represent the optimal value of each tested parameter. Thus, the sample with DC voltage, process time, and citric acid concentration values of 700 V, 45 min, and 10 g·L^{-1} was found to produce the highest TSL intensity around the 692.9 and 694.3 nm [25] luminescence lines of Cr^{3+}.

Lastly, the high purity Al sample was exposed to PEO process with 700 V DC voltage, 45 min process time, and no citric acid added in electrolyte for reference on the effect of Cr presence in Al alloy.

2.3. Measurements

The X-ray diffraction (XRD) spectrometer Rigaku MiniFlex 600 (Rigaku, Tokyo, Japan) was used to determine the crystalline structures. The crystalline phases of the PEO coating were characterized by X-ray powder diffraction using a cathode voltage of 700 V with Cu Kα radiation (1.5418 Å). The scan rate was 1.5 °/min.

The photoluminescence (PL) and X-ray induced luminescence (XRL) measurements were performed at room temperature with the Andor DU-401A-BV IDus CCD camera (Andor Technology Ltd., Belfast, United Kingdom) coupled with the Andor Shamrock B-303i spectrograph. (Andor Technology Ltd., Belfast, United Kingdom) Slit size was 100 μm. The excitation source for PL measurements was CryLaS Nd:YAG laser (CryLaS, Berlin, Germany, 266 nm) and the excitation source for XRL measurements was X-ray tube with W anode operating at 30 kV, 10 mA.

Thermally stimulated luminescence (TSL) measurements were conducted using Lexsygresearch LMS (Freiberg Instruments, Freiberg, Germany) with X-ray and beta sources, however only X-ray irradiation was used. The X-ray source was set to 40 kV and 0.5 mA and the tube consisted of a tungsten target, beryllium window, and was powered by Spellman MNX50P50/XCC (Spellman, Hauppauge, NY, USA) power supply. As multiple samples with slightly varying masses and surface area were prepared, calibration measurements were performed. Between measurements, samples were preheated to remove any previously accumulated dose, irradiated for 600 s (with 33 Gy), and repeatedly measured. The highest registered intensity was taken as a baseline and an equalization coefficient was calculated for other samples, which was applied to avoid invalidation based on inconsistency of surface area.

Spectra measured with CCD in PL, XRL, and TSL were not corrected to accommodate differences in detection at different wavelengths because they were used comparatively only.

Scanning electron microscope (SEM) measurements were made on Phenom Pro scanning electron microscope (Phenom-World, Eindhoven, Netherlands, using 10 kV accelerating voltage.

X-ray fluorescence (XRF) was measured using RIGAKU miniflex 600 X-ray diffractometer (Rigaku, Tokyo, Japan) at 50 kV voltage and 50 μA current.

3. Results

3.1. Structure and Morphology

SEM measurements were performed to study the surface of the coating and to compare the two samples. Porosity of the samples prepared with citric acid (Figure 1a,b) and those prepared in just KOH solution (Figure 1c,d) seems similar, however the citric acid samples

possess marginally larger pores, which can be attributed to the slightly larger current density during the PEO of the undoped sample. The coating surface is coarse and porous, and it is similar to the coating surface of valve metal in universal PEO. Both coatings exhibit porosity, which sometimes can be an advantage [26], and cracks. Zoomed in images (Figure 1b,d) show a similar ceramic-like structure with irregular cracks formed by large temperature gradients. It can be deduced that the pores in the surface are the residual discharge channel during the discharge reaction. The irregularly shaped areas around the pores are formed due to the rapid cooling of the electrolyte. The average diameters of the pores are 0.3–0.4 mm [27].

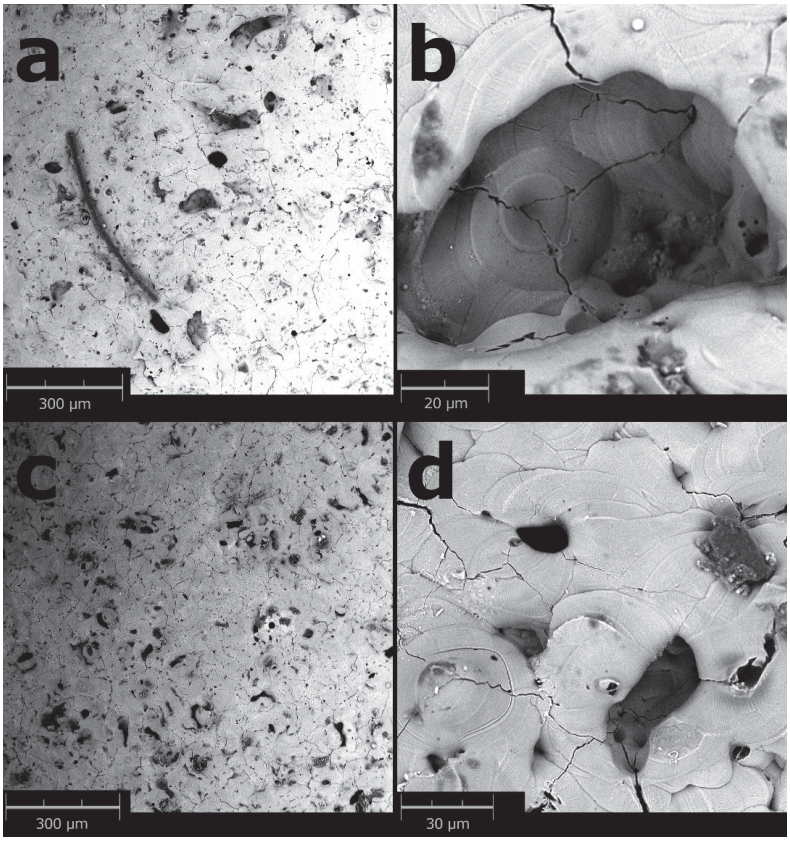

Figure 1. (**a**,**b**) Scanning electron microscope image of doped coating with different scales; (**c**,**d**) Scanning electron microscope image of undoped coating with different scales.

The XRD measurements are crucial in almost any study of PEO coatings as the presence and type of crystalline structure in the coating will manifest most mechanical properties and capabilities. Figure 2 shows the XRD graph of one of the samples, with major peaks identified and connected to different alumina phases corresponding to PDF4+ database. Two main crystalline phases were identified—α-Al_2O_3 rhombohedral and γ-Al_2O_3 cubic [28].

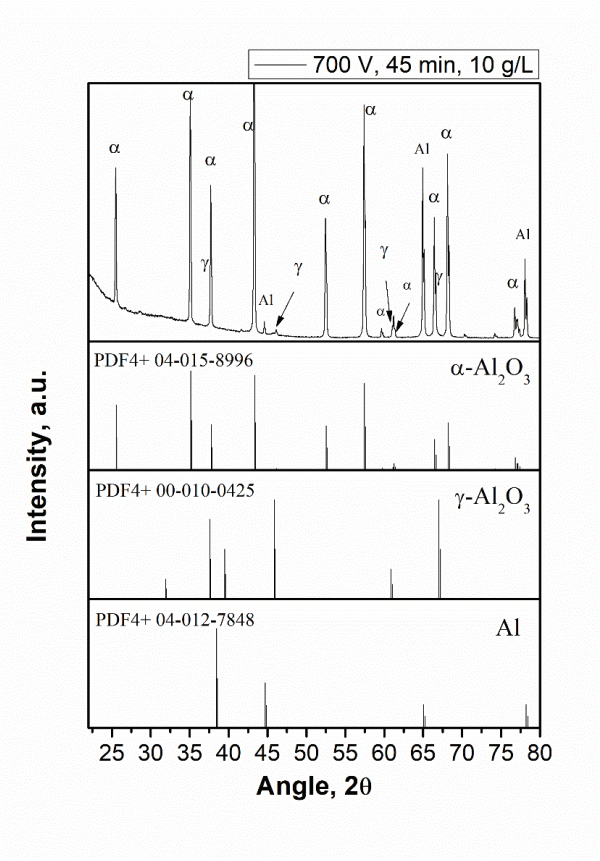

Figure 2. XRD measurement of the sample coating produced with PEO parameters 700 V, 45 min process duration and 10 $g \cdot L^{-1}$ citric acid concentration with all major peaks marked with the corresponding phase.

It was found that the 15 min processing time was enough to produce some amount of α-Al2O3, however at 30 min processing time the mixture of the hardest α-phase and a "softer" γ-phase reaches 13:1 ratio and barely changes with increased process time, as shown in Figure 3, which correlates well with literature [29,30] and previous investigations. As such, the coating is expected to perform well in wear and hardness tests.

During the PEO process, a coating is formed at the interface between the substrate and the electrolyte or the previously formed coating and the electrolyte. Therefore, some of the impurities from the aluminum alloy are expected to migrate to the coating. However, the effect of citric acid inclusion in the electrolyte, voltage applied during PEO process, and duration of the PEO process time has on the concentration of impurity metal ions in the resulting coating is yet unknown.

Photoluminescence of samples consists of three spectral regions of interest—two broad peaks at around 425 nm and 550 nm and a significant peak at 693 nm typical to Cr^{3+} ion presence in α-Al_2O_3 matrix. The three regions in which these peaks are found are often referred to as blue, green, and red, representing visible light spectrum parts.

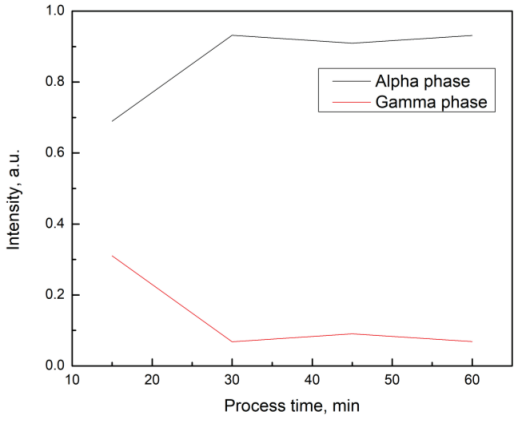

Figure 3. α-Al_2O_3 and γ-Al_2O_3 phase concentrations as derived from XRD measurements for samples with different PEO process duration.

A blue luminescence peak (maximum at 425–450 nm) appears under UV irradiation in both samples, and it relates to alumina F and F^+ centers (oxygen vacancies with one or two electrons) and is often observed in anodic aluminum oxide films. Both F^+ and F centers are present, and the maxima are overlapping, thus producing a broad emission band [31]. A slight variation in integrated intensity at this region between samples is due to the overlap of maxima (F and F^+) with different intensities, as intensities of both bands are highly sensitive to the structure, internal stresses, and preparation conditions of the coating [32–34].

A green luminescence band with maximum at 550 nm is also present under UV irradiation in both samples. This well-known band in amorphous and crystalline alumina is due to intrinsic defects of the alumina matrix, specifically F2 centers. The band is observed in alumina prepared by a wide range of methods [35–38].

Red luminescence observed under UV irradiation is a complex band consisting of a sharp peak (at 693 nm) and a broad-band covering the whole red part of the spectrum. The 693 nm sharp line's intensity is minor compared to the luminescence of the blue band, however still notable over the red broad-band. It is associated with widely studied and abbreviated in literature as R1 and R2 line doublet of Cr^{3+} ions in Al sites of the α-Al_2O_3 matrix. The inability to distinguish R1 and R2 (692.5 nm and 694 nm [39]) lines is explained by the irregularities in the crystalline lattice of the coating and the presence of other impurities [39,40]. Besides Cr^{3+} luminescence, another maximum is also present around the R1 and R2 lines in TSL glow-curves, which most likely correlates with self-luminescence of α-Al_2O_3 (Figure 4).

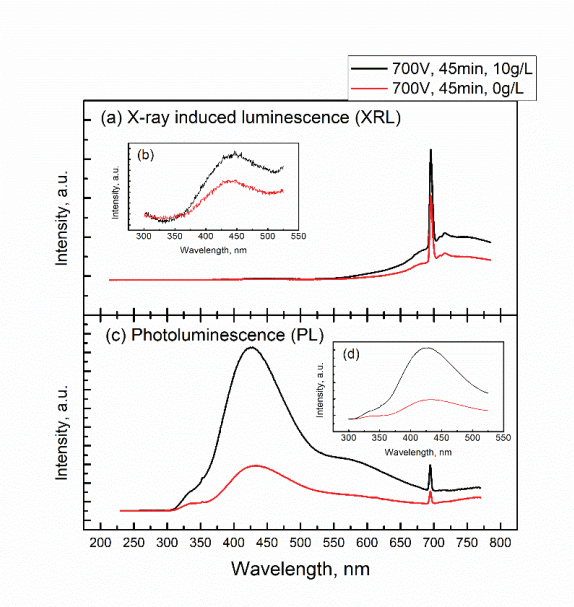

Figure 4. (**a**) XRL spectra of samples with concentrations of 10 g·L^{-1} and 0 g·L^{-1} citric acid used in electrolyte during PEO process, (**b**) intrinsic defect range 300–550 nm; (**c**) PL spectra of samples with concentrations of 10 g·L^{-1} and 0 g·L^{-1} citric acid used in electrolyte during PEO process, (**d**) intrinsic defect range 300–550 nm.

XRL spectrum shows only a weak intensity blue luminescence, peaking at 450 nm and likely relating to the same alumina F and F^+ centers, as observed in PL. Additionally, in the red luminescence part of the spectrum the sharp 693 nm peak, belonging to the R1 and R2 lines of the Cr^{3+} luminescence, can be observed here even more distinct against the broad red luminescence band.

Both PL and XRL measurements show an additional, wide, and particularly complex red luminescence band. Based on previous observations (from XRF), it is evident that a broad red luminescence originates from different metal ions (besides Mn and Cr) present in alumina structure and is obtained from the alloy itself during the growth of the coating [37]. If we compare samples with or without citric acid addition, an improvement in the intensity of luminescence is visible both for XRL and PL (Figure 4).

XRF measurements were performed and, together with thermally stimulated luminescence (TSL) results, are presented in Figure 5. TSL measurements are very important for determining which sample is best suited for dosimetric applications. With increasing duration of PEO process time, a clear peak in TSL intensity can be found for sample with 45 min process duration. Figure 5a shows that the concentration of impurity metal ions in the resulting coating only seems to correlate with these parameters after the 30 min mark. In Figure 5b, a correlation can be seen between an increased PEO process duration, TSL intensity, and Cr ion concentration measured in XRF. The only sample deviating from this correlation is the one created at 700 V DC. The sample series with varied citric acid concentration value yields close to no correlation between TSL intensity and Cr ion concentration. In Figure 5c, the presence of Cr ions in the formed coating peaks at 2 g·L^{-1} of added citric acid in electrolyte, however with increasing the citric acid concentration, TSL intensity seems to also increase up until the 10 g·L^{-1} limit, where the samples began heavily corroding during the PEO process.

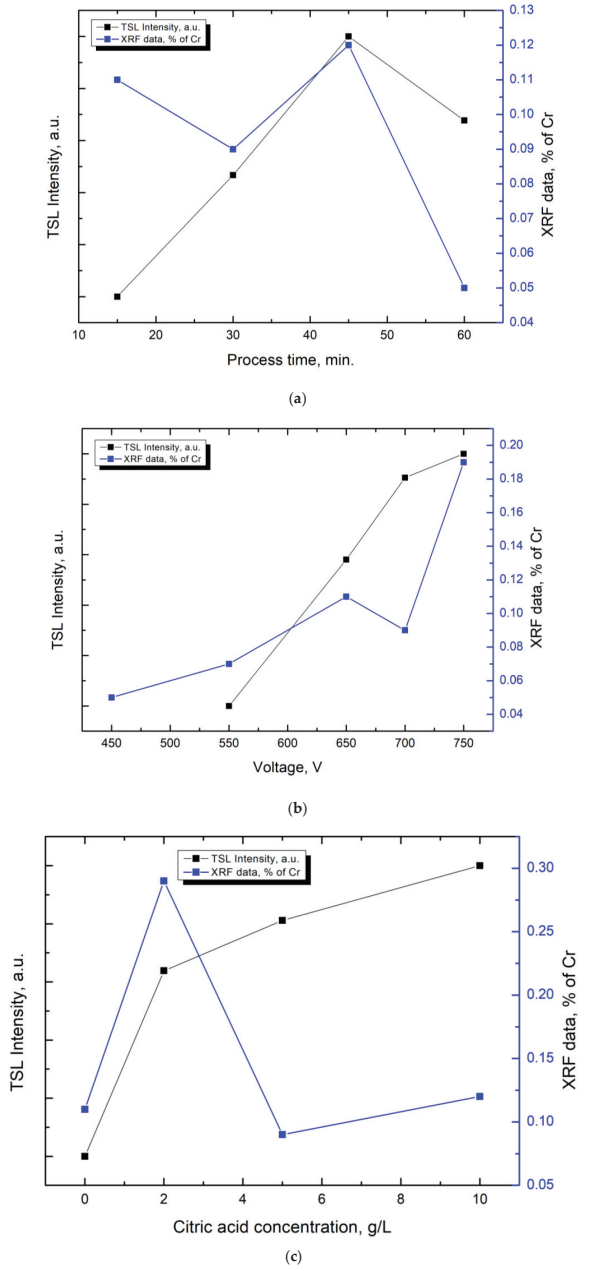

Figure 5. TSL intensity and XRF mass % of Cr based on: (**a**) different PEO process times at 700 V voltage and 10 g·L^{-1} citric acid concentration; (**b**) different PEO voltages at 30 min process time and 10 g·L^{-1} citric acid concentration; (**c**) different citric acid concentrations in PEO electrolyte at 700 V voltage and 45 min process time.

3.2. Optical Properties

TSL glow curves (Figure 6) were measured with CCD, therefore quick analysis of the full spectral distribution can be performed. Although a strong luminescence can be

observed around 420 nm in TSL measurements, the highest intensity maximum corresponds with Cr^{3+} luminescence, meaning that any energy carriers stored in traps present in the lattice recombine on Cr atoms, which correlates well with previous observations even in other matrices. By analyzing only the 693 nm line, one can observe that the Cr-doped sample exhibits intense TSL signal in temperature ranges above room temperature, consisting of two or more overlapping maxima. Low temperature maximum (centered at about 375 K) produces an afterglow at room temperature and its intensity relates to the delay between the "impact" ionizing radiation dose and the measurement itself. The most intense glow curve maximum (at 480 K with FWHM of 50 K) represents the trap center with an activation energy of approximately 1.2 eV (estimated Randall–Wilkins equation [41–43]), well within the broad band-gap of the alumina. The intensity of this maximum might correlate with the acquired radiation dose, as long as the center is stable enough at room temperature. Additionally, a high temperature complex maximum is observed (from 550 K and up); however, the intensity is relatively low, and the limitations of the measurement setup deny comprehensive study of this part of the glow curve). It is important to note that no TSL signal above room temperature was observed for the undoped sample; therefore, all glow curve maxima are due to the increased concentration of defects (impurity ions) in the alumina matrix.

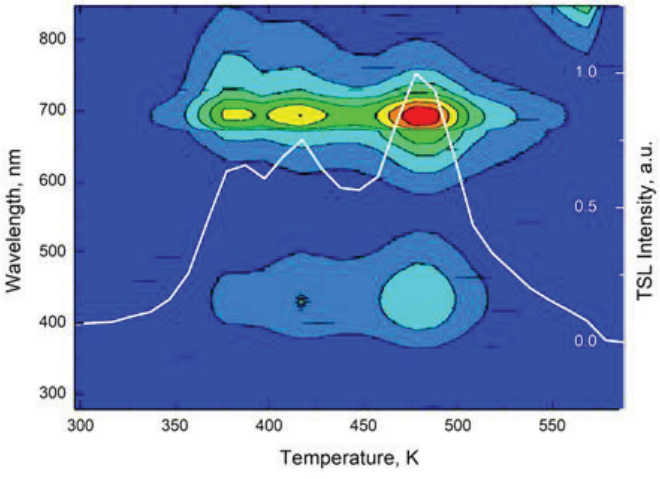

Figure 6. TSL glow curve at 693 nm (white line, right Y scale) overlayed on top of full measurement matrix (left Y scale). X-scale is joined between an overlay and a matrix. Color represents the intensity of the 2D graph (temperature to wavelength).

4. Conclusions

A new approach to produce Cr^{3+}-doped hard ceramic alumina coating on aluminum alloy (Al6082) surface is proposed. The coating is prepared during the PEO process with the use of a modified KOH-based electrolyte by the addition of citric acid. No additional Cr is introduced in the electrolyte as the luminescence centers migrate into the coating from the substrate material. The obtained material exhibits outstanding luminescence properties that are promising for use in the detection and quantification of ionizing radiation. Strong Cr^{3+} emission is observed in PL, XRL, and TSL spectra, providing a basis for a range of sensor applications.

Since the proposed technique does not require an artificial dopant to be added to the electrolyte and in turn uses the impurities already present in most aluminum alloys, this method is easily and inexpensively scalable and is more environmentally friendly than the conventional Cr-based electrolytes. The best performing samples were created with

45 min PEO process time, 700 V DC voltage, and 10 $g \cdot L^{-1}$ concentration of citric acid in the electrolyte.

To evaluate the coating for use as a dosimeter, additional measurements should be performed. Moreover, although the alpha phase is present in the coating, mechanical properties should be studied if the approach is to be considered for use in coating preparation with both mechanical stability and functional properties in mind.

Author Contributions: Conceptualization, K.S. and A.Z. (Aleksejs Zolotarjovs); methodology, A.Z. (Aleksejs Zolotarjovs) and G.T.; software, E.E.; validation, A.Z. (Aleksejs Zolotarjovs), V.V. and K.S.; formal analysis, R.P. and G.T.; investigation, R.P., E.E., V.V. and K.S.; resources, R.P., A.Z. (Arturs Zarins) and G.K.; data curation, G.T. and K.S.; writing—original draft preparation, R.P.; writing—review and editing, A.Z. (Aleksejs Zolotarjovs), V.V. and E.E.; visualization, G.T.; supervision, A.Z. (Aleksejs Zolotarjovs); project administration, K.S.; funding acquisition, K.S. All authors have read and agreed to the published version of the manuscript.

Funding: Financial support provided by the ERDF, European-Union Project No.1.1.1.1/16/A/182 realized at the Institute of Solid State Physics, University of Latvia is greatly acknowledged. Authors are grateful to ElGoo Tech Ltd. for providing PEO equipment. Institute of Solid State Physics, University of Latvia as the Center of Excellence has received funding from the European Union's Horizon 2020 Framework Programme H2020-WIDESPREAD-01-2016-2017-TeamingPhase2 under grant agreement No.739508, project CAMART2.

Institutional Review Board Statement: Not applicable.

Informed Consent Statement: Not applicable.

Data Availability Statement: Data available upon request to the authors.

Conflicts of Interest: The authors declare no conflict of interest.

References

1. Auzins, K.; Zolotarjovs, A.; Bite, I.; Laganovska, K.; Vitola, V.; Smits, K.; Millers, D. Production of Phosphorescent Coatings on 6082 Aluminum Using $Sr_{0.95}Eu_{0.02}Dy_{0.03}Al_2O_4-\delta$ Powder and Plasma Electrolytic Oxidation. *Coatings* **2019**, *9*, 865. [CrossRef]
2. Yerokhin, A.L.; Nie, X.; Leyland, A.; Matthews, A.; Dowey, S.J. Plasma Electrolysis for Surface Engineering. *Surf. Coat. Technol.* **1999**, *122*, 73–93. [CrossRef]
3. Agureev, L.; Savushkina, S.; Ashmarin, A.; Borisov, A.; Apelfeld, A.; Anikin, K.; Tkachenko, N.; Gerasimov, M.; Shcherbakov, A.; Ignatenko, V.; et al. Study of Plasma Electrolytic Oxidation Coatings on Aluminum Composites. *Metals* **2018**, *8*, 459. [CrossRef]
4. Snizhko, L.O.; Yerokhin, A.L.; Pilkington, A.; Gurevina, N.L.; Misnyankin, D.O.; Leyland, A.; Matthews, A. Anodic Processes in Plasma Electrolytic Oxidation of Aluminium in Alkaline Solutions. *Electrochim. Acta* **2004**, *49*, 2085–2095. [CrossRef]
5. White, L.; Koo, Y.; Neralla, S.; Sankar, J.; Yun, Y. Enhanced Mechanical Properties and Increased Corrosion Resistance of a Biodegradable Magnesium Alloy by Plasma Electrolytic Oxidation (PEO). *Mater. Sci. Eng. B* **2016**, *208*, 39–46. [CrossRef]
6. Ramesh, M.; Marimuthu, K.; Karuppuswamy, P.; Rajeshkumar, L. Microstructure and Properties of YSZ-Al2O3 Functional Ceramic Thermal Barrier Coatings for Military Applications. *Boletín Soc. Española Cerámica Vidr.* 2021; *in press*. [CrossRef]
7. Liang, J.; Srinivasan, P.B.; Blawert, C.; Störmer, M.; Dietzel, W. Electrochemical Corrosion Behaviour of Plasma Electrolytic Oxidation Coatings on AM50 Magnesium Alloy Formed in Silicate and Phosphate Based Electrolytes. *Electrochim. Acta* **2009**, *54*, 3842–3850. [CrossRef]
8. Shirai, T.; Watanabe, H.; Fuji, M.; Takahashi, M. Structural Properties and Surface Characteristics on Aluminum Oxide Powders. *Ceram. Res. Lab.* **2009**, *9*, 23–31.
9. da Costa Cunha, G.; Romão, L.P.C.; Macedo, Z.S. Production of Alpha-Alumina Nanoparticles Using Aquatic Humic Substances. *Powder Technol.* **2014**, *254*, 344–351. [CrossRef]
10. Serdechnova, M.; Karpushenkov, S.; Karpushenkava, L.; Starykevich, M.; Ferreira, M.; Hack, T.; Iuzviuk, M.; Zobkalo, I.; Blawert, C.; Zheludkevich, M. The Influence of PSA Pre-Anodization of AA2024 on PEO Coating Formation: Composition, Microstructure, Corrosion, and Wear Behaviors. *Materials* **2018**, *11*, 2428. [CrossRef]
11. Bouali, A.C.; Straumal, E.A.; Serdechnova, M.; Wieland, D.C.F.; Starykevich, M.; Blawert, C.; Hammel, J.U.; Lermontov, S.A.; Ferreira, M.G.S.; Zheludkevich, M.L. Layered Double Hydroxide Based Active Corrosion Protective Sealing of Plasma Electrolytic Oxidation/Sol-Gel Composite Coating on AA2024. *Appl. Surf. Sci.* **2019**, *494*, 829–840. [CrossRef]
12. Grigorjeva, L.; Millers, D.; Smits, K.; Zolotarjovs, A. Gas Sensitive Luminescence of ZnO Coatings Obtained by Plazma Electrolytic Oxidation. *Sens. Actuators A Phys.* **2015**, *234*, 290–293. [CrossRef]
13. Zolotarjovs, A.; Smits, K.; Laganovska, K.; Bite, I.; Grigorjeva, L.; Auzins, K.; Millers, D.; Skuja, L. Thermostimulated Luminescence of Plasma Electrolytic Oxidation Coatings on 6082 Aluminium Surface. *Radiat. Meas.* **2019**, *124*, 29–34. [CrossRef]

14. Zolotarjovs, A.; Smits, K.; Krumina, A.; Millers, D.; Grigorjeva, L. Luminescent PEO Coatings on Aluminum. *ECS J. Solid State Sci. Technol.* **2016**, *5*, R150–R153. [CrossRef]
15. Bite, I.; Krieke, G.; Zolotarjovs, A.; Laganovska, K.; Liepina, V.; Smits, K.; Auzins, K.; Grigorjeva, L.; Millers, D.; Skuja, L. Novel Method of Phosphorescent Strontium Aluminate Coating Preparation on Aluminum. *Mater. Des.* **2018**, *160*, 794–802. [CrossRef]
16. Stojadinović, S.; Vasilić, R. Formation and Photoluminescence of Eu^{3+} Doped Zirconia Coatings Formed by Plasma Electrolytic Oxidation. *J. Lumin.* **2016**, *176*, 25–31. [CrossRef]
17. Bordbar-Khiabani, A.; Yarmand, B.; Mozafari, M. Enhanced Corrosion Resistance and In-Vitro Biodegradation of Plasma Electrolytic Oxidation Coatings Prepared on AZ91 Mg Alloy Using ZnO Nanoparticles-Incorporated Electrolyte. *Surf. Coat. Technol.* **2019**, *360*, 153–171. [CrossRef]
18. Smits, K.; Millers, D.; Zolotarjovs, A.; Drunka, R.; Vanks, M. Luminescence of Eu Ion in Alumina Prepared by Plasma Electrolytic Oxidation. *Appl. Surf. Sci.* **2015**, *337*, 166–171. [CrossRef]
19. Einbergs, E.; Zolotarjovs, A.; Bite, I.; Laganovska, K.; Auzins, K.; Smits, K.; Trinkler, L. Usability of Cr-Doped Alumina in Dosimetry. *Ceramics* **2019**, *2*, 525–535. [CrossRef]
20. Lapraz, D.; Iacconi, P.; Daviller, D.; Guilhot, B. Thermostimulated Luminescence and Fluorescence of α-Al_2O_3:Cr^{3+}Samples (Ruby). Influence of the Cr^{3+} Concentration. *Phys. Status Solidi (A)* **1991**, *126*, 521–531. [CrossRef]
21. Yunusov, M.S.; Tsoi, A.N.; Muminkhodzhaev, K.M.; Khaimov-Mal'kov, V.Y. Using Thermoluminescence of Ruby for the Dosimetry of γ-Radiation. *Sov. At. Energy* **1974**, *36*, 396–398. [CrossRef]
22. Grigorjeva, L.; Zolotarjovs, A.; Millers, D.; Smits, K.; Krug, P.; Stollenwerk, J.; Osman, A.; Tenostendarp, T. Magnetron Sputtering Fabrication of α-Al2O3:Cr Powders and Their Thermoluminescence Properties. *Radiat. Meas.* **2018**, *119*, 140–143. [CrossRef]
23. García-Mayorga, J.C.; Urbano-Reyes, G.; Veloz-Rodríguez, M.A.; Reyes-Cruz, V.E.; Cobos-Murcia, J.A.; Hernández-Ávila, J.; Pérez-Labra, M. Electrochemical Preparation of Precursor Phases for Obtaining Alpha-Alumina from Aluminium Scrap. *Ceram. Int.* **2018**, *44*, 7435–7441. [CrossRef]
24. Pham, T.D.; Kobayashi, M.; Adachi, Y. Interfacial Characterization of α-Alumina with Small Surface Area by Streaming Potential and Chromatography. *Colloids Surf. A Physicochem. Eng. Asp.* **2013**, *436*, 148–157. [CrossRef]
25. Patra, A.; Tallman, R.E.; Weinstein, B.A. Effect of Crystal Structure and Dopant Concentration on the Luminescence of Cr^{3+} in Al_2O_3 Nanocrystals. *Opt. Mater.* **2005**, *27*, 1396–1401. [CrossRef]
26. Curran, J.A.; Clyne, T.W. Porosity in Plasma Electrolytic Oxide Coatings. *Acta Mater.* **2006**, *54*, 1985–1993. [CrossRef]
27. Wang, Y.L.; Wang, M.; Zhou, M.; Li, B.J.; Amoako, G.; Jiang, Z.H. Microstructure Characterisation of Alumina Coating on Steel by PEO. *Surf. Eng.* **2013**, *29*, 271–275. [CrossRef]
28. Gražulis, S.; Chateigner, D.; Downs, R.T.; Yokochi, A.F.T.; Quirós, M.; Lutterotti, L.; Manakova, E.; Butkus, J.; Moeck, P.; le Bail, A. Crystallography Open Database—An Open-Access Collection of Crystal Structures. *J. Appl. Crystallogr.* **2009**, *42*, 726–729. [CrossRef]
29. Tian, J.; Luo, Z.; Qi, S.; Sun, X. Structure and Antiwear Behavior of Micro-Arc Oxidized Coatings on Aluminum Alloy. *Surf. Coat. Technol.* **2002**, *154*, 1–7. [CrossRef]
30. Yerokhin, A.; Snizhko, L.; Gurevina, N.; Leyland, A.; Pilkington, A.; Matthews, A. Matthews Discharge Characterization in Plasma Electrolytic Oxidation of Aluminium. *J. Phys. D Appl. Phys.* **2003**, *36*, 2110. [CrossRef]
31. Huang, G.S.; Wu, X.L.; Yang, L.W.; Shao, X.F.; Siu, G.G.; Chu, P.K. Dependence of Blue-Emitting Property on Nanopore Geometrical Structure in Al-Based Porous Anodic Alumina Membranes. *Appl. Phys. A* **2005**, *81*, 1345–1349. [CrossRef]
32. Li, S.-Y.; Wang, J.; Li, Y. Photoluminescence Properties of Anodic Aluminum Oxide Formed in a Mixture of Ammonium Fluoride and Oxalic Acid. *Opt. Eng.* **2017**, *56*, 067107. [CrossRef]
33. Palanza, V.; Galli, A.; Lorenzi, R.; Moretti, F.; Mozzati, M.C.; Paleari, A.; Spinolo, G. Luminescence Study of Transition Metal Ions in Natural Magmatic and Metamorphic Yellow Sapphires. *IOP Conf. Ser. Mater. Sci. Eng.* **2010**, *15*, 012086. [CrossRef]
34. Brewer, J.D.; Jeffries, B.T.; Summers, G.P. Low-Temperature Fluorescence in Sapphire. *Phys. Rev. B* **1980**, *22*, 4900–4906. [CrossRef]
35. de Azevedo, W.M.; de Oliveira, G.B.; da Silva, E.F.; Khoury, H.J.; Oliveira de Jesus, E.F. Highly Sensitive Thermoluminescent Carbon Doped Nanoporous Aluminium Oxide Detectors. *Radiat. Prot. Dosim.* **2006**, *119*, 201–205. [CrossRef] [PubMed]
36. Baronskiy, M.; Rastorguev, A.; Zhuzhgov, A.; Kostyukov, A.; Krivoruchko, O.; Snytnikov, V. Photoluminescence and Raman Spectroscopy Studies of Low-Temperature γ-Al_2O_3 Phases Synthesized from Different Precursors. *Opt. Mater.* **2016**, *53*, 87–93. [CrossRef]
37. Gorbunov, S.V.; Cholakh, S.O.; Pustovarov, V.A.; Yakovlev, V.Y.; Zatsepin, A.F.; Kucharenko, A.I. Electronic Excitations and Intrinsic Defects in Nanostructural Al_2O_3. *Phys. Status Solidi (C)* **2005**, *2*, 351–354. [CrossRef]
38. Rodriguez, M.G.; Denis, G.; Akselrod, M.S.; Underwood, T.H.; Yukihara, E.G. Thermoluminescence, Optically Stimulated Luminescence and Radioluminescence Properties of Al_2O_3:C,Mg. *Radiat. Meas.* **2011**, *46*, 1469–1473. [CrossRef]
39. Kostyukov, A.; Baronskiy, M.; Rastorguev, A.; Snytnikov, V.; Snytnikov, V.; Zhuzhgov, A.; Ishchenko, A. Photoluminescence of Cr^{3+} in Nanostructured Al_2O_3 Synthesized by Evaporation Using a Continuous Wave CO_2 Laser. *RSC Adv.* **2016**, *6*, 2072–2078. [CrossRef]
40. Ivakin, Y.; Danchevskaya, M.; Muravieva, G.P.; Ovchinnikova, O.G. Physicochemical properties of corundum doped in supercritical water. In Proceedings of the Joint 19th AIRAPT and 41st EHPRG International Conference on High Pressure Science and Technology, Bordeaux, France, 7–11 July 2003.

41. Randall, J.T.; Wilkins, M.H.F. The Phosphorescence of Various Solids. *Proc. R. Soc. Lond. A Math. Phys. Sci.* **1945**, *184*, 347–364. [CrossRef]
42. Randall, J.T.; Wilkins, M.H.F. Phosphorescence and Electron Traps—I. The Study of Trap Distributions. *Proc. R. Soc. Lond. A Math. Phys. Sci.* **1945**, *184*, 365–389. [CrossRef]
43. Randall, J.T.; Wilkins, M.H.F. Phosphorescence and Electron Traps II. The Interpretation of Long-Period Phosphorescence. *Proc. R. Soc. Lond. A Math. Phys. Sci.* **1945**, *184*, 390–407. [CrossRef]

coatings

MDPI

Article

Degradation Rate Control Issues of PEO-Coated Wrought Mg0.5Zn0.2Ca Alloy

Lara Moreno [1,2], Marta Mohedano [1,*], Raul Arrabal [1] and Endzhe Matykina [1,3]

[1] Departamento de Ingeniería Química y de Materiales, Facultad de Ciencias Químicas, Universidad Complutense de Madrid, 28040 Madrid, Spain; lara.morenoturiegano@umons.ac.be (L.M.); rarrabal@ucm.es (R.A.); ematykina@ucm.es (E.M.)
[2] Materials Science Department, Faculty of Engineering, University of Mons, 20, Place du Parc, 7000 Mons, Belgium
[3] Unidad Asociada al ICTP, IQM (CSIC), Grupo de Síntesis Orgánica y Bioevaluación, Instituto Pluridisciplinar (UCM), Paseo de Juan XXIII 1, 28040 Madrid, Spain
* Correspondence: mmohedan@ucm.es

Abstract: Bioactive plasma electrolytic oxidation (PEO) coatings were developed on a wrought Mg0.5Zn0.2Ca alloy using a transparent electrolyte for easy maintenance and waste disposal, compared to a conventional suspension-based solution. Treatment times of 300, 600, and 900 s were evaluated for their effects on coating morphology, composition, and corrosion resistance. A short-time electrochemical impedance spectroscopy (EIS) screening was utilized to identify coatings with optimal corrosion protection. To assess the degradation rate and corrosion mechanisms, hydrogen evolution was monitored under pH-controlled quasi-in vivo conditions over extended immersion periods. Coating thickness increased by only 3% from 300 to 900 s of treatment (13 and 18 μm, respectively), with pore bands formed near the barrier layer at 900 s. The short-term EIS screening revealed that the coatings produced at 600 and 900 s were less protective and consistent than those at 300 s due to the presence of pore bands, which increased permeability. Hydrogen evolution measurements during 5 days of immersion at pH 7.4 indicated a tenfold higher degradation rate of the PEO-coated alloy compared to the bare substrate. Therefore, none of the PEO coatings provided effective corrosion protection after 24 h of immersion, which is attributed to crack formation at the PEO/corrosion products interface. This highlights the importance of crevices in the corrosion of Mg-Zn-Ca alloys. The presence of ZnO exacerbates the corrosion of magnesium in crevice areas.

Keywords: degradation rate; wrought Mg-Zn-Ca alloy; coating; crevice; plasma electrolytic oxidation

Citation: Moreno, L.; Mohedano, M.; Arrabal, R.; Matykina, E. Degradation Rate Control Issues of PEO-Coated Wrought Mg0.5Zn0.2Ca Alloy. *Coatings* **2024**, *14*, 309. https://doi.org/10.3390/coatings14030309

Academic Editor: Shijie Wang

Received: 11 January 2024
Revised: 26 February 2024
Accepted: 27 February 2024
Published: 2 March 2024

1. Introduction

In recent decades, Mg and its alloys have been of great interest as temporary implants due to their good biocompatibility and mechanical properties similar to bone [1,2]. Most biomedical Mg alloys approved for clinical use up to date contain rare earths (RE) which might lead to toxicity problems in the human body [3]. The non-toxicity of alloying elements is becoming a priority in alloy design. In this regard, zinc (Zn) and calcium (Ca) are of great interest; (i) Zn is involved in mineralization, DNA synthesis, hormonal activity, and antibacterial response; (ii) Ca is an essential element in the human body because it is the main component of bone and is involved in cell-signaling reactions [4,5].

Newly developed biodegradable Mg-Zn-Ca alloys have shown excellent mechanical properties and great biocompatibility [6–9]. However, the main concern of that system is a high degradation rate that indirectly delays recovery at the surgical site, due to the generation of gas pockets caused by hydrogen evolution [10]. Most of the degradation studies of Mg-Zn-Ca systems were performed on cast alloys [11–14], while much fewer data exist on extruded alloys [15–18].

Plasma electrolytic oxidation (PEO) is a flexible method of surface protection and functionalization of Mg alloys [19,20]. It allows for a wide variation in composition, microstructure, porosity, and roughness of the coatings through the modification of the electrolyte and process parameters [21]. PEO-coated Mg alloys commonly demonstrate enhanced corrosion resistance [22,23]. However, most of the research has been applied to Mg-Al-Zn system alloys, and less work has been conducted in Al-free systems for biomedical purposes. For instance, in the case of Mg-Zn-Ca systems, PEO has been only applied to as-cast alloys, the findings showing a 2–4 times improvement in the corrosion performance in SBF medium [24–29]. It should be noted that in most cases PEO systems have been evaluated by electrochemical or immersion testing without a tight pH of the medium. Recent studies have indicated that this omission can significantly accelerate the corrosion rate of Mg-Zn-Ca alloys [30].

The Ca-P containing electrolytes used in PEO treatments of Mg alloys are typically based on suspensions which do not offer easy maintenance and waste disposal. Additionally, PEO electrolytes for Mg alloys often contain fluoride compounds for enhanced passivation of Mg. These could negatively affect the cell adhesion and proliferation [26,31]. Transparent Ca-P-based electrolytes have been recently proposed as a more chemically stable and user-friendly alternative and have been applied to Mg-Zn-Ca alloys. To the best of the authors' knowledge, there is no available data on PEO of extruded Mg-Zn-Ca systems.

The present work focuses on a comparative study of the PEO coatings on a wrought Mg0.5Zn0.2Ca alloy using a suspension electrolyte and a transparent electrolyte, both containing bioactive Ca, Si and P species. The coatings were carried out at three different treatment times (300, 600, and 900 s). The influence of the electrolyte and treatment time was evaluated in terms of composition and morphology, thickness, and corrosion behavior of the coatings. Short-term electrochemical impedance screening of the coated systems was followed up by a longer-term hydrogen evolution test, where the pH was kept constant by a CO_2 flow through the medium. The results offer an understanding of the corrosion mechanism of a lean-extruded Mg0.5Zn0.2Ca alloy and highlight the issues with the degradation rate controlled by PEO coating systems.

2. Materials and Experimental Methods

2.1. Materials

The substrate was a wrought Mg0.5Zn0.2Ca alloy supplied by the Institute of Surface Science (Helmholtz-Zentrum Hereon, Geesthacht, Germany), with a composition of (% wt.: 0.5% Zn, 0.2% Ca, 0.001% Ni, 0.001% Cu, 0.002% Fe, 0.01% Si, 0.03% Ag, bal. % Mg) determined by Arc Spark analysis. The alloy was cut into 3.5 mm-thick disks with a diameter of 10 mm. The samples were ground through successive grades of silicon carbide abrasive (up to P1200), rinsed in isopropyl alcohol, and dried in warm air.

2.2. PEO Treatment

PEO treatments were carried out using an alternating current (AC), voltage-controlled power supply (EAC-S2000, ET Systems electronic, Altlußheim, Germany) with a current density of 100 mA/cm^2, 50 Hz frequency and +350/−50 V. The experimental setup was equipped with a stainless-steel mesh (AISI 316 of Ø15 cm) along with a 2 L jacketed cell operating at a constant temperature (20 °C). The PEO process was conducted in transparent and suspension-based alkaline Ca-P-Si electrolytes (Table 1) using three different treatment times of 300, 600, and 900 s. After the PEO process, the specimens were rinsed in deionized water, cleaned with isopropyl, and dried in warm air.

Table 1. Composition and PEO process parameters of electrolytes.

Electrolyte (g/L) Composition	PEO-T Transparent	PEO-S Suspension
$Na_3PO_4 \cdot 12H_2O$	10	10
$Na_2SiO_3 \cdot 5H_2O$	10	9
KOH	8	1
$CaH_7C_3PO_6$	2	-
CaO	-	2.9
Na_2EDTA	2.67	-
NaF	-	-
σ (mS/cm^2)	40.1	24.6
pH	12.7	12.9
Parameters of process		
Voltage (V)	−350/−50	
Current density (mA/cm^2)	100	
Time (s)	300/600/900	

2.3. Characterization

Optical micrographs were obtained under polarized light with a Leica DMi8 optical microscope. A chemical etching with an acetic-picral solution (5 g picric acid, 100 mL ethanol, 5 mL acetic acid and 10 mL water) was used to reveal the microstructure.

The coated specimens were examined in plan-view and cross-section views (polish to 1 μm diamond paste) using JEOL JSM-6400 (Freising-Lerchenfeld, Germany) scanning electron microscopy equipped with an energy dispersive X-ray (EDS). The coating thicknesses were determined with an ISOSCOPE FMP10 eddy current meter (Fischer, Munich, Germany), equipped with an FTA3.3H probe. The coating porosity was analyzed with ImageJ software V.1.8.0 using at least three SEM plan-view micrographs at ×1000 magnification for each coating.

The roughness parameters, S_a (arithmetical mean height of the area) and S_{10z} (Ten-point height), were evaluated using a focus-variation optical 3D profilometer (InfiniteFocus SL, ALICONA, Utrecht, The Netherlands).

Phase identification was carried out by X-ray diffraction (XRD) analysis using Philips X'Pert (Malvern, UK) diffractometer. XRD patterns are analyzed by ICDD PDF4+ database. The XRD spectra were acquired in the range of 2θ range: 10 to 90° with a step size of 0.04° and a dwell time of 1 s per step.

2.4. Electrochemical Measurements

The electrochemical measurements were carried out using a GillAC potentiostat (ACM Instruments, Cartmel Fell, UK). The test was run at 37 °C in a modified α-MEM solution (Minimum Essential Medium Eagle-alpha) prepared in the laboratory and containing only inorganic compounds as follows: 6.8 g/L NaCl, 2.2 g/L $NaHCO_3$, 0.4 g/L KCl, 0.12 g/L Na_2HPO_4, 0.09 g/L $MgSO_4$, 0.2 g/L $CaCl_2$, and pH adjusted at 7.4 with 0.1 M of HCl. A conventional three electrode cell was used with a graphite counter electrode, an Ag/AgCl-3 M KCl reference electrode, and the specimen as the working electrode (exposed area of ~4.3 cm^2).

Potentiodynamic polarization curves were obtained after 1 h of immersion at a scan rate of 0.3 mV/s with potential sweep from −200 mV to +1000 mV (relative to the OCP) using a current density limit of 5 mA/cm^2. The corrosion current density was obtained from an analysis of cathodic Tafel slope.

Electrochemical impedance spectroscopy (EIS) measurements were conducted after 1 h of immersion, applying a sinusoidal perturbation of 10 mV amplitude (vs. OCP) and a frequency sweep from 100 kHz to 10 mHz. ZView software V.3.5i was used to analyze the impedance spectra, and a goodness fit was ensured through the square of the standard

deviation, which should be <0.01, and the weighted sum of squares (proportional to the average percentage error between the original data points and the calculated values) < 0.1.

2.5. Hydrogen Evolution

The corrosion performance of bare alloy and PEO-coated specimens were carried out with an hydrogen evolution test at 37 °C in inorganic α-MEM solution during 5 days of immersion. The total surface area of the immersed specimens was ~4.3 cm^2 and the presented results were tested in triplicate to obtain the average value. The pH of the solution in the immersion tank (~21 L) was continuously adjusted at 7.4 from a flow of CO_2 regulated by a switch coupled with a pH sensor (more details on the set-up can be found elsewhere [32]).

Statistical analysis (mean ± standard deviation) of the resulting data was performed using an unpaired *t*-test with the GraphPad *t*-test calculator (Dotmatics, Boston, MA, USA, https://www.graphpad.com/quickcalcs/ttest1/ (accessed on 25 February 2024).

3. Results and Discussion

3.1. Characterization of Wrought Mg0.5Zn0.2Ca Alloy

Optical and SEM/EDS studies (Figure 1a,b) revealed a microstructure of α-Mg equiaxed grains (25 ± 3 μm) decorated with deformation twins, formed as a result of partial dynamic recrystallization during the alloy manufacturing, and particles distributed along the extrusion direction [33,34]. Some of the particles have dissolved/detached during the metallographic preparation (Figure 1b). An EDS point analysis of the matrix (Figure 1b) reveals that Ca and Zn are partially dissolved in a α-Mg phase at a lower concentration. The X-ray diffraction pattern (Figure 1c) shows high intensity peaks ascribed to the α-Mg phase and lower intensity peaks corresponding to the secondary phases, Mg_2Ca and $Ca_2Mg_6Zn_3$.

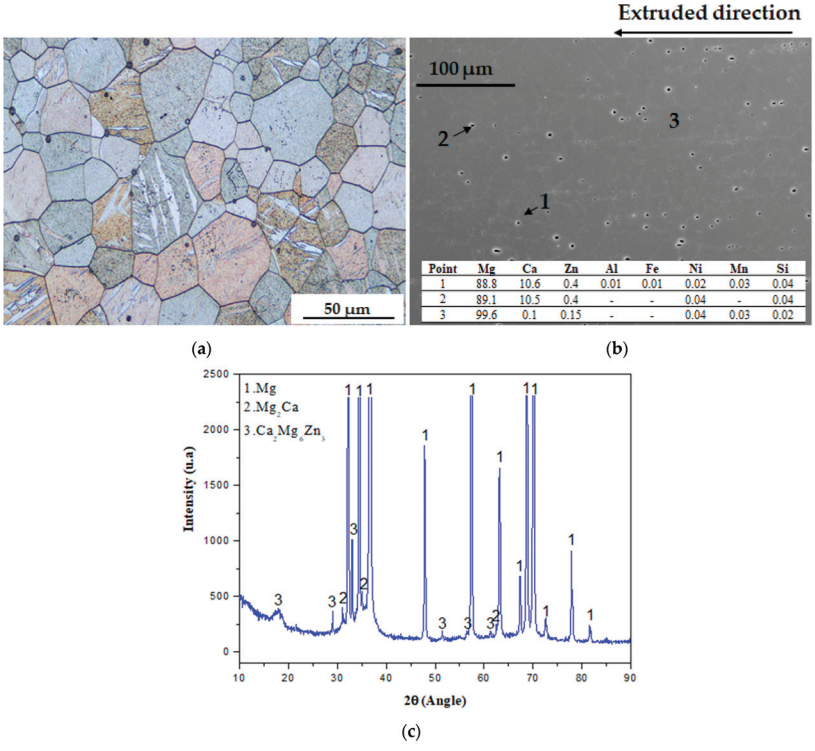

Figure 1. Optical (**a**) and secondary electron (**b**) micrographs of wrought alloy microstructure (inset composition determined by point analyses, EDS (at %)). (**c**) X-ray diffraction pattern of bare substrate.

3.2. Electrical Response and Efficiency of PEO Treatment

Figure 2a illustrates the evolution of the root mean square values of voltage and current density (U_{rms}, i_{rms}) during PEO treatment in transparent (PEO-T) and suspension (PEO-S) electrolytes during 900 s. The treatments performed for shorter times (300 and 600 s) revealed similar behavior.

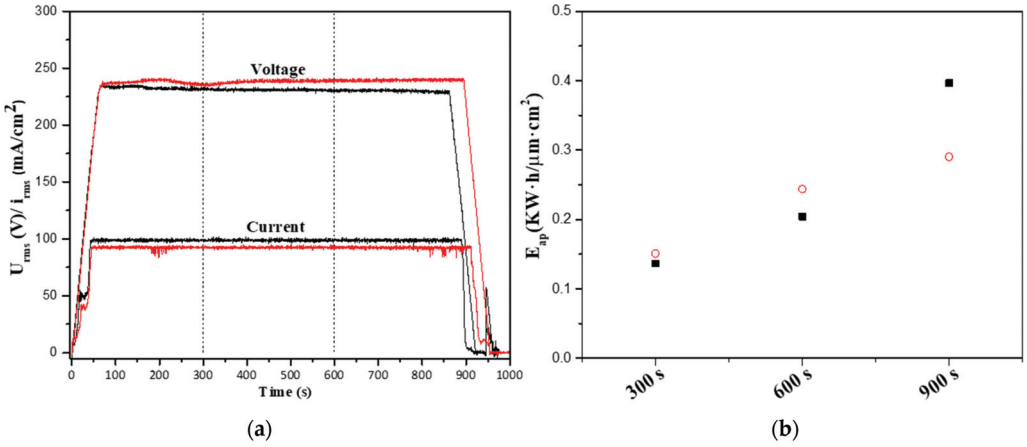

Figure 2. (**a**) Current density-time curves and (**b**) energy consumption for PEO-T and PEO-S coatings for Mg0.5Zn0.2Ca alloy during 900 s. Dashed lines indicate curves corresponding to the 300 and 600 s treatments. PEO-T electrolyte correspond to black colour and squares shape, and PEO-S electrolyte correspond to red colour and circle shape.

A linear voltage is observed during the 60 s ramp followed by a second inflexion at 50 s caused by the initiation of the plasma microdischarges, which corresponds to the oxide layer growth kinetic. A constant value of voltage (~230 V) is observed until the treatments are stopped, due to the increase in the impedance of the coatings during the PEO treatment. It is worth mentioning that microdischarges can be detected visually only in the case of PEO in transparent electrolyte (PEO-T), whereas it is not possible in case of PEO-S, due to the opacity of the milky suspension solution.

The calculated apparent specific energy consumption for all PEO processes is shown in Figure 2b. The calculation is conducted according to the formula: E ($W \cdot s \cdot cm^{-2}$) = $\int_{t0}^{tf}$ (current density ($A \cdot cm^{-2}$) × Voltage (V)), where t_0 = 0 s and t_f is the duration of the PEO coating process. The specific energy consumption is obtained by dividing the energy by the coating thickness and adjusting the units to $kW \cdot h \cdot m^{-2} \cdot \mu m^{-1}$.

An increase in energy consumption for PEO-T and PEO-S is observed with the increase in the treatment time from 0.14 to 0.40 $kW \cdot h \cdot m^{-2} \cdot \mu m^{-1}$ and from 0.15 to 0.29 $kW \cdot h \cdot m^{-2} \cdot \mu m^{-1}$, respectively. The energy efficiency is slightly higher for the PEO-S electrolyte at low treatment times (300 and 600 s), while at longer treatment times (900 s) it is slightly higher for the PEO-T electrolyte. It is important to note that the energy consumption values of this work are comparable with the data available for the PEO treatments in a Ca-free, transparent electrolyte for Mg alloy [35], which is around 0.13 $kW \cdot h \cdot m^{-2} \cdot \mu m^{-1}$. Also, these values are lower compared with those previously reported by the authors in as-cast MgZnCa and Mg3Zn0.4Ca alloys in fluorine-containing electrolyte (1.6 and 1.9 $kW \cdot h \cdot m^{-2} \cdot \mu m^{-1}$, respectively) [30].

3.3. Characterization of the PEO Coatings

The surface and cross-sectional morphologies of all the developed coatings, along with their respective EDS, are shown in Figure 3 and Table 2. Common surface features are found for all the PEO coatings (Figure 3a–c,g–i), characterized by a pumice-like structure

with pores. The latter are formed due to gas ejection out of the discharge channels and gas evolution through molten coating material followed by fast solidification [36].

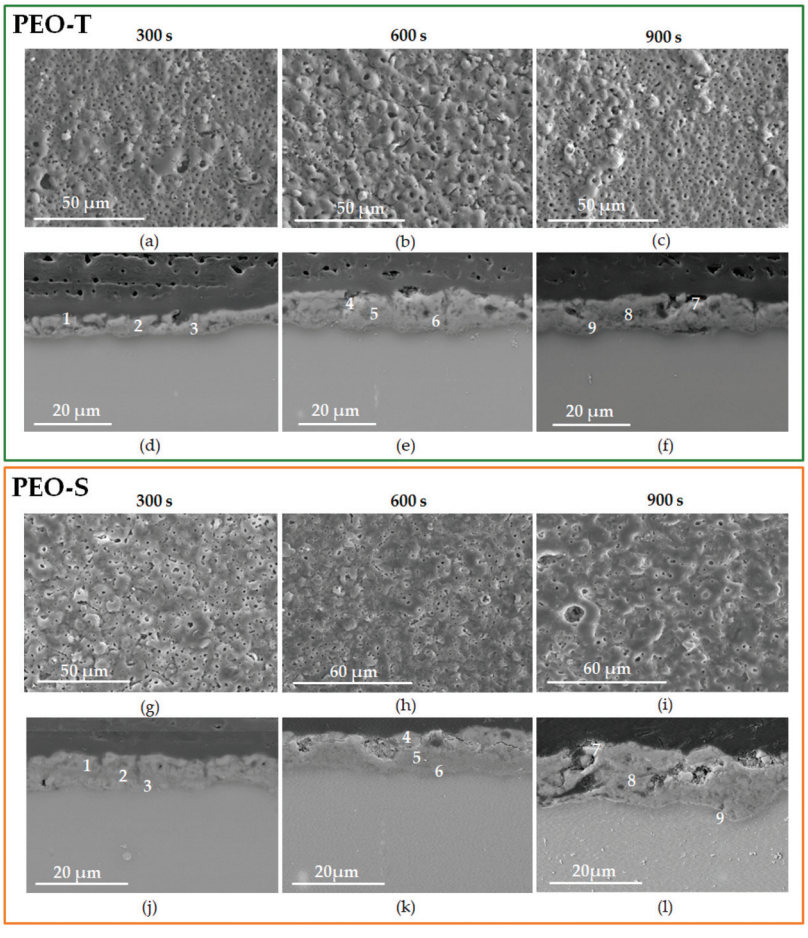

Figure 3. Secondary electron plan-view micrographs and backscattered electron cross-sectional micrographs of the (**a**–**f**) PEO-T and (**g**–**l**) PEO-S coatings. Numbers indicate where the local EDS analysis (Table 2) was performed.

Regarding surface roughness, the average value of S_a of PEO-T and PEO-S coatings tends to decrease (from 3.9 ± 0.7 to 2.7 ± 0.1 µm and 2.4 ± 0.4 to 1.1 ± 0.2 µm, respectively), while that of S_{10z} tends to increase with the treatment time (Supplementary Material, Table S1). Furthermore, the S_a and S_{10z} values for PEO-T are slightly higher compared to PEO-S values for all treatment times. The evolution of the surface pore population density in PEO-T electrolyte decreases from (1 ± 0.3) × 10^6 to (7 ± 1.2) × 10^5 pore·mm^2 (Figure 3a–c) with the increase in treatment time. In addition, the average pore size shows slightly higher values for longer treatments (2.5 ± 0.7 to 1.4 ± 0.4 µm for 600 and 900 s, respectively) compared to 300 s (0.9 ± 0.4 µm).

Coatings developed in suspension electrolyte do not reveal significant changes in the surface characteristics, with values of surface pore population density from (5 ± 0.8 to 3 ± 0.5) × 10^6 pore·mm^2 and the average pore size from 0.5 ± 0.2 to 0.4 ± 0.1 µm. In most PEO/Mg works reported in the literature, the average pore size increases with increasing treatment time because the discharge channels tend to coalesce, contributing

to the increase in pore size [37,38]. The opposite situation is observed here, although the energy consumption is higher with treatment time, as shown in Figure 2b. This may be attributed to the lower intensity of microdischarges on the surface, while most of the energy is involved in the development of a few isolated micro-arcs [39]. In addition, the sub-micrometric pores may be due to gas bubbles passing through the molten oxide material, displaced by the micro-arc events.

Table 2. EDS analysis (at. %) of PEO-T and PEO-S coatings.

Coating	Time (s)	Location	O	Na	Mg	Si	P	K	Ca	Zn	Ca/P
PEO-T	300	Plan view	45.9	1.0	38.1	9.9	4.9	0.0	1.2	0.0	0.24
		1	51.5	1.1	31.5	10.6	4.4	0.2	0.8	0.1	0.18
		2	48.8	0.8	36.9	7.7	4.7	0.5	0.5	0.1	0.11
		3	15.8	0.2	80.5	1.8	1.1	0.1	0.1	0.4	0.09
	600	Plan view	42.5	0.4	40.0	11.7	5.0	0.5	0.8	0.0	0.16
		4	49.4	0.5	36.0	9.3	4.0	0.4	0.3	0.1	0.08
		5	48.9	1.0	38.7	6.2	3.4	1.3	0.3	0.1	0.09
		6	40.5	0.2	51.3	5.1	2.4	0.3	0.1	0.2	0.04
	900	Plan view	45.6	0.9	41.9	9.0	2.9	1.3	0.7	0.1	0.24
		7	49.1	1.1	35.0	8.9	3.9	1.1	0.8	0.1	0.21
		8	49.8	0.3	37.8	7.6	3.9	0.4	0.2	0.1	0.05
		9	39.5	0.3	53.2	4.7	1.8	0.2	0.1	0.2	0.06
PEO-S	300	Plan view	53.7	3.9	26.6	7.8	3.4	0.8	3.8	0.0	1.12
		1	45.8	2.2	34.2	14.1	2.9	0.6	0.1	0.1	0.03
		2	50.3	1.7	35.9	9.1	2.5	0.4	0.1	0.1	0.04
		3	44.1	0.3	50.6	4.0	0.8	0.1	0.1	0.1	0.13
	600	Plan view	44.4	2.6	37.5	14.6	3.0	1.0	1.0	0.3	0.33
		4	37.6	1.3	41.6	14.1	4.5	0.5	0.3	0.4	0.07
		5	36.0	0.9	50.2	8.8	3.7	0.0	0.4	0.1	0.11
		6	37.2	1.6	52.7	8.0	2.1	0.5	0.0	0.0	-
	900	Plan view	38.7	2.1	38.1	12.9	5.8	1.0	1.3	0.1	0.22
		7	36.5	0.9	44.6	13.1	4.2	0.6	0.2	0.1	0.05
		8	36.0	0.5	52.9	7.5	3.3	0.0	0.1	0.3	0.04
		9	41.0	0.1	55.7	1.5	1.0	0.1	0.1	0.4	0.10

Regardless of the treatment time and electrolyte, BSE cross-section images reveal the presence of an inner dense layer and an outer part with internal pores. It is worth mentioning that oxide layers formed at 900 s show the formation of an intermediate pore band which could be related to the evolution of discharges and the specifics of the coating growth mechanism [40]. This may be due to the high solidification rate of the molten coating material. If it solidifies too fast, it forms a vault over the channel, blocking the escape of gases. In addition, this oxidation can also be facilitated by the high amount of Zn in the coating, as illustrated in the EDS analysis of nine points (Table 2) of Figure 3f,l. This type of pore band has been also reported for PEO coatings developed in phosphate-based electrolytes for treatment times longer than 10 min [41,42].

In general, the oxide layers achieved a thickness in the range of (~13–18) μm with slight differences depending on the treatment time and electrolyte (Figure 3d–f,j–l, Supplementary Material, Table S1). The thinnest coating is the one developed in the suspension electrolyte for short time (PEO-T, 300 s). This electrolyte produces an increase in the thickness values (up to 18 for PEO-T 600 s) by increasing the treatment time. This trend is in agreement with observations made in several works conducted on Mg alloys [43–45].

The use of a suspension electrolyte led to the formation of slightly thicker coatings. This fact may be related to the size of the species formed in the electrolyte. In the case of suspension electrolytes, the particles are CaO (size of 1–5 μm), while in the transparent electrolyte, a $[Ca\text{-}EDTA]^{-2}$ complex is formed (the size is few angstroms). According to the literature, the incorporation of particles into PEO coatings in particle-containing

electrolytes [46] depends on their size, with respect to the diameter of the microdischarges channels and coating pores. Once in the plasma discharge channel, the particle is melted and ionized, and the Ca^{2+} and O^{2-} ions migrate under the electric field and form part of the coating material. The CaO particle size is larger than that of the $[Ca\text{-}EDTA]^{-2}$ chelate complex, and there is 0.05 M Ca species in the suspension electrolyte versus only 0.01 M in the transparent one. Therefore, the amount of newly formed coating material per discharge is greater, which translates into a thicker coating. Thicker coatings can be easily achieved in suspension electrolytes compared with particle-free true solutions, this is a well-established and known fact in PEO technology [47,48].

A semiquantitative analysis of the elemental composition of coatings performance by EDS is shown in Table 2. The most important feature is that short PEO treatments (300 s) led to a higher incorporation of Ca, while a slight reduction in Ca occurred for longer treatment times. No clear differences are detected between 300 and 600 s and the type of electrolyte. The decrease in Ca with treatment time could be explained by the development of greater intensity (i.e., longer lasting) microdischarges that could cause a destructive effect with the consequent loss of the previously formed material at the site of microdischarges [49]. It is worth noting that the Ca incorporation for all treatments times is slightly two times higher in the suspension electrolyte than in the transparent electrolyte. The thickness of PEO coatings is affected by the size of the species in the electrolyte as discussed previously. This is related to the fact that the size of the species can also affect their ability to diffuse and transport through the electrolyte to the metal surface and into the growing ceramic layer. Thus, smaller species may have a higher diffusion compared to larger species [50]. Some reports have found that smaller species may have a greater facility to act as "cores" around which ceramic composites form [51]. Therefore, the coatings formed in the suspension electrolyte, although they have a larger particle size, have a higher concentration in the electrolyte (0.05 M vs. 0.01 M), and therefore allow for a higher incorporation of Ca into the coatings.

EDS conducted through the thickness of the coating revealed that Si, K and P migrate inwards from the electrolyte and are mainly incorporated in the outer part of the PEO coatings. Zn incorporation was higher in the inner part of all PEO coatings. This occurs because Si and P migrate from the electrolyte inwards, while Zn migrates from the substrate outwards.

The X-ray diffraction patterns of the (a) PEO-T and (b) PEO-S studied coatings are displayed in Figure 4. All of the coatings reveal high intensity peaks of Mg, MgO, and the presence of amorphous material corresponding to a peak broadening between 25 and 40° (2θ). In addition, Mg_2SiO_4 (forsterite) and ZnO (wurtzite) are formed in all coatings in both electrolytes. During microdischarges, the SiO_2 reacts with MgO to form forsterite in the range 1100–1400 °C [52], while ZnO is formed by the transformation of $Zn(OH)_2$ at 80 °C [53]. The intensity of Mg peaks decreases with an increasing process time while the intensity of those for MgO, ZnO, and Mg_2SiO_4 increases with process time for both electrolytes. The crystallinity of the coating inside the PEO may be also related to the intensity of the discharge. In general terms, the degree of crystallinity/amorphism is around ~71% for PEO-T and ~84% for PEO-S, being slightly higher in the case of the suspension electrolyte. The higher energy required for coating breakdown and the higher discharge intensity can be observed on the Mg surface within the PEO procedure for a longer process time [37]. This means that a higher temperature in the PEO process may favor a greater crystallinity of Mg_2SiO_4, MgO, and ZnO. Crystalline material has a greater electron conductivity and promotes the oxidation of oxygen anions and O_2 evolution, which, together with fast solidification of ejected molten material at the coating/electrolyte interface, explains the presence of a pore band at the 900 s treatments.

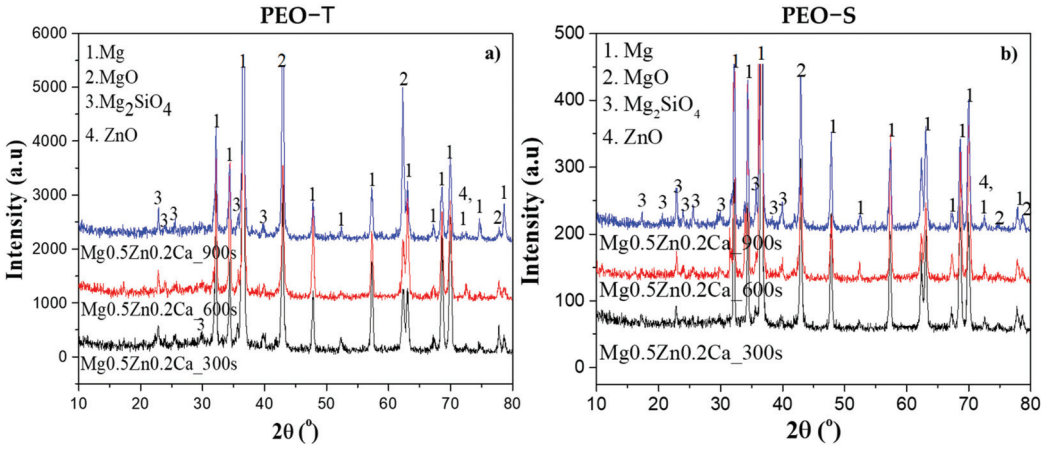

Figure 4. X-ray patterns of (**a**) PEO-T and (**b**) PEO-S on Mg0.5Zn0.2Ca alloy at 300, 600, and 900 s.

As for the semi-quantitative percentage content of Mg, MgO, Mg_2SiO_4, and ZnO phases for the transparent electrolyte, it is in the range of MgO (7–26%), Mg (47–57%), ZnO (1–3%), and Mg_2SiO_4 (27–37%). Similar behavior is observed for the suspension electrolyte, MgO (6–8%), Mg (41–60%), ZnO (1–3%), and Mg_2SiO_4 (31–50%). Overall, the values are slightly higher for the suspension electrolyte due to the incorporation of higher species in the coating, as discussed before. The lack of apatite or hydroxyapatite is due to the fact that a higher positive pulse voltage is required for its formation, as a higher plasma discharge temperature and a lower cooling rate of the material are needed [54].

3.4. Electrochemical Measurements

3.4.1. Potentiodynamic Polarization Curves (PDP)

The polarization curves of PEO-T and PEO-S coatings obtained under different treatment times on the Mg0.5Zn0.2Ca alloy after 1 h of immersion in inorganic α-MEM at 37 °C are displayed in Figure 5. The electrochemical parameters obtained from the curves (corrosion potential (E_{corr}) and corrosion current density (i_{corr})) are presented in Table 3.

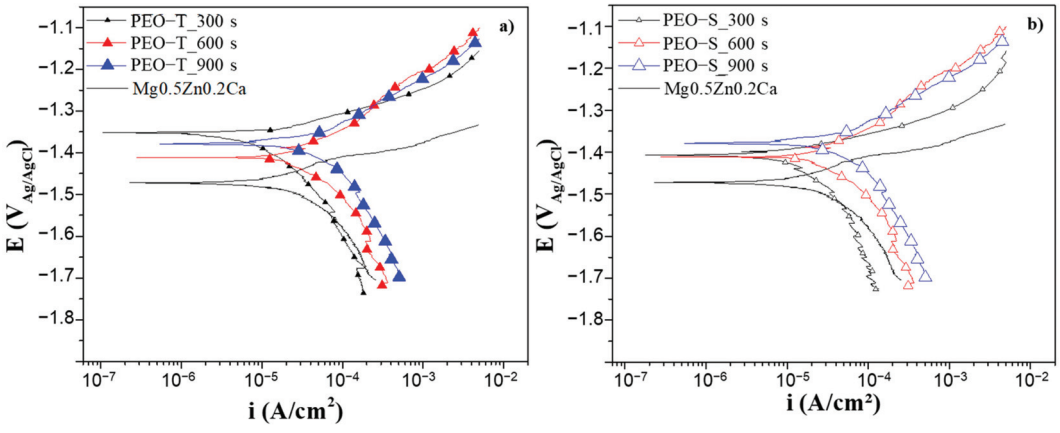

Figure 5. Polarization curves of (**a**) PEO-T and (**b**) PEO-S and for Mg0.5Zn0.2Ca alloy after 1 h of immersion in inorganic α-MEM.

Table 3. Corrosion characteristics obtained from polarization curves.

Electrolyte	Time (s)	E_{corr} (V)	i_{corr} ($\mu A/cm^2$)	E_{pit} (V)
Mg0.5Zn0.2Ca		−1.47	33.41	−1.40
PEO-T	300	−1.35	11.02	-
	600	−1.41	55.40	-
	900	−1.38	60.79	-
PEO-S	300	−1.41	20.20	-
	600	−1.41	47.32	-
	900	−1.38	60.32	-

Regardless of the electrolyte and the treatment time, all PEO coatings shifted the E_{corr} to slightly nobler values (~60–120 mV, depending on the coating). PEO coatings formed during 300 s in both electrolytes reveal protective properties with a decrease in the current density by ~2–3 times, with PEO-T at 300 s being the coating with the best results. It is worth mentioning that increasing the treatment time leads to an increase inf i_{corr}, indicating that the coatings become less protective and could even induce an acceleration of the degradation process, compared with the non-treated substrate. This could be associated with the crevice phenomena and undercoating corrosion, which will be probed further. The pore band formed in the coatings developed under longer times could act as a storage of a more aggressive electrolyte that might also intensify the corrosion process.

It should be noted that the anodic branches of the all PEO-coated specimens do not reveal a well-defined region of pseudo passivity or marked pitting potential, especially for longer treatment times. The latter can reasonably be called pseudo-Tafel behavior, i.e., the anodic behavior of these systems resembles an active dissolution which can be attributed to a uniform undercoating corrosion morphology.

Data unavailability on PEO of extruded Mg-Zn-Ca systems does not allow for a proper comparison with the literature. The closer systems in terms of comparison would be PEO-coated as-cast Mg-Zn-Ca alloys. The current density values of the present work are higher (3–6 times) than those obtained in the literature, e.g., PEO/Mg3Zn0.4Ca and PEO/Mg1.78Zn0.51Ca alloys (i_{corr} of 2.38–7.28 and 5.25 mA/cm^2, respectively) [31,55]. This brings up the fact that the final performance of a PEO system is influenced not only by the electrolyte composition and process parameters, but also by the bulk material including the fabrication process. In fact, in the authors' previous work it was reported that the extruded Mg0.5Zn0.2Ca alloy revealed a slightly higher degradation rate in comparison to as-cast Mg-Zn-Ca alloys, which was associated to the lack of barrier network and the high number of twins which facilitate the corrosion process [17].

It should be noted that the PDP results may not reflect the true protective capability of the coating, taking into account that high polarization is a source of non-stationarity in Mg-based systems. Therefore, additional screening by EIS is always advisable.

3.4.2. Electrochemical Impedance Spectroscopy (EIS)

Figure 6 shows the modulus of total impedance at low frequencies ($|Z|_{10mHz}$) of PEO-coated specimens and the substrate after 1 h of immersion in inorganic α-MEM solution at 37 °C. This value provides a good estimation of the overall corrosion performance of the material.

PEO coatings formed in a transparent electrolyte during 300 and 600 s showed the best repeatability, whereas the rest of the coatings revealed higher differences between the results. This might be related to the heterogeneity of the coatings formed under longer treatment times and the variability between the randomly selected specimens. In general, all of the developed layers do not show a considerably better corrosion performance compared to the bare substrate. This might be attributed to the formation of the pore band close to the inner barrier layer, leading to a premature failure of the sample during the first hour of immersion.

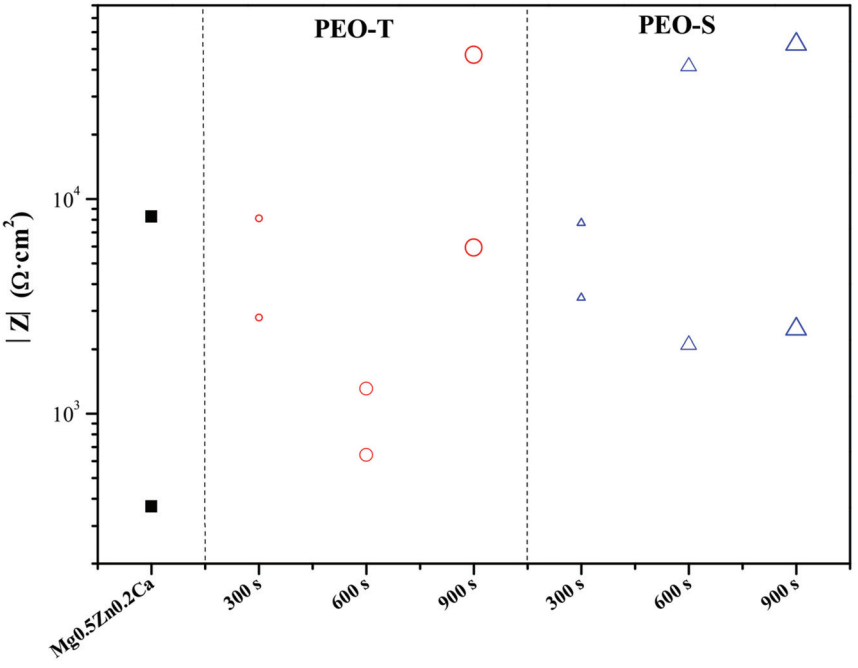

Figure 6. Scatter diagram of the impedance values for studied PEO-T and PEO-S coatings. Black squares indicate bare alloy, red circles indicate PEO-T coatings, blue triangles indicate PEO-S coatings, and symbol size increases in the order of increasing treatment time.

In order to analyze in detail the EIS spectra of PEO coatings formed in different electrolytes, PEO-T (600 s) and PEO-S (300 s) specimens were selected based on their higher repeatability. These two coatings were taken as an example with the aim of understanding the contribution of the coating microstructure and the various electrochemical processes taking place in the coating/substrate systems to their corrosion resistance.

Figure 7a,b shows the Nyquist and Bode plots of the EIS spectra of PEO-T and PEO-S coatings for the selected treatment times (300 and 600 s). The equivalent circuit (inset in Figure 7a) used to interpret the EIS results includes: R_{el}—solution resistance, R_1/CPE_1—the response ascribed to the capacitive and resistance behavior of outer part of the coating, R_2/CPE_2—the capacitive and resistance behavior of the inner barrier layer and R_{ct}/CPE_{dl}—the electrochemical activity at the substrate/electrolyte interface associated with the double layer and charge-transfer phenomena. This equivalent circuit has been previously reported to fit the behavior of this type of PEO systems [30,56]. In cases of the substrate, R_1/CPE_1 and R_2/CPE_2 represent the response of Ca-P-rich deposits that form on the Mg surface in modified α-MEM and on the corrosion products layer, respectively. The impedance of CPE is calculated by the following equation: $Z = 1/(CPE(j\omega)^n)$; where j is the imaginary number and $-1 \leq n \leq 1$.

The fitted values of the circuit elements (Table 4) indicate that the barrier layer is the main factor responsible for the corrosion protection of the PEO coating, where R_1 is lower than R_2 in both cases. It can be seen that the R_1 and R_2 of PEO-S sample are higher compared to the uncoated specimen, indicating that the short-term corrosion resistance of the Mg0.5Zn0.2Ca alloy is improved after the PEO process. Whereas in the case of PEO-T, both values are lower than those of the substrate, suggesting that the coating is not protective and that its barrier layer has degraded, as it has a lower resistance than the corrosion product layer of the substrate. This is because it is not very compact (note

the pores inside the coatings in Figure 3e), which allows for easy permeation of corrosive species from the medium.

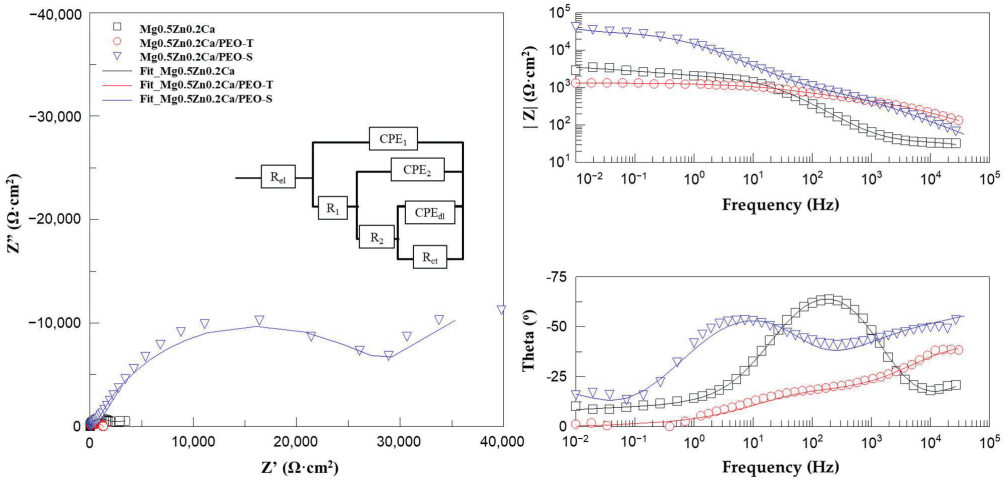

(**a**) (**b**)

Figure 7. (**a**) The Nyquist (inset the equivalent circuit determined for PEO coatings and substrate) and (**b**) Bode plots of PEO-T at 600 s and PEO-S at 300 s on Mg0.5Zn0.2Ca alloy.

Table 4. EIS equivalent circuits after 1 h of immersion in inorganic α-MEM solution.

Sample	R_{el} ($\Omega \cdot cm^2$)	CPE_1 ($\mu S \cdot s^n \cdot cm^2$)	n_1	R_1 ($\Omega \cdot cm^2$)	CPE_2 ($\mu S \cdot s^n \cdot cm^2$)	n_2	R_2 ($\Omega \cdot cm^2$)	CPE_{dl} ($\mu S \cdot s^n \cdot cm^2$)	n_{dl}	R_{ct} ($\Omega \cdot cm^2$)	R_{total} ($\Omega \cdot cm^2$)
Mg0.5Zn0.2Ca	36.8	10.1	0.58	171.3	24.4	0.87	1489	30.6	0.56	1500	3160.3
PEO-T	14	5.14	0.59	187.7	0.003	0.70	342.6	64.4	0.55	777.3	1321.6
PEO-S	10	6.45	0.64	1206	7.44	0.76	32,030	583.13	0.8	32,438	65,684

As for the differences between the two coatings, the R_1 and R_2 values of PEO-S (1206 and 32,438 $\Omega \cdot cm^2$) are 4–10 times higher than those of PEO-T (342.6 and 777.3 $\Omega \cdot cm^2$). These are consistent with the higher pore-area fraction of the latter and the presence of the internal pores. This also explains the lower $|Z|_{10mHz}$ values for PEO-T in the intermediate frequency range. Comparing the results obtained in PDP and EIS, there is a clear concordance in the relative ranking of PEO-T (600 s) and PEO-S (300 s).

Both coatings are further evaluated by hydrogen evolution measurements in modified α-MEM with CO_2 flow-controlled pH for 5 days of immersion, a period that is comparable to the duration of a standard in vitro cell proliferation assay. This is conducted in order to (i) verify the results of the EIS screening; (ii) discriminate the coatings and determine the realistic degradation rate; and (iii) examine the development of corrosion products.

3.4.3. Hydrogen Evolution

Figure 8 shows the hydrogen evolution during 5 days of immersion in an inorganic α-MEM solution at 37 °C for the bulk material and PEO-coated specimens. The pH was controlled at 7.4 by a flow of CO_2 through the medium during the test. It is important to note that the works reported in the literature for PEO-coated Mg alloys in physiological media either use a medium refreshment method [26,55,57] or a 5% CO_2 injection into the incubator atmosphere [58], either of which does not provide a tight pH control and might lead to an underestimation of the corrosion rate [17].

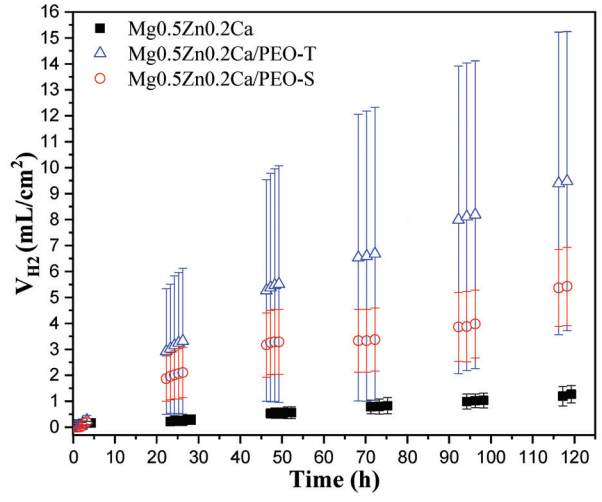

(**a**)

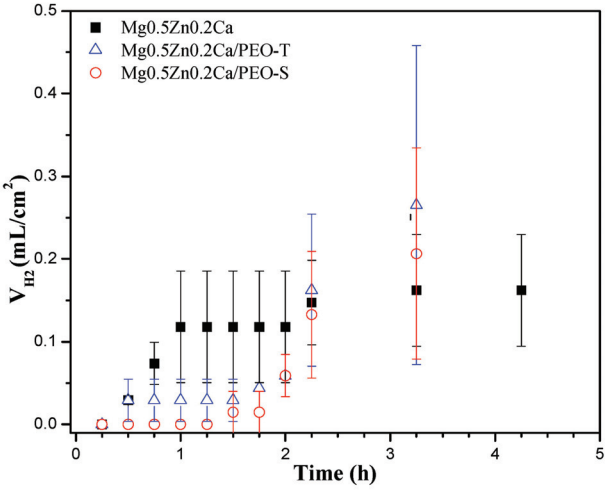

(**b**)

Figure 8. Hydrogen evolution for bare substrate, PEO-T, and PEO-S coatings (**a**) during 5 days of immersion in α-MEM solution; (**b**) amplification of the first 5 h.

Both PEO coatings show a quick, linear acceleration of corrosion rate after 2 h of immersion (Figure 8b) and until the end of the test, with a slight change in the slope after 48 h. This suggests that the coatings are easily permeable due to their internal porosity and the presence of a pore band close to the barrier layer (Figure 3e). In addition, as observed by EIS, the values of the inner barrier layer resistance are lower compared to the literature [8,31,59], which also indicates poor corrosion properties. Considering the total hydrogen volume after 5 days, that of PEO-T coating is two times higher (9.48 mL/cm^2) compared to PEO-S (5.42 mL/cm^2), which is in agreement with the results obtained from the EIS measurements. However, considering the standard deviation values, the differences between the PEO-T and PEO-S cannot be viewed as statistically significant. Remarkably, both PEO coatings exhibited 10–13 times higher corrosion rate (PEO-T: 26.31 and PEO-S:

15.05 mm/year) compared to the substrate (0.94 mm/year), indicating that both oxide layers accelerated the corrosion of Mg, which is opposite to what is typically found in the literature of PEO-treated Mg alloys [26,27]. According to the literature, the degradation rate of an orthopedic implant is expected to be <0.5 mm/year [60,61], which would allow an implant integration with complete bone healing. Comparing these values with the degradation rate by hydrogen evolution (PEO-T: 26.3 and PEO-S: 15.1 mm/year), they are 3–10 times higher than expected for a complete implant integration. This situation would lead to the implant degrading before implant integration occurs, so the implant is not performing its function. The corrosion-accelerating PEO treatment may present as an interest for bone cancer therapy applications, where an accelerated degradation of Mg implant is sought after, in order to treat the tumors [62,63].

The high corrosion rate observed in PEO-coated extruded Mg0.5Zn0.2Ca alloy may be attributed to two factors: (i) the formation of a crevice at the interface PEO/substrate, as described in previous work [30], and (ii) the presence of ZnO within the coatings due to the oxidation of Ca-Mg-Zn intermetallic (in particular $Ca_2Mg_6Zn_3$ as identified by XRD) (Figure 1c). Studies on galvanized steel have indicated that ZnO, in the presence of carbonates (dissolved CO_2 from the air), generates corrosion products in both the anodic region (e.g., $Zn_5(OH)_8Cl_2{\cdot}H_2O$) and cathodic region (e.g., $Zn_5(OH)_6(CO_3)_2$). These corrosion products can function as semi-permeable membranes, facilitating the transportation of anions (as Cl^-) while hindering the movement of cations (e.g., H^+), thus promoting ionic flow and maintaining acidic conditions in the anodic area [64,65]. Consequently, localized corrosion is intensified. Moreover, once the corrosion process commences, it progresses swiftly due to the uniformity of the alloy microstructure and the presence of defects produced during the extrusion process (see Figure 1) [17]. A continuous network of secondary phases that might act as a barrier for corrosion progression, as occurs in cast PEO-F/Mg-Zn-Ca alloys [30], is lacking in the extruded lean alloy.

According to the literature, PEO coatings on a cast-Mg-Zn-Ca alloy showed improved corrosion performance based on electrochemical and immersion measurements [24,27,28,66]. In the present work, taking into consideration only the electrochemical measurements, a slight corrosion protection could be observed for some of the coatings. However, when the pH in the immersion test was kept at 7.4, it became evident that the PEO coatings did not improve the corrosion resistance. A direct comparison with other published results on similar coatings appears difficult due to different factors: (i) most of the PEO work reported so far has been carried out on as-cast Mg-Zn-Ca alloys, with no reports on extruded alloys. (ii) The reported coatings in general are ~2 times thicker than those of this work (in the range of 20–40 μm), not least due to the presence of fluorine species in the electrolytes. (iii) Hydrogen release volume is not measured during immersion tests or constant pH of the corrosive medium is not ensured.

Figure 9 shows the macro- and micro-morphological examination of the corrosion products developed in the studied specimens after 5 days of immersion. The bare substrate has a very uniform appearance (Figure 9a), while in PEO-T and PEO-S coated samples the corrosion products layer is heterogeneous (Figure 9c,d). A detailed cross-sectional analysis of one of the coatings (considering that both PEO-T (600 s) and PEO-S (300 s) performed similarly during H_2 evolution test) has been carried out in order to understand the corrosion mechanism. The examination (Figure 9e) disclosed a 64.3 ± 1.1 μm-thick, cracked corrosion products layer and a notable lack of a PEO layer above it. Cracking of the corrosion products is related to stresses induced by twofold volume changes during dehydration of $Mg(OH)_2$ (Reactions (1) and (2))

$$Mg^{2+} + 2OH^- \rightarrow Mg(OH)_2 \quad (1)$$

$$Mg(OH)_2 \rightarrow MgO + H_2O \quad (2)$$

and evolving H_2 gas.

Table 5. EDS analysis (at.%) of substrate and PEO-S on Mg0.5Zn0.2Ca alloy from Figure 9b,e after 5 days of immersion in inorganic α-MEM solution.

Sample	Location	O	Na	Mg	Si	P	Cl	K	Ca	Zn	Ca/P
Mg0.5Zn0.2Ca	1	47.8	1.3	8.2	0.1	17.1	-	-	20.7	0.1	1.21
	2	40.8	0.7	10.8	0.4	19.6	-	-	26.5	0.7	1.36
PEO-S	3	60.2	0.9	12.0	0.0	9.7	0.7	-	13.8	0.7	1.42
	4	56.0	0.7	17.5	0.0	10.0	1.2	-	12.1	0.9	1.21
	5	48.5	1.1	17.7	0.2	11.2	1.1	0.4	17.7	1.1	1.58
	6	70.1	0.8	19.2	0.0	2.5	0.3	-	5.1	0.5	2.04

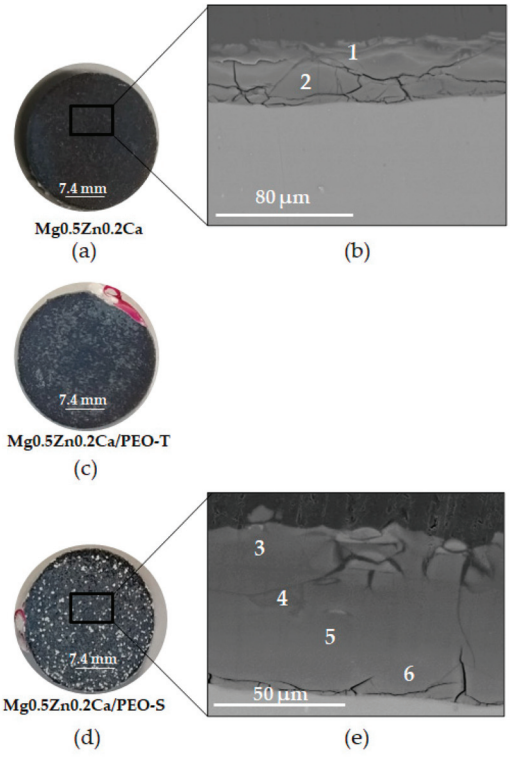

Figure 9. (**a**,**c**,**d**) Macrographs and (**b**,**e**) cross-section of (**b**) Mg0.5Zn0.2Ca substrate and (**e**) PEO-S coatings for Mg0.5Zn0.2Ca alloys after 5 days of immersion in inorganic α-MEM. The numbers (1–6) indicate where the local ESD analysis was displayed (Table 5).

In comparison with the results of other published works, the onset of corrosion in the present systems is rather early. For instance, on PEO-coated Mg0.8Ca the initiation of the undercoating corrosion product layer was reported after 2 weeks of immersion [67], although the coatings in question were four times thicker and contained a high level of fluorine.

The EDS analysis presented in Table 5 illustrates the composition of corrosion products (Figure 9b,e). The corrosion product layer in the PEO-S-coated substrate exhibits high levels of Ca and P (~12–18% and ~10 at.%, respectively) attributed to the precipitation of Ca-P compounds from the inorganic α-MEM solution. They are considerably lower than the respective levels in corrosion layer formed on the bare substrate (~20–27% and ~17–20 at.%), indicating that the coating must have been at least partially present during most of the immersion period and was impeding the ingress of α-MEM species [30].

These results are in agreement with observations made in other studies. The main corrosion products on Mg-Zn-Ca alloys consist of $Mg(OH)_2$, $Ca_{10}(PO_4)_6(OH)_2$, $(Ca,Mg)_3(PO_4)_2$, $Mg(HCO_3)(OH)\cdot 2H_2O$, or $MgCO_3\cdot 3H_2O$ [24,27,68], which is consistent with the high levels of Mg, Ca, P, and O illustrated in Table 5. Additionally, Zn is present in both inner and outer parts of the corrosion products (e.g., points 3 and 5; Table 5) due to the diffusion of Zn from the bulk material and the dissolution of ZnO from the PEO coating. In the present conditions, the ZnO dissolution forms compounds such as $Zn_5(OH)_8Cl_2\cdot H_2O$, $ZnPO_4$, $ZnCO_3$, and/or $Zn(OH)_2$ [64,65]. This supports the idea of (i) the corrosion products layer acting as a crevice between the substrate and the coating, and (ii) ZnO in the PEO participating in reactions creating a more aggressive environment. The latter is corroborated by the high level of Cl^- in the corrosion products in PEO-S sample (points 4 and 5, Table 5, ~1.1%,) causing an accelerated corrosion of the system.

Several important factors corresponding to the corrosion mechanisms are illustrated by post-corrosion characterization: (i) corrosive species from the medium penetrate through the micro-defects of the outer porous layer, causing progressive hydration of the coating and degradation of the inner barrier layer. (ii) Corrosion products react with the medium species causing the precipitation of Ca-P based compounds. (iii) The cracked inner coating corrosion products layer forms a crevice at the PEO/corrosion products interface. (iv) The presence of ZnO in the PEO coatings and its hydration products promote a more aggressive microenvironment in the crevice, accelerating the corrosion rate of the systems.

For the load-bearing applications where an implant is expected to be made of a wrought alloy (for the mechanical properties sake), it is necessary to continue searching for strategies to improve the corrosion behavior of the Mg0.5Zn0.2Ca alloy. A possible strategy may include changing the PEO electrolyte and electrical conditions so that the Zn is incorporated into the coating not as ZnO but in the form of Zn phosphate, or Zn-substituted hydroxyapatite.

4. Conclusions

PEO coatings were produced on a wrought Mg0.5Zn0.2Ca alloy using transparent and suspension electrolytes and were assessed for microstructure, composition, and corrosion behavior. Key findings are as follows:

- Coatings applied for 300 s in both electrolytes were compact, while longer treatments led to the formation of a pore band.
- Suspension electrolyte coatings were marginally thicker (13–18 μm) compared to transparent electrolyte coatings (13–16 μm) due to the relationship between species size in the electrolyte and microdischarges channel diameter.
- The incorporation of species into the coating increased from 300 to 900 s for both electrolytes, with slightly higher incorporation in suspension electrolyte coatings, attributed to species size, diffusion, and electrolyte concentration.
- Coatings comprised MgO, ZnO and Mg_2SiO_4, regardless of treatment time or electrolyte, with slightly higher crystallinity in suspension electrolyte coatings (~84%).
- Short-term electrochemical evaluation by EIS demonstrated protective properties for 300 s coatings ($|Z|_{10mHz}$, PEO-T: 5449.65 and PEO-S: 5582.60 $\Omega\cdot cm^2$), while longer treatments showed impaired repeatability due to pore band formation.
- PEO-T-600s coatings revealed 50 times lower corrosion protection than PEO-S-300s due to higher pore area fraction and slightly larger internal pores.
- Both coatings revealed significantly higher corrosion rates (PEO-T: 26.3 and PEO-S: 15.6 mm/year) over the 5-day period compared to the substrate (0.94 mm/year), attributed to a Cl^--rich aggressive microenvironment in the crevice induced by hydrolysis of ZnO in the coatings.

Supplementary Materials: The following supporting information can be downloaded at: https://www.mdpi.com/article/10.3390/coatings14030309/s1, Table S1: Coating surface porosity characteristics from plan view of PEO-T and PEO-S at three treatment times (Figure 3a–c,g–i).

Author Contributions: L.M.: Conceptualization, investigation, validation, writing—original draft, review and editing. M.M.: conceptualization, resources, software, supervision, writing—review and editing, Funding acquisition. R.A.: conceptualization, resources, software, supervision, writing—original draft, writing—review and editing. E.M.: conceptualization, resources, software, supervision, writing—review and editing, Funding acquisition. All authors have read and agreed to the published version of the manuscript.

Funding: This research was funded by grant number S2018/NMT-4411 (Regional Government of Madrid and EU Structural and Social Funds), grant number PID2021-124341OB-C22 (MCIU), and grant number RYC-2017-21843.

Institutional Review Board Statement: Not applicable.

Informed Consent Statement: Not applicable.

Data Availability Statement: Data available in a publicly accessible repository that does not issue DOIs. All data presented in this work will be available in Docta Complutense repository https://docta.ucm.es/handle/20.500.14352/16 (25 February 2024).

Acknowledgments: The support of the ADITIMAT-CM project (S2018/NMT-4411, Regional Government of Madrid and EU Structural and Social Funds) and PID2021-124341OB-C22 (MCIU) are gratefully acknowledged. M. Mohedano is grateful for the support of RYC-2017-21843.

Conflicts of Interest: The authors declare no conflicts of interest. The funders had no role in the design of the study; in the collection, analyses, or interpretation of data; in the writing of the manuscript; or in the decision to publish the results.

References

1. Munir, K.; Lin, J.; Wen, C.; Wright, P.F.A.; Li, Y. Mechanical, Corrosion, and Biocompatibility Properties of Mg-Zr-Sr-Sc Alloys for Biodegradable Implant Applications. *Acta Biomater.* **2020**, *102*, 493–507. [CrossRef]
2. Kiani, F.; Wen, C.; Li, Y. Prospects and Strategies for Magnesium Alloys as Biodegradable Implants from Crystalline to Bulk Metallic Glasses and Composites—A Review. *Acta Biomater.* **2020**, *103*, 1–23. [CrossRef]
3. Witte, F.; Kaese, V.; Haferkamp, H.; Switzer, E.; Meyer-Lindenberg, A.; Wirth, C.J.; Windhagen, H. In Vivo Corrosion of Four Magnesium Alloys and the Associated Bone Response. *Biomaterials* **2005**, *26*, 3557–3563. [CrossRef]
4. Staiger, M.P.; Pietak, A.M.; Huadmai, J.; Dias, G. Magnesium and Its Alloys as Orthopedic Biomaterials: A Review. *Biomaterials* **2006**, *27*, 1728–1734. [CrossRef]
5. Kellesarian, S.V.; Yunker, M.; Ramakrishnaiah, R.; Malmstrom, H.; Kellesarian, T.V.; Ros Malignaggi, V.; Javed, F. Does Incorporating Zinc in Titanium Implant Surfaces Influence Osseointegration? A Systematic Review. *J. Prosthet. Dent.* **2017**, *117*, 41–47. [CrossRef]
6. Li, Z.H.; Sasaki, T.T.; Uedono, A.; Hono, K. Role of Zn on the Rapid Age-Hardening in Mg-Ca-Zn Alloys. *Scr. Mater.* **2022**, *216*, 114735. [CrossRef]
7. Schäublin, R.E.; Becker, M.; Cihova, M.; Gerstl, S.S.A.; Deiana, D.; Hébert, C.; Pogatscher, S.; Uggowitzer, P.J.; Löffler, J.F. Precipitation in Lean Mg–Zn–Ca Alloys. *Acta Mater.* **2022**, *239*, 118223. [CrossRef]
8. Baigonakova, G.; Marchenko, E.; Zhukov, I.; Vorozhtsov, A. Structure, Cytocompatibility and Biodegradation of Nanocrystalline Coated Mg–Ca–Zn Alloys. *Vacuum* **2023**, *207*, 111630. [CrossRef]
9. Qiu, W.; Huang, G.; Li, Y.; Chen, J.; Huang, W.; Peng, Z.; Liang, J.; Xia, F.; Yao, M.; Xiong, A. Microstructure and Properties of Mg–Ca–Zn Alloy for Thermal Energy Storage. *Vacuum* **2022**, *203*, 111282. [CrossRef]
10. Roche, V.; Koga, G.Y.; Matias, T.B.; Kiminami, C.S.; Bolfarini, C.; Botta, W.J.; Nogueira, R.P.; Jorge Junior, A.M. Degradation of Biodegradable Implants: The Influence of Microstructure and Composition of Mg-Zn-Ca Alloys. *J. Alloys Compd.* **2019**, *774*, 168–181. [CrossRef]
11. Annur, D.; Erryani, A.; Amal, M.I.; Sitorus, L.S.; Kartika, I. The Synthesis and Characterization of Mg-Zn-Ca Alloy by Powder Metallurgy Process. *AIP Conf. Proc.* **2016**, *1725*, 020032. [CrossRef]
12. Abdel-Gawad, S.A.; Shoeib, M.A. Corrosion Studies and Microstructure of Mg−Zn−Ca Alloys for Biomedical Applications. *Surf. Interfaces* **2019**, *14*, 108–116. [CrossRef]
13. Wang, Y. The Effects of Second Phase on Microstructure and Properties of Degradable As-Cast Mg-Zn-Ca Alloy for Intrauterine Device (IUD) Applications. *Int. J. Electrochem. Sci.* **2022**, *17*, 220835. [CrossRef]
14. Xie, L.L.; Chu, J.H.; Li, X.J.; Zou, D.N.; Tong, L.B. Improved Corrosion Resistance of EP Coating on Mg Alloy through GO Hybridization and Silica-Based Superhydrophobic Surface. *Diam. Relat. Mater.* **2022**, *130*, 109476. [CrossRef]
15. Merson, D.; Brilevsky, A.; Myagkikh, P.; Markushev, M.; Vinogradov, A. Effect of Deformation Processing of the Dilute Mg-1Zn-0.2Ca Alloy on the Mechanical Properties and Corrosion Rate in a Simulated Body Fluid. *Lett. Mater.* **2020**, *10*, 217–222. [CrossRef]

16. Jiang, P.; Blawert, C.; Hou, R.; Bohlen, J.; Konchakova, N.; Zheludkevich, M.L. A Comprehensive Comparison of the Corrosion Performance, Fatigue Behavior and Mechanical Properties of Micro-Alloyed MgZnCa and MgZnGe Alloys. *Mater. Des.* **2020**, *185*, 108285. [CrossRef]
17. Moreno, L.; Matykina, E.; Yasakau, K.A.; Blawert, C.; Arrabal, R.; Mohedano, M. As-Cast and Extruded MgZnCa Systems for Biodegradable Implants: Characterization and Corrosion Behavior. *J. Magnes. Alloys* **2023**, *11*, 1102–1120. [CrossRef]
18. Jin, Y.; Blawert, C.; Yang, H.; Wiese, B.; Feyerabend, F.; Bohlen, J.; Mei, D.; Deng, M.; Campos, M.S.; Scharnagl, N.; et al. Microstructure-Corrosion Behaviour Relationship of Micro-Alloyed Mg-0.5Zn Alloy with the Addition of Ca, Sr, Ag, In and Cu. *Mater. Des.* **2020**, *195*, 108980. [CrossRef]
19. Zhang, Y.; Bai, K.; Fu, Z.; Zhang, C.; Zhou, H.; Wang, L.; Zhu, S.; Guan, S.; Li, D.; Hu, J. Composite Coating Prepared by Micro-Arc Oxidation Followed by Sol–Gel Process and in Vitro Degradation Properties. *Appl. Surf. Sci.* **2012**, *258*, 2939–2943. [CrossRef]
20. Gao, J.H.; Shi, X.Y.; Yang, B.; Hou, S.S.; Meng, E.C.; Guan, F.X.; Guan, S.K. Fabrication and Characterization of Bioactive Composite Coatings on Mg–Zn–Ca Alloy by MAO/Sol–Gel. *J. Mater. Sci. Mater. Med.* **2011**, *22*, 1681–1687. [CrossRef]
21. Blawert, C.; Sah, S.P.; Scharnagl, N.; Kannan, M.B. 8—Plasma Electrolytic Oxidation/Micro-Arc Oxidation of Magnesium and Its Alloys. In *Surface Modification of Magnesium and Its Alloys for Biomedical Applications*; Narayanan, T.S.N.S., Park, I.-S., Lee, M.-H., Eds.; Woodhead Publishing Series in Biomaterials; Woodhead Publishing: Sawton, UK, 2015; pp. 193–234, ISBN 978-1-78242-078-1.
22. Jia, P.; Pan, Y.; Yu, L.; Wang, J.; Feng, R.; Wang, Y.; Fang, X.; Chen, C. In Vitro Degradation and Corrosion Evaluations of Plasma Electrolytic Oxidized Mg–Zn–Ca–Si Alloys for Biomedical Applications. *J. Mater. Res. Technol.* **2023**, *23*, 2410–2425. [CrossRef]
23. Keyvani, A.; Kamkar, N.; Chaharmahali, R.; Bahamirian, M.; Kaseem, M.; Fattah-alhosseini, A. Improving Anti-Corrosion Properties AZ31 Mg Alloy Corrosion Behavior in a Simulated Body Fluid Using Plasma Electrolytic Oxidation Coating Containing Hydroxyapatite Nanoparticles. *Inorg. Chem. Commun.* **2023**, *158*, 111470. [CrossRef]
24. Zhang, N.; Zhao, D.; Liu, N.; Wu, Y.; Yang, J.; Wang, Y.; Xie, H.; Ji, Y.; Zhou, C.; Zhuang, J.; et al. Assessment of the Degradation Rates and Effectiveness of Different Coated Mg-Zn-Ca Alloy Scaffolds for in Vivo Repair of Critical-Size Bone Defects. *J. Mater. Sci. Mater. Med.* **2018**, *29*, 138. [CrossRef]
25. Kröger, N.; Kopp, A.; Staudt, M.; Rusu, M.; Schuh, A.; Liehn, E.A. Hemocompatibility of Plasma Electrolytic Oxidation (PEO) Coated Mg-RE and Mg-Zn-Ca Alloys for Vascular Scaffold Applications. *Mater. Sci. Eng. C* **2018**, *92*, 819–826. [CrossRef]
26. Pan, Y.; Chen, C.; Wang, D.; Huang, D. Dissolution and Precipitation Behaviors of Silicon-Containing Ceramic Coating on Mg–Zn–Ca Alloy in Simulated Body Fluid. *Colloids Surf. B Biointerfaces* **2014**, *122*, 746–751. [CrossRef] [PubMed]
27. Ly, X.; Yang, S.; Nguyen, T. Effect of Equal Channel Angular Pressing as the Pretreatment on Microstructure and Corrosion Behavior of Micro-Arc Oxidation (MAO) Composite Coating on Biodegradable Mg-Zn-Ca Alloy. *Surf. Coat. Technol.* **2020**, *395*, 125923. [CrossRef]
28. Dou, J.; Gu, G.; Chen, C.; Pan, Y. Characterization and Biodegradation Behavior of Micro-Arc Oxidation Coatings Formed on Mg–Zn–Ca Alloys in Two Different Electrolytes. *RSC Adv.* **2016**, *6*, 104808–104818. [CrossRef]
29. Pan, Y.; He, S.; Wang, D.; Huang, D.; Zheng, T.; Wang, S.; Dong, P.; Chen, C. In Vitro Degradation and Electrochemical Corrosion Evaluations of Microarc Oxidized Pure Mg, Mg–Ca and Mg–Ca–Zn Alloys for Biomedical Applications. *Mater. Sci. Eng. C* **2015**, *47*, 85–96. [CrossRef]
30. Moreno, L.; Mohedano, M.; Arrabal, R.; Matykina, E. Development and Screening of (Ca-P-Si-F)-PEO Coatings for Biodegradability Control of Mg-Zn-Ca Alloys. *J. Magnes. Alloys* **2022**, *10*, 2220–2237. [CrossRef]
31. Wang, Y.; Chen, M.; Zhao, Y. Preparation and Corrosion Resistance of Microarc Oxidation-Coated Biomedical Mg–Zn–Ca Alloy in the Silicon–Phosphorus-Mixed Electrolyte. *ACS Omega* **2019**, *4*, 20937–20947. [CrossRef]
32. Daavari, M.; Atapour, M.; Mohedano, M.; Sánchez, H.M.; Rodríguez-Hernández, J.; Matykina, E.; Arrabal, R.; Taherizadeh, A. Quasi-in Vivo Corrosion Behavior of AZ31B Mg Alloy with Hybrid MWCNTs-PEO/PCL Based Coatings. *J. Magnes. Alloys* **2021**, *10*, 3217–3233. [CrossRef]
33. Chun, J.S.; Byrne, J.G. Precipitate Strengthening Mechanisms in Magnesium Zinc Alloy Single Crystals. *J. Mater. Sci.* **1969**, *4*, 861–872. [CrossRef]
34. Lu, X.; Zhao, G.; Zhou, J.; Zhang, C.; Yu, J. Microstructure and Mechanical Properties of the As-Cast and As-Homogenized Mg-Zn-Sn-Mn-Ca Alloy Fabricated by Semicontinuous Casting. *Materials* **2018**, *11*, 703. [CrossRef]
35. Santos-Coquillat, A.; Esteban-Lucia, M.; Martinez-Campos, E.; Mohedano, M.; Arrabal, R.; Blawert, C.; Zheludkevich, M.L.; Matykina, E. PEO Coatings Design for Mg-Ca Alloy for Cardiovascular Stent and Bone Regeneration Applications. *Mater. Sci. Eng. C* **2019**, *105*, 110026. [CrossRef]
36. Arrabal, R.; Mohedano, M.; Matykina, E. Electrochemical Surface Treatments for Mg Alloys. In *Encyclopedia of Materials: Metals and Allloys*; Caballero, F.G., Ed.; Elsevier: Oxford, UK, 2022; pp. 87–112. ISBN 978-0-12-819733-2.
37. Chaharmahali, R.; Fattah-alhosseini, A.; Babaei, K. Surface Characterization and Corrosion Behavior of Calcium Phosphate (Ca-P) Base Composite Layer on Mg and Its Alloys Using Plasma Electrolytic Oxidation (PEO): A Review. *J. Magnes. Alloys* **2020**, *9*, 21–40. [CrossRef]
38. Tang, H.; Wu, T.; Wang, H.; Jian, X.; Wu, Y. Corrosion Behavior of HA Containing Ceramic Coated Magnesium Alloy in Hank's Solution. *J. Alloys Compd.* **2017**, *698*, 643–653. [CrossRef]
39. Hussein, R.; Northwood, D. Production of Anti-Corrosion Coatings on Light Alloys (Al, Mg, Ti) by Plasma-Electrolytic Oxidation (PEO). In *Developments in Corrosion Protection*; BoD–Books on Demand: Norderstedt, Germany, 2014; Chapter 11; pp. 201–239. ISBN 978-953-51-1223-5.

40. Hussein, R.O.; Nie, X.; Northwood, D.O. An Investigation of Ceramic Coating Growth Mechanisms in Plasma Electrolytic Oxidation (PEO) Processing. *Electrochim. Acta* **2013**, *112*, 111–119. [CrossRef]
41. Lu, X.; Blawert, C.; Mohedano, M.; Scharnagl, N.; Zheludkevich, M.L.; Kainer, K.U. Influence of Electrical Parameters on Particle Uptake during Plasma Electrolytic Oxidation Processing of AM50 Mg Alloy. *Surf. Coat. Technol.* **2016**, *289*, 179–185. [CrossRef]
42. Lu, X.; Blawert, C.; Huang, Y.; Ovri, H.; Zheludkevich, M.L.; Kainer, K.U. Plasma Electrolytic Oxidation Coatings on Mg Alloy with Addition of SiO_2 Particles. *Electrochim. Acta* **2016**, *187*, 20–33. [CrossRef]
43. Asoh, H.; Asakura, K.; Hashimoto, H. Effect of Alcohol Addition on the Structure and Corrosion Resistance of Plasma Electrolytic Oxidation Films Formed on AZ31B Magnesium Alloy. *RSC Adv.* **2020**, *10*, 9026–9036. [CrossRef]
44. de Tavares, M.M.; de Vitoriano, J.O.; da Silva, R.C.L.; Franco, A.R.; de Souza, G.B.; da Costa, J.A.P.; Alves-Junior, C. Effect of Duty Cycle and Treatment Time on Electrolytic Plasma Oxidation of Commercially Pure Al Samples. *J. Mater. Res. Technol.* **2019**, *8*, 2141–2147. [CrossRef]
45. Zhuang, J.; Song, R.; Xiang, N.; Lu, J.; Xiong, Y. Effects of Oxidation Time on Corrosion Resistance of Plasma Electrolytic Oxidation Coatings on Magnesium Alloy. *Int. J. Mater. Res.* **2017**, *108*, 758–766. [CrossRef]
46. Lu, X.; Mohedano, M.; Blawert, C.; Matykina, E.; Arrabal, R.; Kainer, K.U.; Zheludkevich, M.L. Plasma Electrolytic Oxidation Coatings with Particle Additions—A Review. *Surf. Coat. Technol.* **2016**, *307*, 1165–1182. [CrossRef]
47. Lou, B.-S.; Lin, Y.-Y.; Tseng, C.-M.; Lu, Y.-C.; Duh, J.-G.; Lee, J.-W. Plasma Electrolytic Oxidation Coatings on AZ31 Magnesium Alloys with Si3N4 Nanoparticle Additives. *Surf. Coat. Technol.* **2017**, *332*, 358–367. [CrossRef]
48. Wang, Y.; Wei, D.; Yu, J.; Di, S. Effects of Al_2O_3 Nano-Additive on Performance of Micro-Arc Oxidation Coatings Formed on AZ91D Mg Alloy. *J. Mater. Sci. Technol.* **2014**, *30*, 984–990. [CrossRef]
49. Gu, X.-N.; Zheng, Y.-F. A Review on Magnesium Alloys as Biodegradable Materials. *Front. Mater. Sci. China* **2010**, *4*, 111–115. [CrossRef]
50. Tsai, D.-S.; Chou, C.-C. Influences of Growth Species and Inclusions on the Current–Voltage Behavior of Plasma Electrolytic Oxidation: A Review. *Coatings* **2021**, *11*, 270. [CrossRef]
51. Reichelt, K. Nucleation and Growth of Thin Films. *Vacuum* **1988**, *38*, 1083–1099. [CrossRef]
52. Brindley, G.W.; Hayami, R. Kinetics and Mechanism of Formation of Forsterite (Mg_2SiO_4) by Solid State Reaction of MgO and SiO_2. *Philos. Mag. J. Theor. Exp. Appl. Phys.* **1965**, *12*, 505–514. [CrossRef]
53. Wang, M.; Zhou, Y.; Zhang, Y.; Hahn, S.; Kim, E. From Zn(OH) 2 to ZnO: A Study on the Mechanism of Phase Transformation. *CrystEngComm* **2011**, *13*, 6024–6026. [CrossRef]
54. Tang, H.; Han, Y.; Wu, T.; Tao, W.; Jian, X.; Wu, Y.; Xu, F. Synthesis and Properties of Hydroxyapatite-Containing Coating on AZ31 Magnesium Alloy by Micro-Arc Oxidation. *Appl. Surf. Sci.* **2017**, *400*, 391–404. [CrossRef]
55. Dou, J.; Wang, J.; Lu, Y.; Chen, C.; Yu, H.; Ma, R.L.-W. Bioactive MAO/CS Composite Coatings on Mg-Zn-Ca Alloy for Orthopedic Applications. *Prog. Org. Coat.* **2021**, *152*, 106112. [CrossRef]
56. Moreno, L.; Mohedano, M.; Arrabal, R.; Matykina, E. Screening of Fluoride-Free PEO Coatings on Cast Mg3Zn0.4Ca Alloy for Orthopaedic Implants. *Surf. Coat. Technol.* **2024**, *476*, 130184. [CrossRef]
57. Fang, H.; Wang, C.; Zhou, S.; Zheng, Z.; Lu, T.; Li, G.; Tian, Y.; Suga, T. Enhanced Adhesion and Anticorrosion of Silk Fibroin Coated Biodegradable Mg-Zn-Ca Alloy via a Two-Step Plasma Activation. *Corros. Sci.* **2020**, *168*, 108466. [CrossRef]
58. van Gaalen, K.; Gremse, F.; Benn, F.; McHugh, P.E.; Kopp, A.; Vaughan, T.J. Automated Ex-Situ Detection of Pitting Corrosion and Its Effect on the Mechanical Integrity of Rare Earth Magnesium Alloy—WE43. *Bioact. Mater.* **2022**, *8*, 545–558. [CrossRef] [PubMed]
59. Shahri, Z.; Allahkaram, S.R.; Soltani, R.; Jafari, H. Study on Corrosion Behavior of Nano-Structured Coatings Developed on Biodegradable as Cast Mg–Zn–Ca Alloy by Plasma Electrolyte Oxidation. *Surf. Coat. Technol.* **2018**, *347*, 225–234. [CrossRef]
60. Tsakiris, V.; Tardei, C.; Clicinschi, F.M. Biodegradable Mg Alloys for Orthopedic Implants—A Review. *J. Magnes. Alloys* **2021**, *9*, 1884–1905. [CrossRef]
61. Chandra, G.; Pandey, A. Biodegradable Bone Implants in Orthopedic Applications: A Review. *Biocybern. Biomed. Eng.* **2020**, *40*, 596–610. [CrossRef]
62. Wang, L.; Guo, X.; Chen, J.; Zhen, Z.; Cao, B.; Wan, W.; Dou, Y.; Pan, H.; Xu, F.; Zhang, Z.; et al. Key Considerations on the Development of Biodegradable Biomaterials for Clinical Translation of Medical Devices: With Cartilage Repair Products as an Example. *Bioact. Mater.* **2022**, *9*, 332–342. [CrossRef] [PubMed]
63. Nicolao-Gómez, A.; Martínez-Campos, E.; Moreno, L.; Rodríguez-Hernández, J.; Matykina, E. Hierarchical Hybrid Coatings with Drug-Eluting Capacity for Mg Alloy Biomaterials. *Materials* **2023**, *16*, 7688. [CrossRef]
64. Persson, D.; Thierry, D.; Karlsson, O. Corrosion and Corrosion Products of Hot Dipped Galvanized Steel during Long Term Atmospheric Exposure at Different Sites World-Wide. *Corros. Sci.* **2017**, *126*, 152–165. [CrossRef]
65. Manhabosco, S.M.; Manhabosco, T.M.; Geoffroy, N.; Vignal, V.; Dick, L.F.P. Corrosion Behaviour of Galvanized Steel Studied by Electrochemical Microprobes Applied on Low-Angle Cross Sections. *Corros. Sci.* **2018**, *140*, 379–387. [CrossRef]
66. Dou, J.; Chen, Y.; Chi, Y.; Li, H.; Gu, G.; Chen, C. Preparation and Characterization of a Calcium–Phosphate–Silicon Coating on a Mg–Zn–Ca Alloy via Two-Step Micro-Arc Oxidation. *Phys. Chem. Chem. Phys.* **2017**, *19*, 15110–15119. [CrossRef] [PubMed]

67. Mohedano, M.; Luthringer, B.J.C.; Mingo, B.; Feyerabend, F.; Arrabal, R.; Sanchez-Egido, P.J.; Blawert, C.; Willumeit-Römer, R.; Zheludkevich, M.L.; Matykina, E. Bioactive Plasma Electrolytic Oxidation Coatings on Mg-Ca Alloy to Control Degradation Behaviour. *Surf. Coat. Technol.* **2017**, *315*, 454–467. [CrossRef]
68. Dou, J.; Zhao, Y.; Lu, L.; Gu, G.; Yu, H.; Chen, C. Effect of the Second-Step Voltages on the Structural and Corrosion Properties of Silicon–Calcium–Phosphate (Si–CaP) Coatings on Mg–Zn–Ca Alloy. *R. Soc. Open Sci.* **2018**, *5*, 172410. [CrossRef]

coatings

MDPI

Article

Functionalization of Plasma Electrolytic Oxidation/Sol–Gel Coatings on AZ31 with Organic Corrosion Inhibitors

Borja Pillado [1,2], Endzhe Matykina [1], Marie-Georges Olivier [3], Marta Mohedano [1] and Raúl Arrabal [1,*]

[1] Departamento de Ingeniería Química y de Materiales, Facultad de Ciencias Químicas, Universidad Complutense, 28040 Madrid, Spain; pillado-rios@ill.fr (B.P.); ematykin@ucm.es (E.M.); mmohedan@ucm.es (M.M.)
[2] Institut Laue-Langevin, 71 Avenue des Martyrs, 38000 Grenoble, France
[3] Department of Materials Science, Materials Institute, Faculty of Engineering, University of Mons, 20 Place du Parc, 7000 Mons, Belgium; marjorie.olivier@umons.ac.be
* Correspondence: rarrabal@ucm.es

Abstract: In this investigation, the sol–gel method is employed along with a corrosion inhibitor to seal a plasma electrolytic oxidation (PEO) coating, aiming to improve the long-term corrosion resistance of the AZ31 Mg alloy. Following an initial screening of corrosion inhibitors, 8-hydroxyquinoline (8HQ) is incorporated into the hybrid PEO/sol–gel system using two methods: (i) post-treatment of the PEO layer through immersion in an inhibitor-containing solution; (ii) loading the inhibitor into the sol–gel precursor. The characterization includes scanning electron microscopy (SEM), X-ray diffraction (XRD), Fourier transform infrared spectroscopy (FTIR), ultraviolet-visible spectroscopy (UV-vis), and water drop contact angle measurements. The rheological properties of the inhibitor-loaded sol–gel precursors are assessed by measuring flow curves. The corrosion processes are evaluated in a saline solution through electrochemical impedance spectroscopy (EIS) and immersion tests with unscratched and scratched specimens, respectively. The results demonstrate the successful incorporation of the inhibitor for both loading strategies. Regardless of the loading approach, systems containing 8HQ exhibit the most favourable long-term corrosion resistance.

Keywords: magnesium; plasma electrolytic oxidation; sol–gel; corrosion; inhibitor

Citation: Pillado, B.; Matykina, E.; Olivier, M.-G.; Mohedano, M.; Arrabal, R. Functionalization of Plasma Electrolytic Oxidation/Sol–Gel Coatings on AZ31 with Organic Corrosion Inhibitors. *Coatings* **2024**, *14*, 84. https://doi.org/10.3390/coatings14010084

Academic Editor: Gianni Barucca

Received: 11 December 2023
Revised: 4 January 2024
Accepted: 5 January 2024
Published: 7 January 2024

1. Introduction

Currently, magnesium alloys account for less than 1% of the total weight of automobiles [1], primarily due to their insufficient corrosion resistance and other challenges, including price variability, low formability, flammability and inadequate creep strength. PEO coatings on magnesium can improve the corrosion resistance by up to 4 orders of magnitude in aqueous corrosion media such as sodium chloride (NaCl) [2–6] and simulated body fluid (SBF) [7–11]. However, high porosity of PEO coatings makes Mg alloys susceptible to localized corrosion, particularly pitting and undercoating corrosion. Therefore, corrosion protection provided by PEO coatings usually only lasts a few days [11–14].

Sol–gel sealings have been garnering growing attention in recent years, as evidenced by several papers on hybrid PEO/sol–gel coatings [15–19]. The appeal of sol–gel stems from its capacity to penetrate PEO pores and cracks, along with its versatility and low environmental impact [20–23]. For example, Malayoglu et al. [24] explored various post-treatments, including phosphate and silicate sealings, and concluded that the PEO/sol–gel system demonstrated superior corrosion performance [23,25].

Inorganic–organic sol–gel formulations, also known as hybrid sol–gels (HSGs), prove highly effective in enhancing corrosion performance [21]. The organic component lowers the curing temperature and imparts elasticity, while the silane structure contributes favourable mechanical properties and adhesion [26–28]. Pezzato et al. [12] positively

acknowledged the use of hybrid sol–gel sealings for PEO coatings as they enhance the uniformity of the PEO layer, leading to a notable improvement in corrosion resistance.

While PEO/sol–gel systems show promise, a drawback is that they are often perceived merely as barriers to the substrate, thereby lacking self-healing ability. This is why the incorporation of corrosion inhibitors has become a focal point in PEO coating research.

Recent examples of inhibitor incorporation into either PEO coatings or sol–gels are those concerned with organic species like 8–hydroxyquinoline (8HQ) [29] and 2–mercaprobenzothiazole (MBT) [30], as well as inorganic additives involving Ca, Ce, and Zn [31–35]. However, there is a scarcity of published results on PEO/sol–gel systems incorporating corrosion inhibitors.

Chen et al. [17] developed a PEO/sol–gel system loaded with glycolic acid, 4-aminosalicylic sodium salt, and 2,6-pyridinedicarboxylic acid. Inhibitors were integrated by impregnating the PEO coating, followed by the sol–gel sealing. As per the reported findings, coatings with inhibitors revealed improved corrosion performance. The authors proposed a protective mechanism achieved by suppressing the re-deposition of detrimental Fe impurities and promoting adsorption over the surface. In a similar vein, Ivanou et al. [18] impregnated a PEO coating with 1,2,4-triazole, followed by sol–gel sealing. Notably, high corrosion protection was observed during continuous exposure to the aggressive medium for one month. This enhancement was attributed to the thin and porous PEO layer, which secured the corrosion inhibitor close to the bulk metal where the corrosion process initiates.

In this work, a hybrid sol–gel sealing is used along 8HQ as a corrosion inhibitor for improving the corrosion resistance of a PEO coating on the AZ31 Mg alloy. The selection of a hybrid PEO/sol–gel system was motivated by the potential of sol–gel films to effectively seal pores and cracks within PEO coatings, thus improving their long-lasting corrosion protection for applications spanning transport and consumer products. The incorporation of 8HQ as a corrosion inhibitor seeks to introduce self-healing properties. The research includes an initial screening of various corrosion inhibitors and the exploration of two methods for incorporating the best corrosion inhibitor into the hybrid PEO/sol–gel system: (i) post-treatment of the PEO layer through immersion in an inhibitor-containing solution, and (ii) loading of the inhibitor into the sol–gel precursor. The coatings undergo characterization concerning morphology, composition, and corrosion resistance. The goal is to pinpoint the optimal strategy for enhancing the long-term corrosion protection of hybrid PEO/sol–gel coatings.

2. Materials and Methods

2.1. Mg Alloy

For this study, 60 × 60 × 2 mm square-shaped AZ31 specimens (KG Fridman AB, Karlstad, Sweden), 2.5–3.5% Al, 0.7–1.3% Zn, 0.2% Mn, 0.05% Si, 0.05% Cu, 0.04% Ca, 0.005% Fe, 0.1% Ni (wt.%), and Mg balance) were etched in 2 M nitric acid and rinsed in deionized water. Subsequently, they were subjected to a second etching in 0.25 M nitric acid, followed by another rinse in deionized water. The specimens were air-dried and stored in a desiccator before use.

2.2. Plasma Electrolytic Oxidation

PEO coating was fabricated in a 3 L double-walled cell connected to a continuous water flow to maintain a constant temperature of (293 ± 5) K. The electrolyte consisted of 8.4 g/L KOH, 10.5 g/L Na_2SiO_3, and 1.73 g/L NaF, which were purchased from Alfa Aesar (Tewksbury, MA, USA). The PEO films were formed using an AC power supply (PowerPulse–Micronics, Vilette d'Anthon, France) connected to a stainless-steel sheet as the counter electrode. The electric regime was designed as +400/−30 V, 100 mA cm^{-2}, 5/5 ms up to 4 min of treatment (Table 1). The samples were cleaned in deionized water and air-dried.

Table 1. PEO conditions for surface modification of AZ31 and details of the sol–gel sealing.

Coating	Conditions	
PEO	Na_2SiO_3 10.5 g/L KOH 8.5 g/L NaF 1.73 g/L	(20 ± 1) °C, +400/−30 V, 100 mA cm^{-2}, 50 Hz, 4 min, 60 s ramp
PEO-SG	TEOS [1] 20%, GPTMS 10%, ethanol 10%, water 58% Acetic acid to adjust the pH 2	10 mm/min immersion/withdraw 15 min air drying, 150 °C 2 h curing

[1] TEOS: tetraethoxysilane; GPTMS: 3-glycidyloxypropyl trimethoxysilane.

2.3. Sol–Gel Sealing

Sealing was carried out by the dip-coating method (KSV NIMA dip-coater, Biolin Scientific, Espoo, Finland) using a hybrid sol–gel precursor consisting of TEOS, GPTMS, ethanol, and water at pH 2. TEOS and GPTMS were supplied by Sigma-Aldrich, Steinheim, Germany. Note that the reactants were mixed in the order presented in Table 1.

2.4. Inhibitor Loading

Nine corrosion inhibitors supplied by Sigma-Aldrich (Germany) underwent preliminary screening, involving the immersion of the bare AZ31 Mg alloy in a saline solution (0.5 wt.% NaCl) at pH 8, containing 0.05 M of each corrosion inhibitor (Figure S1 and Table S1). Among them, 8–Hydroxyquinoline (8HQ) revealed the lowest amount of collected hydrogen, closely followed by 5–methyl–2–nitrobenzoic acid and 3–methylsalycilic acid. Consequently, 8HQ was chosen for further investigation.

After immersion in the solution with 8HQ, the exposed surface shows no corroded areas. Instead, a yellowish precipitate covers the entire surface (Figure S2 and Table S2). In agreement with several studies [36–40], 8HQ may behave as an inhibitor by the formation of a complex chelate ($Mg(8HQ)_2$) on the surface, blocking the action of aggressive ions. It is important to note that 8HQ has already been used with good results as an additive in sol–gel systems for steel [41], Mg [29] and Al [40,42–44]; however, those systems did not include an intermediate PEO layer.

Two methods were used for incorporating 8HQ into the hybrid PEO/sol–gel system: (i) post-treatment after PEO processing through immersion in an inhibitor-containing solution for 30 min at pH 10; (ii) loading the inhibitor into the sol–gel precursor. As shown in Table 2, several inhibitor concentrations and times were investigated in each case. Note that high concentrations of corrosion inhibitor were not included in the second strategy due to formation of emulsions.

2.5. Characterization

The plan and cross-section views of the coatings were examined by scanning electron microscopy (SEM, JEOL JSM 6400 and Hitachi SU8020, Tokyo, Japan) and energy dispersive X-ray spectroscopy (EDS, Oxford Link energy-dispersive X-ray, Abingdon, UK) for semi-quantitative analysis. The crystalline composition of the PEO layer was analysed using X-ray diffraction (XRD, Philips X'Pert, Amsterdamm, The Netherlands, Cu Kα = 0.154056 nm, 2θ range between 10° and 90°, 0.05° step size, 6 s per step, 0.5° grazing angle). Fourier transform infrared (FTIR) was performed in a SHIMADZU IRTracer-100 spectrometer (Kyoto, Japan) operated in reflection set-up of 45°. UV-vis spectra were acquired in the 800–200 nm range using a PerkinElmer Lambda 365 equipment (Waltham, MA, USA).

The rheological behaviour of the aqueous preparations was determined through monitoring flow curves, apparent viscosity obtained from shear stress versus shear rate at 26 ± 0.1 °C using a controlled rheometer (MCR302, Anton Paar, Gentbrugge, Belgium) equipped with double-gap cylinders (ISO/WD 3219-2 standard).

Table 2. Designation of studied specimens.

	Sample	Inhibitor [8HQ] Post-Treatment	Sol–Gel Sealing
	AZ31	–	–
	PEO	–	–
	PEO–SG	–	TEOS/GPTMS
Strategy 1	PEO–1 mM–5 min	1 mM–5 min	–
	PEO–5 mM–5 min	5 mM–5 min	–
	PEO–10 mM–5 min	10 mM–5 min	–
	PEO–100 mM–5 min	100 mM–5 min	–
	PEO–5 mM–5 min–SG	5 mM–5 min	TEOS/GPTMS
	PEO–5 mM–10 min–SG	5 mM–10 min	TEOS/GPTMS
	PEO–5 mM–30 min–SG	5 mM–30 min	TEOS/GPTMS
	PEO–10 mM–5 min–SG	10 mM–5 min	TEOS/GPTMS
	PEO–10 mM–10 min–SG	10 mM–10 min	TEOS/GPTMS
	PEO–10 mM–30 min–SG	10 mM–30 min	TEOS/GPTMS
	PEO–100 mM–5 min–SG	100 mM–5 min	TEOS/GPTMS
	PEO–100 mM–10 min–SG	100 mM–10 min	TEOS/GPTMS
	PEO–100 mM–30 min–SG	100 mM–30 min	TEOS/GPTMS
Strategy 2	PEO–SG–1 mM	–	TEOS/GPTMS + 8HQ 1 mM in the aqueous solution (58%)
	PEO–SG–5 mM	–	TEOS/GPTMS + 8HQ 5 mM in the aqueous solution (58%)
	PEO–SG–10 mM	–	TEOS/GPTMS + 8HQ 10 mM in the aqueous solution (58%)

Waterdrop contact angle measurements were carried out by depositing a water drop on top of the surface and recording the evolution of the angle after 2 s by means of a drop shape DSA10−Mk2 analysis system (KRÜSS Scientific, Hamburg, Germany). Presented values are the average of triplicated measurements.

2.6. Corrosion Tests

Electrochemical impedance spectroscopy (EIS) measurements were performed using a SP–300 potentiostat (BioLogic, Grenoble, France) connected to a three-electrode cell. Sodium chloride aqueous solutions of 0.5 wt.% concentration were employed. A 10 mV sinusoidal perturbation of amplitude and a scan in the frequency range of 10 kHz–0.01 Hz were applied after different immersion times.

Immersion tests were carried out with scratched specimens in 0.5 wt.% NaCl solution. The 1 cm long defect was generated with the necessary depth to expose the underlying substrate. The evolution of the corrosion process was monitored by macroscopic photographs at different stages of the immersion test up to a maximum time of 14 days.

3. Results

3.1. PEO/Inhibitor/Sol–Gel Systems

3.1.1. Optimization of Inhibitor Post-Treatment

After selecting 8HQ as the most promising inhibitor, several coating systems were outlined for further optimization. Initially, different concentrations of 8HQ (1, 5, 10, and 100 mM) were examined for the immersion post-treatment. Then, various hybrid PEO/sol–gel systems were evaluated, involving alterations in both the inhibitor concentration and post-treatment time (refer to Table 2) [45–48].

The EIS screening results are presented in Figure 1. All the combinations yielded higher impedance values than the bare alloy. The standalone PEO exhibits an impedance modulus two orders of magnitude higher than that of the substrate. However, its protective effect diminishes rapidly over time, reaching a modulus similar to that of the alloy after 24 h. In contrast, the hybrid system (PEO–SG) shows an initial impedance slightly lower

than that of PEO, yet the response remains nearly constant with time. This long-term protection is attributed to the sealing of defects in the PEO coating [27]. The slightly lower impedance, in comparison to the PEO coating without sealing, may be linked to the partial dissolution of the ceramic coating induced by the slightly acidic conditions of the sol–gel precursor (pH 2).

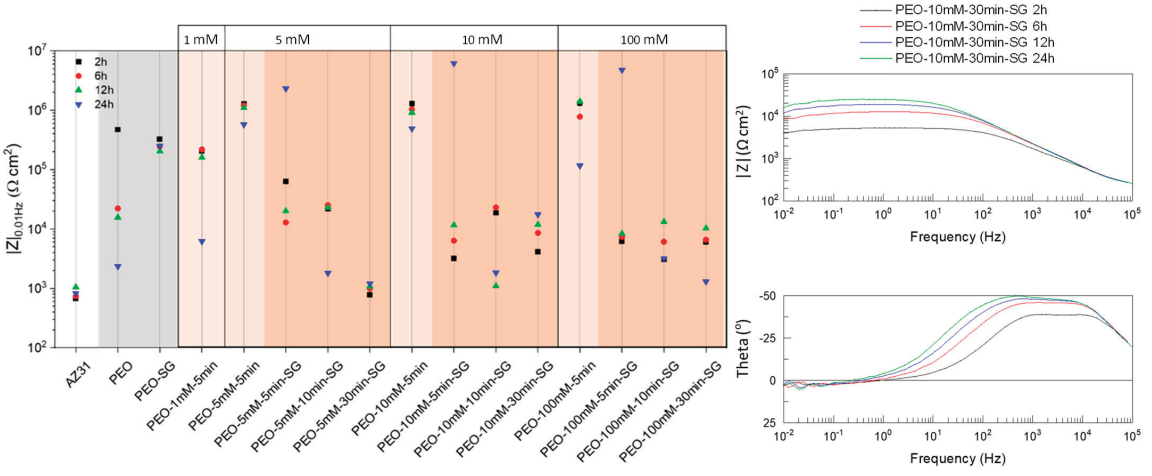

Figure 1. Scatter diagram of impedance modulus at 0.01 Hz of PEO, PEO–SG, PEO–8HQ, and PEO–8HQ–SG coatings on AZ31 alloy up to 24 h of immersion in 0.5 wt.% NaCl. The diagram also includes the bare AZ31 substrate. An example of the Bode diagrams for one of the studied PEO–8HQ–SG coatings is also presented.

The impregnation with 8HQ through the immersion post-treatment improved the performance of the PEO coating, most likely due to the formation of insoluble $Mg(8HQ)_2$ deposit [49]. The sole exception was observed with the 1 mM solution, revealing a lower impedance value. This discrepancy may be attributed to insufficient $Mg(8HQ)_2$ precipitation and potential degradation of the PEO coating in the post-treatment solution (pH 10).

Contrary to expectations, the application of sol–gel on top of the post-treated PEO coating resulted in lower impedance values than the reference PEO–SG film for all the tested combinations. The potential causes for this outcome are diverse. For instance, 8HQ–rich precipitates may disrupt the continuity of the sol–gel film. Additionally, the formation of Si–O–M bonds in the PEO/sol–gel interface could be influenced in the presence of 8HQ, leading to a reduction in the penetration of the sol–gel layer [45]. However, it is noteworthy that some coating systems reveal an increase in the modulus with prolonged immersion time. This improvement suggests active protection and recovery of the corrosion protection.

Except for the PEO–1 mM–5 min specimen, no significant differences are observed among the investigated hybrid PEO/inhibitor/SG systems. Therefore, all the full systems with inhibitor concentrations of 5, 10, and 100 mM were chosen for further evaluation.

3.1.2. Coating Morphology and Composition

FTIR, SEM/EDS, and XRD analyses were employed to characterize the hybrid PEO/sol–gel systems, both with and without inhibitor impregnation, following the PEO processing. It is important to note that only representative systems were examined.

Figure 2 and Table 3 display the FTIR results of 8HQ powder, PEO–8HQ, PEO–SG, and PEO–8HQ–SG coatings [50–52]. In the spectrum of a representative specimen (PEO–5 mM–10 min), bands corresponding to 8HQ are still evident, indicating successful incorporation onto the surface (Figure 2b). However, a notable difference is observed; the 3150 cm^{-1} band associated with the phenol group vanishes due to the formation of metal complexes

between $8HQ^-$ and Mg^{2+} [50]. It is important to note that the spectrum now exhibits bands originating from the PEO layer. The most distinct bands include the one at 3311 cm^{-1}, attributed to ν(H–O), indicating hydration of the outermost region of the PEO layer. Additionally, several signals are observed related to Si–O–Si (1493–960, 960–724 cm^{-1}) and Si–O–Mg bonds (<700 cm^{-1}), indicating the incorporation of silicate from the electrolyte during PEO processing [27,53–55].

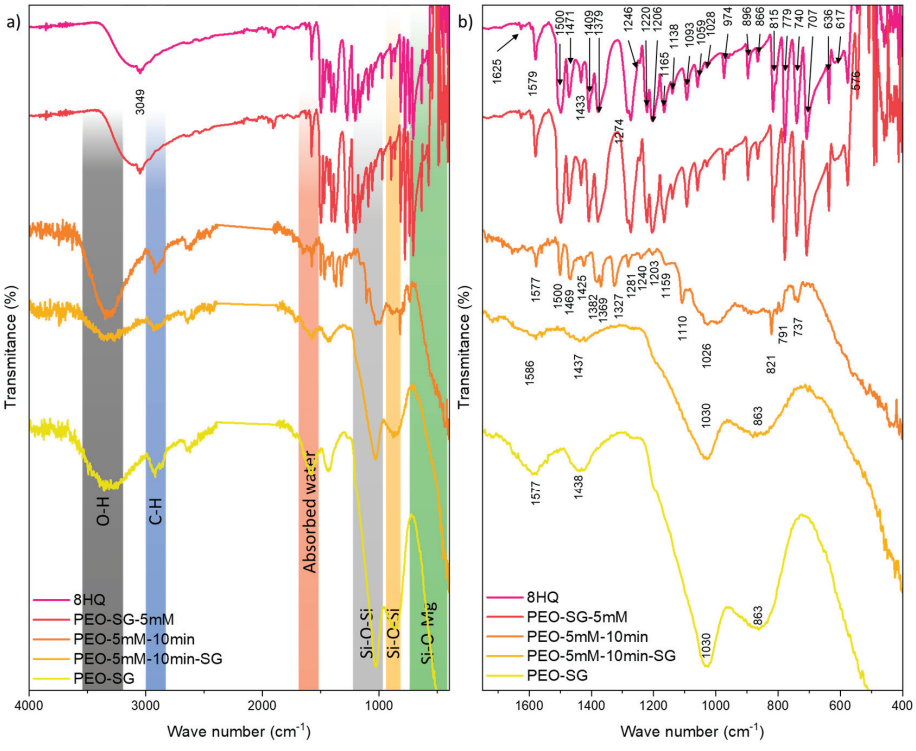

Figure 2. (**a**) FTIR spectra of 8HQ powder and PEO–8HQ, PEO–SG, and PEO–8HQ–SG coatings, and (**b**) detail of the near IR region. Bands related to the 8HQ compound.

Table 3. Band assignments for the FTIR spectra presented in Figure 2.

Band Wave Number (cm^{-1})	Assignation
3311	ν(OH) hydration of PEO
3150	stretching vibration for ν(OH) phenol
3049	aromatic ν(C–H) stretching
1625	ν(C=N) stretching
1579	ν(C=N) ring stretching vibration
1500	ν(C=C) stretching vibration
1471, 779	in–plane and out-of-plane deformations of CH_2 and CH_3 groups
1433	O–H plane bending
1274, 1246	ν(C–O) stretching vibrations
1165, 1138, 1093	N(C–N) stretching bands
1059, 1028	ν(N–O) stretching bands
974	$–CH_2$ rocking
896, 866	ν(C–C) bending vibration
740, 707	ν(C–H) out-of-plane bending band

The spectra obtained for the PEO–SG and PEO–8HQ–SG coatings reveal characteristic bands of sol–gel layers. Signals at 3100–3600 cm^{-1} and 1585 cm^{-1} correspond to vibrations of the ν(H–O) bonds, originating from the Si–OH groups in the sol–gel layer and absorbed water molecules [27,50,51]. The intensity of these bands increases with the number of polar groups, serving as an indicator of the level of sol–gel polymerization. Vibrations of ν(C–H) bonds at 3000–2824 cm^{-1} correspond to the $–CH_3$ and $–CH_2$ groups from the GPTMS precursor. Notably, there is an increased intensity of the Si–O–Si and Si–O–M signals which come from both the PEO and sol–gel layers. The intensity of the band centred at ~1034 cm^{-1} is generally associated with asymmetric Si–O–Si vibrations, indicative of correct sol–gel formation.

It is important to mention that the inhibitor post-treatment with 8HQ leads to less pronounced Si–O–Si and Si–O–Mg bands for the hybrid PEO–8HQ–SG system. Therefore, it can be deduced that the 8HQ post-treatment interferes with the sol–gel process: the hydrolysis and condensation reactions are restricted, limiting the formation of a 3D network. Very few studies have investigated the impact of an intermediate post-treatment step on sol–gel sealing of PEO coatings [56–58], numerous examples exist where species incorporated in the sol–gel affect the degree of polymerisation associated with the inorganic and organic components [27].

Before discussing the SEM micrographs of the hybrid systems, the stand-alone PEO coating is presented first. SEM images of the surface of the PEO-coated AZ31 Mg alloy are presented in Figure 3 alongside the EDS maps. The unsealed coating reveals a crater-like morphology, with microcracks and micropores concentrated at the sites of the discharge channels, which formed due to residual stresses and gas evolution during coating formation (Figure 3a,b).

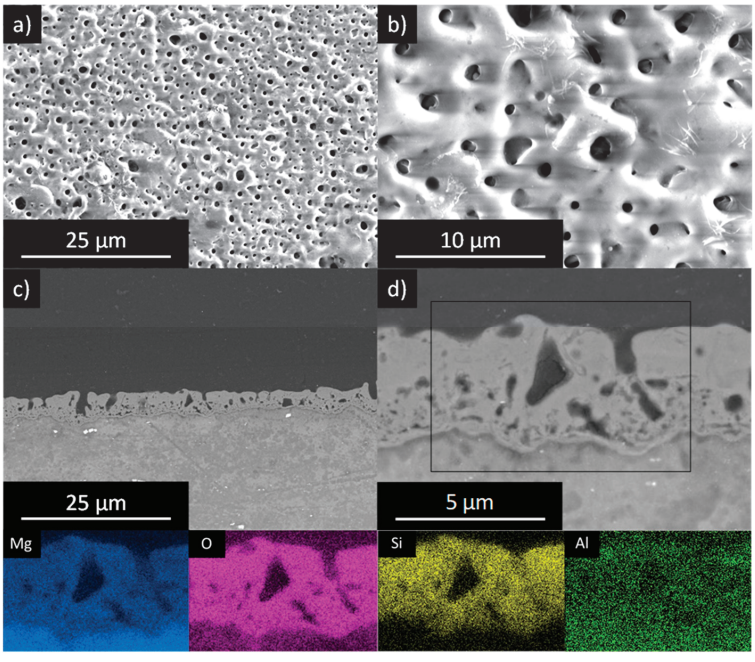

Figure 3. Scanning electron micrographs corresponding to the (**a**,**b**) planar and (**c**,**d**) cross-sectional views of PEO-coated AZ31. Cross-sectional observation along with EDS mapping of the PEO layer.

Cross-sectional micrographs (Figure 3c,d) reveal a well-defined barrier layer in combination with a thicker and porous outer layer (thickness 7.3 ± 0.4 µm). The EDS Si map of the PEO layer displays a significant contribution from Si, which is expected as the PEO

coating was produced in an alkaline–silicate electrolyte [59–61]. The outer regions of the coating exhibit some Al enrichment, originating from the substrate.

The XRD results of the unsealed PEO coating (Figure 4) indicate the presence of magnesium oxide (MgO, JCPDS 75-1525) and forsterite (Mg_2SiO_4, JCPDS 34-0189). Crystalline phases of aluminium (e.g., $MgAl_2O_4$) were not detected. Therefore, the aluminium detected in the coating is primarily in the form of amorphous phases or as a dopant in the aforementioned compounds. The peaks corresponding to magnesium originate from the substrate (Mg, JCPDS 35-0821), a result of X-ray penetration.

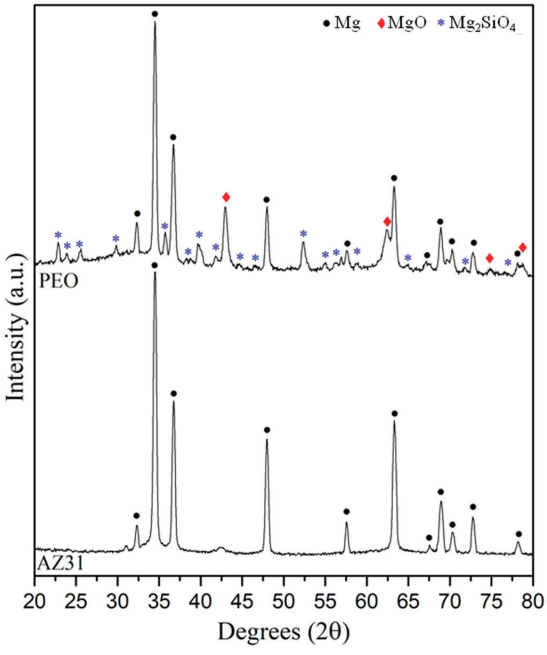

Figure 4. XRD patterns of the bare alloy and the fabricated PEO coating.

Comparative SEM micrographs of the PEO-coated AZ31 alloy without and with post-treatment and sol–gel sealings are depicted in Figure 5, including planar and cross-view micrographs. Following a 10 min post-treatment, the surface of the PEO coating shows flakes of 8HQ complexes with two distinct morphologies (Figure 5c); (i) agglomerates of small flakes deposited on the flat surface of the PEO layer, surrounding smaller pores; and (ii) large flakes near bigger pores, resembling the morphology observed in Figure S2. No flakes were found in the cross-sectional micrographs, presumably washed away during cross-section preparation. Cross-view examination suggests a slight dissolution of the PEO coating after the inhibitor post-treatment (PEO 7.3 $\pm$ 0.4 μm vs. PEO–5 mM–10 min 6.7 $\pm$ 0.3 μm, Figure 5b,d).

The variation in the size of the flakes is attributed to the availability of Mg^{2+} ions. The dissolution of Mg is presumed to be more substantial within the pores, supplied by the substrate and PEO layer, leading to the formation of larger flakes. EDS analysis indicates that these flakes show elevated levels of C, O, and Mg, suggesting the formation of $Mg(8HQ)_2$. These observations align with the findings of Vaghefinazari et al. [45], who reported the formation of $Mg(8HQ)_2$ on a bare substrate exposed to a solution containing 8HQ.

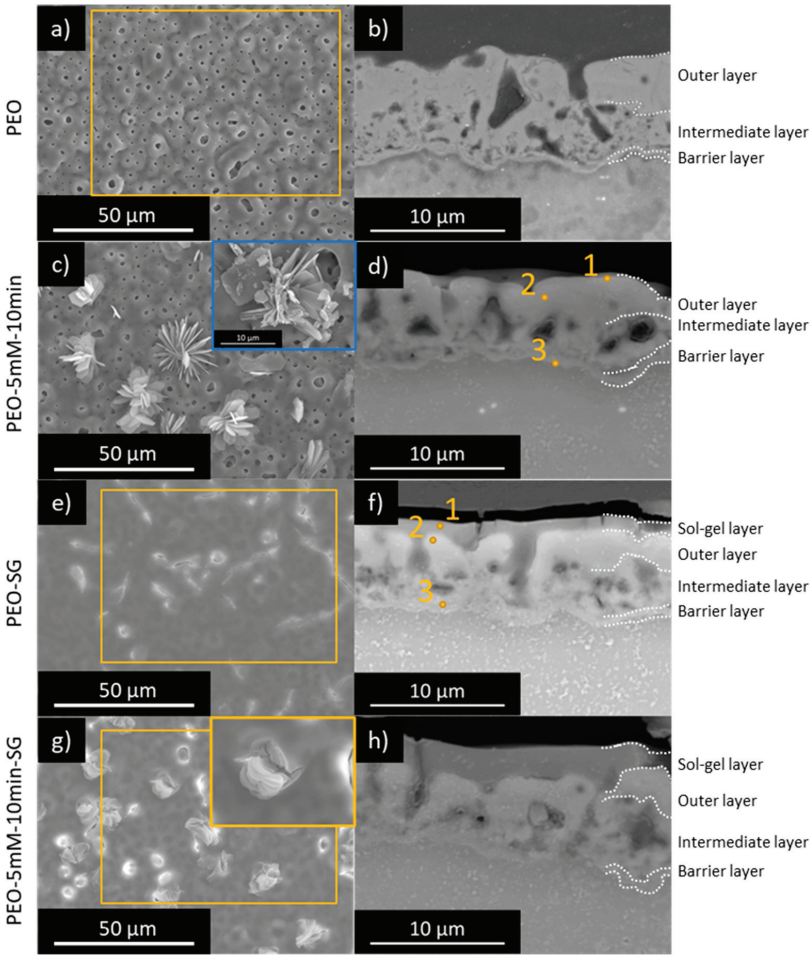

Figure 5. Scanning electron micrographs corresponding to the planar and cross-views of (**a**,**b**) PEO, (**c**,**d**) PEO–5 mM–10 min, (**e**,**f**) PEO–SG, and (**g**,**h**) PEO–5 mM–10 min–SG. Corresponding EDS analysis are presented in Table 4.

Table 4. Results of the local EDS surface analysis of the studied coatings (at.%). Refer to the locations shown in Figure 5.

		Element										
		C	**N**	**O**	**F**	**Na**	**Mg**	**Al**	**Si**	**K**	**Mn**	**Zn**
PEO	Area	8.8	–	54.3	–	1.0	24.6	0.7	10.4	0.2	–	–
PEO–5 mM–10 min	Area	13.0	0.6	52.1	0.9	1.0	20.6	1.0	10.0	0.2	0.5	0.1
	1	24.0	–	52.7	1.0	0.7	15.4	0.4	5.7	0.1	–	–
	2	22.7	–	47.9	0.8	0.8	19.0	0.6	8.1	0.1	–	–
	3	17.0	–	22.7	1.5	0.2	52.1	1.3	4.5	0.1	–	0.5
PEO–SG	Area	27.0	–	41.5	–	0.4	16.7	0.5	13.9	0.1	–	–
	1	46.7	–	43.0	0.5	0.2	4.6	0.1	4.8	0.1	–	–
	2	33.4	–	41.6	0.3	0.5	15.6	0.4	8.0	0.1	–	–
	3	18.4	–	29.7	2.0	0.2	42.1	1.2	5.9	0.1	–	0.3
PEO–5 mM–10 min–SG	Area	31.7	–	44.3	–	0.5	12.5	0.6	10.2	0.2	–	–

Figure 5e reveals that the sol–gel sealing forms a uniform layer (1.8 ± 0.5 μm) that effectively fills the pores and cracks in the PEO layer. However, some surface defects, primarily cracks resulting from dehydration of the sol–gel layer during curing, are observed. These cracks are also visible in the cross-view (Figure 5f). The thickness of the PEO coating decreased to 5.4 ± 0.5 μm due to the acidic conditions during sol–gel sealing. The overall thickness of the PEO–SG system was 6.4 ± 0.2 μm. It is noteworthy that the inner barrier layer of the PEO coating remains intact.

Micrographs of specimens with a sol–gel layer on top of a PEO layer post-treated with 8HQ are presented in Figure 5g,h. Similar to the observations on the PEO–SG surface, the sol–gel layer fills the pores and cracks in the PEO layer; however, here, the $Mg(8HQ)_2$ deposits emerge from the surface of sol–gel layer at certain points. Dehydration cracks in the sol–gel layer are also noticeable. Once again, no $Mg(8HQ)_2$ flaky deposits are observed in the cross-view, but minor bulky precipitates are visible inside the pores. The overall thickness increases to 8.2 ± 0.4 μm, with the sol–gel layer being thicker than in previous cases (2.9 ± 0.2 μm). The sol–gel thickening is attributed to the increase in surface roughness due to the presence of the $Mg(8HQ)_2$ precipitates. It is noteworthy that the PEO layer exhibits some dissolution (5.5 ± 0.7 μm), with the intermediate layer being less evident than in the PEO and PEO–SG systems (see labels in Figure 5).

3.1.3. Corrosion Test: Immersion Tests

Figure 6 shows digital macrographs of the PEO–8HQ–SG specimens with an artificial scribe after 14 days of immersion in a 0.5 wt.% NaCl solution, with PEO and PEO–SG specimens included as references. The stand-alone PEO coating reveals corrosion across the entire surface (Figure 6a), while the PEO–SG system demonstrates slightly improved performance. Nevertheless, there are noticeable signs of corrosion adjacent to the scratch and some localized damages away from it.

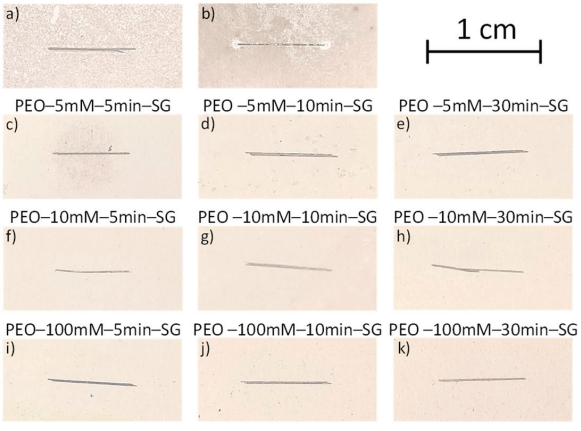

Figure 6. Surface appearance of (**a**) PEO, (**b**) PEO–SG, and (**c**–**k**) PEO–8HQ–SG scribed coatings after 14 days of immersion in a 0.5 wt.% NaCl solution at room temperature.

The PEO–8HQ–SG systems reveal significantly less corrosion damage than the reference coatings (Figure 6c–k), although the 5 mM 8HQ post-treatments show some corrosion around the scratch. This aligns with the EIS results, where post-treatments with low 8HQ concentration displayed a lower modulus of impedance after 24 h (e.g., PEO–5 mM–5 min–SG; 1.1×10^6 Ω cm^{-2} vs. PEO–10 mM–5 min–SG; 5.1×10^6 Ω cm^{-2}). The PEO–10 mM–30 min–SG coating stands out as one of the best performers and was selected for further characterization (Figure 6h). Therefore, these results suggest a positive effect of increasing the 8HQ concentration. It is proposed here that the dissolution of $Mg(8HQ)_2$ flakes and

their redeposition in regions with high pH (above 7, [45]) provides a self-healing ability, thereby enhancing the long-term corrosion resistance of the hybrid systems.

SEM/EDS results of the scribed systems after 14 days of immersion in 0.5 wt.% NaCl are presented in Figure 7 and Table 5. PEO–10 mM–30 min–SG was selected as a representative of PEO–8HQ–SG systems due to its superior corrosion performance.

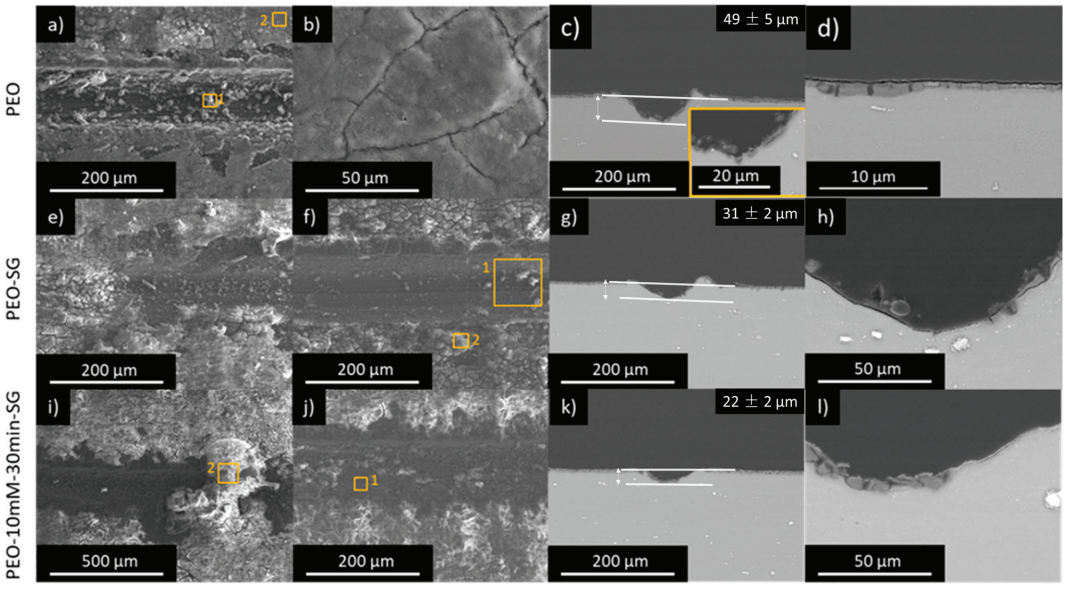

Figure 7. SEM microscopy images of (**a**–**d**) PEO, (**e**–**h**) PEO–SG, and (**i**–**l**) PEO–10 mM–30 min–SG scribed coatings after 14 days immersion test in 0.5 wt.% NaCl solution at room temperature.

Table 5. EDS analysis performed of the scribed PEO, PEO–SG and PEO–10 mM–30 min–SG coatings after 14 days immersion in 0.5 wt.% NaCl (in at.%).

Sample	Area	Elements							
		C	O	F	Na	Mg	Al	Si	K
PEO	1	18.4	59.7	1.4	0.4	14.8	1.0	4.3	–
	2	20.5	59.0	–	0.2	15.9	0.3	4.1	–
PEO–SG	1	22.2	47.0	0.1	0.5	28.3	0.9	1.0	–
	2	19.9	58.5	0.3	0.7	12.0	0.6	8.0	–
PEO–10 mM–30 min–SG	1	32.1	26.7	0.3	0.2	39.2	0.8	0.7	–
	2	11.5	64.7	–	0.1	22.3	0.3	0.1	0.8

The scratch in the PEO specimen shows voluminous corrosion products rich in O and Mg (Figure 7a, Table 5). As illustrated in Figure 7b, typical PEO micropores are no longer visible due to coating hydration, with some cracks formed as a consequence of partial dehydration. The cross-sectional view reveals that the corrosion attack is quite deep, especially at the centre of the defect where small pits are revealed (inset in Figure 7c). The incorporation of F and Si in these corrosion products is noteworthy. These elements can only be released from the PEO coating. It is believed that SiO_3^{2-} anions originating from the dissolution of the PEO coating combine with Mg^{2+} in the solution, forming precipitates such as $MgSiO_3$. Despite these self-repairing properties, the level of protection is insufficient, and some of the non-scribed areas also display corrosion damage, indicating failure of the inner barrier layer (Figure 7d).

In comparison with the stand-alone PEO coating, the PEO–SG system shows a lesser amount of corrosion products (Figure 7e–h). Corrosion products are primarily present at the artificial defect and its surroundings, with the cracked appearance of the sol–gel layer being particularly noticeable. The cross-sectional view of the defect (Figure 7g) reveals a small amount of corrosion products within the scribe. The EDS analysis at the centre of the scribe also shows some Si, which can originate from either the PEO coating or the sol–gel layer.

The PEO–10 mM–30 min–SG demonstrates the best corrosion behaviour, as evidenced by the shallow depth of the scratch (Figure 7i–l). The initial depth of the scratch is 20 ± 2 μm and it reaches values of 49 ± 5 μm, 31 ± 2 μm and 22 ± 2 μm for PEO, PEO–SG, and PEO–10 mM–30 min–SG, respectively, after 14 days of immersion. The presence of C and O along with Mg in EDS area 1 may be indicative of the presence of $Mg(8HQ)_2$ (Table 5).

3.1.4. Contact Angle

The contact angle measurements were conducted to evaluate the hydrophilicity/-phobicity of the developed coatings (Table 6 and Figure S3). All the coatings show hydrophilic behaviour with values below 66°. Minor differences are observed between the PEO and the sol–gel sealed samples. The inherent porosity of the PEO coating is strongly correlated with the obtained contact angle value, and its tendency to hydrate also contributes to this behaviour. The sol–gel layer significantly reduces the contribution of surface defects; therefore, the hydrophobic character is mostly related to the chemistry of the sol–gel surface rather than its roughness.

Table 6. Water contact angle measurements.

Sample	Contact Angle (°)
PEO	58 ± 3
PEO–SG	59 ± 0.4
PEO–5 mM–5 min–SG	63 ± 2
PEO–5 mM–10 min–SG	65.3 ± 0.9
PEO–5 mM–30 min–SG	59 ± 3
PEO–10 mM–5 min–SG	59.9 ± 0.9
PEO–10 mM–10 min–SG	58 ± 1
PEO–10 mM–30 min–SG	60.2 ± 0.5
PEO–100 mM–5 min–SG	59.9 ± 0.9
PEO–100 mM–10 min–SG	66 ± 3
PEO–100 mM–30 min–SG	58 ± 3

According to SEM and FTIR results, the PEO–8HQ–SG specimens should be more hydrophilic due to the following two factors: (i) disrupted sol–gel layer in the presence of $Mg(8HQ)_2$ flakes; and (ii) a lower degree of sol–gel polymerization in the presence of 8HQ, resulting in an increased number of hydrophilic silanol groups and, therefore, increased hydrophilicity [27,62]. However, as shown in Table 6, the difference between specimens with and without treatment is not significant.

3.2. Results on PEO/Sol–Gel(Inhibitor) Systems

3.2.1. Sol–Gel/8HQ Precursors

Sol–gel precursors with varying amounts of incorporated 8HQ corrosion inhibitor were prepared for sealing the PEO coating on the AZ31 alloy. The PEO processing was identical to that already described. Therefore, the inhibitor loading approach in this hybrid PEO/sol–gel system differs from that of the previous section, where the inhibitor was incorporated after PEO and before the sol–gel sealing.

The inhibitor was incorporated into the precursor by dissolving 8HQ in the aqueous solution, constituting 58% of the sol–gel. Figure 8 depicts the rheological characterization of the sol–gel precursors before polymerization. The shear rate increases with the shear

stress with a constant slope for all cases, indicating Newtonian behaviour. The presence of 8HQ causes a slight reduction in viscosity, with the 10 mM concentration yielding the lowest values. The viscosity values in mPa·s were as follows: 3.87 ± 0.02, 3.74 ± 0.02, 3.74 ± 0.02, and 3.71 ± 0.02 for SG, SG–1 mM, SG–5 mM, and SG–10 mM, respectively. These values suggest that the addition of 8HQ may slightly facilitate the penetration of the sol–gel precursor into the PEO coating.

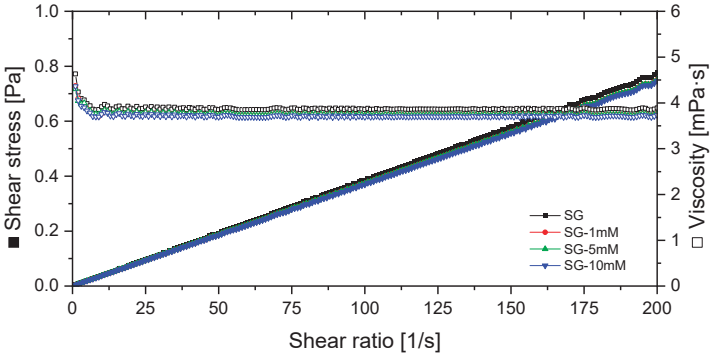

Figure 8. Flow curves for various 8HQ concentrations in the sol–gel solutions.

Figure 9 presents the UV–visible spectra of the sol–gel solutions with and without 8HQ. It is important to note that a 10 times dilution in deionized water was used to avoid detector saturation. The 8HQ (0.05 M) aqueous solution is included as a reference, showing a saturated peak at 250 nm and an absorption maximum at 305 nm, characteristic of the neutral prototropic species of 8HQ in water [38]. When 8HQ is incorporated into the acidic sol–gel precursor (pH 2 after hydrolysis) a new broad band emerges at 358 nm, corresponding to the lowest electronic transition of the acidic prototropic species of 8HQ (both O and N are protonated). The intensity of this band is higher for the precursor with the highest amount of 8HQ. Therefore, UV–Vis spectra confirm the presence of 8HQ in the sol–gel precursor.

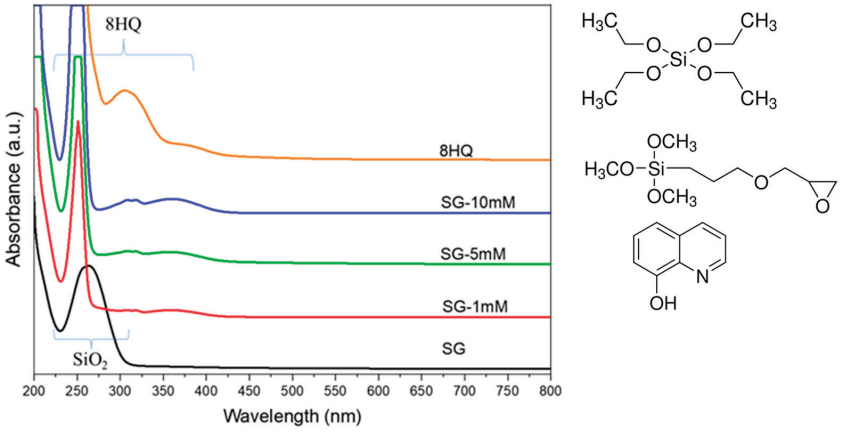

Figure 9. UV–Visible spectra of the sol–gel solutions for various concentrations of 8HQ corrosion inhibitor.

The SG solution without the inhibitor exhibits an absorption maximum at 263 nm, attributed here to electronic transitions of SiO_2 [63] due to partial polymerization of the precursor. Specifically, the absorption band is related to non-bridging oxygen hole centres [64].

3.2.2. Optimization of Sol–Gel Precursors Loaded with Inhibitor

Figure 10 depicts the impedance modulus of the examined coatings at 0.01 Hz in 0.5 wt.% NaCl up to 48 h of immersion, with reference impedance results for AZ31, PEO and PEO–SG included. After 2h of immersion, PEO–SG–8HQ specimens exhibit a lower impedance modulus than the inhibitor-free PEO–SG system. Notably, the impedance is lowest for the highest 8HQ concentration (PEO–SG–10 mM), with decreasing values for increasing 8HQ concentration in the sol–gel film. Despite this negative effect of 8HQ incorporation, PEO–SG–1 mM and PEO–SG–5 mM specimens demonstrate improved performance after 24 h (e.g., $|Z| > 10^7\ \Omega\ cm^2$ for PEO–SG–1 mM).

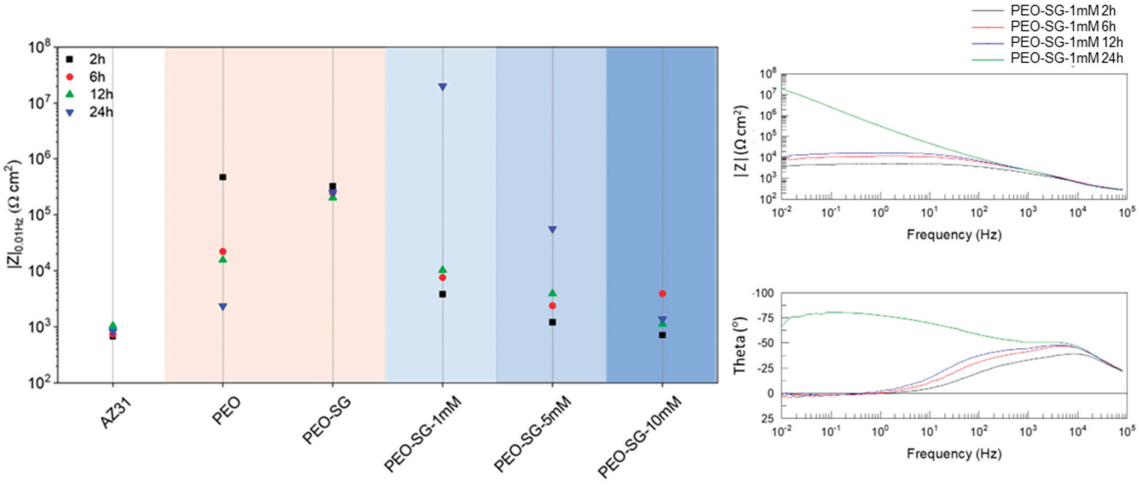

Figure 10. Scatter diagram of impedance modulus at 0.01 Hz of the PEO–SG coatings with 1, 5, and 10 mM 8HQ in the sol–gel layer up to 24 h of immersion in 0.5 wt.% NaCl. The diagram also includes the reference coatings (PEO and PEO–SG). An example of the Bode diagrams for one of the studied PEO–SG–8HQ coatings is also presented.

These findings suggest that 8HQ has conflicting effects when integrated into the sol–gel precursor. On one hand, it impedes sol–gel polymerization (see Section 3.2.3), decreasing the barrier effect against the corrosive medium. On the other hand, when added in a small concentration (1 mM), 8HQ significantly improves the impedance response after extended immersion times. The positive effect is likely associated with the precipitation of complexes formed between the 8HQ molecules released from the sol–gel layer and the Mg^{2+} ions originating from the corroding substrate.

3.2.3. Coating Morphology and Composition

FTIR results of PEO–SG–8HQ systems are depicted in Figure 11 and Table 7, with the spectrum of 8HQ powder included for reference. Si–O–Si bonds show their characteristic signals at 1493–960 and 960–724 cm^{-1} [27]. Once again, the prominent band at ~1034 cm^{-1}, associated with asymmetric vibrations, signifies successful sol–gel polymerization. Comparatively, the presence of 8HQ results in less intense Si–O–Si signals, suggesting that 8HQ has a detrimental effect on the polymerization process. Similarly, the band below 700 cm^{-1}, corresponding to Si–O–M bonds, is more intense for PEO–SG, indicating a better interaction between the PEO and the inhibitor-free sol–gel layer. Note that bands corresponding to the 8HQ molecule are nearly invisible when incorporated into the sol–gel layer.

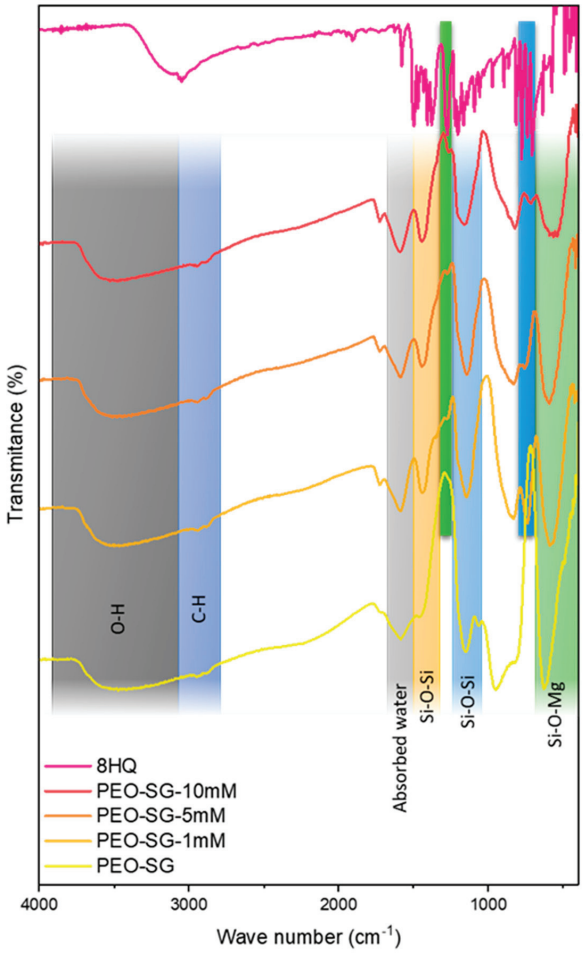

Figure 11. FTIR spectra of PEO–SG–8HQ systems on AZ31 alloy. The spectra of PEO–SG coating and 8HQ powder are included for reference.

Table 7. Band assignments for the FTIR spectra presented in Figure 11.

Band Wave Number (cm^{-1})	Assignation
3311	ν(OH) hydration of PEO
3150	stretching vibration for ν(OH) phenol
3049	aromatic ν(C–H) stretching
1625	ν(C=N) stretching
1579	ν(C=N) ring stretching vibration
1500	ν(C=C) stretching vibration
1471, 779	in-plane and out-of-plane deformations of CH_2 and CH_3 groups
1433	O–H plane bending
1274, 1246	ν(C–O) stretching vibrations
1165, 1138, 1093	N(C–N) stretching bands
1059, 1028	ν(N–O) stretching bands
974	–CH_2 rocking
896, 866	ν(C–C) bending vibration
740, 707	ν(C–H) out-of-plane bending band

Surface and cross-sectional SEM micrographs for the PEO–SG–1 mM specimen, representative of the studied systems, are presented in Figure 12. Some cracks are evident in the sol–gel layer (Figure 12a), but the porosity of the PEO layer is almost completely sealed (Figure 12b). The thickness of the sol–gel film is 2.1 ± 0.7 µm, as measured with the eddy current method, without significant influence from 8HQ. The EDS analysis of the sol–gel layer is consistent with previous results, but there is a relatively high amount of C, indicative of 8HQ incorporation in the sol–gel layer.

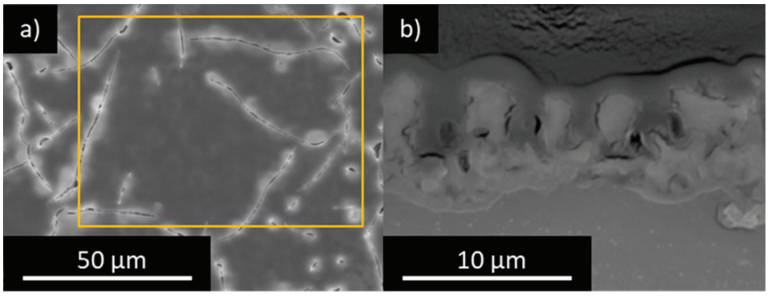

Figure 12. Scanning electron micrographs corresponding to the (**a**) planar and (**b**) cross-views of PEO–SG–1 mM coated AZ31. Results of the local EDS surface analysis of the coatings (at.%) are: C 36.3, O 38.8, Na 0.3, M 9.9, Al 0.3, Si 13.4, and K 0.1. The marked yellow rectangle represents area of EDS analysis.

3.2.4. Corrosion Test: Immersion Test

The surface appearance of PEO–SG–8HQ systems with an artificial scribe after 14 days in 0.5 wt.% NaCl is presented in Figure 13. Overall, the specimens show much better corrosion performance than PEO and PEO–SG (see Figure 6a,b). However, some small corrosion spots are visible at the scratch for the PEO–SG–5 mM and PEO–SG–10 mM specimens. Therefore, the addition of 8HQ into the sol–gel precursor improves the long-term corrosion resistance of hybrid PEO/SG systems, although their performance is slightly compromised when the concentration of 8HQ is above 1 mM.

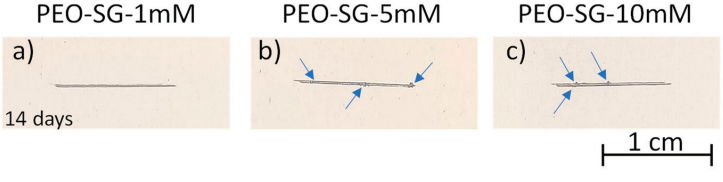

Figure 13. Surface appearance of PEO–SG–8HQ scribed coatings after 14 days of immersion in 0.5 wt.% NaCl solution at room temperature. Arrows mark the location of corrosion spots.

The PEO–SG–1 mM specimen, which combines the highest |Z| value with best surface appearance after the scribe test, was selected for SEM/EDS examination (Figure 14 and Table 8). As shown in the plan-view, the scribe shows some corrosion products and there is cracking of the sol–gel layer, attributed to water permeation and hydrolysis of the Si–O–Si bonds [65]. (Figure 14a,b). However, the depth of the attack is significantly less than that of the inhibitor-free systems (PEO, PEO–SG in Figure 14), being very similar to the original depth of the defect (~20 µm, Figure 14c). In the regions away from the scratch, it can be seen that the cracks penetrate the entire sol–gel thickness, although the PEO coating remains relatively unaffected, with only some signs of hydration (Figure 14d).

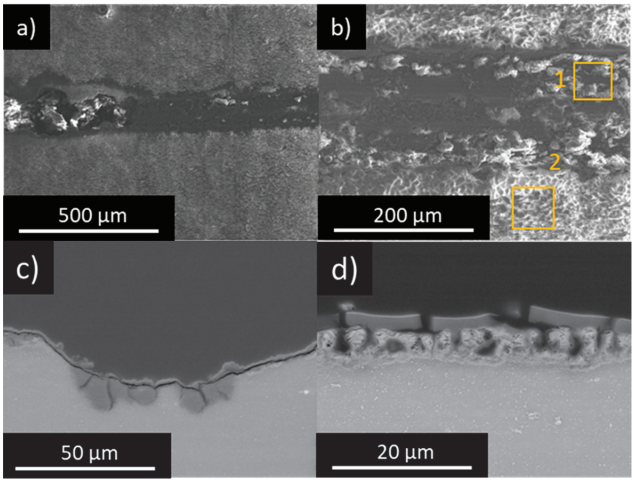

Figure 14. SEM microscopy images of PEO–SG–1mM scribed coatings after immersion in 0.5 wt.% NaCl solution at room temperature for 14 days. (**a**,**b**) General view and detail of the scribe. (**c**) Cross-section of the scribe and (**d**) cross-section away from the scribe.

Table 8. EDS analysis performed of the scribed PEO–SG–1 mM coating after 14 days immersion in 0.5 wt.% NaCl (in at.%). See Figure 14 for locations.

Spectrum	Elements							
	C	O	F	Na	Mg	Al	Si	Cl
1	15.6	60.0	1.2	0.1	21.5	0.5	0.8	0.3
2	24.2	53.7	0.8	0.3	13.4	0.2	7.4	–

EDS analysis on the scribe's surface shows a relatively high level of O, suggesting the formation of magnesium hydroxide as the main corrosion product. There is also some Si and F, which can originate from chemical dissolution of the PEO and/or sol–gel films (in case of Si), and C, although no $Mg(8HQ)_2$ flakes were detected on the surface of the scratch.

4. Discussion

PEO coatings are known to be susceptible to corrosion in saline environments due to the limited protection provided by MgO and the absence of self-healing ability. To address this drawback, various strategies have been employed to incorporate inhibitors into PEO coatings. This study explores two approaches: inhibitor impregnation of the PEO layer before sol–gel sealing and the modification of the sol–gel precursor with the organic inhibitor 8HQ. The selection of 8HQ was made following an initial screening process using EIS tests.

The inhibitory effect of 8HQ is linked to the formation of insoluble metal chelates on the surface [29]. This mechanism has been demonstrated on materials such as aluminium [65] and copper [37]. On magnesium surfaces, $Mg(8HQ)_2$ precipitates in alkaline solutions in the form of large flakes [45]. In the present study, these flakes were clearly visible on the surface of AZ31 alloy after a 14-day immersion in a 0.5 wt.% NaCl solution containing 0.05 M 8HQ. A recent study by Vaghefinazari et al. [45] also highlighted the formation of $Mg(8HQ)_2$ flakes on the surface of a PEO-coated AZ21 alloy, leading to improved corrosion resistance. Precisely, in the present work, the immersion post-treatment approach was successfully applied to incorporate 8HQ into the so-called hybrid PEO–8HQ–SG systems.

The second approach for incorporating 8HQ, denoted as PEO–SG–8HQ, aligns with findings from earlier studies [29], where sol–gel formulations doped with 8HQ demon-

strated enhanced corrosion resistance on AZ31. The innovation in this study lies in the combination of the barrier properties of the PEO layer, the sealing effect of the sol–gel, and the active protection imparted by the 8HQ inhibitor. In this context, 8HQ is proposed to function through a release–precipitation mechanism, effectively impeding corrosion in areas where damage has occurred.

In the present study, a comparison between the PEO–8HQ–SG and PEO–SG–8HQ strategies revealed that, irrespective of the approach, the incorporation of 8HQ improved the long-term corrosion resistance. This effect was particularly evident in scribed specimens, indicating an active protection mechanism in the presence of 8HQ. Both PEO–8HQ–SG and PEO–SG–8HQ systems demonstrated similar outcomes, displaying minimal corrosion depth at the scratch site after 14 days of immersion in 0.5 wt.% NaCl. The influence of variables such as inhibitor post-treatment time and 8HQ concentration did not exhibit a clear trend. Nonetheless, the PEO–100 mM–30 min–SG and PEO–SG–1 mM configurations emerged as among the top performers, considering EIS results and corrosion tests with scribed specimens. Additional research is needed to identify the advantages and disadvantages of the strategies under study. Specifically, the assessment should include parameters such as inhibitor release rate, compatibility with paints and inhibitor effectiveness when employed in conjunction with alternative sol–gel formulations.

Figure 15 shows the schematics illustrating the proposed protection mechanisms for the developed hybrid systems. In the case of the PEO–8HQ–SG combination, obtained through immersion post-treatment in an 8HQ solution followed by sol–gel sealing, a composite structure is formed, with flakes of $Mg(8HQ)_2$ embedded in the sol–gel matrix and protruding at certain locations (Figure 15a). These areas exhibit greater heterogeneity and show the presence of small cracks. On the other hand, the PEO–SG–8HQ combination does not exhibit $Mg(8HQ)_2$ flakes (Figure 15b). However, UV–visible and FTIR spectra provided sufficient evidence of successful incorporation of 8HQ into the sol–gel film. Remarkably, FTIR results indicated a lower degree of sol–gel polymerization and interaction between the sol–gel layer and the PEO coating when 8HQ was added to the precursor.

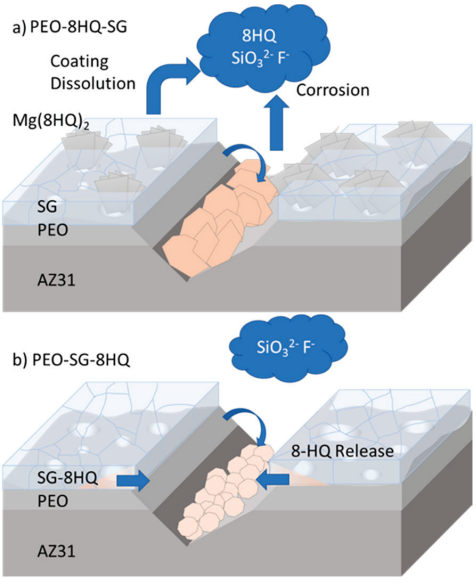

Figure 15. Schematic illustration of the corrosion mechanism for scratched (**a**) PEO–8HQ–SG and (**b**) PEO–SG–8HQ coatings on AZ31 Mg alloy.

In light of the findings from this study, when mechanical damage occurs in PEO–8HQ–SG and PEO–SG–8HQ systems, the following steps are likely to take place:

1. Corrosion occurs at the location of the scribe with liberation of Mg^{2+} ions.

$$Mg(s) \rightarrow Mg^{2+}(aq) + 2e^{-}$$

2. Water uptake and hydrolysis of the Si–O–Si bonds causes cracking of the sol–gel layer and Si release [66].

$$SiO_2(s) + 2H_2O(l) \rightarrow Si(OH)_4(aq)$$

3. Chemical dissolution of the PEO coating with liberation of $SiO_3{}^{2-}$, Mg^{2+}, and F^{-} ions occurs when acidic pH of the sol–gel solution penetrates across pores of the layer. Some dissolution is also expected to occur in the damaged regions next to the scratch. This chemical dissolution process is well documented in the literature [67,68].

$$MgO(s) + 2H^{+}(aq) \rightarrow Mg^{2+}(aq) + H_2O(l)$$

$$Mg_2SiO_4(s) + 4H^{+}(aq) \rightarrow 2Mg^{2+}(aq) + SiO_3{}^{2-}(aq) + H_2O(l)$$

4. In neutral or slightly acidic conditions, $8HQ^{-}$ ions are released from the $Mg(8HQ)_2$ flakes [29] in the PEO–8HQ–SG system and from the bulk of the sol–gel layer [69] in the PEO–SG–8HQ system. Subsequently, as the pH increases over the cathodic regions due to the water reduction reaction, $8HQ^{-}$ combines with Mg^{2+} and precipitates as $Mg(8HQ)_2$. These precipitates remain insoluble under the highly alkaline conditions developed in the scratch region [45,70].
5. The combination of Mg^{2+} with other species in the solution ($SiO_3{}^{2-}$, F^{-}, OH^{-}) leads to the formation of additional precipitates, further contributing to the delay of the corrosion attack. This precipitation is more prominent at the location of the scratch due to a higher amount of Mg^{2+} ions and confinement of the solution. EDS analyses in this study have demonstrated the presence of Si and F on the surface of the scribe. However, additional studies are required to confirm the precipitation of $Mg(8HQ)_2$ in the damaged areas, for example, through testing for longer immersion times.

5. Conclusions

Key conclusions drawn from the investigation into inhibitor loading on PEO/sol–gel systems include:

- Hydrogen evolution tests identified 8HQ as the most effective organic corrosion inhibitor for the AZ31 alloy in a saline solution, operating through the formation of insoluble $Mg(8HQ)_2$ flakes.
- Successful incorporation of 8HQ inhibitor species into hybrid PEO/sol–gel systems was achieved through two strategies: (i) inhibitor post-treatment before sol–gel sealing (PEO–8HQ–SG); (ii) inhibitor loading into the sol–gel precursor (PEO–SG–8HQ).
- The PEO–8HQ–SG system exhibited a composite structure with embedded $Mg(8HQ)_2$ flakes in the SG film, while the PEO–SG–8HQ incorporated 8HQ into its structure, albeit with a reduction in the cross–linking of the sol–gel layer.
- Both PEO–8HQ–SG and PEO–SG–8HQ systems demonstrated comparable results, displaying minimal depth of corrosion attack at the scratch location after 14 days of immersion in 0.5 wt.% NaCl. This improvement primarily stemmed from an active protection mechanism involving the release and precipitation of 8HQ species and other species ($SiO_3{}^{2-}$, F^{-}).
- Notably, the PEO–10 mM–30 min–SG and PEO–SG–1 mM coatings emerged as top performers in the tests involving EIS and immersion with scribed specimens.

Supplementary Materials: The following supporting information can be downloaded at: https://www.mdpi.com/article/10.3390/coatings14010084/s1. Table S1: Kinetic laws, with and without inhibitor, calculated from hydrogen measurements. Table S2: Results of the local EDS surface analysis of the coatings (at.%). Figure S1: Volume of hydrogen evolved from the cathodic reaction during immersion in 0.5 wt.% NaCl solution and surface appearance of the exposed area after the test. Figure S2: (a) Surface morphology of bare AZ31 exposed to 0.5 wt.% NaCl containing 8HQ after 14 days. A higher magnification view of the flakes is presented in (b). Marked areas corresponds to the EDS analysis collected in Table S2. Figure S3: Water contact angle measurements: (a) PEO, (b) PEO–SG, and (c–k) PEO–8HQ–SG.

Author Contributions: Conceptualization, B.P., E.M., M.-G.O., M.M. and R.A.; Formal analysis, B.P., M.M. and R.A.; Funding acquisition, M.-G.O., M.M. and R.A.; Investigation, B.P.; Methodology, B.P., M.-G.O., M.M. and R.A.; Project administration, M.-G.O., M.M. and R.A.; Resources, M.-G.O., M.M. and R.A.; Writing—original draft, B.P.; Writing—review and editing, E.M., M.-G.O. and R.A. All authors have read and agreed to the published version of the manuscript.

Funding: The authors gratefully acknowledge the support of PID2021-124341OB-C22 project (MCIN/AEI/FEDER, EU) and the Materials Institute of UMONS. M. Mohedano is grateful for the support of RYC-2017 21843.

Institutional Review Board Statement: Not applicable.

Data Availability Statement: All data presented in this work is available in Docta Complutense repository https://docta.ucm.es/handle/20.500.14352/16 (accessed on 5 December 2023).

Conflicts of Interest: The authors declare no conflicts of interest.

References

1. Oak Ridge National Laboratory. *Transportation Energy Data Book*, 40th ed.; Oak Ridge National Laboratory: Oak Ridge, TN, USA, 2022.
2. Demirci, E.E.; Arslan, E.; Ezirmik, K.V.; Baran, Ö.; Totik, Y.; Efeoglu, İ. Investigation of wear, corrosion and tribocorrosion properties of AZ91 Mg alloy coated by micro arc oxidation process in the different electrolyte solutions. *Thin Solid Film.* **2013**, *528*, 116–122. [CrossRef]
3. Shang, W.; Chen, B.; Shi, X.; Chen, Y.; Xiao, X. Electrochemical corrosion behavior of composite MAO/sol–gel coatings on magnesium alloy AZ91D using combined micro-arc oxidation and sol–gel technique. *J. Alloys Compd.* **2009**, *474*, 541–545. [CrossRef]
4. Guo, X.; Du, K.; Guo, Q.; Wang, Y.; Wang, F. Experimental study of corrosion protection of a three-layer film on AZ31B Mg alloy. *Corros. Sci.* **2012**, *65*, 367–375. [CrossRef]
5. Chen, Q.; Zheng, Y.; Dong, S.; Chen, X.-B.; Dong, J. Effects of fluoride ions as electrolyte additives for a PEO/Ni-P composite coating onto Mg alloy AZ31B. *Surf. Coat. Technol.* **2021**, *417*, 126883. [CrossRef]
6. Wierzbicka, E.; Vaghefinazari, B.; Lamaka, S.V.; Zheludkevich, M.L.; Mohedano, M.; Moreno, L.; Visser, P.; Rodriguez, A.; Velasco, J.; Arrabal, R.; et al. Flash-PEO as an alternative to chromate conversion coatings for corrosion protection of Mg alloy. *Corros. Sci.* **2021**, *180*, 109189. [CrossRef]
7. Oleshko, O.; Kornienko, V.; Kyrylenko, S.; Simka, W.; Husak, Y.; Oleshko, T.; Dryhval, B. Physical and Chemical Characterization of the Magnesium Surface Modified by Plasma Electrolytic Oxidation—Influence of Immersion in Simulated Body Fluid. In Proceedings of the 2020 IEEE 10th International Conference Nanomaterials: Applications Properties (NAP), Sumy, Ukraine, 9–13 November 2022; p. 02BA11-01. [CrossRef]
8. Ghanbari, A.; Bordbar-Khiabani, A.; Warchomicka, F.; Sommitsch, C.; Yarmand, B.; Zamanian, A. PEO/Polymer hybrid coatings on magnesium alloy to improve biodegradation and biocompatibility properties. *Surf. Interfaces* **2023**, *36*, 102495. [CrossRef]
9. Xu, L.; Fu, X.; Su, H.; Sun, H.; Li, R.; Wan, Y. Corrosion and tribocorrosion protection of AZ31B Mg alloy by a hydrothermally treated PEO/chitosan composite coating. *Prog. Org. Coat.* **2022**, *170*, 107002. [CrossRef]
10. Sampatirao, H.; Amruthaluru, S.; Chennampalli, P.; Lingamaneni, R.K.; Nagumothu, R. Fabrication of ceramic coatings on the biodegradable ZM21 magnesium alloy by PEO coupled EPD followed by laser texturing process. *J. Magnes. Alloys* **2021**, *9*, 910–926. [CrossRef]
11. Li, Y.; Lu, F.; Li, H.; Zhu, W.; Pan, H.; Tan, G.; Lao, Y.; Ning, C.; Ni, G. Corrosion mechanism of micro-arc oxidation treated biocompatible AZ31 magnesium alloy in simulated body fluid. *Prog. Nat. Sci. Mater. Int.* **2014**, *24*, 516–522. [CrossRef]
12. Pezzato, L.; Rigon, M.; Martucci, A.; Brunelli, K.; Dabalà, M. Plasma Electrolytic Oxidation (PEO) as pre-treatment for sol–gel coating on aluminum and magnesium alloys. *Surf. Coat. Technol.* **2019**, *366*, 114–123. [CrossRef]
13. Pezzato, L.; Babbolin, R.; Cerchier, P.; Marigo, M.; Dolcet, P.; Dabalà, M.; Brunelli, K. Sealing of PEO coated AZ91magnesium alloy using solutions containing neodymium. *Corros. Sci.* **2020**, *173*, 108741. [CrossRef]

14. Gnedenkov, A.; Sinebryukhov, S.; Nomerovskii, A.; Filonina, V.; Ustinov, A.; Gnedenkov, S. Design of self-healing PEO-based protective layers containing in-situ grown LDH loaded with inhibitor on the MA8 magnesium alloy. *J. Magnes. Alloys* **2023**, *11*, 3688–3709. [CrossRef]
15. Telmenbayar, L.; Gopal Ramu, A.; Erdenebat, T.-O.; Choi, D. Anticorrosive lanthanum embedded PEO/GPTMS coating on magnesium alloy by plasma electrolytic oxidation with silanization. *Mater. Today Commun.* **2022**, *33*, 104662. [CrossRef]
16. Fernández-Hernán, J.P.; López, A.J.; Torres, B.; Martínez-Campos, E.; Matykina, E.; Rams, J. Anticorrosion and cytocompatibility assessment of graphene-doped hybrid silica and plasma electrolytic oxidation coatings for biomedical applications. *ACS Biomater. Sci. Eng.* **2021**, *7*, 5861–5877. [CrossRef]
17. Chen, Y.; Lu, X.; Lamaka, S.V.; Ju, P.; Blawert, C.; Zhang, T.; Wang, F.; Zheludkevich, M.L. Active protection of Mg alloy by composite PEO coating loaded with corrosion inhibitors. *Appl. Surf. Sci.* **2020**, *504*, 144462. [CrossRef]
18. Ivanou, D.; Yasakau, K.; Kallip, S.; Lisenkov, A.D.; Starykevich, M.; Lamaka, S.V.; Ferreira, M.; Zheludkevich, M.L. Active corrosion protection coating for ZE41 magnesium alloy created by combining PEO and sol–gel techniques. *RSC Adv.* **2016**, *6*, 12553–12560. [CrossRef]
19. Li, T.; Li, L.; Qi, J.; Chen, F. Corrosion protection of Ti6Al4V by a composite coating with a plasma electrolytic oxidation layer and sol–gel layer filled with graphene oxide. *Prog. Org. Coat.* **2020**, *144*, 105632. [CrossRef]
20. Joo, J.; Kim, D.; Moon, H.-S.; Kim, K.; Lee, J. Durable Anti-Corrosive Oil-Impregnated Porous Surface of Magnesium Alloy by Plasma Electrolytic Oxidation with Hydrothermal Treatment. *Appl. Surf. Sci.* **2020**, *509*, 145361. [CrossRef]
21. Qian, Z.; Wang, S.; Wu, Z. Corrosion Behavior Study of AZ31B magnesium Alloy by Sol–gel Silica-based Hybrid. *Coating. Int. J. Electrochem. Sci.* **2017**, *12*, 8269–8279. [CrossRef]
22. Toorani, M.; Aliofkhazraei, M. Review of electrochemical properties of hybrid coating systems on Mg with plasma electrolytic oxidation process as pretreatment. *Surf. Interfaces* **2019**, *14*, 262–295. [CrossRef]
23. Zheng, S.; Li, J. Inorganic-organic sol gel hybrid coatings for corrosion protection of metals. *J. Sol–Gel Sci. Technol.* **2010**, *54*, 174–187. [CrossRef]
24. Malayoglu, U.; Tekin, K.; Shrestha, S. Influence of post-treatment on the corrosion resistance of PEO coated AM50B and AM60B Mg alloys. *Surf. Coat. Technol.* **2010**, *205*, 1793–1798. [CrossRef]
25. Figueira, R.; Silva, C.; Pereira, E. Organic-inorganic hybrid sol–gel coatings for metal corrosion protection: A review of recent progress. *J. Coat. Technol. Res.* **2014**, *12*, 1–35. [CrossRef]
26. Wen, J.; Wilkes, G. Organic/Inorganic Hybrid Network Materials by the Sol–gel Approach. *Chem. Mater.* **1996**, *8*, 1667–1681. [CrossRef]
27. Akbarzadeh, S.; Santos, L.; Vitry, V.; Paint, Y.; Olivier, M.G. Improvement of the corrosion performance of AA2024 alloy by a duplex PEO/clay modified sol–gel nanocomposite coating. *Surf. Coat. Technol.* **2022**, *434*, 128168. [CrossRef]
28. Balgude, D.; Sabnis, A. Sol–gel derived hybrid coatings as an environment friendly surface treatment for corrosion protection of metals and their alloys. *J. Sol–Gel Sci. Technol.* **2012**, *64*, 124–134. [CrossRef]
29. Galio, A.; Lamaka, S.V.; Zheludkevich, M.L.; Dick, L.; Muller, I.; Ferreira, M. Inhibitor-doped sol–gel coatings for corrosion protection of magnesium alloy AZ31. *Surf. Coat. Technol.* **2010**, *204*, 1479–1486. [CrossRef]
30. Kartsonakis, I.; Balaskas, A.; Koumoulos, E.P.; Charitidis, C.A.; Kordas, G. Evaluation of corrosion resistance of magnesium alloy ZK10 coated with hybrid organic–inorganic film including containers. *Corros. Sci.* **2012**, *65*, 325–333. [CrossRef]
31. Lim, T.; Ryu, H.; Hong, S.-H. Electrochemical corrosion properties of CeO2-containing coatings on AZ31 magnesium alloys prepared by plasma electrolytic oxidation. *Corros. Sci.* **2012**, *62*, 104–111. [CrossRef]
32. Barranco, V.; Carmona, N.; Galvan, J.C.; Grobelny, M.; Kwiatkowski, L.; Velasco, M.A. Electrochemical study of tailored sol–gel thin films as pre-treatment prior to organic coating for AZ91 magnesium alloy. *Prog. Org. Coat.* **2010**, *68*, 347–354. [CrossRef]
33. Zanotto, F.; Grassi, V.; Frignani, A.; Zucchi, F. Protection of the AZ31 magnesium alloy with cerium modified silane coatings. *Mater. Chem. Phys.* **2011**, *129*, 1–8. [CrossRef]
34. Montemor, M.F.; Ferreira, M.G.S. Electrochemical study of modified bis-[triethoxysilylpropyl] tetrasulfide silane films applied on the AZ31 Mg alloy. *Electrochim. Acta* **2007**, *52*, 7486–7495. [CrossRef]
35. Fajardo, S.; Frankel, G.S. Gravimetric method for hydrogen evolution measurements on dissolving magnesium. *J. Electrochem. Soc.* **2015**, *162*, C693–C701. [CrossRef]
36. Shangyi, S.; Zuo, Y.; Zhao, X. The effects of 8-hydroxyquinoline on corrosion performance of a Mg-rich coating on AZ91D magnesium alloy. *Corros. Sci.* **2013**, *76*, 275–283. [CrossRef]
37. Cicileo, G.P.; Rosales, B.M.; Varela, F.E.; Vilche, J.R. Inhibitory action of 8-Hydroxyquinoline on the copper corrosion process. *Corros. Sci.* **1998**, *40*, 1915–1926. [CrossRef]
38. Tang, L.; Li, X.; Si, Y.; Mu, G.; Liu, G. The synergistic inhibition between 8-hydroxyquinoline and chloride ion for the corrosion of cold rolled steel in 0.5M sulfuric acid. *Mater. Chem. Phys.* **2006**, *95*, 29–38. [CrossRef]
39. Lamaka, S.V.; Zheludkevich, M.L.; Yasakau, K.A.; Montemor, M.F.; Ferreira, M.G.S. High effective organic corrosion inhibitors for 2024 aluminium alloy. *Electrochim. Acta* **2007**, *52*, 7231–7247. [CrossRef]
40. Yasakau, K.A.; Zheludkevich, M.L.; Karavai, O.V.; Ferreira, M.G.S. Influence of inhibitor addition on the corrosion protection performance of sol–gel coatings on AA2024. *Prog. Org. Coat.* **2008**, *63*, 352–361. [CrossRef]

41. Stankiewicz, A. Self-healing nanocoatings for protection against steel corrosion. In *Nanotechnology in Eco-Efficient Construction*; Pacheco-Torgal, F., Diamanti, M.V., Nazari, A., Granqvist, C.G., Pruna, A., Amirkhanian, S., Eds.; Woodhead Publishing: Cambridge, UK, 2019; pp. 303–335. [CrossRef]
42. Snihirova, D.; Lamaka, S.V.; Taheri, P.; Mol, J.M.C.; Montemor, M.F. Comparison of the synergistic effects of inhibitor mixtures tailored for enhanced corrosion protection of bare and coated AA2024-T3. *Surf. Coat. Technol.* **2016**, *303*, 342–351. [CrossRef]
43. Tian, Z.; Shi, H.; Liu, F.; Xu, S.; Han, E.-H. Inhibiting effect of 8-hydroxyquinoline on the corrosion of silane-based sol–gel coatings on AA 2024-T3. *Prog. Org. Coat.* **2015**, *82*, 81–90. [CrossRef]
44. Arunoday, M.; Premkumar, K.P.; Kumar, R.; Subasri, R. Multifunctional, environmental coatings on AA2024 by combining anodization with sol–gel process. *Ceram. Int.* **2022**, *48*, 10969–10978. [CrossRef]
45. Vaghefinazari, B.; Lamaka, S.V.; Blawert, C.; Serdechnova, M.; Scharnagl, N.; Karlova, P.; Wieland, D.C.; Zheludkevich, M. Exploring the corrosion inhibition mechanism of 8-hydroxyquinoline for a PEO-coated magnesium alloy. *Corros. Sci.* **2022**, *203*, 110344. [CrossRef]
46. Arrabal, R.; Matykina, E.; Hashimoto, T.; Skeldon, P.; Thompson, G.E. Characterization of AC PEO coatings on magnesium alloys. *Surf. Coat. Technol.* **2009**, *203*, 2207–2220. [CrossRef]
47. Arrabal, R.; Matykina, E.; Pardo, A.; Merino, M.C.; Paucar, K.; Mohedano, M.; Casajús, P. Corrosion behaviour of AZ91D and AM50 magnesium alloys with Nd and Gd additions in humid environments. *Corros. Sci.* **2012**, *55*, 351–362. [CrossRef]
48. Pardo, A.; Casajús, P.; Mohedano, M.; Coy, A.E.; Viejo, F.; Torres, B.; Matykina, E. Corrosion protection of Mg/Al alloys by thermal sprayed aluminium coatings. *Appl. Surf. Sci.* **2009**, *255*, 6968–6977. [CrossRef]
49. Lamaka, S.V.; Shchukin, D.G.; Andreeva, D.V.; Zheludkevich, M.L.; Möhwald, H.; Ferreira, M.G.S. Sol–gel/Polyelectrolyte Active Corrosion Protection System. *Adv. Funct. Mater.* **2008**, *18*, 3137–3147. [CrossRef]
50. Abbas, R.; Jarad, A.; Nafliu, I.; Nechifor, A. Synthesis, Characterization and Antibacterial Activity from Mixed Ligand Complexes of 8-Hydroxyquinoline and Tributylphosphine for Some Metal Ions. *Rev. Chim.* **2019**, *70*, 36–40. [CrossRef]
51. Karuppanan, A.; Govindan, A.B.; Perumalsamy, R. Growth of <201> 8-hydroxyquinoline organic crystal by Czochralski method and its characterizations. *J. Therm. Anal. Calorim.* **2012**, *110*, 1333–1339. [CrossRef]
52. Kumar, S.; Kumar, B. Growth of an 8-hydroxyquinoline single crystal by a modified Czochralski growth technique, and crystal characterization. *CrystEngComm* **2018**, *20*, 624–630. [CrossRef]
53. Noor, S.A.M.; Ahmad, A.; Talib, I.A.; Rahman, M.Y.A. Morphology, chemical interaction, and conductivity of a PEO-ENR50 based on solid polymer electrolyte. *Ionics* **2009**, *16*, 161–170. [CrossRef]
54. Hernández-Barrios, C.A.; Cuao, C.A.; Jaimes, M.A.; Coy, A.E.; Viejo, F. Effect of the catalyst concentration, the immersion time and the aging time on the morphology, composition and corrosion performance of TEOS-GPTMS sol–gel coatings deposited on the AZ31 magnesium alloy. *Surf. Coat. Technol.* **2017**, *325*, 257–269. [CrossRef]
55. Narayanan, S.; Lee, M.H. A simple strategy to modify the porous structure of plasma electrolytic oxidation coatings on magnesium. *RSC Adv.* **2016**, *6*, 16100–16114. [CrossRef]
56. Xu, J.; Yu, Q.; Liu, J.; Yin, Y.; Han, Y.; Li, B. Preparation and characterization of polyfluoroaniline/organosiloxane hybrid films. *J. Sol–Gel Sci. Technol.* **2013**, *69*, 580–585. [CrossRef]
57. Molaeipour, P.; Ramezanzadeh Karati, M.; Ramezanzadeh, B. Stachys byzantina extract: A green biocompatible molecules source for graphene skeletons generation on the carbon steel for superior corrosion mitigation. *Bioelectrochemistry* **2021**, *143*, 107970. [CrossRef] [PubMed]
58. Tan, A.; Soutar, A.; Annergren, I.F.; Liu, Y.N. Multilayer Sol–Gel Coatings for Corrosion Protection of Magnesium. *Surf. Coat. Technology.* **2005**, *198*, 478–482. [CrossRef]
59. Mohedano, M.; Blawert, C.; Zheludkevich, M.L. Silicate-based Plasma Electrolytic Oxidation (PEO) coatings with incorporated CeO2 particles on AM50 magnesium alloy. *Mater. Des.* **2015**, *86*, 735–744. [CrossRef]
60. Alabbasi, A.; Kannan, M.B.; Walter, R.; Störmer, M.; Blawert, C. Performance of pulsed constant current silicate-based PEO coating on pure magnesium in simulated body fluid. *Mater. Lett.* **2013**, *106*, 18–21. [CrossRef]
61. Gnedenkov, S.V.; Khrisanfova, O.A.; Zavidnaya, A.G.; Sinebryukhov, S.L.; Egorkin, V.S.; Nistratova, M.V.; Yerokhin, A.; Matthews, A. PEO coatings obtained on an Mg–Mn type alloy under unipolar and bipolar modes in silicate-containing electrolytes. *Surf. Coat. Technol.* **2010**, *204*, 2316–2322. [CrossRef]
62. Nguyen, V.N.; Perrin, F.; Vernet, J.L. Water permeability of organic/inorganic hybrid coatings prepared by sol–gel method: A comparison between gravimetric and capacitance measurements and evaluation of non-Fickian sorption models. *Corros. Sci.* **2005**, *47*, 397–412. [CrossRef]
63. Salh, R. Defect Related Luminescence in Silicon Dioxide Network: A Review. In *Crystalline Silicon—Properties and Uses*; InTech: London, UK, 2011. [CrossRef]
64. Zhao, W.; Ji, W.; Zhang, Y.; Du, L.; Wang, S. A competitive fluorescence quenching-based immunoassay for bisphenol A employing functionalized silica nanoparticles and nanogold. *RSC Adv.* **2016**, *6*, 38950–38956. [CrossRef]
65. Hernández-Escolano, M.; Juan-Díaz, M.; Martínez-Ibáñez, M.; Jiménez-Morales, A.; Goñi, I.; Gurruchaga, M.; Suay, J. The design and characterisation of sol–gel coatings for the controlled-release of active molecules. *J. Sol–Gel Sci. Technol.* **2012**, *64*, 442–451. [CrossRef]
66. Spinthaki, A.; Kamaratou, M.; Matheis, J.; Disci, D.; Hater, W. The precipitation of "aluminum silicate" under geothermal stresses: Identifying its idiosyncrasies. *Geothermics* **2021**, *92*, 102060. [CrossRef]

67. Mingo, B.; Arrabal, R.; Mohedano, M.; Llamazares, Y.; Matykina, E.; Yerokhin, A.; Pardo, A. Influence of sealing post-treatments on the corrosion resistance of PEO coated AZ91 magnesium alloy. *Appl. Surf. Sci.* **2018**, *433*, 653–667. [CrossRef]
68. Mohedano, M.; Blawert, C.; Zheludkevich, M.L. Cerium-based sealing of PEO coated AM50 magnesium alloy. *Surf. Coat. Technol.* **2015**, *269*, 145–154. [CrossRef]
69. El Ojaimi, M.; Thummel, R.P. Polydentate Analogues of 8-Hydroxyquinoline and Their Complexes with Ruthenium. *Inorg. Chem.* **2011**, *50*, 10966–10973. [CrossRef]
70. Prachayasittikul, V.; Prachayasittikul, S.; Ruchirawat, S.; Prachayasittikul, V. 8-Hydroxyquinolines: A review of their metal chelating properties and medicinal applications. *Drug Des. Dev. Ther.* **2013**, *7*, 1157–1178. [CrossRef]

coatings

MDPI

Article

Influence of Cathodic Polarization on Plasma Electrolytic Oxidation of Magnesium and AZ31 and AZ91 Magnesium Alloys

Zhengzhou Le, Zihua Liu, Xiaorui He, Yulin Cheng, Panfeng Hu and Yingliang Cheng *

College of Materials Science and Engineering, Hunan University, Changsha 410082, China
* Correspondence: chengyingliang@hnu.edu.cn; Tel.: +86-731-88821727; Fax: +86-731-88823554

Abstract: In this study, the influence of cathodic polarization on the plasma electrolytic oxidation (PEO) behaviors of pure magnesium and AZ31 and AZ91 magnesium alloys with varied Al alloying contents was systematically examined in a dilute alkaline silicate electrolyte by adjusting the cathodic-to-anodic current density ratio ($R = j_c/j_a$) from 0 to 3.2. The results show that moderate cathodic polarization (R = 0.6) led to the thickest coatings on the Mg and Mg alloys, and the coatings grew in an outward-and-inward mode compared with the inward growth at R = 0. Excessive cathodic polarization (high R ratios) differently influenced the PEO behaviors of the magnesium alloys. For the pure magnesium and AZ31 alloy, the coatings blistered or peeled off when the $R \geq 0.9$. However, the tolerance to cathodic polarization was significantly improved for the AZ91 Mg alloy. The coatings were undamaged even with the highest R ratio of 3.2, and their compactness was further improved as the R ratio increased to 0.9 and 1.2. An increase in cathodic polarization led to a reduction in the anodic potential and spark softening but did not result in an improvement in the coating quality. Optical emission spectroscopy identified two spectral lines at 559.79 and 570.11 nm, which are assigned to the Mg species but not found in databases or the literature. The corrosion and wear resistance of the PEO coatings were also investigated. The coating formed on the AZ91 magnesium alloy at R = 1.2 displayed the narrowest wear track due to its high compactness.

Keywords: plasma electrolyte oxidation; Mg and Mg alloys; cathodic polarization; soft sparking; wear

Citation: Le, Z.; Liu, Z.; He, X.; Cheng, Y.; Hu, P.; Cheng, Y. Influence of Cathodic Polarization on Plasma Electrolytic Oxidation of Magnesium and AZ31 and AZ91 Magnesium Alloys. *Coatings* **2023**, *13*, 1736. https://doi.org/10.3390/coatings13101736

Academic Editor: Vincent Ji

Received: 2 September 2023
Revised: 20 September 2023
Accepted: 1 October 2023
Published: 6 October 2023

1. Introduction

Magnesium (Mg) and magnesium alloys, as the lightest structural materials, have many advantages, including light weight, high stiffness and strength, excellent dimensional stability, good electromagnetic shielding and damping characteristics [1–3]. For decades, a lot of research work has been devoted to magnesium and its alloys, aimed at improving their roles in engineering applications [4–7]. However, the low hardness and high chemical activity of magnesium and its alloys seriously limit their wide-spread applications, especially in aggressive environments. Surface treatment is one of the effective methods to improve the surface properties of magnesium alloys. Plasma electrolytic oxidation (PEO) technology is an advanced surface treatment technology that was developed from traditional anodization [8,9]. By using this technology, metals and their alloys, such as Al [10], Mg [11–13], Ti [14,15], Zr [16], Ta [17] and Cu [18,19], can grow a layer of oxide ceramic coating on the surface. These coatings have strong bonding with the substrate, good wear and corrosion resistance, thermal stability and high hardness [8,9].

Unlike conventional anodization, which has a simple electrochemical mechanism that involves the migration of anions and cations to form a film [20–22], PEO works at potentials above the breakdown potential of the oxide coating, resulting in the occurrence of plasma discharges, which trigger complex physical–chemical processes other than electrochemical reactions, including the plasma chemical process, thermal process and sintering [23–26]. Hussein et al. [27] described the growth of magnesium alloy PEO coatings as a process in

which dielectric breakdown occurs at the weak point of the oxide, and then the molten oxide is ejected from the coating/substrate interface, rapidly solidified and recrystallized when it reaches the coating/electrolyte interface. Such repeated steps form a thick coating with complex compounds. However, Zhu et al. [28] found that a slow growth process controlled by an ion migration mechanism helps the formation of the barrier layer in the PEO of pure aluminum. PEO discharges are normally accompanied by the release of large amounts of gases, which inevitably cause pores and various defects within the coatings [29–33].

The introduction of cathodic polarization (such as AC, bipolar pulses) can improve the homogeneity, thickness and quality of PEO coatings [34–36]. In particular, when the ratio of the cathodic-to-anodic current or charge ($R = j_c/j_a$ or $R = Q_c/Q_a$) is greater than 1, a so-called "soft sparking" PEO regime will be triggered for aluminum and its alloys [37–39]. The soft sparking occurs after the coating has grown to a certain thickness and is normally manifested by an obvious drop in the anodic potential and decreases in the acoustic sound emissions and micro-discharge size [34,37,39]. The occurrence of soft sparks can result in a faster coating growth rate, fewer defects and higher uniformity [34].

The mechanisms of cathodic polarization and soft sparking are very complex and are still the key research topics in PEO. Yerokhin et al. reported that the main role of cathodic polarization is to interrupt the continuous anode discharge, and to provide a gas environment for plasma discharge and the possible cathodic-discharge phenomenon [26]. Sah et al. [40,41] proposed that cathodic polarization can randomize the position of the subsequent anodic breakdown, avoiding repeated breakdowns at the same position and the formation of large discharge channels. Hussein et al. [35] believe that the application of cathodic currents can weaken the strong plasma discharges. Cheng et al. [36] think that cathodic hydrogen evolution can promote the transport of electrolyte ions to the electrode surface, thereby facilitating the formation of uniform and thick coatings.

The explanation for the phenomenon of soft sparking is more complex. Regarding the drop in the anodic potential in the soft-sparking state, Gębarowski and Pietrzyk considered that it is due to the large amount of hydrogen evolution in the cathodic stage, which destroys the barrier layer [38]. Rogov et al. [42] proposed the local acidification hypothesis and the "active zone" theory to explain the related phenomena of the soft-sparking process. They believe that once the oxide coating reaches a certain thickness, localized acidification eliminates voltage barriers at the oxide coating/electrolyte interface, resulting in a drop in the anodic potential. Martin et al. [43] found that increased cathodic polarization leads to delayed spark discharges, and they thus propose a mechanism of electrical-charge accumulation. Martin et al. [43] and Cheng et al. [39] found that there is an optimum cathodic-to-anodic current or charge ratio (R) for the soft-sparking effect in aluminum alloys, with a value of approximately R = 1.2. Beyond this ratio, the coatings become thinner or even cannot form [39,43]. Interestingly, Cheng et al. showed that the anodic potential does not necessarily decrease under the optimum R value [39]. In addition, He et al. [44] demonstrate that the internal temperature of the coating under the condition of soft sparking is higher than those under conventional discharges, leading to the formation of more alpha alumina phase and black copper (II) oxide. The reason is that the amorphous outer layer formed under soft sparking and the amorphous barrier layer at the oxide/substrate interface can effectively prevent the heat from escaping out of the coating system. In addition, Martin et al. also found that increasing the anodic current density and frequency is beneficial for establishing an earlier soft-sparking state [45]. A recent study found that adding carbon nanotubes to the electrolyte can also lead to the earlier occurrence of soft sparking [46].

The research on the phenomenon of soft sparking mainly focuses on Al and its alloys. Due to the advantages of soft sparking on Al alloys, people have also strived to achieve the soft-sparking effect on other metals. However, the research on soft sparking on other metals is not satisfactory and has not achieved similar effects to those of Al alloys [35,47–50]. Rogov et al. [42] found that the relatively consistent soft-sparking phenomenon will appear

in those metals forming insulating oxide on the surface, such as Mg, Al, Zr and Ta, while the typical anodic-potential drop of soft sparking will not appear in those metals forming the semiconductor oxide, such as Ti and Nb, but a certain degree of spark softening can also be observed on these metals. At present, there are also a few literature works dedicated to achieving soft sparking on Mg. Tjiang et al. [47] triggered soft sparking on pure magnesium in a solution containing zirconium K2ZrF6 at R = ~1.16, resulting in a PEO coating with fewer pores and a relatively dense structure. However, there were still cracks and pores in the coating. Arrabal [50] studied different types of magnesium alloys at R = ~1.2 and found that the occurrence time of the soft sparking depends on the type of magnesium alloy matrix, and defects in the coating are improved. However, the densification of the inner layer on the Mg alloy surface has not been completed. Maryam [51,52] triggered the soft sparking of an AZ31 magnesium alloy by changing the cathodic duty cycle, resulting in a coating with good wear and corrosion resistance. Pan et al. [53] and Gao et al. [54] indicated that hydrogen evolution via the appropriate cathodic current promotes ion diffusion and exchange, but excessive cathodic current can hinder the movement of the required anions in the coating, and a large amount of hydrogen can even damage the integrity of the coating. In addition, the PEO coatings of magnesium and magnesium alloys obtained under the aforementioned soft sparking still have some pores and are not dense compared to the effect of soft sparking on aluminum alloys. Even if pure magnesium is in a soft-sparking state, the coating will peel off after 60 min, as confirmed by Tjiang [47]. This also indicates that there is a difference in the growth of oxide coatings between magnesium and aluminum in the soft-sparking state.

Surveying the PEO literature on Mg-based alloys, Tsai [55] found that the strategy of softened plasma works best on the coatings on Mg alloys when the electrolytic solution contains a substantial amount of aluminate, commonly $NaAlO_2$. Therefore, the authors believe that researchers essentially resort to the rectifying aluminum oxide on Mg-based metals in replicating soft sparking and its associated dense inner layer. For the electrolytic solutions without aluminate, Tsai thought that the cathodic component in the waveform is ineffective in obtaining a dense inner layer by citing several works on the PEO of Mg alloys [56–59].

In this work, the PEO behaviors of pure magnesium and AZ31 and AZ91 magnesium alloys were systematically studied at different R ratios in a typical silicate solution, which is used in the study of the soft-sparking phenomenon on Al alloy. The Al contents of these three alloys increased sequentially, which can be used to investigate the effect of the Al content on the PEO behavior of Mg substrate.

2. Experimental

2.1. Materials

Samples with a dimension of 10 mm × 20 mm × 4 mm were cut from the rolled plates of pure magnesium (Mg 99 wt.%) and AZ31 magnesium alloy (nominal composition in wt.%: Al 3%, Zn 1%, Mn 0.2% and Mg balance). Samples of the same dimension for the AZ91 magnesium alloy (nominal composition in wt.%: Al 9%, Zn 1%, Mn 0.2% and Mg balance) were cut from an extruded rod with a diameter of 27 mm. Each specimen was then connected with a copper wire and mounted with resin, leaving a working area of 10 mm × 20 mm. The working surface of each specimen was successively ground to a 2000-grit SiC finish, degreased in ethanol, rinsed in distilled water and dried in a stream of warm air.

2.2. PEO

PEO was carried out in a 1 L glass cell equipped with mechanical stirring and a water-cooling system. The temperature of the cooling water was set at 20 °C. The electrolyte was 5 g L^{-1} $Na_2SiO_3 \cdot 9H_2O$ + 1 g L^{-1} KOH, which was prepared by dissolving analytical-grade chemicals (Sinopharm Chemical Reagent Co., Ltd., Shanghai, China) in distilled water. During the PEO process, the anode was the magnesium samples, and the cathode was a

large stainless-steel plate. The power supply was a 5 KW pulse electrical source (MAO-5D, Pulsetech Electrical Co., Ltd., Chengdu, China). The duty cycle of the waveform was 20% and the frequency was 100 Hz. An oscilloscope (Tektronix TDS 1002C-SC) was used to monitor the current waveforms during PEO. The applied average anodic current density was 0.172 A cm^{-2}, and the average cathodic current densities were kept at 0, 0.103, 0.155, 0.206, 0.275 and 0.550 A cm^{-2}, constituting cathodic-to-anodic current density ratios (Rs) of 0, 0.6, 0.9, 1.2, 1.6 and 3.2, respectively.

2.3. Characterization

Real-time imaging and optical emission spectroscopy (OES) were employed to investigate the plasma discharges during PEO. A digital camera (Canon Powershot G5) was used to record the plasma discharges and the appearance of the PEO coatings. The thicknesses of the coatings were measured by using an eddy-current thickness gauge (TT260, Times Group, Beijing, China). The OES spectra were acquired using a spectrometer (Ocean Optics, HR4000) in the wavelength range of 250–710 nm. The system for the spectrum collection was placed outside of the quartz window of the glass vessel, with the distance between the collimating lens and the specimen fixed at ~10 mm. An integration time of 2 s was adopted to record the light emissions in this study. Atomic and ionic lines in the collected spectra were identified using the NIST online spectral database [60].

The corrosion resistances of the substrates and PEO coatings were evaluated via polarization curves. Polarization curves were produced using an electrochemical workstation (CHI660C). The corrosive medium was a 3.5 wt.% NaCl solution. The configuration of a 3-electrode system was employed. The working electrode was the samples with exposed areas of 2 cm^2, the counter electrode was a large platinum plate and the reference electrode was a saturated calomel electrode (SCE). To eliminate the influence of the crevices between the specimen edges and mounting resin on the measured polarization curves, the edges of all the samples were sealed with paraffin. Prior to the polarization curves, the open-circuit potential (OCP) was recorded for 1800 s in order to obtain a stable state. The polarization curves were recorded between −0.5 V and +1.5 V with reference to the OCP, using a scanning rate of 1 mV/s.

A field-emission scanning electron microscope (SEM) (QUANTA FEG 250) with energy-dispersive X-ray spectroscopy (EDS) was used to examine the morphologies and compositions of the coatings. The cross sections of the coatings were observed via the conventional mounting and polishing method. All samples were sputtered with platinum or gold for 180 s before SEM.

In order to investigate the growth mechanism of the coating, a small piece of rectangular magnesium metal was encapsulated together with the aforementioned 10 mm × 20 mm × 4 mm pure magnesium specimen with epoxy resin. The small piece of magnesium was very close to the pure magnesium specimen but was kept insulated from it. The two were then polished to the same plane with 5000-grit SiC paper. After that, the small piece of magnesium was protected by 704 silicon rubber. Subsequently, the pure magnesium specimen was subjected to PEO treatment. A cross section of the specimen was prepared to observe the relative position of the PEO coating to the original surface (the protected magnesium piece) under SEM.

A Rigaku D/max 2500 X-ray diffractometer (XRD) (Cu K_α radiation, 40 kV, 250 mA) was used to detect the phase compositions of the coatings. The scanning range is 10–80° in 2θ and the scanning rate is 4°/min.

The friction performances of the substrates and coatings were analyzed via dry sliding wear tests. For the pure magnesium and AZ31 alloy, PEO coatings formed under R = 0 and R = 0.6 for 2400 s were tested. Coatings formed under R = 0, 0.6 and 1.2 for 2400 s were tested for the AZ91 magnesium alloy. Tests were performed on the HT1000 friction and wear tribometer (Zhongke Kaihua Technology Co., Ltd., Lanzhou, China). The load is 5 N, and the counter material is a Cr steel ball with a diameter of 4 mm and a hardness value of 62 HRC. The wear radius was set to 2 mm, the rotation speed was 318 rpm and the

sliding time was 1200 s. After the wear tests, the cross-section profiles of the wear scars were examined via the probe attached to an SFT-2M pin-disc-friction and wear-testing instrument (Zhongke Kaihua Technology Co., Ltd., Lanzhou, China). Wear rates were calculated by dividing the calculated wear volume losses by the total sliding distance and load.

3. Results

3.1. Cell Potential–Time Responses

Figure 1 shows the cell potential–time responses of the pure magnesium and AZ31 and AZ 91 magnesium alloys during PEO under R ratios from 0 to 3.2 for 2400 s. In the initial period, the anodic potential of the pure magnesium at different R values rapidly increased at a nearly linear rate to ~500 V. Then, the rising rate of the anodic potential was significantly reduced, accompanied by the appearance of sparks. However, in the subsequent PEO stage, there were differences in the cell potential–time curves for different R values. The anodic potentials of R = 0 and R = 0.6 increased slowly to the final values of 577 V and 631 V at 2400 s, respectively. During most of the PEO period, the potential at R = 0.6 remained higher than that at R = 0. However, the potential at R = 0.9 did not rise continuously. At the PEO time of 760 s, the potential at R = 0.9 suddenly decreased from ~571 V to ~224 V, accompanied by a weakening of the plasma discharges. Afterwards, the potential remained at relatively low values (~200 V), with fluctuations being observed, and this stage lasted for ~385 s. At ~1145 s, the anodic potential rose again, reaching 524 V at 1242 s, accompanied by the reappearance of strong sparks. Afterwards, the potential decreased again at ~1857 s. Visual observation showed that the decrease in the potential was due to the destruction of the coating. However, after the coating was completely detached from the sample, strong sparks reappeared and the potential rose again. The cell potential–time responses of the pure magnesium at higher R values were similar to that at R = 0.9, except for an earlier decrease at greater R values. In addition, the cell potential at R = 1.6 did not show recoveries after the potential dropped.

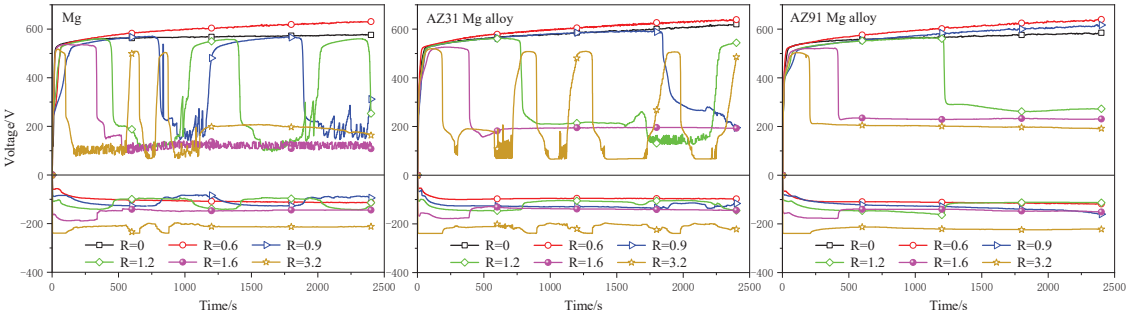

Figure 1. Cell potential–time curves during PEO of the three different metals under different R values: (**a**) pure magnesium; (**b**) AZ31 magnesium alloy; (**c**) AZ91 magnesium alloy.

The cell potential–time responses at different R values for the AZ31 magnesium alloy were similar to those of the pure magnesium. The anodic potential at R = 0.6 was higher than that at R = 0, with final values of 637 V and 616 V at 2400 s, respectively. When the R $\geq$ 0.9, the potential of the AZ31 magnesium alloy underwent a sudden drop or multiple drop-and-rise cycles at the later stage of the PEO treatment.

Unlike the pure magnesium and AZ31 magnesium alloy, the cell potential–time responses of the AZ91 magnesium alloy did not show a decrease in the anodic potential at R = 0.9. At the termination of the PEO, the anodic-potential values were 585 V (R = 0), 641 V (R = 0.6) and 616 V (R = 0.9) at 2400 s, respectively. When R $\geq$ 1.2, the AZ91 magnesium

alloy also experienced a decrease in the anodic potential, but there was no oscillation in the anodic potential.

The amplitudes of the cathodic potentials were much lower than those of the positive ones. In R values ranging from 0.6 to 3.2, the cathodic potentials of the three samples were normally lower than −250 V. The cathodic potentials were usually more negative at higher R values.

3.2. Real-Time Imaging of Sparks

Figure 2 shows the plasma discharges of the pure magnesium and AZ91 magnesium alloy at different R values during the PEO process. The images were recorded at an exposure time of 1/100 s. When the pure magnesium was treated without cathodic polarization (R = 0), numerous small sparks were seen on the metal surface during the initial stage, such as at 46 s. The number of sparks decreased but their intensity increased with time, as shown by the image at 534 s. However, after 534 s, the sparks were basically kept in a similar state. The increase in the spark intensity was usually accompanied by louder acoustic emissions, and a few green sparks could be observed. The green sparks may have been related to the excitation of the Mg in the plasma. The discharging behavior of the pure magnesium at R = 0.6 was similar to that at R = 0, but, in the later stage of the PEO, the sizes of the sparks were significantly larger than those in the condition without cathodic polarization. At the further increased cathodic polarization of R = 1.2, the initial sparks of the pure magnesium at 134 s were similar to those at R = 0 and 0.6. However, the spark intensity weakened at 448 s, accompanied by the drop in the anodic potential to ~490 V, despite a few large sparks at the right-hand edge of the sample. The anodic potential further dropped to 198 V at 778 s, with the near extinguishment of the sparks. At this moment, it was observed with the naked eye that the coating almost peeled off from the surface. However, the potential rose again after the coating was completely peeled off, and strong sparks occurred again, as shown by the image at 1271 s. At 2400 s, the potential dropped again, accompanied by a decrease in the spark intensity, as the formed coating underwent another flaking-off and growth cycle.

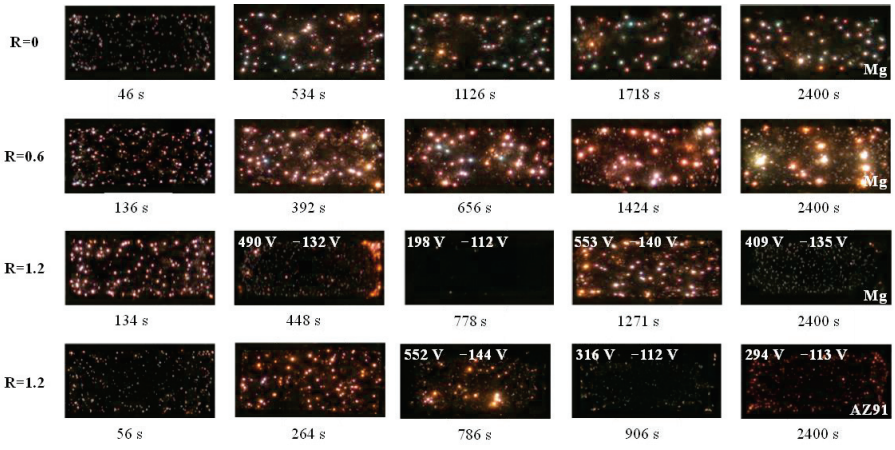

Figure 2. Plasma discharges recorded by the digital camera at different stages of PEO for pure magnesium and AZ91 magnesium alloy under different R ratios. The exposure time of the camera was 1/100 s. For some images under R = 1.2, the anodic and cathodic potentials are also indicated. The size of the samples is 10 mm × 20 mm.

The relationship between the spark discharges and R ratio for the AZ31 magnesium alloy was largely similar to that of the pure magnesium; thus, the plasma discharges of the AZ31 alloy are not shown here. The AZ91 magnesium alloy did not exhibit a potential drop

until R = 0.9, and the discharging behavior was similar to that of the pure magnesium at R values of 0 or 0.6. Figure 2 only includes the discharges under R = 1.2 for the AZ91 alloy. The plasma discharges intensified from 0 to 786 s, as was the case for the pure magnesium at R = 0.6. However, the plasma discharges drastically weakened at 906 s and 2400 s, accompanied by the decrease in the anodic potential.

3.3. OES

Figure 3 shows the OES spectra recorded at 600 s for the pure magnesium and AZ31 and AZ91 magnesium alloys at R = 0 and R = 0.6. The results indicate that, in the sodium silicate solution, the strongest emission lines collected for the pure magnesium at R = 0 were the Na I lines at 588.99 and 589.59 nm. Characteristic emission lines of other elements from the electrolyte, such as O II and Há, Hâ and OH, were also present on the spectrum. In addition, multiple spectral lines of Mg, which came from the substrate, were recorded. It is worth noting that we attribute the two spectral lines at 559.79 and 570.11 nm to Mg. However, databases and the literature do not show the presence of spectral lines at the two positions for species of Mg. The assignment to the Mg lines is based on our deduction. We collected the emission spectra of pure Al in the same solution, showing the absence of the two spectral lines. Therefore, it can be ruled out that these two spectral lines came from the electrolyte. As a result, we can only attribute the two spectral lines to the substrate metal (Mg) at present. The spectral lines collected for the pure magnesium at R = 0.6 are almost identical to those at R = 0.

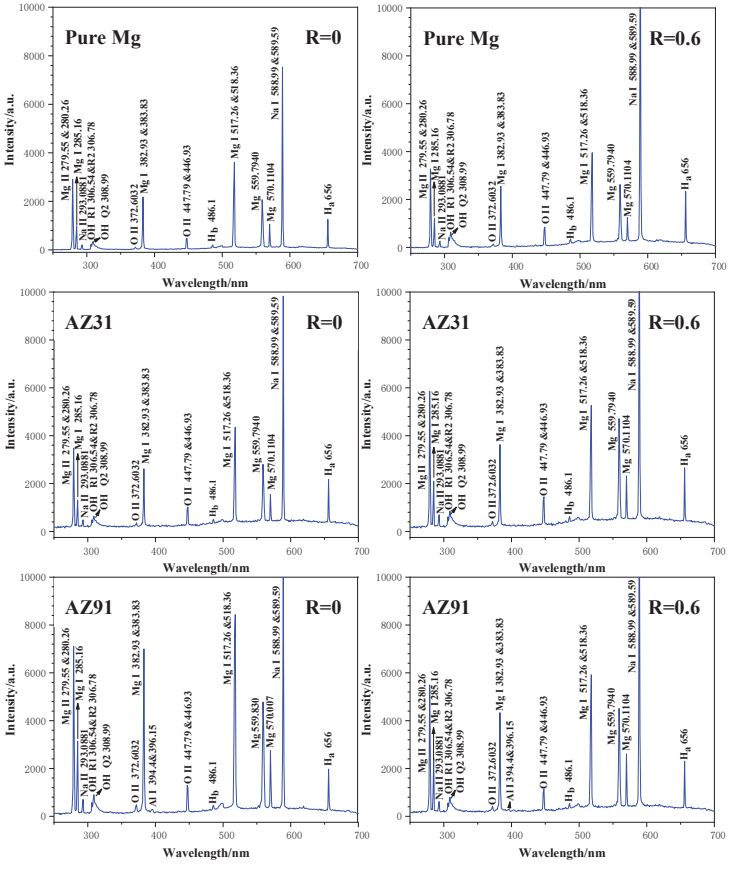

Figure 3. OES spectra recorded at 600 s for PEO of Mg and AZ31 and AZ91 magnesium alloys at R = 0 and R = 0.6.

The emission spectra for the AZ31 and AZ91 magnesium alloys at R = 0 and R = 0.6 are almost the same as that of the pure magnesium. The only difference is that the AZ91 magnesium alloy had weak Al I doublet peaks at 394.4 and 396.1 nm at R = 0, which had even lower intensities at R = 0.6. The results of this experiment showed that the OES spectra were not sensitive to the alloying element of Al.

3.4. Macroscopic Appearances

The appearances of PEO coatings on the pure magnesium and AZ31 and AZ91 magnesium alloys at different R ratios and treatment times, taken by a digital camera, are displayed in Figure 4. When there was no cathodic polarization (i.e., R = 0), many pits were observed on the surface of the PEO coating of pure magnesium after 600 s. The density of the pits was relatively high at the edge of the sample, and, over time, they gradually extended towards the center. When cathodic current was applied, such as at R = 0.6, the surface porosity of the coatings decreased significantly compared to that at R = 0. Further increasing the cathodic polarization to R = 0.9 led to more compact coatings in the early PEO stages. However, long-term-coating surfaces may experience blistering, detachment and re-oxidation. The coating at 1200 s was grown via the secondary oxidation of the pure magnesium after the preliminary coating was completely detached, and the coating at 2400 s once again exhibited blistering on the surface. At R = 1.2, the PEO coatings on the pure magnesium blistered, broke and oxidized again, just like the behavior at R = 0.9. However, the time to blistering was significantly shortened (see the image at 600 s for R = 1.2).

The performance of the AZ31 magnesium alloy under different R ratios was basically consistent with that of the pure magnesium. Uniform and dense coatings were formed only at R = 0.6. Further increasing the cathodic polarization resulted in blistering, cracking and re-oxidation.

The PEO of the AZ91 magnesium alloy showed numerous pits on the coatings at R = 0, which were similar to those on the pure magnesium and AZ31 alloy. The coatings formed on the AZ91 alloy at R = 0.6 also improved in uniformity. However, the AZ91 magnesium alloy responded differently to cathodic polarization at higher R ratios. The coatings formed under higher R ratios did not exhibit blistering or detachment as those in the first two alloys. The appearances of the coatings grown on the alloys under the highest R value of 3.2 are shown in Figure 4. No significant damage to the coatings was found throughout any of the entire PEO process.

3.5. Coating Thickness

Figure 5 shows the relationship between the coating thickness and time during the PEO of the pure magnesium and AZ31 and AZ91 magnesium alloys. Overall, for the three samples, the maximum thicknesses at 2400 s under R = 0.6 were 106.4, 109.5 and 124.2 μm, respectively. However, the PEO of the pure magnesium and magnesium alloys without cathodic polarization showed significantly reduced thicknesses at 2400 s, being 45.6, 94.2 and 67.1 μm, respectively. Therefore, the application of cathodic polarization at R = 0.6 significantly increased the thicknesses of the coatings. The thickness data on the pure magnesium and AZ31 magnesium alloy are absent at long times, due to the damage of the coatings. However, the thickness data for the AZ91 magnesium alloy are complete, as the coatings were not damaged in this case. In an R range from 0.6 to 1.2, the thickness of the coatings on the AZ91 alloy at a specific time was higher than that under R = 0. However, the coating thicknesses obtained at too-high R values (1.6 and 3.2) were smaller than those of the coatings formed under R = 0.

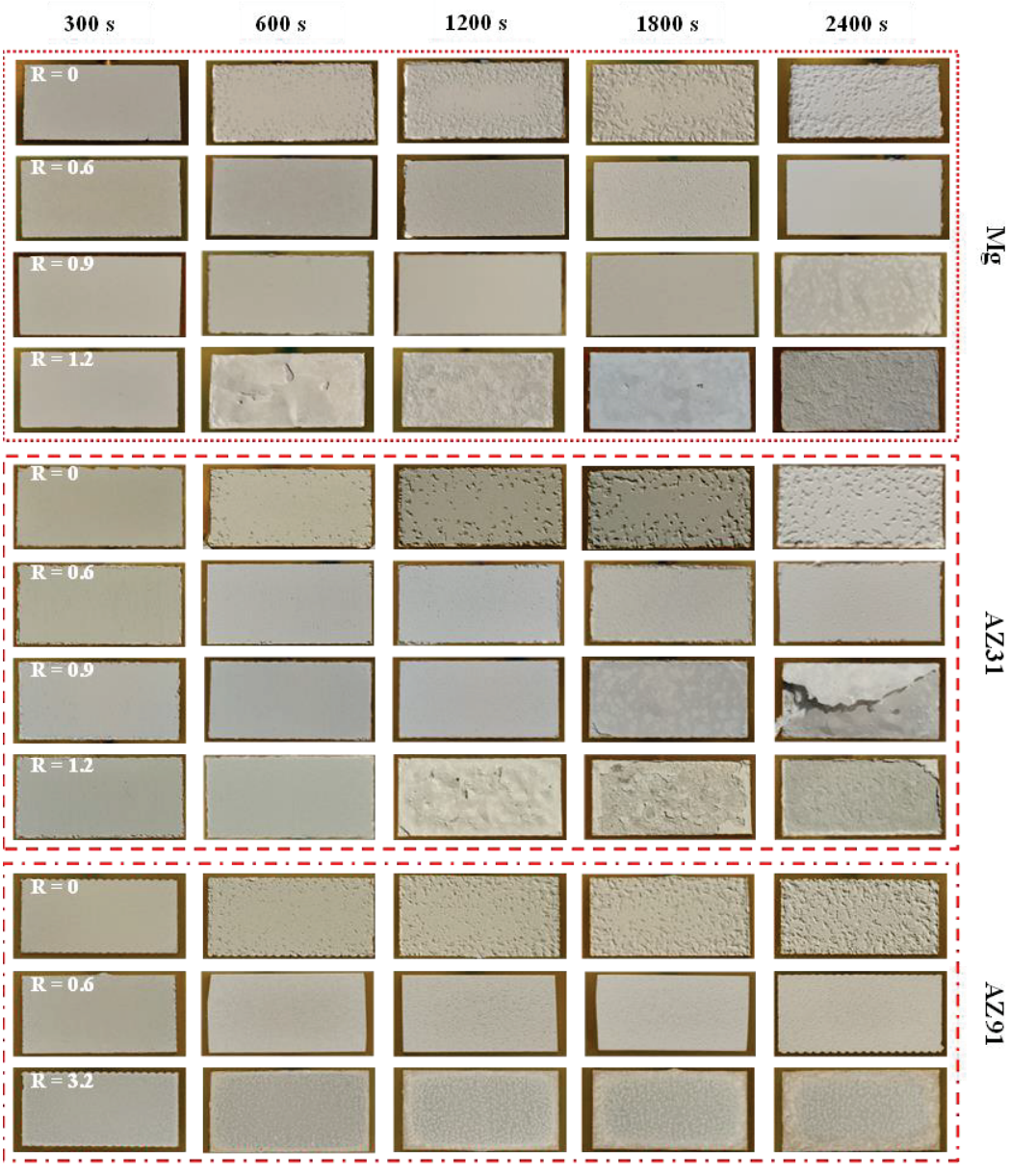

Figure 4. The appearances of pure magnesium and AZ31 and AZ91 magnesium alloys after being PEO-treated for different times under different R ratios. The size of the samples is 10 mm × 20 mm.

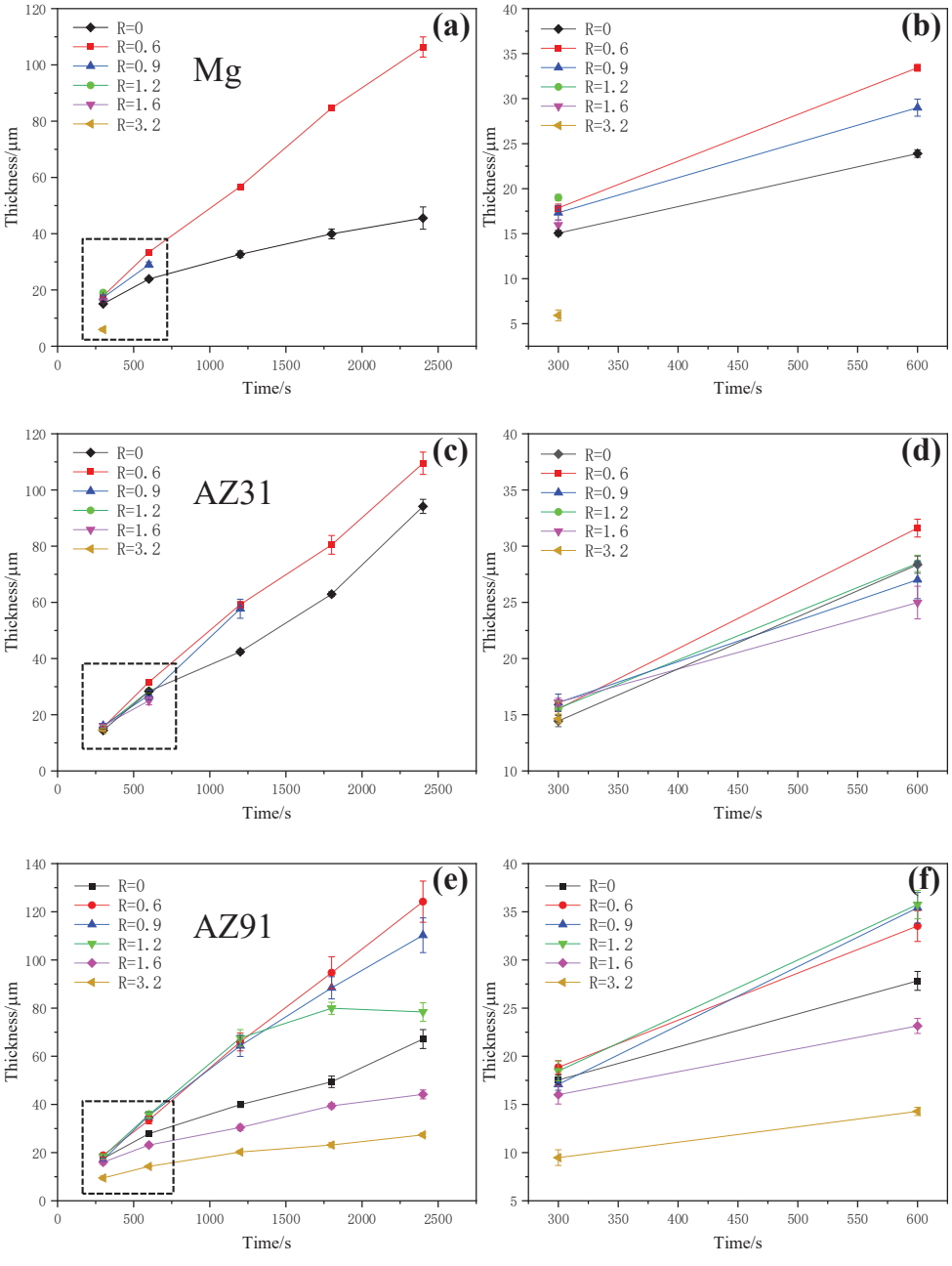

Figure 5. Thicknesses (eddy-current method) as a function of time for the PEO coatings formed under different R ratios on (**a**) pure magnesium and (**c**) AZ31 and (**e**) AZ91 magnesium alloys. (**b**,**d**,**f**) are the boxed regions in (**a**,**c**,**e**), respectively.

3.6. SEM Morphology

Figure 6 shows the surfaces of the coatings formed for 600 s at different R values on the pure magnesium and AZ31 and AZ91 magnesium alloys. It can be seen that at 600 s,

the oxide coatings of the pure magnesium and AZ31 and AZ91 magnesium alloys exhibited similar morphologies in most conditions, with irregular or pancake-shaped solidified oxides distributed on the coating surfaces, and there were also many circular or irregular pores on the surfaces. Points A and B in Figure 6a belong to the PEO coating of the pure magnesium formed under R = 0, and they represent the flat areas around a discharging pore and nodular feature, respectively. EDS analysis shows that point A has a composition of 34.3 wt% O, 48.4 wt% Mg and 15.6 wt% Si, whereas point B consists of 40.9 wt% O, 33.1 wt% Mg, 23.3 wt% Si and 1.5 wt% K. Therefore, the nodular feature (point B) has a higher Si content from the electrolyte than that of point A near the large pore. The high Mg content of point A indicates that the flat areas around the discharge pores are formed by the penetrating discharges from the substrate [5]. Due to the high cathodic polarization (R = 1.2), the coating on the pure magnesium was damaged, as can be seen in Figure 6c. However, the coatings formed under the same condition on the AZ31 and AZ91 alloys were undamaged (Figure 6f,i).

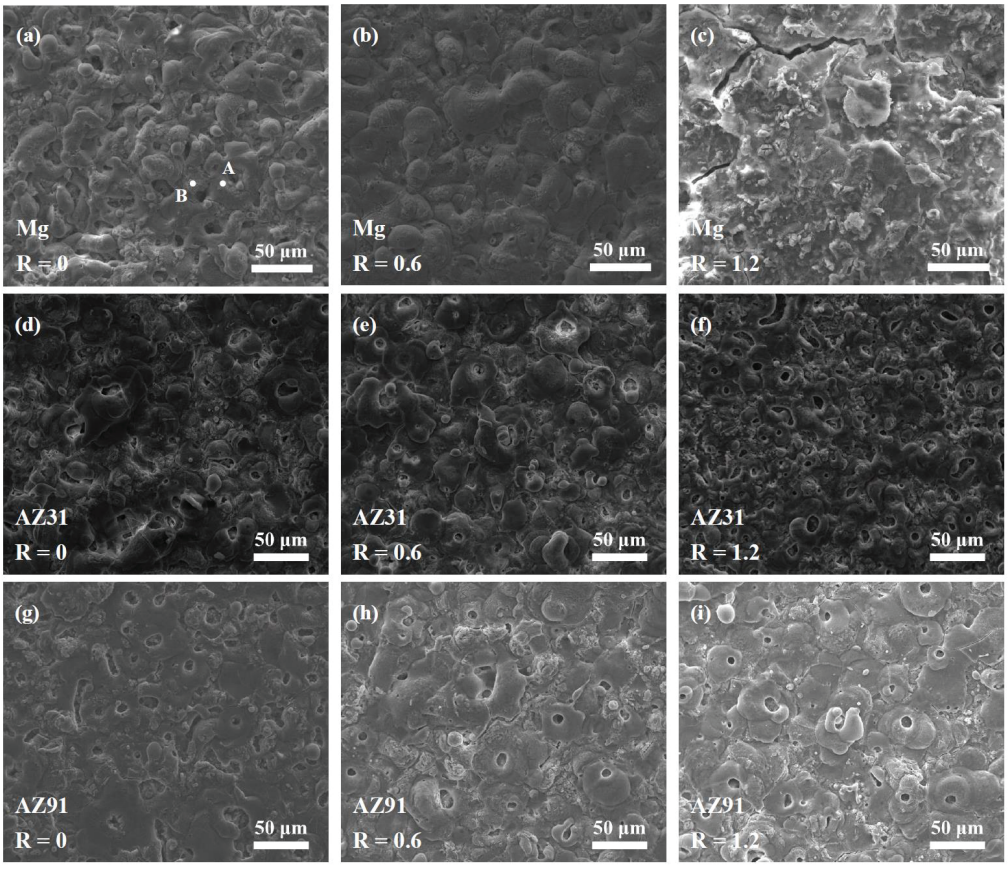

Figure 6. Scanning electron micrographs showing the surfaces of PEO coatings formed for 600 s under different R ratios on (**a**–**c**) pure magnesium and (**d**–**f**) AZ31 and (**g**–**i**) AZ91 magnesium alloys.

The cross sections of the coatings formed for 600 s on different samples are shown in Figure 7. The cross sections show more and less pores as well as unevenness within the different samples. For the pure magnesium, the original coating peeled off at R = 1.2, only showing the remains of an inner coating (see Figure 7c). EDS analyses were performed on the outer parts of the cross sections of the coatings on the AZ31 and AZ91 magnesium

alloys. The results are listed in Table 1. The results show that the Al content was present within the coatings on the AZ31 and AZ91 alloys, and a higher fraction of Al was found with the PEO coatings of the AZ91 magnesium alloy.

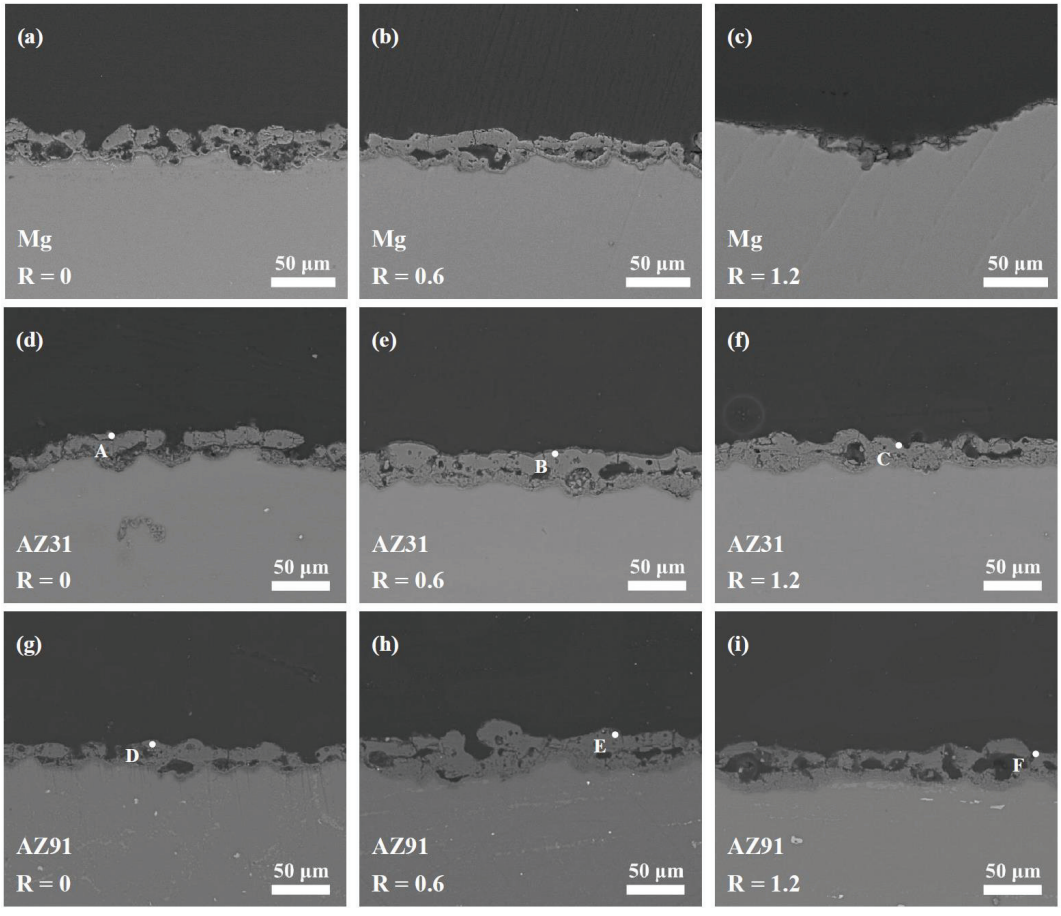

Figure 7. Scanning electron micrographs showing the cross sections of PEO coatings formed for 600 s under different R ratios on (**a**–**c**) pure magnesium and (**d**–**f**) AZ31 and (**g**–**i**) AZ91 magnesium alloys. Points "A-F" are locations for EDS analyses.

Table 1. Elemental compositions of the marked points in Figure 7.

Sample	Point	Element (wt%)					
		O	Na	Mg	Si	K	Al
AZ31	A	26.00	0.74	52.67	17.53	0.60	2.47
	B	37.87	0.31	49.66	8.92	1.41	1.83
	C	30.54	0.10	53.11	14.81	1.20	0.24
AZ91	D	35.80	0.07	48.12	9.92	0.02	6.08
	E	28.07	0.00	48.86	17.57	0.54	4.96
	F	25.51	0.38	56.70	10.63	0.25	6.53

Figure 8 shows the surface morphologies of the coatings formed for 2400 s on different samples under the R ratios of 0 and 0.6. The surface roughness of the coatings is significantly

increased compared to that at 600 s. Solidified oxides in irregular shapes are distributed on the surfaces of the coatings. There are a few pores on the surfaces of the coatings, and the numbers of pores are reduced compared with those coatings formed for 600 s. Some coatings have pancake- or crater-like morphologies on their surfaces, as indicated by the arrows in the figure. The pancake structure is more pronounced on the surfaces of the coatings formed at R = 0.6. These pancake structures are commonly encountered in PEO, which are caused by the repeated penetrating discharges during PEO [5]. At the same time, the PEO process produces a large amount of gas, and the pores are believed to be caused by gas emissions from the PEO process [5].

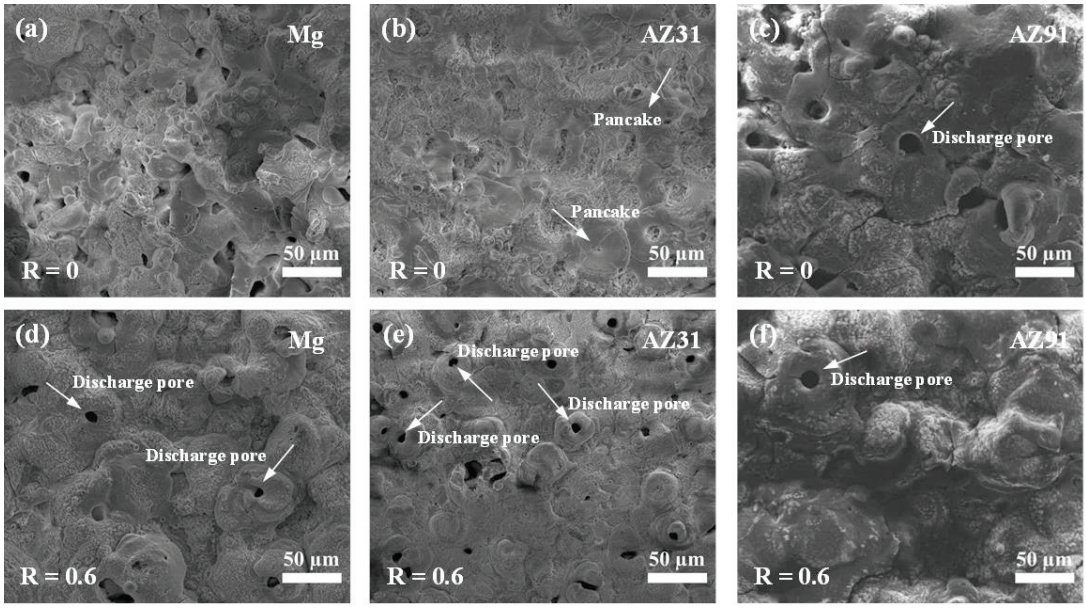

Figure 8. Scanning electron micrographs showing the surfaces of PEO coatings formed for 2400 s under different R ratios on (**a**,**d**) pure magnesium and (**b**,**e**) AZ31 and (**c**,**f**) AZ91 magnesium alloys.

Figure 9 shows the cross sections of the coatings formed for 2400 s under R = 0 and 0.6 on the pure magnesium and AZ31 and AZ91 magnesium alloys. At R = 0, the coating thicknesses for the different samples were around 50 μm, and the uniformities of the coatings were poor. The coatings can be roughly divided into a thicker outer layer and an inner layer. Large, elongated pores are observed between the inner and outer layers of the coatings on the pure magnesium and AZ91 alloy. Significant undulations are observed with the coating/substrate interfaces for all coatings formed under R = 0. The enlarged view of the coating/substrate interface in Figure 9a (the inset) indicates the presence of a dense barrier layer. This barrier layer is often mentioned in the literature, and it can provide the main corrosion resistance for PEO coatings [61,62]

After applying cathodic polarization (R = 0.6), the thicknesses and uniformities of the coatings were significantly improved (see Figure 9d–f). The coating thicknesses were 71.9, 89.3 and 128.9 μm for the pure magnesium and AZ31 and AZ91 magnesium alloys, respectively.

Uniform PEO coatings could be formed for longer times on the AZ91 magnesium alloy up to a high R ratio of 3.2. Figure 10 compares the cross sections of the coatings formed for 2400 s under R = 0.6 and R = 0.9. The coatings formed under R = 0.6 have a few elongated pores within the cross section. However, the elongated pores are significantly reduced

within the cross section under R = 0.9. Therefore, a higher R is beneficial for the growth of denser coatings with fewer defects on AZ91 magnesium alloy.

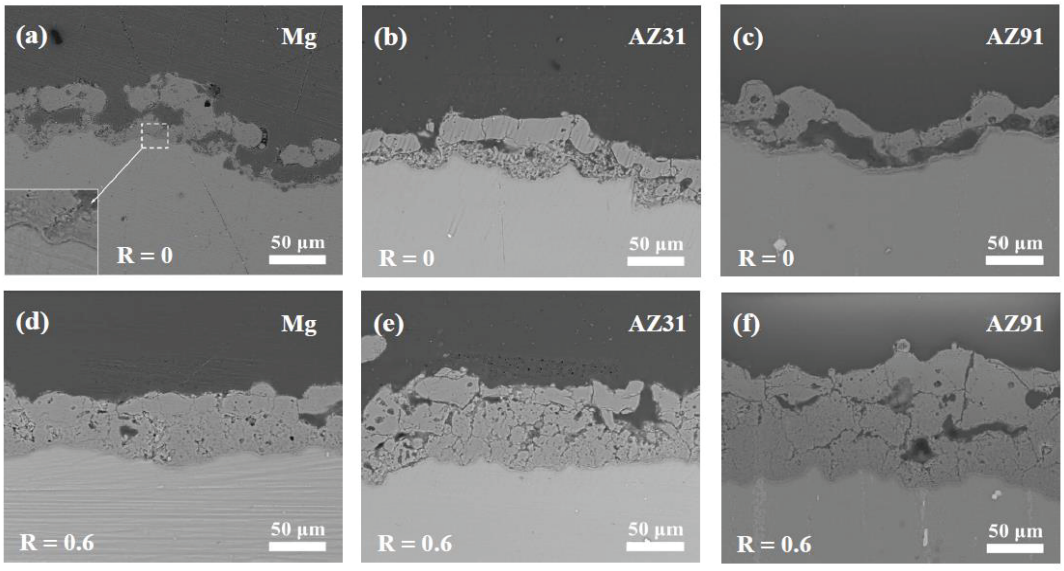

Figure 9. Scanning electron micrographs showing the cross sections of the PEO coatings formed for 2400 s under R = 0 and 0.6 on (**a**,**d**) pure magnesium and (**b**,**e**) AZ31 and (**c**,**f**) AZ91 magnesium alloys.

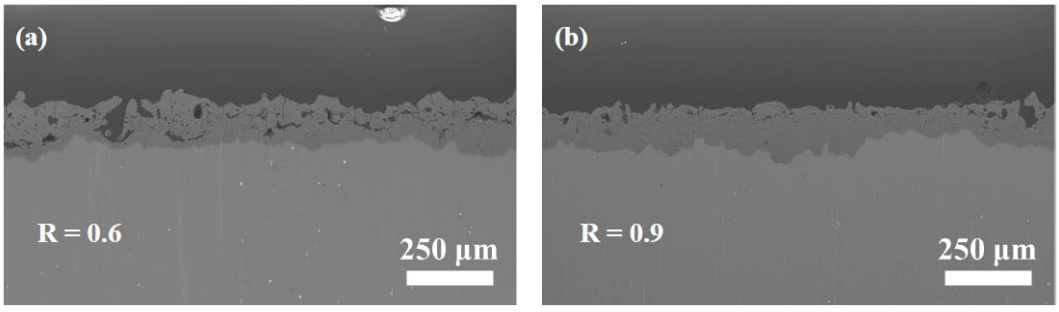

Figure 10. Scanning electron micrographs showing the cross sections of PEO coatings on the AZ91 mg alloy formed for 2400 s at (**a**) R = 0.6 and (**b**) R = 0.9.

3.7. XRD

Figure 11a shows the XRD patterns of the PEO coatings on the pure magnesium and AZ31 and AZ91 magnesium alloys formed for 2400 s under R = 0, whereas Figure 11b compares the XRD patterns of the PEO coatings on the AZ91 magnesium alloys formed for 2400 s with different R values. According to Figure 11a, the phase compositions for the three samples were nearly the same, consisting of mainly MgO and Mg_2SiO_4. Perhaps due to the low content of aluminum, no XRD diffraction peaks related to the species of Al were found for the PEO coatings formed on the AZ31 and AZ91 magnesium alloys. The diffraction peaks of Mg are clearly seen on the XRD patterns of all the PEO coatings, which can be attributed to the fact that X-rays penetrated the thin and porous coatings during the examination.

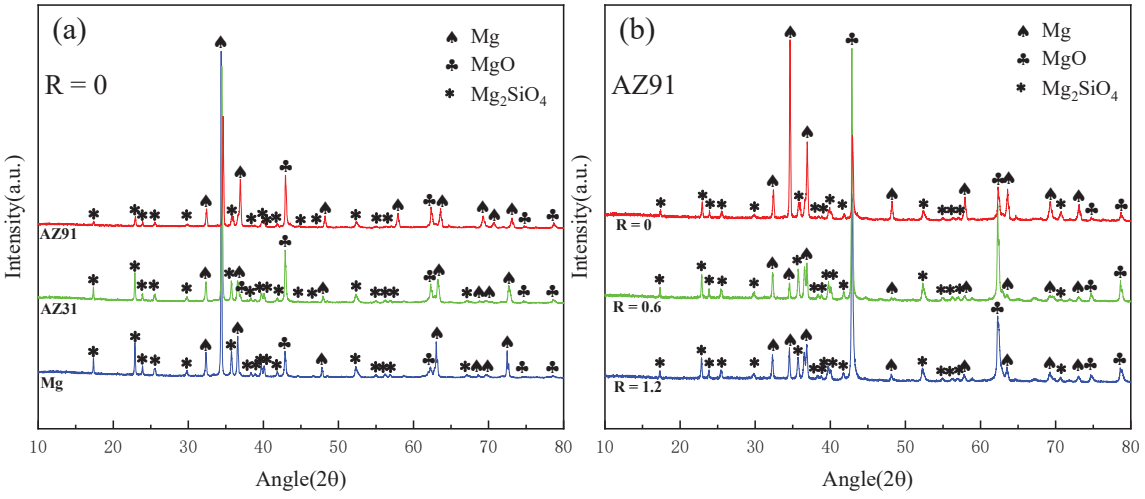

Figure 11. (**a**) A comparison of the XRD patterns of the coatings formed for 2400 s under R = 0 on pure magnesium and AZ31 and AZ91 magnesium alloys. (**b**) XRD patterns of the coatings formed on AZ91 magnesium alloy for 2400 s under R = 0, 0.6 and 1.2.

Figure 11b shows that the phase compositions of the coatings formed on the AZ91 magnesium alloy under R = 0.6 and R = 0 were the same as that of the coating formed without the application of cathodic polarization (R = 0), except for increased diffraction peaks for Mg_2SiO_4 and MgO on the former coatings. The result shows that cathodic polarization did not alter the phase compositions of the coatings. The reduction in the intensity of the Mg peaks in the XRD patterns at R = 0.6 and 1.2 is due to the formation of thicker and denser coatings after the application of cathodic polarization.

3.8. Growth Regularity

Figure 12 depicts the effect of cathodic polarization on the growth regularity of the PEO coatings on the pure magnesium. Figure 12a,b show the cross sections of the coatings formed for 2400 s at R = 0 and R = 0.6. A piece of un-oxidized magnesium adjacent to the left side of the PEO coatings is served to show the original surface prior to oxidation. From Figure 12(a), it can be seen that for the sample prepared at R = 0, a large-sized pit was formed not far from the left sample edge. The enlarged image in Figure 12c shows that the size of the pit is ~550 μm. This feature should correspond to the macroscopic pits observed in Figure 4. The oxide-coating thickness on the surface of the sample at R = 0 is ~37 μm, evenly covering the sample surface, including the surfaces of the pits. According to Figure 12c, even for the oxide coating at the left edge, most of the coating is located below the original sample surface, indicating that the coating basically grew inward.

After the application of the cathodic current, the uniformity and thickness of the coating were significantly improved, and no pits similar to those at R = 0 were found with the cross section at R = 0.6. From Figure 12b,d, it can be seen that the coating formed at R = 0.6 grew both outward and inward, with an outward growth of approximately 48.9 μm and an inward growth of ~65.3 μm.

3.9. Polarization Curves

Figure 13 shows the polarization curves tested in a 3.5 wt% NaCl solution for the pure magnesium and AZ31 and AZ91 magnesium alloys and their PEO coatings formed in the dilute silicate electrolyte for 2400 s at different R values. The parameters of the corrosion potential (E_{corr}) and free-corrosion current density (I_{corr}) are listed in Table 2. The values of

the E_{corr} were read from the inversion points on the polarization curves, while the corrosion current densities were obtained via the Tafel extrapolation method.

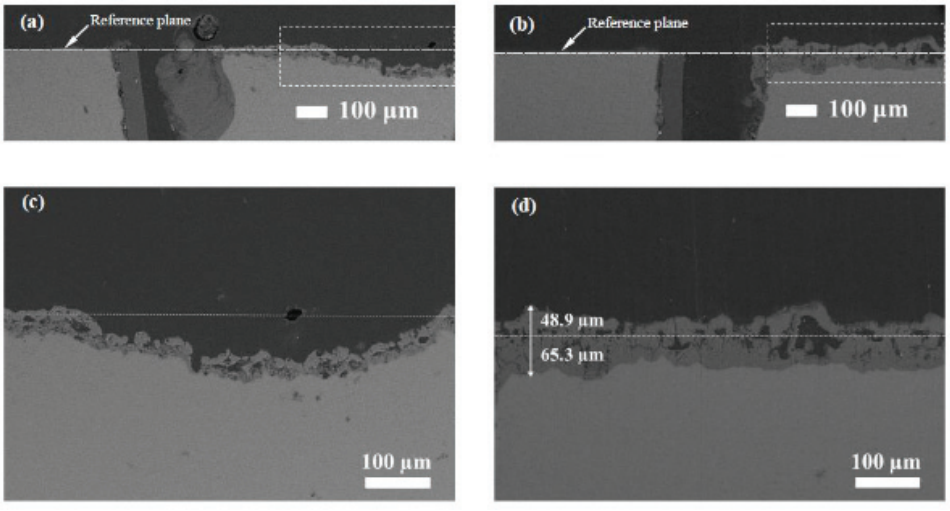

Figure 12. The influence of cathodic polarization on coating growth regularity: (**a**) the cross section of a coating formed for 2400 s under R = 0 on pure magnesium; (**b**) the cross section of a coating formed for 2400 s under R = 0.6 on pure magnesium; (**c**,**d**) the boxed areas in (**a**,**b**), respectively. A piece of untreated magnesium adjacent to the left side of each sample is used to show the original surface.

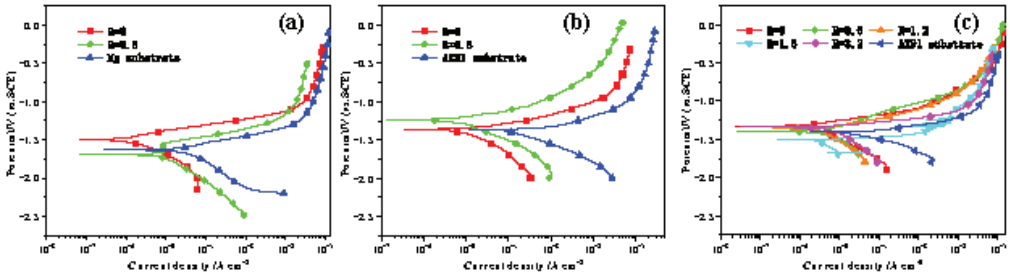

Figure 13. Polarization curves of the uncoated substrates and the PEO coatings on (**a**) pure magnesium and (**b**) AZ31 and (**c**) AZ91 magnesium alloys formed for 2400 s under different R ratios.

According to Table 2, the E_{corr} values of the pure Mg and AZ31 and AZ91 magnesium alloys are −1.625, −1.371 and −1.398 V (vs. SCE), respectively, indicating that the corrosion potential was improved after the addition of the alloying elements. The standard equilibrium electrode potentials for Mg and Al are −2.34 and −1.67 V (vs. SHE), respectively. Therefore, it is not surprising that the AZ31 and AZ91 magnesium alloys had higher corrosion potentials than that of the pure magnesium. Samples with more positive corrosion potentials usually indicate less of a thermodynamic tendency towards corrosion. It is also noted from Figure 13 that the PEO treatment normally led to improved corrosion potentials for the samples. However, the coating formed on the pure magnesium at R = 0.6 and the coating formed on the AZ91 magnesium alloy at R = 1.6 exhibited lower corrosion potentials compared with the untreated metal. In our recent work, PEO coatings formed on tantalum under high cathodic polarization also exhibited considerably lower corrosion potentials, which was attributed to the incorporation of hydrogen species or cations [63].

Table 2. Parameters derived from the polarization curves in Figure 13.

Sample	E_{corr} (V vs. SCE)	i_{corr} (A cm^{-2})
Mg Substrate	−1.625	3.80×10^{-5}
R = 0	−1.493	1.66×10^{-6}
R = 0.6	−1.695	1.26×10^{-5}
AZ31 Substrate	−1.371	8.07×10^{-5}
R = 0	−1.363	5.69×10^{-6}
R = 0.6	−1.243	1.60×10^{-5}
AZ91 Substrate	−1.398	2.26×10^{-5}
R = 0	−1.327	3.52×10^{-6}
R = 0.6	−1.392	5.78×10^{-6}
R = 1.2	−1.353	4.68×10^{-6}
R = 1.6	−1.498	4.48×10^{-6}
R = 3.2	−1.338	9.08×10^{-6}

The corrosion current densities of the different samples are further plotted in the histogram of Figure 14. The I_{corr} of the pure magnesium is 3.80×10^{-5} A cm^{-2}. The AZ31 magnesium alloy shows a higher corrosion current density of 8.07×10^{-5} A cm^{-2}. However, the I_{corr} of the AZ91 magnesium alloy is the lowest among the three uncoated samples (2.26×10^{-5} A cm^{-2}). PEO treatment can improve the corrosion resistance of pure magnesium and AZ31 and AZ91 magnesium alloys. However, the corrosion resistance of the coatings does not improve with an increase in the R value. It can be seen in Figure 13 that the coatings formed under R = 0 normally possessed lower I_{corr} values than those of the coatings formed with cathodic polarization. The coating formed under R = 0 on the pure magnesium displays the lowest corrosion current density ($I_{corr} = 1.66 \times 10^{-6}$ A cm^{-2}). However, the corrosion current densities of the coatings formed under R = 0 on the AZ31 and AZ91 magnesium alloys are 5.69×10^{-6} A cm^{-2} and 3.52×10^{-6} A cm^{-2}, respectively. The application of a cathodic polarization of R = 0.6 led to coatings with improved corrosion current densities of 1.26×10^{-5} A cm^{-2} and 1.60×10^{-5} A cm^{-2} on the pure magnesium and AZ31 magnesium alloy, respectively. The coatings formed with different cathodic polarizations on the AZ91 magnesium alloy normally had higher corrosion resistances than the coatings formed on the pure magnesium and AZ31 magnesium alloy under R = 0.6.

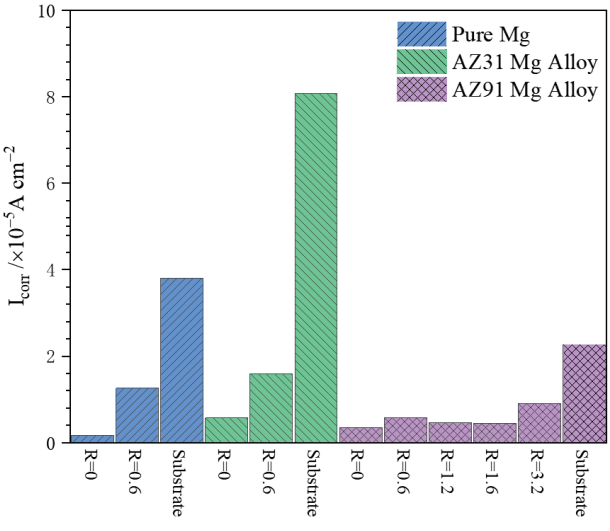

Figure 14. Histogram of the corrosion current densities of the uncoated and coated samples in Figure 13.

3.10. Wear

Figure 15 shows the variation in the friction coefficients during the 1800 s dry sliding tests under a load of 5 N against a Cr steel ball for the uncoated and PEO-coated pure magnesium and AZ31 and AZ91magnesium alloys.

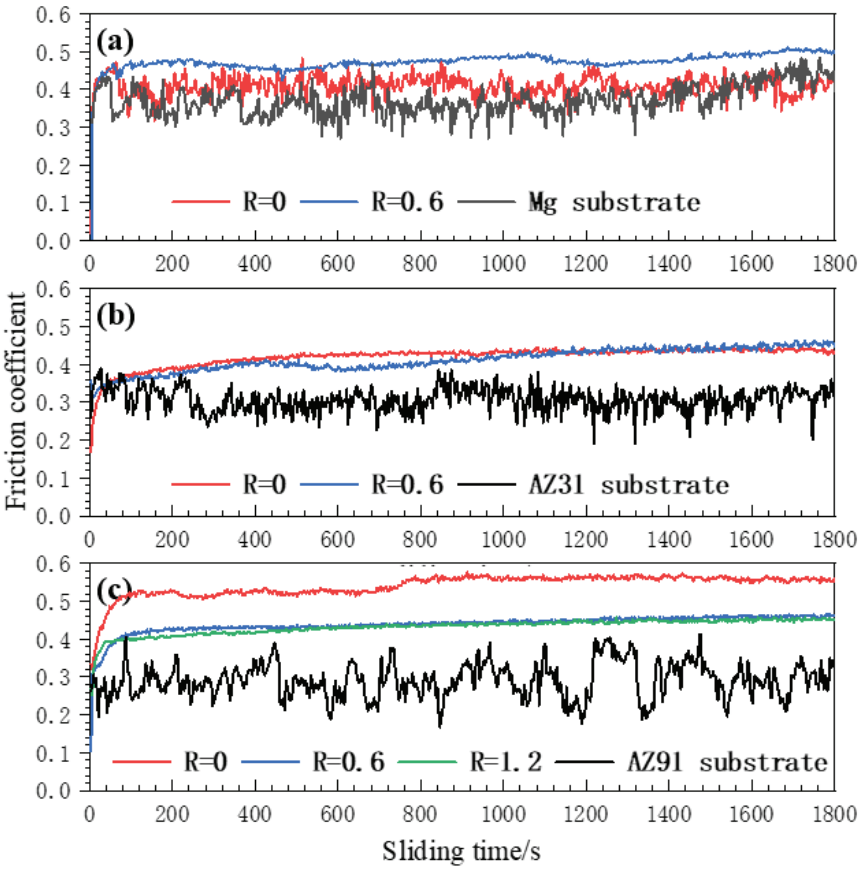

Figure 15. Coefficients of friction as a function of sliding time for (**a**) pure magnesium and (**b**) AZ31 and (**c**) AZ91 magnesium alloys and their PEO coatings formed in 5 g/L Na_2SiO_3 + 1 g/L KOH for 2400 s under different R ratios.

For the pure magnesium, the friction coefficient curves of the substrate and the R = 0 coating were similar, showing significant fluctuations after the initial surge in the friction coefficient. The friction coefficient of the substrate and R = 0 coating normally ranged between 0.32 and 0.48. In contrast, the friction coefficient curve of the PEO coating formed under R = 0.6 was more stable, with a slightly higher friction coefficient value throughout the entire process than those of the other two samples, and its value was around 0.5 in the later stage.

For the uncoated and coated AZ31 alloy samples, only the substrate showed fluctuations in the friction coefficient, the values of which remained between approximately 0.28 and 0.36. The curves of the friction coefficients for the oxide coatings formed under R = 0 and R = 0.6 are higher than that of the substrate, and the curves are relatively stable. Moreover, their values are very close, showing values of around 0.45 for the later stage of the friction tests.

Similarly, only the substrate of the AZ91 magnesium alloy exhibited significant fluctuations in the friction coefficient, with values ranging between ~0.2 and ~0.4. The sample with an R = 0 coating had the highest friction coefficient, showing values between 0.5 and 0.56 after the initial surge. The friction coefficient curves of the coatings formed under R = 0.6 and 1.2 almost coincide, with values ranging from 0.4 to 0.46 during most of the process.

Figure 16 shows the appearances of the different samples after the dry sliding tests. It can be seen that all the metal substrates and the R = 0 coating on the pure magnesium are heavily worn, showing broad wear tracks with metallic luster. Except for the coating formed on the pure magnesium under R = 0, all the coated samples formed dark-brown wear tracks. The dark-brown wear tracks are the "transfer layers", which were formed due to material transfer and the tribo-oxidation of the steel counterpart under the combined action of mechanical stresses and frictional heating [64]. For the pure magnesium and AZ91 magnesium alloy, the coatings formed under R = 0.6 exhibit narrower wear tracks than the coatings formed under R = 0, indicating the better wear resistance of the former. However, for the AZ31 alloy, the coatings formed under R = 0 and R = 0.6 show comparable wear tracks in width. It is noted that the narrowest wear track is found with the coating formed under R = 1.2 on the AZ91 magnesium alloy.

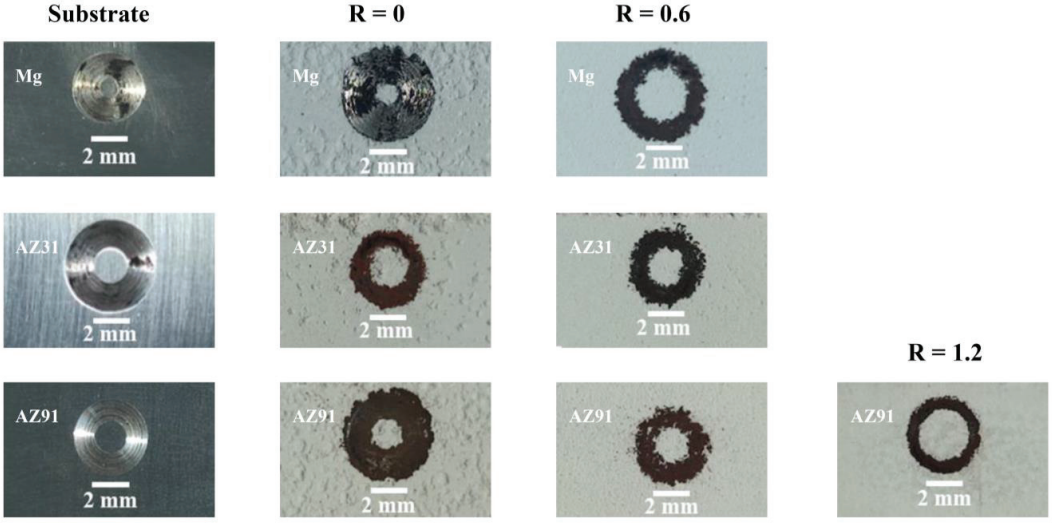

Figure 16. Appearance of wear scars after dry sliding tests for the uncoated pure magnesium and AZ31 and AZ91 magnesium alloys and their PEO coatings formed for 2400 s under different R ratios.

Figure 17 shows the corresponding cross-sectional profiles for the wear tracks. It can be seen that the wear track depths on the uncoated substrates are in the range of 62.42–79.21 μm. The coating formed under R = 0 on the pure magnesium shows the deepest wear scar at 116.08 μm. It is believed that the debris of broken coating material was entrapped within the wear track, imposing an additional micro-cutting effect on the substrate, thereby leading to a deeper wear track. In contrast, the wear depth on the coating formed on the pure magnesium under R = 0.6 is only 19.77 μm, indicating the significant improvement in the wear resistance. Other coatings formed on the AZ31 and AZ91 alloys show wear depths in the same order; their values are between 6.98 and 18.23 μm. However, the narrowest wear scar width is recorded for the coating formed on the AZ91 alloy under R = 1.2, with a value of 801 μm.

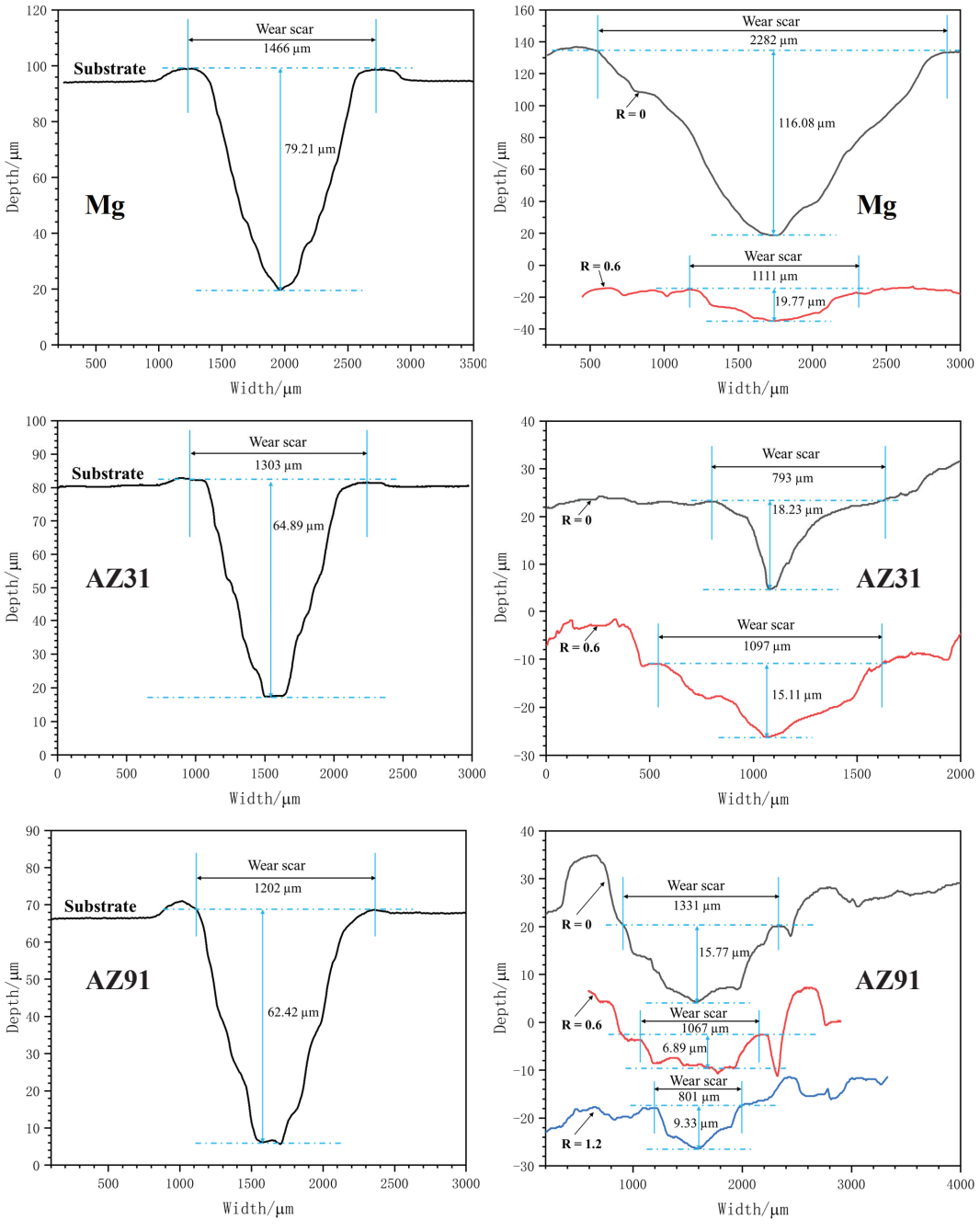

Figure 17. Cross-sectional profiles of the wear tracks on pure magnesium and AZ31 and AZ91 magnesium alloys and their coatings.

The wear rates of the different samples are calculated and plotted in Figure 18. The PEO coating formed under R = 0 on the pure magnesium shows the highest wear rate of

279.6 × 10^{-6} mm^3/(N·m), whereas the lowest wear rate is registered for the PEO coating formed under R = 1.2 on the AZ91 magnesium alloy, which is 8.6 × 10^{-6} mm^3/(N·m).

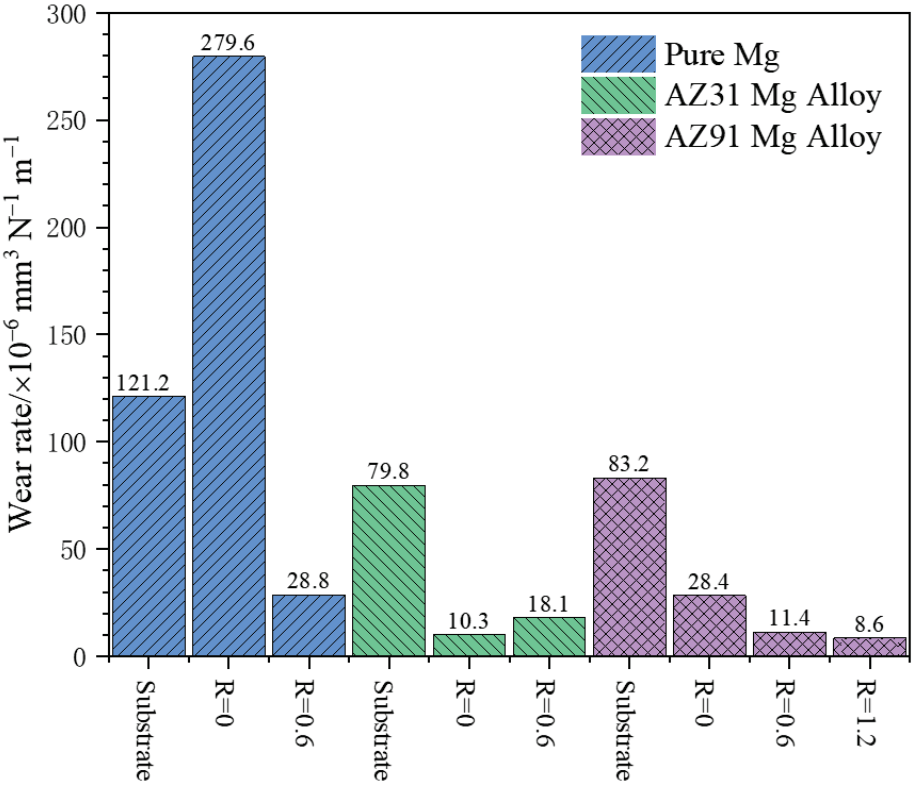

Figure 18. Wear rates of the uncoated and coated samples for pure magnesium and AZ31 and AZ91 magnesium alloys.

4. Discussion

In this work, the effect of cathodic polarization on the PEO behaviors and coating properties of pure magnesium and AZ31, and AZ91 magnesium alloys was systematically studied in a dilute silicate solution. The main findings are as follows:

- The PEO of the pure magnesium and AZ31 and AZ91 magnesium alloys without cathodic polarization led to a large number of pores on the coatings in the later stage. The thicknesses of the coatings were low, with poor uniformity, and the coatings mainly grew inward;
- The lower cathodic polarization (R = 0.6) greatly improved the thickness and uniformity of the coatings, and the growth mechanism of the coatings shifted to both inward and outward growth;
- When the cathodic polarization was high, the anodic potential decreased or fluctuated during the PEO process. At this point, some features of soft sparking appeared, such as weakened sparks and lower acoustic emissions, but their impacts on the quality of the coating were negative, leading to the blistering or flaking off of the coating;
- The increase in the Al content in the magnesium alloys seemed to improve the tolerance to high cathodic polarization and was beneficial for the compactness of the coating. When the R values were 0.9 and 1.2, the coating thickness on the AZ91 magnesium alloy was only slightly lower than that at R = 0.6, and the compactness of the coating

was improved. Even at the highest R value of 3.2, there was no coating flaking-off phenomenon for the AZ91 alloy;

- The PEO coatings improved the corrosion resistance of the substrates. Compared with the coatings formed under R = 0, cathodic polarization slightly decreased the corrosion resistance of the coatings. Excessive cathodic polarization damaged the coatings on the pure magnesium and AZ31 alloy. For the AZ91 magnesium alloy, excessive cathodic polarization led to a lowered corrosion potential and decreased corrosion resistance;
- The coatings formed under R = 0.6 usually possessed high wear resistances than the coatings formed under R = 0. The PEO coating on the AZ91 magnesium alloy formed under R = 1.2 displays the narrowest wear scar.

This study further demonstrates that the significant improvement in the coating thickness and uniformity related to soft sparking reported in the literature may be only confined to aluminum alloys. Although the soft sparking of the magnesium and magnesium alloys in this study was not related to an improvement in the coating quality, the effect of cathodic polarization on the PEO coating formation process was similar to that of aluminum alloys. After applying a certain cathodic current (e.g., R = 0.6), the uniformity and thickness of the coating first significantly increased, which is consistent with those of aluminum alloys [39]. In addition, it has been found in the relevant research on aluminum alloys that excessive cathodic polarization can also result in a reduced coating thickness, blistering, flaking off and other phenomena [39,43]

According to the literature [52,65,66], for the PEO of magnesium and magnesium alloys, the main anodic reactions can be written as follows:

$$Mg \rightarrow Mg^{2+} + 2e \quad (1)$$

$$4OH^- \rightarrow O_2 + 2H_2O + 4e \quad (2)$$

$$Mg^{2+} + O^{2-} \rightarrow MgO \quad (3)$$

$$Mg^{2+} + 2OH^- \rightarrow Mg(OH)_2 \quad (4)$$

$$2Mg^{2+} + SiO_3^{2-} + 2OH^- \rightarrow Mg_2SiO_4 + H_2O \quad (5)$$

$$Mg(OH)_2 \rightarrow MgO + H_2O \quad (6)$$

$$SiO_3^{2-} + 2H^- \rightarrow SiO_2 + H_2O \quad (7)$$

$$2SiO_3^{2-} \rightarrow O_2 + 2SiO_2 + 4e \quad (8)$$

$$SiO_2 + 2MgO \rightarrow Mg_2SiO_4 \quad (9)$$

$$2Mg + O_2 \rightarrow 2MgO \quad (10)$$

According to Reaction (1), Mg^{2+} is produced via the dissolution of the magnesium substrate under a strong electric field. Reaction (2) is a side reaction of oxygen generation under anodic polarization. In the initial PEO stage, traditional anodic film is formed under the electric field via the ion migration mechanism: Mg^{2+} ions move towards the electrolyte/coating interface, whereas the anions of O^{2-}, OH^- and SiO_3^{2-} move towards the substrate. The cations and anions meet within the film, leading to the formation of MgO (Reaction (3)), $Mg(OH)_2$ (Reaction (4)) and Mg_2SiO_4 (Reaction (5)). Mg^{2+} can also

enter the electrolyte directly. After reaching the breakdown potential, the magnesium in the substrate will directly react with oxygen in the molten-discharge channels to form MgO (Reaction (10)). Similarly, in the presence of high-temperature-discharge channels, $Mg(OH)_2$ and SiO_3^{2-} may undergo thermal decomposition to form SiO_2 and MgO, manifested by Reactions (6)–(8). MgO can also react with SiO_2 to form magnesium olivine (Reaction (9)).

For PEO without the application of cathodic polarization, many large-sized pits are formed on the surfaces of magnesium and magnesium alloys in the later stage of PEO (see Figure 4). The formation of these pits may be related to the strong anodic dissolution of the Mg substrate. The greater possibility for the pit formation may be that the formed oxide coating has been damaged by the strong discharges. Within the PEO discharge channels, there are high temperatures (10^3–10^4 K) and pressures (~10^2 MPa) [8], accompanied by plasma generation and gas release. When the cohesive force of the oxide coating itself is less than the mechanical stress associated with the gas release within the discharge channels, the oxide coating may break down locally, forming the pits.

After applying a certain cathodic polarization (R = 0.6), the formation of pits on the surface of the oxide coating is basically suppressed, and the uniformity and thickness of the coating are significantly improved. The growth mechanism of the coating also becomes a mode of both inward and outward growth. The reactions involved during the cathodic polarization may include the following:

$$2H^+ + 2e \rightarrow H_2 \quad (11)$$

$$2H_2O + 2e \rightarrow H_2 + 2OH^- \quad (12)$$

$$H^+ + e \rightarrow [H^*]_{ox} \quad (13)$$

The cathodic process generally involves the release of hydrogen gas (Reactions (11) and (12)), but, according to Rogov et al. [42], it is also possible to generate neutral hydrogen complexes (Reaction (13)). Neutral hydrogen species exist in the lattice of the oxide, leading to an increase in the conductivity of the oxide coating, which may be the reason for the decrease in the anodic potential during soft sparking [42].

The improvement in the coating thickness and uniformity after the application of cathodic polarization is a common phenomenon in PEO studies that has been reported in PEO studies of various metals [35,36,39,63]. Cheng et al. [36] believe that the hydrogen evolution during the cathodic process promotes the transport of reactant particles in the electrolyte. Therefore, more electrolyte components participate in the coating formation, leading to an increase in the coating thickness and uniformity. The increase in the thicknesses of the PEO coatings on the magnesium and magnesium alloys after the application of cathodic polarization in this study can be explained by the same mechanism. In this study, the species involved in the coating formation in the electrolyte was mainly SiO_3^{2-} ions. Due to the participation of more electrolytic species in the coating formation, the growth pattern of the coatings also shifted to both outward and inward growth.

The blistering and flaking off of the coating under excessive cathodic polarization is associated with the internal stress caused by hydrogen evolution. Hydrogen ions or water molecules can travel through the porosity of the oxide coating to the barrier layer near the coating/substrate interface, where they receive electrons to produce hydrogen bubbles. When the cathodic polarization is too high, a large amount of hydrogen gas is generated, causing the coating to blister or detach. In addition, excessive cathodic polarization can also lead to a decrease in the coating thickness, which has been observed in the PEO of aluminum [39,43] and tantalum [63], which is consistent with this study.

The reason for the decrease in the coating thickness caused by excessive cathodic polarization is believed to be related to the repulsion of the cathodic electric field on the anions. During the formation of the oxide coatings, anions such as SiO_3^{2-}, OH^- and O^{2-} also participate in the coating-forming reactions. An excessively high cathodic electric field

will repel the anions adjacent to the surface liquid layer and within the coating, thereby reducing the number of anions participating in the coating formation reactions and leading to a decrease in the coating thickness. This mechanism was proposed in our research on the effect of cathodic polarization on the PEO of tantalum [63].

An interesting phenomenon in this study was the tolerance to cathodic polarization in the AZ91 magnesium alloy. Although the EDS and XRD show that the compositions and phase compositions of the coatings on the pure magnesium and magnesium alloys are similar, the PEO coatings on the AZ91 magnesium alloy exhibited a completely different capability to resist the peeling caused by cathodic hydrogen evolution. For the pure magnesium and AZ31 magnesium alloys, the coatings blistered and peeled off at R = 0.9, whereas the AZ91 alloy did not show significant damage to the coating until R = 3.2. The anti-exfoliation ability of the PEO coatings on the AZ91 magnesium alloy may be related to the Al content in the substrate. Interestingly, the tolerance of the AZ91 magnesium alloy to cathodic polarization in this study was even better than that of the aluminum alloy. In our previous study, when an Al-Cu-Li alloy was PEO-treated under R = 2.0 and 3.3, the coatings exhibited significant blistering and flaking off in the later stage [39]. It is possible for the Al component to improve the compactness of the PEO coating on magnesium alloys, as Tsai et al. [55] found that only in a sodium aluminate electrolyte can magnesium-based metals obtain a dense inner layer under the soft-sparking condition. The mechanism of the anti-exfoliation of the PEO coatings on AZ91 magnesium alloy under excessive cathodic polarization is very complex and requires further research.

For pure magnesium and AZ31 magnesium alloy, the optimal cathodic polarization is R = 0.6. Under this condition, the thickness and uniformity of the coatings are improved, as well as the wear resistance of the coatings. However, a further increase in the R value will result in damage to the resultant coatings.

Due to the higher tolerance of the AZ91 magnesium alloy to cathodic polarization, although the coating thickness was highest at R = 0.6, further increasing the R value led to denser coatings, and the wear scar width on the coating formed under R = 1.2 was the narrowest. This indicates that a higher R value may result in more wear-resistant coatings.

As for the corrosion resistance, the coatings without cathodic polarization were slightly more corrosion-resistant than the coatings formed under the moderate cathodic polarization of R = 0.6. This phenomenon may be related to the fact that the barrier layers at the coating/substrate interfaces of the coatings formed under R = 0 were denser than those formed under R = 0.6. As mentioned previously, the barrier layers provide the main corrosion resistance for PEO coatings [61,62]. For the pure magnesium and AZ31 magnesium alloy, excessive cathodic polarization was detrimental to the corrosion resistance of the samples, as the coatings were damaged. For the AZ91 alloy, excessive cathodic polarization was also detrimental, as these coatings had lowered corrosion potentials and larger corrosion current densities compared with those of the coating formed under R = 0. The same phenomenon has been observed in previous studies [39,63]. It is believed that the incorporation of hydrogen species leads to a decrease in the corrosion resistance [63].

Regarding the soft-sparking phenomenon, the pure magnesium and AZ31 alloy exhibited anodic-potential drops and reductions in the intensity of sparks at high R values, but the coatings were damaged when these characteristics of soft sparking occurred. The AZ91 alloy also experienced decreases in the anodic potential and strength of the discharging sparks under R = 1.2, which correspond to the optimum R value for the soft sparking of aluminum alloys [39], but, in this study, the efficiency of the coating formation under this R value decreased (see Figure 5). Therefore, in this study, the soft sparking on the magnesium and its alloys is possibly not related to the improvement in the coating quality.

5. Conclusions

In this study, the effect of cathodic polarization on the PEO behaviors of pure magnesium and AZ31 and AZ91 magnesium alloys in 5 g L^{-1} $Na_2SiO_3 \cdot 9H_2O$ + 1 g L^{-1} KOH was

investigated. The corrosion and wear performances of the coatings formed for 2400 s were evaluated. The main conclusions are as follows:

1. The OES detected two spectral lines at 559.79 nm and 570.11 nm, which are attributed to the excitation of the Mg species during PEO;
2. For PEO without cathodic polarization (R = 0), the coatings on the pure magnesium and magnesium alloys were damaged by the strong plasma discharges, forming large pits on the coating surfaces, and the uniformities and thicknesses of the coatings were significantly lower than those of the coatings formed with cathodic polarization. In this case, the coatings mainly grew inward;
3. The pure magnesium and AZ31 and AZ91 magnesium alloys showed the highest coating growth efficiencies under R = 0.6, with thick coatings (>100 μm in thickness) being formed following 2400 s of PEO treatment. The uniformities of the coatings were also significantly improved, and the coating growth mechanism was transformed into both inward and outward growth;
4. When $R \geq 0.9$, the formed coatings on the pure magnesium and AZ31 magnesium alloy experienced blistering and flaking off in the later stage of the PEO, resulting in incomplete coating formation;
5. The AZ91 magnesium alloy had excellent tolerance to cathodic polarization, and the coatings did not experience blistering or peeling, even under the highest R value of 3.2. Meanwhile, denser coatings seemed to form under higher R values;
6. The PEO treatment improved the corrosion resistances of the pure magnesium and magnesium alloys. The coatings formed under R = 0 possessed slightly better corrosion resistances than the coatings formed with cathodic polarization;
7. The uncoated samples and the coating formed on the pure magnesium under R = 0 showed large fluctuations in their coefficients of friction. However, the other PEO coatings displayed more stable coefficient-of-friction curves with higher values;
8. Most of the PEO coatings could improve the wear resistance of the magnesium and magnesium alloys. For the pure magnesium and AZ31 magnesium alloys, the protective performances of the coatings formed under R = 0.6 were better. For the AZ91 magnesium alloy, the wear scar width on the coating formed under R = 1.2 was the narrowest;
9. Magnesium and magnesium alloys may experience soft sparking after the application of a certain degree of cathodic polarization, but this is not related to an improvement in the coating quality.

Author Contributions: Conceptualization, Y.C. (Yingliang Cheng); investigation, Z.L. (Zhengzhou Le), Z.L. (Zihua Liu), X.H., Y.C. (Yulin Cheng) and P.H.; project administration, Y.C. (Yingliang Cheng); validation, Z.L. (Zhengzhou Le), Y.C. (Yingliang Cheng); visualization, Z.L. (Zhengzhou Le), Z.L. (Zihua Liu), X.H., Y.C. (Yulin Cheng) and P.H.; writing—original draft, Z.L. (Zhengzhou Le); writing—review and editing, Y.C. (Yingliang Cheng). All authors have read and agreed to the published version of the manuscript.

Funding: This work is funded by the National Natural Science Foundation of China [51671084].

Institutional Review Board Statement: Not applicable.

Informed Consent Statement: Not applicable.

Data Availability Statement: Not applicable.

Acknowledgments: We thank the National Natural Science Foundation of China for supporting this work. We also thank Bin Su for providing the samples of AZ91 magnesium alloy.

Conflicts of Interest: The authors declare no conflict of interest.

References

1. Esmaily, M.; Svensson, J.E.; Fajardo, S.; Birbilis, N.; Frankel, G.S.; Virtanen, S.; Arrabal, R.; Thomas, S.; Johansson, L.G. Fundamentals and advances in magnesium alloy corrosion. *Prog. Mater. Sci.* **2017**, *89*, 92–193. [CrossRef]

2. Mordike, B.L.; Ebert, T. Magnesium: Properties—Applications—Potential. *Mater. Sci. Eng. A.* **2001**, *302*, 37–45. [CrossRef]
3. Pezzato, L.; Brunelli, K.; Napolitani, E.; Magrini, M.; Dabalà, M. Surface properties of AZ91 magnesium alloy after PEO treatment using molybdate salts and low current densities. *Appl. Surf. Sci.* **2015**, *357*, 1031–1039. [CrossRef]
4. Wei, B.J.; Cheng, Y.L.; Liu, Y.Y.; Zhu, Z.D.; Cheng, Y.L. Corrosion and wear resistance of AZ31 Mg alloy treated by duplex process of magnetron sputtering and plasma electrolytic oxidation. *T. Nonferr. Metal. Soc.* **2021**, *31*, 2287–2306. [CrossRef]
5. Tu, W.; Cheng, Y.; Wang, X.; Zhan, T.; Han, J.; Cheng, Y. Plasma electrolytic oxidation of AZ31 magnesium alloy in aluminate-tungstate electrolytes and the coating formation mechanism. *J. Alloys Compd.* **2017**, *725*, 199–216. [CrossRef]
6. Cai, L.; Song, X.; Liu, C.-B.; Cui, L.-Y.; Li, S.-Q.; Zhang, F.; Kannan, M.B.; Chen, D.-C.; Zeng, R.-C. Corrosion resistance and mechanisms of Nd(NO3)3 and polyvinyl alcohol organic-inorganic hybrid material incorporated MAO coatings on AZ31 Mg alloy. *J. Colloid. Interface. Sci.* **2023**, *630*, 833–845. [CrossRef]
7. Bakkar, A.; Neubert, V. Electrodeposition onto magnesium in air and water stable ionic liquids: From corrosion to successful plating. *Electrochem. Commun.* **2007**, *9*, 2428–2435. [CrossRef]
8. Yerokhin, A.L.; Nie, X.; Leyland, A.; Matthews, A.; Dowey, S.J. Plasma electrolysis for surface engineering. *Surf. Coat. Technol.* **1999**, *122*, 73–93. [CrossRef]
9. Parfenov, E.V.; Yerokhin, A.; Nevyantseva, R.R.; Gorbatkov, M.V.; Liang, C.J.; Matthews, A. Towards smart electrolytic plasma technologies: An overview of methodological approaches to process modelling. *Surf. Coat. Technol.* **2015**, *269*, 2–22. [CrossRef]
10. Xue, W.; Deng, Z.; Lai, Y.; Chen, R. Analysis of Phase Distribution for Ceramic Coatings Formed by Microarc Oxidation on Aluminum Alloy. *J. Am. Ceram. Soc.* **2005**, *81*, 1365–1368. [CrossRef]
11. Chen, Y.; Lu, X.; Lamaka, S.V.; Ju, P.; Blawert, C.; Zhang, T.; Wang, F.; Zheludkevich, M.L. Active protection of Mg alloy by composite PEO coating loaded with corrosion inhibitors. *Appl. Surf. Sci.* **2020**, *504*, 144462. [CrossRef]
12. Shi, X.; Wang, Y.; Li, H.; Zhang, S.; Zhao, R.; Li, G.; Zhang, R.; Sheng, Y.; Cao, S.; Zhao, Y.; et al. Corrosion resistance and biocompatibility of calcium-containing coatings developed in near-neutral solutions containing phytic acid and phosphoric acid on AZ31B alloy. *J. Alloys Compd.* **2020**, *823*, 153721. [CrossRef]
13. Qin, J.; Shi, X.; Li, H.; Zhao, R.; Li, G.; Zhang, S.; Ding, L.; Cui, X.; Zhao, Y.; Zhang, R. Performance and failure process of green recycling solutions for preparing high degradation resistance coating on biomedical magnesium alloys. *Green Chem.* **2022**, *24*, 8113–8130. [CrossRef]
14. Aliofkhazraei, M.; Macdonald, D.; Matykina, E.; Parfenov, E.; Egorkin, V.; Curran, J.; Troughton, S.; Sinebryukhov, S.; Gnedenkov, S.; Lampke, T.; et al. Review of plasma electrolytic oxidation of titanium substrates: Mechanism, properties, applications and limitations. *Appl. Surf. Sci. Adv.* **2021**, *5*, 100121. [CrossRef]
15. Qin, J.; Chen, Y.; Chen, C.; Zhong, S.; Yan, Z.; Liu, W.; Wang, Y.; Lai, X.; Zhao, Y.; Zhao, R.; et al. Preparation of HA-containing coating by one-step MAO on titanium alloys through synergistic effect of calcium gluconate and calcium glycerophosphate. *Surf. Coat. Technol.* **2023**, *466*, 129655. [CrossRef]
16. Santos, J.S.; Lemos, S.G.; Gonçalves, W.N.; Bruno, O.M.; Pereira, E.C. Characterization of electrical discharges during spark anodization of zirconium in different electrolytes. *Electrochim. Acta* **2014**, *130*, 477–487. [CrossRef]
17. Sowa, M.; Woszczak, M.; Kazek-Kęsik, A.; Dercz, G.; Korotin, D.M.; Zhidkov, I.S.; Kurmaev, E.Z.; Cholakh, S.O.; Basiaga, M.; Simka, W. Influence of process parameters on plasma electrolytic surface treatment of tantalum for biomedical applications. *Appl. Surf. Sci.* **2017**, *407*, 52–63. [CrossRef]
18. Cheng, Y.; Wei, B.; Liu, Y.; Cheng, Y. Plasma electrolytic oxidation of copper in an aluminate based electrolyte with the respective additives of Na_3PO_4, NaH_2PO_4 and NaH_2PO_2. *Appl. Surf. Sci.* **2021**, *565*, 150477. [CrossRef]
19. Cheng, Y.; Zhu, Z.; Zhang, Q.; Zhuang, X.; Cheng, Y. Plasma electrolytic oxidation of brass. *Surf. Coat. Technol.* **2020**, *385*, 125366. [CrossRef]
20. Mizutani, Y.; Kim, S.J.; Ichino, R.; Okido, M. Anodizing of Mg alloys in alkaline solutions. *Surf. Coat. Technol.* **2003**, *169*, 143–146. [CrossRef]
21. Zhou, X.; Thompson, G.e.; Skeldon, P.; Wood, G.C.; Shimizu, K.; Habazaki, H. Film formation and detachment during anodizing of Al–Mg alloys. *Corros. Sci.* **1999**, *41*, 1599–1613. [CrossRef]
22. Blawert, C.; Dietzel, W.; Ghali, E.; Song, G. Anodizing Treatments for Magnesium Alloys and Their Effect on Corrosion Resistance in Various Environments. *Adv. Eng. Mater.* **2006**, *8*, 511–533. [CrossRef]
23. Guo, H.F.; An, M.Z.; Xu, S.; Huo, H.B. Formation of oxygen bubbles and its influence on current efficiency in micro-arc oxidation process of AZ91D magnesium alloy. *Thin. Solid. Films* **2005**, *485*, 53–58. [CrossRef]
24. Wang, L.; Chen, L.; Yan, Z.C.; Fu, W. Optical emission spectroscopy studies of discharge mechanism and plasma characteristics during plasma electrolytic oxidation of magnesium in different electrolytes. *Surf. Coat. Technol.* **2010**, *205*, 1651–1658. [CrossRef]
25. Ikonopisov, S. Theory of electrical breakdown during formation of barrier anodic films. *Electrochim. Acta* **1977**, *22*, 1077–1082. [CrossRef]
26. Yerokhin, A.L.; Snizhko, L.O.; Gurevina, N.L.; Leyland, A.; Pilkington, A.; Matthews, A. Discharge characterization in plasma electrolytic oxidation of aluminium. *J. Phys. D Appl. Phys.* **2003**, *36*, 2110–2120. [CrossRef]
27. Hussein, R.O.; Nie, X.; Northwood, D.O. An investigation of ceramic coating growth mechanisms in plasma electrolytic oxidation (PEO) processing. *Electrochim. Acta* **2013**, *112*, 111–119. [CrossRef]
28. Zhu, L.J.; Guo, Z.X.; Zhang, Y.F.; Li, Z.X.; Sui, M.L. A mechanism for the growth of a plasma electrolytic oxide coating on Al. *Electrochim. Acta* **2016**, *208*, 296–303. [CrossRef]

29. Hussein, R.O.; Nie, X.; Northwood, D.O.; Yerokhin, A.; Matthews, A. Spectroscopic study of electrolytic plasma and discharging behaviour during the plasma electrolytic oxidation (PEO) process. *J. Phys. D Appl. Phys.* **2010**, *43*, 105203. [CrossRef]
30. Cheng, Y.-l.; Xue, Z.-g.; Wang, Q.; Wu, X.-Q.; Matykina, E.; Skeldon, P.; Thompson, G.E. New findings on properties of plasma electrolytic oxidation coatings from study of an Al–Cu–Li alloy. *Electrochim. Acta* **2013**, *107*, 358–378. [CrossRef]
31. Nominé, A.; Troughton, S.C.; Nominé, A.V.; Henrion, G.; Clyne, T.W. High speed video evidence for localised discharge cascades during plasma electrolytic oxidation. *Surf. Coat. Technol.* **2015**, *269*, 125–130. [CrossRef]
32. Troughton, S.C.; Nomine, A.; Dean, J.; Clyne, T.W. Effect of individual discharge cascades on the microstructure of plasma electrolytic oxidation coatings. *Appl. Surf. Sci.* **2016**, *389*, 260–269. [CrossRef]
33. Vladimirovich Timoshenko, A.; Vladimirovna Magurova, Y. Application of oxide coatings to metals in electrolyte solutions by microplasma methods. *Rev. Metal. Madr.* **2010**, *36*, 323–330. [CrossRef]
34. Gebarowski, W.; Pietrzyk, S. Influence of the Cathodic Pulse on the Formation and Morphology of Oxide Coatings on Aluminium Produced by Plasma Electrolytic Oxidation. *Arch. Metall. Mater.* **2013**, *58*, 241–245. [CrossRef]
35. Hussein, R.O.; Zhang, P.; Nie, X.; Xia, Y.; Northwood, D.O. The effect of current mode and discharge type on the corrosion resistance of plasma electrolytic oxidation (PEO) coated magnesium alloy AJ62. *Surf. Coat. Technol.* **2011**, *206*, 1990–1997. [CrossRef]
36. Cheng, Y.; Wang, T.; Li, S.; Cheng, Y.; Cao, J.; Xie, H. The effects of anion deposition and negative pulse on the behaviours of plasma electrolytic oxidation (PEO)—A systematic study of the PEO of a Zirlo alloy in aluminate electrolytes. *Electrochim. Acta* **2017**, *225*, 47–68. [CrossRef]
37. Jaspard-Mécuson, F.; Czerwiec, T.; Henrion, G.; Belmonte, T.; Dujardin, L.; Viola, A.; Beauvir, J. Tailored aluminium oxide layers by bipolar current adjustment in the Plasma Electrolytic Oxidation (PEO) process. *Surf. Coat. Technol.* **2007**, *201*, 8677–8682. [CrossRef]
38. Gębarowski, W.; Pietrzyk, S. Growth Characteristics of the Oxide Layer on Aluminium in the Process of Plasma Electrolytic Oxidation. *Arch. Metall. Mater.* **2014**, *59*, 407–411. [CrossRef]
39. Cheng, Y.L.; Feng, T.; Cheng, Y.L. A Systematic Study of the Role of Cathodic Polarization and New Findings on the Soft Sparking Phenomenon from Plasma Electrolytic Oxidation of an Al-Cu-Li Alloy. *J. Electrochem. Soc.* **2022**, *169*, 071505. [CrossRef]
40. Sah, S.P.; Tsuji, E.; Aoki, Y.; Habazaki, H. Cathodic pulse breakdown of anodic films on aluminium in alkaline silicate electrolyte–Understanding the role of cathodic half-cycle in AC plasma electrolytic oxidation. *Corros. Sci.* **2012**, *55*, 90–96. [CrossRef]
41. Sah, S.P.; Tatsuno, Y.; Aoki, Y.; Habazaki, H. Dielectric breakdown and healing of anodic oxide films on aluminium under single pulse anodizing. *Corros. Sci.* **2011**, *53*, 1838–1844. [CrossRef]
42. Rogov, A.B.; Yerokhin, A.; Matthews, A. The Role of Cathodic Current in Plasma Electrolytic Oxidation of Aluminum: Phenomenological Concepts of the "Soft Sparking" Mode. *Langmuir* **2017**, *33*, 11059–11069. [CrossRef]
43. Martin, J.; Nominé, A.; Brochard, F.J.L.B.; Briançon, J.L.; Noël, C.; Belmonte, T.; Czerwiec, T.; Henrion, G. Delay in microdischarges appearance during PEO of Al: Evidence of a mechanism of charge accumulation at the electrolyte/oxide interface. *Appl. Surf. Sci.* **2017**, *410*, 29–41. [CrossRef]
44. He, X.; Feng, T.; Cheng, Y.; Hu, P.; Le, Z.; Liu, Z.; Cheng, Y. Fast formation of a black inner α-Al2O3 layer doped with CuO on Al–Cu–Li alloy by soft sparking PEO process. *J. Am. Ceram. Soc.* **2023**, *106*, 7019–7042. [CrossRef]
45. Martin, J.; Melhem, A.; Shchedrina, I.; Duchanoy, T.; Nomine, A.; Henrion, G.; Czerwiec, T.; Belmonte, T. Effects of electrical parameters on plasma electrolytic oxidation of aluminium. *Surf. Coat. Technol.* **2013**, *221*, 70–76. [CrossRef]
46. Tousch, C.D.S.; Magniez, L.; Fontana, S.; Marcos, G.; Hérold, C.; Henrion, G.; Czerwiec, T.; Martin, J. Influence of carbon nanotubes on the plasma electrolytic oxidation process of aluminum under "soft" sparking conditions. *Surf. Coat. Technol.* **2023**, *468*, 129779. [CrossRef]
47. Tjiang, F.; Ye, L.W.; Huang, Y.J.; Chou, C.C.; Tsai, D.S. Effect of processing parameters on soft regime behavior of plasma electrolytic oxidation of magnesium. *Ceram. Int.* **2017**, *43*, S567–S572. [CrossRef]
48. Hussein, R.O.; Northwood, D.O.; Su, J.F.; Nie, X. A study of the interactive effects of hybrid current modes on the tribological properties of a PEO (plasma electrolytic oxidation) coated AM60B Mg-alloy. *Surf. Coat. Technol.* **2013**, *215*, 421–430. [CrossRef]
49. Hussein, R.O.; Northwood, D.O.; Nie, X. The influence of pulse timing and current mode on the microstructure and corrosion behaviour of a plasma electrolytic oxidation (PEO) coated AM60B magnesium alloy. *J. Alloys Compd.* **2012**, *541*, 41–48. [CrossRef]
50. Arrabal, R.; Matykina, E.; Hashimoto, T.; Skeldon, P.; Thompson, G.E. Characterization of AC PEO coatings on magnesium alloys. *Surf. Coat. Technol.* **2009**, *203*, 2207–2220. [CrossRef]
51. Rahmati, M.; Raeissi, K.; Toroghinejad, M.R.; Hakimizad, A.; Santamaria, M. Effect of Pulse Current Mode on Microstructure, Composition and Corrosion Performance of the Coatings Produced by Plasma Electrolytic Oxidation on AZ31 Mg Alloy. *Coatings* **2019**, *9*, 688. [CrossRef]
52. Rahmati, M.; Raeissi, K.; Toroghinejad, M.R.; Hakimizad, A.; Santamaria, M. Corrosion and wear resistance of coatings produced on AZ31 Mg alloy by plasma electrolytic oxidation in silicate-based K2TiF6 containing solution: Effect of waveform. *J. Magnes. Alloy* **2022**, *10*, 2574–2587. [CrossRef]
53. Pan, Y.K.; Chen, C.Z.; Wang, D.G.; Zhao, T.G. Improvement of corrosion and biological properties of microarc oxidized coatings on Mg-Zn-Zr alloy by optimizing negative power density parameters. *Colloids Surf. B Biointerfaces* **2014**, *113*, 421–428. [CrossRef] [PubMed]

54. Gao, Y.H.; Yerokhin, A.; Matthews, A. Effect of current mode on PEO treatment of magnesium in Ca- and P-containing electrolyte and resulting coatings. *Appl. Surf. Sci.* **2014**, *316*, 558–567. [CrossRef]
55. Tsai, D.S.; Chou, C.C. Review of the Soft Sparking Issues in Plasma Electrolytic Oxidation. *Metals* **2018**, *8*, 105. [CrossRef]
56. Liang, J.; Srinivasan, P.B.; Blawert, C.; Dietzel, W. Influence of chloride ion concentration on the electrochemical corrosion behaviour of plasma electrolytic oxidation coated AM50 magnesium alloy. *Electrochim. Acta* **2010**, *55*, 6802–6811. [CrossRef]
57. Liang, J.; Srinivasan, P.B.; Blawert, C.; Störmer, M.; Dietzel, W. Electrochemical corrosion behaviour of plasma electrolytic oxidation coatings on AM50 magnesium alloy formed in silicate and phosphate based electrolytes. *Electrochim. Acta* **2009**, *54*, 3842–3850. [CrossRef]
58. Bala Srinivasan, P.; Liang, J.; Balajeee, R.G.; Blawert, C.; Störmer, M.; Dietzel, W. Effect of pulse frequency on the microstructure, phase composition and corrosion performance of a phosphate-based plasma electrolytic oxidation coated AM50 magnesium alloy. *Appl. Surf. Sci.* **2010**, *256*, 3928–3935. [CrossRef]
59. Bala Srinivasan, P.; Liang, J.; Blawert, C.; Störmer, M.; Dietzel, W. Effect of current density on the microstructure and corrosion behaviour of plasma electrolytic oxidation treated AM50 magnesium alloy. *Appl. Surf. Sci.* **2009**, *255*, 4212–4218. [CrossRef]
60. NIST: Atomic Spectra Database Lines Form. Available online: https://physics.nist.gov/PhysRefData/ASD/lines_form.html (accessed on 30 September 2023).
61. Arrabal, R.; Mohedano, M.; Matykina, E.; Pardo, A.; Mingo, B.; Merino, M.C. Characterization and wear behaviour of PEO coatings on 6082-T6 aluminium alloy with incorporated α-Al2O3 particles. *Surf. Coat. Technol.* **2015**, *269*, 64–73. [CrossRef]
62. Nie, X.; Meletis, E.I.; Jiang, J.C.; Leyland, A.; Yerokhin, A.L.; Matthews, A. Abrasive wear/corrosion properties and TEM analysis of Al2O3 coatings fabricated using plasma electrolysis. *Surf. Coat. Technol.* **2002**, *149*, 245–251. [CrossRef]
63. Liu, Z.; Le, Z.; He, X.; Cheng, Y.; Hu, P.; Cheng, Y. Plasma electrolytic oxidation of tantalum in an aluminate electrolyte: Effect of cathodic polarization and frequency. *Ceram. Int.* **2023**, *in press*. [CrossRef]
64. Martini, C.; Ceschini, L.; Tarterini, F.; Paillard, J.M.; Curran, J.A. PEO layers obtained from mixed aluminate–phosphate baths on Ti–6Al–4V: Dry sliding behaviour and influence of a PTFE topcoat. *Wear* **2010**, *269*, 747–756. [CrossRef]
65. Duan, H.; Yan, C.; Wang, F. Growth process of plasma electrolytic oxidation films formed on magnesium alloy AZ91D in silicate solution. *Electrochim. Acta* **2007**, *52*, 5002–5009. [CrossRef]
66. Chen, D.; Wang, R.; Huang, Z.; Wu, Y.; Zhang, Y.; Wu, G.; Li, D.; Guo, C.; Jiang, G.; Yu, S.; et al. Evolution processes of the corrosion behavior and structural characteristics of plasma electrolytic oxidation coatings on AZ31 magnesium alloy. *Appl. Surf. Sci.* **2018**, *434*, 326–335. [CrossRef]

coatings

MDPI

Article

Production of Porous ZrO_2–TiO_2 Ceramic Coatings on the Biomedical Ti-6Al-4V Alloy via AC PEO Treatment and Their Effects on the Corrosion Behavior in 0.9% NaCl

Aline C. N. da Silva [1], Rafael P. Ribeiro [2], Elidiane C. Rangel [2], Nilson C. da Cruz [2] and Diego R. N. Correa [3,*]

[1] Department of Chemical Engineering and Civil Engineering, University of Sorocaba (UNISO), Sorocaba 18023-000, SP, Brazil; aline.nanuh@unesp.br
[2] Laboratory of Technological Plasma, Institute of Science and Technology, São Paulo State University (UNESP), Campus Sorocaba, Sorocaba 18087-180, SP, Brazil; rafael-parra.ribeiro@unesp.br (R.P.R.); elidiane.rangel@unesp.br (E.C.R.); nilson.cruz@unesp.br (N.C.d.C.)
[3] Laboratory of Anelasticity and Biomaterials, School of Sciences, São Paulo State University (UNESP), Campus Bauru, Bauru 17033-360, SP, Brazil
* Correspondence: diego.correa@unesp.br; Tel.: +55-(14)-31036179

Abstract: Ti and its alloys have been vastly employed in the manufacturing of biomedical implants for orthopedy and dentistry, especially the Ti-6Al-4V alloy (wt%), which is the most-used Ti alloy worldwide. However, the ion release of Al and V in the long term has been related to harmful effects on the human body. In this scenario, surface modification strategies, such as plasma electrolytic oxidation (PEO), have often been performed in Ti alloys to match the clinical needs. This study evaluated the effect of electrical AC parameters on the surface of the commercial Ti-6Al-4V alloy immersed in ZrO_2-rich electrolytic solution regarding the chemical, physical, structural, and topographical aspects. Then, the selected PEO-treated samples surpassed the electrochemical test in saline solution. The results indicated that the electrical AC parameters affect the duration and intensity of the oxidative reactions and plasma micro-discharge steps, resulting in porous and thick oxide layers. PEO treatment promoted bio-camouflage of the surface, enriching it with TiO_2, ZrO_2, and $ZrTiO_4$ compounds and depleting it of Al and V. After screening the PEO-treated samples and their corrosion behavior, the results indicated that the porous ZrO_2–TiO_2 ceramic coatings in the Ti-6Al-4V alloy can be a viable alternative for the manufacturing of biomedical implants.

Keywords: biomaterial; Ti-6Al-4V; AC; PEO; ZrO_2; corrosion

Citation: da Silva, A.C.N.; Ribeiro, R.P.; Rangel, E.C.; da Cruz, N.C.; Correa, D.R.N. Production of Porous ZrO_2–TiO_2 Ceramic Coatings on the Biomedical Ti-6Al-4V Alloy via AC PEO Treatment and Their Effects on the Corrosion Behavior in 0.9% NaCl. *Coatings* **2024**, *14*, 866. https://doi.org/10.3390/coatings14070866

Academic Editors: Marta Mohedano and Raul Arrabal

Received: 24 May 2024
Revised: 2 July 2024
Accepted: 4 July 2024
Published: 10 July 2024

1. Introduction

Metallic biomaterials play an essential role in current medicine, mainly in the repair, substitution, or fixation of hard tissues in the human body. Moreover, these materials significantly contribute to the treatment of traumas and diseases; the current biometals did not completely reproduce the complex cell and tissue functions in the human body, thus requiring the development of new strategies for manufacturing and processing [1]. Commercial metallic biomaterials, such as stainless steel, Co–Cr alloys, and Ti and its alloys, are extensively employed in orthopedic and dental implants for the replacement of bones and joints, especially in the hip and knee, where they are exposed to distinct biomedical loads under contact with body fluids [2]. To enhance the biocompatibility and durability of these implants, there is a growing demand for research and development of surface modification strategies to guarantee long-term success in their usage.

Titanium and its alloys have been the primary choice for the fabrication of biomedical implants due to their exceptional properties, including high mechanical strength-to-density ratio, low elastic modulus, corrosion resistance, biocompatibility, and osseointegration ability [3]. Ti-6Al-4V (wt%) ELI (Extra-Low Interstitial), also known as commercially pure titanium grade 5 (CP-Ti V), is the most used Ti alloy worldwide, especially in medicine, as

implants, plates, pins, and screws [4]. However, the Al and V ion release after long-term implantation via corrosion and wear mechanisms have been related to neurological and toxic reactions in the human body [5]. For example, studies have demonstrated the presence of Al ions in the brain tissue on patients with Alzheimer's disease, multiple sclerosis, and autism, while V was related to neurological problems. Thus, there is a growing demand for research in surface modification to obtain biomedical implants with surfaces that match the clinical needs [6–8].

Plasma electrolytic oxidation (PEO) is a conventional technique used to modify the surface of valve metals, like Ti and its alloys. The technique applied an anodic AC or DC potential in the metallic surface immersed in an electrolytic solution, resulting in the growth of a thick oxide layer. As this layer acts as an electrical insulator, it accumulates electrical charges until the advent of dielectric breakdown, which promotes plasma micro-discharges that turn the outer surface porous [9]. The local high temperature and pressure induces the synthesis of metastable phases, while the electrical field supplies the necessary driving force for chemical species in the electrolytic solution to be incorporated in the oxide layer [10]. Thus, the PEO-treated surfaces generally exhibit a thick and porous layer, firmly adherent to the substrate and decorated with strategic chemical species [11]. However, only a few reports have exploited the effect of the electrical parameters in the surface during PEO treatment with an AC power source due to its complex group of electrical parameters, which opens possibilities to obtain coatings with unique properties compared to those reported so far.

Zirconia (ZrO_2) is a non-harmful transition metal oxide with vast biomedical applications as ceramic materials and coatings [12,13]. It has demonstrated outstanding anticancer, antibacterial, and antioxidant actions in the human organism [14]. In addition, its excellent biocompatibility and chemical stability make the compound attractive for use in medicine, dentistry, and pharmacy, especially as endosseous implants, abutments, and drug deliveries [15]. Nikoomanzari et al. [16] investigated the surface aspects of PEO-treated Ti-6Al-4V alloy in a ZrO_2-rich nanoparticle (NP) solution under a DC power source. The authors found a porous and thick oxide layer, with the ZrO_2 NPs absorbed through the pore walls, which significantly enhanced the antibacterial effect against *Escherichia coli*, *Staphylococcus aureus*, and *Staphylococcus epidermidis*, and the anticorrosive behavior in Hank's solution. More recently, Nikoomanzari et al. [17] demonstrated the beneficial effect of the $ZrTiO_4/TiO_2$ composite coating, obtained via the same PEO treatment on the Ti-6Al-4V alloy, in the electrochemical, cytotoxicity, and photocatalytic behavior, which confirmed the great potential for biomedical application.

This study aims to evaluate the effect of electrical AC parameters on the growth of a porous ZrO_2–TiO_2 coating on the biomedical Ti-6Al-4V alloy by performing a PEO treatment in ZrO_2-rich electrolyte. The surface of the PEO-treated samples was evaluated in terms of topography, chemical composition, phase proportion, thickness, roughness, and contact angle. Then, the preliminary electrochemical aspects in 0.9% NaCl were analyzed in selected samples to assess their potential for use as a biomedical implant.

2. Materials and Methods

Disk-shaped samples of Ti-6Al-4V (wt%) alloy (ASTM F136) [18], with dimensions of 10 mm diameter (Ø) × 3 mm thickness, were used as a substrate. Powders of zirconium oxide (ZrO_2; 99%; 5 μm) and potassium hydroxide (KOH; 90%; ~50 μm), purchased from Sigma-Aldrich Inc. (Cotia, Brazil), were used in the PEO treatments. The samples were preliminarily polished with waterproof SiC emery papers (#220 to #1000 mesh), sonicated in acetone, isopropyl alcohol, distilled water baths, and dried with air stream.

The electrolyte comprised an aqueous solution of 0.08 $mol \cdot L^{-1}$ ZrO_2 and 0.04 $mol \cdot L^{-1}$ KOH. The PEO treatments were performed in a system consisting of a pulsed alternating current (AC) power supply (MAO-30, Plasma Technology Ltd., Hong Kong, China) in a water-cooled stainless-steel tank, which also served as the cathode, and a suspended electrode connected to the sample as the anode. The surface treatments were carried out

at voltages between 300 and 500 V, frequencies from 60 to 1000 Hz, duty cycles ranging from 10 to 70%, and treatment times of 1 up to 20 min. The sample nomenclatures and PEO parameters are summarized in Table 1.

Table 1. Evaluated electrical AC parameters.

Sample Designation	Voltage (V)	Time (min)	Duty Cycle (%)	Frequency (Hz)
300 V	300	5	40	1000
350 V	350			
375 V	375			
400 V	400			
425 V	425			
450 V	450			
500 V	500			
1 min	375	1	40	1000
3 min		3		
5 min		5		
7 min		7		
10 min		10		
15 min		15		
20 min		20		
10%	375	5	10	1000
20%			20	
30%			30	
40%			40	
50%			50	
60%			60	
70%			70	
60 Hz	375	5	40	60
100 Hz				100
250 Hz				250
400 Hz				400
550 Hz				550
700 Hz				700
850 Hz				850
1000 Hz				1000

The surface morphology was examined using scanning electron microscopy (SEM; JSM-6010LA, JEOL Ltd., Peabody, MA, USA), using the secondary electron beam mode (SE), with a spot size of 30 μm, at a voltage of 3 kV. Semi-quantitative chemical microanalysis and elemental mapping were performed using X-ray dispersive energy spectroscopy (EDS; JEOL Ltd., Peabody, MA, USA), with the detector coupled to the SEM equipment, operating at 10 kV. In the transmittance mode, the vibrational characteristics of molecular groups absorbed in the surfaces were analyzed using Fourier transform infrared spectroscopy (FTIR; Jasco Corp., Tokyo, Japan) at room temperature, with 128 scans and a resolution of 4 cm^{-1}. Further chemical characterization of the surface was determined with X-ray photoelectron spectroscopy (XPS; Thermo K-Alpha model, Thermo Scientific, Inc., Waltham, MA, USA), operating with a monochromatic radiation source of Al-K_α (1486 eV), a spot size of 400 μm, an energy step of 200 eV (resolution of 1 eV) for long-scan spectra, and an energy step 50 eV (resolution of 0.01 eV) for high-resolution spectra (short scan). The spectra were analyzed using the CasaXPS® software version 2.3.24, and the calibration was performed with the C1s peak. The phase composition was evaluated using X-ray diffraction (XRD; Panalytical X'Pert PRO, Westborough, MA, USA), with monochromatic Cu-K_α radiation (λ = 0.1544 nm), at a voltage of 45 kV, a current of 40 mA, in the θ-2θ mode, with a scan speed of 0.02° per sec, and a step size of 0.02°. Phase indexation was performed using the Highscore Plus® 3.0 software version 3.0 and crystallographic datasheets from

the International Centre for Diffraction Data (ICDD). The surface wettability was checked with contact angle measurements (Ramé-hart Instrument Co., Succasunna, NJ, USA) using a droplet of distilled water (30 μL) at room temperature. Arithmetic roughness (Ra) was measured using optical profilometry (Dektak 150 profilometer, Veeco Metrology, Tucson, AZ, USA), with a stylus radius of 12.5 μm, scan length of 100 μm, for 12 s, and with an applied load of 3 mg. Eddy's current method (Minipa equipment, model MCT 401) was used to estimate the coatings' thicknesses. The average values were calculated from ten different regions in each sample.

The electrochemical tests were conducted in a three-electrode system, with the sample placed as the working electrode, a platinum wire (Pt) as the counter electrode, and an Ag/AgCl wire as the reference electrode. The electrolyte was composed of an aqueous 0.9% NaCl solution, simulating physiological body fluid [19], kept at room temperature for all the experiments. The sample area in contact with the electrolyte was limited by an O-ring (Ø = 1 cm). The experiments were performed in an Autolab PGSAT128N potentiostat/galvanostat (Metrohm Ltd., Riverview, FL, USA). The open circuit potential (OCP) was measured for 3600 s, while the potentiodynamic polarization (PDP) test was measured in the range of −1 to 2 V vs. OCP, at a scan rate of 1 $mV \cdot s^{-1}$, and a step of 1 mV. The obtained results were evaluated using NOVA 2.0® software version 2.1.5. An electrochemical impedance spectroscopy (EIS) test was conducted with 10 points per decade, in the range 10^{-2}–10^{5} Hz, and with an amplitude of 10 mV vs. OCP.

3. Results

3.1. Effect of Electrical AC Parameters

The current density evolution as a function of the time for each electrical AC parameter of the PEO treatment is shown in Figure 1. Overall, all curves initially depicted a typical sharp decay resulting from the fast oxide layer growth under the anodic voltages, which limits the movement of electrical charges between the electrolyte and the metallic surface. The consecutive plateau in the current density can be linked with the equilibrium between the anodic oxidative reactions and the plasma micro-discharges locally occurring on the surface after the dielectric breakdown [9]. However, distinct aspects can be seen in the curves when varying the electrical AC parameters. The rise of the applied voltage produced more intense current densities, starting from ~1.25 $A \cdot cm^2$ to values above ~1.50 $A \cdot cm^2$, but all curves achieved ~0.50 $A \cdot cm^2$ at the end of the treatment. The augment of the duration time did not change the overall aspect of the curves, following the same plateau after 3 min of treatment. The duty cycle variation produced a non-linear augment in the current density, from ~0.50 $A \cdot cm^2$ to values above 1.00 $A \cdot cm^2$. The same trend can be seen for the frequency, where values above 700 Hz depicted the most intense current density values at the beginning of the treatment. From these results, it is possible to notice that the PEO parameters effectively modified the current density's magnitude in detriment of the curves' overall shape, which can directly impact the surface aspects of the samples. As pointed out by Vekateswarlu et al. [20], the distinct regions of the curves denote specific steps of the PEO treatments, such as anodic oxidation, dielectric breakdown, and steady-state regime, which can directly interfere with the surface aspects and incorporation of additives from the electrolyte.

The surface topography of the PEO-treated samples with the varying applied voltage is shown in Figure 2. The substrate depicted a smooth surface, with some grooves resulting from the metallographic preparation. Between 300 and 425 V, the samples were entirely covered by a thick oxide layer, having some minor pores uniformly distributed. Besides the oxidative reactions dominating this range, the increase in voltage produces a visible increase in pore size. Along 425 to 500 V, the surfaces seemed rough, with micro-sized pores surrounded by pancake-like structures resulting from solidifying melted species generated during the plasma micro-discharges. As pointed out by Wang et al. [21], the voltage can have a direct impact on the generation of energetic plasma micro-discharges, resulting in large pore sizes, which can positively promote cell viability and bone ingrowth.

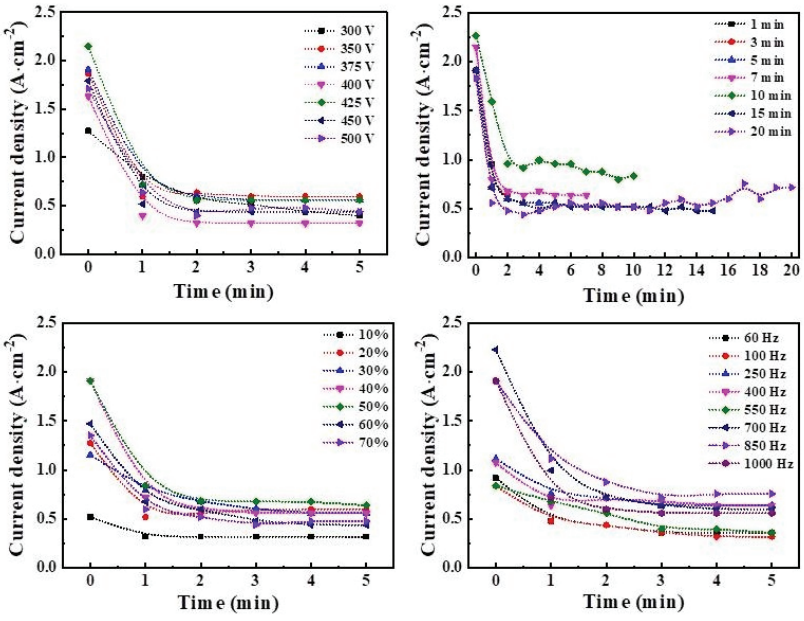

Figure 1. Current density vs. time plot for each electrical AC parameter.

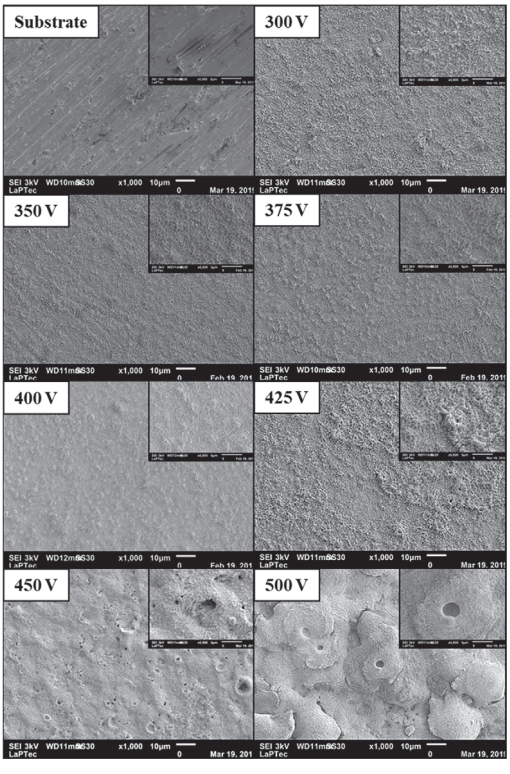

Figure 2. SEM imaging of the PEO-treated samples as a function of the applied voltage and zoomed view of the pore as inset.

The dependence of the surface topography with the duration time of the PEO treatment is shown in Figure 3. In the range of 1 and 3 min, the surface was coated by a smooth oxide layer, which completely covered the grooves from the substrate. Between 3 and 10 min, it is possible to note the distribution of minor pores along the oxide layer, indicating that the time was enough for the dielectric breakdown and the plasma micro-discharges. However, the treatment period between 10 and 20 min was too long, producing an exceeding growth of the oxide layer and resulting in the coverage of the pores. Li et al. [22] discussed that the duration time can be linked with the distinct PEO treatment steps illustrated in the current density plot. Thus, the time setup can interfere with the overall surface aspect, like topography and pores distribution.

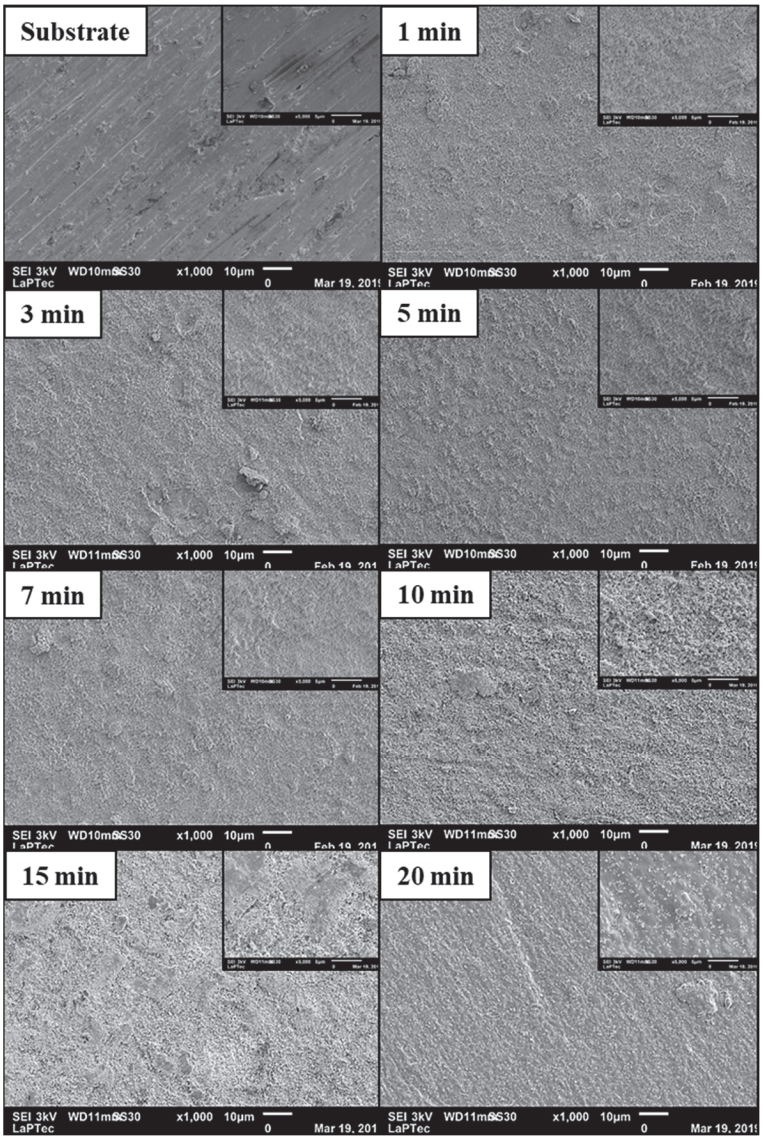

Figure 3. SEM imaging of the PEO-treated samples as a function of the duration time and zoomed view of the pore as inset.

The effect of the duty cycle in the surface topography of the PEO-treated samples is shown in Figure 4. The values between 10% and 40% did not effectively induce enough oxidative reactions on the surface once the grooves from the substrate are seen in the images. However, it was effective between 40% and 70%, where the surfaces depicted a rough aspect without marks of the grooves. Similarly, Abbas et al. [23] investigated the effect of duty cycle on the surface of commercially pure titanium grade 4 (CP-Ti IV) under PEO treatment in Ca- and P-rich electrolyte. The authors found that 60% of the duty cycle promoted the best combination of porous size, thickness, and roughness in the oxide layer, which enhanced the corrosion resistance in saline 3.5% NaCl solution.

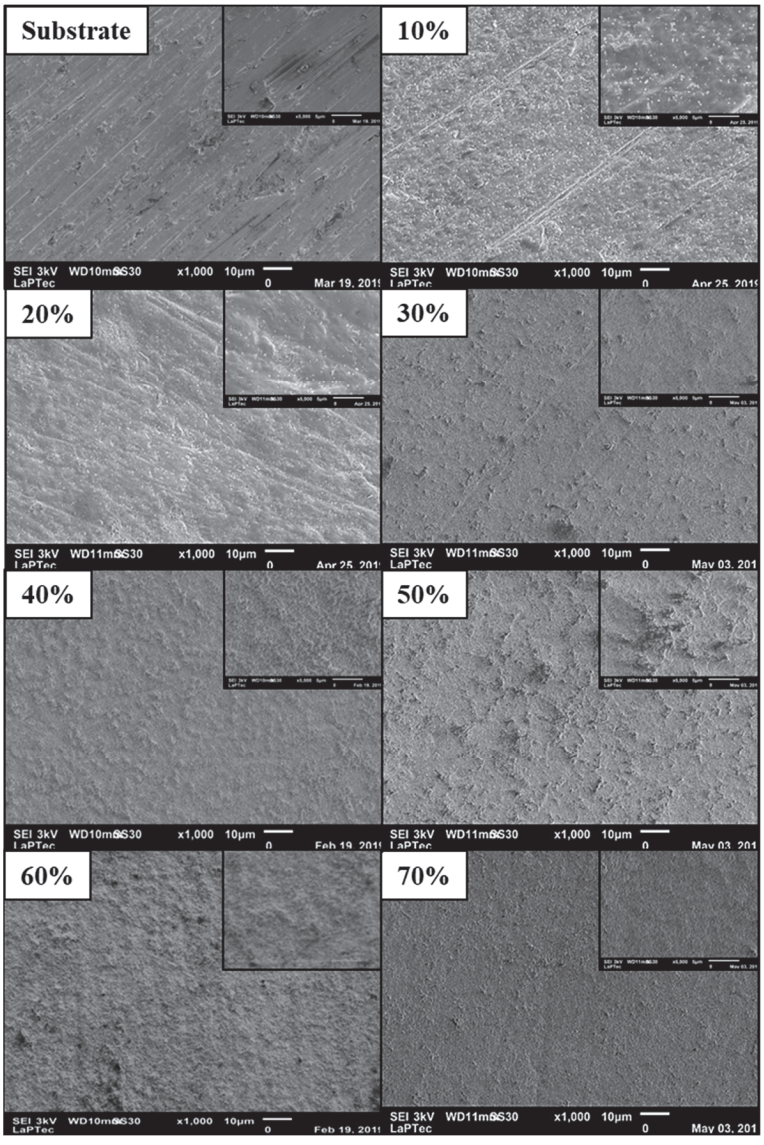

Figure 4. SEM imaging of the PEO-treated samples as a function of the duty cycle and zoomed view of the pore as inset.

The relationship between the frequency and surface topography of the PEO-treated samples can be seen in Figure 5. The samples treated between 60 and 550 Hz exhibited only a smooth surface without a precise pore distribution. However, some pores appeared between 550 and 1000 Hz and gradually increased in quantity and size. In particular, the PEO-treated sample at 1000 Hz depicted the most porous surface, with micro-sized pores distributed uniformly on the entire surface. Sobolev et al. [24] investigated the effect of frequency on the surface of the Ti-6Al-4V alloy after PEO treatment in a Na_2CO_3 and Na_2SiO_3-rich electrolyte. After evaluating the frequency range of 200 to 1000 Hz, the authors found that, besides the similar topographies, the PEO-treated sample at 1000 Hz depicted a more compact and thick oxide layer, having better corrosion resistance in saline 3.5% NaCl solution.

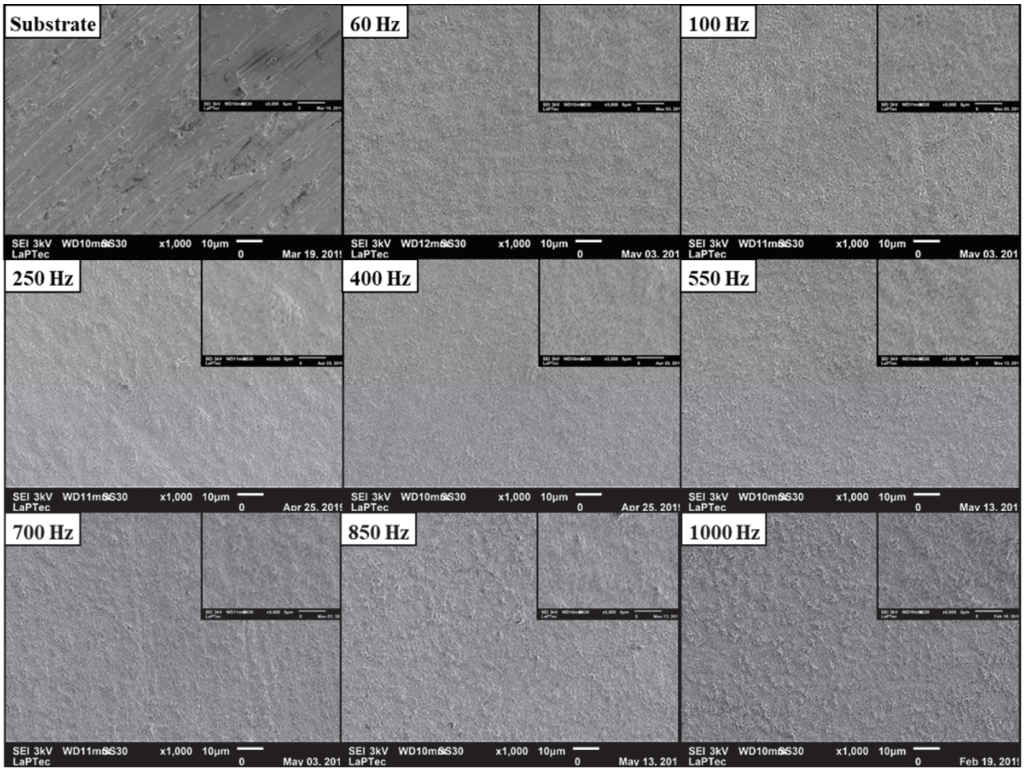

Figure 5. SEM imaging of the PEO-treated samples as a function of the frequency and zoomed view of the pore as inset.

The chemical proportion of the elements taken from EDS analysis for each electrical AC parameter is depicted in Figure 6. The results indicated that all the PEO-treated samples depicted a majority of oxygen (~60 at%), confirming the presence of a thick oxide layer. In addition, Ti and Zr elements were also predominant in the PEO-treated samples, probably in the form of metallic oxides. At the same time, Al and V elements remained as traces, with values lower than those detected for the substrate. This result shows that the PEO treatment was effective in bio-camouflaging the surface of the Al and V elements from the bulk in all evaluated parameters of this study. As Gabor et al. [25] highlighted, the PEO treatment on the Ti-6Al-4V alloy can favorably reduce the presence of Al and V elements on the surface, positively impacting the cell behavior for use as biomedical implants.

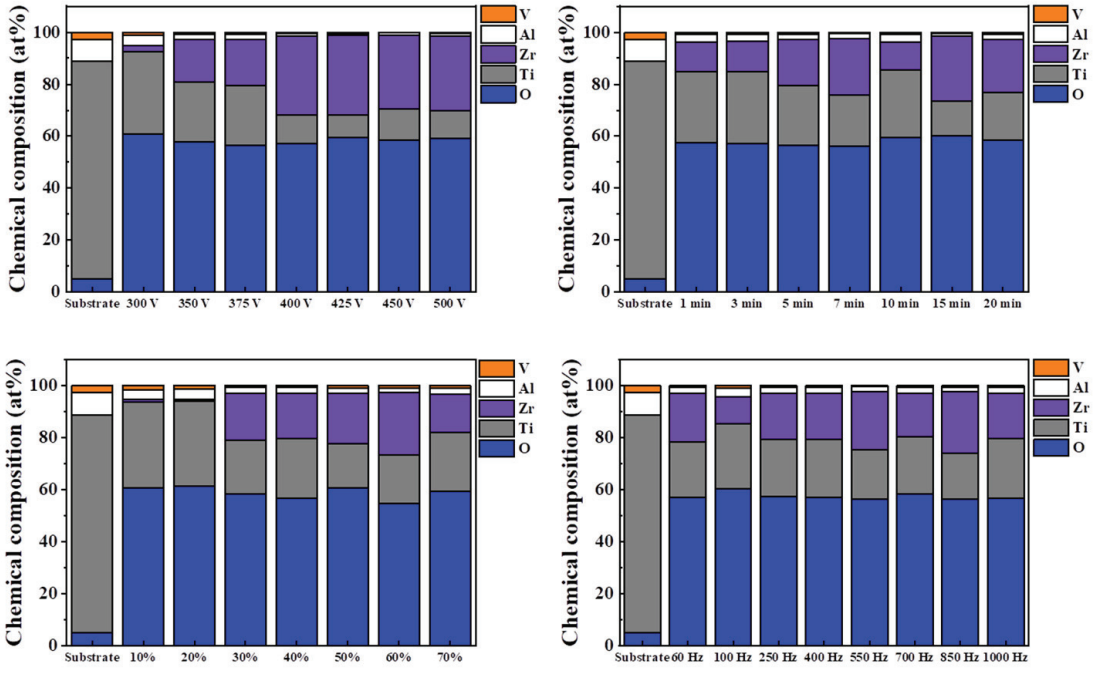

Figure 6. Semi-quantitative EDS analysis of the PEO-treated samples.

A view of the absorbed species in the outer surface of each sample can be seen in the FTIR spectrum exhibited in Figure 7. Overall, all samples depicted similar bands of chemical species naturally absorbed from the environment, indicating that the electrical AC parameters did not affect the chemical reactivity of the outer surface. It was possible to note vibrational bands related to organic compounds, like stretching H-O-H (1625 cm^{-1}), stretching C-O (1103 cm^{-1}), bending CH=CH (754 cm^{-1}), and also metallic oxides, like bending Ti-O-Ti (493 and 488 cm^{-1}) and Zr-O-Zr (568 and 478 cm^{-1}). The peak located at 568 cm^{-1} is attributed specifically to the monoclinic phase of ZrO_2 [26,27]. FTIR easily identifies the monoclinic ZrO_2 phase once its crystalline structure has a more significant number of active vibration modes in the infrared region than those presented by the tetragonal ZrO_2 phase and other Zr-based inorganic compounds [28]. In addition, the absorption bands attributed to Zr-O-Zr and Ti-O-Ti corroborate the results detected in the EDS results, which showed a predominance of Ti, Zr, and O in the coatings. It is possible to observe that the band attributed to H-O-H at 1625 cm^{-1} was wide, indicating different coordination states related to absorbed water molecules and other organic compounds. According to Mohsen et al. [28], the O-H terminal groups on the zirconia surface possess two coordination sites, one linked with a single Zr ion and the other with multi-coordinated two or three Zr ions. Thus, the presence of broad O-H bands reinforces the existence of the crystalline phase of ZrO_2.

Further details about the chemical composition in the outer layer of selected PEO-treated samples can be seen in Figure 8, which depicts the survey spectrums of the XPS analysis. The samples treated at 375 and 450 V were chosen to better comprehend the chemical aspects during the change from smooth to rough topography. Moreover, the EDS analysis indicated that the 15 min, 60 Hz, and 50% sample conditions were selected considering the amount of crystalline Zr oxide incorporated in the surfaces. The survey spectrums and the quantitative results indicated the prominent presence of C and O on the outer surface in the form of organic molecules, as corroborated with FTIR. The Zr and Ti

appeared as secondary elements, indicating the formation of metallic oxides, probably the most stable being TiO_2 and ZrO_2. Interestingly, the voltage increase from 375 V to 450 V increased the incorporation of Zr and diminished the amount of Ti, being a direct action of the driving force provided by the electric field, making it possible for more chemical species to be incorporated from the electrolyte [9]. The peculiar amount of Al detected in the 450 V sample can be related to the energetic plasma micro-discharges provided by the elevated anodic potential, which makes possible the removal of melted particles from the substrate, which solidify in the outer surface when in contact with the electrolyte [10]. The Au4f peak depicted in the 15 min sample is related to the sample holder and fixation of the equipment. Similarly, Maj et al. [29] investigated the chemical aspects of PEO-treated CP-Ti IV surfaces in a Na_2HPO_4-rich electrolyte. The EDS and XPS results indicated a gradual enrichment of chemical species from the electrolyte in the oxide layer, being considerably different in the inner and outer regions of the coating.

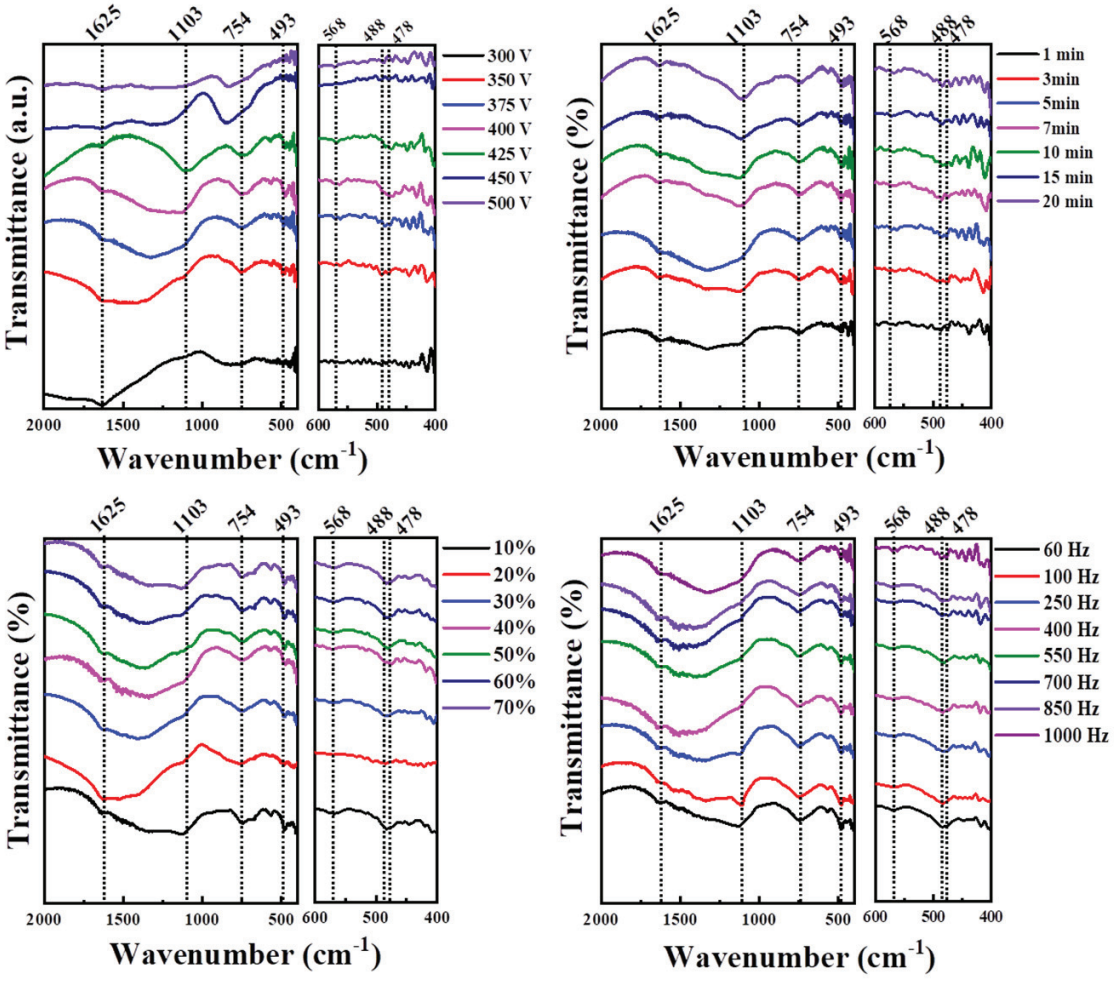

Figure 7. FTIR spectrum and zoomed view of the PEO-treated samples.

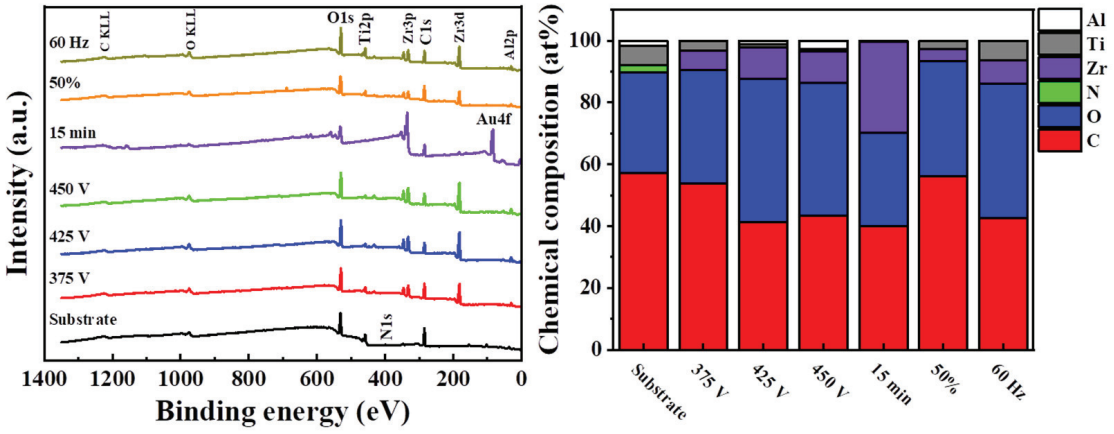

Figure 8. XPS analysis of the selected PEO-treated samples: (**left**) survey spectrums and (**right**) quantitative results.

The respective high-resolution spectrums for elements of interest in the samples are shown in Figure 9, and the quantitative results are depicted in Figure 10. The O1s spectrums of all samples exhibited peaks from O-H, C-O, and C=O groups; it is possible to conclude that the O-H peak in the O1s XPS spectrum should be mainly attributed to the presence of water, as already indicated with the FTIR results, and also a peak related to metallic oxides (M-O group). However, the PEO treatment resulted in a significant increase in the proportion of the M-O group and a decay in the O-H and C-O groups, evidencing the significant presence of the metallic oxides on the surfaces after the PEO treatment. The Ti2p spectrum of the substrate exhibited doublet peaks related to the Ti^{4+} (TiO_2) and sub-oxides, e.g., Ti^{2+} (TiO) and Ti^{3+} (Ti_2O_3), in similar proportions, and metal Ti^0 as a trace. After PEO treatment, all samples depicted a majority of TiO_2 and only minor amounts of sub-oxides. Similarly, the Zr3d spectrums of the PEO-treated samples showed doublet peaks related mainly to Zr^{4+} (ZrO_2) and a minor amount of sub-oxides, e.g., Zr^{2+} (ZrO) and Zr^{1+} (ZrOH), which could be formed during the plasma micro-discharges. Further details about the peak fitting of the high-resolution curves can be found in the Supplementary Materials. The presence of sub-oxides in the PEO-treated surfaces results from the local high pressure and temperature kept during the plasma micro-discharge and pore formation, favoring traces of amorphous and metastable phases [30].

The phase composition acquired from XRD measurements for each sample is shown in Figure 11. Overall, all the electrical AC parameters contributed significantly to modify the phase composition of the surfaces, depicting distinct amounts of anatase TiO_2 (CIF #7206075), monoclinic ZrO_2 (CIF #2108451), and $ZrTiO_4$ (CIF #176429) phases, together with the α-Ti (CIF #43416) phase originated from the bulk. All the PEO-treated samples depicted some diffraction peaks referred to oxide phases, indicating the successful covering of the surface by a uniform oxide layer. In terms of the applied voltage, the XRD profiles were composed mainly of monoclinic ZrO_2 and traces of anatase TiO_2 until 425 V, which were later replaced by a mixture of monoclinic ZrO_2 and $ZrTiO_4$, with traces of anatase TiO_2, over 450 V. Regarding the duration time, extended times just provided intense diffraction peaks related to the oxides, without apparent changes in the phase proportion, which remained mainly composed of monoclinic ZrO_2, with traces of $ZrTiO_4$ and anatase TiO_2. For the duty cycle, the XRD profiles depicted significant peaks from oxides only above 30%, which remained almost composed of monoclinic ZrO_2, with minor amounts of $ZrTiO_4$ and anatase TiO_2. Lastly, the frequency did not change abruptly the phase composition of the oxides, altering only the intensity of the α-Ti peaks, which can be related to the distinct thicknesses of the coatings. Altogether, the results can be linked with the primary roles of

each electrical AC parameter in the PEO treatment [9,11]. The higher voltages directly affect the driving force of the chemical species and the energy of the plasma micro-discharges, favoring the growth of the oxide layer and the synthesis of other compounds, such as $ZrTiO_4$. The extended duration time resulted in more incorporation of chemical species, the growth of a thick oxide layer, and intense diffraction peaks from oxide compounds. As the duty cycle is related to the percentage time of the applied voltage, it is natural that high duty cycles result in more oxide phases. Moreover, the frequency is related to the form of the periodic voltage, having more effect on the chemical and topographical aspects than the phase composition. As Echeverry-Rendón et al. [31] pointed out, adjusting of the electrical parameters in the PEO treatment of titanium surfaces can impact the surface characteristics such as phase composition, for instance. As a result, it can benefit the biological response, such as cell viability, adhesion, and proliferation.

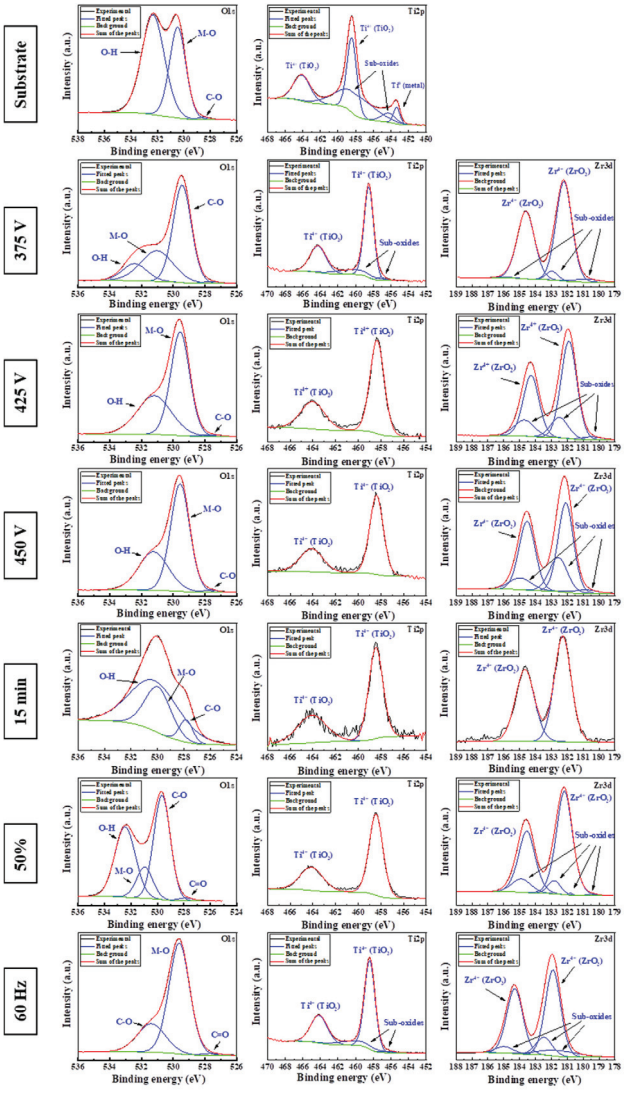

Figure 9. High-resolution XPS spectrums of the selected PEO-treated samples.

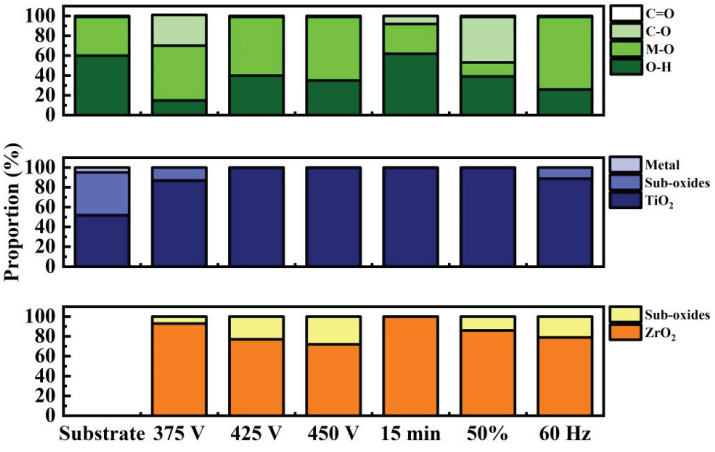

Figure 10. High-resolution XPS quantitative results.

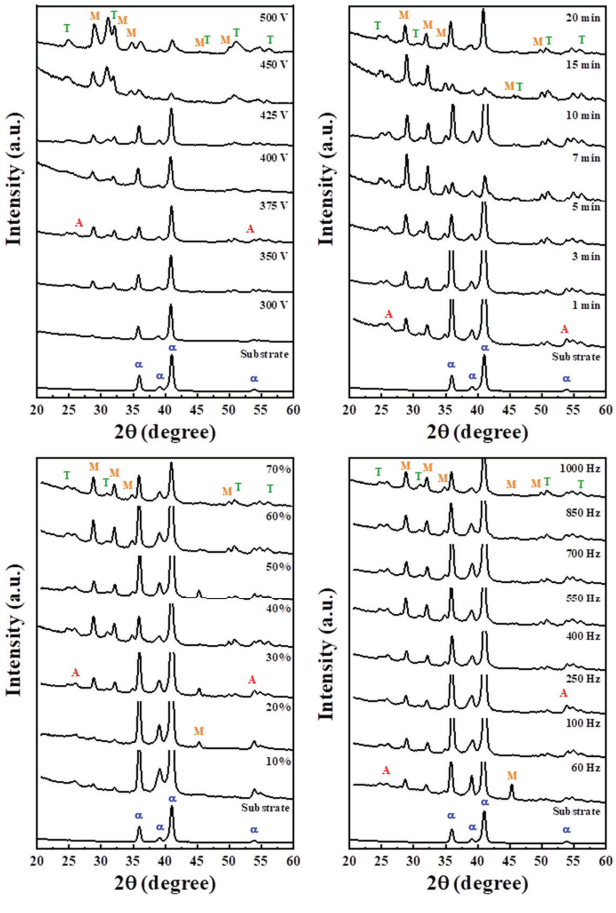

Figure 11. XRD profiles of the PEO-treated samples. Phases label: α-Ti (α), anatase TiO_2 (A), monoclinic (M) ZrO_2, and $ZrTiO_4$ (T).

The thickness, roughness, and contact angle values of the PEO-treated samples are depicted in Figure 12. The thickness values remained in the range of 3–5 μm for all PEO-treated samples, having a non-linear relationship with each electrical parameter. The roughness values remained in the order of some micrometers of all samples. Besides the roughness not producing a clear dependence on the electrical AC parameters, the rising of the applied voltage resulted in a gradual increase in the values, probably due to the large pore size as indicated through the SEM imaging. Lastly, all the PEO-treated samples possessed hydrophobic behavior, with contact angle values above 100°, higher than the substrate. This aspect can be directly linked with the enrichment of ZrO_2 in the outer layer, which has effective hydrophobic action in aqueous environments [17]. In summary, the distinct values of thickness, roughness, and contact angle result from the combined effect of anodic oxidation and plasma micro-charge generation, which impact the incorporation of chemical species from the electrolyte, porous formation, and coating growth [9].

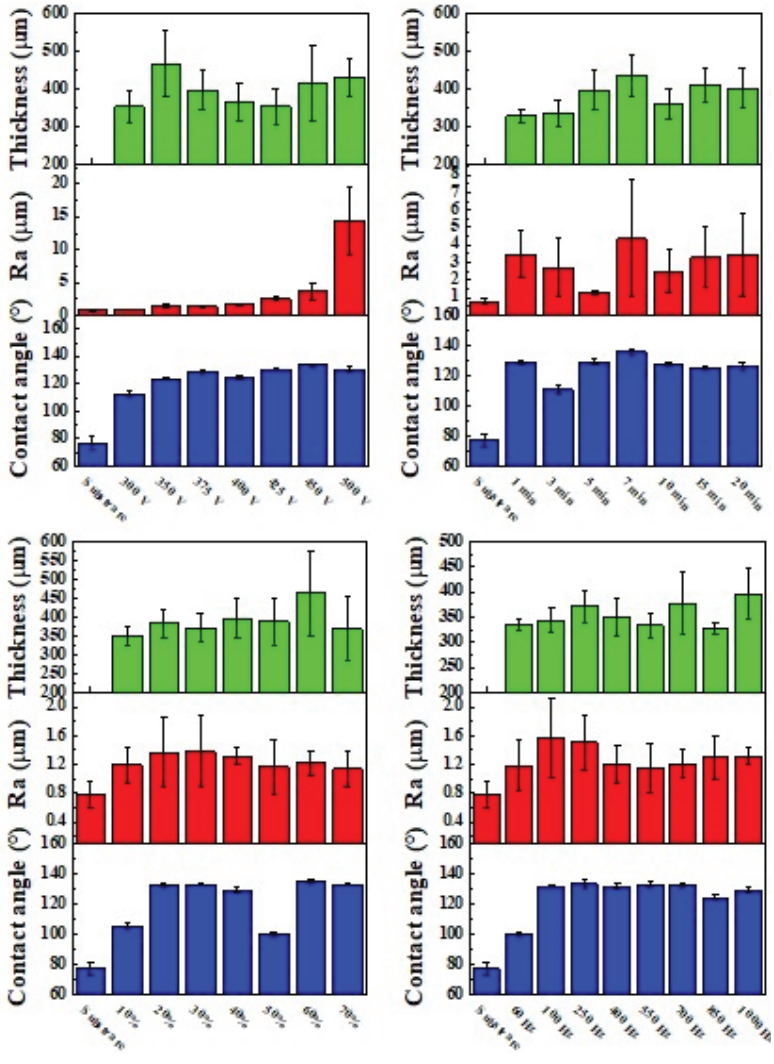

Figure 12. Physical aspects of the PEO-treated samples.

3.2. Preliminary Electrochemical Evaluation for Biomedical Applications

After screening the physical, chemical, structural, and topographical aspects of the PEO-treated samples regarding the electrical AC parameters, three conditions were selected for electrochemical evaluation: The sample treated at 375 V that exhibited a smooth surface with some minor pores, having similar amounts of Ti and Zr in the main form of anatase TiO_2 and monoclinic ZrO_2. The sample treated at 500 V that had a rough surface with large pore and pancake structures, massive amounts of Zr, a mixture of anatase TiO_2, monoclinic ZrO_2, and $ZrTiO_4$. Moreover, the sample treated at 20 min was chosen due to its characteristics being similar to the 375 V sample, differing in the higher amount of Zr incorporated into the surface.

The electrochemical behavior of the PEO-treated samples and the substrate in 0.9% NaCl solution is shown in Figure 13, and the respective quantitative results are depicted in Table 2. The OCP value indicates the thermodynamic stability of the test electrode (samples) in the given medium (electrolyte) [32,33]. Therefore, more negative OCP values reveal a predominance of anodic dissolution reactions during the corrosion [34]. In Figure 13a, the OCP curve of the substrate presented an upward behavior as a function of the immersion time. The increase in the OCP value after immersion suggests an improvement in the passive film formed, which leads to the inhibition of anodic surface reactions due to the forming of a protective barrier that isolates the metal from the medium [33]. The OCP result indicated that all the selected PEO-treated samples depicted nobler values than the substrate, with positive average values, indicating a more stable and protective oxide layer. The Zr-rich 20 min and 500 V samples had higher values than the 375 V sample. These results indicate that for the coatings investigated, the Zr content on the surface is more important than the roughness in terms of protection against corrosion, as the 375 V sample presented a lower Ra value (Figure 12), but with OCP values lower than the 20 min and 500 V samples. It is a result of the fact that Zr is a transition metal that, like Ti, presents a passivation behavior generating a protective film that is highly resistant to corrosion [32,34]. This factor justifies the more positive values presented for samples with higher Zr content. In the PDP curves (Figure 13b), it is possible to observe two regions: the cathodic region, which has more negative potential values than the corrosion potential, E_{corr}, and the anodic region, which has more positive values than E_{corr}. In the cathode region, water reduction and oxygen dissolution occur. In the anode region, hydrogen reduction and dissolution of metallic material (corrosion) occur [33]. Comparing the PDP curves of the coated samples with that of the substrate, a shift towards more positive potentials is observed. This anodic displacement represents the presence of a passive film that is more stable and, therefore, more protective than that present in the substrate [35]. The PDP curves indicated that the PEO-treated samples presented similar current density values to the substrate, in the order of 100 $nA \cdot cm^{-2}$. However, The PEO coatings significantly enhanced the corrosion potential with a similar R_p value, evidencing the better protection ability of the PEO-treated surfaces enriched with Zr. The Bode diagrams, illustrated in the impedance modulus $|Z|$ and phase angle as a function of frequency (Figure 13c,d), indicated a gradual decrease in $|Z|$ from ~10^2 $k\Omega \cdot cm^2$ to ~10^{-1} $k\Omega \cdot cm^2$ and a peak in the phase angle at intermediary frequencies, respectively. It denotes the presence of a protective layer on the surfaces of the PEO-treated samples. The Nyquist plot (Figure 13e) exhibited a single semi-circle, which is characteristic of a unique constant phase element (CPE) related to the oxide layer. The respective electrochemical electric circuit (EEC), depicted in Figure 13f, comprised a solution, oxide, and metal components in a series connection. The quantitative results (Table 2) indicated a dominant capacitive behavior of the oxide layer, indicated by the n/p value being close to 1.0 [36], with polarization resistance (R_{ox}) higher than those of the solution (R_s) and the metallic surface (R_{ct}). Thus, it can be noted that the PEO-treated samples depicted better electrochemical behavior under 0.9% NaCl than the bare substrate, as expected by the earlier studies, which also evidenced the role of ZrO_2 in corrosion resistance [37].

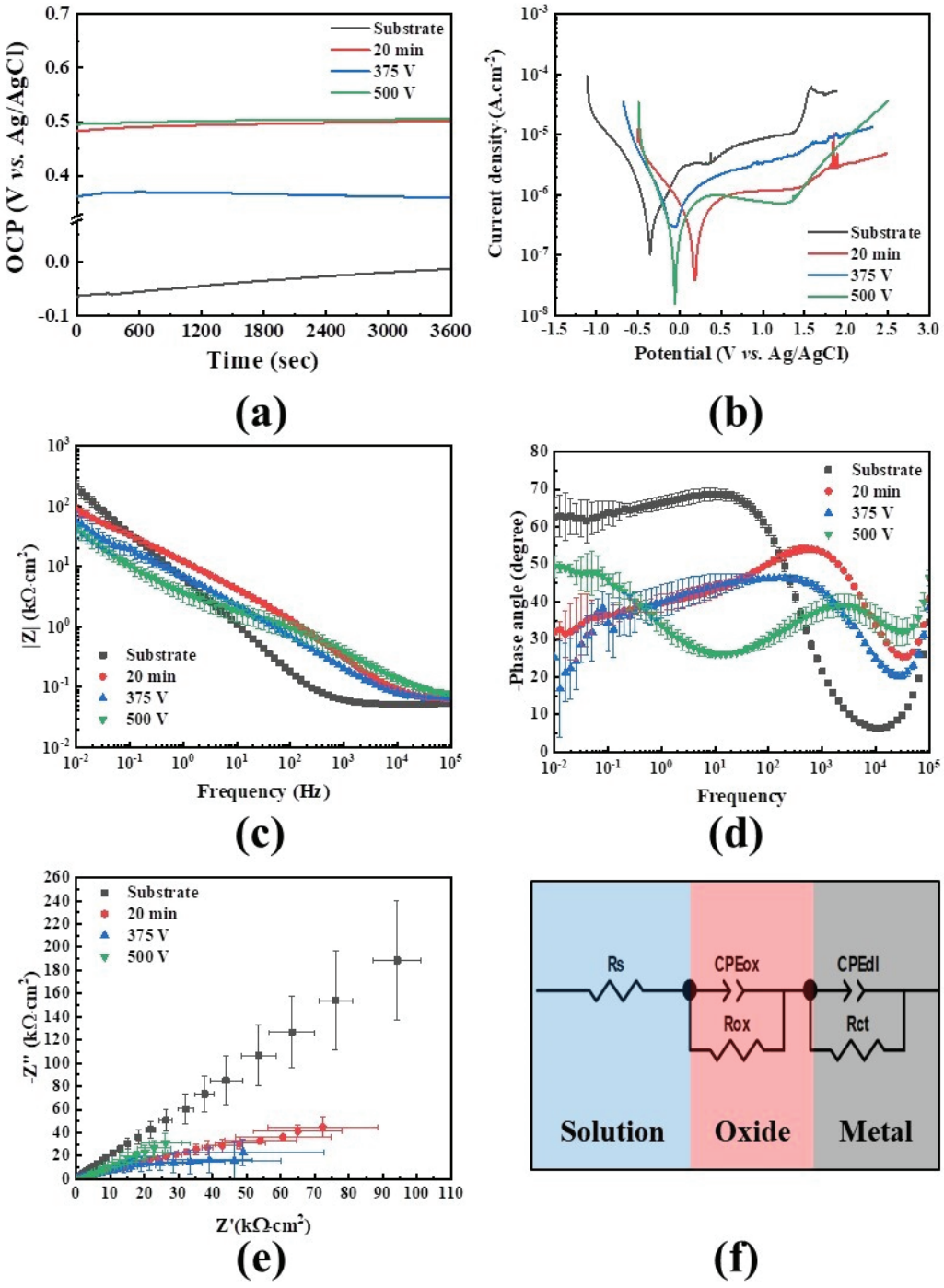

Figure 13. Electrochemical results of the selected PEO-treated samples: (**a**) OCP curves, (**b**) PDP curves, (**c**) Bode plot, (**d**) phase angle, (**e**) Nyquist plot, and (**f**) EEC diagram.

Table 2. Electrochemical parameters of the selected PEO-treated samples.

Analysis	Parameters	Substrate	20 min	375 V	500 V
OCP	Average OCP (V)	−0.067	0.493	0.326	0.505
PDP	E_{corr} (mV)	−381.3	182.5	−68.7	−55.5
	I_{corr} (nA·cm^{-2})	302.3	532.5	659.3	105.5
EIS	R_p (MΩ·cm^2)	0.244	0.267	0.183	0.276
	R_s (MΩ·cm^2)	5.27×10^{-5}	4.67×10^{-5}	4.10×10^{-5}	3.33×10^{-5}
	CPE_{ox} (μF·cm^2)	78.8	11.9	9.1	20.9
	n/p	0.83	0.72	0.75	0.54
	R_{ox} (MΩ·cm^2)	3.38×10^{-3}	4.11×10^{-3}	4.87×10^{-3}	2.26×10^{-3}
	C_{dl} (μF·cm^2)	40.8	36.4	52.4	119.4
	n/p	0.83	0.60	0.58	0.61
	R_{ct} (MΩ·cm^2)	1.30×10^{-3}	0.13×10^{-3}	0.17×10^{-3}	0.35×10^{-3}
	χ^2	5.14×10^{-4}	2.17×10^{-3}	3.94×10^{-3}	6.37×10^{-4}

4. Discussion

During the PEO treatment, the surface underwent an anodic potential, which induced oxidative reactions in the metallic titanium's surface placed as an anodic electrode (Equation (1)) and further TiO_2 growth (Equation (2)). At the same time, the water molecules in the electrolyte suffer hydrolysis (Equation (3)), while there is a reduction in hydrogen atoms in the cathodic electrode (Equation (4)) [10]. If the oxide coating grows, ZrO_2 particles from the electrolyte are gradually incorporated into the surface, enriching the outer region of the surface, as indicated with the EDS, FTIR, and XPS results.

$$Ti \rightarrow Ti^{4+} + 4e^- \quad (1)$$

$$Ti^{4+} + 4OH^- \rightarrow TiO_2 + 2H_2O \quad (2)$$

$$H_2O \rightarrow H^+ + OH^- \quad (3)$$

$$2H^+ + 2e^- \rightarrow H_2 \uparrow \quad (4)$$

With further oxide growth, the charge accumulation in the outer region promotes the dielectric breakdown and favors plasma micro-discharge generation. Thus, this step results in porous and rough topography, as indicated with the SEM images. However, the local high pressure and temperature during the plasma micro-discharges favor the synthesis of the $ZrTiO_4$ compounds, as indicated in Equation (5) [12], and the XRD results corroborate this.

$$TiO_2 + ZrO_2 \rightarrow ZrTiO_4 \quad (5)$$

According to Li et al. [38], when immersed in saline solution, the TiO_2 passive layer on the titanium surface reacts with NaCl, O_2, and water molecules to form Na_2TiO_3 (Equations (6) and (7)), which can be easily delaminated from the surface. Then, the reactive products HCl and Cl_2 diffuse through the passive layer and react with the metallic titanium, resulting in $TiCl_4$ (Equations (8) and (9)), which further transforms to TiO_2 (Equation (10)) and re-takes the reaction with NaCl. As indicated from the corrosion tests, the enrichment of ZrO_2 particles and the presence of $ZrTiO_4$ compound in the TiO_2 oxide layer hinder the corrosion mechanisms and protect the surface from degradation. Thus, it can be noted that the formation of porous ZrO_2–TiO_2 ceramic coatings on the Ti-6Al-4V al-

loys via the PEO treatment can be a helpful strategy to avoid the degradation of biomedical implants made of titanium.

$$4NaCl + 2TiO_2 + 2H_2O \rightarrow 2Na_2TiO_3 + 4HCl \quad (6)$$

$$4NaCl + 2TiO_2 + O_2 \rightarrow 2Na_2TiO_3 + 2Cl_2 \quad (7)$$

$$Ti + 2Cl_2 \rightarrow TiCl_4 \quad (8)$$

$$Ti + 4HCl \rightarrow TiCl_4 + 2H_{2\uparrow} \quad (9)$$

$$TiCl_4 + 2H_2O \rightarrow TiO_2 + 4HCl \quad (10)$$

5. Conclusions

This study used PEO treatment with a ZrO_2-rich electrolyte in the commercial Ti-6Al-4V alloy. The effect of the electrical AC parameters on the chemical, physical, structural, and topographical aspects of the surface was addressed. Then, selected PEO-treated samples were submitted to electrochemical evaluation in 0.9% NaCl solution. From the results reported in the present study, it is possible to conclude the following:

- The electrical AC parameters affected the initial current density without significant modification in the overall shape of the curves, indicating some minor changes in the oxidative reactions and plasma micro-discharges;
- The topography of the PEO-treated samples depended differently on each electrical AC parameter, interfering in the domain of oxidative reactions or plasma micro-discharges, resulting in a smooth and thick oxide layer with porous structures;
- The chemical analyses indicated that the PEO treatment successfully incorporated ZrO_2 in the TiO_2 layer, bio-camouflaging the surface of the potentially harmful Al and V ions. Moreover, the electrical AC parameters did not modify the ability to absorb organic molecules from the ambient environment, the plasma micro-discharges promote the formation of a considerable amount of $ZrTiO_4$;
- All the PEO-treated samples depicted micro-scaled thickness and roughness without clear dependence on the electrical AC parameters. However, all the PEO-treated samples showed considerable hydrophobic behavior compared to the bare substrate, which was related to the role of ZrO_2 enrichment on the surface;
- Electrochemical evaluation of selected PEO-treated samples in 0.9% NaCl indicated a considerable enhancement of the average OCP, corrosion current density, corrosion potential, and impedance values compared to the bare substrate. The EIS results indicated the presence of a single CPE element with a significant capacitive aspect, which provided protection and nobler behavior of the metallic surface;
- The selected PEO-treated samples resulted in porous ZrO_2–TiO_2 ceramic coatings with superior corrosion strength, which could benefit biomedical implants, especially those used for hard-tissue replacements in the long-term. Further biological and antimicrobial testing can be helpful to screen its potential thoroughly as a biomaterial.

Supplementary Materials: The following supporting information can be downloaded at: https://www.mdpi.com/article/10.3390/coatings14070866/s1, Figure S1—High-resolution XPS spectrums of the substrate; Figure S2—High-resolution XPS spectrums of the PEO-treated sample at 375 V; Figure S3—High-resolution XPS spectrums of the PEO-treated sample at 425 V; Figure S4—High-resolution XPS spectrums of the PEO-treated sample at 450 V; Figure S5—High-resolution XPS spectrums of the PEO-treated sample at 15 min; Figure S6—High-resolution XPS spectrums of the PEO-treated sample at 50%; Figure S7—High-resolution XPS spectrums of the PEO-treated sample at 60 Hz; Table S1—Quantitative results of the high-resolution XPS spectrums.

Author Contributions: A.C.N.d.S.: Validation, Formal analysis, Investing, Data curation, Writing—Original Draft. R.P.R.: Formal analysis, Investigation, Writing—Review and Editing. E.C.R.: Data curation, Resources, Writing—Review and Editing. N.C.d.C.: Resources, Writing—Review and Editing, Funding acquisition. D.R.N.C.: Conceptualization, Methodology, Resources, Writing—Review and Editing, Supervision, Project administration, Funding acquisition. All authors have read and agreed to the published version of the manuscript.

Funding: This study was funded by the National Council for Scientific and Technological Research (CNPq grants #407251/2018-9 and #404020/2023-2) and São Paulo Research Foundation (FAPESP grants #2018/24931-7 and #2021/13921-3) funding agencies.

Institutional Review Board Statement: Not applicable.

Informed Consent Statement: Not applicable.

Data Availability Statement: Data can be shared upon request.

Acknowledgments: The authors thank the Brazilian Nanotechnology National Laboratory (LNNano) for the XPS experiment (Proposal #24721/2019 and #20232420).

Conflicts of Interest: The authors declare no conflicts of interest.

References

1. Sarraf, M.; Rezvani Ghomi, E.; Alipour, S.; Ramakrishna, S.; Liana Sukiman, N. A State-of-the-Art Review of the Fabrication and Characteristics of Titanium and Its Alloys for Biomedical Applications. *Bio-Des. Manuf.* **2022**, *5*, 371–395. [CrossRef] [PubMed]
2. Pesode, P.; Barve, S. A Review—Metastable β Titanium Alloy for Biomedical Applications. *J. Eng. Appl. Sci.* **2023**, *70*, 25. [CrossRef]
3. SHao, L.; Du, Y.; Dai, K.; Wu, H.; Wang, Q.; Liu, J.; Tang, Y. β-Ti Alloys for Orthopedic and Dental Applications: A Review. *Coatings* **2021**, *11*, 1446. [CrossRef]
4. Kaur, M.; Singh, K. Review on Titanium and Titanium Based Alloys as Biomaterials for Orthopaedic Applications. *Mater. Sci. Eng. C* **2019**, *102*, 844–862. [CrossRef] [PubMed]
5. Eliaz, N. Corrosion of Metallic Biomaterials: A Review. *Materials* **2019**, *12*, 407. [CrossRef] [PubMed]
6. Mirza, A.; King, A.; Troakes, C.; Exley, C. Aluminium in Brain Tissue in Familial Alzheimer's Disease. *J. Trace Elem. Med. Biol.* **2017**, *40*, 30–36. [CrossRef] [PubMed]
7. Exley, C.; Clarkson, E. Aluminium in Human Brain Tissue from Donors without Neurodegenerative Disease: A Comparison with Alzheimer's Disease, Multiple Sclerosis and Autism. *Sci. Rep.* **2020**, *10*, 7770. [CrossRef] [PubMed]
8. Mold, M.; Chmielecka, A.; Rodriguez, M.R.R.; Thom, F.; Linhart, C.; King, A.; Exley, C. Aluminium in Brain Tissue in Multiple Sclerosis. *Int. J. Environ. Res. Public Health* **2018**, *15*, 1777. [CrossRef]
9. Simchen, F.; Sieber, M.; Kopp, A.; Lampke, T. Introduction to Plasma Electrolytic Oxidation—An Overview of the Process and Applications. *Coatings* **2020**, *10*, 628. [CrossRef]
10. Sikdar, S.; Menezes, P.V.; Maccione, R.; Jacob, T.; Menezes, P.L. Plasma Electrolytic Oxidation (PEO) Process—Processing, Properties, and Applications. *Nanomaterials* **2021**, *11*, 1375. [CrossRef]
11. Aliofkhazraei, M.; Macdonald, D.D.; Matykina, E.; Parfenov, E.V.; Egorkin, V.S.; Curran, J.A.; Troughton, S.C.; Sinebryukhov, S.L.; Gnedenkov, S.V.; Lampke, T.; et al. Review of Plasma Electrolytic Oxidation of Titanium Substrates: Mechanism, Properties, Applications and Limitations. *Appl. Surf. Sci. Adv.* **2021**, *5*, 100121. [CrossRef]
12. Molaei, M.; Nouri, M.; Babaei, K.; Fattah-Alhosseini, A. Improving Surface Features of PEO Coatings on Titanium and Titanium Alloys with Zirconia Particles: A Review. *Surf. Interfaces* **2021**, *22*, 100888. [CrossRef]
13. Jiang, X.J.; Bao, S.J.; Zhang, L.W.; Zhang, X.Y.; Jiao, L.S.; Qi, H.B.; Wang, F. Effect of Zr on Microstructure and Properties of TC4 Alloy Fabricated by Laser Additive Manufacturing. *J. Mater. Res. Technol.* **2023**, *24*, 8782–8792. [CrossRef]
14. Bapat, R.A.; Yang, H.J.; Chaubal, T.V.; Dharmadhikari, S.; Abdulla, A.M.; Arora, S.; Rawal, S.; Kesharwani, P. Review on Synthesis, Properties and Multifarious Therapeutic Applications of Nanostructured Zirconia in Dentistry. *RSC Adv.* **2022**, *12*, 12773–12793. [CrossRef]
15. Patil, N.A.; Kandasubramanian, B. Biological and Mechanical Enhancement of Zirconium Dioxide for Medical Applications. *Ceram. Int.* **2020**, *46*, 4041–4057. [CrossRef]
16. Nikoomanzari, E.; Fattah-alhosseini, A.; Pajohi Alamoti, M.R.; Keshavarz, M.K. Effect of ZrO_2 Nanoparticles Addition to PEO Coatings on Ti–6Al–4V Substrate: Microstructural Analysis, Corrosion Behavior and Antibacterial Effect of Coatings in Hank's Physiological Solution. *Ceram. Int.* **2020**, *46*, 13114–13124. [CrossRef]
17. Nikoomanzari, E.; Fattah-alhosseini, A.; Karbasi, M.; Nourian, A. A Versatile TiO_2/ZrO_2 Nanocomposite Coating Produced on Ti-6Al-4V via Plasma Electrolytic Oxidation Process. *Surf. Interfaces* **2022**, *32*, 102128. [CrossRef]
18. *ASTM F136-13*; Standard Specification for Wrought Titanium-6Aluminum-4Vanadium ELI (Extra Low Interstitial) Alloy for Surgical Implant Applications (UNS R56401). ASTM International: West Conshohocken, PA, USA, 2021.

19. Marcuz, N.; Ribeiro, R.P.; Rangel, E.C.; Cruz, N.C.; Possato, L.G.; Coan, K.S.; Grandini, C.R.; Correa, D.R.N. Exploiting the Effect of PEO Parameters on the Surface of AISI 1020 Low-Carbon Steel Treated in a TaOH-Rich Electrolyte. *Surf. Coat. Technol.* **2024**, *477*, 130374. [CrossRef]
20. Venkateswarlu, K.; Rameshbabu, N.; Sreekanth, D.; Bose, A.C.; Muthupandi, V.; Babu, N.K.; Subramanian, S. Role of Electrolyte Additives on In-Vitro Electrochemical Behavior of Micro Arc Oxidized Titania Films on Cp Ti. *Appl. Surf. Sci.* **2012**, *258*, 6853–6863. [CrossRef]
21. Wang, R.; Ni, S.; Ma, L.; Li, M. Porous Construction and Surface Modification of Titanium-Based Materials for Osteogenesis: A Review. *Front. Bioeng. Biotechnol.* **2022**, *10*, 973297. [CrossRef]
22. Li, G.; Ma, F.; Liu, P.; Qi, S.; Li, W.; Zhang, K.; Chen, X. Review of Micro-Arc Oxidation of Titanium Alloys: Mechanism, Properties and Applications. *J. Alloys Compd.* **2023**, *948*, 169773. [CrossRef]
23. Abbas, A.; Kung, H.-P.; Lin, H.-C. Effects of Electrical Parameters on Micro-Arc Oxidation Coatings on Pure Titanium. *Micromachines* **2023**, *14*, 1950. [CrossRef] [PubMed]
24. Sobolev, A.; Kossenko, A.; Borodianskiy, K. Study of the Effect of Current Pulse Frequency on Ti-6Al-4V Alloy Coating Formation by Micro Arc Oxidation. *Materials* **2019**, *12*, 3983. [CrossRef] [PubMed]
25. Gabor, R.; Doubkova, M.; Gorosova, S.; Malanik, K.; Vandrovcova, M.; Cvrcek, L.; Drobikova, K.; Mamulova Kutlakova, K.; Bacakova, L. Preparation of Highly Wettable Coatings on Ti–6Al–4V ELI Alloy for Traumatological Implants Using Micro-Arc Oxidation in an Alkaline Electrolyte. *Sci. Rep.* **2020**, *10*, 19780. [CrossRef]
26. Tikhani, F.; Shirkavand Hadavand, B.; Fakharizadeh Bafghi, H.; Jouyandeh, M.; Vahabi, H.; Formela, K.; Hosseini, H.; Paran, S.M.R.; Esmaeili, A.; Mohaddespour, A.; et al. Polyurethane/Silane-Functionalized ZrO_2 Nanocomposite Powder Coatings: Thermal Degradation Kinetics. *Coatings* **2020**, *10*, 413. [CrossRef]
27. Gao, Y.; Masuda, Y.; Seo, W.-S.; Ohta, H.; Koumoto, K. TiO_2 Nanoparticles Prepared Using an Aqueous Peroxotitanate Solution. *Ceram. Int.* **2004**, *30*, 1365–1368. [CrossRef]
28. Mohsen, Q.; Al-Gethami, W.S.; Zaki, Z.; Alotaibi, S.H.; Ibrahim, M.M.; Ezzat, M.; Amin, M.A.; Kamel, M.M.; Mostafa, N.Y. Effect of PH on Hydrothermal Synthesis of ZrO_2 Nanoparticles and Their Electrocatalytic Activity for Hydrogen Production. *Int. J. Electrochem. Sci.* **2022**, *17*, 22073. [CrossRef]
29. Maj, Ł.; Muhaffel, F.; Jarzębska, A.; Trelka, A.; Balin, K.; Bieda, M.; Cimenoglu, H. Unveiling the Mechanisms of Coating Formation during Micro-Arc Oxidation of Titanium in Na_2HPO_4 Electrolyte. *Surf. Coat. Technol.* **2024**, *476*, 130224. [CrossRef]
30. Yang, G.; Meng, Y.; Qian, C.; Chen, X.; Liu, P.; Zhou, H.; Kang, B.; Tang, X.; Diao, L.; Zhou, F. Review of Microarc Oxidation of Titanium Implant. *J. Vac. Sci. Technol. B* **2023**, *41*, 060801. [CrossRef]
31. Echeverry-Rendón, M.; Galvis, O.; Aguirre, R.; Robledo, S.; Castaño, J.G.; Echeverría, F. Modification of Titanium Alloys Surface Properties by Plasma Electrolytic Oxidation (PEO) and Influence on Biological Response. *J. Mater. Sci. Mater. Med.* **2017**, *28*, 169. [CrossRef]
32. Rahmouni, K.; Besnard, A.; Oulmi, K.; Nouveau, C.; Hidoussi, A.; Aissani, L.; Zaabat, M. In Vitro Corrosion Response of CoCrMo and Ti-6Al-4V Orthopedic Implants with Zr Columnar Thin Films. *Surf. Coat. Technol.* **2022**, *436*, 128310. [CrossRef]
33. Moura de Souza Soares, F.; Barbosa, D.M.; Reis Corado, H.P.; de Carvalho Santana, A.I.; Elias, C.N. Surface Morphology, Roughness, and Corrosion Resistance of Dental Implants Produced by Additive Manufacturing. *J. Mater. Res. Technol.* **2022**, *21*, 3844–3855. [CrossRef]
34. Zhang, Y.M.; Chai, F.; Hornez, J.-C.; Li, C.L.; Zhao, Y.M.; Traisnel, M.; Hildebrand, H.F. The Corrosion and Biological Behaviour of Titanium Alloys in the Presence of Human Lymphoid Cells and MC3T3-E1 Osteoblasts. *Biomed. Mater.* **2009**, *4*, 015004. [CrossRef] [PubMed]
35. Barril, S.; Mischler, S.; Landolt, D. Electrochemical Effects on the Fretting Corrosion Behaviour of Ti_6Al_4V in 0.9% Sodium Chloride Solution. *Wear* **2005**, *259*, 282–291. [CrossRef]
36. Ejenstam, L.; Tuominen, M.; Haapanen, J.; Mäkelä, J.M.; Pan, J.; Swerin, A.; Claesson, P.M. Long-Term Corrosion Protection by a Thin Nano-Composite Coating. *Appl. Surf. Sci.* **2015**, *357*, 2333–2342. [CrossRef]
37. Zhang, W.; Guo, H.; Sun, H.; Zeng, R.-C. Photogenerated Cathodic Protection and Invalidation of Silane/TiO_2 Hybrid Coatings. *J. Coat. Technol. Res.* **2017**, *14*, 417–424. [CrossRef]
38. Li, R.; Liu, L.; Cui, Y.; Liu, R.; Wang, F. Corrosion Behavior of Pure Ti under Continuous NaCl Solution Spraying at 600 °C. *npj Mater. Degrad.* **2022**, *6*, 53. [CrossRef]

coatings

MDPI

Article

Passivation and pH-Induced Precipitation during Anodic Polarization of Steel in Aluminate Electrolytes as a Precondition for Plasma Electrolytic Oxidation

Roy Morgenstern [1,*], Claudia Albero Rojas [1], Frank Simchen [1], Vanessa Meinhold [2], Thomas Mehner [1] and Thomas Lampke [1]

[1] Materials and Surface Engineering Group, Faculty of Mechanical Engineering, Chemnitz University of Technology, 09107 Chemnitz, Germany
[2] FMT Flexible Montagetechnik GmbH, 09212 Limbach-Oberfrohna, Germany
* Correspondence: roy.morgenstern@mb.tu-chemnitz.de; Tel.: +49-371-531-32818

Abstract: Potentiodynamic and potentiostatic polarization tests in the potential range between open circuit potential (OCP) − 0.1 V and OCP + 4 V were carried out in aluminate–phosphate electrolytes with an aluminate concentration of 0.2 mol/L and varying phosphates contents between 0 and 0.1 mol/L. The pH was adjusted between 11.5 and 12.0 due to phosphate and optional KOH addition. A high-strength, dual-phase steel, which is relevant for lightweight construction, served as the substrate material. The layer microstructure was investigated by optical and scanning electron microscopy. Energy-dispersive X-ray spectroscopy and Raman spectroscopy were used for element and phase analyses. We found that iron hydroxides or oxides are initially formed independently of the electrolyte composition at low potentials. At around 1 V vs. standard hydrogen electrode (SHE), the current density suddenly increases as a result of oxygen evolution, which causes a significant reduction in the pH value. Precipitation leads to the formation of porous layers with thicknesses of 10 µm to 20 µm. In the case of a pure aluminate solution, the layer mainly consists of amorphous alumina. When adding phosphate to the electrolyte, the layer additionally contains the hydrous phosphate evansite. At the highest phosphate content in the electrolyte, the highest P content and the most pronounced crack network were observed.

Keywords: passivation; precipitation; polarization; aluminate; phosphate; pH; dual-phase steel

Citation: Morgenstern, R.; Albero Rojas, C.; Simchen, F.; Meinhold, V.; Mehner, T.; Lampke, T. Passivation and pH-Induced Precipitation during Anodic Polarization of Steel in Aluminate Electrolytes as a Precondition for Plasma Electrolytic Oxidation. *Coatings* **2023**, *13*, 656. https://doi.org/10.3390/coatings13030656

Academic Editors: Giorgos Skordaris and Tadeusz Hryniewicz

Received: 31 January 2023
Revised: 8 March 2023
Accepted: 16 March 2023
Published: 20 March 2023

1. Introduction

Electrochemical passivation is considered an important prerequisite for plasma electrolytic oxidation (PEO) [1,2]. Passivation is generally understood as the deposition of a poorly soluble compound from the dissolved metal ions and ions of a corrosive solution after the solubility product has been exceeded [3]. This causes the formation of a protecting layer on the substrate, which kinetically inhibits both the anodic metal dissolution and the electrolysis of the water, i.e., the oxygen evolution at the anode. A significant part of the current occurs due to the outward migration of metal ions towards the passive layer/electrolyte interface and the migration of the oxygen ions in the opposite direction. Lohrengel summarizes the mechanisms of ion transport and passive layer growth according to the high-field model in [4]. With increasing oxide layer thickness, the anodic potential for maintaining the current must be continuously increased. As a result of the oxygen generation and the electrolyte evaporation due to Joule heating, a gas envelope forms on the anode surface. According to the model by Yerokhin, microarc initiation occurs above the breakdown potential between a quasi-cathode on the surface of the gas envelope and the anode [5].

In contrast to chemical elements such as Al, Nb, and Zr, Fe does not spontaneously form a dense and adherent oxide layer under humid conditions but a porous and loose

mixture of iron oxides and hydroxides, which is well known as rust [6]. However, numerous studies describe the anodic passivation of Fe in strongly alkaline solutions above a pH of 13 [7–11]. At low anodic polarization, iron(II) oxide and hydroxide are initially formed according to Equations (1) and (2) [7]. A corrosion-protective passivation is observed after further oxidation to iron(II,III) oxide (magnetite) according to Equations (3) and (4) [7–9]. With increasing anodic potential, iron(II,III) oxide is oxidized to iron(III) oxide or hydroxide [7–9], resulting in a multilayer structure with a higher proportion of Fe(II) oxide close to the substrate and Fe(III) oxide and hydroxide on the surface [10]. The thickness of the passive layers is in the range of a few nanometers [11]. The corrosion and passivation behavior of high-strength multiphase steels, e.g., dual phase (DP) steels, which consist of the ferrite and martensite phases [12], are more complex than in case of single-phase ferritic iron. It is known from numerous corrosion studies that at pH values around 7, martensite behaves more electrochemically noble and that the ferrite phase corrodes preferentially. Therefore, the corrosion rate increases with increasing martensite content on the surface [13–16]. However, in alkaline solutions, the anodic passivation of the ferrite phase due to Equations (1) to (6) might be supported by the galvanic coupling with martensite. Abdo et al. found that a more stable passivation layer was formed during anodic polarization in 0.8 mol/L NaOH after a DP heat treatment compared with the normalized ferrite-perlite condition [17].

$$\mathrm{Fe} + 3\mathrm{H_2O} \rightarrow \mathrm{FeO} + 2\mathrm{H_3O^+} + 2\mathrm{e^-} \quad (1)$$

$$\mathrm{Fe} + 4\mathrm{H_2O} \rightarrow \mathrm{Fe(OH)_2} + 2\mathrm{H_3O^+} + 2\mathrm{e^-} \quad (2)$$

$$3\mathrm{Fe(OH)_2} + 2\mathrm{OH^-} \rightarrow \mathrm{Fe_3O_4} + 4\mathrm{H_2O} + 2\mathrm{e^-} \quad (3)$$

$$3\mathrm{FeO} + 2\mathrm{OH^-} \rightarrow \mathrm{Fe_3O_4} + \mathrm{H_2O} + 2\mathrm{e^-} \quad (4)$$

$$2\mathrm{Fe_3O_4} + 2\mathrm{OH^-} \rightarrow 3\mathrm{Fe_2O_3} + \mathrm{H_2O} + 2\mathrm{e^-} \quad (5)$$

$$\mathrm{Fe_3O_4} + \mathrm{OH^-} + \mathrm{H_2O} \rightarrow 3\mathrm{FeO(OH)} + \mathrm{e^-} \quad (6)$$

The formation of a corrosion-protecting layer can be promoted by the addition of further anions to the solution. For example, the addition of silicate leads to the formation of a thin protective layer, effectively inhibiting Fe dissolution at pH 12 [18]. Pronounced passivation at pH 12 was also observed in electrolytes containing aluminate [19]. Two different mechanisms for the formation of an aluminum oxide or aluminum hydroxide surface layer from aluminate-containing electrolytes have been proposed in the literature: electrochemical oxidation and the precipitation reaction [20,21]. Electrochemical oxidation of aluminate can produce insoluble aluminum hydroxide according to Equation (7) or alumina according to Equation (8). Due to oxygen evolution at the anode, a drop in the pH value is expected. With a decreasing pH value and thus a decreasing ratio of OH^- to Al^{3+}, polymers of the type $[Al(OH)_4]_n(OH)_2^{(n+2)-}$ are initially formed. In the pH range between 8.2 and 9.3 and at an OH^-/Al^{3+} ratio in the range of 3.01 to 3.3, colloidal $Al(OH)_3$ eventually precipitates [21,22]. According to Ginsberg et al., crystalline $Al(OH)_3$ precipitates in the pH range between 10 and 12.5 after prolonged storage [23]. In order to prevent premature precipitation, aluminate solutions in this pH range must be stabilized with complexing agents [20,24]. Furthermore, gels form between pH 8 and 10, with an increasing proportion of crystalline AlO(OH) at increasing pH. Stable solutions of Al^{3+} and $[Al(OH)_4]^-$ exist below pH 8 and above pH 13 [23]. For the precipitation of $Al(OH)_3$ as a result of anodic acidification, the pH value of the solution and the anodic potential must be set within narrow limits [24]. The precipitation reactions of $Al(OH)_3$ and Al_2O_3 are represented in simplified form in Equations (9) and (10) [20,21].

$$[\mathrm{Al(OH)_4}]^- \rightarrow \mathrm{Al(OH)_3} + {}^1/_2\mathrm{O_2} + 2\mathrm{H_2O} + \mathrm{e^-} \quad (7)$$

$$2[\mathrm{Al(OH)_4}]^- \rightarrow \mathrm{Al_2O_3} + {}^1/_2\mathrm{O_2} + 4\mathrm{H_2O} + 2\mathrm{e^-} \quad (8)$$

$$[\mathrm{Al(OH)_4}]^- + \mathrm{H^+} \rightarrow \mathrm{Al(OH)_3} + \mathrm{H_2O} \quad (9)$$

$$2[Al(OH)_4]^- + 2H^+ \rightarrow Al_2O_3 + 5H_2O \quad (10)$$

At high anodic potentials of several 100 V and with intense oxygen evolution, Karpushenkov et al. concluded that the layer formation is mainly based on a precipitation reaction according to Equations (9) or (10) [21]. For alkaline electrolytes, which additionally contain hydrogen phosphate ions, Li et al. proposed a precipitation reaction at the anode, which leads to the deposition of a mix of aluminum oxide and aluminum phosphate [25]. Equation (11) describes the overall reaction. In contrast, Kurze considered that a precipitation reaction caused by anodic acidification is unlikely, since the concentration of H^+ ions in alkaline media is very low. Furthermore, H^+ ions would be immediately repelled from the anode due to their positive charge, and a strong oxygen evolution would prevent the formation of an adherent oxide layer. They advocate the mechanism of electrochemical oxidation of aluminate ions according to Equations (7) or (8) [20].

$$3[Al(OH)_4]^- + [HPO_4]^{2-} \rightarrow Al_2O_3 \cdot AlPO_4 + 5OH^- + 4H_2O \quad (11)$$

Based on a broad design of experiments, Kurze described the production of dense and adherent layers by anodic polarization in the potential range up to 75 V, which mainly consist of amorphous, water-containing $Al(OH)_3$ [20]. As a result of the dehydration of the layer by drying in air or accelerated drying at elevated temperatures or under vacuum conditions, there is a significant reduction in volume, which leads to the formation of a crack network [20]. Li et al. described the formation of a surface layer, which mainly consists of Al, O, and P, at around 450 V (still below the ignition voltage), with the alumina aluminum phosphate (see Equation (11)) or aluminum phosphate phases predominating [18]. After the formation of Al-oxide- or Al-hydroxide-rich top layers and after the breakdown potential is exceeded, microarc discharges were initiated and thus the PEO process began on Fe substrates, similar to the PEO of Al alloys [20,21,25].

A temperature of about 7000 K to 10,000 K is reached in the center of the discharge channel [26]. There, substrate regions close to the surface, the passive layer, and anions from the electrolyte present at the quasi-cathode are vaporized and form plasma. This is followed by a region where the oxide formation reaction mainly takes place, where the preferentially formed oxides are in the liquid state [27] and the components of the passive layer and the electrolyte are incorporated into the PEO layer. This enables the modification of the layer composition, e.g., for the production of Al- or Si-rich oxide layers during the PEO of steel substrates in aluminate- or silicate-containing solutions with the aim of increased corrosion and/or wear resistance (summarized in [28]). The results of Li et al. showed that the initially formed surface layer, which contains Al and P, is converted into a porous PEO layer with a similar chemical composition by the first wave of microarc discharges [25]. With increasing duration, the layer thickness and the Al and Fe contents of the layer increase. This results in a PEO layer consisting of $FeAl_2O_4$ and Fe_3O_4 phases [25]. Other publications have described the production of PEO layers which largely consist of amorphous and crystalline Al_2O_3 phases using aluminate-containing electrolytes [19,21,29]. These PEO layers possess a very high hardness of up to 1680 HV and improve both the tribological behavior and the corrosion resistance of the steel substrate [29]. From the state-of-the-art research, it can be deduced that the formation of a surface layer of insoluble compounds such as aluminum oxide, hydroxide, and/or phosphate not only ensures the necessary substrate passivation, but also ensures that the top layer provides a significant portion of the chemical elements to be incorporated into the layer (e.g., Al), especially in the early phase of PEO. The formation of the top layer is therefore of central importance for the PEO of steels in aluminate electrolytes.

It can be shown from the Nernst equation that the anode potential for oxygen evolution decreases with increasing pH value and is well below 1 V in alkaline media. If the surface layer is formed by precipitation due to acidification at the anode, it can be expected that layer formation will already start in this potential range. The classic passivation by the formation of iron hydroxides or oxides takes place at anodic potentials of a few

100 millivolts. To our knowledge, polarization experiments in aluminate electrolytes in a potential range of up to 4 V have not yet been described in the scientific literature. Therefore, it is the aim of this paper to clarify whether, and if so, in which potential range, passivation- and pH-induced precipitation take place and which microstructural features characterize the layers. This approach allows to obtain novel findings, which enable a more precise control of the insulating layer formation prior to the PEO process.

2. Materials and Methods

2.1. Materials

The DP steel CR440Y780T-DP/HCT780XD (mass fraction in %: <0.17 C, <0.3 Si, <2.0 Mn, <0.05 P, <0.01 S, 0.015–0.08 Al, <1.0 Cr + Mo, <0.05 Nb + Ti), provided by Salzgitter Flachstahl GmbH, Germany, as hot-dip galvanized sheets with a thickness of about 1.7 mm, served as the substrate material. The samples were cut to a size of 15 × 15 mm^2 by water jet cutting. Subsequently, about 0.1 mm to 0.2 mm of the sheet thickness was removed by grinding on one side. In this way, the hot dip galvanizing coating (thickness < 10 µm) and an edge region with a slightly different metallographic appearance (thickness approx. 50 µm, possibly decarburized) were removed. Furthermore, a blank metal surface with a defined roughness of $R_a \approx 0.4$ µm and $R_z \approx 3.0$ µm (transverse to the grinding direction) was obtained by grinding. Directly before the electrochemical measurements, the samples were degreased with ethanol. The samples appeared metallically bright. Pickling was avoided in order not to preferentially dissolve electrochemically fewer noble phases and thus change the phase composition on the surface.

2.2. Electrochemical Polarization

The schematic set-up of the electrochemical polarization measurements is shown in the left of Figure 1. The DP steel sample was clamped in a cylindrical sample holder in a way that it is contacted on the back and masked on the front. The measurement area was about 78.5 mm^2 (circular opening with a diameter of 10 mm). A platinum foil with an area of about 15 × 15 mm^2 was used as the counter-electrode. Ag/AgCl/3M KCl served as the reference electrode. For the qualitative measurement of the pH value change during polarization, polarization experiments were carried out in a vertical electrode arrangement (schematically shown in Figure 1, right). The surface of the working electrode was also 78.5 mm^2, a platinum foil with an area of about 15 × 15 mm^2 served as the counter electrode, and Ag/AgCl/3M KCl was used as the reference electrode. In addition, a pH electrode EGA 133 (Sensortechnik Meinsberg, Waldheim, Germany) was positioned at a small angle at a distance of about 10 mm from the working electrode. The pH electrode was grounded via a high-impedance resistor.

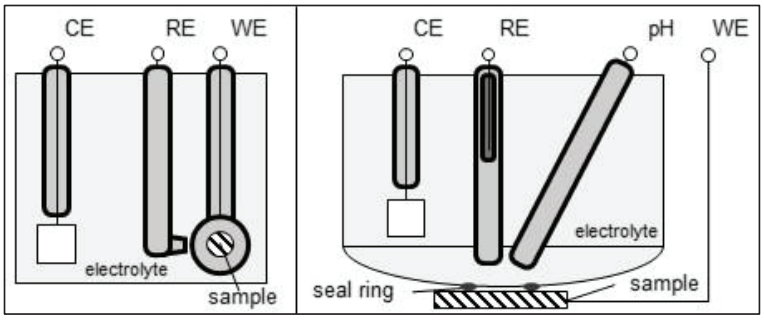

Figure 1. Schematic set-ups of the electrochemical measurements without (**left**) and with a pH electrode (**right**).

Table 1 gives an overview of the electrolytes used. The starting point was the results of Simchen et al., who observed the strongest substrate passivation in an aluminate electrolyte

at pH 12 and low phosphate content [19]. The aluminate content was set at 0.2 mol/L, as this causes a pH value of about 12 (electrolyte 1). The phosphate concentration was increased to 0.05 and 0.1 mol/L to investigate the influence of increased phosphate levels and the associated pH change. The electrolyte was synthesized by first quickly adding $NaAlO_2$ to stirred distilled water, as the aluminate addition itself causes the alkaline pH that is required for obtaining a stable solution. Afterwards, Na_2HPO_4 was added in the required amounts. In order to distinguish the effects of pH and phosphate concentration, reference electrolytes with pH 12 were also prepared by adding KOH. All chemicals were of analytical grade.

Table 1. Chemical composition and pH of the electrolyte solutions used in this study.

Electrolyte No.	Concentration in mol/L		pH
	$NaAlO_2$	Na_2HPO_4	
1	0.2	0	12.0
2	0.2	0.05	11.7
3	0.2	0.05	12.0 *
4	0.2	0.1	11.5
5	0.2	0.1	12.0 *

* pH adjusted to 12 by adding KOH.

Before each electrochemical measurement, the open-circuit potential (OCP) was first recorded for 30 min. For all electrolytes, potentiodynamic "screening" measurements (OCP − 100 mV to OCP + 4000 mV with a scan rate of 10 mV/s), as well as higher resolution measurements near the OCP (OCP − 100 mV to OCP + 100 mV with 1 mV/s) were performed. Based on these higher resolution measurements, the corrosion potential, φ_{corr}, was determined and the corrosion current density, j_{corr}, was calculated according to the method of Stern [30] using Equations (12) and (13), where R_{pol} is the polarization resistance, j is the current density, R is the universal gas constant, T is the electrolyte temperature (295.15 K), F is the Faraday constant, and A is the measurement area.

$$R_{pol} = \frac{(\varphi_{corr} + 10\ mV) - (\varphi_{corr} - 10\ mV)}{I(\varphi_{corr} + 10\ mV) - I(\varphi_{corr} - 10\ mV)} \quad (12)$$

$$j_{corr} = \frac{R \cdot T}{z \cdot F \cdot R_{pol} \cdot A} \quad (13)$$

Additionally, potentiostatic polarization measurements were carried out for all electrolytes at OCP + 4 V to produce thick surface layers for further material and scientific characterization, as well as further potentiostatic measurements at defined potentials. For statistical validation, all electrochemical measurements were carried out at least 3 times under the same conditions. The electrochemical work station Zennium X (Zahner, Kronach, Germany) served as the voltage source and for recording the current curves and the pH value.

2.3. Microstructural Analysis

All specimens were routinely documented using a stereo microscope MVX 10 (Olympus, Tokyo, Japan). Metallographic preparation was carried out on samples that were polarized at an anodic potential of OCP + 4 V. For this purpose, the samples were cut, embedded in conductive resin, ground on SiC paper to 4000 grit, polished on cloths to a diamond size of 1 µm, and finally polished with a suspension of colloidal silicon dioxide. The optical microscopic examinations were carried out using an inverse optical microscope GX 51 (Olympus, Japan) in bright field mode. Prior to scanning electron microscopy (SEM) measurements, the cross-sections were rinsed in ethanol and isopropanol and then dried in an oven at 60 °C. In order to ensure a sufficient electrical conductivity of the electrically insulating layers for the SEM investigations, all ground surfaces were vapor coated with carbon. The scanning electron microscopic investigations were carried out with an SEM

LEO1455VP (Zeiss, Oberkochen, Germany) at an acceleration voltage of 25 kV and a working distance of 14.5 mm using the secondary electron (SE) and backscattered electron (BSE) contrasts. In addition, the chemical composition of the surface layers was determined using energy-dispersive X-ray microanalysis (EDX) in the middle of the layer.

In order to determine the phase composition, an X-ray diffraction (XRD) analysis was carried out using the D8 Discover (Bruker, USA) diffractometer with Co-Kα radiation. The measurements were performed on the surface of samples that were polarized at OCP + 4 V with a point focus (diameter pinhole aperture 0.5 mm) and the LYNXEYE XE-T detector. Measurements for the qualitative determination of the phase composition were carried out on the same sample surfaces using a confocal Raman microscope inVia (Renishaw, United Kingdom). The measurement was carried out with a 20× lens and a laser wavelength of 532 nm at 100% excitation energy for 10 s (thick precipitated layers) or 50 s (thin passive layers) with 10 accumulations. The reference data of possible phases were taken from the RRUFF database [31] and from the scientific literature.

3. Results

3.1. Polarization Experiments

3.1.1. Potentiodynamic Polarization

In order to obtain an overview of the electrochemical processes, potentiodynamic polarization measurements were first carried out in the potential range from OCP − 100 mV to OCP + 4000 V. Figure 2 shows the average current–density curves (solid lines) including the curves of the standard deviations of the current–density values at a specific potential for different electrolytes in the range between φ_{corr} and OCP + 4 V, as well as a representative curve of the pH change during polarization in electrolyte 1. The secondary ordinate (pH change) has a linear scale and is not labeled with absolute values of the pH change, since the pH measurements were not carried out in the immediate vicinity of the anode but at a distance of about 10 mm. It is to be expected that the pH change in the immediate vicinity of the substrate will be significantly higher than measured.

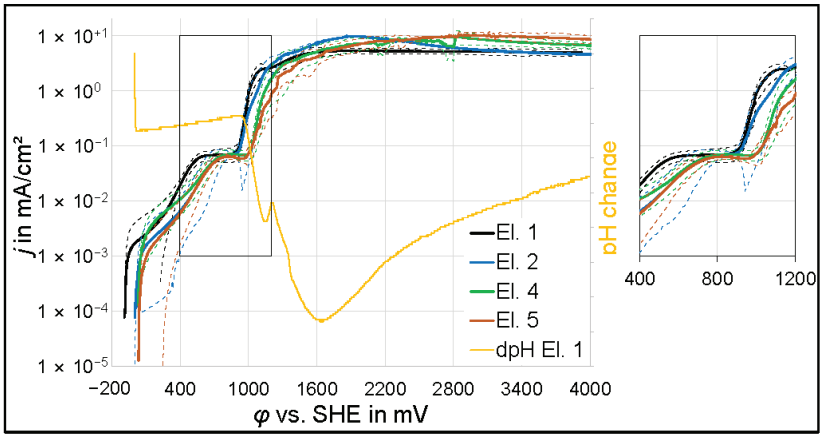

Figure 2. j–φ curves due to potentiodynamic polarization in electrolytes (El.) 1, 2, 4, and 5 within the range of φ_{corr} to OCP + 4 V with a magnified image of the section between 400 and 1200 mV vs. SHE (right) and qualitative pH change (dpH) during a measurement in electrolyte 1 (linear scale). The dashed lines represent the standard deviation between the repetition samples.

The current–density curves are qualitatively similar for all electrolytes. After a steep increase when crossing φ_{corr}, the curves flatten slightly at about φ_{corr} + 10 mV. In the region of the steep current–density increase, a sudden pH decrease can be observed. Another steep current–density increase can be identified starting at about φ_{corr} + 350 mV. Again, a

flattening of the curves can be seen at around φ_{corr} + 600 mV (electrolyte 1) and at around φ_{corr} + 700 mV (other electrolytes). In the case of electrolytes 4 and 5 (highest phosphate concentration of 0.1 mol/L), there is even a slight decrease in current density and a local minimum is passed (see magnified section in Figure 2). Another steep increase in current density follows at around 900 mV vs. standard hydrogen electrode (SHE) for electrolytes 1 and 2 and at around 1000 mV vs. SHE for the other electrolytes. Compared to the current–density increase, the pH starts to decrease during polarization in electrolyte 1 with a slight delay at around 950 mV vs. SHE. The pH value reacts very sensitively to a change in current density. For example, the current–density fluctuation during polarization in electrolyte 1 at around 1200 mV vs. SHE leads to a measurable pH fluctuation. The increase in current density is the steepest for electrolyte 1 and begins to level off at around 1000 mV vs. SHE. After passing through the minimum pH value at around 1650 mV vs. SHE, the maximum current density of 5.3 mA/cm^2 is reached for electrolyte 1 at around 2000 mV vs. SHE. The flattening of the curves and the current–density maxima shift towards higher potentials with increasing phosphate content in the electrolyte. In addition, the magnitudes of the maxima increase to around 9.5–10.5 mA/cm^2. During polarization in electrolyte 5 (high phosphate content, adjusted to pH 12), the highest measured current–density maximum is reached at about 2850 mV vs. SHE. At the end of the polarization at OCP + 4 V, the lowest current densities in the range of 4.5 mA/cm^2 to 5 mA/cm^2 are reached for electrolytes 1 and 2. After polarization in the potential range OCP − 100 mV to OCP + 4000 mV, light gray to white covering layers can be observed on all sample surfaces with the naked eye.

As can be seen in Figure 2, different free corrosion potentials are obtained in the different electrolytes. The OCP drifts significantly during the 30 min OCP measurement prior to the potentiodynamic polarization measurements. Both increases and decreases in the OCP were measured in the same electrolyte. A detailed investigation of the electrochemical behavior was carried out using polarization tests in the OCP ± 100 mV range. Figure 3 shows the courses of the current density for the polarization in electrolytes 1, 3, and 5 (which have the same pH value of 12 and differ in terms of the phosphate content) in the potential range φ_{corr} ± 40 mV using a Tafel plot. The points marked with the symbol × represent the corrosion potential, φ_{corr}, and the corrosion current density, j_{corr}, calculated according to Equation (13). The average values, including standard deviations of φ_{corr} and j_{corr}, are summarized for all electrolytes in Table 2.

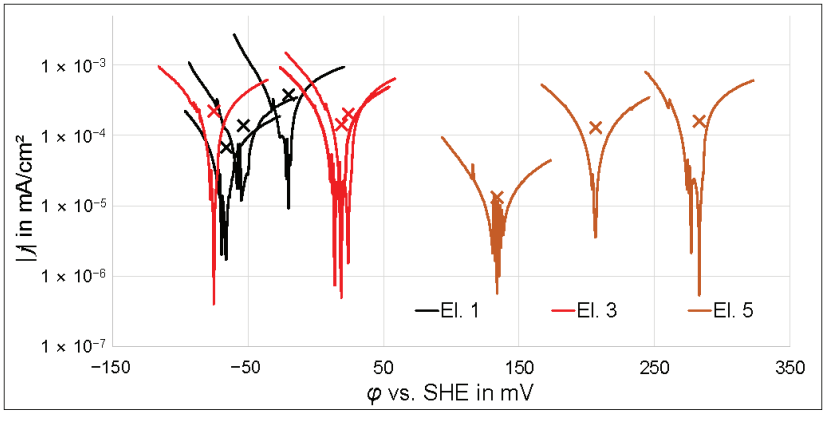

Figure 3. j–φ curves in electrolytes no. 1, 3, and 5 within the range of φ_{corr} ± 40 mV; the crosses mark the φ_{corr} and j_{corr} values of every curve.

The most negative corrosion potentials were measured for the electrolytes without phosphate and with 0.05 mol/L phosphate. No clear influence of the pH value on the corrosion potential can be identified for these electrolytes when considering the large standard deviations. In contrast, for electrolytes 4 and 5 with a phosphate concentration of

0.1 mol/L, a shift in the corrosion potential towards more positive values was observed (see Table 2), especially after adjustment of the pH value to 12 (electrolyte 5). The corrosion current density tends to be lower for electrolytes 4 and 5 compared to electrolytes 1, 2, and 3. After the polarization tests in the OCP ± 100 mV range, no macroscopic changes or layers can be seen on the sample surface.

Table 2. Average values and standard deviations of φ_{corr} and j_{corr} (Equation (13)) in different electrolytes.

Electrolyte No.	φ_{corr} in mV	j_{corr} in 10^{-5}·mA/cm^2
1	−47 ± 24	19 ± 16
2	−70 ± 150	13 ± 7
3	−10 ± 60	19 ± 5
4	90 ± 80	9 ± 7
5	210 ± 80	10 ± 8

3.1.2. Polarization at Constant Potential

The layer formation was examined in more detail using potentiostatic polarization experiments at OCP + 4 V. As can be seen from Figure 4, the current–density curves for electrolytes 1, 2, and 3 are very similar and differ only within the range of their standard deviations. They can be described to a very good approximation ($R^2 \approx 0.99$) by power functions of the form $j = a \cdot t^b$, with a between 33 mA/(cm^2·s) and 45 mA/(cm^2·s) and b between −0.43 and −0.47.

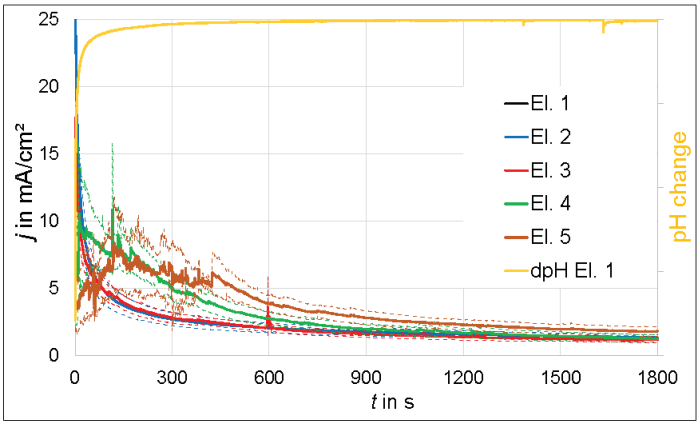

Figure 4. *j*–*t* curves due to polarization at constant potential (OCP + 4 V) in the different electrolytes and qualitative pH change (dpH) during a measurement in electrolyte 1. The dashed lines represent the standard deviation between the repetition samples.

In addition to a high current density at the beginning of the polarization, a considerable decrease in the pH value from 12 to 8.5 can be observed at a distance of about 10 mm from the anode, which is a pH change of −3.5 within the first seconds. With the rapid decrease in current density, the pH value quickly approaches the original pH value of the electrolyte. When polarizing in electrolyte 4 and in particular in electrolyte 5, higher current densities and stronger current–density fluctuations can be seen shortly after the start. Later during the experiment, a continuous decrease in the current density can also be observed for these electrolytes. After 1800 s polarization in electrolytes 1 to 4, the average current densities are about 1.17 mA/cm^2 to 1.35 mA/cm^2. These differences are still within the standard deviation of the individual curves. At the same time, a higher average current density of about 1.8 mA/cm^2 can be measured at the end of the polarization in electrolyte 5.

The surface layers after 30 min of polarization at OCP + 4 V have a light gray to white color and are partially opaque so that the grinded steel substrate is visible. In Figure 5, stereomicroscopic surface images of one representative sample per electrolyte are arranged in a table structure according to the phosphate content of the electrolyte (e.g., "0.05 PO_4^{3-}" stands for 0.05 mol/L phosphate) and pH value. The images were always taken at the center of the measuring surface. After polarization in electrolyte 1 (0 PO_4^{3-}, pH 12), a microscopically heterogeneous top layer is formed. There are finely distributed light gray, opaque areas next to fine pores (darker areas) where the steel substrate shines through the layer more strongly. The top layers produced in electrolytes 2 (0.05 PO_4^{3-}, pH 11.7) and 4 (0.1 PO_4^{3-}, pH 11.5) appear homogeneous and less porous. In the case of the latter layer (0.1 PO_4^{3-}, pH 11.5), sharp-edged layer spallation can be seen, which indicates a high degree of brittleness. After polarization in electrolytes 3 (0.05 PO_4^{3-}, pH 12) and 5 (0.1 PO_4^{3-}, pH 12), larger pores are visible on the surface, which are presumably caused by the temporary adhesion of gas bubbles and the associated hindrance of layer formation. This is most pronounced after polarization in electrolyte 5.

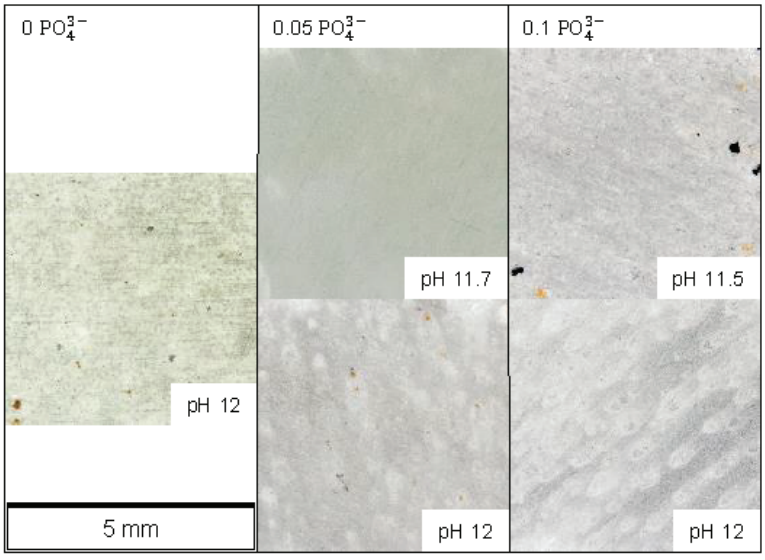

Figure 5. Optical microscopic images of the sample areas after polarization at constant potential (OCP + 4 V) in the different electrolytes, categorized by the phosphate content in the electrolyte (PO_4^{3-}) in mol/L and the pH. The scale bar applies to all images.

When examining the surfaces at higher magnification using optical microscopy, it is noticeable that all layers are microcracked. After polarization in electrolytes 1, 2, and 3, a fine network of closed cracks can be observed. As shown in the left of Figure 6, the layer, which was produced by polarization in electrolyte 2 and appeared very evenly in Figure 5, also has fine porosity and roughness. This may cause light scattering, which is the reason why the layer appears cloudy and the substrate cannot be seen. For the same reason, the crack network can only be seen in some places (see Figure 6, left). Dense crack networks are clearly visible in layers that were created by polarization in electrolytes 4 and 5. This is particularly pronounced after polarization in electrolyte 4. As can be seen from the right of Figure 6, some cracks have widened so much that layer fragments are present as islands. In addition, these layers are optically transparent so that the grinding marks on the base material can be clearly seen in the background. The macroscopic gray appearance may not be due to fine porosity or roughness but because of light scattering at the crack edges.

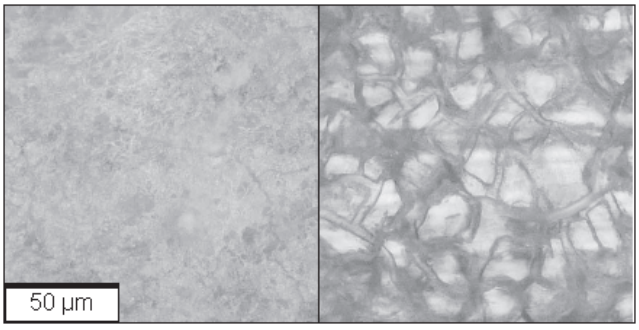

Figure 6. Optical microscopic images of the sample surface after polarization at constant potential (OCP + 4 V) in electrolytes 2 (**left**) and 4 (**right**). The scale bar applies to both images.

As already described in Section 3.1.1, the potentiodynamic polarization experiments depicted in Figure 2 show a flattening of the current–density curve in the potential range between about 550 mV and 1000 mV vs. SHE (depending on the electrolyte), and sometimes there is even a slight decrease in current density. To examine this potential range more closely, potentiostatic polarization tests were carried out at OCP + 500 mV. Figure 7 shows the current–density curves for electrolytes 1 and 4, which differ most in terms of phosphate content and pH value. In both cases, a clear decrease in current density is recorded shortly after the start. Compared to the polarization at OCP + 4 V (Figure 4), the current densities after 1800 s are about 20 to 30 times higher. Up to about 1100 s, both average current–density curves (solid lines) run almost congruently.

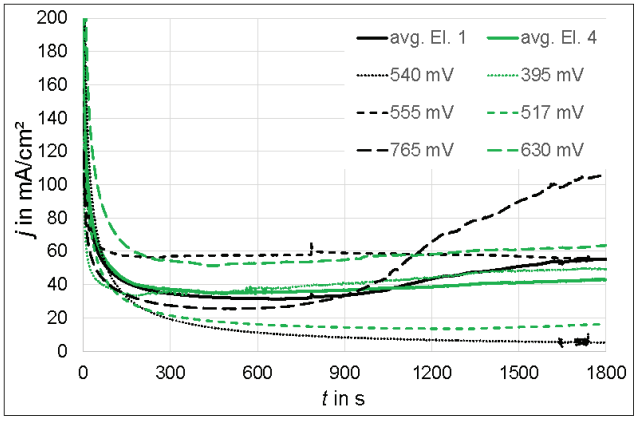

Figure 7. *j*–*t* curves due to polarization at constant OCP + 500 mV in electrolytes 1 and 4. The solid lines represent the averaged curves; the dashed lines represent the curves of the individual samples with the potentials of the individual measurements vs. SHE.

However, it can be observed that the courses of the individual curves in Figure 7 are very different. It must be taken into account that the individual measurements were carried out at different potentials vs. SHE, since the OCPs varied considerably. The potentials vs. SHE of the individual measurements are given in the legend of Figure 7. For both electrolytes, the lowest current densities of about 4 mA/cm^2 for electrolyte 1 and about 13 mA/cm^2 for electrolyte 4 were reached after 1800 s polarization at 540 mV (electrolyte 1) and 517 mV (electrolyte 4) vs. SHE. These values are close to the oxygen evolution potentials of 522 mV and 552 mV vs. SHE at pH 12 and 11.5, respectively. Relatively high current densities of over 50 mA/cm^2 were observed both above 550 mV vs. SHE and below

400 mV vs. SHE. At the highest potential of 765 mV vs. SHE, a significant increase in the current density was observed at the end of the measurement. After the tests, no surface layer formation can be seen macroscopically or by means of optical microscopy.

3.2. Microstructure

To illustrate the layer microstructure, Figure 8 shows optical microscopy images of the layer cross-section of a representative sample of each electrolyte. The arrangement of the images is the same as in Figure 5. In accordance with the observation of pores in the surface images, significant layer thickness fluctuations can be observed in the layer cross-section. However, it cannot be clearly assigned which regions with a thin layer actually formed during polarization. The surface layers showed a high degree of brittleness and low adhesion, which led to partial layer detachment during the cross-section preparation. The amount of cracks visible in Figure 8 and the gaps between the layer and the substrate probably increased during preparation. Layer thicknesses of about 10 µm and 20 µm within the uniform regions (shown in Figure 8) were probably only slightly changed by the preparation of the cross-section. These uniform layer areas have a similar appearance in all cases.

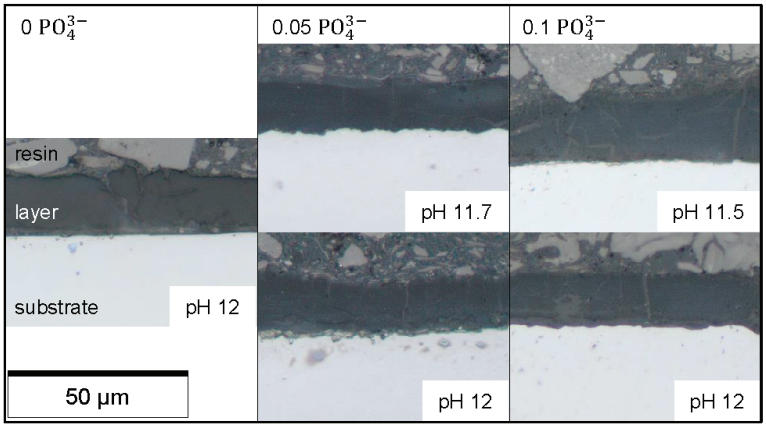

Figure 8. Optical microscopic images of the cross-sections after polarization at constant potential (OCP + 4 V) in the different electrolytes, categorized by the phosphate content in the electrolyte (PO_4^{3-}) in mol/L and the pH. The scale bar applies to all images.

Generally, the same layer characteristics can be recognized by means of SEM. Figure 9 shows homogeneous layer regions that were created by polarization at OCP + 4 V in electrolytes 1, 3, and 5 with different phosphate concentrations and at the same pH of 12. These layer areas still appear compact in the SE contrast. In the BSE contrast, a very faint horizontal, slightly wavy layering can be seen at some places. This is an indication of slight variations in the chemical composition. However, a systematic change in the composition over the layer thickness is not recognizable. In order to determine representative average values of the chemical element content, EDX measurements were always carried out over a larger measuring area in the middle of the layer, with a sufficient distance to the edges. The results of the EDX measurements are summarized in Table 3. Polarization in electrolyte 1 (without phosphate) creates layers that almost exclusively consist of the elements Al and O, with the ratio of Al to O being about 2 to 3. With the addition of 0.05 mol/L and 0.1 mol/L phosphate to the electrolyte, the P content of the layers increases to an average molar fraction of 7.9% and 9.3%, respectively. At the same time, the O content increases from 61.4% to 66.4% and 68.7%, respectively. These increases are at the expense of the Al content, which drops significantly from 38.4% to 25.0% and 20.5%, respectively. In any case, the element Fe can only be measured in small amounts. It cannot be clearly determined whether the layer actually contains Fe. It is also conceivable that Fe particles

were transferred to the layer during the preparation of the cross-section or that the substrate was slightly excited during the EDX measurement.

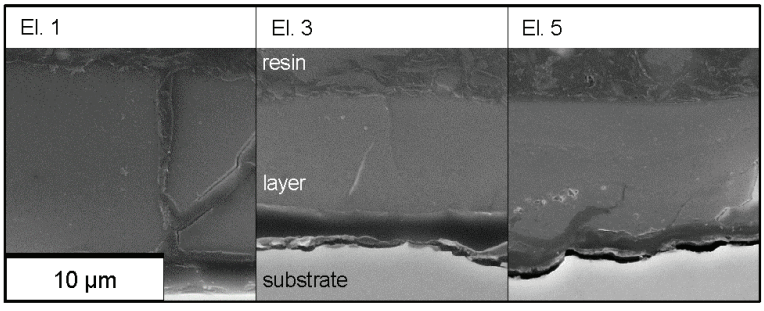

Figure 9. SEM images (SE contrast) of the cross-sections of samples that were polarized at constant OCP + 4 V in electrolytes 1, 3, and 5. The scale bar applies to all images.

Table 3. Chemical compositions measured by EDX analyses at the cross-sections of samples that were polarized at constant potential (OCP + 4 V) in electrolytes 1, 3, and 5.

Electrolyte No.	Molar Fraction in %			
	Al	O	P	Fe
1	38.4 ± 0.8	61.4 ± 0.7	<0.1	0.3 ± 0.1
3	25.0 ± 1.9	66 ± 3	7.9 ± 0.9	0.8 ± 0.2
5	20.5 ± 0.7	68.7 ± 2.1	9.3 ± 0.1	1.5 ± 1.3

Despite the high layer thicknesses in the range of 10 µm to 20 µm after polarization at OCP + 4 V for 30 min, only the characteristic peaks of the substrate material can be registered with XRD surface measurements. Obviously, the layers are X-ray amorphous or nanocrystalline.

The surface layers that were generated by polarization at OCP + 4 V for 30 min in electrolytes 1 and 4, which differ most in terms of phosphate content and pH value, were analyzed using Raman spectroscopy. As can be seen from the bottom spectrum in Figure 10, the layer produced in electrolyte 1 primarily shows a broad peak with a maximum at 590 cm^{-1} and a double peak at around 1070 cm^{-1} and 1100 cm^{-1}. Based on the results of the EDX measurements, only phases containing Al, O, and possibly light elements such as H, which are not detectable by EDX, can be considered. Suitable reference spectra of the $Al(OH)_3$ modifications gibbsite (RRUFF ID: R190038) and nordstrandite (RRUFF ID: R050592) were taken from [31] and inserted in Figure 10. The pronounced gibbsite band at about 475 cm^{-1} and the weak band at about 1080 cm^{-1} may be included in the broad peaks of the electrolyte 1 spectrum, but do not explain them sufficiently. The nordstrandite reference spectrum contains a series of bands between 470 cm^{-1} and 750 cm^{-1}. In the case of an amorphous or nanocrystalline layer, these bands could appear broader and overlap to form a broad peak as measured at the sample produced in electrolyte 1. However, the other bands of the nordstrandite spectrum between 210 cm^{-1} and 450 cm^{-1} and between 810 cm^{-1} and 1000 cm^{-1} do not correspond to the measured spectrum. It is known from the literature that the $Al(OH)_3$ modification bayerite has characteristic bands at the following Raman shifts (in cm^{-1}): 1079, 1068, 898, 866, 545, 525, 484, 443, 434, 388, 359, 322, 297, 250, 239, and 205 [32]. These also do not specifically match the bands of the measured spectrum of the layer produced in electrolyte 1. Furthermore, there is no striking conformance with boehmite (RRUFF ID: R120123) either, which is characterized by bands at around 360 cm^{-1}, 500 cm^{-1}, and 680 cm^{-1} [31]. According to Sudare et al., the Raman spectra of amorphous Al_2O_3 and γ-Al_2O_3 show bands at about 555 cm^{-1} and 1060 cm^{-1} within the applied measurement range (vertical, black lines in Figure 10) [33]. Both bands are close to the characteristic bands of the spectrum of the layer produced in electrolyte 1.

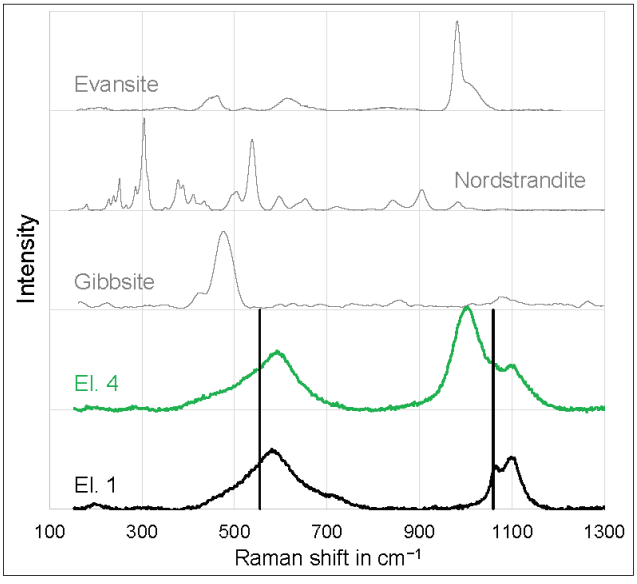

Figure 10. Raman spectra of layers produced in electrolytes 1 and 4 at OCP + 4 V and reference spectra of gibbsite, nordstrandite, and evansite from [31]. The vertical black lines mark characteristic bands of amorphous Al_2O_3/γ-Al_2O_3 according to [33].

Compared to the layer from electrolyte 1, the layer produced in electrolyte 4 primarily shows an additional broad peak at about 1000 cm^{-1}. In addition, the left shoulder of the broad peak with the maximum at 590 cm^{-1} extends more towards lower values. Based on the results of the EDX measurements, the conformability of phases containing P in addition to Al, O, and potentially H was checked. The best match was found for the evansite phase. This is a hydrous phosphate that also contains Al ions and is described by the chemical formula $Al_3(PO_4)(OH)_6{\cdot}6H_2O$. As can be seen in Figure 10, the deviations between the spectra of the layers of electrolytes 1 and 4 can be explained very well by the characteristic bands in the Raman spectrum of Evansite at around 980 cm^{-1} and 460 cm^{-1}. The broad peak around 590 cm^{-1} possibly covers another band of Evansite at around 620 cm^{-1}. In order to clarify the phase composition of surface layers, which are generated during polarization at OCP + 500 mV, the individual samples from electrolytes 1 and 4, which showed the strongest current–density decrease during polarization, were examined using Raman spectroscopy as well. A five times higher measurement duration was applied in order to obtain peaks which can be clearly distinguished from the background. As can be seen in Figure 11, the Raman spectra of the samples produced in electrolytes 1 and 4 are very similar. They essentially show the same peaks, but the latter spectrum shows higher peak intensities at 1130 cm^{-1}, 1290 cm^{-1}, and 1440 cm^{-1}. Both spectra differ significantly from the spectra of the macroscopically visible layers that were produced by polarization at OCP + 4 V. A Raman spectrum with the same peaks but lower intensities was measured at the edge of a steel sample. This area was not polarized in either electrolyte but subjected to the same rinsing routine and storage. For phase identification, the reference spectra of phases containing Fe, O, and potentially H were checked. By far the best match was found for the maghemite phase (γ-Fe_2O_3) in [34]. As can be seen in Figure 11, there is a high level of agreement with the reference spectrum (RRUFF ID: R140712) from [31] for almost all peaks in the range between about 200 cm^{-1} and 1300 cm^{-1}, with the exceptions that the measured spectra exhibit a much more pronounced peak at about 770 cm^{-1} and no peaks around 500 cm^{-1}. The measured peaks above 1300 cm^{-1} were compared with references of the maghemite phase from the literature. Hanesch et al. identified a characteristic

band at 1330 cm^{-1} [35]. This agrees approximately with the findings of Mazzetti and Thistlethwaite, according to whom there is a band at 1320 cm^{-1} [36]. In addition, Mazzetti and Thistlethwaite identified a band at 1560 cm^{-1} [36]. These bands are shown as black lines in Figure 11 and are close to the measured peaks at 1290 cm^{-1} and 1550 cm^{-1}. Furthermore, Modesto Lopez et al. reported a broad band between about 1360 cm^{-1} and 1480 cm^{-1} [37]. The measured peak at 1435 cm^{-1} is located within this range.

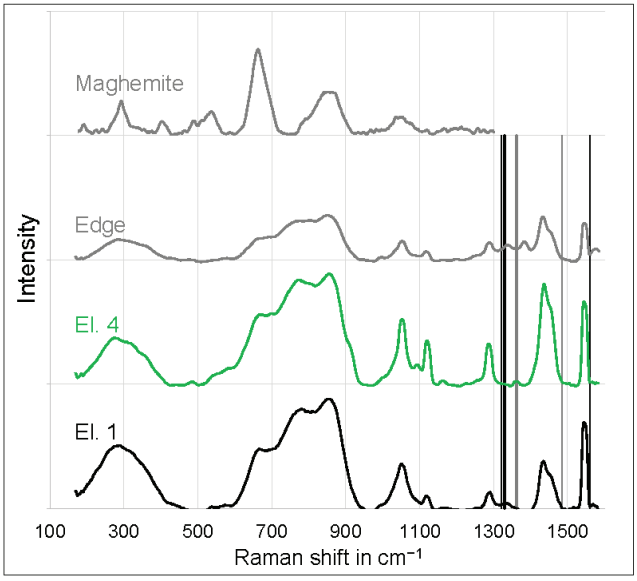

Figure 11. Raman spectra of layers produced in electrolytes 1 and 4 at OCP + 500 mV and reference spectra of the untreated sample edge and maghemite from [31], the vertical lines mark characteristic bands (black) and a broad peak (gray) of maghemite according to the literature [35–37].

4. Discussion

The results of the polarization experiments indicate that several different processes take place on the substrate surface in the potential range from φ_{corr} to OCP + 4 V. This approach provides novel insights into the electrochemical behavior of steel in alkaline aluminate solution. The fluctuations during the OCP measurements and the different OCPs of individual samples in the same electrolyte appear to be stochastic and must therefore be caused by randomly varying factors. One reason could be the multi-phase microstructure of the DP steel, which essentially consists of ferrite and martensite. The microstructure shows a slight banding parallel to the rolling direction. When grinding the surface, a line rich in the electrochemically more noble martensite or the less noble ferrite may randomly be exposed, resulting in different OCP values and a more or less pronounced drift of the OCP due to the passivation of the less noble ferrite phase. The corrosion potential of -47 ± 24 mV vs. SHE, measured in electrolyte 1, is in good agreement with the corrosion potential of around -56 mV vs. SHE of a DP steel in 0.8 mol/L NaOH reported in the literature [17]. A corrosion-inhibiting effect in alkaline media (pH 12 to 13) due to the adhesion of phosphates to the steel surface is described in the literature [38]. This could explain the slightly lower average corrosion current densities at the highest phosphate concentration. The interactions between the phosphate ions and the steel surface are not described in the literature in detail.

Since the potentiodynamic polarization experiments always started in the cathodic region at OCP − 100 mV, in order to reliably polarize slightly cathodically when starting the measurement despite the OCP fluctuation over time, adhering anions were probably

initially repelled. For this reason, the OCPs after 30 min of immersion do not exactly match the φ_{corr} values of the potentiodynamic polarization experiments. Immediately after passing φ_{corr}, the current density initially increases sharply, which is probably due to the anodic dissolution of the iron. The subsequent flattening of the current–density curve might be explained by the formation of an iron(II) oxide or hydroxide layer. According to the cyclic voltammetric investigations by Joiret et al., this layer formation is associated with the formation of hydronium ions according to Equations (1) and (2) [7]. This might explain the decrease in pH measured after passing φ_{corr}. This layer is locally destroyed with increasing anodic potential, so the current density increases sharply again.

The subsequent current–density plateau between about 600 mV and 900 mV vs. SHE for the polarization in electrolytes 1 and 2 and between about 780 mV and 1000 mV vs. SHE for the polarization in electrolytes 4 and 5 (see Figure 2) indicates formation of another layer. Joiret et al. state that iron(II) oxide and hydroxide are firstly oxidized to iron(II,III) oxide (magnetite) according to Equations (3) and (4) and then further oxidized to iron(III) oxide and hydroxide according to Equations (5) and (6) [7]. It is known from the literature that a protective passive layer is only observed after the formation of iron(II,III) oxide [8,9]. This coincides with the observation that the flattening of the increase in current density is much more pronounced here.

Using potentiostatic polarization experiments in the vicinity of this potential range, it was possible to demonstrate the formation of a passive layer. The greatest decrease in current density over time was found at a potential of 500 mV vs. SHE, independent of the phosphate content and pH value of the electrolyte. This is a few 100 mV before the current–density plateau was reached in the potentiodynamic measurements, which can be explained by the kinetics of oxide formation. As can be seen in Figure 5, the current density drops quickly at the beginning of the polarization. As an example, it still takes around 30 s before the current density falls below twice the value of the current density minimum. Given the potential scan rate of 10 mV/s in potentiodynamic polarization up to OCP + 4 V, the anodic potential increases by 300 mV during this time.

On the measuring surfaces of the samples, which showed the strongest current density decrease during polarization at OCP + 500 mV, no phase other than maghemite could be detected by means of Raman spectroscopy. This also means that both other iron oxides or hydroxides and chemical compounds containing P or Al are not present in detectable amounts. The formation of maghemite (γ-Fe_2O_3) by oxidation of the iron(II,III) oxide according to Equation (5) is plausible [7]. Both the differences between the spectra of the samples, which were polarized in electrolytes 1 and 4, and the differences between the measured spectra and the maghemite reference could not be attributed to plausible phases. Since a Raman spectrum with the same characteristic peaks was measured at the edge of the sample that was not in contact with the electrolyte, it cannot be definitively proven whether the maghemite layer formation was actually due to polarization or as a result of sample storage. However, it might be concluded from the higher peak intensities that slightly thicker oxide layers were formed in the polarized areas. The layers cannot be distinguished from the substrate neither macroscopically nor under the optical microscope. This is consistent with the literature, which states that the thickness of an oxide layer formed in this potential range on iron is only a few nanometers [11].

According to the Nernst equation, oxygen evolution starts at 522 mV and 552 mV vs. SHE at pH 12 and 11.5, respectively. It is possible that this impairs the formation of dense layers during potentiostatic polarization and leads to the detachment of porous and non-adherent top layers. This would explain that at potentials above about 550 mV vs. SHE, a less pronounced decrease in current density could be measured and that in case of the highest potential of 765 mV vs. SHE, the current even increased again towards the end. In the case of the potentiodynamic measurements, the oxygen evolution appears with a significant delay at around 900 mV vs. SHE or 1000 mV vs. SHE, which can be seen by the significant increase in the current density and the significant decrease in the pH value that is delayed by about another 50 mV. It is possible that the passive layer initially inhibited oxygen evolution until it finally

detaches from the surface. As the comparisons of the current–density curves for electrolytes 1 and 2 and in particular for electrolytes 4 and 5 in Figure 2 shows, this breakthrough potential is not significantly influenced by the pH value of the solution. The increased breakdown potential in electrolytes 4 and 5 with the highest phosphate content is possibly due to an interaction of the attached phosphate with the surface.

In the case of potentiodynamic polarization in electrolyte 1, the increase in current density levels off immediately after the start of the pH value reduction. These observations are consistent with the theory that a precipitation reaction according to Equations (9) or (10) takes place as a result of the pH drop and that the precipitated layer inhibits the current. Similarly, layer formation in phosphate-containing electrolytes at potentials above 1 V vs. SHE can be explained by the precipitation reaction described in Equation (11). During potentiodynamic polarization in phosphate-containing electrolytes, the maximum current density is reached at higher potentials and is at a higher current density level. Possibly, the development of oxygen is initially slightly inhibited by phosphate adhering to the anode. However, the precipitation layer appears to be more permeable to the released oxygen, resulting in the formation of more and bigger oxygen bubbles, which adhere to the surface temporarily. This coincides with the observation that after polarization at OCP + 4 V in electrolyte 5 (highest phosphate content, pH 12), the layer surface shows the most pronounced porosity due to gas evolution.

It can be expected that for any anodic potential between about 1 V and several hundred V, just below the breakthrough potential of microarc ignition, layer formation occurs due to a precipitation reaction, which is consistent with the findings of Li et al. [25]. At an anodic potential of OCP + 4 V, a pH reduction of up to 3.5 could be measured in electrolyte 1 at a distance of about 10 mm from the anode. A significantly greater reduction in the pH value is to be expected directly at the anode surface. This could at least partially invalidate the argument formulated in [20] that there are not enough H^+ ions in alkaline solutions, which enable a precipitation reaction according to Equations (9) or (10). Precipitation layers with a thickness between 10 μm and 20 μm are created by polarization at OCP + 4 V for 30 min. This layer thickness is approximately 1000 times greater than would be expected in the case of electrochemical passivation at the same anodic potential. In contrast to a dense and firmly adhering passive layer, the precipitation layers tend to be loosely adherent and porous and can easily be removed by rubbing. The precipitation layers are amorphous or nanocrystalline and mainly consist of the elements Al, O, and (in the case of phosphate-containing electrolytes) P. The Al:O ratio of about 2 to 3 measured by EDX and the results of the Raman measurements indicates that the layers formed after polarization in electrolyte 1 at OCP + 4 V probably consist of amorphous alumina or nanocrystalline γ-alumina. Sufficient agreement with the literature-reported Raman spectra of $Al(OH)_3$ c was not found. This contradicts the observations of Kurze that mainly $Al(OH)_3$ is formed due to anodic polarization in the potential range up to 75 V [13]. However, it cannot be ruled out that $Al(OH)_3$ or $AlO(OH)$ were present immediately after the polarization experiments and decomposed as a result of drying during sample storage. This is also indicated by the existence of a fine crack network, which probably arose as a result of the internal stresses caused by dehydration. The fine porosity may also have facilitated the drying of the layers and reduced the internal stresses so cracks were not widened significantly.

With increasing phosphate content in the electrolyte, the water-containing aluminum phosphate evansite ($Al_3(PO_4)(OH)_6 \cdot 6H_2O$) is increasingly incorporated into the layer. This is in good agreement with Li et al., who describe the formation of alumina aluminum phosphate [25], with the difference that additional OH^- ions and H_2O molecules formed according to Equation (11) are also incorporated into the layer. It is likely that there was more intense drying in the course of the SEM investigations of Li et al. [25], which could have resulted in a more pronounced conversion of the evansite into alumina aluminum phosphate. In particular, a crack network, which can be seen in Figure 6, characterizes the layers that were produced in electrolytes 4 and 5 with a high phosphate content (right). Since the crack network is more pronounced compared to the layers of electrolytes with a

lower phosphate content, it can be assumed that the water-containing aluminum phosphate was at least partially dehydrated.

5. Conclusions

In addition to the existing state of knowledge, the formation of surface layers during polarization of a dual-phase steel in alkaline, aluminate-containing electrolytes in the potential range between OCP − 100 mV and OCP + 4000 mV was investigated. The potentiodynamic polarization was applicable to the screening of the potential range and potentiostatic polarization proved to be useful for the investigation of passivation or pH-induced precipitation at a distinct potential. The following potential ranges can be classified according to the dominating mechanisms:

1. At an anodic potential of about 500 mV vs. SHE, slightly below the potential of oxygen evolution, electrochemical passivation takes place by the formation of an iron oxide, which probably consists of the maghemite phase.
2. In the potential range between about 550 mV and 900 mV vs. SHE, passivation is still apparent. However, the passive layer is increasingly damaged with rising anodic potential due to oxygen evolution.
3. At anodic potentials above about 1 V vs. SHE, oxygen evolution causes a sufficiently high pH drop at the anode surface, leading to the precipitation of a thick and porous oxide layer, which predominantly consists of amorphous alumina or nanocrystalline γ-alumina and, in the case of phosphate-containing electrolytes, the hydrous phosphate evansite.

According to the findings of this work, a pre-polarization step before the actual PEO process could be introduced in order to generate a precipitation layer with defined properties. For example, polarization at 4 V vs. SHE should be performed for at least 5 min in aluminate solution at pH 12 and for at least 15 min in an aluminate solution which additionally contains 0.1 mol/L phosphate at a similar pH. Furthermore, it was shown that this approach can also be applied to high-strength, multi-phase steels, even though the electrochemical behaviors of the ferrite and martensite phases differ significantly.

Author Contributions: Conceptualization, R.M.; methodology, R.M., C.A.R., F.S. and V.M.; validation, R.M., C.A.R., F.S., V.M., T.M. and T.L.; formal analysis, R.M., C.A.R., F.S. and V.M.; investigation, R.M., C.A.R., F.S. and V.M.; resources, T.L.; data curation, R.M., C.A.R., F.S. and V.M.; writing—original draft preparation, R.M.; writing—review and editing, R.M., C.A.R., F.S., V.M., T.M. and T.L.; visualization, R.M.; supervision, T.M. and T.L.; project administration, R.M, T.M. and T.L.; funding acquisition, T.L. All authors have read and agreed to the published version of the manuscript.

Funding: This research was funded by Deutsche Forschungsgemeinschaft (DFG, German Research Foundation), grant number 464291298.

Data Availability Statement: The authors confirm that the data supporting the findings of this study are available within the article.

Acknowledgments: The technical assistance of Anu George (polarization measurements, sample preparation, and optical microscopy), Saravanan Palaniyappan (Raman), and Marc Pügner (XRD) is gratefully acknowledged.

Conflicts of Interest: The authors declare no conflict of interest.

References

1. Krysmann, W. Beitrag Zur Anodischen Oxydation von Aluminium Unter Funkenentladung. Ph.D. Thesis, Technische Hochschule Karl-Marx-Stadt, Karl-Marx-Stadt, Germany, 1982.
2. Simchen, F.; Sieber, M.; Mehner, T.; Lampke, T. Characterisation method of the passivation mechanisms during the pre-discharge stage of plasma electrolytic oxidation indicating the mode of action of fluorides in peo of magnesium. *Coatings* **2020**, *10*, 965. [CrossRef]
3. Holze, R. *Leitfaden der Elektrochemie*, 1st ed.; Teubner: Leipzig, Germany, 1998; p. 190.
4. Lohrengel, M.M. Thin anodic oxide layers on aluminium and other valve metals: High field regime. *Mater. Sci. Eng. R Rep.* **1993**, *11*, 243–294. [CrossRef]

5. Yerokhin, A.L.; Snizhko, L.O.; Gurevina, N.L.; Leyland, A.; Pilkington, A.; Matthews, A. Discharge characterization in plasma electrolytic oxidation of aluminium. *J. Phys. D Appl. Phys.* **2003**, *36*, 2110–2120. [CrossRef]
6. Guo, S.; Si, R.; Dai, Q.; You, Z.; Ma, Y.; Wang, J. A critical review of corrosion development and rust removal techniques on the structural/environmental performance of corroded steel bridges. *J. Clean. Prod.* **2019**, *233*, 126–146. [CrossRef]
7. Joiret, S.; Keddam, M.; Nóvoa, X.R.; Pérez, M.C.; Rangel, C.; Takenouti, H. Use of EIS, ring-disk electrode, EQCM and Raman spectroscopy to study the film of oxides formed on iron in 1M NaOH. *Cem. Concr. Compos.* **2002**, *24*, 7–15. [CrossRef]
8. Zou, J.Y.; Chin, D.T. Anodic Behaviour of Carbon Steel in Concentrated NaOH Solutions. *Electrochim. Acta* **1988**, *33*, 477–485. [CrossRef]
9. Hugot-Le Goff, A.; Flis, J.; Boucherit, N.; Joiret, S.; Wilinski, J. Use of Raman Spectroscopy and Rotating Split Ring Disk Electrode for Identification of Surface Layers on Iron in 1M NaOH. *J. Electrochem. Soc.* **1990**, *137*, 2684–2690. [CrossRef]
10. Freire, L.; Nóvoa, X.R.; Montemor, M.F.; Carmezim, M.J. Study of passive films formed on mild steel in alkaline media by the application of anodic potentials. *Mater. Chem. Phys.* **2009**, *114*, 962–972. [CrossRef]
11. DorMohammadi, H.; Pang, Q.; Murkutec, P.; Árnadóttir, L.; Isgor, O.B. Investigation of iron passivity in highly alkaline media using reactive-force field molecular dynamics. *Corros. Sci.* **2019**, *157*, 31–40. [CrossRef]
12. Nanda, T.; Singh, V.; Singh, V.; Chakraborty, A.; Sharma, S. Third generation of advanced high-strength steels: Processing routes and properties. *Proc. Inst. Mech. Eng. Pt. L J. Mater. Des. Appl.* **2019**, *233*, 209–238. [CrossRef]
13. Sarkar, P.P.; Kumar, P.; Kumar Manna, M.; Chakraborti, P.C. Microstructural influence on the electrochemical corrosion behaviour of dual-phase steels in 3.5% NaCl solution. *Mater. Lett.* **2005**, *59*, 2488–2491. [CrossRef]
14. Nadlene, R.; Esah, H.; Norliana, S.; Mohd Irwan, M.A. Study on the Effect of Volume Fraction of Dual Phase Steel to Corrosion Behaviour and Hardness. *Int. J. Sci. Res.* **2011**, *5*, 393–396.
15. Hai, C.; Cheng, X.; Du, C.; Li, X. Role of Martensite Structural Characteristics on Corrosion Features in Ni-Advanced Dual-Phase Low-Alloy Steels. *Acta Metall. Sin. (Engl. Lett.)* **2021**, *34*, 802–812. [CrossRef]
16. Chen, H.; Lv, Z.; Lu, L.; Huang, Y.; Li, X. Correlation of micro-galvanic corrosion behavior with corrosion rate in the initial corrosion process of dual phase steel. *J. Mater. Res. Technol.* **2021**, *15*, 3310–3320. [CrossRef]
17. Abdo, H.S.; Seikh, A.H.; Mohammed, J.A.; Luqman, M.; Ragab, S.A.; Almotairy, S.M. Influence of Chloride Ions on Electrochemical Corrosion Behavior of Dual-Phase Steel over Conventional Rebar in Pore Solution. *Appl. Sci.* **2020**, *10*, 4568. [CrossRef]
18. Amaral, S.T.; Müller, I.L. A RRDE study of the electrochemical behavior of iron in solutions containing silicate and sulphate at pH 10–13. *Corros. Sci.* **1999**, *41*, 759–771. [CrossRef]
19. Simchen, F.; Masoud-Nia, N.; Mehner, T.; Lampke, T. Formation of corundum-rich alumina coatings on low-carbon steel by plasma electrolytic oxidation. *IOP Conf. Ser. Mater. Sci. Eng.* **2021**, *1147*, 012007. [CrossRef]
20. Kurze, P. Herstellung, Charakterisierung und Anwendung von Al_2O_3-Schichten insbesondere auf Aluminium- und Eisenwerkstoffen. Ph.D. Thesis, Technische Hochschule Karl-Marx-Stadt, Karl-Marx-Stadt, Germany, 1981.
21. Karpushenkov, S.A.; Shchukin, G.L.; Belanovich, A.L.; Savenko, V.P.; Kulak, A.I. Plasma electrolytic ceramic-like aluminum oxide coatings on iron. *J. Appl. Electrochem.* **2010**, *40*, 365–374. [CrossRef]
22. Eremin, N.I.; Volokhov, Y.A.; Mironov, V.E. Structure and Behaviour of Aluminate Ions in Solution. *Russ. Chem. Rev.* **1974**, *43*, 92–104. [CrossRef]
23. Ginsberg, H.; Hüttig, W.; Stiehl, H. Über die Bildung von kristallinem $AI(OH)_3$ und die Umwandlung von Bayerit in Hydrargillit. *Z. Anorg. Allg. Chem.* **1962**, *318*, 238–256. [CrossRef]
24. Dao Huu, N. Untersuchungen zur Anodischen Abscheidung von Schutzschichten aus Wäßrigen Aluminatlösungen auf Eisenwerkstoffen. Ph.D. Thesis, Technische Hochschule Karl-Marx-Stadt, Karl-Marx-Stadt, Germany, 1979.
25. Li, Z.; Cheng, Y.; Kang, S.H.; Tu, W.; Cheng, Y. Re-understanding of the breakdown theory from the study of the plasma electrolytic oxidation of a carbon steel—A non-valve metal. *Electrochim. Acta* **2018**, *284*, 681–695. [CrossRef]
26. Klapkiv, M.D.; Nykyforchyn, H.M.; Posuvailo, V.M. Spectral Analaysis of an Elctrolytic Plasma in the Process of Synthesis of Aluminum Oxide. *Mater. Sci.* **1995**, *30*, 333–343. [CrossRef]
27. Klapkiv, M.D. Simulation of Sythesis of Oxide-Ceramic Coatings in Discharge Channels of a Metal-Electrolyte System. *Mater. Sci.* **1999**, *35*, 279–283. [CrossRef]
28. Attarzadeh, N.; Molaei, M.; Babaei, K.; Fattah-Alhosseini, A. New Promising Ceramic Coatings for Corrosion and Wear Protection of Steels: A Review. *Surf. Interfaces* **2021**, *23*, 100997. [CrossRef]
29. Yang, W.; Li, Q.; Liu, W.; Liang, J.; Peng, Z.; Liu, B. Characterization and properties of plasma electrolytic oxidation coating on low carbon steel fabricated from aluminate electrolyte. *Vacuum* **2017**, *144*, 207–216. [CrossRef]
30. Stern, M. A Method For Determining Corrosion Rates From Linear Polarization Data. *Corrosion* **1958**, *9*, 60–64. [CrossRef]
31. Database of Raman Spectroscopy, X-ray Diffraction and Chemistry Data for Minerals. Available online: https://rruff.info (accessed on 29 January 2023).
32. Ruan, H.D.; Frost, R.L.; Kloprogge, J.T. Comparison of the Raman spectra of Bayerite, Boehmite, Diaspore and Gibbsite. *J. Raman Spectrosc.* **2001**, *32*, 745–750. [CrossRef]
33. Sudare, T.; Zenzai, A.; Tamura, S.; Kiyama, M.; Hayashi, F.; Teshima, K. Hierarchical spheres of Mg–Al LDH for the removal of phosphate ions: Effect of alumina polymorph as precursor. *CrystEngComm* **2019**, *47*, 7211–7216. [CrossRef]

34. Majzlan, J.; Lang, B.E.; Stevens, R.; Navrotsky, A.; Woodfield, B.F.; Boerio-Goates, J. Thermodynamics of Fe oxides: Part I. Entropy at standard temperature and pressure and heat capacity of goethite (α-FeOOH), lepidocrocite (γ-FeOOH), and maghemite (γ-Fe_2O_3). *Am. Mineral.* **2003**, *88*, 846–854. [CrossRef]
35. Hanesch, M. Raman spectroscopy of iron oxides and (oxy)hydroxides at low laser power and possible applications in environmental magnetic studies. *Geophys. J. Int.* **2009**, *177*, 941–948. [CrossRef]
36. Mazzetti, L.; Thistlethwaite, P.J. Raman spectra and thermal transformations of ferrihydrite and schwertmannite. *J. Raman Spectrosc.* **2002**, *33*, 104–111. [CrossRef]
37. Modesto Lopez, L.B.; Pasteris, J.D.; Biswas, P. Sensitivity of Micro-Raman Spectrum to Crystallite Size of Electrospray-Deposited and Post-Annealed Films of Iron-Oxide Nanoparticle Suspensions. *Appl. Spectrosc.* **2009**, *63*, 627–635. [CrossRef]
38. Etteyeb, N.; Dhouibi, L.; Sanchez, M.; Alonso, C.; Andrade, C.; Triki, E. Electrochemical study of corrosion inhibition of steel reinforcement in alkaline solutions containing phosphates based components. *J. Mater. Sci.* **2007**, *42*, 4721–4730. [CrossRef]

coatings

MDPI

Article

Photoluminescent Coatings on Zinc Alloy Prepared by Plasma Electrolytic Oxidation in Aluminate Electrolyte

Hanna Maltanava [1,2,*], Stevan Stojadinovic [3], Rastko Vasilic [3,*], Sergey Karpushenkov [4], Nikita Belko [2], Michael Samtsov [2] and Sergey Poznyak [1]

[1] Research Institute for Physical Chemical Problems, Belarusian State University, Leningradskaya Str. 14, 220006 Minsk, Belarus; poznyak@bsu.by
[2] A.N. Sevchenko Institute of Applied Physical Problems, Belarusian State University, Kurchatova Str. 7, 220045 Minsk, Belarus; belkonv@bsu.by (N.B.); samtsov@bsu.by (M.S.)
[3] Faculty of Physics, University of Belgrade, Studentski Trg 12-16, 11000 Belgrade, Serbia; sstevan@ff.bg.ac.rs
[4] Faculty of Chemistry, Belarusian State University, Nezavisimosti Ave. 4, 220030 Minsk, Belarus; karpushenkov@bsu.by
* Correspondence: maltanava@bsu.by (H.M.); rastko.vasilic@ff.bg.ac.rs (R.V.)

Abstract: Thick $ZnO/ZnAl_2O_4$ coatings were synthesized on zinc alloy Z1 substrates through plasma electrolytic oxidation (PEO) for different anodization times. The prepared coatings were characterized by scanning SEM, XRD, diffuse reflectance and photoluminescence spectroscopy in order to establish the relationship between their structural and optical properties and PEO processing parameters. Under different PEO processing conditions (anodization time—1–10 min and applied voltage—370 and 450 V) ceramic coatings with a mean thickness of 2–12 μm were prepared. XRD analysis explored the coating structure composed of zinc oxide (wurtzite) and zinc aluminate spinel. The content of $ZnAl_2O_4$ in the coatings grows with increasing the applied voltage and anodization time. Photoluminescence (PL) measurements showed that the PEO coatings have several bands in the visible and near-infrared regions associated with their composite structure. The PL spectra significantly depend on the PEO processing parameters due to varying ZnO and $ZnAl_2O_4$ content in the coatings. The insight in the relationship between the $ZnAl_2O_4$ structure and the photoluminescent properties of $ZnO/ZnAl_2O_4$ coatings has been provided using the combination of XRD and luminescence spectroscopy.

Keywords: zinc alloy; plasma electrolytic oxidation; ZnO; $ZnAl_2O_4$; photoluminescence

Citation: Maltanava, H.; Stojadinovic, S.; Vasilic, R.; Karpushenkov, S.; Belko, N.; Samtsov, M.; Poznyak, S. Photoluminescent Coatings on Zinc Alloy Prepared by Plasma Electrolytic Oxidation in Aluminate Electrolyte. *Coatings* **2023**, *13*, 848. https://doi.org/10.3390/coatings13050848

Academic Editor: Frederic Sanchette

Received: 18 March 2023
Revised: 21 April 2023
Accepted: 25 April 2023
Published: 28 April 2023

1. Introduction

Plasma electrolytic oxidation (PEO) is a powerful tool to create functional layers on the surface of active metals such as aluminium, magnesium, titanium and their alloys [1,2]. This method is based on the material treatment with shortly living (in milliseconds range) discharges in environmentally friendly electrolytes. These discharges are responsible for the conversion of components from substrate and electrolyte into well adherent ceramic-like layers on metal surfaces [3].

At the beginning of PEO treatment, anodic oxide films are typically formed using direct current DC polarization of a metal electrode under potentiostatic, galvanostatic or potentiodynamic control. In most cases, a compact barrier-type film initially grows. As the thickness of oxide film reaches a certain critical value, the film is broken due to impact or tunneling ionization [4–7]. Although the breakdown of anodic layers is considered to be harmful, since it leads to the degradation of their dielectric and protection characteristics, this phenomenon "converts" the process to a next step of metal treatment named "microplasma oxidation" or "plasma electrolytic oxidation" [1,2,8–10]. This process operates at potentials above the breakdown voltage of an anodic film and is characterized by luminescence sparks moving over the treated surface. Anodic layers prepared by the

PEO technique are usually rather thick (from fractions of a micron to tens or hundreds of micrometers) [11,12] because a barrier-type film is needed to be formed on a metal surface before the spark discharges can be observed on the electrode surface. Owing to plasma thermochemical interactions in the multiple surface discharges, this method allows obtaining a wide range of the film composition and properties and, therefore, is considered as technologically promising [3]. PEO anodizing has several advantages such as the use of ecological-friendly electrolytes, the preparation of thick coatings without expensive equipment and the absence of special surface treatment before applying the PEO process.

The most of the coatings produced by plasma electrolytic oxidation were investigated on aluminium [12,13], titanium [14], tantalum [15], niobium [16] and zirconium [17], which belongs to the group of valve metals. Nevertheless, in recent years, considerable interest of researchers has been directed to the production of PEO coatings on some non-valve metals, such as magnesium [18], zinc [19,20], iron [21–23], etc. Compared to magnesium, studies on the PEO process on zinc are very limited, although the first patent was published in 1967 [14]. For preparation of PEO coatings on Zn, non-concentrated alkaline solutions were used without any additives or with addition of sodium silicate, sodium aluminate or sodium phosphate [15–18]. Although the possibility of obtaining anodic coatings on zinc in the PEO regime was demonstrated, the various physico-chemical properties of such coatings have not been studied sufficiently.

PEO coatings obtained in aluminate electrolytes can demonstrate improved functional properties due to the formation of $ZnAl_2O_4$/ZnO heterostructures [24]. Zinc aluminate ($ZnAl_2O_4$) is a spinel type oxide which characterized a wide band gap (~3.8 eV), chemical and thermal stability, low surface acidity, high mechanical resistance, superior optical transmittance and high fluorescence efficiency [25,26]. All these properties make $ZnAl_2O_4$ a suitable material for various applications, such as photoelectronic devices [27], optical coatings [28], electroluminescence displays [29], catalyst and catalytic support [30–33]. Recently, $ZnAl_2O_4$ spinel has given interest as a cathode material in Li-ion batteries [34], UV-emitter [35], supercapacitor [36] and $ZnAl_2O_4$@$NiFe_2O_4$ composite magnetic sensor [37]. Zinc oxide is an extensively studied semiconductor material that is of interest for photocatalysis and light-emitting diodes [38,39]. ZnO/$ZnAl_2O_4$ heterostructure has given the new possibility for science and industry due to diversity of morphology, composition and long term stability of the composite. Thus, a series of ZnO/$ZnAl_2O_4$ composites have been prepared for photocatalytic degradation of organic dyes [40,41]. However, photoluminescence and optical properties of ZnO/$ZnAl_2O_4$ heterostructures have not been completely understood. It is clearly of relevance to explore such properties of the $ZnAl_2O_4$/ZnO composites obtained via PEO process since some synergy effect between ZnO and $ZnAl_2O_4$ semiconductors can be anticipated.

The goal of the present work is the preparation of oxide coatings on zinc alloy in alkaline sodium aluminate-containing electrolyte in PEO mode to improve photoluminescence (PL) properties of the metal surface. In addition, the relationship between the microstructure, chemical and phase composition of the PEO coatings on the Zn alloy and their semiconducting and photoluminescence properties was studied.

2. Materials and Methods

2.1. Materials

For preparation of PEO coatings, zinc alloy Z1 (according to EN988) (VMZinc, Bagnolet, France) with a nominal composition [wt.%]: 0.08 ÷ 1.00% Cu, 0.06 ÷ 0.20% Ti, $\leq$0.015% Al and Zn balance was used as a substrate. 1.5 mm thick metal foil was cut into 12.5 mm × 20 mm pieces and a small hole was drilled in the upper part of each piece for an electrical contact. The Zn alloy samples were cleaned with ethanol in an ultrasonic bath, washed with deionized water, and then attached to a titanium rod coated with Teflon. The connection spot was insulated with silicone sealant.

An aqueous solution containing 8.2 g/L $NaAlO_2$ (Sigma Aldrich, Louis, MO, USA, technical, anhydrous) and 2 g/L KOH (Sigma Aldrich, Louis, MO, USA, 90%) was used

as the electrolyte. The electrolyte was prepared using deionized water and analytical-grade chemicals.

2.2. Setup for PEO Anodization

The power source for PEO anodizing was a home-made DC power supply unit, providing rectified voltage from 0 to 500 V and current up to 3 A. Anodic oxidation of zinc electrodes was carried out in a cylindrical glass cell with a volume of 700 mL. A zinc alloy plate and a 40 mm × 15 mm stainless steel plate were used as the anode and cathode in the experiments, respectively. During the anodizing process, the electrolyte in the cell was mixed with a magnetic stirrer. The temperature of the electrolyte was maintained in the range of 10–50 °C using a cooling system.

A voltmeter and an amperometer were used to control the output parameters of anodizing. To measure the transient current in the system, a precision resistor (shunt) was connected in series to the circuit and the potential drop on this resistor was recorded by a digital oscilloscope.

2.3. Characterization Techniques

The phase composition of the prepared coatings was examined by X-ray diffraction (XRD) method on a PANalytical X'Pert PRO MRD (Multi-Purpose Research Diffractometer, Almelo, The Netherlands) in Bragg-Brentano geometry using CuK_{α}-radiation. Recording speed was 0.4°/min. A JEOL 840 A scanning electron microscope (SEM) (JEOL Ltd., Tokyo, Japan) equipped with an X-ray energy dispersive spectroscopy (EDS) setup was used to characterize the morphology and chemical composition of the formed oxide films.

PL spectral measurements were performed on a Horiba Jobin Yvon Fluorolog FL3-22 spectrofluorimeter (Horiba, Palaiseau, France) at room temperature, with a 450 W Xe lamp as the excitation light source. The obtained spectra were corrected for the spectral response of the measuring system and spectral distribution of the Xe lamp. UV–vis diffuse reflectance spectra (DRS) of the formed coatings were recorded using a UV–vis spectrophotometer (Shimadzu UV-3600, Kyoto, Japan).

Spectral characterization of the sparks appearing during the PEO process was performed using a grating spectrometer with an intensified charge coupled device (ICCD). Optical detection system consisted of a large-aperture achromatic lens, a 0.3 m Czerny-Turner type monochromator (Hilger spectrometer, diffraction grating 1200 grooves/mm, inverse linear dispersion of 2.7 nm/mm in the first diffraction order and wavelength range of 43 nm) (Hilger Crystals, London, UK) and a very sensitive PI-MAX ICCD thermoelectrically cooled camera (−40 °C) manufactured by Princeton Instruments. (Trenton, NJ, USA) Inverse linear dispersion of the optical detection system was 0.07 nm per pixel. The system was used with several grating positions with overlapping wavelength range of 20 nm. Spectra of sparks obtained by this system were recorded using the integration time of 0.1 s. In all experiments the image of the cathode surface was projected with unity magnification to the entrance slit of the spectrometer. The obtained spectra were adjusted to the spectral response of the measuring system.

A low dispersion system fiber optic spectrometer USB4000 UV/VIS (Ocean Optics) (Orlando, FL, USA) was used for the measurements in the spectral range from 400 nm to 800 nm. The spectrometer detector consisted of a 3648-elementar linear CCD array with a diffraction grating of 600 grooves/mm. The light emitted during PEO process was transmitted from Ocean Optics QP400-2-UV/BX on the spectrometer slit and recorded with integration time of 1 s.

3. Results and Discussion

3.1. Electrochemical Behavior of Zinc Alloy Electrodes at Anodic Polarization in Alkaline Aluminate-Containing Electrolyte

In the present research, a unipolar pulsed DC mode, i.e., under only positive polarization of the metal electrode, for PEO anodization was used. Initially, the voltage on

the electrochemical cell was increased with a rate of 1 V/min until a certain voltage was reached. Then anodization was carried out in the potentiostatic mode. Figure 1 shows typical current density data as a function of time during the PEO anodization of zinc alloy. During linear increase of the voltage to about 370 V, the current density passed through a maximum followed by a sharp drop. At this stage, the appearance of a large number of small microdischarges with white color was observed ("soft sparking" mode). In potentiostatic mode at 370 V, the coating continues to grow and the current drops because of this. The appearance of a current density peak after ~200 s of anodization is associated with an increase in the size of the microdischarges and a decrease of their total number. This phenomenon is ascribed to reduced number of discharging sites through which a higher anodic current is able to pass [42]. After 300 s at 370 V of PEO treatment, the change of color of sparks into yellow ("spark" mode) was observed.

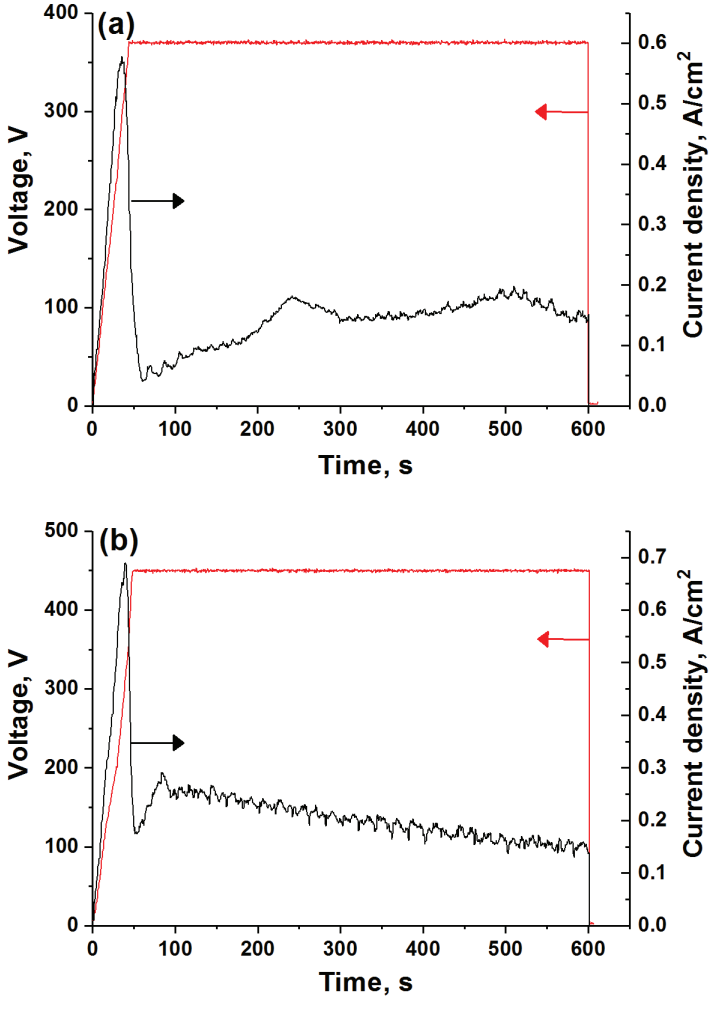

Figure 1. Temporal evolution of the current density and peak voltage during anodization of Zn alloy (**a**) peak voltage 370 V; (**b**) peak voltage 450 V.

The increase of voltage to 450 V leads to a larger current density peak associated with more intensive oxygen bubbling. Moreover, first sparks appear after about 3 s of anodizing and rapidly change their color from white to yellow. After ~100 s of anodizing,

the current density gradually decreases with anodizing time, and visual observations reveal the occurrence of fine homogeneously dispersed microarcs. Increasing the voltage above 450 V intensifies the microarcs formation and gas release, which leads to peeling of the oxide layer. Since the PEO coatings prepared at 370 and 450 V are uniform and have rather good adhesion to the Zn substrate (see Appendix A), this peak voltage range was selected for further studies of the coating growth on Zn alloy. The wear behavior of prepared PEO coatings is presented in Appendix A (Figures A1 and A2).

3.2. PEO Coating Morphology and Elemental Composition

The typical surface morphologies of two sets of PEO coatings, prepared under 370 and 450 V for different time periods, are presented in the SEM micrographs in Figures 2–5. SEM inspection showed that the prepared samples have the fused surface with randomly distributed microcraters. These microcraters or micropores are characteristic of the PEO coatings and were previously assigned to the gas bubble emission through the molten materials or to the formation of very energetic discharges across the growing film [43,44]. As can be seen from Figures 2–5, the size of the microcraters grows with increasing the voltage and anodization time. Moreover, the coatings grown at higher voltage (450 V) exhibit a rougher surface with some microcracks (Figure 4). These microcracks could be attributed to the thermal stresses during the coating growth as a result of melting and solidification of the ceramic compounds such as zinc oxide.

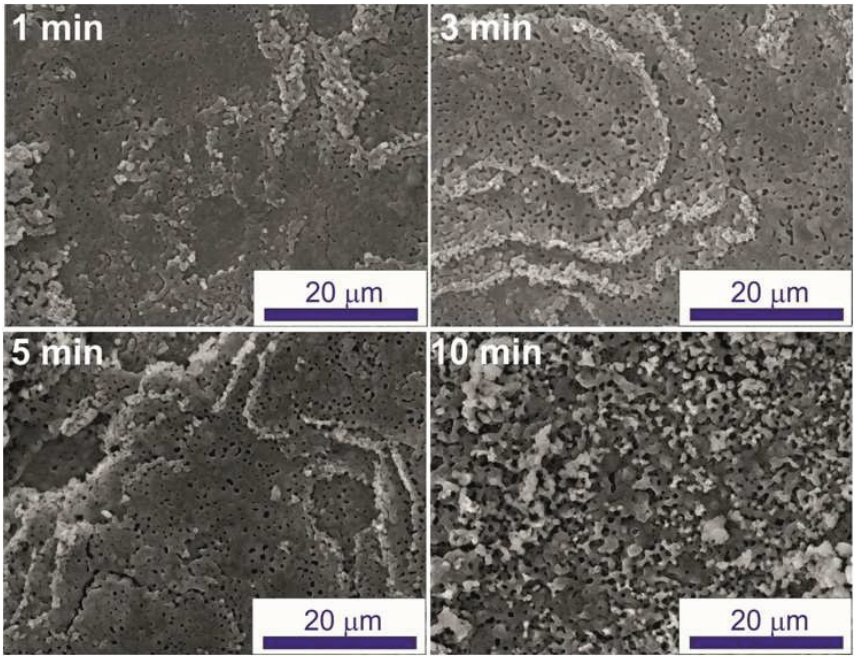

Figure 2. SEM micrographs (lower magnification) showing surface morphology of the PEO coatings prepared at 370 V for different anodization time.

The presence of a significant Al content along with Zn and O in the EDS spectra of these coatings indicates that Al is included into the coatings owing to aluminate anions present in the electrolyte. It is important to note that an increase in the processing voltage from 370 to 450 V leads to a rise in the aluminium content and a decrease in the zinc content in the PEO coatings.

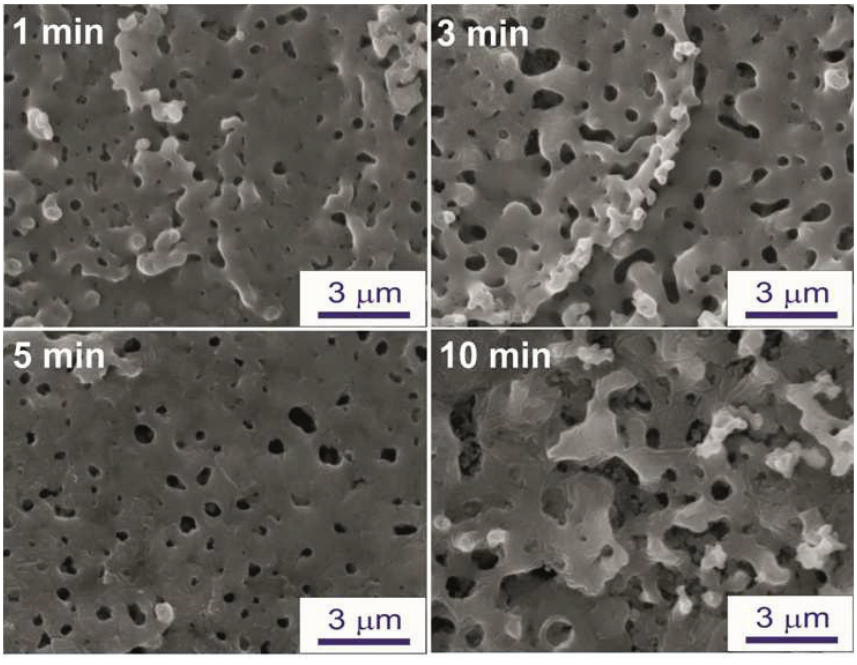

Figure 3. SEM micrographs (higher magnification) showing surface morphology of the PEO coatings prepared at 370 V for different anodization time.

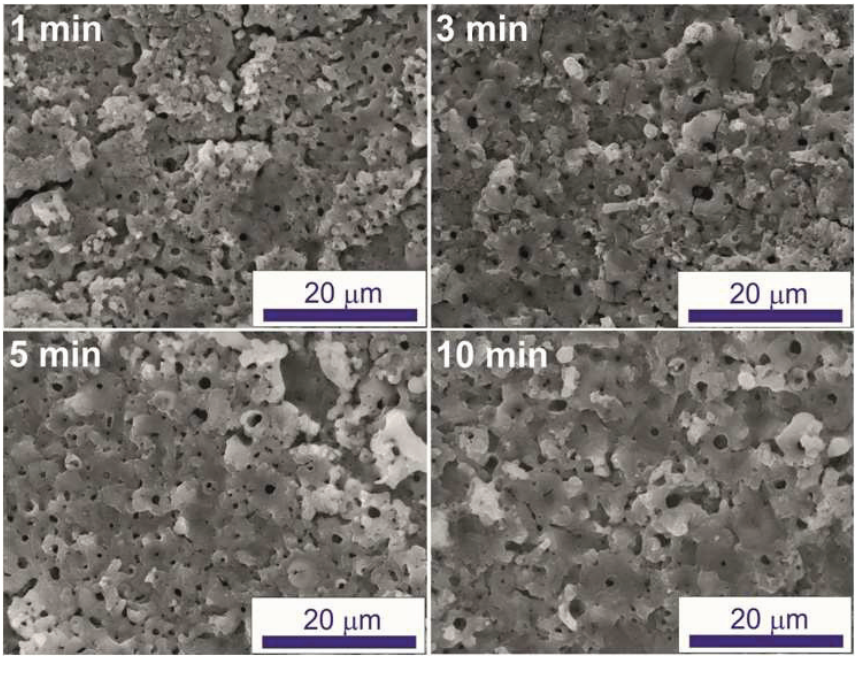

Figure 4. SEM micrographs (lower magnification) showing surface morphology of the PEO coatings prepared at 450 V for different anodization time.

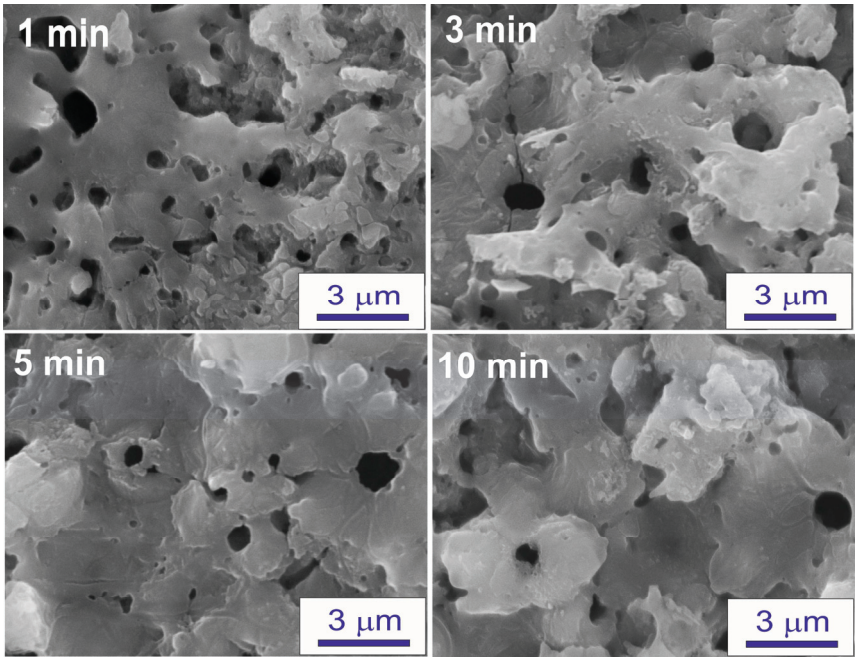

Figure 5. SEM micrographs (higher magnification) showing surface morphology of the PEO coatings prepared at 450 V for different anodization time.

Results of the EDS analysis of the PEO coatings on Zn are shown in Table 1. Main elements of the coatings are determined as O, Zn, and Al.

Table 1. Chemical composition of the PEO coatings (in at.%).

Time of the Treatment, min	Applied Voltage: 370 V			Applied Voltage: 450 V		
	O	Al	Zn	O	Al	Zn
1	59.62	26.30	14.09	60.66	26.40	12.93
3	60.72	27.62	11.61	60.97	31.05	7.98
5	60.71	27.13	12.16	62.90	30.61	6.49
10	59.74	24.09	16.17	59.93	33.04	7.03

Figures 6 and 7 show SEM micrographs of cross-sections of the PEO coated Zn alloy samples prepared at two different voltages (370 and 450 V) for treatment times of 1 and 10 min. All coating-substrate interfaces have an uneven appearance, which may be the result of melting or dissolution of the substrate during the PEO treatment. The coating thickness after 1 min treatment at 370 V is about 2–4.5 μm at different locations of the cross sections. This thickness increases to 4.5–6.5 μm with a rise in processing time up to 10 min (Figure 6). PEO anodization of Zn electrodes at 450 V leads to an increase in the coating thickness (4–6.5 μm after 1 min treatment and 8–12 μm after 10 min treatment) (Figure 7). The obtained data demonstrate that an increase in the processing time from 1 to 10 min results in only a 2-fold rise in the coating thickness. This fact can be explained by the partial detachment of the coating material due to the abundant gas evolution during the anodizing process.

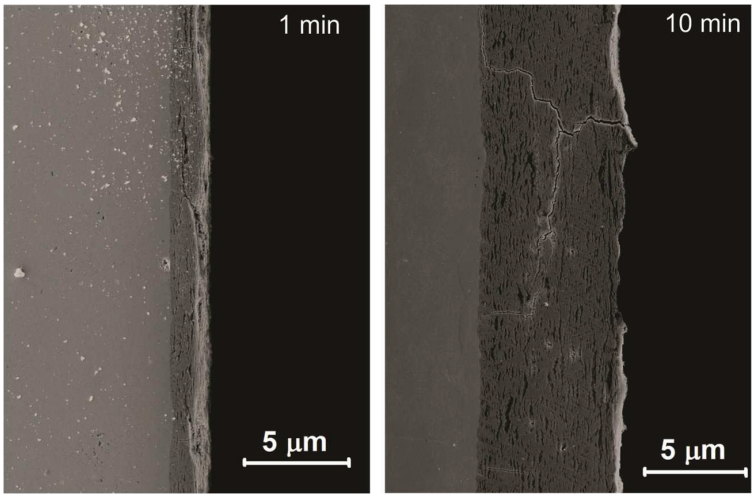

Figure 6. SEM micrographs of cross-sections of the PEO coatings grown at 370 V for 1 and 10 min.

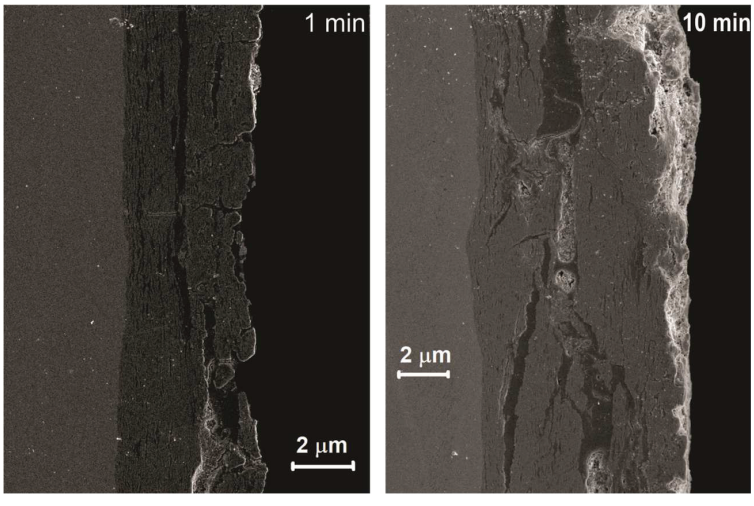

Figure 7. SEM micrographs of cross-sections of the PEO coatings grown at 450 V for 1 and 10 min.

The EDS mapping of the cross-sections of the PEO coatings obtained at 370 and 450 V revealed uneven distribution of zinc and aluminium over the depth of the coatings. It has been identified that the incorporation of aluminium as zinc aluminate into the coatings is preceded by the formation of a zinc oxide layer (as will be shown below). The cross-sectional view of the PEO coatings obtained at 370 V demonstrated the deposition of alternating layers of zinc oxide and zinc aluminate as the coating thickness grows (Figure 8a). Such structure can result from the synthesis of $ZnAl_2O_4$ during high energy plasma discharges. At the same time, two regions are observed for coatings obtained at 450 V (Figure 8b). The inner region is composed of ZnO, whereas the outer region is mainly presented by a thick layer of zinc aluminate. The structural features of the samples treated at 450 V can be related to avalanches generated in zinc oxide, which lead to the occurrence of microarcs and contribute to the synthesis of the aluminate layer.

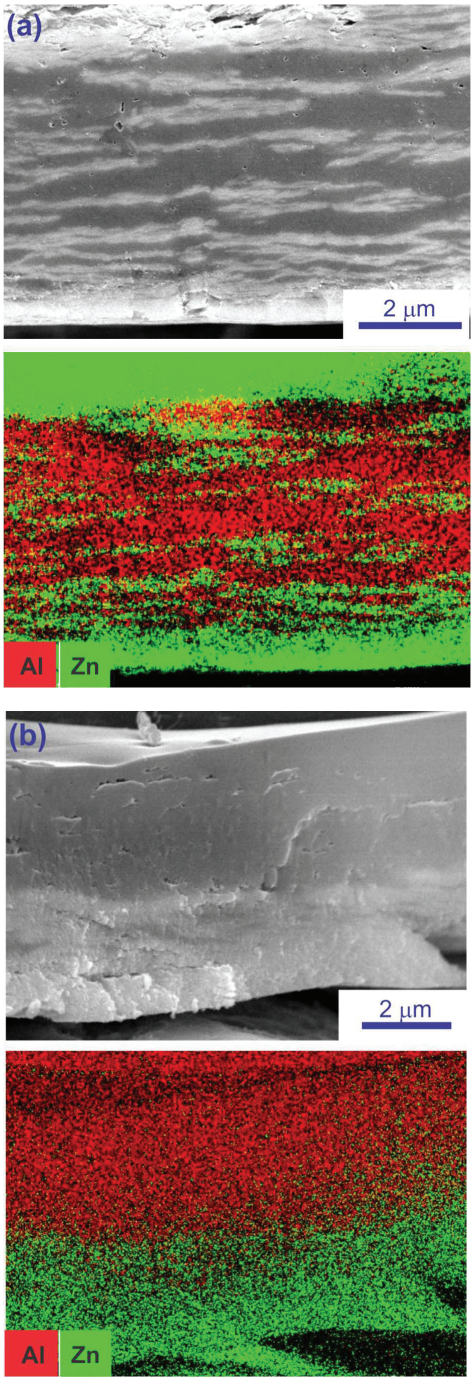

Figure 8. SEM micrographs and associated EDS mapping of cross-sections of the PEO coatings grown at 370 V (**a**) and 450 V (**b**).

3.3. Crystalline Structure of the PEO Coatings

The XRD patterns of the PEO coatings formed at 370 V for different processing time are shown in Figure 9. Beside the characteristic diffraction peaks of the Zn alloy substrate (due to thin thickness of the coatings), ZnO and $ZnAl_2O_4$ phases were detected in all the X-ray diffractograms. ZnO has wurtzite structure with (100), (002), (101), (110), (103), (200), (112), (201), (004) and (201) diffraction peaks at 31.8, 34.4, 36.3, 56.6, 62.9, 66.4, 68.0, 69.1, 72.6 and 77°, respectively. $ZnAl_2O_4$ exhibits a spinel structure with (220), (311), (400), (422), (511), (440), (620) and (533) diffraction peaks at 31.2, 36.8, 44.8, 55.6, 59.3, 65.2, 74.1 and 77.3°. It is known that aluminates (such as $MgAl_2O_4$ [45]) can be of different stoichiometry. The XRD peaks for $ZnAl_2O_4$ show excellent agreement with the literature data indicating that the stoichiometry for ZnO to Al_2O_3 in this phase is close to 1:1. At short processing times, the ZnO phase is the main one, while with an increase in the anodization time, the $ZnAl_2O_4$ phase becomes predominant (Figure 9). When the anodization voltage is increased to 450 V, the relative $ZnAl_2O_4$ content in the coating grows even at short processing times (Figure 10).

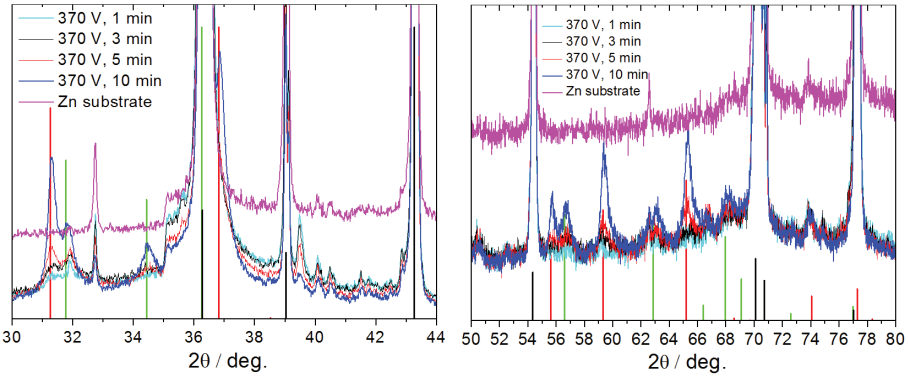

Figure 9. X-ray diffractograms of the pure Zn alloy substrate and PEO coatings prepared on the Zn alloy substrate at 370 V for different anodization time in an alkaline aluminate based electrolyte. Vertical lines correspond to the XRD peaks of ZnO (green; JCPDS: 36-1451), $ZnAl_2O_4$ (red; JCPDS: 82-1036) and metallic Zn (black; JCPDS: 04-0831) phases.

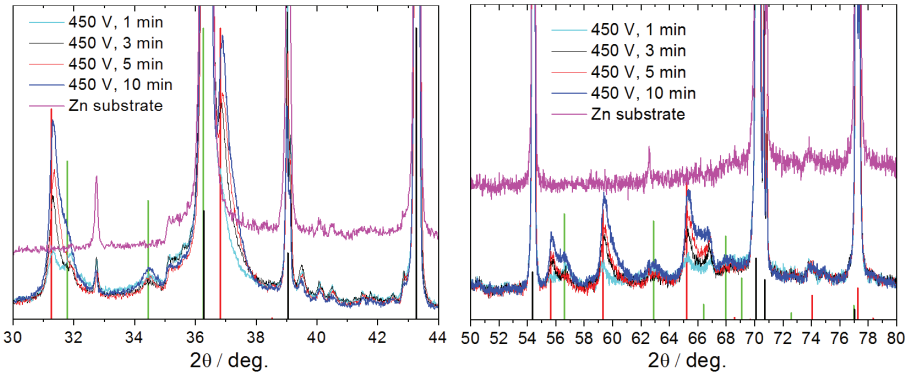

Figure 10. X-ray diffractograms of the pure Zn alloy substrate and PEO coatings prepared on the Zn alloy substrate at 450 V for different anodization time in an alkaline aluminate based electrolyte. Vertical lines correspond to the XRD peaks of ZnO (green; JCPDS: 36-1451), $ZnAl_2O_4$ (red; JCPDS: 82-1036) and metallic Zn (black; JCPDS: 04-0831) phases.

The appearance of the zinc aluminate phase in the PEO coating can be associated with the participation of aluminate anions, contained in the electrolyte, in various chemical and thermochemical processes that occur during PEO treatment. In particular, the aluminate anions react with water in alkaline solutions to produce aluminium tetrahydroxy anions (Reaction 1) that can be decomposed near the anode surface due to the pH and thermal conditions created in the local regions of electrolyte adjacent to the surface discharges (Reaction 2) [14,46]:

$$AlO_2^- + 2H_2O \rightarrow Al(OH)_4^- \quad (1)$$

$$2Al(OH)_4^- \rightarrow Al_2O_3 + 2OH^- + 3H_2O \quad (2)$$

Finally, owing to a very high temperature in the microplasma channels, $ZnAl_2O_4$ can be formed in accordance to the Reaction 3:

$$ZnO + Al_2O_3 \rightarrow ZnAl_2O_4 \quad (3)$$

3.4. Diffuse Reflectance Spectra of the PEO Coatings

To characterize the optical properties of the PEO coatings on Zn, which are important for different applications such as photocatalysis, the diffuse reflectance spectra (DRS) of the coatings formed at various stages of PEO process were analyzed. Figure A3 presents the DRS spectra of the coatings grown at 370 V and 450 V for different time. These spectra were recorded relative to the reference standard—$BaSO_4$ powder.

For analysis of DRS spectra, the Kubelka-Munk theory [47] generally is applied. According to this theory, the relative reflectance of the powder, R_∞, can be converted into an equivalent absorption coefficient, α, using the Kubelka-Munk function $F(R_\infty)$ calculated by the equation:

$$F(R_\infty) = (1 - R_\infty)/2R_\infty = \alpha/S, \quad (4)$$

where S is the coefficient of light scattering.

The calculated spectra of $F(R_\infty)$ for the PEO coatings are shown in Figure 11.

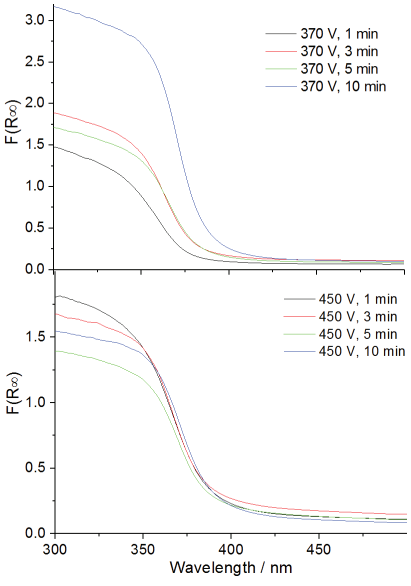

Figure 11. Absorption spectra of the PEO coatings prepared at 370 and 450 V for different anodization time in alkaline aluminate based electrolyte.

The energy dependence of the absorption coefficient α for semiconductors in the region near the absorption edge is given by the equation:

$$\alpha = A\ (h\nu)^{-1}\ (h\nu - E_g)^{1/n}, \quad (5)$$

where E_g is the optical absorption edge energy, ν is the frequency of the incident photon, h is the Planck constant, A is a constant, n = 1/2 and n = 2 for allowed indirect and direct optical transitions, respectively.

Taking into account Equations (4) and (5), the energy intercept of a plot $(F(R_\infty)\ h\nu)^2$ as a function of $h\nu$ (Tauc plot) will give the band gap values for a direct allowed transition when the linear region of the plot is extrapolated to the zero ordinate. We used n = 2 in these calculations, because direct optical transitions are characteristic of both ZnO and $ZnAl_2O_4$. Using this method, the apparent band gaps for the PEO coatings are calculated (Figure A4) and listed in the Table 2. Since the studied coatings are highly defective, the values shown in Table 2 reflect both the changes in the bandgap and the appearance of defective states. The calculated values should be considered as apparent bandgap that does not necessarily reflect the fundamental absorption edge [48].

Table 2. Apparent band gap values calculated using DRS spectra of the PEO coatings prepared at 370 and 450 V for different anodization time.

Time of the PEO Treatment, min	Applied Voltage, V	
	370	**450**
1	3.38 eV	3.29 eV
3	3.33 eV	3.29 eV
5	3.32 eV	3.27 eV
10	3.28 eV	3.26 eV

As can be seen from Table 2, the optical band gap of the PEO films is in the range from 3.38 to 3.26 eV, depending on the applied voltage and the PEO treatment time. These E_g values are close to or slightly higher than the band gap of ZnO (about 3.2 eV [49]), but noticeably lower than the band gap reported for $ZnAl_2O_4$ (3.8 ÷ 4.2 eV [50–53]). According to the XRD data discussed above, the relative $ZnAl_2O_4$ content in the coating grows with increasing the applied voltage and treatment time. Therefore, the apparent E_g of the composite coating is also expected to increase, but in reality it is reduced (see Table 2). The observed contradiction can be explained by the presence of a pronounced shoulder at the long-wavelength edge of the absorption spectrum of $ZnAl_2O_4$ powders, which was observed in the wavelength range of 320–400 nm [51,54]. This shoulder was tentatively related to electronic transitions between filled O 2p orbitals and empty 4s orbitals and would be representative of a defective structure [51]. The contribution from this shoulder to the total absorption in the wavelength range from 300 to 400 nm could be responsible for reduced values of the apparent E_g for the PEO coatings with an enhanced content of $ZnAl_2O_4$.

3.5. Spectral Characterization of Microdischarge Emission during PEO Process on Zn Electrodes in Aluminate-Based Electrolyte

Measurement and analysis of radiation spectra from microdischarges using optical emission spectroscopy (OES) provides a valuable diagnostic tool for studying the PEO process [55–57]. As mentioned above, the PEO process on Zn alloy begins from "soft sparking" mode when small microdischarges with white color appear on the electrode surface. The spectrum of these microdischarges observed during the first 5 min at 370 V does not demonstrate specific emission lines and only a broad halo in the visible region (450–850 nm) is registered. The appearance of small white sparks can be explained via the presence of free electrons in the plasma interacting with solid and/or liquid compounds and bremsstrahlung radiation [56]. When microdischarges become more intense and their

color changes from white to yellow, the spectrum of emission is changed. Typical spectrum corresponding to this stage is shown in Figure 12. The strong lines appear in the spectra and can be attributed to Na I (588.99 nm, 589.59 nm) and K I (766.57 nm, 769.94 nm) lines originating from the electrolytes.

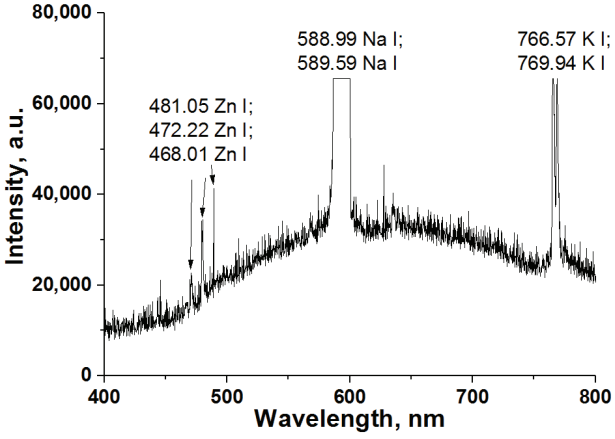

Figure 12. Optical emission spectrum recorded during PEO of Zn alloy in aluminate electrolyte.

In order to better identify less intensive species originated from zinc anode and electrolytes, the detailed optical emission spectra have been analyzed in range 370–420 nm and 450–500 nm, respectively (Figures 13 and 14). Three emission lines of Zn I at 468.01 nm, 472.22 nm and 481.05 nm are observed, which originate from the zinc anode (Figure 13). With increasing the applied voltage up to 450 V when the sparks become significantly larger, additional lines appear in the optical emission spectra. These lines arise from components of aluminate electrolyte and can be assigned to Al I at 394.40 nm, Al I at 396.15 nm, O II at 404.49 nm, H I at 656.28 nm (Figure 14).

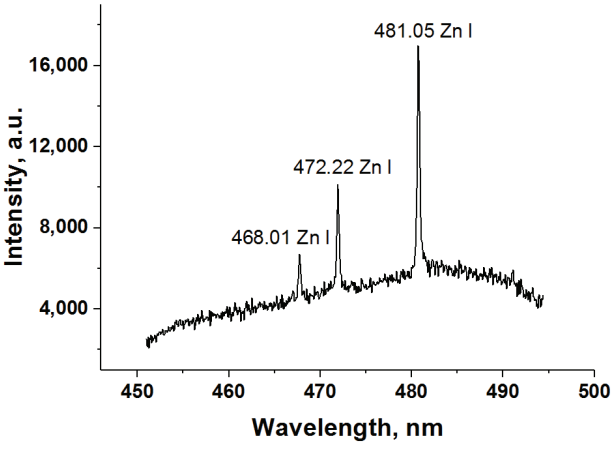

Figure 13. Optical emission spectrum in the range from 450 to 500 nm recorded during PEO of Zn alloy at 370 V.

According to Ref. [56], three discharge models have been developed for the interpretation of the discharge appearance during PEO process: metal-oxide interface discharge (type B), oxide-electrolyte interface discharge within the coating upper layer (type A) and at the coating top layer (type C). Since the melting point of Zn (419.6 °C) is relatively low,

the type B of microdischarge appearance may be present during PEO process. At the same time, oxygen, potassium, sodium and aluminium lines in the optical emission spectra are related to processes of type A and type C. The XRD and EDS data of the obtained PEO coatings (presented above) coincide with the OES results.

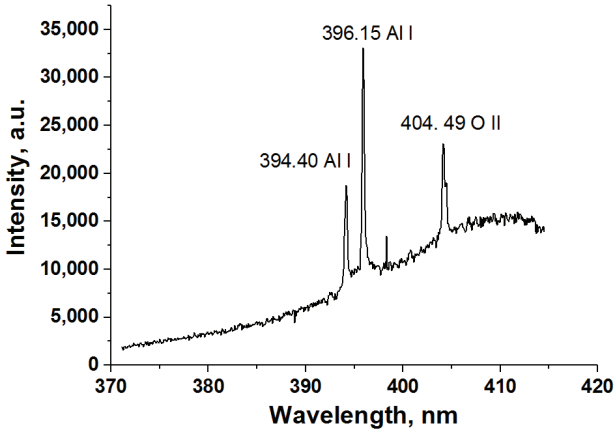

Figure 14. Optical emission spectrum in the range from 370 to 415 nm recorded during PEO of Zn alloy at 450 V.

3.6. Photoluminescence Properties of the PEO Coatings

Interest in studying the photoluminescence (PL) properties of zinc oxide based materials is associated with the perspectives for the practical application of such materials in various fields [58,59]. In particular, the use of luminescence of ZnO materials with a large specific surface as a probe of gas adsorption has been highlighted in some previous works [60,61].

Typical PL excitation spectra (monitored at 570 nm) and corresponding emission spectra (excited at 340 nm) of the PEO coatings prepared at 370 and 450 V for different anodization time are shown in Figures 15 and 16, respectively.

There are two bands in the excitation spectra of the PEO coatings prepared at 370 V for 1–5 min and at 450 V for 1 min (Figure 15). Maximum of the first band located at 335 ÷ 360 nm is shifted to shorter wavelengths with decreasing the treatment time. Position of the other band located at ~275 nm slightly depends on the processing parameters. This band practically disappears with an increase in processing time up to 10 min at 370 V and up to 3 min or more at 450 V. Instead of this band, an exponential rise in the PL intensity appears, starting from 300 nm towards shorter wavelengths (Figure 15). The observed evolution of the PL excitation spectra with a change in the PEO processing parameters can be related to a change in the phase composition of the PEO coatings. As it is shown by XRD analysis (Section 3.3), the relative $ZnAl_2O_4$ content in the coatings grows with increasing the treatment time and applied voltage. Thus, the PL excitation spectrum with exponential growth in the short-wavelength region can be attributed to $ZnAl_2O_4$ phase. Actually, this semiconductor material has a wider band gap than ZnO, and similar PL excitation spectra were reported previously for $ZnAl_2O_4$ powders [25,28,62].

It should be noted that the shape of excitation and emission spectra is changed with changing the emission and excitation wavelengths. Figure 17 shows the evolution of the PL spectra excited at 275 nm, depending on the parameters of the PEO process.

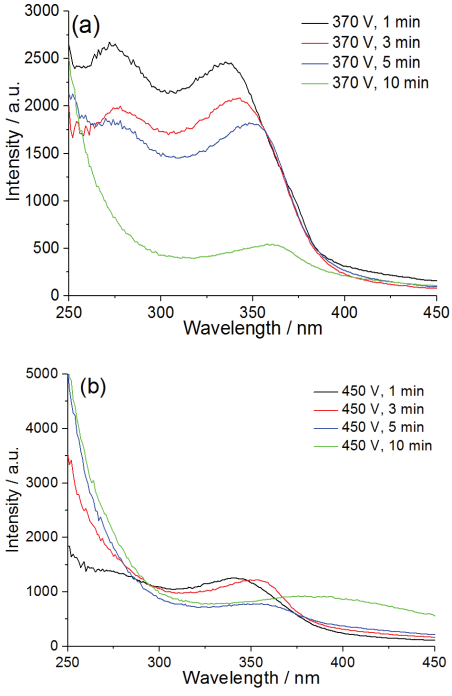

Figure 15. PL excitation spectra of the PEO coatings prepared at 370 V (**a**) and 450 V (**b**) for different anodization time. PL emission was monitored at 570 nm.

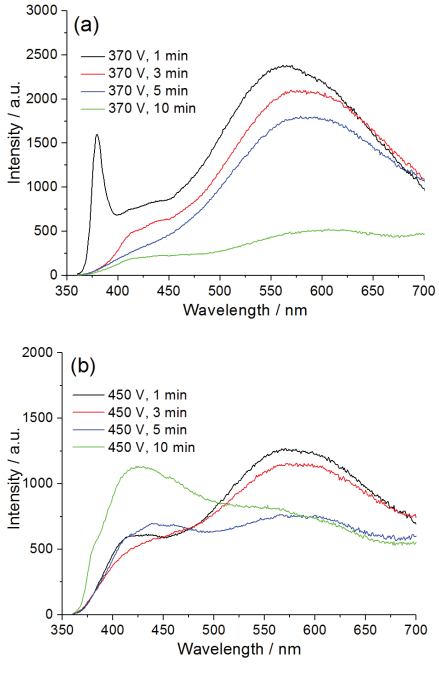

Figure 16. PL emission spectra of the PEO coatings prepared at 370 V (**a**) and 450 V (**b**) for different anodization time. PL was excited at 340 nm.

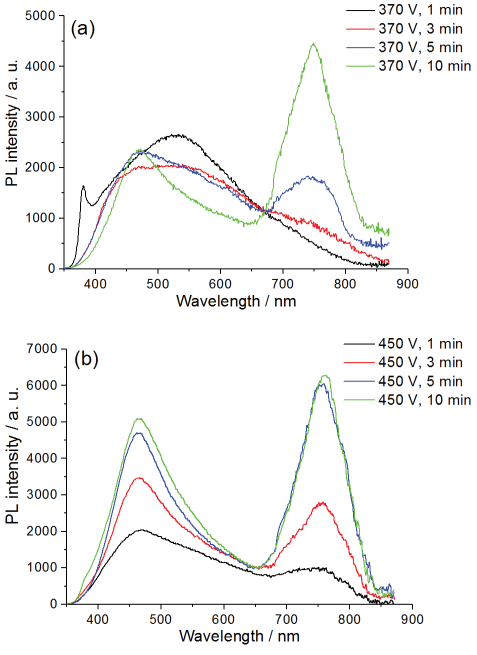

Figure 17. PL emission spectra of the PEO coatings prepared at 370 V (**a**) and 450 V (**b**) for different anodization time. PL was excited at 275 nm.

PL emission spectra of the PEO coatings are composed of several bands located mainly in the visible region (Figures 16 and 17). It should be noted that the total photoluminescence of the coatings is a sum of the PL originating from ZnO and $ZnAl_2O_4$. Based on the XRD data, it is logical to assume that for the coatings grown at 370 V for 1 min, the main contribution to the PL will be made by ZnO. Actually, only these coatings are characterized by a sharp near-ultraviolet PL band centered at ~380 nm, which can be assigned to radiative recombination of free excitons in ZnO [63]. In addition to this short-wavelength band, other wide overlapping bands are observed in the visible region. ZnO commonly demonstrates PL properties in the visible spectral range due to the different intrinsic or extrinsic defects. The origin of this visible PL (green, yellow, orange, and red emission) is still highly controversial. Generally, the green PL is typically associated with oxygen deficiency (e.g., excess Zn^{2+} ions or double ionized oxygen vacancies), and the yellow/orange PL is related to excess oxygen (e.g., oxygen interstitial defects) [64–67]. The wide visible PL band in the 400–800 nm range observed for the PEO coatings grown at 370 V for 1 min indicates that simultaneously several types of defects can contribute to the radiative recombination (Figures 16 and 17). With increasing anodization time and applied voltage in the PL spectra of coatings, this wide PL band shifts to shorter wavelengths and its width decreases. This effect is especially pronounced in the case of PL excited by shorter wavelength light (275 nm) (Figure 17). The emerging PL band peaked at ~460 nm can be assigned to $ZnAl_2O_4$. Similar PL emission spectra were previously reported for pure $ZnAl_2O_4$ powders, and the observed blue emission was ascribed to intra-band-gap defects, such as oxygen vacancies, in $ZnAl_2O_4$ crystals [68]. At the same time, near infrared emission around 760 nm appears under 275 nm excitation. This band grows with increasing the anodization time and applied voltage, which may be due to an increase of $ZnAl_2O_4$ content in the coating. To confirm this observation, the $ZnAl_2O_4$ powder has been obtained. The synthesis of $ZnAl_2O_4$ powder is described in Appendix A. The $ZnAl_2O_4$ spinel structure of prepared powder has been confirmed by XRD (Figure A5). We found two bands (one weak band centered at 570 nm and another strong band at 765 nm) in the emission spectra of the

prepared $ZnAl_2O_4$ powder annealed at 800 °C. Increasing the annealing temperature to 1000 °C leads to a shift of the emission to lower wavelengths and a significant decrease in emission in the near-infrared range (Figure 18).

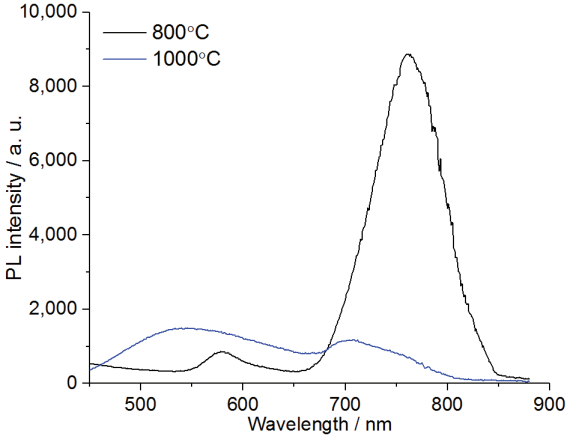

Figure 18. PL emission spectra of the $ZnAl_2O_4$ powders annealed at 800 °C and 1000 °C for 5 h. PL was excited at 275 nm.

According to Ref. [62], such near-infrared emission is strongly dependent on annealing temperature of $ZnAl_2O_4$ and originates from structural defects due to formation of oxygen vacancies. This observation allows concluding that $ZnAl_2O_4$ synthesized during PEO is poorly crystallized and have high level of structural defects. Thus, varying the processing parameters of PEO treatment of Zn alloy can be effective tool for tuning luminescent properties of ZO/$ZnAl_2O_4$ coatings.

4. Conclusions

Plasma electrolytic oxidation of zinc alloy Z1 has been studied in an alkaline aluminate-based electrolyte. SEM study showed that the prepared PEO coatings have fused surfaces with randomly distributed microcraters. According to EDS analysis, the main elemental components of the obtained coatings are Zn, Al and O. XRD results demonstrated that the coatings are crystallized and composed of ZnO (wurtzite) and $ZnAl_2O_4$ (spinel) phases. The phase composition of the coatings is changed with increasing the applied voltage and anodization time: the content of ZnO phase decreases and the proportion of $ZnAl_2O_4$ increases. The excited atoms of H, O, Na, K, Zn and Al, which were identified in optical emission spectra of microdischarges, originate from zinc substrate or electrolyte components. A set of characterization techniques (XRD, EDS-mapping and OES) revealed that the formation of a zinc oxide layer precedes the incorporation of aluminium in the form of zinc aluminate into the coatings as energy of plasma discharges increases. The apparent optical band gap of the PEO composite coatings is estimated from DRS spectra and is in the range from 3.38 to 3.26 eV depending on the applied voltage and PEO treatment time. It has been found that the band gap is reducing during the increase of $ZnAl_2O_4$ content in the PEO coatings. PL excitation and emission spectra of the PEO coatings prepared on the Zn alloy demonstrate a complex evolution of the shape with changing the excitation and emission wavelengths. PL of coatings prepared at 370 V for short times is basically associated to ZnO, whereas increasing the applied voltage and anodization time leads to the appearance of PL bands (peaked at 460 and 760 nm) characteristic of $ZnAl_2O_4$. The appearance of PL band in near-IR region is associated with the defective structure of $ZnAl_2O_4$. The luminescent properties of PEO coatings can be flexibly tuned by PEO processing parameters due to the combination of $ZnAl_2O_4$ and ZnO. Thus, the regulation of the $ZnAl_2O_4$ content and struc-

ture revealed the possibility for the creation of new optical devices and electroluminescence displays with desirable functionalities.

Author Contributions: Conceptualization, S.P. and M.S.; methodology, R.V. and S.P.; software, N.B.; validation, S.P. and S.S.; formal analysis, H.M., M.S. and S.P.; investigation, H.M., S.S., S.K. and S.P.; resources, S.P. and R.V.; data curation, H.M. and N.B.; writing—original draft preparation, H.M. and S.P.; writing—review and editing, H.M., R.V., N.B., S.K. and S.P.; visualization, N.B.; supervision, S.P. and R.V.; project administration, R.V.; funding acquisition, R.V. All authors have read and agreed to the published version of the manuscript.

Funding: This work was partially supported by FUNCOAT project ("Development and design of novel multiFUNctional PEO COATings") in frame of H2020-MSCA-RISE-2018, (Grant Agreement No. 823942), the Belarusian Republican Foundation for Fundamental Research (Grant No. X21M-073) and the State Program for Scientific Research of Belarus "Chemical processes, reagents and technologies, bioregulators and bioorganic chemistry" (Project No. 2.1.04.02).

Institutional Review Board Statement: Not applicable.

Informed Consent Statement: Not applicable.

Data Availability Statement: Data available in a publicly accessible repository.

Acknowledgments: The authors thank Anastasiya Tabolich and the Center for Analytical and Spectral Measurements of the B.I. Stepanov Institute of Physics for measuring photoluminescence spectra.

Conflicts of Interest: The authors declare no conflict of interest.

Appendix A

Appendix A.1. Adhesion/Cohesion Behavior

The adhesion/cohesion of the PEO coatings prepared at 370 V and 450 V has been evaluated by pull-off tests using ONIKS 1.AP adhesion tester (Interpribor, Chelyabinsk, Russia).

Adhesion of $ZnO/ZnAl_2O_4$ coatings on Zn alloy prepared at 450 V and 370 V was approximately the same (0.95 ± 0.21 MPa). The slightly greater adhesion (1.3 ± 0.11 MPa) was achieved for PEO coatings prepared at 370 V for 1 and 3 min. It can be related to the increase of defects, internal stresses and cracks in the PEO coatings with increasing the treatment time. However, some part of PEO coating remains on the substrate after pull-off test due to formation of microstresses and cracks within the PEO layer. The obtained results are in a good agreement with the data presented in [24].

Appendix A.2. Wear Behavior

The dry sliding wear behaviour of the PEO coatings was assessed with an oscillating ball-on-disc tribometer (Tribotec AB, Clichy-France, France), with an AISI 52100 steel ball of 6 mm diameter as the static friction counterpart (IHSD-Klarmann, Bamberg, Germany). The wear tests were performed at ambient conditions (25 ± 2 °C and 36–44% relative humidity) with load of 1 N and an oscillating amplitude of 10 mm with a sliding velocity of 5 $mm \cdot s^{-1}$. The test was terminated after a total sliding distance of 12 m. Laser scanning confocal microscope (LSM 800, ZEISS, Jena, Germany) was used for analysis of the wear tracks after the test. ConfoMapST software (ZEISS, Jena, Germany) (version 1.0) was used for subsequent data treatment and analysis.

Figure A1 demonstrates the comparison of the coefficient of friction for the PEO coatings prepared at 370 and 450 V. The curves initially increase sharply and then equalizes to the average value of the coefficient of friction. The latter was approximately the same during 20 min of the measurement. However, the coatings prepared at 370 V after 20 min of the abrasion show the decrease of the friction coefficient. SEM images (Figure A2) of the wear tracks evidence totally removing the PEO coatings prepared at 370 V during the wear test. At the same time, the coatings obtained at 450 V do not fail during the test and the Zn substrate is not reached. The trend emerged from the wear measurement evidence that the regime of sparking contributes to the formation of more wear-resistant

PEO coatings. Thus, the coatings formed at "microarcs" mode are characterized by thick and well-crystallized PEO layers which demonstrate higher wear resistance in comparison with coatings prepared at "soft sparking" or/and "sparking" modes.

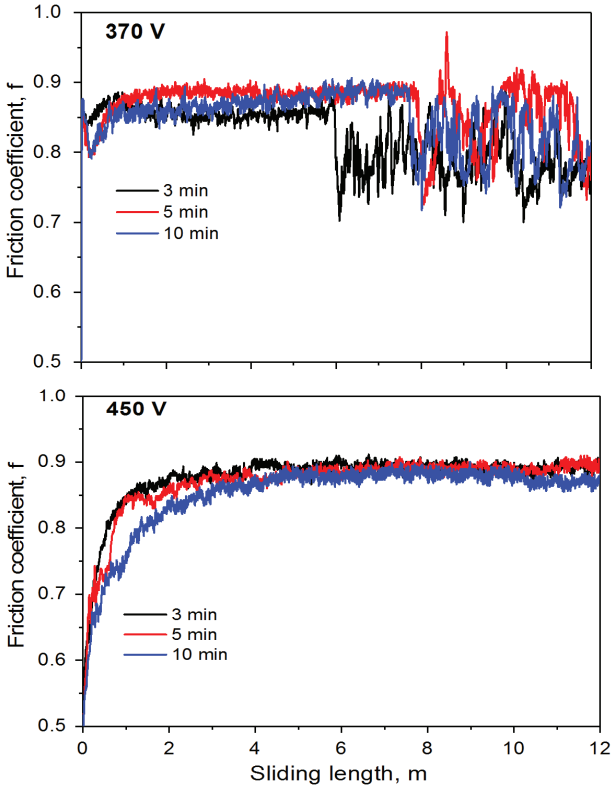

Figure A1. Comparison of the coefficient of friction for the PEO coatings prepared at 370 and 450 V during 3, 5 and 10 min at load of 1 N.

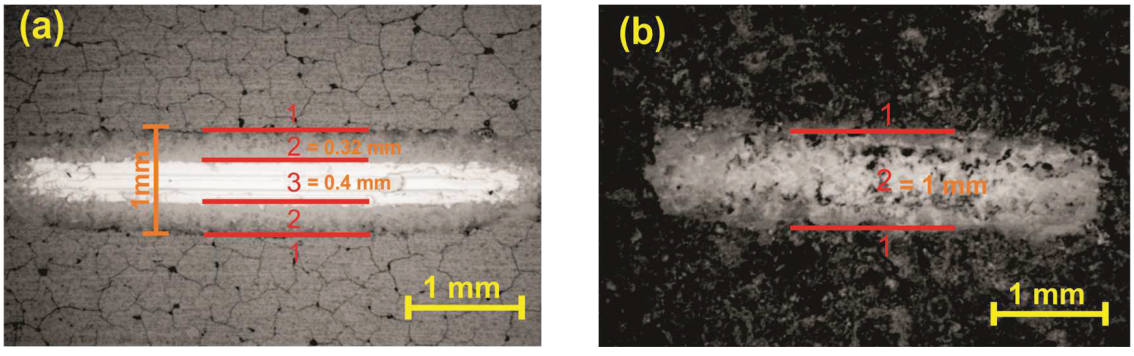

Figure A2. SEM images of the surface of PEO coatings prepared at 370 V (**a**) and 450 V (**b**) for 10 min after the wear tests.

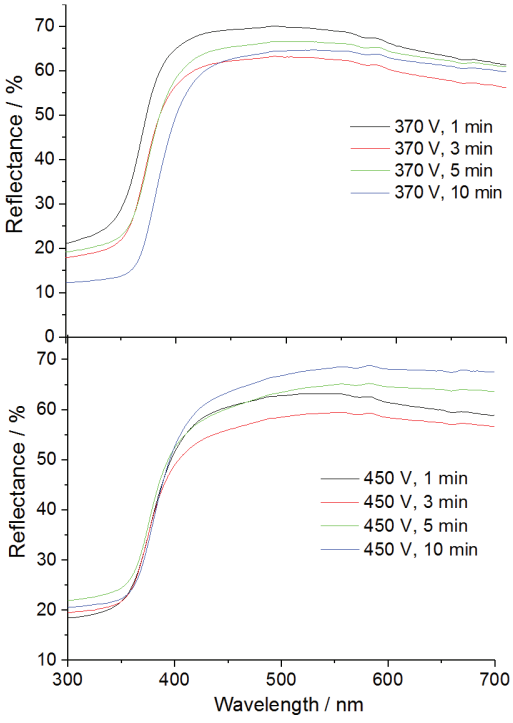

Figure A3. Diffuse reflectance spectra of the PEO coatings prepared at 370 and 450 V for different anodization time in alkaline aluminate based electrolyte.

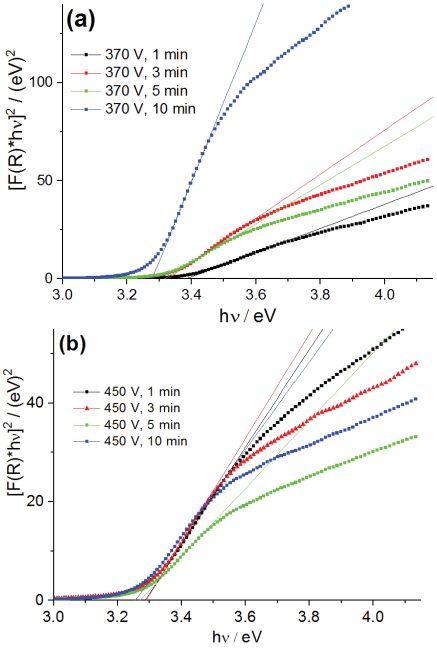

Figure A4. Tauc plots of the PEO coatings prepared at 370V (**a**) and 450V (**b**) for different anodization time.

Appendix A.3. The Synthesis of $ZnAl_2O_4$ Powder

$ZnAl_2O_4$ powder was synthesized by the co-precipitation method as described below followed by thermal treatment at 800 and 1000 °C. 500 mL of 0.02 M $NaAlO_2$ was mixed with 500 mL of 0.01 M $Zn(NO_3)_2$ under vigorous stirring. The obtained precipitate was separated from the solution and washed by centrifugation. Then, the powder was annealed at different temperatures (at 800 and 1000 °C) for 5 h. XRD patterns of prepared powders are presented in Figure A5.

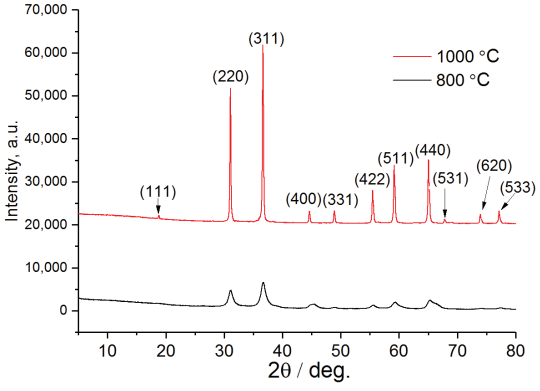

Figure A5. XRD patterns of $ZnAl_2O_4$ annealed at 800 and 1000 °C.

References

1. Sikdar, S.; Menezes, P.V.; Maccione, R.; Jacob, T.; Menezes, P.L. Plasma Electrolytic Oxidation (Peo) Process—Processing, Properties, and Applications. *Nanomaterials* **2021**, *11*, 1375. [CrossRef] [PubMed]
2. Kaseem, M.; Fatimah, S.; Nashrah, N.; Ko, Y.G. Recent Progress in Surface Modification of Metals Coated by Plasma Electrolytic Oxidation: Principle, Structure, and Performance. *Prog. Mater. Sci.* **2021**, *117*, 100735. [CrossRef]
3. Yerokhin, A.L.; Nie, X.; Leyland, A.; Matthews, A.; Dowey, S.J. Plasma Electrolysis for Surface Engineering. *Surf. Coat. Technol.* **1999**, *122*, 73–93. [CrossRef]
4. Wood, G.C.; Pearson, C. Dielectric Breakdown of Anodic Oxide Films on Valve Metals. *Corros. Sci.* **1967**, *7*, 119–125. [CrossRef]
5. Yahalom, J.; Hoar, T.P. Galvanostatic Anodizing of Aluminium. *Electrochim. Acta* **1970**, *15*, 877–884. [CrossRef]
6. Dyer, C.K.; Leach, J.S.L. Breakdown and Efficiency of Anodic Oxide Growth on Titanium. *J. Electrochem. Soc.* **1978**, *125*, 1032–1038. [CrossRef]
7. Kadary, V.; Klein, N. Electrical Breakdown: I. During the Anodic Growth of Tantalum Pentoxide. *J. Electrochem. Soc.* **1980**, *127*, 139–151. [CrossRef]
8. Bakovets, V.V.; Polyakov, O.V.; Dolgovesova, I.P. *Plasma Electrolytic Anodic Treatment of Metals*; Nauka: Novosibirsk, Russia, 1991.
9. Chernenko, V.I.; Snezhko, L.A.; Papanova, I.I. *Coating Preparation by Anodic Spark Electrolysis*; Khimiya: Leningrad, Russia, 1991.
10. Voevodin, A.A.; Yerokhin, A.L.; Lyubimov, V.V.; Donley, M.S.; Zabinski, J.S. Characterization of Wear Protective Al-Si-O Coatings Formed on Al-Based Alloys by Micro-Arc Discharge Treatment. *Surf. Coat. Technol.* **1996**, *86–87*, 516–521. [CrossRef]
11. Egorkin, V.S.; Gnedenkov, S.V.; Sinebryukhov, S.L.; Vyaliy, I.E.; Gnedenkov, A.S.; Chizhikov, R.G. Increasing Thickness and Protective Properties of PEO-Coatings on Aluminum Alloy. *Surf. Coat. Technol.* **2018**, *334*, 29–42. [CrossRef]
12. Matykina, E.; Arrabal, R.; Pardo, A.; Mohedano, M.; Mingo, B.; Rodríguez, I.; González, J. Energy-Efficient PEO Process of Aluminium Alloys. *Mater. Lett.* **2014**, *127*, 13–16. [CrossRef]
13. Sieber, M.; Simchen, F.; Morgenstern, R.; Scharf, I.; Lampke, T. Plasma Electrolytic Oxidation of High-Strength Aluminium Alloys—Substrate Effect on Wear and Corrosion Performance. *Metals* **2018**, *8*, 365. [CrossRef]
14. Yerokhin, A.L.; Leyland, A.; Matthews, A. Kinetic Aspects of Aluminium Titanate Layer Formation on Titanium Alloys by Plasma Electrolytic Oxidation. *Appl. Surf. Sci.* **2002**, *200*, 172–184. [CrossRef]
15. Fattah-Alhosseini, A.; Molaei, M.; Babaei, K. Influence of Electrolyte Composition and Voltage on the Microstructure and Growth Mechanism of Plasma Electrolytic Oxidation (PEO) Coatings on Tantalum: A Review. *Anal. Bioanal. Electrochem.* **2020**, *12*, 517–535. [CrossRef]
16. Quintero, D.; Gómez, M.A.; Araujo, W.S.; Echeverría, F.; Calderón, J.A. Influence of the Electrical Parameters of the Anodizing PEO Process on Wear and Corrosion Resistance of Niobium. *Surf. Coat. Technol.* **2019**, *380*, 125067. [CrossRef]
17. Cengiz, S.; Uzunoglu, A.; Stanciu, L.; Tarakci, M.; Gencer, Y. Direct Fabrication of Crystalline Hydroxyapatite Coating on Zirconium by Single-Step Plasma Electrolytic Oxidation Process. *Surf. Coat. Technol.* **2016**, *301*, 74–79. [CrossRef]

18. Echeverry-Rendon, M.; Duque, V.; Quintero, D.; Harmsen, M.C.; Echeverria, F. Novel Coatings Obtained by Plasma Electrolytic Oxidation to Improve the Corrosion Resistance of Magnesium-Based Biodegradable Implants. *Surf. Coat. Technol.* **2018**, *354*, 28–37. [CrossRef]
19. Stojadinović, S.; Tadić, N.; Vasilić, R. Formation and Characterization of ZnO Films on Zinc Substrate by Plasma Electrolytic Oxidation. *Surf. Coat. Technol.* **2016**, *307*, 650–657. [CrossRef]
20. Rocca, E.; Veys-Renaux, D.; Guessoum, K. Electrochemical Behavior of Zinc in KOH Media at High Voltage: Micro-Arc Oxidation of Zinc. *J. Electroanal. Chem.* **2015**, *754*, 125–132. [CrossRef]
21. Malinovschi, V.; Marin, A.; Mihalache, M.; Iosub, I. Preparation and Characterization of Coatings on Carbon Steel Obtained by PEO in Silicate/Carbonate Electrolyte. *Surf. Coat. Technol.* **2016**, *296*, 96–103. [CrossRef]
22. Karpushenkov, S.A.; Shchukin, G.L.; Belanovich, A.L.; Savenko, V.P.; Kulak, A.I. Plasma Electrolytic Ceramic-like Aluminum Oxide Coatings on Iron. *J. Appl. Electrochem.* **2010**, *40*, 365–374. [CrossRef]
23. Yang, W.; Peng, Z.; Liu, B.; Liu, W.; Liang, J. Influence of Silicate Concentration in Electrolyte on the Growth and Performance of Plasma Electrolytic Oxidation Coatings Prepared on Low Carbon Steel. *J. Mater. Eng. Perform.* **2018**, *27*, 2345–2353. [CrossRef]
24. Serdechnova, M.; Blawert, C.; Karpushenkov, S.; Karpushenkava, L.; Shulha, T.; Karlova, P.; Vasilić, R.; Stojadinović, S.; Stojanović, S.; Damjanović-Vasilić, L.; et al. Properties of ZnO/$ZnAl_2O_4$ Composite PEO Coatings on Zinc Alloy Z1. *Surf. Coat. Technol.* **2021**, *410*, 126948. [CrossRef]
25. Miron, I.; Enache, C.; Vasile, M.; Grozescu, I. Optical Properties of $ZnAl_2O_4$ Nanomaterials Obtained by the Hydrothermal Method. *Phys. Scr.* **2012**, *T149*, 014064. [CrossRef]
26. Ghribi, F.; Sehailia, M.; Aoudjit, L.; Touahra, F.; Zioui, D.; Boumechhour, A.; Halliche, D.; Bachari, K.; Benmaamar, Z. Solar-Light Promoted Photodegradation of Metronidazole over ZnO-$ZnAl_2O_4$ Heterojunction Derived from 2D-Layered Double Hydroxide Structure. *J. Photochem. Photobiol. A Chem.* **2020**, *397*, 112510. [CrossRef]
27. Menon, S.; Dhabekar, B.; Alagu Raja, E.; More, S.P.; Gundu Rao, T.K.; Kher, R.K. TSL, OSL and ESR Studies in $ZnAl_2O_4$:Tb Phosphor. *J. Lumin.* **2008**, *128*, 1673–1678. [CrossRef]
28. Sampath, S.K.; Cordaro, J.F. Optical Properties of Zinc Aluminate, Zinc Gallate, and Zinc Aluminogallate Spinels. *J. Am. Ceram. Soc.* **1998**, *81*, 649–654. [CrossRef]
29. Lou, Z.; Hao, J. Cathodoluminescence of Rare-Earth-Doped Zinc Aluminate Films. *Thin Solid Films* **2004**, *450*, 334–340. [CrossRef]
30. Farhadi, S.; Panahandehjoo, S. Spinel-Type Zinc Aluminate ($ZnAl_2O_4$) Nanoparticles Prepared by the Co-Precipitation Method: A Novel, Green and Recyclable Heterogeneous Catalyst for the Acetylation of Amines, Alcohols and Phenols under Solvent-Free Conditions. *Appl. Catal. A Gen.* **2010**, *382*, 293–302. [CrossRef]
31. Matveyeva, A.N.; Omarov, S.O.; Nashchekin, A.V.; Popkov, V.I.; Murzin, D.Y. Catalyst support based on ZnO-$ZnAl_2O_4$ nanocomposites with enhanced selectivity and coking resistance in isobutane dehudrogenation. *Dalton Trans.* **2022**, *51*, 12213. [CrossRef]
32. Liu, L.; Lin, Y.; Hu, Y.; Lin, Z.; Lin, S.; Du, M.; Zhang, L.; Zhang, X.; Lin, J.; Zhang, Z.; et al. $ZnAl_2O_4$ Spinel-Supported $PdZn_\beta$ Catalyst with Parts per Million Pd for Methanol Steam Reforming. *ACS Catal.* **2022**, *12*, 2714–2721. [CrossRef]
33. Song, L.; Wang, H.; Wang, S.; Qu, Z. Dual-site activation of H_2 over Cu/$ZnAl_2O_4$ boosting CO_2 hydrogenation to methanol. *Appl. Catal. B.* **2023**, *322*, 122137. [CrossRef]
34. Moustafa, M.G.; Sanad, M.M.S. Green fabrication of $ZnAl_2O_4$-coated $LiFePO_4$ nanoparticles for enhanced electrochemical performance in Li-ion batteries. *J. Alloy. Compd.* **2022**, *903*, 163910. [CrossRef]
35. Rojas-Hernandez, R.E.; Rubio-Marcos, F.; Romet, I.; del Campo, A.; Gorni, G.; Hussainova, I.; Fernandez, J.F.; Nagirnyi, V. Deep-Ultraviolet Emitter: Rare-Earth-Free $ZnAl_2O_4$ Nanofibers via a Simple Wet Chemical Route. *Inorg. Chem.* **2022**, *61*, 11886–11896. [CrossRef]
36. Gouadria, S.; Abudllah, M.; Ahmad, Z.; John, P.; Nisa, M.U.; Manzoor, S.; Aman, S.; Ashiq, M.N.; Ghori, M.I. Development of bifunctional Mo doped $ZnAl_2O_4$ spinel nanorods array directly grown on carbon fiber for supercapacitor and OER application. *Ceram. Int.* **2023**, *49*, 4281–4289. [CrossRef]
37. Sankaranarayanan, R.; Shailajha, S.; Seema, S.; Mubina, M.S.K. Enhanced Magneto-Electric Properties of $ZnAl_2O_4$@$NiFe_2O_4$ Nanocomposites in Magnetic Sensor Applications. *J. Supercond. Nov. Magn.* **2023**, *36*, 693–709. [CrossRef]
38. Maltanava, H.; Poznyak, S.; Ovodok, E.; Ivanovskaya, M.; Maia, F.; Kudlash, A.; Scharnagl, N.; Tedim, J. Synthesis of ZnO Mesoporous Powders and Their Application in Dye Photodegradation. *Mater. Today Proc.* **2018**, *5*, 17414–17421. [CrossRef]
39. Byeon, K.J.; Cho, J.Y.; Jo, H.B.; Lee, H. Fabrication of High-Brightness GaN-Based Light-Emitting Diodes via Thermal Nanoimprinting of ZnO-Nanoparticle-Dispersed Resin. *Appl. Surf. Sci.* **2015**, *346*, 354–360. [CrossRef]
40. Battiston, S.; Rigo, C.; Da Cruz Severo, E.; Mazutti, M.A.; Kuhn, R.C.; Gündel, A.; Foletto, E.L. Synthesis of Zinc Aluminate ($ZnAl_2O_4$) Spinel and Its Application as Photocatalyst. *Mater. Res.* **2014**, *17*, 734–738. [CrossRef]
41. Nasr, M.; Viter, R.; Eid, C.; Warmont, F.; Habchi, R.; Miele, P.; Bechelany, M. Synthesis of Novel ZnO/$ZnAl_2O_4$ Multi Co-Centric Nanotubes and Their Long-Term Stability in Photocatalytic Application. *RSC Adv.* **2016**, *6*, 103692–103699. [CrossRef]
42. Moon, S.; Jeong, Y. Generation Mechanism of Microdischarges during Plasma Electrolytic Oxidation of Al in Aqueous Solutions. *Corros. Sci.* **2009**, *51*, 1506–1512. [CrossRef]
43. Guo, H.F.; An, M.Z. Growth of Ceramic Coatings on AZ91D Magnesium Alloys by Micro-Arc Oxidation in Aluminate-Fluoride Solutions and Evaluation of Corrosion Resistance. *Appl. Surf. Sci.* **2005**, *246*, 229–238. [CrossRef]
44. Mécuson, F.; Czerwiec, T.; Belmonte, T.; Dujardin, L.; Viola, A.; Henrion, G. Diagnostics of an Electrolytic Microarc Process for Aluminium Alloy Oxidation. *Surf. Coat. Technol.* **2005**, *200*, 804–808. [CrossRef]

45. Prieditis, G.; Feldbach, E.; Kudryavtseva, I.; Popov, A.I.; Shablonin, E.; Lushchik, A. Luminescence Characteristics of Magnesium Aluminate Spinel Crystals of Different Stoichiometry. In *IOP Conference Series: Materials Science and Engineering*; IOP Publishing Ltd.: Bristol, UK, 2019; Volume 503, p. 012021. [CrossRef]
46. Sun, X.; Jiang, Z.; Yao, Z.; Zhang, X. The Effects of Anodic and Cathodic Processes on the Characteristics of Ceramic Coatings Formed on Titanium Alloy through the MAO Coating Technology. *Appl. Surf. Sci.* **2005**, *252*, 441–447. [CrossRef]
47. Kubelka, P. New Contributions to the Optics of Intensely Light-Scattering Materials. *J. Opt. Soc. Am.* **1948**, *38*, 448–457. [CrossRef] [PubMed]
48. Brik, M.G.; Srivastava, A.M.; Popov, A.I. A Few Common Misconceptions in the Interpretation of Experimental Spectroscopic Data. *Opt. Mater.* **2022**, *127*, 112276. [CrossRef]
49. Srikant, V.; Clarke, D.R. On the Optical Band Gap of Zinc Oxide. *J. Appl. Phys.* **1998**, *83*, 5447–5451. [CrossRef]
50. Arbi, M.; Benramdane, N.; Kebbab, Z.; Miloua, R.; Chiker, F.; Khenata, R. First Principles Calculations of Structural, Electronic and Optical Properties of Zinc Aluminum Oxide. *Mater. Sci. Semicond. Process.* **2012**, *15*, 301–307. [CrossRef]
51. Rafla-Yuan, H.; Cordaro, J.F. Optical Reflectance of Aluminum-Doped Zinc Oxide Powders. *J. Appl. Phys.* **1991**, *69*, 959–964. [CrossRef]
52. Ragupathi, C.; John Kennedy, L.; Judith Vijaya, J. A New Approach: Synthesis, Characterization and Optical Studies of Nano-Zinc Aluminate. *Adv. Powder Technol.* **2014**, *25*, 267–273. [CrossRef]
53. Sampath, S.K.; Kanhere, D.G.; Pandey, R. Electronic Structure of Spinel Oxides: Zinc Aluminate and Zinc Gallate. *J. Phys. Condens. Matter* **1999**, *11*, 3635–3644. [CrossRef]
54. Mathur, S.; Veith, M.; Haas, M.; Shen, H.; Lecerf, N.; Huch, V.; Hüfner, S.; Haberkorn, R.; Beck, H.P.; Jilavi, M. Single-Source Sol-Gel Synthesis of Nanocrystalline $ZnAl_2O_4$: Structural and Optical Properties. *J. Am. Ceram. Soc.* **2001**, *84*, 1921–1928. [CrossRef]
55. Stojadinović, S.; Jovović, J.; Petković, M.; Vasilić, R.; Konjević, N. Spectroscopic and Real-Time Imaging Investigation of Tantalum Plasma Electrolytic Oxidation (PEO). *Surf. Coat. Technol.* **2011**, *205*, 5406–5413. [CrossRef]
56. Hussein, R.O.; Nie, X.; Northwood, D.O.; Yerokhin, A.; Matthews, A. Spectroscopic Study of Electrolytic Plasma and Discharging Behaviour during the Plasma Electrolytic Oxidation (PEO) Process. *J. Phys. D Appl. Phys.* **2010**, *43*, 105203. [CrossRef]
57. Dunleavy, C.S.; Golosnoy, I.O.; Curran, J.A.; Clyne, T.W. Characterisation of Discharge Events during Plasma Electrolytic Oxidation. *Surf. Coat. Technol.* **2009**, *203*, 3410–3419. [CrossRef]
58. Sharma, D.K.; Shukla, S.; Sharma, K.K.; Kumar, V. A Review on ZnO: Fundamental Properties and Applications. *Mater. Today Proc.* **2022**, *49*, 3028–3035. [CrossRef]
59. Ayoub, I.; Kumar, V.; Abolhassani, R.; Sehgal, R.; Sharma, V.; Sehgal, R.; Swart, H.C.; Mishra, Y.K. Advances in ZnO: Manipulation of Defects for Enhancing Their Technological Potentials. *Nanotechnol. Rev.* **2022**, *11*, 575–619. [CrossRef]
60. Du, B.; Zhang, M.; Ye, J.; Wang, D.; Han, J.; Zhang, T. Novel Au Nanoparticle-Modified ZnO Nanorod Arrays for Enhanced Photoluminescence-Based Optical Sensing of Oxygen. *Sensors* **2023**, *23*, 2886. [CrossRef]
61. Jiang, T.T.; Du, B.S.; Zhang, H.; Yu, D.F.; Sun, L.; Zhao, G.Y.; Yang, C.H.; Sun, Y.; Yu, M.; Ashfold, M.N.R. High-performance photoluminescence-based oxygen sensing with Pr-modified ZnO nanofibers. *Appl. Surf. Sci.* **2019**, *483*, 922–928. [CrossRef]
62. da Silva, A.A.; Gonçalves, A.S.; Davolos, M.R.; Santagneli, S.H. Al^{3+} environments in nanostructured $ZnAl_2O_4$ and their effects on the luminescence properties. *J. Nanosci. Nanotechnol.* **2008**, *8*, 5690–5695. [CrossRef]
63. Zeng, H.; Duan, G.; Li, Y.; Yang, S.; Xu, X.; Cai, W. Blue Luminescence of ZnO Nanoparticles Based on Non-Equilibrium Processes: Defect Origins and Emission Controls. *Adv. Funct. Mater.* **2010**, *20*, 561–572. [CrossRef]
64. Vanheusden, K.; Warren, W.L.; Seager, C.H.; Tallant, D.R.; Voigt, J.A.; Gnade, B.E. Mechanisms behind Green Photoluminescence in ZnO Phosphor Powders. *J. Appl. Phys.* **1996**, *79*, 7983–7990. [CrossRef]
65. Greene, L.E.; Law, M.; Goldberger, J.; Kim, F.; Johnson, J.C.; Zhang, Y.; Saykally, R.J.; Yang, P. Low-Temperature Wafer-Scale Production of ZnO Nanowire Arrays. *Angew. Chem.—Int. Ed.* **2003**, *42*, 3031–3034. [CrossRef] [PubMed]
66. Van Dijken, A.; Meulenkamp, E.A.; Vanmaekelbergh, D.; Meijerink, A. Luminescence of Nanocrystalline ZnO Particles: The Mechanism of the Ultraviolet and Visible Emission. *J. Lumin.* **2000**, *87*, 454–456. [CrossRef]
67. Studenikin, S.A.; Golego, N.; Cocivera, M. Fabrication of Green and Orange Photoluminescent, Undoped ZnO Films Using Spray Pyrolysis. *J. Appl. Phys.* **1998**, *84*, 2287–2294. [CrossRef]
68. Sun, G.; Sun, G.; Zhong, M.; Wang, S.; Zu, X.; Xiang, X. Coordination Mechanism, Characterization, and Photoluminescence Properties of Spinel $ZnAl_2O_4$ Nanoparticles Prepared by a Modified Polyacrylamide Gel Route. *Russ. J. Phys. Chem. A* **2016**, *90*, 691–699. [CrossRef]

MDPI AG
Grosspeteranlage 5
4052 Basel
Switzerland
Tel.: +41 61 683 77 34

Coatings Editorial Office
E-mail: coatings@mdpi.com
www.mdpi.com/journal/coatings

Academic Open
Access Publishing

mdpi.com

ISBN 978-3-7258-2032-0